



HAL
open science

Competition between global and local instabilities in the failure of aeronautical structures

Moubine Al Kotob

► **To cite this version:**

Moubine Al Kotob. Competition between global and local instabilities in the failure of aeronautical structures. Materials. Université Paris sciences et lettres, 2019. English. NNT : 2019PSLEM002 . tel-02386956

HAL Id: tel-02386956

<https://pastel.hal.science/tel-02386956>

Submitted on 29 Nov 2019

HAL is a multi-disciplinary open access archive for the deposit and dissemination of scientific research documents, whether they are published or not. The documents may come from teaching and research institutions in France or abroad, or from public or private research centers.

L'archive ouverte pluridisciplinaire **HAL**, est destinée au dépôt et à la diffusion de documents scientifiques de niveau recherche, publiés ou non, émanant des établissements d'enseignement et de recherche français ou étrangers, des laboratoires publics ou privés.

THÈSE DE DOCTORAT
DE L'UNIVERSITÉ PSL

Préparée à MINES ParisTech

**Competition between global and local instabilities
in the failure of aeronautical structures**

**Compétition entre instabilités globales et locales
lors de la ruine de structures aéronautiques**

Soutenue par

Moubine AL KOTOB

Le 14 janvier 2019

École doctorale n°621

**Ingénierie des Systèmes,
Matériaux, Mécanique,
Énergétique**

Spécialité

Mécanique

Composition du jury :

René de Borst University of Sheffield	<i>Président</i>
Ahmed Benallal ENS Cachan	<i>Rapporteur</i>
Henryk Petryk Polish Academy of Sciences	<i>Rapporteur</i>
Corrado Maurini Sorbonne Université	<i>Examineur</i>
Christelle Combescure Université Paris Est	<i>Examineur</i>
Tonya Rose Safran	<i>Examineur</i>
Samuel Forest Mines ParisTech CNRS	<i>Directeur de thèse</i>
Matthieu Mazière Mines ParisTech	<i>Co-directeur de thèse</i>

*"Tu ne m'aimeras jamais autant que je t'aime mon enfant :
toi, tu m'aimes et tu vas faire ta vie ;
moi, je t'aime et c'est toi ma vie."
Mon père*

Remerciements Acknowledgements شكر وتقدير

Les remerciements ... La section du manuscrit la plus stressante à écrire. Stressante parce que c'est bien là que je ne veux oublier de citer aucune de ces personnes qui m'ont soutenu, supporté, écouté, motivé, chéri, fait rire, inspiré et encouragé dans mon parcours. Alors ça risque d'être long, mais j'ai finalement rarement eu l'occasion de vous remercier.

والداي العزيزان ... تقف الكلمات عاجزة أمام ما أحمله من تقدير لكما، فأنتما سر النجاح والتفوق. فكلمة "شكرا" تبدو بسيطة أمام كل ما في قلبي.

أشكركم على تربيتي وعلى إمساك يدي عندما كنت أتعثر، أشكركم على كل ما فعلتماه لأجلي من تعليمٍ لأعظم المسائل، وإرشادٍ إلى أفضل طريق، وحملٍ وإلباسٍ وسهرٍ وتنظيفٍ وعقابٍ ومحبةٍ وتشجيعٍ... أشكركم على ما علمتماه لنا من أهمية المحبة بين الإخوة وأي شكرٍ يستطيع أن يقابل التضحية والصبر اللذان بذلتماهما لنا أشكركم أيضا على كل ما لم أذكره في سطوري وعلى الأشياء التي فعلتموها ولكنها خفيت عني.

أمي ... تمتلكين حدسا قويا، لن أصل إليه مهما فعلت. أشكرك لأنك صبرت معي ورفعت لي رأسي كي أنظر بعيدا بينما كنت أحنيه
أمي ... أشكرك على تشجيعي لأخذ أعلى الشهادات عندما كنت مترددا
أمي ... أشكرك على تنوير طريقي كلما ضعف ضوءها سامحيني دوما على تقصيري

أمي، أمي، أمي ... ثم أبي

أبي ... تتسابق العبارات ويتزاحم الكلام لشكرك، أشكرك على شغفك الذي نقلته لنا وعلى تحفيزي لفعل الأفضل دائما وعلى حياتك التي ضحيت بها لأجلنا وعلى جهودك الكبيرة في مختلف الأوقات.

خالتي حليلة ... أنت بمنزلة أمي الثانية، أشكرك على تلبية دعوتي، لقد كنت مصدرا للطمأنينة عندما قدمت أطروحتي. وأخيرا أشكر خالي وكل خالاتي، وأتمنى لكم جميعا الأفضل في هذه الدنيا وفي الآخرة.

Évidemment, je ne peux continuer qu'en remerciant Samuel et Matthieu mes co-directeurs de thèse à l'école des Mines, ainsi que Christelle et Tonya mes encadrantes à Safran Tech pour leur patience pendant nos discussions enflammées, leur bienveillance lorsque je proposais une idée et leur disponibilité malgré un emploi du temps très chargé. Samuel, je t'avoue qu'il était parfois douloureux de voir qu'il te fallait un rien de temps pour comprendre une idée que j'avais mis trois semaines à décortiquer, ce qui n'a pas manqué de m'inspirer. Nos discussions à la première heure sur les lois en grandes déformations vont me manquer ! Matthieu, j'ai pu profiter de ta pédagogie, ton impressionnant recul scientifique et tes encouragements dans les moments difficiles. J'espère avoir un peu hérité de ta pédagogie, tu es de ceux qui expliquent si bien que ça semble évident. Christelle, je te remercie pour ton enthousiasme dans nos échanges et pour m'avoir appris à lier clarté et esthétique dans mes présentations (une pensée particulière pour cette courbe qui a changé huit fois de couleur, quatre fois d'épaisseur et trois fois de niveau de transparence). Encore merci d'avoir continué à te rendre disponible après ton départ à l'U-PEM. Tonya, I want to thank you for your involvement in my work, for proofreading my rough English again and again, and for supporting me in my most difficult days. I will always have a thought for you when I will see nice doooors. J'espère que le futur nous réserve encore de nombreux

projets ensemble. Ca peut sembler bateau, mais cette expérience n'aurait vraiment pas été la même sans vous.

Members of the jury, I would like to express my most sincere thanks to you for accepting to participate in my defence. Pr. Benallal and Pr. Petryk I want to particularly thank you for reviewing my manuscript and allowing me to defend. Also, our discussions in ESMC in Bologna were very helpful and a great source of inspiration for my last developments. Ahmed, c'était un vrai plaisir et ce n'est que partie remise ... on finira par être d'accord sur cette histoire de van Hove.

Une mention spéciale pour Hélène Dumontet et Yves Berthaud, vous m'avez admis dans le parcours CMI à l'UPMC alors que mon dossier était pour le moins atypique. Cette opportunité que vous m'avez donnée a été de loin un tournant des plus décisifs dans mon parcours et dans le développement de ma passion pour la mécanique. Notamment, c'est pendant ce parcours que j'ai eu l'occasion de faire un stage avec Arnaud et Corrado sur les instabilités de l'arrête d'un prisme, une expérience clé pour mes travaux de doctorat. C'est aussi là bas que j'ai pu échanger avec Djimedo que je remercie très très chaleureusement pour son écoute et ses conseils pour mon orientation vers une formation doctorale. Plus généralement, un grand merci à tous les enseignants de l'UPMC pour leur implication dans l'enseignements.

Dans le cadre de mes travaux j'ai eu la chance d'échanger avec de nombreux intervenants du groupe Safran. A Safran Tech, Nicolas et Alexandre, je vous remercie très sincèrement pour le temps que vous m'avez accordé, pour parler de sciences entre autre. Vous avez joué un rôle très important dans mon épanouissement au CMH et avez su me soutenir dans des moments difficiles. Je remercie Arjen et chaque membre de ZeTeam pour l'accueil et les bons moments passés ensemble (B. ce fut bref mais intense), et plus largement, les membres des autres équipes du pôle M&S dont Frédéric pour le temps que tu as réussi à libérer pour me parler parcours ou Zset, Augustin et Felipe pour vos coups de main avec les outils numériques. Enfin, cette expérience n'aurait pas été la même sans Mumu ... Merci Mumu !

Aussi, il est difficile de penser à ces trois dernières années sans parler des plénières que nous avons organisées avec SLS, SAE et SHE. René et Franck, je vous remercie d'avoir pris le temps de suivre mes travaux et d'avoir toujours alimenté mes réflexions. Nicolas et Martin, je vous remercie pour l'accueil à SLS et pour le temps que vous m'avez accordé pour la génération des abaqués, l'étude de la chape et pour nos nombreuses discussions qui ont été une grande source d'inspiration. Pierre-Antoine et Adriana, je vous remercie pour votre implication dans mes travaux et pour m'avoir fourni un cas d'étude pour mettre mes outils à l'épreuve.

Enfin, les derniers mais pas les moindres, merci à tous mes collègues doctorants (ou docteurs) Clément, Clément et Clément (je vous laisse deviner l'ordre), Adrien (je continuerai à t'envoyer des selfies pris de trop près), Camille pour ta bienveillance, Maxence le sage, Loic pour ton sourire et ta patate à toute épreuve, Florian (n'abandonne pas tes jeux de mots, je suis fan), Yannis pour ton humour subtile, Perle et Anthony pour les bons moments passés ensemble. Vous avez sublimé mon expérience à Safran Tech ! N'oubliez pas de me prévenir quand vous trouverez la sortie que je vienne à votre soutenance, parce que finalement, la thèse c'est un escape game avec un chrono de trois ans et une seule petite énigme pour trouver la clé. Je sais comme vous êtes bons à cet exercice, je ne m'inquiète pas pour vous.

Si on m'avait dit qu'un jour je me lèverais à 7h du matin pour aller prendre une navette pendant 45 minutes, occasionnellement l'attendre dix ou quinze minutes dans le froid et parfois subir une heure de bouchons, mais surtout que je le ferais avec grand plaisir, j'aurais eu du mal à y croire ... En fait je n'y aurais jamais cru. Sauf que ce qui manque dans cette histoire, c'est la

destination. J'ai probablement passé parmi mes plus délicieuses années au Centre des Matériaux. Évidemment, ce n'est pas pour la vue qu'on s'y plaît, mais pour les rencontres exceptionnelles que l'on y fait. Alors oui ça va être un peu long, mais comme vous êtes exceptionnels, difficile de vous remercier par paquets.

Jacques, je te remercie de m'avoir accordé de ton temps, même si je n'étais pas un de tes doctorants. Anne-Francoise, merci de m'avoir raccompagné en voiture les fois où je me faisais kidnapper par Samuel juste avant le départ de la navette, ces trajets en ta compagnie étaient toujours un plaisir. Georges, merci pour l'autographe et merci d'avoir pris le temps de répondre à mes questions quand je toquais à ta porte. Vlad, merci d'avoir été disponible et pour le reading club au début de la thèse. Cathy, merci pour l'accueil et ta bienveillance. Véronique et Claudine, merci pour votre aide et votre disponibilité pour toutes les démarches que je savais rarement faire seul. Didile! La meilleure documentaliste et ma psy dans les moments difficiles, merci Didile! Djamel, merci pour ton aide et ta bonne humeur.

Basile et Laurent¹, vous avez été des piliers pendant la deuxième moitié de la thèse, merci pour votre soutien et votre écoute. Raphael, mes papilles et moi même te remercie de nous avoir allimenté en bonne fourme de Mont Brison et pour ta bonne compagnie. Mariem et Lyliat², merci pour ces déjeuners qu'on a toujours eu du mal à organiser mais auquel j'étais toujours ravi de participer (j'attends encore de goûter votre plats légendaires, à moins que ce ne soit que des légendes?). D'ailleurs en parlant nourriture, Chiraz, je te remercie d'avance pour le bon couscous que tu m'as promis! Merci William, mon générateur aléatoire de ragots préféré, pour nos échanges et ton humour cinglant. Mes collègues de bureau, Fang (le rayon de soleil du Centre des Matériaux) merci pour ton sourire, ton énergie et ta bonne humeur à toute épreuve; Alexianne merci d'avoir tenu le bureau et de nous avoir empêché de le transformer en champ de bataille tout en maintenant la bonne ambiance; Andrei, you were my companion in this unique experience, let us talk about science or about the blinking light any time you like, thank you for always being around; Basava the wise, thank you for chuckling at my jokes when I was teasing Andrei, that was a great source of support. Et puis y'avait les gars du bureau d'en face : Nicolas, Juan et Jonathan merci d'avoir supporté mes sifflements impromptus. Kamel, notre pilote, le seul à être capable de déplacer un car de cinquantes personnes et de se faufiler comme si c'était un scooter, merci d'avoir levé le pied de l'accélérateur toutes les fois où je t'envoyais un message désespéré à 7H40 quand j'avais peur de rater la navette. Nikolay et Stéphane je tiens à vous remercier pour votre soutien durant la thèse et pour l'opportunité que m'avez offerte à la fin de mon contrat de thèse. Enfin, merci au personnel de l'atelier, même si je n'ai jamais touché une éprouvette pendant ma thèse, vous m'avez gentiment dépanné en bouchon d'oreille pour la rédaction ...

Valentin, merci de m'avoir prêté ton regard d'expert et d'avoir pris le temps de débattre avec moi de mes folles idées sur l'utilisation de la transformée de Fourier. Ce café place du Luxembourg m'a vraiment beaucoup apporté. Merci aussi d'avoir été mon binôme d'encadrement de TP, c'était un vrai plaisir!

Martin, j'ai tellement de raisons de te remercier que je ne sais pas par où commencer. Justement, quand on parle de commencer, qui aurait cru qu'on pouvait rencontrer l'ami d'une vie en recevant un pain au lait au Nutella en pleine figure? Alors 16 ans plus tard, je te remercie d'être encore là. Merci de m'avoir supporté, soutenu, encouragé, poussé à croire en mes idées et d'avoir fait semblant que ce que je disais avait du sens quand je te parlais d'instabilité. Merci de m'avoir supporté pendant deux ans de coloc, pour les rires, les films et les bonnes bouffes ...

1. Un jour, vous n'aurez peut-être plus besoin de vous y mettre à deux pour engager une joute verbale avec moi. Ne vous emballez pas, je ne suis pas encore sénile, ça n'arrivera pas de si tôt.

2. Directrice artistique de ce manuscrit.

Merci d'avoir été là dans les moments difficiles, de m'avoir réveillé les moments où moi même je ne réalisais pas que ça n'allait pas. Merci aussi à ta famille, Joette, Joe et Karine pour leur soutien dans ma scolarité. Sans eux je n'aurais probablement pas eu le même parcours. Enfin, merci pour les années à venir, parce que je n'ai aucun doute sur la longévité de notre amitié.

Enfin, ma famille, je vous remercie pour tout. Mon parcours en mécanique a probablement commencé avec papa tout petit, mais mon parcours en sciences a commencé avec toi Ahmad. Merci de t'être patiemment occupé de ton petit frère et de m'avoir appris à apprécier les mathématiques et la physique. Je n'oublierai pas ce jour où tu m'as expliqué l'optique, c'est sûrement là que tout a commencé. Oublie pas, ça fait quinze ans que tu m'as promis une randoroller ! Nour, merci d'avoir gardé un oeil sur moi, de m'avoir encouragé et de m'avoir laissé te regarder jouer quand on était petit (mais bon si tu m'avais lâché la manette avant que maman rentre ça aurait été bien aussi !). Merci de m'avoir aidé à réparer mon vélo alors que c'est quand même moi le mécanicien qui devrait savoir faire. On ne peut pas tous être de talentueux autodidactes. Hoda, il n'y a pas à se poser de question, Gauss, Euler et Cauchy n'ont qu'à bien se tenir ... tu es de loin ma mathématicienne et grande sœur préférée (à part que dans ton arithmétique $3 \times 4 = 11$) ! Tu as beau dire que tu comprenais pas toujours ce que je racontais pendant ces trois ans, il n'en reste pas moins que tes questions étaient toujours pertinentes et ne manquaient pas de me faire avancer. Merci de m'avoir écouté et supporté pendant ma rédaction. Marwa et Karine, merci pour votre bonne compagnie, votre énergie et pour mes nièces Layane Bahijah et Sarah et mon neveu Adam \Leftarrow je laisse de la place pour les suivants ... sans pression. Ali, merci pour le temps que tu m'as accordé quand je me posais des questions sur mon parcours et mes candidatures. Ton écoute et tes conseils m'ont été très précieux. Wafae, merci d'être venue à ma soutenance, arrivée avant les autres, ta présence m'a réconforté.

Je souhaite aussi remercier le personnel de l'école et de la cafétéria pour leur accueil et pour leur bonne humeur à toute épreuve. Une petite pensée pour la L017, cette salle au rez de jardin qui m'a accueilli pour une grande partie de la rédaction de ce manuscrit. Évidemment, je ne peux parler de cet endroit sans avoir une pensée particulière pour Michel Amestoy avec qui j'ai eu la chance d'y avoir quelques échanges.

Enfin, je remercie aussi le personnel du restaurant Istanbul Kehribar qui nous a toujours très bien accueilli lorsque ma seule chance de voir un de mes encadrants était de l'appâter avec leurs magnifiques brochettes.

Contents

1	Introduction	15
1.1	Designing methods	16
1.2	Failure of an elastoplastic structure	17
1.3	Finite deformation framework	19
1.4	Imperfections and boundary conditions	20
1.5	Aim of this work	21
1.6	Outline	22
2	Finite Deformation Framework	29
2.1	General framework	30
2.1.1	Equilibrium	30
2.1.2	Boundary conditions	31
2.1.3	Rate problem and local tangent operator	32
2.2	Hypo-elastoplastic formulations	32
2.2.1	Objectivity	33
2.2.2	Elastoplastic behaviour	36
2.2.3	Tangent operators and rate potential	37
2.2.4	Summary	40
2.3	FEM formulation of finite deformation problems	41
2.3.1	Weak formulations	42
2.3.2	Discretization	43
2.3.3	Numerical global problem	44
2.3.4	Application of Dirichlet boundary conditions	46
3	Global instabilities	51
3.1	Uniqueness and stability in elastoplastic problems: Hill 1958	53
3.1.1	Uniqueness criterion for the rate boundary value problem	53
3.1.2	Global stability criterion	54
3.1.3	Numerical method: Loss of stability in a FEM framework	55
3.1.4	Eigenvalue problem on the global tangent operator	55
3.1.5	Implementation in <code>Zset</code>	56
3.1.6	Necking	58
3.2	Structural applications	61
3.2.1	Necking in a tensile sample	61
3.2.2	Buckling of a tube loaded in torsion	66
3.2.3	Thin plate loaded in tension: sensitivity to DBCs	69
3.3	Conclusions	73

4	Material Instabilities	77
4.1	Elastoplastic localization bands: Rice 1976	79
4.1.1	Loss of ellipticity in a finite deformation framework	79
4.1.2	Loss of ellipticity and loss of strong ellipticity in an infinite homogeneous domain	84
4.2	Localization in structures	85
4.2.1	Ellipticity and local uniqueness: van Hove's rate boundary value problem	86
4.2.2	A minor extension to van Hove's theorem and loss of uniqueness	87
4.2.3	Discussion	88
4.3	Numerical methods for detection of loss of ellipticity	89
4.3.1	Literature review	89
4.3.2	Minimization problem	91
4.3.3	Algorithm	92
4.3.4	Initialization and general scheme	96
4.3.5	Validation	97
4.3.6	Performance and robustness	99
4.4	Structural applications	102
4.4.1	Loss of uniqueness and loss of ellipticity in a FEM framework: homogeneous shear in a square	102
4.4.2	Application to a simple tube loaded in torsion	109
4.4.3	Application to a full torsion sample	118
4.5	Conclusions	122
5	Weakened stability analysis	127
5.1	Influence of the type of boundary conditions	129
5.1.1	Euler buckling: Sensitivity to BCs	129
5.1.2	External stiffness	132
5.2	Weakened stability analysis	133
5.2.1	Weakened stability criterion	134
5.2.2	Hierarchy and interpretation of instabilities	135
5.2.3	Numerical method	136
5.2.4	Validation with Euler buckling	138
5.3	Applications of the weakened stability criterion	140
5.3.1	Application to a tube loaded in torsion	140
5.3.2	Loss of ellipticity and loss of uniqueness in a homogeneous media in FEM	144
5.3.3	Competition between loss of ellipticity and global loss of uniqueness in a discretized problem: tube loaded in torsion	159
5.4	Conclusions	163
6	Structural Applications	167
6.1	Localization and buckling in ML340 tubes loaded in torsion	169
6.1.1	Numerical problem	173
6.1.2	Buckling analysis	173
6.1.3	Localization analysis	176
6.1.4	Consequences of linear hardening	179
6.1.5	Weakened stability analysis	179
6.2	High yield vs slow saturating hardening	182
6.2.1	Materials and weakened problems	182
6.2.2	Influence of the finite deformation framework: comparison with reference curves	184

6.2.3	Comparison between materials	184
6.2.4	Weakened stability analysis	185
6.2.5	Discussion about design methods	193
6.3	Weakened instability analysis for contact	197
6.3.1	Mechanical problem	197
6.3.2	Proposed approach for instabilities with contact	198
6.3.3	Numerical results	199
6.3.4	Discussions and prospects	204
7	Conclusions – Prospects	207
7.1	Main results and tools	208
7.1.1	Incremental and rate boundary value problems	208
7.1.2	Discretized Hill’s loss of uniqueness criterion	208
7.1.3	Localization and loss of ellipticity	209
7.1.4	Modeling assumptions and weakened stability analysis	209
7.1.5	Structural applications	210
7.1.6	Numerical developments	211
7.2	Prospects	212
7.2.1	Stability of sub-part	212
7.2.2	Curvature and corners on the yield surfaces and non-associative flows	213
7.2.3	Localization in the sense of Rice in heterogeneous media	213
7.2.4	Reduced order modeling	213
8	Appendix	217
8.1	Additive Lagrangian formulations	218
8.1.1	Seth-Hill strain measures	218
8.1.2	Mesures des contraintes et déformations	218
8.1.3	Formulation thermodynamique	219
8.1.4	Tangent operator	220
8.1.5	Summary	221
8.2	Multiplicative decomposition formulations	222
8.2.1	Gradient de la transformation	222
8.2.2	Formulation thermodynamique	222
8.2.3	Opérateur tangent élastoplastique (configuration locale relâchée)	224
8.2.4	Opérateur tangent	226
8.3	Loss of uniqueness in elastoplastic solids: Rodney Hill 1958	229
8.3.1	Contraintes, déformations et équilibre	229
8.3.2	Loi de comportement en référentiel local objectif	231
8.3.3	Identités remarquables	232
8.3.4	Critère d’unicité	233
8.4	Dynamic discontinuity and acoustic tensor	236
8.5	Loss of ellipticity specified to small deformation	238
8.5.1	General analysis:	238
8.5.2	Elastic unloading/plastic loading condition	241
8.6	Loss of ellipticity: analytical simple cases (small deformation)	243
8.6.1	Simple shear	243
8.6.2	Simple tension (or 3D case)	244
8.6.3	Tension in plane strain	245
8.6.4	Plane stress bidimensional case	246
8.6.5	Application of numerical algo	247

8.7	Design curves summary	257
8.7.1	Material properties:	257
8.7.2	Comparison of localization curves	258
8.7.3	Comparison of reference curves with instability analysis	261
8.7.4	Material comparison : Design curves	271
8.7.5	Weakened stability analysis comparison	274

Notations

“Les mathématiques sont un jeu que l’on exerce selon des règles simples en manipulant des symboles ou des concepts qui n’ont en soi, aucune importance particulière.”
David Hilbert

Tensors

<i>Description</i>	<i>Notation</i>
Scalar (order 0)	a
Vector (order 1)	$\underline{\mathbf{a}}$
Second order	$\underline{\underline{\mathbf{A}}}$
Third order	$\underline{\underline{\underline{\mathbf{A}}}}$
Fourth order	$\underline{\underline{\underline{\underline{\mathbf{A}}}}}$
Transposed second order tensor	$\underline{\underline{\mathbf{A}}}^T$
Right transposed third order tensor	$(\underline{\underline{\underline{\mathbf{A}}}}^T)_{ijk} = A_{ikj}$
Left transposed third order tensor	$({}^T\underline{\underline{\underline{\mathbf{A}}}})_{ijk} = A_{jik}$
Inverse second order	$\underline{\underline{\mathbf{A}}}^{-1}$
Symmetric part	$\underline{\underline{\mathbf{A}}}^{sy} = \frac{1}{2} (\underline{\underline{\mathbf{A}}} + \underline{\underline{\mathbf{A}}}^T)$
Skew symmetric part	$\underline{\underline{\mathbf{A}}}^{sk} = \frac{1}{2} (\underline{\underline{\mathbf{A}}} - \underline{\underline{\mathbf{A}}}^T)$
Major symmetry for a fourth order tensor	$A_{ijkl} = A_{klij}$
Minor symmetries for a fourth order tensor	$A_{ijkl} = A_{jikl} = A_{ijlk}$

Contractions

Compact notation

$$a = \underline{\mathbf{x}} \cdot \underline{\mathbf{y}}$$

$$\underline{\mathbf{a}} = \underline{\underline{\mathbf{X}}} \cdot \underline{\underline{\mathbf{y}}}$$

$$\underline{\underline{\mathbf{A}}} = \underline{\underline{\mathbf{X}}} \underline{\underline{\mathbf{Y}}}$$

$$a = \underline{\underline{\mathbf{X}}} : \underline{\underline{\mathbf{Y}}}$$

$$\underline{\underline{\mathbf{A}}} = \underline{\underline{\mathbf{X}}} : \underline{\underline{\mathbf{Y}}}$$

$$\underline{\underline{\mathbf{A}}} = \underline{\underline{\mathbf{x}}} \odot \underline{\underline{\mathbf{Y}}}$$

$$\underline{\underline{\mathbf{A}}} = \underline{\underline{\mathbf{x}}} \odot \underline{\underline{\mathbf{Y}}} \cdot \underline{\underline{\mathbf{z}}}$$

$$\underline{\underline{\mathbf{A}}} = \underline{\underline{\mathbf{X}}} : \underline{\underline{\mathbf{Y}}}$$

$$\underline{\underline{\mathbf{A}}} = \underline{\underline{\mathbf{X}}} : \underline{\underline{\mathbf{Y}}}$$

Index notation (Euclidean tensors)

$$a = x_i y_i$$

$$a_i = X_{ij} y_j$$

$$A_{ij} = X_{ik} Y_{kj}$$

$$a = X_{ij} Y_{ij}$$

$$A_{ij} = X_{ijkl} Y_{kl}$$

$$A_{ijk} = x_l Y_{iljk}$$

$$A_{ij} = x_k Y_{ikjl} z_l$$

$$A_{ij} = X_{ikl} Y_{klj}$$

$$A_{ijkl} = X_{ijrs} Y_{rskl}$$

Dyadic products

Compact notation

$$\underline{\underline{\mathbf{A}}} = \underline{\underline{\mathbf{x}}} \otimes \underline{\underline{\mathbf{y}}}$$

$$\underline{\underline{\mathbf{A}}} = \underline{\underline{\mathbf{X}}} \otimes \underline{\underline{\mathbf{Y}}}$$

$$\underline{\underline{\mathbf{A}}} = \underline{\underline{\mathbf{X}}} \boxtimes \underline{\underline{\mathbf{Y}}}$$

$$\underline{\underline{\mathbf{A}}} = \underline{\underline{\mathbf{X}}} \boxplus \underline{\underline{\mathbf{Y}}}$$

Index notation (Euclidean tensors)

$$A_{ij} = x_i y_j$$

$$A_{ijkl} = X_{ij} Y_{kl}$$

$$A_{ijkl} = X_{ik} Y_{jl}$$

$$A_{ijkl} = X_{il} Y_{jk}$$

Matrices

Compact notation

$$\{\mathbf{a}\}$$

$$\{\underline{\mathbf{a}}\}$$

$$\{\underline{\underline{\mathbf{A}}}\}$$

$$[\mathbf{A}]$$

Index notation

Column vector of a_i 's

Column vector of a_i 's ($\underline{\mathbf{a}}$ first order tensor)

Column vector of A_{ij} 's (11,22,33,12,23,31,21,32,13)

Rectangular matrix of A_{ij} 's

Identities

$$\underline{\underline{A}} \cdot \underline{\underline{b}} = \underline{\underline{b}} \cdot \underline{\underline{A}}^T \quad (0.1)$$

$$\underline{\underline{A}} \underline{\underline{C}} \underline{\underline{B}}^T = (\underline{\underline{A}} \boxtimes \underline{\underline{B}}) : \underline{\underline{C}} \quad (0.2)$$

$$\underline{\underline{A}} \underline{\underline{C}}^T \underline{\underline{B}}^T = (\underline{\underline{A}} \boxplus \underline{\underline{B}}) : \underline{\underline{C}} \quad (0.3)$$

$$(\underline{\underline{A}} \boxtimes \underline{\underline{B}}) : (\underline{\underline{C}} \boxtimes \underline{\underline{D}}) = (\underline{\underline{A}} \underline{\underline{C}}) \boxtimes (\underline{\underline{B}} \underline{\underline{D}}) \quad (0.4)$$

$$(\underline{\underline{A}} \boxplus \underline{\underline{B}}) : (\underline{\underline{C}} \boxplus \underline{\underline{D}}) = (\underline{\underline{A}} \underline{\underline{D}}) \boxtimes (\underline{\underline{B}} \underline{\underline{C}}) \quad (0.5)$$

$$(\underline{\underline{A}} \boxtimes \underline{\underline{B}}) : (\underline{\underline{C}} \boxplus \underline{\underline{D}}) = (\underline{\underline{A}} \underline{\underline{C}}) \boxplus (\underline{\underline{B}} \underline{\underline{D}}) \quad (0.6)$$

$$(\underline{\underline{A}} \boxplus \underline{\underline{B}}) : (\underline{\underline{C}} \boxtimes \underline{\underline{D}}) = (\underline{\underline{A}} \underline{\underline{D}}) \boxplus (\underline{\underline{B}} \underline{\underline{C}}) \quad (0.7)$$

$$(\underline{\underline{A}} \boxtimes \underline{\underline{B}})^{-1} = (\underline{\underline{A}}^{-1} \boxtimes \underline{\underline{B}}^{-1}) \quad (0.8)$$

$$(\underline{\underline{A}} \boxplus \underline{\underline{B}})^{-1} = (\underline{\underline{B}}^{-1} \boxtimes \underline{\underline{A}}^{-1}) \quad (0.9)$$

$$\underline{\underline{A}} = \underline{\underline{A}}^{sym} \Rightarrow \underline{\underline{A}} : \underline{\underline{B}} = \underline{\underline{A}} : \underline{\underline{B}}^{sym} \quad (0.10)$$

$$A_{ijkl} = A_{ijlk} \Rightarrow \underline{\underline{A}} : \underline{\underline{B}} = \underline{\underline{A}} : \underline{\underline{B}}^{sym} \quad (0.11)$$

Particular quantities

<i>Notation</i>	<i>Description</i>
t	Fictitious time
Ω_0	Material domain in initial configuration at $t = 0$
Ω	Material domain in actual configuration
$\partial\Omega$	Boundary of Ω
$\partial\Omega^T$ ou S^T	Boundary of Ω subject to external forces (Neumann)
$\partial\Omega^u$ ou S^u	Boundary of Ω subject to imposed displacements (Dirichlet)
$\partial\Omega^v$ ou S^v	Boundary of Ω subject to imposed velocities
$\underline{\underline{X}}$	Position of a material point in Ω_0
$\underline{\underline{x}}$	Position of a material point in Ω (initial $\underline{\underline{X}}$ in Ω_0)
$\underline{\underline{u}} = \underline{\underline{x}} - \underline{\underline{X}}$	Displacement field
$\underline{\underline{I}}$	Second order identity tensor
∇	Gradient operator with respect to reference configuration: $\underline{\underline{\nabla}} \underline{\underline{a}} = \frac{\partial a_i}{\partial J_j}$.
$\underline{\underline{F}} = \frac{\partial \underline{\underline{x}}}{\partial \underline{\underline{X}}}$	Deformation gradient tensor
$\underline{\underline{\dot{F}}} = \underline{\underline{\nabla}} \underline{\underline{\dot{u}}}$	Lagrangian velocity gradient tensor
$J = \det(\underline{\underline{F}})$	Jacobian of the deformation
$\underline{\underline{L}} = \underline{\underline{\dot{F}}} \underline{\underline{F}}^{-1}$	Eulerian velocity gradient tensor

$\underline{\underline{D}} = \underline{\underline{L}}^{sym}$	Strain-rate tensor
$\underline{\underline{\Omega}} = \underline{\underline{L}}^{skew}$	Spin tensor
$\underline{\underline{D}}^e$	Elastic strain rate tensor
$\underline{\underline{D}}^p = \underline{\underline{D}} - \underline{\underline{D}}^e$	Plastic strain rate tensor
$\hat{\underline{\underline{F}}}$	Updated Lagrangian deformation gradient: $\hat{\underline{\underline{F}}} = \underline{\underline{I}}$ and $\dot{\hat{\underline{\underline{F}}}} = \underline{\underline{L}}$
$\underline{\underline{\sigma}}$	Cauchy stress tensor
$\underline{\underline{\tau}} = J \underline{\underline{\sigma}}$	Kirchhoff stress tensor
$\hat{\underline{\underline{\tau}}} = \hat{J} \underline{\underline{\sigma}}$	Updated Lagrangian Kirchhoff stress tensor
$\underline{\underline{S}} = \underline{\underline{\tau}} \underline{\underline{F}}^{-T}$	Boussinesq stress tensor (First Piola Kirchhoff or transposed nominal stress tensor)
$\underline{\underline{\Pi}} = \underline{\underline{F}}^{-1} \underline{\underline{S}}$	Piola stress tensor (Second Piola Kirchhoff)
$\underline{\underline{C}} = \underline{\underline{F}}^T \underline{\underline{F}}$	Right Cauchy Green tensor
$\underline{\underline{E}} = \frac{1}{2}(\underline{\underline{C}} - \underline{\underline{I}})$	Green-Lagrange strain tensor
$\underline{\underline{F}}^e$	Elastic multiplicative part of strain gradient (multiplicative decomposition)
$J_e = \det(\underline{\underline{F}}^e)$	Elastic volume variation
$\underline{\underline{F}}^p$	plastic multiplicative part of strain gradient (multiplicative decomposition)
$\underline{\underline{M}} = \underline{\underline{F}}^{eT} \underline{\underline{\tau}} \underline{\underline{F}}^{e-T} = \underline{\underline{C}}^e \underline{\underline{\Pi}}^e$	Mandel stress tensor

Chapter 1

Introduction

*"Mets l'intention, et fais ce que tu peux."
Mon père*

Résumé : Les ingénieurs en aéronautique sont constamment mis au défi de réduire la consommation de carburant dans le but de réduire l'impact environnemental et le coût des vols. En parallèle, la conception aéronautique est soumise à de nombreuses réglementations ayant pour but d'assurer l'intégrité des avions durant le décollage, le vol et l'atterrissage, et de ce fait la sécurité des passagers et de l'équipage. Pour ce faire, les limites de la connaissance en mécanique des matériaux et des structures sont continuellement repoussées donnant naissance à de nouveaux outils mathématiques, de production et d'expérimentation.

Parmi les phénomènes mécaniques les plus extrêmes pour la tenue d'un composant mécanique, nous trouvons l'émergence d'instabilités globales, comme le flambement d'un arbre mécanique, ou locales, comme la localisation de la déformation plastique. Dans ces travaux nous souhaitons participer au défi ci-avant en proposant des méthodes mathématiques et des outils numériques pour la détection de ces phénomènes.

Plus précisément, nous proposons de revisiter le critère de perte d'unicité proposé dans [Hill, 1958] (instabilité globale) et le critère de perte d'ellipticité énoncé dans [Rice, 1976] (instabilité locale). Cette étude nous mènera alors à illustrer et interpréter les résultats de ces critères, à proposer de nouvelles méthodes numériques pour leur évaluation, ainsi qu'à proposer la formulation d'un nouveau critère dit "critère affaibli de stabilité" permettant d'avoir une première approche systématique de l'analyse de stabilité d'un composant dans un problème incluant une surface de contact.

1.1	Designing methods	16
1.2	Failure of an elastoplastic structure	17
1.3	Finite deformation framework	19
1.4	Imperfections and boundary conditions	20
1.5	Aim of this work	21
1.6	Outline	22

Aeronautical engineers are constantly challenged to provide lighter structures in order to reduce fuel consumption, and thus the environmental impact and flight costs. At the same time, the design of aeronautical structures is subjected to strict regulation rules aiming to ensure the integrity of the aircraft and the safety of the passengers. To address this challenge, the limits of structural and material mechanics are consistently explored which in turn leads to the development of new, mathematical, numerical, experimental and manufacturing tools.

1.1 Designing methods

“The application of methods such as Finite Element Method or engineering formulae to complex structures in modern aircraft is considered reliable only when validated by full scale tests (ground and/or flight tests). Experience relevant to the product in the utilisation of such methods should be considered.” [European Aviation Safety Agency, 2018].

Established in 2002, the European Aviation Safety Agency regulates the aviation industry in order to ensure the safe design of aircraft. For a structure to be certified, various strength requirements must be fulfilled: they may concern the limit loads (maximum loads expected during service) or the ultimate loads (limit loads multiplied by prescribed factors of safety) [European Aviation Safety Agency, 2018]. These load specifications have been set by European aeronautical experts on the basis of previous experience.

In order to comply with the requirements, engineers must use specified approaches depending on the part and material of interest. For instance, in the design of landing systems, only experimental certification is necessary for the wheels, while analytical justifications are also necessary for the landing shafts. In the first case, engineers can use any tool they trust in the design process, and only the final experimental certification tests confirm the reliability of the part. In the second case, the engineers must refer to analytical approaches trusted by the aeronautical community ¹.

Typically, analytical justifications are based on mathematical results derived in a continuum mechanics framework. For instance, in [Lee and Ades, 1957] the authors analyzed the ultimate loads of metallic tubes loaded in torsion using small strain finite rotation shell theory. However, due to the complexity of the mathematical framework, approximate (yet relatively accurate) solutions were used in order to compute the plastic torsional buckling strength of cylinders.

Even though these results were obtained sixty years ago, they are still the references used in the design of elastoplastic tubes loaded in torsion [Department of Defense, 1998, 2003]. Nonetheless, because of their complexity these analyses are usually restricted to basic geometries, relatively simple materials and monotonic loadings. Of course, in optimized designs, simple geometries are rare (see Figure 1.1). Therefore, the present work aims to bring this type of analysis a step further by evaluating the ultimate behavior of arbitrary elastoplastic structures in a finite deformation framework using the Finite Elements Method (FEM).

¹ [European Aviation Safety Agency, 2018]: “*Structural analysis may be used only if the structure conforms to that for which experience has shown this method to be reliable.*”

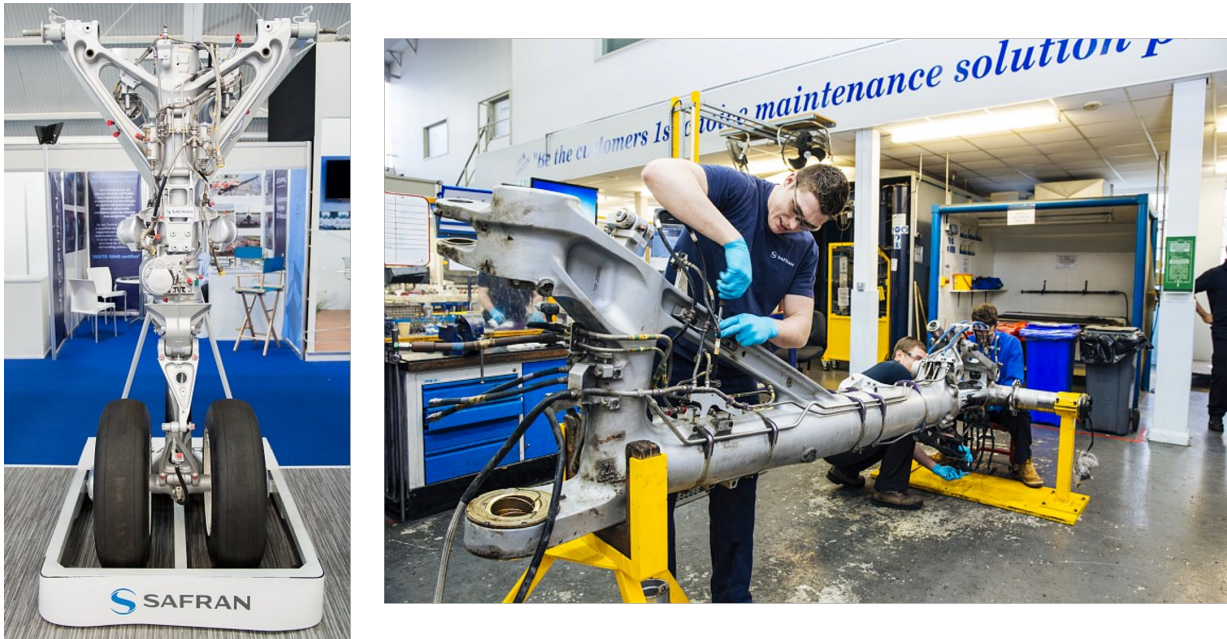


Figure 1.1: Pictures of a A320 landing system design by Safran Group (Safran Landing Systems).

1.2 Failure of an elastoplastic structure

In a broad sense, the failure of a structure is characterized by the initiation and propagation of cracks or by a sudden drop in its overall stiffness. The first case is not considered in the present work. It is generally studied as a consequence of a stress concentration (fracture mechanics) or as a material failure (coalescence of micro-voids and damage-like approaches²). For the second case two phenomena are generally distinguished: *strain localization*³ and *buckling*. The distinction between localization and buckling was also made by the authors in [Lee and Ades, 1957] (see Figures 1.2 and 1.3).

² In [Defaïsse et al., 2018] no micro-voids were observed and an incremental damage like parameter was defined in order to capture the initiation of material failure.

³ This includes diffused necking and shear band localization.

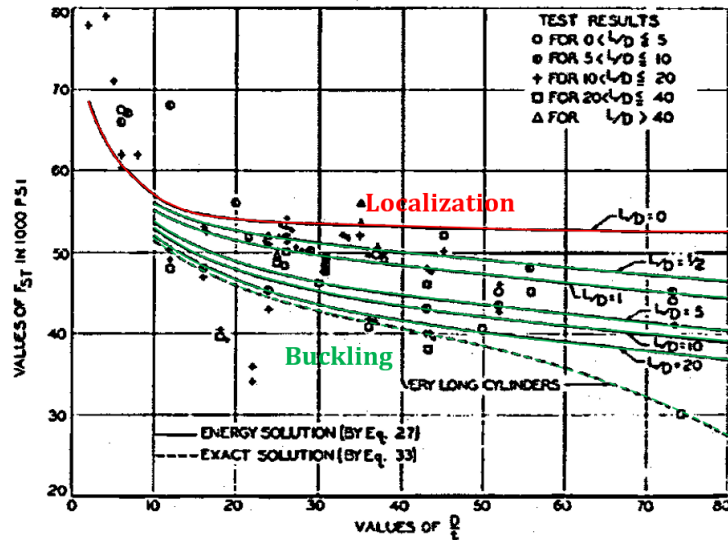


FIG. 11. Comparison of theory with experimental results—steel cylinders.

Figure 1.2: Design curves for tubes loaded in torsion in [Lee and Ades, 1957]. Two phenomena are distinguished: strain localization deduced from the ultimate engineering shear stress (in red), and buckling based on an energy minimization criterion (in green).

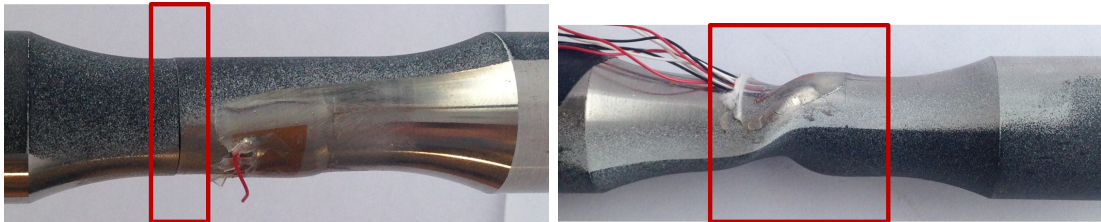


Figure 1.3: Experiments on steel tubes loaded in torsion (source: ONERA): on the left, emergence of a shear localization band in a thick tube: external diameter of 16 mm and thickness of 4 mm; on the right, buckling of a thin tube: external diameter of 16 mm and thickness of 1 mm.

Localization refers to many phenomena. The most well-known example is probably the emergence of necking in a bar loaded in tension (see Figure 1.4). This phenomenon has long been interpreted as a consequence of material heterogeneity. For the first time, in 1885, it was studied as a structural phenomenon by Considère: “*Nous n’avons entendu assigner à ce phénomène d’autre cause que le manque d’homogénéité des métaux qui, étant essentiellement variable, ne saurait expliquer un fait constant. Nous croyons en conséquence qu’il faut chercher ailleurs et que les faits se passent comme nous allons l’exposer.*”⁴ [Considère, 1885]. The author also states: “*à un certain moment qui correspond au début de la striction, le barreau est en équilibre instable.*”⁵. In further explanations, the author discusses a kind of competition

⁴ “There have not been any other cause given to this phenomenon but the heterogeneity of metals which, being essentially variable, can not explain a constant behavior. We therefore believe that the cause must be sought elsewhere and that the facts happen as we will expose them.”

⁵ “at a certain point that corresponds to the emergence of necking, the bar is in an unstable equilibrium state.”

between the geometrical variations and the material properties.

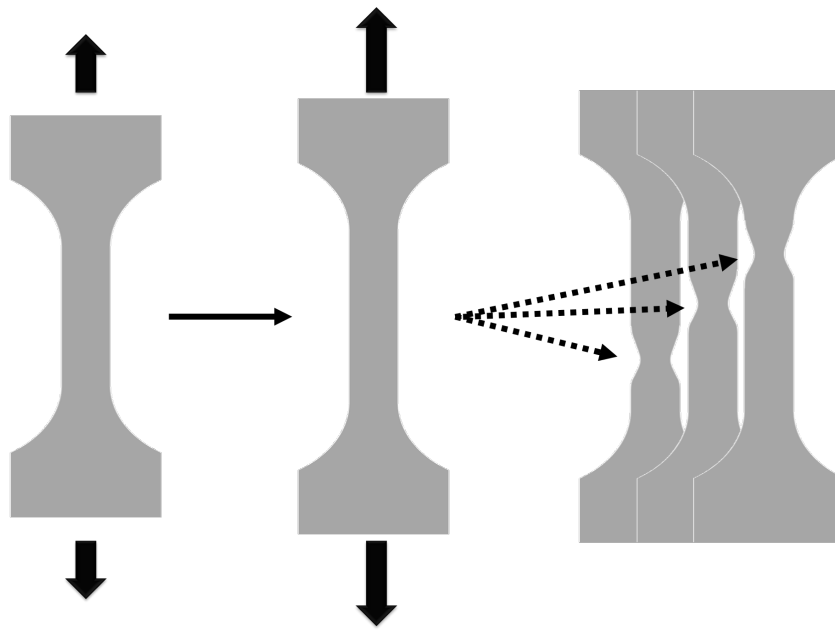


Figure 1.4: Schematic representation of the emergence of necking in a tensile experiment.

This notion of instability has been generalized and linked to the loss of uniqueness⁶ by [Hill, 1958] in the analysis of elastoplastic problems in a finite deformation framework. In [Mazière, 2007], a link has been established between the latter and Considère's necking criterion.

Finally, in [Rice, 1976] another founding criterion, known as the loss of ellipticity criterion, has been presented and linked to [Hill, 1958] in order to explain the emergence of arbitrarily thin shear bands as a consequence of the possible existence of jumps in strain rate. This criterion has been shown to be linked to the loss of uniqueness and regularity of the solution of the boundary value problem.

These pioneering references have been the source of numerous studies that led to classify elastoplastic instabilities into two major types:

- *Global instabilities* such as diffused necking and buckling, as in [Hill, 1958, Hutchinson, 1974, Petryk, 2000, Durand and Combescure, 1999, Nefussi and Combescure, 2002, Ibrahimbegovic, 2009, Abed-Meraim, 2009, de Borst et al., 2012, Bigoni, 2012, Asmolovski et al., 2015, Lestringant et al., 2017, Gardner, 2018];
- *Material instabilities* such as shear band localization, as in [Hill, 1952, Mandel, 1964, 1966, Rudnicki and Rice, 1975, Stören and Rice, 1975, Hutchinson and Tvergaard, 1981, Ortiz, 1987, Rice, 1976, Bigoni and Hueckel, 1991, Petryk, 1992, Pijaudier-Cabot and Benallal, 1993, Benallal and Comi, 1996, Doghri and Billardon, 1995, Petryk, 1997, Benallal et al., 2006, Lemaitre et al., 2009, Ryzhak, 1994, Thermann, 2000, d'Avila et al., 2016, Mota et al., 2016, Akparna et al., 2017]

1.3 Finite deformation framework

Already in the work of the famous mathematician and physicist Euler [Euler, 1759], the effects of geometrical changes were taken into account in the analysis of the buckling of a

⁶ Uniqueness of the solution to the rate boundary value problem.

beam loaded in compression. In other words, he found it necessary to distinguish initial and equilibrium configurations. Given that it was necessary for the study of the simplest instability case, it is essential for the present work. Therefore, the finite deformation framework is used for our analysis.

When working in such a framework, there are two main difficulties in addition to the complexity of the mathematical derivations: the formulation of the constitutive law, and the characterization of the material properties. The first has led to numerous studies, each one introducing its own notations, but none have managed to provide a unifying approach (see for instance [Truesdell and Toupin, 1960, Mandel, 1971, Halphen, 1975, Bigoni and Zaccaria, 1993, Meyers et al., 2000, Rubin and Nadler, 2016]). For the second, the challenge lies in the identification of the post-necking behavior (see Figure 1.5).

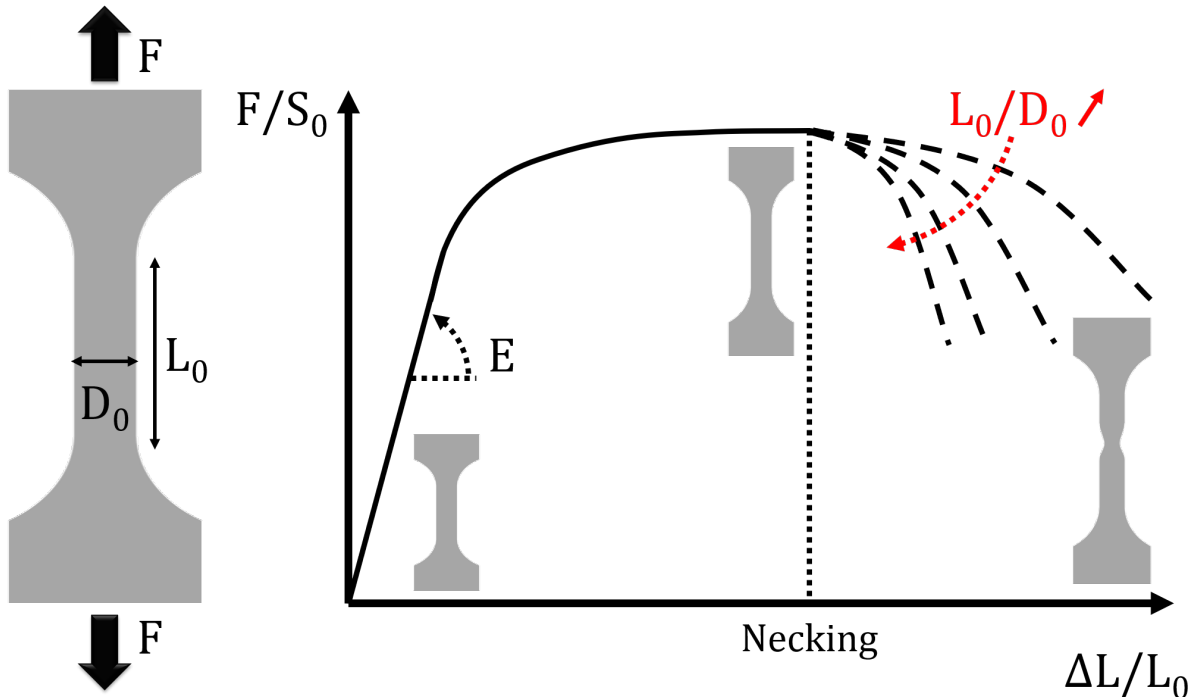


Figure 1.5: Schematic representation of the influence of the geometry on the post-necking behavior, with: F the tensile force; ΔL the elongation; E the Young modulus; D_0 , S_0 and L_0 the initial geometrical parameters.

Even though the tensile force decreases when necking arises, the local material behavior does not necessarily soften. In order to resolve this issue, some methods have been proposed for estimating the material properties beyond the maximum tensile strength, as in [Bridgman, 1964]. More recently, significant improvements in the post-necking identification have been made by coupling Direct Image Correlation technologies and FEM, as in [Kamaya and Kawakubo, 2011, Gerbig et al., 2016, Defaïsse et al., 2018, Li et al., 2018]. Such refined identifications will be shown to be decisive in the analysis of instabilities.

1.4 Imperfections and boundary conditions

In reality, “perfect” geometries, “homogeneous” materials and “perfect” loading directions do not exist. In linear mechanics, this problem is rarely studied since such imperfections are

considered to be negligible. This assumption is based on the stability of the linear problems in a mathematical sense: for a small smooth variation of the geometry, material properties, or loading conditions, the effect on the results vary smoothly and tend to vanish.

Also commonly used in linear mechanics, Saint-Venant's principle states that the way the boundary conditions are prescribed has a negligible effect on the solution of the problem far from the boundary in question. This means, for instance, that loading a tensile sample with prescribed vertical displacements, or vertical traction forces does not have significant effects on the strains and stresses in the gauge length.

While these two principles are valid for linear mechanics, they are less relevant when it comes to the analysis of elastoplastic problems in a finite deformation framework. In fact, sensitivity to imperfections is a well-known problem when analyzing the uniqueness and stability of a structure's response. While there are many studies which focus on the sensitivity to the loading direction, geometrical and material imperfections, as in [Hill and Hutchinson, 1975, Lee and Ades, 1957, Hutchinson and Tvergaard, 1981, Mear and Hutchinson, 1985, Remmers and de Borst, 2001, Regulation, 2005, Kriegsmann et al., 2012, Asmolovskiy et al., 2015, Di Pasqua et al., 2016, Dæhli et al., 2017, Wang et al., 2017, Walport et al., 2018], only a few focus on the sensitivity to the way the load is prescribed: imposed displacement or traction forces, such as in [Mandel, 1964, Ryzhak, 1994, Nguyen, 2000].

For simple elastoplastic structures, the analysis of small geometrical or loading imperfections can be done explicitly as in [Lee and Ades, 1957]. However, these analyses usually have strong restrictions regarding the material's constitutive law and are limited to simple geometries. When numerical modeling is required for more complex structures, an exhaustive analysis of the sensitivity to geometrical or loading imperfections may be impracticable due to the computation costs and the diversity of possible imperfections. Some recent developments in High Performance Computation (HPC) methods [Gosselet and Rey, 2006], and in Hybrid Reduced Order Modeling (HROM) [Ryckelynck, 2005, Eftang and Patera, 2014] could possibly provide the required tools for such analyses.

When designing complex structures, it is common to study sub-parts independently. A usual assumption is to apply kinematic constraints that maintain the *cut surface's* geometry⁷. In civil engineering structures, standardization of the geometries and material has made it possible to thoroughly study the effects of such modeling methods on the critical loads [Regulation, 2005, Gardner, 2018]. Such standards do not exist in aeronautical structures.

1.5 Aim of this work

As presented above, the analysis of elastoplastic instabilities has motivated numerous studies over the last sixty years. Global and local instabilities were often presented separately, and generally only studied together for homogeneous problems. The principal aim of this work is to combine both approaches in order to analyze and better understand the competition between localization and buckling in elastoplastic structures within a FEM framework.

Moreover, the analysis of the effects of the way the loading is prescribed (displacements or traction forces) on the stability and uniqueness of the solution has usually been neglected in favor of the study of the consequences of the loading direction, geometry or material imperfections. When it comes to the analysis of sub-parts, some over-constraining kinematic conditions are commonly applied and may have a significant impact on the analysis of the stability of the structure. Therefore, a method must be identified to address this problem.

Finally, contact interfaces are often considered when studying an assembly or experimental

⁷ The *cut surface* here relates to the surface obtained after splitting the sub-part from the larger structure. It is the surface that would appear after "cutting the sub-part out".

setups. However, the evaluation of the stability of a problem involving contact cannot be studied using the classical global instability analysis. Therefore, a systematic method, still to be improved, is presented in order to study the stability of a part in multi-bodies problems.

1.6 Outline

Since there exists no universal conventions, the finite deformation notations are introduced in chapter 2. The constitutive law formulation adopted in the present work and the corresponding FEM formulation are also detailed in order to facilitate further discussions.

Hill’s stability and uniqueness criteria are presented in chapter 3. The link between the stability condition given in an infinite functional space in [Hill, 1958] and the singularity of the global stiffness matrix in FEM (finite functional space) is thoroughly detailed. The latter has been implemented in the C++ FEM-software *Zset* (<http://www.zset-software.com/> [Besson and Foerch, 1997]) and validated on the analysis of the necking of a bar loaded in tension. Three structural problems are then presented in order to illustrate the capacity and limits of this method: the simulation of a tensile sample to show the sensitivity to changes in the geometry; the analysis of the buckling of a thin tube loaded in torsion; and the sensitivity of the instability criterion to the boundary conditions is demonstrated with the analysis of a thin plate loaded in tension.

In chapter 4, Rice’s localization criterion⁸ is thoroughly detailed. So as to link the local and global instability criteria, the uniqueness of the van Hove rate boundary value problem⁹ is discussed, and a minor extension is proposed. On the basis of this extension, the loss of stability and loss of ellipticity of a homogeneous problem in a FEM framework are discussed. Then, a new efficient and robust minimization algorithm for the evaluation of the Rice’s localization criterion is detailed. The numerical method is validated with a simple shear problem and compared to methods available in the literature. Then, discussion about loss of stability and loss of ellipticity in a FEM framework will be illustrated in the analysis of a square loaded in shear under the plane strain hypothesis. Finally, the analysis of loss of ellipticity and loss of stability of a non-homogeneous problem will be discussed and illustrated in the analysis of a tube loaded in torsion. The conclusions of the latter study will help us discuss and better understand the modeling of the failure of an actual ML340 steel sample used in [Defaisse et al., 2018, Defaisse, 2018].

In order to analyze the stability of a structure for various boundary conditions, the “weakened stability analysis” is proposed in chapter 5. To motivate this new approach, Euler’s famous buckling analysis of a beam loaded in compression is re-derived starting from Hill’s loss of stability criterion. Also, similar approaches already used in civil engineering will be briefly presented. The weakened stability analysis is then rigorously derived and the implementation in *Zset* is given. The numerical method is validated using Euler’s buckling problem. The utility of this approach for the analysis of the stability of various problems is demonstrated in three cases: the sensitivity of the buckling load of a tube loaded in torsion to various kinematic constraints is studied and will show the significant consequences of various modeling assumptions; the instability modes of a homogeneous square loaded in shear is thoroughly studied for various boundary conditions, leading to a discussion about the interpretation of the loss of ellipticity criterion regarding the emergence of localization bands in a structure by introducing the Ryzhak, Mandel, and “Left Fixed” boundary value problems; the latter study will foster the discussion about the emergence of localization bands and the loss of regularity of the FEM model of a thick tube loaded in torsion.

All of these analyses are then combined and applied to various structural problems in the

⁸ Also called “loss of ellipticity criterion”.

⁹ First introduced in [van Hove, 1947], and briefly discussed in [Rice, 1976].

chapter 6, all instability analyses are applied to various structural problems. The first example is a thorough parametric study of the failure of ML340 tubes loaded in torsion compared with the reference results obtained in [Lee and Ades, 1957]. In particular, the differences observed concerning the localization loads is related to the use of a full finite deformation framework. This parametric analysis is then performed for two fictitious materials that exhibit the same maximum tensile strength, lower yield stresses but a much larger plastic deformation before necking occurs. The aim of this study is to identify which parameters control the emergence of localization or buckling modes. The comparison of the numerical results with the analysis presented in [Department of Defense, 2003] shows that significantly different trends may be observed. The third and final structural example focuses on the analysis of instabilities when contact is involved. A method based on the weakened stability analysis is presented and applied to the analysis of the failure of a lug loaded in tension.

Bibliography

- Abed-Meraim, F. (2009). *Contributions à la prédiction d'instabilités de type structure et matériau : modélisation de critères et formulation d'éléments finis adaptés à la simulation des structures minces*. Mémoire HDR dissertation, Arts et Métiers ParisTech.
- Akparna, H., Ben-Bettaieb, M., and Abed-Meraim, F. (2017). Prediction of plastic instability in sheet metals during forming processes using the loss of ellipticity approach. *Latin American Journal of Solids and Structures*, 14:1816–1836.
- Asmolovskiy, N., Tkachuk, A., and Bischoff, M. (2015). Numerical approaches to stability analysis of cylindrical composite shells based on load imperfections. *Engineering Computations*, 32(2):498–518.
- Benallal, A., Botta, A. S., and Venturini, W. S. (2006). On the description of localization and failure phenomena by the boundary element method. *Computer Methods in Applied Mechanics and Engineering*, 195(44):5833 – 5856.
- Benallal, A. and Comi, C. (1996). Localization analysis via a geometrical method. *International Journal of Solids and Structures*, 33:99–119.
- Besson, J. and Foerch, R. (1997). Large scale object-oriented finite element code design. *Computer Methods in Applied Mechanics and Engineering*, 142(1):165–187.
- Bigoni, D. (2012). *Nonlinear Solid Mechanics: Bifurcation Theory and Material Instability*. Cambridge University Press.
- Bigoni, D. and Hueckel, T. (1991). Uniqueness and localization - i - associative and non-associative elastoplasticity. *International Journal of Solids and Structures*, 28:197–213.
- Bigoni, D. and Zaccaria, D. (1993). On strain localization analysis of elastoplastic materials at finite strains. *International Journal of Plasticity*, 9:21–33.
- Bridgman, P. (1964). *Studies in Large Plastic Flow and Fracture*. Harvard University Press.
- Considère, A. (1885). Mémoire sur l'emploi du fer et de l'acier dans les constructions. *Annales des Ponts et Chaussées*, 9:574–775.
- d'Avila, M. S., Triantafyllidis, N., and Wen, G. (2016). Localization of deformation and loss of macroscopic ellipticity in microstructured solids. *Journal of the Mechanics and Physics of Solids*, 97:275–298.
- de Borst, R., Crisfield, M. A., Remmers, J., and Verhoosel, C. (2012). *Non-Linear Finite Element Analysis of Solids and Structures*. Wiley.
- Defaisse, C. (2018). *Étude de la rupture ductile d'un acier à très haute résistance pour des applications aéronautiques*. PhD thesis, École de Mines Paristech.

- Defaisse, C., Mazière, M., Marcin, L., and Besson, J. (2018). Ductile fracture of an ultra-high strength steel under low to moderate stress triaxiality. *Engineering Fracture Mechanics*, 194:301–318.
- Department of Defense (1998). *Military Handbook: Metallic Materials and Elements for Aerospace Vehicle Structures*. USA.
- Department of Defense (2003). *Military Handbook: Metallic Materials and Elements for Aerospace Vehicle Structures*. USA.
- Dæhli, L., Morin, D., Børvik, T., and Hopperstad, O. (2017). Influence of yield surface curvature on the macroscopic yielding and ductile failure of isotropic porous plastic materials. *Journal of the Mechanics and Physics of Solids*, 107:253–283.
- Di Pasqua, M., Khakimova, R., Castro, S., Arbelo, M., Riccio, A., Raimondo, A., and Degenhardt, R. (2016). Investigation on the geometric imperfections driven local buckling onset in composite conical shells. *Applied Composite Materials*, 23(4):879–897.
- Doghri, I. and Billardon, R. (1995). Investigation of localization due to damage in elasto-plastic materials. *Mechanics of Materials*, 19(2):129–149.
- Durand, S. and Combescure, A. (1999). Analytical and numerical study of the bifurcation of a cylindrical bar under uniaxial tension. *Revue européenne des éléments finis*, 8:725–745.
- Eftang, J. and Patera, A. (2014). A port-reduced static condensation reduced basis element method for large component-synthesized structures: approximation and a posteriori error estimation. *Advanced Modeling and Simulation in Engineering Sciences*, 1(1):49 p.
- Euler, L. (1759). Sur la force des colonnes. *Memoires de l'academie des sciences de Berlin*, 13:252–282.
- European Aviation Safety Agency (2018). *Certification Specifications and Acceptable Means of Compliance for Large Aeroplanes CS-25 - Amendment 22*. EASA.
- Gardner, L. (2018). Elastic local buckling stresses for full structural steel cross-sections (oral presentation). In *European Solid Mechanics Conference*. (July-2018) Bologna, Italy.
- Gerbig, D., Bower, A., Savic, V., and Hector, L. (2016). Coupling digital image correlation and finite element analysis to determine constitutive parameters in necking tensile specimens. *International Journal of Solids and Structures*, 97-98:496–509.
- Gosselet, P. and Rey, C. (2006). Non-overlapping domain decomposition methods in structural mechanics. *Archives of Computational Methods in Engineering*, 13:515–572.
- Halphen, B. (1975). Sur le champ des vitesses en thermoplasticité finie. *International Journal of Solid Structures*, pages 947–960.
- Hill, R. (1952). On discontinuous plastic states, with special reference to localized necking in thin sheets. *Journal of the Mechanics and Physics of Solids*, 1:19–30.
- Hill, R. (1958). A general theory of uniqueness and stability in elastic-plastic solids. *Journal of the Mechanics and Physics of Solids*, 6:236–249.
- Hill, R. and Hutchinson, J. (1975). Bifurcation phenomena in the plane tension test. *Journal of the Mechanics and Physics of Solids*, 23:239–264.

- Hutchinson, J. (1974). Plastic buckling. *Advances in applied mechanics*, 14:67–144.
- Hutchinson, J. and Tvergaard, V. (1981). Shear band formation in plane strain. *International Journal of Solids and Structures*, 17(5):451 – 470.
- Ibrahimbegovic, A. (2009). *Geometric and material instabilities*. Springer.
- Kamaya, M. and Kawakubo, M. (2011). A procedure for determining the true stress–strain curve over a large range of strains using digital image correlation and finite element analysis. *Mechanics of Materials*, 43(5):243 – 253.
- Kriegsmann, B., Hilburger, M., and Rolfes, R. (2012). The effects of geometric and loading imperfections on the response and lower-bound buckling load of a compression-loaded cylindrical shell. *53rd AIAA/ASME/ASCE/AHS/ASC Structures, Structural Dynamics and Materials Conference*, 1:10 p.
- Lee, L. and Ades, C. (1957). Plastic torsional buckling strength of cylinders including effects of imperfections. *Journal of the Aeronautical Sciences*, 24:241–248.
- Lemaitre, J., Chaboche, J. L., Benallal, A., and Desmorat, R. (2009). *Mécanique des matériaux solides - 3ème édition*. Dunod.
- Lestringant, C., Maurini, C., Lazarus, A., and Audoly, B. (2017). Buckling of an elastic ridge: Competition between wrinkles and creases. *Phys. Rev. Lett.*, 118:165501.
- Li, J., Yang, G., Siebert, T., Shi, M. F., and Yang, L. (2018). A method of the direct measurement of the true stress–strain curve over a large strain range using multi-camera digital image correlation. *Optics and Lasers in Engineering*, 107:194 – 201.
- Mandel, J. (1964). Propagation des surfaces de discontinuité dans un milieu élastoplastique. In *Stress waves in anelastic solids*, pages 331–340. Springer.
- Mandel, J. (1966). Conditions de stabilité et postulat de drucker. In *Rheology and Soil Mechanics*, pages 58–68. Springer.
- Mandel, J. (1971). Plasticité classique et viscoplasticité. In *CISM Courses and lectures*, volume 97, pages 1–187.
- Mazière, M. (2007). *Éclatement des disques de Turbomachines*. PhD thesis, École des Mines de Paris.
- Mear, M. and Hutchinson, J. (1985). Influence of yield surface curvature on flow localization in dilatant plasticity. *Mechanics of Materials*, 4:395–407.
- Meyers, A., Bruhns, O., and Xiao, H. (2000). Large strain response of kinematic hardening elastoplasticity with the logarithmic rate: Swift effect in torsion. *Meccanica*, 35(3):229–247.
- Mota, A., Chen, Q., Foulk, J., Ostien, J., and Lai, Z. (2016). A cartesian parametrization for the numerical analysis of material instability. *International Journal for Numerical Methods in Engineering*, 108(2):156–180.
- Nefussi, G. and Combescure, A. (2002). Coupled buckling and plastic instability for tube hydroforming. *International Journal of Mechanical Sciences*, 44:899–914.
- Nguyen, Q. S. (2000). *Stability and nonlinear solid mechanics*. Wiley.

- Ortiz, M. (1987). An analytical study of the localized failure modes of concrete. *Mechanics of Materials*, 6:159–174.
- Petryk, H. (1992). Material instability and strain-rate discontinuities in incrementally nonlinear continua. *Journal of Mechanics and Physics of Solids*, 40:1227–1250.
- Petryk, H. (1997). Plastic instability : Criteria and computational approaches. *Archives of Computational Methods in Engineering*, 4:111–151.
- Petryk, H. (2000). *Material Instabilities in Elastic and Plastic Solids*. CISM International Centre for Mechanical Sciences 414. Springer, 1 edition.
- Pijaudier-Cabot, G. and Benallal, A. (1993). Strain localization and bifurcation in a nonlocal continuum. *International Journal of Solids and Structures*, 30(13):1761–1775.
- Regulation, T. E. U. P. (2005). *Eurocode 3: Design of steel structures - Part 1-1: General rules and rules for buildings*. The European Union.
- Remmers, J. and de Borst, R. (2001). Delamination buckling of fibre–metal laminates. *Composites Science and Technology*, 61(15):2207–2213.
- Rice, J. (1976). The localization of plastic deformation. In *W.T. Koiter (Ed.), Theoretical and Applied Mechanics*, pages 207–220. North-Holland.
- Rubin, M. and Nadler, B. (2016). An eulerian formulation for large deformations of elastically isotropic elastic-viscoplastic membranes. *Journal of Mechanics of Materials and Structures*, 11:197–216.
- Rudnicki, J. and Rice, J. (1975). Conditions for the localization of deformation in pressure sensitive dilatant materials. *Journal of Mechanics and Physics of Solids*, 23:371–394.
- Ryckelynck, D. (2005). A priori hyperreduction method: an adaptive approach. *Journal of Computational Physics*, 202(1):346–366.
- Ryzhak, E. (1994). On stability of homogeneous elastic bodies under boundary conditions weaker than displacement conditions. *The Quarterly Journal of Mechanics and Applied Mathematics*, 47(4):663–672.
- Stören, S. and Rice, J. (1975). Localized necking in thin sheets. *Journal of the Mechanics and Physics of Solids*, 23(6):421–441.
- Thermann, K. (2000). *Post-critical plastic deformation pattern in incrementally nonlinear materials at finite strain*. CISM International Centre for Mechanical Sciences 414. Springer.
- Truesdell, C. and Toupin, R. (1960). *The classical field theory of mechanics*. Springer.
- van Hove, L. (1947). Sur l’extension de la condition de Legendre du calcul des variations aux intégrales multiples à plusieurs fonctions inconnues. *Proceedings of the Koninklijke Nederlandse Akademie van Wetenschappen*, 50:18–23.
- Walport, F., Gardner, L., Real, E., Arrayago, I., and Nethercot, D. (2018). Effects of material nonlinearity on the global analysis and stability of stainless steel frames. *Journal of Constructional Steel Research*, page in press: <https://doi.org/10.1016/j.jcsr.2018.04.019>.
- Wang, H., Yao, X., Li, L., Sang, Z., and Krakauer, B. (2017). Imperfection sensitivity of externally-pressurized, thin-walled, torispherical-head buckling. *Thin-Walled Structures*, 113:104–110.

Chapter 2

Finite Deformation Framework

“Si je te vends le plus beau des châteaux à 1€, mais que tu n’as pas 1€, il est trop cher.”
Mon père

Résumé : Ce chapitre a pour but d’introduire les notations en grandes déformations utilisées, ainsi que la formulation de la loi de comportement exploitée dans la suite des travaux. Une attention particulière est apportée à l’expression des opérateurs tangents, ces derniers jouant un rôle majeur dans les critères d’instabilité. Enfin, la formulation des éléments finis en grandes déformations est détaillée pour faciliter la présentation des développements numériques dans les autres chapitres.

2.1	General framework	30
2.2	Hypo-elastoplastic formulations	32
2.3	FEM formulation of finite deformation problems	41

By default most Finite Element Method (FEM) analyzes assume small deformations, that is to say the change in geometry of the structure is small enough not to affect the load paths and subsequently the final results. However in some cases, such as the buckling of beams and shells [Lee and Ades, 1957] and the forming processes of thin metal sheets [Ben-Bettaieb and Abed-Meraim, 2017], these assumptions are invalid. In these cases, which occur whenever there is a need to distinguish initial and current configurations [Mora et al., 2013], the more general finite deformation framework is required.

Due to the wide applicability of the finite deformation framework and the number of researchers in the field, there exist a multiplicity of sets of notations. The present chapter mainly aims to introduce the notations used in this manuscript. The hypo-elastoplastic formulations used in this work are also thoroughly defined. Finally, the FEM formulation needed for the later discussions will be described for both incremental and rate problems. Due to the possible multiple implementations that can be found in FEM software, multiple formulations will be derived so that the developments of this manuscript can be adapted to other codes.

2.1 General framework

Since a thorough understanding of how the finite deformation framework is formulated is required to fully grasp the work presented, the following section introduces the required concepts. Let $\underline{\mathbf{X}}$ be the position of a material point in the initial configuration Ω_0 . At any time t the position of this point in the current configuration Ω is given by $\underline{\mathbf{x}}(\underline{\mathbf{X}}, t)$ (see Figure 2.1).

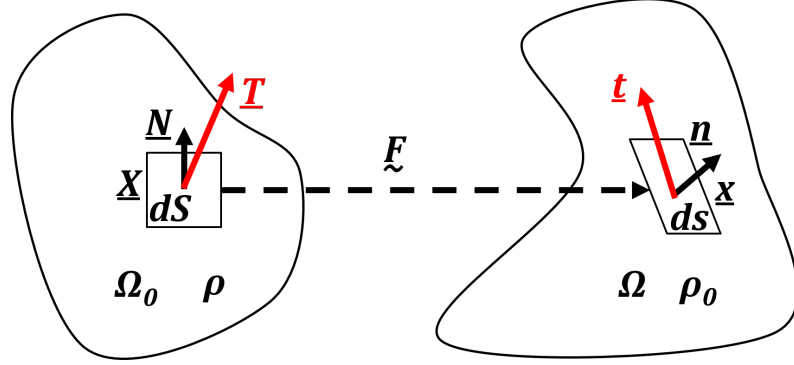


Figure 2.1: Finite deformation of a continuum media.

where the deformation gradient $\underline{\mathbf{F}}$ is given by:

$$\underline{\mathbf{F}}(\underline{\mathbf{X}}, t) = \frac{\partial \underline{\mathbf{x}}}{\partial \underline{\mathbf{X}}} \quad (2.1)$$

$$F_{ij} = \frac{\partial x_i}{\partial X_j} \quad (2.2)$$

$\underline{\mathbf{N}}$ denotes the unit normal to a surface element dS in the initial configuration, and $\underline{\mathbf{n}}$ denotes the unit normal to a surface element ds in the current configuration. They are linked by Nanson's formula:

$$\underline{\mathbf{n}} ds = J \underline{\mathbf{F}}^{-T} \underline{\mathbf{N}} dS \quad (2.3)$$

where:

$$J = \det(\underline{\mathbf{F}}) = \frac{dv}{dV} \quad (2.4)$$

with dV and dv the material volume element respectively in the initial and current configuration, and J the Jacobian of the transformation (volume variation).

2.1.1 Equilibrium

In order to formulate the local equilibrium problem, one needs to introduce a stress measure. First of all, let $\underline{\boldsymbol{\sigma}}$ denote the **Cauchy** stress tensor. It associates a given surface element in the current configuration to the traction forces applied to that surface element:

$$\underline{\boldsymbol{\sigma}} \cdot \underline{\mathbf{n}} ds = \underline{\mathbf{t}} ds \quad (2.5)$$

Combining equation (2.3) and (2.5), naturally leads to the expression of the **Boussinesq** stress tensor $\underline{\mathbf{S}}$ (also called "Piola Kirchhoff 1" or "transposed nominal stress tensor" [Ogden, 2000]):

$$\underline{\mathbf{S}} = J \underline{\boldsymbol{\sigma}} \underline{\mathbf{F}}^{-T} \quad (2.6)$$

such that:

$$\underline{\mathbf{T}} = \underline{\mathcal{S}} \cdot \underline{\mathbf{N}} = \underline{\mathbf{t}} \frac{ds}{dS} \quad (2.7)$$

And finally we introduce the **Kirchhoff** stress tensor $\underline{\boldsymbol{\tau}}$, which will be necessary later. It is defined as:

$$\underline{\boldsymbol{\tau}} = J \underline{\boldsymbol{\sigma}} \quad (2.8)$$

Static equilibrium is then equivalently formulated as:

$$\underline{\mathbf{div}} (\underline{\boldsymbol{\sigma}}) + \underline{\mathbf{f}} = \mathbf{0} \quad (2.9)$$

$$\underline{\mathbf{Div}} (\underline{\mathcal{S}}) + J \underline{\mathbf{f}} = \mathbf{0} \quad (2.10)$$

where $\underline{\mathbf{f}}$ are the volumic forces applied to a volume element in the current configuration “div” is the divergence operator in the current configuration (in a fixed Cartesian coordinate system):

$$[\underline{\mathbf{div}} (\underline{\boldsymbol{\sigma}})]_i = \frac{\partial \sigma_{ij}}{\partial x_j} \quad (2.11)$$

and “Div” is the divergence operator in the initial configuration:

$$[\underline{\mathbf{Div}} (\underline{\mathcal{S}})]_i = \frac{\partial \mathcal{S}_{ij}}{\partial X_j} \quad (2.12)$$

Since the initial configuration is fixed, one can easily express the rate form of equation 2.10 and gets:

$$\underline{\mathbf{Div}} (\underline{\dot{\mathcal{S}}}) + \frac{d}{dt} (J \underline{\mathbf{f}}) = \mathbf{0} \quad (2.13)$$

where $\dot{a} = \frac{da}{dt}$ denotes the time derivative of the quantity a .

2.1.2 Boundary conditions

Boundary conditions can be expressed on either the current and initial configuration. However, for some cases, one definition might be more natural than the other. For example:

- On the current configuration in the case of following forces such as fluid pressure;
- On the initial configuration in the case of global forces such as the tension force applied to a sample for which the initial geometry is known.

In the case of traction forces applied to the current configuration, $\underline{\mathbf{t}}^a = \underline{\boldsymbol{\sigma}} \cdot \underline{\mathbf{n}}$, one can transport them to the initial configuration such that $\underline{\mathbf{T}}^a = \underline{\mathcal{S}} \cdot \underline{\mathbf{N}}$. The relation between $\underline{\mathbf{T}}^a$ and $\underline{\mathbf{t}}^a$ is given by:

$$\underline{\mathbf{T}}^a = J \left\| \underline{\mathbf{F}}^{-T} \cdot \underline{\mathbf{N}} \right\| \underline{\mathbf{t}}^a \quad (2.14)$$

The traction (Neumann) boundary conditions can therefore always be expressed in the form:

$$\underline{\mathcal{S}} \cdot \underline{\mathbf{N}} = \underline{\mathbf{T}}^a \quad \forall \underline{\mathbf{X}} \in \partial\Omega_0^T \quad (2.15)$$

and the displacement (Dirichlet) boundary conditions as:

$$\underline{\mathbf{u}} = \underline{\mathbf{u}}^a \quad \forall \underline{\mathbf{X}} \in \partial\Omega_0^u \quad (2.16)$$

where $\partial\Omega_0^u$ and $\partial\Omega_0^T$ are complementary parts of the boundary of the material domain denoted $\partial\Omega_0$. The Boundary Conditions (BCs) (2.15) and (2.16) can be expressed in their rate form:

$$\underline{\dot{\mathcal{S}}} \cdot \underline{\mathbf{N}} = \underline{\dot{\mathbf{T}}}^a \quad \forall \underline{\mathbf{X}} \in \partial\Omega_0^T \quad (2.17)$$

$$\underline{\dot{\mathbf{u}}} = \underline{\dot{\mathbf{u}}}^a \quad \forall \underline{\mathbf{X}} \in \partial\Omega_0^u \quad (2.18)$$

2.1.3 Rate problem and local tangent operator

In order to build the rate boundary value problem, necessary for the stability analyses presented in the next chapters, the rate constitutive law must be specified. However, there exists a multiplicity of constitutive law formulations in a finite deformation framework, see for instance [Hill, 1958, Truesdell and Toupin, 1960, Mandel, 1971, Hutchinson and Miles, 1974, Hutchinson, 1974, Petryk, 1992, Bigoni and Zaccaria, 1993, Besson et al., 2010, Nguyen, 2000, Mora et al., 2013, Ben-Bettaieb and Abed-Meraim, 2017, d'Avila et al., 2016, Rubin and Nadler, 2016]. In the present work only the hypo-elastoplastic formulations, in particular the corotational formulation, will be used (details in section 2.2). Still, other formulations can be found in section 8.1 and section 8.2 and could also be applied to the present work. In fact, these formulations all have in common the fact that the Boussinesq stress rate ($\dot{\underline{\underline{S}}}$) and the Lagrangian velocity gradient ($\dot{\underline{\underline{F}}}$) can be related by:

$$\dot{\underline{\underline{S}}} = \underline{\underline{\mathcal{L}}} : \dot{\underline{\underline{F}}} \quad (2.19)$$

where $\underline{\underline{\mathcal{L}}}$ is a fourth order tensor, **possibly multibranch**, that depends only on current quantities and a plastic loading/elastic unloading condition. In particular, it can depend on the deformation gradient $\underline{\underline{F}}$, the Cauchy stress $\underline{\underline{\sigma}}$ and the explicit material properties such as the elastic moduli, the strain hardening and the plastic flow rule.

Let us summarize the rate boundary value problem (in the absence of body forces):

$$\underline{\underline{S}} = J \underline{\underline{\sigma}} \underline{\underline{F}}^{-T} \quad \text{Stress measure} \quad (2.20)$$

$$\dot{\underline{\underline{F}}} = \frac{\partial \dot{\underline{\underline{u}}}}{\partial \underline{\underline{X}}} \quad \text{Lagrangian velocity gradient} \quad (2.21)$$

$$\dot{\underline{\underline{S}}} = \underline{\underline{\mathcal{L}}} : \dot{\underline{\underline{F}}} \quad \text{Rate constitutive law} \quad (2.22)$$

$$\text{Div}(\dot{\underline{\underline{S}}}) = \underline{\underline{0}} \quad \text{Local rate equilibrium} \quad (2.23)$$

$$\dot{\underline{\underline{S}}} \cdot \underline{\underline{N}} = \underline{\underline{T}}^a \quad \forall \underline{\underline{X}} \in \partial\Omega_0^T \quad \text{Dead load rate} \quad (2.24)$$

$$\underline{\underline{u}} = \underline{\underline{u}}^a \quad \forall \underline{\underline{X}} \in \partial\Omega_0^u \quad \text{Velocity BC} \quad (2.25)$$

Velocity potential and major symmetry

It is interesting to remark that $\underline{\underline{\mathcal{L}}}$ does not possess the minor symmetries, but it might possess the major symmetry such that $\mathcal{L}_{ijkl} = \mathcal{L}_{klij}$. In this case, there exists a velocity potential \mathcal{V} such that:

$$\dot{\underline{\underline{S}}} = \frac{\partial \mathcal{V}}{\partial \dot{\underline{\underline{F}}}} \quad (2.26)$$

$$\text{with: } \mathcal{V}(\dot{\underline{\underline{F}}}) = \frac{1}{2} \dot{\underline{\underline{F}}} : \underline{\underline{\mathcal{L}}} : \dot{\underline{\underline{F}}} \quad (2.27)$$

The existence of such a potential has some implications regarding the uniqueness and stability of the velocity problem, as discussed for instance in [Hill, 1958, Nguyen, 2000, Petryk, 1992, 1993].

2.2 Hypo-elastoplastic formulations

The formulation of hypo-elastoplastic laws leads to a set of equations that strongly resembles the one obtained in a standard elastoplastic small deformation framework. This has the twin benefits of using a framework well-known to mechanical engineers, as well as facilitating its

implementation in a numerical framework. One way to define such laws is to chose a local objective frame on which the elastoplastic law is formulated, another is to directly choose an objective derivative for the stress evolution. In this section, the notion of local objective frame is first introduced¹. Then, a formulation is detailed for elastoplastic materials and specified for some choices of local objective frame. Finally, the local tangent operator $\underline{\underline{\mathcal{L}}}$ is specified for such formulations.

2.2.1 Objectivity

The notion of *local objective frame* is closely related to the notion of an observer. If one chooses to respect the principle of material frame indifference, then the constitutive formulation should also be insensitive to the choice of observer. One way to fulfill this principle is to formulate the constitutive law with objective quantities. While this is intrinsic for Lagrangian formulations (see section 8.1 and section 8.2 for more details), it is necessary to be aware of this principle when working with Eulerian quantities.

Let us consider two points, M_1 and M_2 , respectively occupying the positions $\underline{\mathbf{x}}_1$ and $\underline{\mathbf{x}}_2$ in the referential \mathcal{E} , and the positions $\underline{\mathbf{x}}'_1$ and $\underline{\mathbf{x}}'_2$ in the referential \mathcal{E}' . In the present work, the difference between \mathcal{E} and \mathcal{E}' is a mere rigid body motion. Thus one has:

$$\underline{\mathbf{x}}'_i = \underline{\underline{\mathcal{Q}}}(t) \cdot \underline{\mathbf{x}} + \underline{\mathbf{a}}(t) \quad (2.28)$$

where $\underline{\underline{\mathcal{Q}}}$ is an arbitrary time dependent orthogonal second order tensor (rotation)², and $\underline{\mathbf{a}}$ an arbitrary first order tensor (translation).

Let us denote the difference of position between M_1 and M_2 by $\underline{\mathbf{u}} = \underline{\mathbf{x}}_2 - \underline{\mathbf{x}}_1$ in \mathcal{E} and by $\underline{\mathbf{u}}' = \underline{\mathbf{x}}'_2 - \underline{\mathbf{x}}'_1$ in \mathcal{E}' such that:

$$\underline{\mathbf{u}}' = \underline{\underline{\mathcal{Q}}}(t) \cdot \underline{\mathbf{u}} \quad (2.29)$$

A vector field that follows equation (2.29) when the referential changes fulfill equation (2.28) is an **objective vector field**.

In a more general way [Besson et al., 2010], a n^{th} order tensor field:

$$T_{(n)} = \underline{\mathbf{u}}_1 \otimes \dots \otimes \underline{\mathbf{u}}_n \quad (2.30)$$

is an objective tensor field if:

$$T'_{(n)} = \underline{\mathbf{u}}'_1 \otimes \dots \otimes \underline{\mathbf{u}}'_n \quad (2.31)$$

For instance, a second order tensor, $\underline{\underline{\mathcal{T}}} = \underline{\mathbf{u}} \otimes \underline{\mathbf{v}}$, is objective if:

$$\underline{\underline{\mathcal{T}}}' = \underline{\mathbf{u}}' \otimes \underline{\mathbf{v}}' = \underline{\underline{\mathcal{Q}}} \cdot \underline{\underline{\mathcal{T}}} \cdot \underline{\underline{\mathcal{Q}}}^T \quad (2.32)$$

Based on this definition, it is simple to prove that $\underline{\underline{\sigma}}$ (as well as $\underline{\underline{\tau}}$) is an objective tensor field if one admits that forces are objective quantities:

$$\begin{cases} \underline{\underline{\sigma}}' \cdot \underline{\mathbf{n}}' = \underline{\mathbf{t}}' = \underline{\underline{\mathcal{Q}}} \cdot \underline{\mathbf{t}} \\ \underline{\mathbf{n}}' = \underline{\underline{\mathcal{Q}}} \cdot \underline{\mathbf{n}} \end{cases} \quad (2.33)$$

$$\Rightarrow (\underline{\underline{\mathcal{Q}}}^T \cdot \underline{\underline{\sigma}}' \cdot \underline{\underline{\mathcal{Q}}}) \cdot \underline{\mathbf{n}} = \underline{\mathbf{t}} = \underline{\underline{\sigma}} \cdot \underline{\mathbf{n}} \quad \forall \underline{\mathbf{n}} \quad (2.34)$$

$$\Rightarrow \underline{\underline{\sigma}}' = \underline{\underline{\mathcal{Q}}} \cdot \underline{\underline{\sigma}} \cdot \underline{\underline{\mathcal{Q}}}^T \quad (2.35)$$

¹ This section is mainly based on the chapter 6 in [Besson et al., 2010]

² One has: $\underline{\underline{\mathcal{Q}}} \cdot \underline{\underline{\mathcal{Q}}}^T = \underline{\underline{\mathcal{I}}} \Rightarrow \overbrace{(\underline{\underline{\mathcal{Q}}} \cdot \underline{\underline{\mathcal{Q}}}^T)} = \underline{\underline{\mathbf{0}}} \Rightarrow \dot{\underline{\underline{\mathcal{Q}}}} \cdot \underline{\underline{\mathcal{Q}}}^T = -(\dot{\underline{\underline{\mathcal{Q}}}} \cdot \underline{\underline{\mathcal{Q}}}^T)^T$

On the other hand, the gradient of deformation $\underline{\mathbf{F}}$ is not objective:

$$\underline{\mathbf{d}}\underline{\mathbf{x}}' = \underline{\mathbf{Q}} \cdot \underline{\mathbf{d}}\underline{\mathbf{x}} = \underline{\mathbf{Q}} \cdot \underline{\mathbf{F}} \cdot \underline{\mathbf{d}}\underline{\mathbf{X}} \Rightarrow \underline{\mathbf{F}}' = \underline{\mathbf{Q}} \cdot \underline{\mathbf{F}} \quad (2.36)$$

And the Eulerian velocity gradient $\underline{\mathbf{L}}$:

$$\underline{\mathbf{d}}\underline{\mathbf{x}} = \underline{\dot{\mathbf{F}}} \cdot \underline{\mathbf{d}}\underline{\mathbf{X}} = \underline{\dot{\mathbf{F}}} \cdot \underline{\mathbf{F}}^{-1} \cdot \underline{\mathbf{d}}\underline{\mathbf{x}} = \underline{\mathbf{L}} \cdot \underline{\mathbf{d}}\underline{\mathbf{x}} \quad (2.37)$$

is also not objective:

$$\underline{\mathbf{L}}' = \underline{\dot{\mathbf{F}}}' \cdot \underline{\mathbf{F}}'^{-1} \quad (2.38)$$

$$= (\underline{\mathbf{Q}} \cdot \underline{\dot{\mathbf{F}}} + \underline{\dot{\mathbf{Q}}} \cdot \underline{\mathbf{F}})(\underline{\mathbf{F}}^{-1} \cdot \underline{\mathbf{Q}}^T) \quad (2.39)$$

$$= \underline{\mathbf{Q}} \cdot \underline{\mathbf{L}} \cdot \underline{\mathbf{Q}}^T + \underline{\dot{\mathbf{Q}}} \cdot \underline{\mathbf{Q}}^T \quad (2.40)$$

$$\Rightarrow \begin{cases} (\underline{\mathbf{L}}')^{sym} = \frac{1}{2}(\underline{\mathbf{L}}' + \underline{\mathbf{L}}'^T) = \underline{\mathbf{D}}' = \underline{\mathbf{Q}} \cdot \underline{\mathbf{D}} \cdot \underline{\mathbf{Q}}^T \\ (\underline{\mathbf{L}}')^{skew} = \frac{1}{2}(\underline{\mathbf{L}}' - \underline{\mathbf{L}}'^T) = \underline{\mathbf{\Omega}}' = \underline{\mathbf{Q}} \cdot \underline{\mathbf{\Omega}} \cdot \underline{\mathbf{Q}}^T + \underline{\dot{\mathbf{Q}}} \cdot \underline{\mathbf{Q}}^T \end{cases} \quad (2.41)$$

where $\underline{\mathbf{D}}$ denotes the strain rate tensor, and $\underline{\mathbf{\Omega}}$ the spin tensor. Equation (2.41) is obtained using the fact that $\underline{\mathbf{Q}}$ is orthogonal and shows that $\underline{\mathbf{D}}$ is an objective tensor but $\underline{\mathbf{\Omega}}$ is not.

Objective derivatives

For a given objective quantity one has no reason to believe that its time derivative is also objective. In fact, if we return to the example at the beginning of section 2.2.1, and consider that $\underline{\mathbf{u}}$ is constant in time, $\underline{\dot{\mathbf{u}}} = \underline{\mathbf{0}}$, then:

$$\underline{\dot{\mathbf{u}}}' = \underline{\dot{\mathbf{Q}}} \cdot \underline{\mathbf{u}} = \underline{\dot{\mathbf{Q}}} \cdot \underline{\mathbf{Q}}^T \cdot \underline{\mathbf{u}}' \neq \underline{\mathbf{0}} \quad (2.42)$$

While this is not surprising for a velocity field, this might be a problem when the constitutive law is formulated on stress and strain rates measures. Therefore, the notion of *objective derivative* is introduced. Let $D(\cdot)$ denote the operator of such a derivative. It fulfills:

$$D(\underline{\mathbf{u}}') = \underline{\mathbf{Q}} D(\underline{\mathbf{u}}) \quad (2.43)$$

This notion can be expanded to n^{th} order tensors as well:

$$D(T_n) = [D(\underline{\mathbf{u}}_1) \otimes \dots \otimes \underline{\mathbf{u}}_n] + [\underline{\mathbf{u}}_1 \otimes D(\underline{\mathbf{u}}_2) \otimes \dots \otimes \underline{\mathbf{u}}_n] \dots + [\underline{\mathbf{u}}_1 \otimes \dots \otimes D(\underline{\mathbf{u}}_n)] \quad (2.44)$$

A well known objective derivative is the Jaumann derivative:

$$D^J(\underline{\mathbf{u}}) = \underline{\dot{\mathbf{u}}} - \underline{\mathbf{\Omega}} \cdot \underline{\mathbf{u}} \quad (2.45)$$

Proof:

$$D^J(\underline{\mathbf{u}}') = \underline{\dot{\mathbf{u}}}' - \underline{\mathbf{\Omega}}' \cdot \underline{\mathbf{u}}' \quad (2.46)$$

$$= \underline{\dot{\mathbf{Q}}} \cdot \underline{\mathbf{u}} + \underline{\mathbf{Q}} \cdot \underline{\dot{\mathbf{u}}} - (\underline{\mathbf{Q}} \cdot \underline{\mathbf{\Omega}} \cdot \underline{\mathbf{Q}}^T + \underline{\dot{\mathbf{Q}}} \cdot \underline{\mathbf{Q}}^T) \cdot (\underline{\mathbf{Q}} \cdot \underline{\mathbf{u}}) \quad (2.47)$$

$$= \underline{\dot{\mathbf{Q}}} \cdot \underline{\mathbf{u}} + \underline{\mathbf{Q}} \cdot \underline{\dot{\mathbf{u}}} - \underline{\mathbf{Q}} \cdot \underline{\mathbf{\Omega}} \cdot \underline{\mathbf{u}} - \underline{\dot{\mathbf{Q}}} \cdot \underline{\mathbf{u}} \quad (2.48)$$

$$= \underline{\mathbf{Q}} \cdot (\underline{\dot{\mathbf{u}}} - \underline{\mathbf{\Omega}} \cdot \underline{\mathbf{u}}) \quad (2.49)$$

$$\Rightarrow D^J(\underline{\mathbf{u}}') = \underline{\mathbf{Q}} \cdot D^J(\underline{\mathbf{u}}) \quad (2.50)$$

For a second order tensor one gets:

$$D^J(\underline{\mathbf{T}}) = \underline{\dot{\mathbf{T}}} + \underline{\mathbf{T}} \cdot \underline{\mathbf{\Omega}} - \underline{\mathbf{\Omega}} \cdot \underline{\mathbf{T}} \quad (2.51)$$

While this derivative is commonly found as such in the literature, it can be derived another way. Let us consider a local referential for each material element in the structure. In fact, while the notion of referential is tightly linked to the notion of observer, one can imagine that a different observer is attached to each material point. For each material point, the change in referential can be characterized by a tensor of space and time $\underline{\mathbf{Q}}^*(\underline{\mathbf{x}}, t)$. In our case, such a local referential field is an orthogonal second order tensor field that respects:

$$\left\{ \begin{array}{l} \underline{\mathbf{Q}}^*(\underline{\mathbf{x}}, t = 0) = \underline{\mathbf{I}} \\ \det(\underline{\mathbf{Q}}(x), t) = 1 \\ \underline{\mathbf{Q}}^{*T} = \underline{\mathbf{Q}}^{*-1} \\ \underline{\mathbf{Q}}^{*' } = \underline{\mathbf{Q}}' \cdot \underline{\mathbf{Q}}^* \quad \text{for any change of global referential by } \underline{\mathbf{Q}}'. \end{array} \right. \quad (2.52)$$

One can then imagine the following procedure:

1. Transport any quantity to the local referential;
2. Take its time derivative;
3. Transport back the result to the global referential.

This procedure leads to the definition of the local objective derivative $D^*(\cdot)$ associated to the local referential $\underline{\mathbf{Q}}^*$ of a second order tensor $\underline{\mathbf{T}}$ as³:

$$D^*(\underline{\mathbf{T}}) = \underline{\mathbf{Q}}^{*T} \cdot \underline{\dot{\mathbf{T}}}^* \cdot \underline{\mathbf{Q}}^* \quad (2.53)$$

$$= \underline{\mathbf{Q}}^{*T} \cdot \overbrace{(\underline{\mathbf{Q}}^* \cdot \underline{\mathbf{T}} \cdot \underline{\mathbf{Q}}^{*T})} \cdot \underline{\mathbf{Q}}^* \quad (2.54)$$

$$= \underline{\dot{\mathbf{T}}} + \underline{\mathbf{Q}}^{*T} \cdot \underline{\dot{\mathbf{Q}}}^* \cdot \underline{\mathbf{T}} + \underline{\mathbf{T}} \cdot \underline{\dot{\mathbf{Q}}}^{*T} \cdot \underline{\mathbf{Q}}^* \quad (2.55)$$

One can then choose the local referential in which the spin tensor vanishes. This is the **corotational frame**⁴, $\underline{\mathbf{Q}}^c$, defined such that $\underline{\mathbf{\Omega}}^c = \underline{\mathbf{0}}$. Based on equation (2.41), such a referential fulfills:

$$\underline{\mathbf{\Omega}}^c = \underline{\mathbf{Q}}^c \cdot \underline{\mathbf{\Omega}} \cdot \underline{\mathbf{Q}}^{cT} + \underline{\dot{\mathbf{Q}}}^c \cdot \underline{\mathbf{Q}}^{cT} = \underline{\mathbf{0}} \quad (2.56)$$

$$\Rightarrow \underline{\mathbf{\Omega}} = -\underline{\mathbf{Q}}^{cT} \cdot \underline{\dot{\mathbf{Q}}}^c = \underline{\dot{\mathbf{Q}}}^{cT} \cdot \underline{\mathbf{Q}}^c \quad (2.57)$$

By injecting equation (2.57) into equation (2.55) one directly gets the Jaumann derivative defined in equation (2.51):

$$D^c = D^J \quad (2.58)$$

Also, another well known objective local frame is the polar frame defined such that:

$$\underline{\mathbf{Q}}^R = \underline{\mathbf{R}}^T \quad (2.59)$$

where $\underline{\mathbf{R}}$ comes from the polar decomposition: $\underline{\mathbf{F}} = \underline{\mathbf{R}} \cdot \underline{\mathbf{U}}$. One then gets:

$$\underline{\mathbf{F}}^R = \underline{\mathbf{R}}^T \cdot \underline{\mathbf{R}} \cdot \underline{\mathbf{U}} = \underline{\mathbf{U}} \quad \text{and} \quad D^R(\underline{\mathbf{T}}) = \underline{\dot{\mathbf{T}}} + \underline{\mathbf{R}} \cdot \underline{\dot{\mathbf{R}}}^T \cdot \underline{\mathbf{T}} + \underline{\mathbf{T}} \cdot \underline{\dot{\mathbf{R}}} \cdot \underline{\mathbf{R}}^T \quad (2.60)$$

where $\underline{\mathbf{U}}$ in the (symmetric) right stretch tensor.

³ This of course can be generalized to n^{th} order tensors.

⁴“Referential in which the observer instantaneously rotates with the material point”.

2.2.2 Elastoplastic behaviour

Given the definition of objective derivatives, it is now possible to formulate a particular category of elastoplastic laws in finite deformation: *Hypo-elastoplastic formulations*. The name of these formulations, “hypo”, is due to the fact that the existence of an elastic potential is not ensured⁵ in contrast to *Hyperelasticity*. These formulations should be avoided for cycling problems or problems with high elastic strain. While aware of this issue, this formulation has been used in the present work since mainly monotonic loading is performed and the materials of interest have small elastic strains.

These formulations are considered Eulerian. Three strain measures are commonly used in such formulations: $\underline{\boldsymbol{\sigma}}$ [Rice, 1976, Nguyen, 2000, Besson et al., 2010], $\underline{\boldsymbol{\tau}}$ [Petryk, 1992, Hutchinson and Miles, 1974], and $\hat{\boldsymbol{\tau}}$ [Hill, 1958, Nguyen, 2000]. The latter is the Kirchhoff stress tensor in an updated Lagrangian framework:

$$\hat{\boldsymbol{\tau}} = \hat{J} \boldsymbol{\sigma} \quad (2.61)$$

where $\hat{J} = \det(\hat{\boldsymbol{F}})$:

$$\hat{J} = 1 \quad (2.62)$$

$$\dot{\hat{J}} = \text{Tr}(\underline{\boldsymbol{D}}) = \text{Tr}(\underline{\boldsymbol{L}}) \quad (2.63)$$

where $\text{Tr}(\underline{\boldsymbol{A}}) = \underline{\boldsymbol{A}} : \underline{\boldsymbol{I}} = A_{ii}$ is the trace operator. Depending on the choice made for the stress measure, the tangent operator may, or may not, possess major symmetry. This is further discussed in section 2.2.3. Nevertheless, it is often possible to neglect this difference when the plastic flow is incompressible and elastic strains are small ($\text{Tr}(\underline{\boldsymbol{L}})$ vanishes). $D^*(\underline{\boldsymbol{\sigma}})$, $D^*(\underline{\boldsymbol{\tau}})$, and $D^*(\hat{\boldsymbol{\tau}})$ can be related as follows:

$$D^*(\underline{\boldsymbol{\tau}}) = J D^*(\underline{\boldsymbol{\sigma}}) + J \text{Tr}(\underline{\boldsymbol{L}}) \underline{\boldsymbol{\sigma}} \quad (2.64)$$

$$D^*(\hat{\boldsymbol{\tau}}) = D^*(\underline{\boldsymbol{\sigma}}) + \text{Tr}(\underline{\boldsymbol{L}}) \underline{\boldsymbol{\sigma}} \quad (2.65)$$

$$\text{and } \dot{\hat{\boldsymbol{\tau}}} = \frac{\dot{\hat{\boldsymbol{\tau}}}}{J} \quad (2.66)$$

In order to formulate an elastoplastic law in a local objective frame, one needs:

- A local objective frame: $\underline{\boldsymbol{Q}}^*(t)$;
- An additive decomposition of the strain rate tensor: $\underline{\boldsymbol{D}}^* = \underline{\boldsymbol{D}}^{*e} + \underline{\boldsymbol{D}}^{*p}$;
- An Eulerian stress tensor: $\underline{\boldsymbol{\tau}}$, $\underline{\boldsymbol{\sigma}}$ or $\hat{\boldsymbol{\tau}}$. (*The rest of the analysis will be done with $\underline{\boldsymbol{\tau}}$* ⁶);
- A rate elasticity law in the local objective frame: $\dot{\hat{\boldsymbol{\tau}}}^* = \underline{\boldsymbol{\Lambda}}^* : \underline{\boldsymbol{D}}^{*e}$;
- A yield surface: $f(\underline{\boldsymbol{\tau}}^*, \underline{\boldsymbol{X}}^*)$. (*Structural FEM analyses here are done with a von Mises criterion with an isotropic hardening $R(p)$, $f = \sqrt{\frac{3}{2} \underline{\boldsymbol{\tau}}^{dev} : \underline{\boldsymbol{\tau}}^{dev}} - R(p)$;*)
- A plastic flow rule: $\underline{\boldsymbol{D}}^{*p} = \dot{\lambda} \frac{\partial g}{\partial \underline{\boldsymbol{\tau}}^*} = \dot{\lambda} \underline{\boldsymbol{P}}^* \Rightarrow \underline{\boldsymbol{D}}^p = \dot{\lambda} \underline{\boldsymbol{Q}}^{*T} \cdot \frac{\partial g}{\partial \underline{\boldsymbol{\tau}}^*} \cdot \underline{\boldsymbol{Q}}^* = \dot{\lambda} \underline{\boldsymbol{P}}$;
- A hardening law: $\dot{\boldsymbol{\alpha}}^* = -\dot{\lambda} \frac{\partial F}{\partial \underline{\boldsymbol{X}}^*} = -\dot{\lambda} \underline{\boldsymbol{M}}^*$.

⁵ There might be residual stresses after an elastic cycle

⁶ This stress measure implies the existence of an elastoplastic potential (see section 2.1.3) [Nguyen, 2000, Petryk, 2000].

where $\underline{\alpha}^*$ denotes the tensor of internal variables defined in the local objective frame, and \underline{X}^* the associated forces. Note that the elasticity law can easily be reformulated to link it to the formulations based on objective derivatives:

$$\overbrace{(\underline{Q}^* \underline{\tau} \underline{Q}^{*T})} = \underline{\Lambda}^* : (\underline{Q}^* \underline{D}^e \underline{Q}^{*T}) \quad (2.67)$$

$$\underline{Q}^* (\dot{\underline{\tau}} + \underline{Q}^{*T} \dot{\underline{Q}}^* \underline{\tau} + \underline{\tau} \dot{\underline{Q}}^{*T} \underline{Q}^*) \underline{Q}^{*T} = \underline{\Lambda}^* : (\underline{Q}^* \underline{D}^e \underline{Q}^{*T}) \quad (2.68)$$

$$(\underline{Q}^* \boxtimes \underline{Q}^*) : D^*(\underline{\tau}) = \underline{\Lambda}^* : (\underline{Q}^* \boxtimes \underline{Q}^*) : \underline{D}^e \quad (2.69)$$

$$D^*(\underline{\tau}) = (\underline{Q}^{*T} \boxtimes \underline{Q}^{*T}) : \underline{\Lambda}^* : (\underline{Q}^* \boxtimes \underline{Q}^*) : D_{kl}^e \quad (2.70)$$

$$\Rightarrow D^*(\underline{\tau}) = \underline{\Lambda} : \underline{D}^e \quad (2.71)$$

where $\Lambda_{ijkl} = \Lambda_{pqrs}^* Q_{pi}^* Q_{qj}^* Q_{rk}^* Q_{sl}^*$; for isotropic elasticity: $\underline{\Lambda}^* = \underline{\Lambda}$.

2.2.3 Tangent operators and rate potential

The set of equations given in the previous paragraph does not define an explicit relationship between the stress rates and the strain rates. It is shown in section 2.3 that this relation is necessary for the FEM problem. In the following equations, the tangent operator $\underline{\mathcal{L}}^*$ defined in equation (2.72) is derived for such formulations⁷.

$$D^*(\underline{\tau}) = \underline{\mathcal{L}}^* : \underline{D} = \underline{\mathcal{L}}^* : \underline{L} \quad (2.72)$$

First, the consistency condition gives:

$$\dot{f}(\underline{\tau}^*, \underline{X}^*) = 0 \quad (2.73)$$

$$\underline{n}^* : \dot{\underline{\tau}}^* + \frac{\partial f}{\partial \underline{X}^*} : \dot{\underline{X}}^* = 0 \quad \text{where} \quad \underline{n}^* = \frac{\partial f}{\partial \underline{\tau}^*} \quad (2.74)$$

$$\underline{n}^* : \dot{\underline{\tau}}^* + \frac{\partial f}{\partial \underline{X}^*} : \frac{\partial \underline{X}^*}{\partial \underline{\alpha}^*} : \dot{\underline{\alpha}}^* = 0 \quad (2.75)$$

$$\underline{n}^* : (\underline{Q}^* D^*(\underline{\tau}) \underline{Q}^{*T}) - h \dot{\lambda} = 0 \quad \text{where} \quad h = \frac{\partial f}{\partial \underline{X}^*} : \frac{\partial \underline{X}^*}{\partial \underline{\alpha}^*} : \frac{\partial F}{\partial \underline{X}^*} \quad (2.76)$$

$$\Rightarrow h \dot{\lambda} = (\underline{Q}^{*T} \underline{n}^* \underline{Q}^*) : D^*(\underline{\tau}) \quad (2.77)$$

Injecting (2.71) in (2.77) and using the plastic flow rule, one gets the expression of the plastic multiplier:

$$h \dot{\lambda} = \underline{n} : \underline{\Lambda} : \underline{D}^e \quad (2.78)$$

$$h \dot{\lambda} = \underline{n} : \underline{\Lambda} : (\underline{D} - \underline{D}^p) \quad (2.79)$$

$$h \dot{\lambda} + \underline{n} : \underline{\Lambda} : \underline{D}^p = \underline{n} : \underline{\Lambda} : \underline{D} \quad (2.80)$$

$$h \dot{\lambda} + \dot{\lambda} \underline{n} : \underline{\Lambda} : \underline{P} = \underline{n} : \underline{\Lambda} : \underline{D} \quad (2.81)$$

$$\dot{\lambda} = \frac{\underline{n} : \underline{\Lambda} : \underline{D}}{h + \underline{n} : \underline{\Lambda} : \underline{P}} \quad (2.82)$$

⁷ $\underline{\mathcal{L}}^*$ necessarily possesses minor symmetries since \underline{D} and $D^*(\underline{\tau})$ possess minor symmetry.

From equation (2.71), one can then deduce:

$$D^*(\boldsymbol{\tau}) = \underline{\underline{\Lambda}} : (\underline{\underline{D}} - \underline{\underline{D}}^p) \quad (2.83)$$

$$D^*(\boldsymbol{\tau}) = \underline{\underline{\Lambda}} : \underline{\underline{D}} - \dot{\lambda} \underline{\underline{\Lambda}} : \underline{\underline{P}} \quad (2.84)$$

$$(2.82) \Rightarrow D^*(\boldsymbol{\tau}) = \underline{\underline{\Lambda}} : \underline{\underline{D}} - \left(\frac{\underline{\underline{n}} : \underline{\underline{\Lambda}} : \underline{\underline{D}}}{h + \underline{\underline{n}} : \underline{\underline{\Lambda}} : \underline{\underline{P}}} \right) \underline{\underline{\Lambda}} : \underline{\underline{P}} \quad (2.85)$$

$$\Rightarrow D^*(\boldsymbol{\tau})_{ij} = \Lambda_{ijkl} D_{kl} - \frac{n_{pq} \Lambda_{pqkl} D_{kl}}{h + n_{ab} \Lambda_{abcd} P_{cd}} \Lambda_{ijtv} P_{tv} \quad (2.86)$$

$$D^*(\boldsymbol{\tau})_{ij} = \left[\Lambda_{ijkl} - \frac{(\Lambda_{ijtv} P_{tv})(n_{pq} \Lambda_{pqkl})}{h + n_{ab} \Lambda_{abcd} P_{cd}} \right] D_{kl} \quad (2.87)$$

$$\Rightarrow D^*(\boldsymbol{\tau}) = \left[\underline{\underline{\Lambda}} - \frac{\left(\underline{\underline{\Lambda}} : \underline{\underline{P}} \right) \otimes \left(\underline{\underline{n}} : \underline{\underline{\Lambda}} \right)}{h + \underline{\underline{n}} : \underline{\underline{\Lambda}} : \underline{\underline{P}}} \right] : \underline{\underline{D}} \quad (2.88)$$

This leads to the definition of the elastoplastic tangent operator:

$$\underline{\underline{\mathcal{L}}}^* = \underline{\underline{\Lambda}} - \begin{cases} 0 & \text{if } \underline{\underline{n}} : \underline{\underline{\Lambda}} : \underline{\underline{D}} < 0 ; \\ \frac{\left(\underline{\underline{\Lambda}} : \underline{\underline{P}} \right) \otimes \left(\underline{\underline{n}} : \underline{\underline{\Lambda}} \right)}{h + \underline{\underline{n}} : \underline{\underline{\Lambda}} : \underline{\underline{P}}} & \text{if not.} \end{cases} \quad (2.89)$$

Defined as such, $\underline{\underline{\mathcal{L}}}^*$ does not necessarily possess major symmetry⁸. Yet, when the plastic flow rule is associative ($f = g$), it fulfills the normality rule:

$$\underline{\underline{D}}^p = \dot{\lambda} \underline{\underline{P}} = \dot{\lambda} \underline{\underline{n}} \quad (2.90)$$

The elastoplastic tangent operator then becomes:

$$\underline{\underline{\mathcal{L}}}^* = \underline{\underline{\Lambda}} - \begin{cases} 0 & \text{if } \underline{\underline{n}} : \underline{\underline{\Lambda}} : \underline{\underline{D}} < 0 ; \\ \frac{\left(\underline{\underline{\Lambda}} : \underline{\underline{n}} \right) \otimes \left(\underline{\underline{n}} : \underline{\underline{\Lambda}} \right)}{h + \underline{\underline{n}} : \underline{\underline{\Lambda}} : \underline{\underline{n}}} & \text{if not.} \end{cases} \quad (2.91)$$

and possesses major symmetry.

A little more work is still required to formulate the expression of $\underline{\underline{\mathcal{L}}}$ defined in equation (2.22). To simplify calculations, the work will be done with respect to updated Lagrangian quantities ($\hat{\underline{\underline{S}}}$, $\underline{\underline{L}}$)⁹, and linked to the mixed Eulerian/Lagrangian quantities ($\dot{\underline{\underline{S}}}$, $\dot{\underline{\underline{F}}}$):

$$\dot{\underline{\underline{S}}} = \underline{\underline{\mathcal{L}}} : \dot{\underline{\underline{F}}} \Leftrightarrow \hat{\underline{\underline{S}}} = \hat{\underline{\underline{\mathcal{L}}}} : \underline{\underline{L}} \quad (2.92)$$

$$\text{with } \hat{\underline{\underline{S}}} = \frac{1}{J} (\underline{\underline{I}} \boxtimes \underline{\underline{F}}) : \dot{\underline{\underline{S}}} = \hat{\underline{\underline{\tau}}} - \boldsymbol{\sigma} \underline{\underline{L}} \quad (2.93)$$

$$\text{and } \underline{\underline{\mathcal{L}}} = J (\underline{\underline{I}} \boxtimes \underline{\underline{F}}^{-1}) : \hat{\underline{\underline{\mathcal{L}}}} : (\underline{\underline{I}} \boxtimes \underline{\underline{F}}^{-T}) \quad (2.94)$$

⁸ Minor symmetries are implicit since it works on $\underline{\underline{D}}$, and outputs $D^* \boldsymbol{\tau}$ which are both symmetric second order tensors.

⁹ Reminder: $\hat{\underline{\underline{F}}} = \underline{\underline{I}}$, $\hat{\underline{\underline{F}}} = \underline{\underline{L}}$, $\hat{J} = 1$, and $\hat{J} = \text{Tr } \underline{\underline{L}}$.

where \boxtimes denotes the product:

$$(\mathbf{A} \boxtimes \mathbf{B})_{ijkl} = A_{ik}B_{jl} \quad (2.95)$$

Starting from equation (2.93), and after substituting equations (2.66), (2.55) and (2.72), one gets:

$$\dot{\hat{\mathbf{S}}} = \frac{1}{J} \dot{\hat{\boldsymbol{\tau}}} - \boldsymbol{\sigma} \mathbf{L} \quad (2.96)$$

$$J \dot{\hat{\mathbf{S}}} = D^*(\boldsymbol{\tau}) - \mathbf{Q}^{*T} \cdot \dot{\mathbf{Q}}^* \cdot \mathbf{T} - \mathbf{T} \cdot \dot{\mathbf{Q}}^{*T} \cdot \mathbf{Q}^* - \boldsymbol{\tau} \mathbf{L} \quad (2.97)$$

$$J \dot{\hat{\mathbf{S}}} = \mathcal{L}^* : \mathbf{L} - \mathbf{Q}^{*T} \cdot \dot{\mathbf{Q}}^* \cdot \mathbf{T} - \mathbf{T} \cdot \dot{\mathbf{Q}}^{*T} \cdot \mathbf{Q}^* - \boldsymbol{\tau} \mathbf{L} \quad (2.98)$$

Then if it is possible to express $\dot{\mathbf{Q}}^{*T} \mathbf{Q}^*$ as:

$$\dot{\mathbf{Q}}^{*T} \mathbf{Q}^* = \mathbf{A}^* : \mathbf{L} \quad (2.99)$$

where \mathbf{A}^* does not explicitly depend on the rate of any quantity. Then:

$$J \dot{\hat{\mathbf{S}}} = \mathcal{L}^* : \mathbf{L} - (\mathbf{A}^* : \mathbf{L})^T \boldsymbol{\tau} - \boldsymbol{\tau} (\mathbf{A}^* : \mathbf{L}) - \boldsymbol{\tau} \mathbf{L}^T \quad (2.100)$$

$$J \dot{\hat{\mathbf{S}}} = \mathcal{L}^* : \mathbf{L} - (\mathbf{I} \boxplus \boldsymbol{\tau}) : \mathbf{A}^* : \mathbf{L} - (\boldsymbol{\tau} \boxtimes \mathbf{I}) : \mathbf{A}^* : \mathbf{L} - (\boldsymbol{\tau} \boxplus \mathbf{I}) : \mathbf{L}^T \quad (2.101)$$

$$\dot{\hat{\mathbf{S}}} = \frac{1}{J} \left(\mathcal{L}^* - (\mathbf{I} \boxplus \boldsymbol{\tau}) : \mathbf{A}^* - (\boldsymbol{\tau} \boxtimes \mathbf{I}) : \mathbf{A}^* - (\boldsymbol{\tau} \boxplus \mathbf{I}) \right) : \mathbf{L} \quad (2.102)$$

$$\dot{\hat{\mathbf{S}}} = \hat{\mathcal{L}} : \mathbf{L} \quad \text{with} \quad \hat{\mathcal{L}} = \frac{1}{J} \left(\mathcal{L}^* - (\mathbf{I} \boxplus \boldsymbol{\tau}) : \mathbf{A}^* - (\boldsymbol{\tau} \boxtimes \mathbf{I}) : \mathbf{A}^* - (\boldsymbol{\tau} \boxplus \mathbf{I}) \right) \quad (2.103)$$

which gives:

$$\hat{\mathcal{L}} = (\mathbf{I} \boxtimes \mathbf{F}^{-1}) : \left(\mathcal{L}^* - (\mathbf{I} \boxplus \boldsymbol{\tau}) : \mathbf{A}^* - (\boldsymbol{\tau} \boxtimes \mathbf{I}) : \mathbf{A}^* - (\boldsymbol{\tau} \boxplus \mathbf{I}) \right) : (\mathbf{I} \boxtimes \mathbf{F}^{-T}) \quad (2.104)$$

Yet this will be possible only if \mathbf{A}^* exists. In the case of the corotational formulation:

$$\dot{\mathbf{Q}}^{cT} \mathbf{Q}^c = \boldsymbol{\Omega} \quad (2.105)$$

$$= \frac{1}{2} (\mathbf{L} - \mathbf{L}^T) \quad (2.106)$$

$$= \frac{1}{2} [(\mathbf{I} \boxtimes \mathbf{I}) : \mathbf{L} - (\mathbf{I} \boxplus \mathbf{I}) \mathbf{L}] \quad (2.107)$$

$$= \frac{1}{2} (\mathbf{I} \boxtimes \mathbf{I} - \mathbf{I} \boxplus \mathbf{I}) : \mathbf{L} = \mathbf{A}^c : \mathbf{L} \quad (2.108)$$

Which gives:

$$\hat{\mathcal{L}} = \frac{1}{J} \left[\mathcal{L}^* - (\mathbf{I} \boxplus \boldsymbol{\tau}) : \left(\frac{1}{2} \mathbf{I} \boxtimes \mathbf{I} - \frac{1}{2} \mathbf{I} \boxplus \mathbf{I} \right) - (\boldsymbol{\tau} \boxtimes \mathbf{I}) : \left(\frac{1}{2} \mathbf{I} \boxtimes \mathbf{I} - \frac{1}{2} \mathbf{I} \boxplus \mathbf{I} \right) - (\boldsymbol{\tau} \boxplus \mathbf{I}) \right] \quad (2.109)$$

$$= \frac{1}{J} \left[\mathcal{L}^* - \frac{1}{2} \mathbf{I} \boxplus \boldsymbol{\tau} + \frac{1}{2} \mathbf{I} \boxtimes \boldsymbol{\tau} - \frac{1}{2} \boldsymbol{\tau} \boxtimes \mathbf{I} + \frac{1}{2} \boldsymbol{\tau} \boxplus \mathbf{I} - \boldsymbol{\tau} \boxplus \mathbf{I} \right] \quad (2.110)$$

$$= \frac{1}{J} \left[\mathcal{L}^* + \frac{1}{2} \mathbf{I} \boxtimes \boldsymbol{\tau} - \frac{1}{2} \mathbf{I} \boxplus \boldsymbol{\tau} - \frac{1}{2} \boldsymbol{\tau} \boxtimes \mathbf{I} - \frac{1}{2} \boldsymbol{\tau} \boxplus \mathbf{I} \right] \quad (2.111)$$

Remark: $\underline{\underline{\mathcal{L}}}^*$ is usually called “material stiffness”, and the added stress terms are often called “geometrical stiffness”. Yet, this name can be confusing since they do not only depend on the geometry and the current stresses, but also on the finite deformation formulation one uses. This is further detailed in chapter 8 for other formulations. Yet this is already clear whether one chooses to use $\underline{\underline{\boldsymbol{\tau}}}$, $\underline{\underline{\hat{\boldsymbol{\tau}}}}$ or $\underline{\underline{\boldsymbol{\sigma}}}$ as the stress measure. In particular, for the last option, a term of the form: $\underline{\underline{\boldsymbol{\sigma}}} \otimes \underline{\underline{\mathbf{I}}}$, which does not possess major symmetry, would be added. In contrast, as can be seen in equation (2.111), $\underline{\underline{\mathcal{L}}}$ possesses global symmetry when formulated with $\underline{\underline{\boldsymbol{\tau}}}$ or $\underline{\underline{\hat{\boldsymbol{\tau}}}}$. This property is lost when formulated with $\underline{\underline{\boldsymbol{\sigma}}}$ [Hill, 1958, Pinsky et al., 1986, Ortiz, 1987, Bigoni and Hueckel, 1991, Bigoni and Zaccaria, 1993]. Furthermore, this loss of symmetry generally leads to a slow convergence of the Newton algorithm in the FEM problem. Therefore, in the present work, $\underline{\underline{\boldsymbol{\tau}}}$ and $\underline{\underline{\hat{\boldsymbol{\tau}}}}$ are generally used.

Sometimes, one cannot explicitly formulate a tensor $\underline{\underline{\mathbf{A}}}^*$. For example, for the polar local referential, the expression of $\underline{\underline{\mathbf{A}}}^*$ that is commonly used is the same as the one derived for the corotational formulation. However, $\underline{\underline{\boldsymbol{\Omega}}} \neq \underline{\underline{\dot{\mathbf{R}}}}\underline{\underline{\mathbf{R}}}^T$ and one can express the difference as follows:

$$\underline{\underline{\boldsymbol{\Omega}}} = \frac{1}{2}(\underline{\underline{\mathbf{L}}} - \underline{\underline{\mathbf{L}}}^T) \quad (2.112)$$

$$= \frac{1}{2}(\underline{\underline{\dot{\mathbf{R}}}}\underline{\underline{\mathbf{R}}}^T + \underline{\underline{\mathbf{R}}}\underline{\underline{\dot{\mathbf{U}}}}\underline{\underline{\mathbf{U}}}^{-1}\underline{\underline{\mathbf{R}}}^T - (\underline{\underline{\mathbf{R}}}\underline{\underline{\dot{\mathbf{R}}}}^T + \underline{\underline{\mathbf{R}}}\underline{\underline{\mathbf{U}}}^{-1}\underline{\underline{\dot{\mathbf{U}}}}\underline{\underline{\mathbf{R}}}^T)) \quad (2.113)$$

$$= \underline{\underline{\dot{\mathbf{R}}}}\underline{\underline{\mathbf{R}}}^T + \frac{1}{2}\underline{\underline{\mathbf{R}}}(\underline{\underline{\dot{\mathbf{U}}}}\underline{\underline{\mathbf{U}}}^{-1} - \underline{\underline{\mathbf{U}}}^{-1}\underline{\underline{\dot{\mathbf{U}}}})\underline{\underline{\mathbf{R}}}^T \quad (2.114)$$

$$\underline{\underline{\boldsymbol{\Omega}}} - \underline{\underline{\dot{\mathbf{R}}}}\underline{\underline{\mathbf{R}}}^T = \frac{1}{2}\underline{\underline{\mathbf{R}}}(\underline{\underline{\dot{\mathbf{U}}}}\underline{\underline{\mathbf{U}}}^{-1} - \underline{\underline{\mathbf{U}}}^{-1}\underline{\underline{\dot{\mathbf{U}}}})\underline{\underline{\mathbf{R}}}^T \quad (2.115)$$

In this case, the resulting error strongly depends on the norm of the skew part of $\underline{\underline{\dot{\mathbf{U}}}}\underline{\underline{\mathbf{U}}}^{-1}$. For instance, when $\underline{\underline{\mathbf{U}}}$ is diagonal, then both polar and corotational formulations are equivalent. More generally, when $\underline{\underline{\dot{\mathbf{U}}}}$ and $\underline{\underline{\mathbf{U}}}^{-1}$ commute the difference vanishes.

2.2.4 Summary

For future reference the equations described above are summarized here:

- $\forall \underline{\underline{\mathbf{X}}} \in \Omega_0$:

$$\left\{ \begin{array}{ll} \underline{\underline{\mathbf{F}}} = \frac{\partial \underline{\underline{\mathbf{x}}}}{\partial \underline{\underline{\mathbf{X}}}} & \text{Deformation gradient} \\ \underline{\underline{\mathbf{L}}} = \underline{\underline{\dot{\mathbf{F}}}}\underline{\underline{\mathbf{F}}}^{-1} & \text{Eulerian velocity gradient} \\ \underline{\underline{\boldsymbol{\Omega}}} = \frac{1}{2}(\underline{\underline{\mathbf{L}}} - \underline{\underline{\mathbf{L}}}^T) & \text{Spin tensor} \\ \underline{\underline{\mathbf{D}}} = \frac{1}{2}(\underline{\underline{\mathbf{L}}} + \underline{\underline{\mathbf{L}}}^T) & \text{Strain rate tensor} \\ \underline{\underline{\mathbf{D}}} = \underline{\underline{\mathbf{D}}}^e + \underline{\underline{\mathbf{D}}}^p & \text{Additive decomposition} \\ \underline{\underline{\mathbf{A}}}^* = \underline{\underline{\mathbf{Q}}}^* \underline{\underline{\mathbf{A}}}\underline{\underline{\mathbf{Q}}}^{*T} & \text{Rotation in a local objective frame} \\ \underline{\underline{\dot{\boldsymbol{\tau}}}}^* = \underline{\underline{\boldsymbol{\Lambda}}}^* : \underline{\underline{\mathbf{D}}}^* \text{ or } \underline{\underline{D}}^*(\underline{\underline{\boldsymbol{\tau}}}) = \underline{\underline{\boldsymbol{\Lambda}}} : \underline{\underline{\mathbf{D}}}^e & \text{Rate elasticity law} \\ \text{avec } \Lambda_{ijkl} = \Lambda_{pqrs}^* Q_{pi}^* Q_{qj}^* Q_{rk}^* Q_{sl}^* & \\ \underline{\underline{D}}^*(\underline{\underline{\boldsymbol{\tau}}}) = \underline{\underline{\dot{\boldsymbol{\tau}}}} + \underline{\underline{\mathbf{Q}}}^{*T} \underline{\underline{\dot{\mathbf{Q}}}}^* \underline{\underline{\boldsymbol{\tau}}} + \underline{\underline{\boldsymbol{\tau}}}\underline{\underline{\dot{\mathbf{Q}}}}^{*T} \underline{\underline{\mathbf{Q}}}^* & \text{Objective derivative of associated with} \\ & \text{the local referential“*”} \end{array} \right.$$

- Plastic flow rule ($\underline{\mathbf{n}} : \underline{\underline{\Lambda}} : \underline{\underline{D}} \geq 0$ and $f(\underline{\underline{\tau}}^*, \underline{\underline{X}}^*) = 0$):

$$\left\{ \begin{array}{ll} \underline{\mathbf{n}} = \underline{\underline{Q}}^{*T} \cdot \frac{\partial f}{\partial \underline{\underline{\tau}}^*} \cdot \underline{\underline{Q}}^* & \text{Normal to yield surface} \\ \underline{\underline{D}}^p = \lambda \underline{\underline{Q}}^{*T} \cdot \frac{\partial g}{\partial \underline{\underline{\tau}}^*} \cdot \underline{\underline{Q}}^* = \lambda \underline{\underline{P}} & \text{Plastic strain rate} \\ \dot{\underline{\underline{\alpha}}}^* = -\lambda \frac{\partial F}{\partial \underline{\underline{X}}^*} = -\lambda \underline{\underline{M}} & \text{Hardening} \\ h = \frac{\partial f}{\partial \underline{\underline{X}}^*} : \frac{\partial \underline{\underline{X}}^*}{\partial \underline{\underline{\alpha}}^*} : \frac{\partial F}{\partial \underline{\underline{X}}^*} & \text{Hardening modulus} \\ \lambda = \frac{\underline{\underline{n}}^* : \underline{\underline{\Lambda}}^* : \underline{\underline{D}}^*}{h + \underline{\underline{n}}^* : \underline{\underline{\Lambda}}^* : \underline{\underline{P}}^*} \geq 0 & \text{Plastic multiplier} \end{array} \right.$$

- Elastoplastic tangent operator in local objective frame:

$$\left\{ \begin{array}{l} D^*(\underline{\underline{\tau}}) = \underline{\underline{\mathcal{L}}}^* : \underline{\underline{D}} \\ \text{where } \underline{\underline{\mathcal{L}}}^* = \underline{\underline{\Lambda}} - \begin{cases} 0 & \text{If } \underline{\underline{n}} : \underline{\underline{\Lambda}} : \underline{\underline{D}} < 0 ; \\ \frac{(\underline{\underline{\Lambda}} : \underline{\underline{P}}) \otimes (\underline{\underline{n}} : \underline{\underline{\Lambda}})}{h + \underline{\underline{n}} : \underline{\underline{\Lambda}} : \underline{\underline{P}}} & \text{else.} \end{cases} \\ \underline{\underline{P}} = \underline{\underline{n}} \text{ for associative flow rule.} \end{array} \right.$$

- Elastoplastic tangent operator for corotational formulation on $\underline{\underline{\tau}}$:

$$\left\{ \begin{array}{l} \dot{\underline{\underline{S}}} = \underline{\underline{\mathcal{L}}} : \dot{\underline{\underline{F}}} \\ \text{where } \underline{\underline{\mathcal{L}}} = (\underline{\underline{I}} \boxtimes \underline{\underline{F}}^{-1}) : \left[\underline{\underline{\mathcal{L}}}^* + \frac{1}{2}(\underline{\underline{I}} \boxtimes \underline{\underline{\tau}} - \underline{\underline{I}} \boxplus \underline{\underline{\tau}} - \underline{\underline{\tau}} \boxtimes \underline{\underline{I}} - \underline{\underline{\tau}} \boxplus \underline{\underline{I}}) \right] : (\underline{\underline{I}} \boxtimes \underline{\underline{F}}^{-T}) \end{array} \right.$$

2.3 FEM formulation of finite deformation problems

In the following sections, the FEM is presented for a finite deformation framework. First the weak formulations for the boundary and rate boundary value problem are presented, then the construction of the tangent and global stiffness matrix are detailed. Finally, the application of Dirichlet boundary conditions is briefly presented.

For the sake of brevity, let us introduce the Lagrangian quantities: the Piola Kirchhoff stress tensor $\underline{\underline{\Pi}}$, and the Green Lagrange strain tensors $\underline{\underline{E}}$:

$$\underline{\underline{\Pi}} = \underline{\underline{F}}^{-1} \underline{\underline{\tau}} \underline{\underline{F}}^{-T} \quad (2.116)$$

$$\underline{\underline{E}} = \frac{1}{2}(\underline{\underline{F}}^T \underline{\underline{F}} - \underline{\underline{I}}) \quad (2.117)$$

which are both Lagrangian tensors. The tangent operator $\underline{\underline{\mathcal{L}}}^{\Pi}$ can also be formulated (under the same restrictions as $\underline{\underline{\mathcal{L}}}$) so that it fulfills:

$$\dot{\underline{\underline{\Pi}}} = \underline{\underline{\mathcal{L}}}^{\Pi} : \dot{\underline{\underline{E}}} \quad (2.118)$$

Like $\underline{\underline{\mathcal{L}}}$, $\underline{\underline{\mathcal{L}}}^{\Pi}$ may contain some "geometrical terms" depending on how the constitutive law is formulated (see Appendix, section 8.1).

2.3.1 Weak formulations

Equilibrium boundary value problem

Based on section 2.1.1 and section 2.1.2 the following equilibrium problem can be formulated (in the absence of volume forces)¹⁰:

$$\mathbf{Div}(\underline{\mathcal{S}}) = \mathbf{0} \quad \forall \underline{\mathbf{X}} \in \Omega_0 \quad (2.119)$$

$$\underline{\mathbf{u}} = \underline{\mathbf{u}}^a \quad \forall \underline{\mathbf{X}} \in \partial\Omega_0^u \quad (2.120)$$

$$\underline{\mathcal{S}} \cdot \underline{\mathbf{N}} = \underline{\mathbf{T}}^a \quad \forall \underline{\mathbf{X}} \in \partial\Omega_0^T \quad (2.121)$$

In equation (2.121) only dead loads are considered¹¹.

Let $\delta\underline{\hat{\mathbf{u}}}$ be some arbitrary test field (regular and derivable). Projection of equation (2.119) on $\delta\underline{\hat{\mathbf{u}}}$ and integration over the whole domain Ω_0 gives:

$$0 = \int_{\Omega_0} \mathbf{div}(\underline{\mathcal{S}}) \cdot \delta\underline{\hat{\mathbf{u}}} dV_0 \quad (2.122)$$

$$\int_{\Omega_0} \underline{\mathcal{S}} : \underline{\nabla}(\delta\underline{\hat{\mathbf{u}}}) dV_0 = \int_{\partial\Omega_0} (\underline{\mathcal{S}} \cdot \underline{\mathbf{N}}) \cdot \delta\underline{\hat{\mathbf{u}}} dS \quad (2.123)$$

$$\int_{\Omega_0} \underline{\mathcal{S}} : \delta\underline{\hat{\mathbf{F}}} dV_0 = \int_{\partial\Omega_0^T} (\underline{\mathcal{S}} \cdot \underline{\mathbf{N}})_i (\delta\underline{\hat{\mathbf{u}}})_i dS + \int_{\partial\Omega_0^u} (\underline{\mathcal{S}} \cdot \underline{\mathbf{N}})_i (\delta\underline{\hat{\mathbf{u}}})_i dS \quad (2.124)$$

$$\int_{\Omega_0} \underline{\mathcal{S}} : \delta\underline{\hat{\mathbf{F}}} dV_0 = \int_{\partial\Omega_0^T} T_i^a (\delta\underline{\hat{\mathbf{u}}})_i dS + \int_{\partial\Omega_0^u} (\underline{\mathcal{S}} \cdot \underline{\mathbf{N}})_i (\delta\underline{\hat{\mathbf{u}}})_i dS \quad (2.125)$$

where $\delta\underline{\hat{\mathbf{F}}} = \underline{\nabla}(\delta\underline{\hat{\mathbf{u}}})$. Since $\delta\underline{\hat{\mathbf{u}}}$ is arbitrary, one can choose $\delta\underline{\hat{\mathbf{u}}}$ kinematically admissible to 0:

$$(\delta\underline{\hat{\mathbf{u}}})_i = 0 \quad \forall \underline{\mathbf{X}} \in \partial\Omega_0^u \quad (2.126)$$

$$\text{noted: } \delta\underline{\hat{\mathbf{u}}} \in \text{CA0} \quad (2.127)$$

Then one has:

$$\int_{\Omega_0} \underline{\mathcal{S}} : \delta\underline{\hat{\mathbf{F}}} dV_0 = \int_{\partial\Omega_0^T} T_i^a (\delta\underline{\hat{\mathbf{u}}})_i dS \quad \forall \delta\underline{\hat{\mathbf{u}}} \in \text{CA0} \quad (2.128)$$

Without any restriction, this problem can equivalently be written as:

$$\int_{\Omega_0} \underline{\mathbf{\Pi}} : \delta\underline{\hat{\mathbf{E}}} dV_0 = \int_{\partial\Omega_0^T} T_i^a (\delta\underline{\hat{\mathbf{u}}})_i dS \quad \forall \delta\underline{\hat{\mathbf{u}}} \in \text{CA0} \quad (2.129)$$

$$\int_{\Omega} \underline{\hat{\mathcal{S}}} : \underline{\mathbf{L}} dV = \int_{\partial\Omega_0^T} T_i^a (\delta\underline{\hat{\mathbf{u}}})_i dS \quad \forall \delta\underline{\hat{\mathbf{u}}} \in \text{CA0} \quad (2.130)$$

where $\delta\underline{\hat{\mathbf{L}}} = \delta\underline{\hat{\mathbf{F}}}\underline{\mathbf{F}}^{-1}$, $\delta\underline{\hat{\mathbf{D}}} = \delta\underline{\hat{\mathbf{L}}}^{sym}$ and $\delta\underline{\hat{\mathbf{E}}} = \underline{\mathbf{F}}^T \delta\underline{\hat{\mathbf{D}}}\underline{\mathbf{F}}$. The three formulations will be derived in this section since all are used in FEM software for various purposes. While they all imply solving the exact same problem, one should be aware of the difference when implementing a material law.

¹⁰ These are not difficult to add, but are not of interest in the present work [Hill, 1958].

¹¹ Considering following forces like pressure are possible, yet have no particular interest for the general FEM formulation. Following forces would imply another term to add to the global stiffness matrix, and this is detailed in [Nefussi and Combescure, 2002, Mazière, 2007, Mazière et al., 2009].

Rate boundary value problem

Following the same procedure but starting with the set of equations given in 2.1.3 one has:

$$\begin{aligned} \int_{\Omega_0} \dot{\underline{\mathbf{S}}} : \delta \hat{\underline{\mathbf{F}}} dV_0 &= \int_{\partial\Omega_0^T} \dot{T}_i^a(\delta \hat{\underline{\mathbf{u}}})_i dS \\ \int_{\Omega_0} \dot{\underline{\mathbf{F}}} : \underline{\underline{\mathcal{L}}} : \delta \hat{\underline{\mathbf{F}}} dV_0 &= \int_{\partial\Omega_0^T} \dot{T}_i^a(\delta \hat{\underline{\mathbf{u}}})_i dS \quad \forall \delta \hat{\underline{\mathbf{u}}} \in \text{CA0} \end{aligned} \quad (2.131)$$

or equivalently:

$$\begin{aligned} \int_{\Omega_0} \dot{\underline{\mathbf{\Pi}}} : \delta \hat{\underline{\mathbf{E}}} + \underline{\underline{\mathbf{\Pi}}} : (\dot{\underline{\mathbf{F}}}^T \delta \hat{\underline{\mathbf{F}}}) dV_0 &= \int_{\partial\Omega_0^T} \dot{T}_i^a(\delta \hat{\underline{\mathbf{u}}})_i dS \quad \forall \delta \hat{\underline{\mathbf{u}}} \in \text{CA0} \\ \int_{\Omega_0} \dot{\underline{\mathbf{E}}} : \underline{\underline{\mathcal{L}}}^{\text{II}} : \delta \hat{\underline{\mathbf{E}}} + \underline{\underline{\mathbf{\Pi}}} : (\dot{\underline{\mathbf{F}}}^T \delta \hat{\underline{\mathbf{F}}}) dV_0 &= \int_{\partial\Omega_0^T} \dot{T}_i^a(\delta \hat{\underline{\mathbf{u}}})_i dS \quad \forall \delta \hat{\underline{\mathbf{u}}} \in \text{CA0} \end{aligned} \quad (2.132)$$

and:

$$\begin{aligned} \int_{\Omega} \dot{\underline{\mathbf{S}}} : \delta \hat{\underline{\mathbf{L}}} dV &= \int_{\partial\Omega_0^T} \dot{T}_i^a(\delta \hat{\underline{\mathbf{u}}})_i dS \quad \forall \delta \hat{\underline{\mathbf{u}}} \in \text{CA0} \\ \Rightarrow \int_{\Omega} \dot{\underline{\mathbf{F}}} : \underline{\underline{\mathcal{L}}} : \delta \hat{\underline{\mathbf{F}}} dV &= \int_{\partial\Omega_0^T} \dot{T}_i^a(\delta \hat{\underline{\mathbf{u}}})_i dS \quad \forall \delta \hat{\underline{\mathbf{u}}} \in \text{CA0} \end{aligned} \quad (2.133)$$

2.3.2 Discretization

A FEM problem is based on the projection of the solution onto a finite number of shape functions defined for each node. This leads to the definition of a discretized problem that, when well-posed¹², has a solution that approximates the exact solution. Let us denote by n the number of nodes that define the mesh, u_i^k the value of the i^{th} component of the k^{th} node, and $N^k(\underline{\mathbf{X}})$ the shape function associated to the k^{th} node. From here, a displacement field in this finite space can be decomposed as:

$$u_i = \sum_{k=1}^n N^k(\underline{\mathbf{x}}) u_i^k \quad (2.134)$$

Equation (2.134) can be written with a matrix vector product by introducing $[\mathbf{N}(\underline{\mathbf{x}})]$, such that:

$$\underline{\mathbf{u}}(x) = [\mathbf{N}(\underline{\mathbf{x}})] \cdot \{\underline{\mathbf{u}}\} \quad (2.135)$$

where $\{\underline{\mathbf{u}}\}$ denotes the column matrix of the u_i^k . The gradient can then be expressed as:

$$\frac{\partial u_i}{\partial x_j} = \sum_{k=1}^n \frac{\partial N^k(\underline{\mathbf{x}})}{\partial x_j} u_i^k \quad (2.136)$$

This leads to the definition of a derivation matrix $[\mathbf{B}_{\underline{\mathbf{F}}}]$, defined such that:

$$\{\underline{\nabla}(\underline{\mathbf{u}})\} = [\mathbf{B}_{\underline{\mathbf{F}}}] \cdot \{\underline{\mathbf{u}}\} \quad (2.137)$$

where $\{\underline{\nabla}(\underline{\mathbf{u}})\}$ the column matrix of the $\frac{\partial u_i}{\partial x_j}$. In a general way, we will denote $\{\underline{\mathbf{A}}\}$ the vector of the A_{ij} components of a second order tensor $\underline{\underline{\mathbf{A}}}$. There are different ways to set such a vector, yet, in the present work the order is consistent with the one in `Zset` code : $\{A_{11}, A_{22}, A_{33}, A_{12}, A_{23}, A_{31}, A_{21}, A_{32}, A_{13}\}$.

¹² Which is actually the critical question for the present work.

2.3.3 Numerical global problem

The variational problem defined in equation (2.128) (or equivalently for the problems defined by equations (2.129) and (2.130)), becomes after discretization ($\forall \delta \hat{\mathbf{u}} \in \text{CA0}$) :

$$\begin{aligned} \int_{\Omega_0} \{\underline{\mathcal{S}}\}^T \cdot [\underline{\mathbf{B}}_{\dot{\mathbf{F}}}] \cdot \{\delta \hat{\mathbf{u}}\} dV_0 &= \int_{\partial\Omega_0} \{\underline{\mathbf{T}}^a\}^T \cdot [\underline{\mathbf{N}}] \cdot \{\delta \hat{\mathbf{u}}\} dS_0 + \\ \left[\int_{\Omega_0} \{\underline{\mathcal{S}}\}^T \cdot [\underline{\mathbf{B}}_{\dot{\mathbf{F}}}] dV_0 \right] \cdot \{\delta \hat{\mathbf{u}}\} &= \int_{\partial\Omega_0} \{\underline{\mathbf{T}}^a\}^T \cdot [\underline{\mathbf{N}}] dS_0 \cdot \{\delta \hat{\mathbf{u}}\} \\ \Rightarrow \{\mathbf{F}_i(\underline{\mathbf{u}}(t))\} &= \int_{\Omega_0} [\underline{\mathbf{B}}_{\dot{\mathbf{F}}}]^T \cdot \{\underline{\mathcal{S}}\} dV_0 = \int_{\partial\Omega_0} [\underline{\mathbf{N}}]^T \cdot \{\underline{\mathbf{T}}^a\} dS_0 = \{\mathbf{F}_e(t)\} \end{aligned} \quad (2.138)$$

where $\{\mathbf{F}_i(\underline{\mathbf{u}}(t))\}$ and $\{\mathbf{F}_e(t)\}$ respectively denote the vectors of internal and external forces¹³.

As elastoplastic problems are path dependent, it is necessary to compute equilibrium configurations while gradually loading the structure. Therefore, a time discretization fine enough to consider path dependency has to be defined to compute the final solution of the problem incrementally. At each load step, the incremental problem to solve is given by:

$$\{\mathbf{F}_i(\underline{\mathbf{u}}(t + \Delta t))\} = \{\mathbf{F}_e(t + \Delta t)\} \quad (2.139)$$

Global stiffness matrix

For each load increment from the instant t to the instant $t + \Delta t$, a displacement increment $\underline{\Delta \mathbf{u}} = \underline{\mathbf{u}}(t + \Delta t) - \underline{\mathbf{u}}(t)$ must be computed. In order to evaluate $\underline{\Delta \mathbf{u}}$, a sequence $\underline{\Delta \mathbf{u}}^k$ is defined such that $\underline{\Delta \mathbf{u}}^{k+1} = \underline{\Delta \mathbf{u}}^k + \underline{\delta \mathbf{u}}^{k+1}$ converges toward $\underline{\Delta \mathbf{u}}$. $\underline{\Delta \mathbf{u}}^0$ is generally chosen to be zero to initialize the sequence. However, it can be specified to other values in order to accelerate convergence¹⁴. For each iteration, $\underline{\delta \mathbf{u}}^{k+1}$ can be evaluated based on a first order expansion of $\{\mathbf{F}_i(\underline{\mathbf{u}}(t + \Delta t))\}$:

$$\{\mathbf{F}_i(\underline{\mathbf{u}}(t) + \underline{\Delta \mathbf{u}}^k + \underline{\delta \mathbf{u}}^{k+1})\} = \{\mathbf{F}_e(t + \Delta t)\} \quad (2.140)$$

$$\{\mathbf{F}_i(\underline{\mathbf{u}}(t) + \underline{\Delta \mathbf{u}}^k)\} + \frac{\partial \{\mathbf{F}_i(\underline{\mathbf{u}} + \underline{\Delta \mathbf{u}}^k)\}}{\partial \{\underline{\mathbf{u}}\}} \cdot \{\underline{\delta \mathbf{u}}^{k+1}\} = \{\mathbf{F}_e(t + \Delta t)\} \quad (2.141)$$

$$\frac{\partial \{\mathbf{F}_i(\underline{\mathbf{u}} + \underline{\Delta \mathbf{u}}^k)\}}{\partial \{\underline{\mathbf{u}}\}} \cdot \{\underline{\delta \mathbf{u}}^{k+1}\} = \{\mathbf{F}_e(t + \Delta t)\} - \{\mathbf{F}_i(\underline{\mathbf{u}}(t) + \underline{\Delta \mathbf{u}}^k)\} \quad (2.142)$$

$$[\mathbf{K}^k] \cdot \{\underline{\delta \mathbf{u}}^{k+1}\} = \{\mathbf{R}^k\} \quad (2.143)$$

$$\text{where } [\mathbf{K}^k] = \frac{\partial \{\mathbf{F}_i(\underline{\mathbf{u}} + \underline{\Delta \mathbf{u}}^k)\}}{\partial \{\underline{\mathbf{u}}\}} \quad (2.144)$$

$$\text{and } \{\mathbf{R}^k\} = \{\mathbf{F}_e(t + \Delta t)\} - \{\mathbf{F}_i(\underline{\mathbf{u}}(t) + \underline{\Delta \mathbf{u}}^k)\} \quad (2.145)$$

This is the well-known Newton Raphson scheme to solve nonlinear problems. It has a quadratic convergence if the problem is sufficiently smooth and the last estimate is sufficiently close to the solution. To do so, one needs to evaluate the global stiffness matrix, $[\mathbf{K}^k]$, which is obtained

¹³ Note that ‘‘internal’’ can be an ambiguous term in a finite deformation framework since it can also include terms due to following forces

¹⁴ Typically, for a monotonic loading, using the displacement increment obtained for the previous time-step can be a very good starting point.

by assembling the element stiffness matrices $[\mathbf{K}^k]_{elem}$:

$$\begin{aligned}
[\mathbf{K}^k]_{elem} &= \frac{\partial \int_{\Omega_0^e} [\mathbf{B}_{\dot{\mathbf{F}}}]^T \cdot \{\mathfrak{S}(\mathbf{u} + \Delta \mathbf{u}^k)\} dV_0^e}{\partial \{\mathbf{u}\}} \\
&= \int_{\Omega_0^e} [\mathbf{B}_{\dot{\mathbf{F}}}]^T \cdot \frac{\partial \{\mathfrak{S}(\mathbf{u} + \Delta \mathbf{u}^k)\}}{\partial \{\mathbf{u}\}} dV_0^e \\
&= \int_{\Omega_0^e} [\mathbf{B}_{\dot{\mathbf{F}}}]^T \cdot \frac{\partial \{\mathfrak{S}(\mathbf{u} + \Delta \mathbf{u}^k)\}}{\partial \{\mathfrak{F}\}} \cdot \frac{\partial \{\mathfrak{F}\}}{\partial \{\mathbf{u}\}} dV_0^e \\
&= \int_{\Omega_0^e} [\mathbf{B}_{\dot{\mathbf{F}}}]^T \cdot \left[\mathfrak{L}(\mathbf{u} + \Delta \mathbf{u}^k) \right] \cdot [\mathbf{B}_{\dot{\mathbf{F}}}] dV_0^e
\end{aligned} \tag{2.146}$$

where $\left[\mathfrak{L} \right]$ is the matrix defined such that:

$$\{\dot{\mathfrak{S}}\} = \left\{ \mathfrak{L} : \dot{\mathfrak{F}} \right\} = \left[\mathfrak{L} \right] \cdot \{\dot{\mathfrak{F}}\} \tag{2.147}$$

$$\tag{2.148}$$

and Ω_0^e is the volume filled by the element in the reference configuration. Usually, in an incremental framework, $\left[\mathfrak{L} \right]$ is replaced by $\left[\mathfrak{L}_c \right]$ where “c” stands for “consistent” tangent operator, meaning consistent with the integration scheme.

Finite deformation formulation in Z-set [Besson and Foerch, 1997]

It has been shown that the weak formulation of the problem can be calculated in different strictly equivalent ways (see equations (2.131), (2.132) and (2.133)). As detailed in section 8.1, some laws are defined using $\mathfrak{\Pi}$, therefore, it seems more convenient to use equation (2.132) to formulate the problem. Then the element stiffness matrix should be defined [Besson et al., 2010] as:

$$[\mathbf{K}^k]_{elem} = \int_{\Omega_0^e} [\mathbf{B}_{\dot{\mathbf{E}}}]^T \cdot \left[\mathfrak{L}^{\mathfrak{\Pi}}(\mathbf{u} + \Delta \mathbf{u}^k) \right] \cdot [\mathbf{B}_{\dot{\mathbf{E}}}] + [\mathbf{B}_{\dot{\mathbf{F}}}]^T \left[M_L(\mathfrak{\Pi}(\mathbf{u} + \Delta \mathbf{u}^k)) \right] \cdot [\mathbf{B}_{\dot{\mathbf{F}}}] dV_0^e \tag{2.149}$$

$$\text{where } [\mathbf{B}_{\dot{\mathbf{E}}}] \text{ is defined such that: } \{\dot{\mathfrak{E}}\} = [\mathbf{B}_{\dot{\mathbf{E}}}] \cdot \{\dot{\mathbf{u}}\} \tag{2.150}$$

$$\text{and } [M_L(\mathfrak{A})] \text{ is the matrix such that: } \{\mathfrak{A}\mathfrak{B}\} = [M_L(\mathfrak{A})] \cdot \{\mathfrak{B}\} \tag{2.151}$$

Remark 1: It turns out there is no particular advantage and it requires calculating and assembling more terms. It also leads to more complex coding. Finally, the matrix $[\mathbf{B}_{\dot{\mathbf{E}}}]$ does not have a simple expression [Besson et al., 2010]. Therefore, it may be more convenient to do the work on the tangent operator: express \mathfrak{L} based on $\mathfrak{L}^{\mathfrak{\Pi}}$ and $\mathfrak{\Pi}$, as detailed in section 8.1.

Remark 2: Note that the stiffness matrix is updated for each iteration and depends on the last evaluation for this process: stresses, displacements, internal variables, etc. This has two consequences:

1. *For elastoplastic problems, it is necessary to evaluate if the elastic unloading / plastic unloading condition is fulfilled in order to calculate the local tangent operator. This condition is usually estimated to be the same as the last load increment: Gauss points where the plastic loading condition is fulfilled at the last load increment are assumed to stay in plastic loading for the next load increment (same for elastic unloading);*

2. Re-evaluating $[\mathbf{K}]$ at each iteration can be very expensive. In fact, the most expensive part is not the local evaluation of the elementary matrices, or the assembly (although, it is expensive), but the Cholesky factorization of $[\mathbf{K}]$ into a $[\mathbf{L}][\mathbf{U}]$ form. Still, it might be necessary to re-evaluate it for highly non linear problems (like finite deformation elastoplastic problems).

Global tangent matrix

In section 2.3.3, the discretization of the incremental problem led to the definition of a global stiffness matrix. In the following paragraph, the same procedure is applied to the rate problem and will lead to the definition of a global tangent matrix.

Starting from equation (2.131) the discretized problem is given by:

$$\begin{aligned} \int_{\Omega_0} \{\delta \hat{\mathbf{u}}\}^T \cdot [\mathbf{B}_{\dot{\mathbf{F}}}]^T \cdot \left[\underset{\approx}{\mathcal{L}}(\mathbf{u}) \right] \cdot [\mathbf{B}_{\dot{\mathbf{F}}}] \cdot \{\dot{\mathbf{u}}\} dV_0 &= \int_{\partial\Omega_0^T} \{\dot{\mathbf{T}}^a\}^T \cdot [\mathbf{N}] \cdot \{\delta \hat{\mathbf{u}}\} dS_0 \\ \{\delta \hat{\mathbf{u}}\}^T \cdot \left[\int_{\Omega_0} [\mathbf{B}_{\dot{\mathbf{F}}}]^T \cdot \left[\underset{\approx}{\mathcal{L}}(\mathbf{u}) \right] \cdot [\mathbf{B}_{\dot{\mathbf{F}}}] dV_0 \right] \cdot \{\dot{\mathbf{u}}\} &= \{\delta \hat{\mathbf{u}}\}^T \cdot \left[\int_{\partial\Omega_0^T} [\mathbf{N}]^T \cdot \{\dot{\mathbf{T}}^a\} dS_0 \right] \\ &\Rightarrow \{\dot{\mathbf{F}}_i(\mathbf{u})\} = [\mathbf{K}_{tan}(\mathbf{u})] \cdot \{\dot{\mathbf{u}}\} = \{\dot{\mathbf{F}}_e\} \end{aligned}$$

where $\delta \hat{\mathbf{u}}$ is an arbitrary test field ($\delta \hat{\mathbf{u}} \in \text{CA0}$), and $[\mathbf{K}_{tan}(\mathbf{u})]$ is global tangent matrix obtained by assembling the elementary tangent matrices:

$$[\mathbf{K}_{tan}(\mathbf{u})]_{elem} = \int_{\Omega_0^e} [\mathbf{B}_{\dot{\mathbf{F}}}]^T \cdot \left[\underset{\approx}{\mathcal{L}}(\mathbf{u}) \right] \cdot [\mathbf{B}_{\dot{\mathbf{F}}}] dV_0^e \quad (2.152)$$

Assuming that the elastic unloading/plastic loading condition is known at every Gauss point, one can build the global tangent matrix for any equilibrium configuration. Comparing with the incremental problem, the global and tangent matrices are the same when the time-steps are infinitesimal [Besson et al., 2001]. Therefore, for sufficiently small time-steps:

$$[\mathbf{K}_{tan}(\mathbf{u}(t + \Delta t))] = [\mathbf{K}(\mathbf{u} + \Delta \mathbf{u}^\infty)] \quad (2.153)$$

where $[\mathbf{K}(\mathbf{u} + \Delta \mathbf{u}^\infty)]$ is the global stiffness matrix evaluated after convergence of the last increment.

Remark: In the rest of the work no major difference will be made between the global stiffness matrix and the global tangent matrix. In all the numerical computations presented later, the time-stepping is sufficiently small for both matrices to essentially coincide.

2.3.4 Application of Dirichlet boundary conditions

Up to now, nothing has been said about how Dirichlet Boundary Conditions (DBC) are taken into account. To build the global stiffness matrix, only the equilibrium equation was necessary; and to build the external forces vector, only the Neumann Boundary Conditions (NBC) were used. In fact, the DBCs are implicitly hidden in the displacement vector $\{\mathbf{u}\}$:

$$\{\mathbf{u}\}^T = \left\{ u_1^1, u_2^1, \dots, (u^a)_1^k, (u^a)_2^k, \text{etc.} \right\} \quad (2.154)$$

where $(u^a)_i^k$ are fixed displacements from the DBCs. Thus it is possible to define a vector $\{\mathbf{DoF}\}$ (where *DoF* stands for ‘‘Degree of freedom’’), such that no DBCs are stored in this vector:

$$\{\mathbf{DoF}\}^T = \left\{ u_1^1, u_2^1, \dots, u_1^{k+1}, u_2^{k+1}, \text{etc.} \right\} \quad (2.155)$$

then one can modify $[K]$ to build the associated matrix $[K^{DBC}]$ such that:

$$[K^{DBC}] \cdot \{Dof\} = \{R\} \quad (2.156)$$

Where $\{R\}$ is the new residual consistent with the reduced problem. If there are n nodes, each having dim number of degrees of freedom, and f number of degrees of freedom that are fixed, then the real system to solve should be of size $(n * dim - f)$.

There are multiple ways to apply the DBCs. For instance, one can strictly reduce the size of all vectors and matrices adding the adequate terms in $[K^{DBC}]$ and $\{R\}$. Also, one can use a penalty method or even a Lagrange multiplier method. Yet, all these methods modify the initial global stiffness matrix built by assembling the element stiffness matrices.

Remark: before applying any DBCs, the global stiffness matrix should have three or six, respectively for 2D or 3D, vanishing eigenvalues corresponding to the rigid body motions.

Bibliography

- Ben-Bettaieb, M. and Abed-Meraim, F. (2017). Effect of kinematic hardening on localized necking in substrate supported metal layers. *International Journal of Mechanical Sciences*, 123:177–197.
- Besson, J., Cailletaud, G., Chaboche, J.-L., and Forest, S. (2010). *Non-linear mechanics of materials*. Springer.
- Besson, J. and Foerch, R. (1997). Large scale object-oriented finite element code design. *Computer Methods in Applied Mechanics and Engineering*, 142(1):165–187.
- Besson, J., Steglich, D., and Brocks, W. (2001). Modeling of crack growth in round bars and plane strain specimens. *International Journal of Solids and Structures*, 38:8259–8284.
- Bigoni, D. and Hueckel, T. (1991). Uniqueness and localization - i - associative and non-associative elastoplasticity. *International Journal of Solids and Structures*, 28:197–213.
- Bigoni, D. and Zaccaria, D. (1993). On strain localization analysis of elastoplastic materials at finite strains. *International Journal of Plasticity*, 9:21–33.
- d’Avila, M. S., Triantafyllidis, N., and Wen, G. (2016). Localization of deformation and loss of macroscopic ellipticity in microstructured solids. *Journal of the Mechanics and Physics of Solids*, 97:275–298.
- Hill, R. (1958). A general theory of uniqueness and stability in elastic-plastic solids. *Journal of the Mechanics and Physics of Solids*, 6:236–249.
- Hutchinson, J. (1974). Plastic buckling. *Advances in applied mechanics*, 14:67–144.
- Hutchinson, J. and Miles, J. (1974). Bifurcation analysis of the onset of necking in an elastic/plastic cylinder under uniaxial tension. *Journal of the Mechanics and Physics of Solids*, 22:61–71.
- Lee, L. and Ades, C. (1957). Plastic torsional buckling strength of cylinders including effects of imperfections. *Journal of the Aeronautical Sciences*, 24:241–248.
- Mandel, J. (1971). Plasticité classique et viscoplasticité. In *CISM Courses and lectures*, volume 97, pages 1–187.
- Mazière, M. (2007). *Éclatement des disques de Turbomachines*. PhD thesis, École des Mines de Paris.
- Mazière, M., Besson, J., Forest, S., Tanguy, B., Chalons, H., and Vogel, F. (2009). Overspeed burst of elastoviscoplastic rotating disks – part i: Analytical and numerical stability analyses. *European Journal of Mechanics - A/Solids*, 28(1):36–44.

- Mora, S., Maurini, C., Phou, T., Fromental, J.-M., Audoly, B., and Pomeau, Y. (2013). Solid drops: Large capillary deformations of immersed elastic rods. *Physical Review Letters*, 111:114301.
- Nefussi, G. and Combescure, A. (2002). Coupled buckling and plastic instability for tube hydroforming. *International Journal of Mechanical Sciences*, 44:899–914.
- Nguyen, Q. S. (2000). *Stability and nonlinear solid mechanics*. Wiley.
- Ogden, R. (2000). *Elastic and pseudo-elastic instability and bifurcation*. Springer Vienna, Vienna.
- Ortiz, M. (1987). An analytical study of the localized failure modes of concrete. *Mechanics of Materials*, 6:159–174.
- Petryk, H. (1992). Material instability and strain-rate discontinuities in incrementally nonlinear continua. *Journal of Mechanics and Physics of Solids*, 40:1227–1250.
- Petryk, H. (1993). Theory of bifurcation and instability in time-independent plasticity. In *Bifurcation and Stability of Dissipative Systems*, volume 327, pages 95–152, Vienna. Springer Vienna.
- Petryk, H. (2000). *Material Instabilities in Elastic and Plastic Solids*. CISM International Centre for Mechanical Sciences 414. Springer, 1 edition.
- Pinsky, P., Ortiz, M., and Pister, K. (1986). Numerical integration of rate constitutive equations in finite deformation analysis. *Computer Methods in Applied Mechanics and Engineering*, 40:137–158.
- Rice, J. (1976). The localization of plastic deformation. In *W.T. Koiter (Ed.), Theoretical and Applied Mechanics*, pages 207–220. North-Holland.
- Rubin, M. and Nadler, B. (2016). An eulerian formulation for large deformations of elastically isotropic elastic-viscoplastic membranes. *Journal of Mechanics of Materials and Structures*, 11:197–216.
- Truesdell, C. and Toupin, R. (1960). *The classical field theory of mechanics*. Springer.

Chapter 3

Global instabilities

*”Mon enfant, quand une plante pousse de travers, on lui met un bâton pour l’aider à pousser droit ... Toi c’est pareil.”
Mon père*

Résumé : Le flambement et la striction sont communément liés à l’émergence d’instabilités globales. Lorsqu’ils apparaissent au cours d’un chargement, ils sont généralement synonymes de ruine de la structure. D’un point de vue mathématique, ces phénomènes sont étroitement liés à la perte d’unicité de la solution du problème en vitesse. De ce fait, dans la présente étude nous proposons d’analyser l’émergence de ces comportement en s’appuyant sur le critère de perte d’unicité en vitesse de Hill formulé dans [Hill, 1958]. Dans le présent chapitre, nous réintroduisons ce critère avec les notations introduites précédemment et donnons sa formulation dans le cadre des éléments finis. Pour finir, ce critère sera validé et illustré dans le cas de la striction d’un barreau, du flambement d’un tube en torsion et la double striction d’une éprouvette plate en traction.

3.1	Uniqueness and stability in elastoplastic problems: Hill 1958	53
3.2	Structural applications	61
3.3	Conclusions	73

Necking and buckling can both be seen as global instabilities. The emergence of such modes usually leads to the failure of the structure. As shown in 1.1, they can often be linked to a loss of uniqueness or stability of the solution. In order to detect such behaviors, Hill’s loss of uniqueness criterion formulated in [Hill, 1958], was adopted in the present work. This criterion gives a general framework for investigating the uniqueness of the solution of a rate boundary value problem¹. Also, the author proposed a stability criterion now referred to as “stability in the Hill sense” [Bigoni, 2012].

In order to analyze complex structures, this criterion will be specified for a FEM framework. For this purpose, a link between the criterion formulated in a continuum medium and its commonly used discrete formulation will be made. The numerical method to evaluate this discrete criterion will be presented, implemented in `Zset` and validated on the case of necking in a bar loaded in tension. Then, this analysis will be applied to three structural problems: necking of a full tensile sample (“dog-bone” specimen) is first analyzed to illustrate the sensitivity of the method to a variation in geometry; then buckling of a tube loaded in torsion is presented (a more detailed discussion of this case is given in sections 6.1 and 6.2); and finally the sensitivity

¹ A detailed analysis of [Hill, 1958] can be found in Appendix 8.3. A discussion of the notations and their adaptation to this work can also be found there.

of such a method to a variation in the boundary conditions is illustrated with the analysis of a thin plate loaded in tension. Finally, these applications will lead to conclusions on the limits of the method.

3.1 Uniqueness and stability in elastoplastic problems: Hill 1958

The global loss of uniqueness criterion of the rate boundary value problem proposed by R. Hill in [Hill, 1958] is presented in this section. The analytical developments of this criterion, and a detailed discussion of the first part of the article are given in appendix 8.3. Based on this fundamental criterion, a discretized form is derived for a FEM framework, and the link between the discrete incremental problem and continuum rate boundary value problem is detailed. In order to validate the method, necking in a simple bar is presented.

3.1.1 Uniqueness criterion for the rate boundary value problem

Let us consider a domain Ω_0 in equilibrium at the current time τ , for which the actual state is known (stresses, internal variables, etc.). In the absence of body forces or following forces the rate boundary value problem is written as:

$$\underline{\text{Div}} (\underline{\dot{S}}) = \underline{0} \quad \forall \underline{X} \in \Omega_0 \quad (3.1)$$

$$\underline{\dot{u}} = \underline{\dot{u}}^d \quad \forall \underline{X} \in \partial\Omega_0^u \quad (3.2)$$

$$\underline{\dot{S}} \cdot \underline{N} = \underline{\dot{T}}^d \quad \forall \underline{X} \in \partial\Omega_0^T \quad (3.3)$$

$$\underline{\dot{S}} = \underline{\mathcal{L}} : \underline{\dot{F}} \quad (3.4)$$

where $\partial\Omega_0^u$ and $\partial\Omega_0^T$ are respectively the boundaries of Ω_0 with prescribed velocities and dead load rates, and $\underline{\mathcal{L}}$ accounts for elastic unloading or plastic loading conditions.

If one assumes that two different solutions exist to the rate boundary value problem, then their difference $\Delta\underline{\dot{u}} = \underline{\dot{u}}^2 - \underline{\dot{u}}^1$ fulfills the following rate boundary value problem:

$$\underline{\text{Div}} (\Delta\underline{\dot{S}}) = \underline{0} \quad \forall \underline{X} \in \Omega_0 \quad (3.5)$$

$$\Delta\underline{\dot{u}} = \underline{0} \quad \forall \underline{X} \in \partial\Omega_0^u \quad (3.6)$$

$$(\Delta\underline{\dot{S}}) \cdot \underline{N} = \underline{0} \quad \forall \underline{X} \in \partial\Omega_0^T \quad (3.7)$$

$$\underline{\dot{S}}^i = \underline{\mathcal{L}}^i : \underline{\dot{F}}^i \quad i = 1, 2 \quad (3.8)$$

By simply contracting equation (3.5) with $\Delta\underline{\dot{u}}$, applying the fundamental divergence theorem and using (3.6) and (3.7), one gets the following loss of uniqueness condition:

$$\boxed{\int_{\Omega_0} \Delta\underline{\dot{S}} : \Delta\underline{\dot{F}} \quad dV_0 = 0} \quad (3.9)$$

also called loss of positive definiteness of the global second order work.

Assuming that both solutions fulfill the elastic unloading/plastic loading condition in the same way at every point in the structure:

$$\underline{\mathcal{L}}^1 = \underline{\mathcal{L}}^2 = \underline{\mathcal{L}} \quad (3.10)$$

equation (3.9) becomes:

$$\boxed{\int_{\Omega_0} \Delta\underline{\dot{F}} : \underline{\mathcal{L}} : \Delta\underline{\dot{F}} \quad dV_0 = 0} \quad (3.11)$$

Equivalently, since the term inside the integral is a quadratic form, equation (3.11) can be rewritten:

$$\boxed{\int_{\Omega_0} \Delta\underline{\dot{F}} : \underline{\mathcal{L}}^{sym} : \Delta\underline{\dot{F}} \quad dV_0 = 0} \quad (3.12)$$

where $\mathcal{L}_{ijkl}^{sym} = \frac{1}{2}(\mathcal{L}_{ijkl} + \mathcal{L}_{klij})$. It is quite convenient to note that, formulated as such, equation (3.11) possesses the same structure as equation (2.131). In fact, these two equations are closely related and lead to the analysis of the global stiffness matrix used for the incremental problem.

Finally, in [Hill, 1958], an “extremum” principle is derived and linked to the existence of a velocity potential. In fact, when there exists such a velocity potential, for instance when \mathcal{L} possesses major symmetry, both the loss of uniqueness criterion, and the existence of a minimum for the global velocity potential are equivalent. These problems are discussed in [Petryk, 2000, Thermann, 2000].

3.1.2 Global stability criterion

The stability of an equilibrium and the uniqueness of the solution are two merging concepts for elastic solids. However, when it comes to elastoplastic problems, a difference needs to be made due to the multi-branch definition of the tangent operator (plastic loading/elastic unloading condition, see section 2.2.3). In order to understand this difference, Hill’s stability criterion is derived in the present section.

Let us consider a domain Ω with applied displacements on $\partial\Omega^u$ and dead loads applied on $\partial\Omega^T$. Consider that the displacement conditions are temporarily fixed and that a small disturbance is applied to the structure. The equilibrium is considered to be stable if the effects of the disturbance remain sufficiently small during the entire motion subsequent to its application.

In the case of elastoplastic solids, the evolution of the internal variables makes a thorough analysis of the evolution of these perturbations impossible [Bigoni, 2012]. However, for constitutive law formulations that possess a rate potential (\mathcal{L} possesses the major symmetry), a “directional stability” was formulated in [Hill, 1958]. In this context, the word direction comes with the meaning of “a direction in which the body can be disturbed”. This consists in considering that the perturbation is infinitesimal and that the internal variables are fixed. Then, the work of deformation in Ω (W) after a perturbation of displacement by a field $\Delta\mathbf{u}$ (with $\Delta\mathbf{u} = \mathbf{0}$ on $\partial\Omega^u$) associated to a variation in Boussinesq stresses $\Delta\mathcal{S}$ can be expressed:

$$W = \int_{\Omega} \mathcal{S} : \nabla(\Delta\mathbf{u}) \, dV + \frac{1}{2} \int_{\Omega} \Delta\mathcal{S} : \nabla(\Delta\mathbf{u}) \, dV \quad (3.13)$$

In this case Δ does not denote the difference between two solutions, but the difference between the perturbed and unperturbed configurations. Since $\Delta\mathbf{u}$ vanishes on $\partial\Omega^u$ and by virtue of the principle of virtual powers, the first term is identified to be the work done by the external dead loads, W^{load} , caused by the displacement $\Delta\mathbf{u}$. Then equation (3.13) can be rewritten:

$$W - W^{load} = \frac{1}{2} \int_{\Omega} \Delta\mathcal{S} : \nabla(\Delta\mathbf{u}) \, dV \quad (3.14)$$

$\Delta\mathcal{S}$ and $\Delta\mathbf{u}$ are infinitesimal variations with reference to the actual equilibrium configuration during an increment Δt of the fictitious time. Assuming that the rates were constant during this increment, one gets:

$$\Delta\mathbf{u} = \Delta t \dot{\mathbf{u}} \quad (3.15)$$

$$\Delta\mathcal{F} = \Delta t \dot{\mathcal{F}}(\dot{\mathbf{u}}) \quad (3.16)$$

$$\Delta\mathcal{S} = \Delta t \dot{\mathcal{S}} = \Delta t \mathcal{L} : \dot{\mathcal{F}} \quad (3.17)$$

Finally, injecting equations (3.16) and (3.17) in equation (3.14) gives:

$$W - W^{load} = \frac{(\Delta t)^2}{2} \int_{\Omega} \dot{\mathcal{F}}(\dot{\mathbf{u}}) : \mathcal{L} : \dot{\mathcal{F}}(\dot{\mathbf{u}}) \, dV \quad (3.18)$$

Then stability of an equilibrium configuration is ensured if equation (3.19) is fulfilled for any velocity field $\underline{\dot{\mathbf{u}}}$ kinematically admissible to 0 ($\underline{\dot{\mathbf{u}}} = \mathbf{0}$ on $\partial\Omega^u$).

$$\int_{\Omega} \underline{\dot{\mathbf{F}}} : \underline{\mathcal{L}} : \underline{\dot{\mathbf{F}}} dV > 0 \quad (3.19)$$

In other words, stability is ensured as long as it is necessary to provide some additional energy from an external source to maintain the perturbation $\Delta \underline{\mathbf{u}}$.

It is important to remark that equation (3.19) and equation (3.12) differ by construction. For elastoplastic solids, stability and uniqueness may coincide as long as no elastic unloading occurs. Yet, loss of uniqueness in its most general form is given in equation (3.9) and admits that the two solutions to the rate boundary value problem may differ in the fulfillment of the plastic loading or elastic unloading conditions. Therefore, stability of the equilibrium configuration does not necessarily imply uniqueness of the rate boundary value problem, but loss of stability of the current equilibrium implies that uniqueness is lost for the rate boundary value problem.

In the present work, we assume that no elastic unloading takes place at the instant of bifurcation. This assumption is mainly due to our incapacity to compute all possible combinations of elastic loading and plastic unloading, even in a FEM problem. Therefore stability in its main form cannot be investigated, and only uniqueness of the equilibrium may be investigated numerically.

3.1.3 Numerical method: Loss of stability in a FEM framework

Following the same procedure of discretization as the one performed in section 2.3, one can rewrite equation (3.12) to get in a FEM framework:

$$\{\Delta \underline{\dot{\mathbf{u}}}\}^T \cdot [\mathbf{K}_{tan}]^{sym} \cdot \{\Delta \underline{\dot{\mathbf{u}}}\} = \{\mathbf{0}\} \quad (3.20)$$

where $[\mathbf{K}_{tan}]^{sym} = \frac{1}{2}([\mathbf{K}_{tan}] + [\mathbf{K}_{tan}]^T)$. When using a small enough time-step, the global tangent matrix $[\mathbf{K}_{tan}]$ and global stiffness matrix $[\mathbf{K}]$ almost coincide (see section 2.3.3). Therefore in a numerical incremental process the problem to solve after convergence towards equilibrium is:

$$\{\Delta \underline{\dot{\mathbf{u}}}\}^T \cdot [\mathbf{K}]^{sym} \cdot \{\Delta \underline{\dot{\mathbf{u}}}\} = 0 \quad (3.21)$$

Finally, since $\Delta \underline{\dot{\mathbf{u}}}$ is kinematically admissible to 0, the problem to solve is:

$$\{\mathbf{DoF}\}^T \cdot [\mathbf{K}^{DBC}]^{sym} \cdot \{\mathbf{DoF}\} = 0 \quad (3.22)$$

Where $\{\mathbf{DoF}\}$ is the vector of the non-zero components of $\{\Delta \underline{\dot{\mathbf{u}}}\}$.

3.1.4 Eigenvalue problem on the global tangent operator

In order to find a non-trivial solution to (3.22), the following eigenvalue problem is solved:

$$[\mathbf{K}^{DBC}]^{sym} \cdot \{\mathbf{X}\} = \lambda \{\mathbf{X}\} \quad (3.23)$$

where $\{\mathbf{X}\}$ is the eigenvector associated to the eigenvalue λ . When a vanishing eigenvalue exists, equation (3.22) is fulfilled. However, in a numerical process, one might not capture the exact moment for which the eigenvalue vanishes, since only a finite number of equilibrium configurations can be considered. However, the eigenvalues are initially all positive, so that when an eigenvalue becomes negative, one knows that a loss of stability has been bypassed. Therefore, the following procedure, also proposed in [Petryk, 2000, Durand and Combescure, 1999, Besson et al., 2010, Nguyen, 2000, Nefussi and Combescure, 2002, Okazawa, 2010, de Borst et al., 2012, Bigoni, 2012], is followed:

1. Solve the incremental problem;
2. Evaluate, after convergence, the smallest eigenvalues of the global stiffness matrix;
3. Conclude about the uniqueness of the solution of the rate boundary value problem.

Linear buckling analysis:

Note that when the changes in geometry can be neglected, linearizing equation (2.149) to small deformations would give:

$$[\mathbf{K}^k]_{elem} = \int_{\Omega^e} [\mathbf{B}_{\dot{\varepsilon}}]^T \cdot \left[\underset{\approx}{\mathcal{L}} \right] \cdot [\mathbf{B}_{\dot{\varepsilon}}] + [\mathbf{B}_{\dot{F}}]^T [\mathbf{M}_L(\underline{\varrho})] \cdot [\mathbf{B}_{\dot{F}}] dV^e \quad (3.24)$$

with $[\mathbf{B}_{\dot{\varepsilon}}]$ defined such that:

$$\{\underline{\varepsilon}\} = [\mathbf{B}_{\dot{\varepsilon}}] \{\underline{u}\} \quad (3.25)$$

If the material is linear elastic, and if it is possible to define a scalar loading parameter λ , then:

$$\underset{\approx}{\mathcal{L}} = \underset{\approx}{\mathbf{\Lambda}} \quad (3.26)$$

$$\underline{\varrho}(\lambda) = \lambda \underline{\varrho}(1) \quad (3.27)$$

with $\underset{\approx}{\mathbf{\Lambda}}$ the elasticity tensor, and $\underline{\varrho}(1)$ the stress field for a unitary load. Under these conditions, the generalized eigenvalue problem defined in equation 3.28 can be solved to evaluate the stability of the structure. This is the well-known “linear buckling analysis”.

$$([\mathbf{K}_{mat}] - \lambda [\mathbf{K}_{geo}(\underline{\varrho}(1))]) \{\mathbf{X}\} = \{\mathbf{0}\} \quad (3.28)$$

where $[\mathbf{K}_{mat}]$ and $[\mathbf{K}_{geo}(\underline{\varrho}(1))]$ take into account the DBCs, and are respectively obtained by assembling the elementary matrices:

$$[\mathbf{K}_{mat}]_{elem} = \int_{\Omega^e} [\mathbf{B}_{\dot{\varepsilon}}]^T \cdot \left[\underset{\approx}{\mathbf{\Lambda}} \right] \cdot [\mathbf{B}_{\dot{\varepsilon}}] dV^e \quad (3.29)$$

$$[\mathbf{K}_{geo}(\underline{\varrho}(1))]_{elem} = - \int_{\Omega^e} [\mathbf{B}_{\dot{F}}]^T [\mathbf{M}_L(\underline{\varrho}(1))] \cdot [\mathbf{B}_{\dot{F}}] dV^e \quad (3.30)$$

In this analysis, the sign of λ is not important. A negative eigenvalue means that one would have to load in the other direction to reach the instability².

3.1.5 Implementation in Zset

The method described in section 3.1.4 has been implemented in **Zset**, a FEM software developed in C++ by the school of Mines, Safran Tech and ONERA. In this software, static problems can be solved with a Newton Raphson (NR) algorithm, as described in section 2.3.3. The architecture is designed to allow the developers/users to implement plugins, called “**Problem Components**”, that can insert numerical procedures at key moments of the computation. In particular, the insertion can be done:

1. At the beginning of a new increment by implementing a “**start_increment()**” method;
2. At the end of an increment by implementing a “**end_increment()**” method.

² As an example, if one wants to capture buckling of a beam in compression, but the unit load is defined as a unit force tension on the beam, this analysis will lead to the opposite values of the well known Euler buckling loads.

It is shown in Figure 3.1 that the proposed global stability analysis is implemented to be evaluated at the end of an increment (after convergence of the NR loop). For this purpose, the C++ library `Spectra` (<https://spectralib.org/>) has been interfaced with `Zset`. This library offers multiple options to compute the eigenvalues of a large sparse matrix. In particular, a “selection rule” can be set to select eigenvalues by smallest (or largest) magnitude/algebraic values.0. After testing the various combinations, it was concluded that the most efficient way to evaluate the smallest algebraic eigenvalues was to compute the eigenvalues with the largest magnitude of the inverted matrix and take their inverse.

This choice is linked to the fact that `Spectra` is a non intrusive library. The user does not need to store the sparse global matrix in a particular way, instead the library requests to implement a method that evaluates matrix-vector products with any preferred method. In our case, we are interested in the eigenvalues with the largest magnitude of $[\mathbf{K}]^{-1}$. Thus, `Spectra` will require to solve:

$$[\mathbf{K}]^{-1} \cdot \{x_{in}\} = \{y_{out}\} \quad (3.31)$$

where $\{x_{in}\}$ is the vector given by `Spectra` and $\{y_{out}\}$ is the vector to compute. Since the global tangent matrix $[\mathbf{K}]$ was previously factorized to solve the incremental problem, it is possible to efficiently evaluate the product given in equation (3.31) multiple times. The eigenvalue extraction algorithm is then done by the `Spectra` library independently.

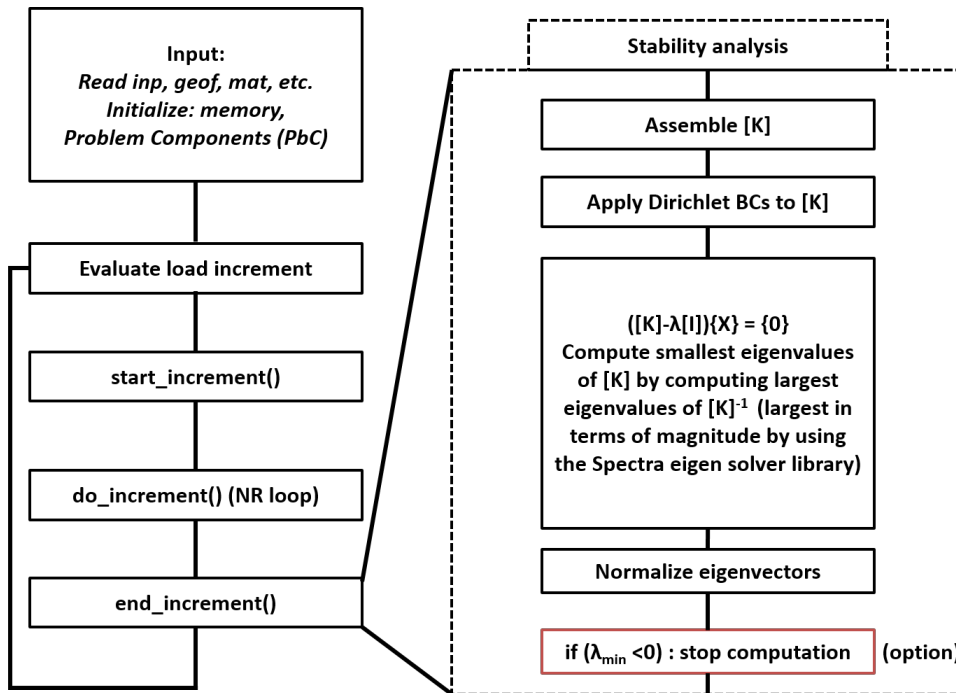


Figure 3.1: Evolution of the smallest eigenvalues during loading process.

In order to perform this analysis, it is sufficient to insert the following lines in the input file:

```

***global_bifurcation
  [**stop_if_unstable]
  **standard <number of eigen values> <Size of Krylov subspace>
  
```

To activate the output of the eigen modes and eigenvalues, one must also add the following keywords (or the eigenvalues only are output in the “message” file):

***output

**extra global_bifurcation % use global_bifurcation_2D for 2D models

During the computation, the eigen vectors are output as nodal fields and a text file “XXX.eigen” is created to store the eigenvalues.

3.1.6 Necking

Necking of a bar loaded in tension is analyzed in order to illustrate and validate this method. This problem is introduced in section 1.2, and necking should occur when (3.32) is fulfilled (tension direction is \underline{e}_2 in this case).

$$\dot{S}_{22} = 0 \quad (3.32)$$

which corresponds to the maximum force condition [Considère, 1885].

The simulation is run on an axi-symmetric model of a perfect cylinder (mesh shown in figure 3.2). Boundary conditions are given by:

- $u_y = 0$ for $y = 0$ (symmetry condition);
- $u_x = 0$ for $x = 0$ (symmetry condition);
- $u_y = u^d$ for $y = \frac{L}{2}$;
- $\underline{\sigma}\underline{n} = \underline{0}$ for $x = \frac{D}{2}$.

The constitutive law is defined by (see section 2.2.2) [Defaisse et al., 2018]:

- Corotational : Jaumann derivative of the Kirchhoff stress tensor;
- Elasticity: $E = 184$ GPa and $\nu = 0.29$;
- Criterion: von Mises;
- Isotropic non-linear hardening: $R(p) = R_0 + Q_1(1 - e^{-b_1 p}) + Q_2(1 - e^{-b_2 p}) + Ap$.
 - $R_0 = 1600$ MPa;
 - $A = 236$ MPa;
 - $Q_1 = 510$ MPa ; $b_1 = 773$
 - $Q_2 = 190$ MPa ; $b_2 = 81$

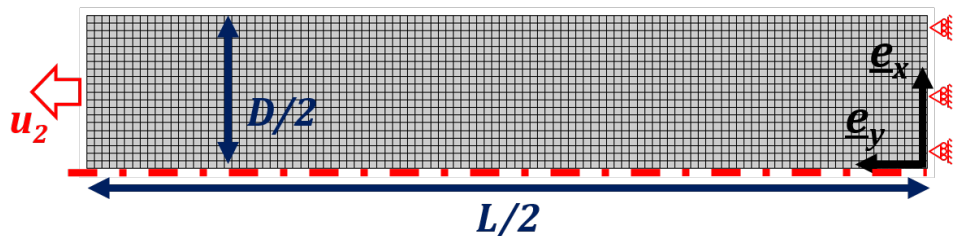


Figure 3.2: Mesh and boundary conditions of the axi-symmetric model of a simple bar loaded in tension.

During the simulation the solution of the incremental problem stays homogeneous in terms of deformation (displacements are linear as shown in Figure 3.6). However, when Considère's criterion is fulfilled, the smallest eigenvalue vanishes (see Figure 3.4) and the associated mode, shown in Figure 3.5, corresponds to a necking mode. This happens around $p = 0.025$ for this material, as shown in Figure 3.3. Even though the uniqueness of the solution of the rate boundary value problem is lost, the bar stayed straight during the whole computation and necking has been bypassed.

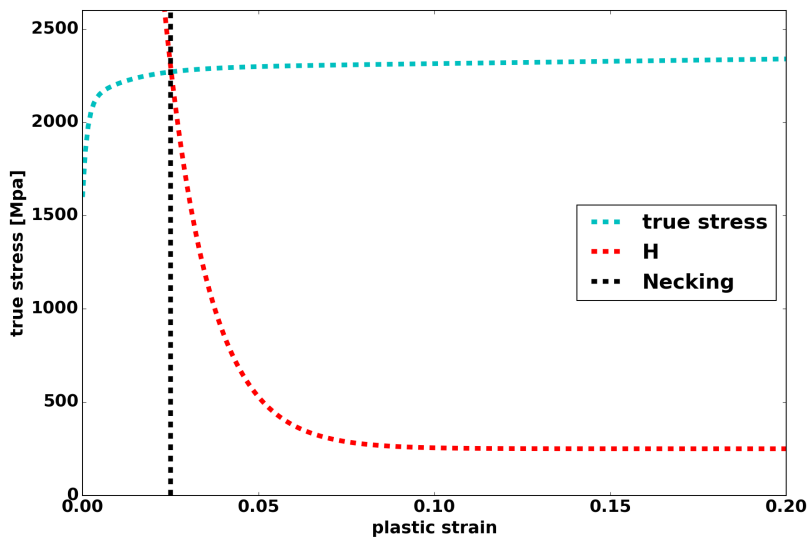


Figure 3.3: Evolution of the true stress and the hardening modulus $H = \frac{\partial R}{\partial p}$ as a function of the plastic strain. Necking should occur at $p = 0.025$.

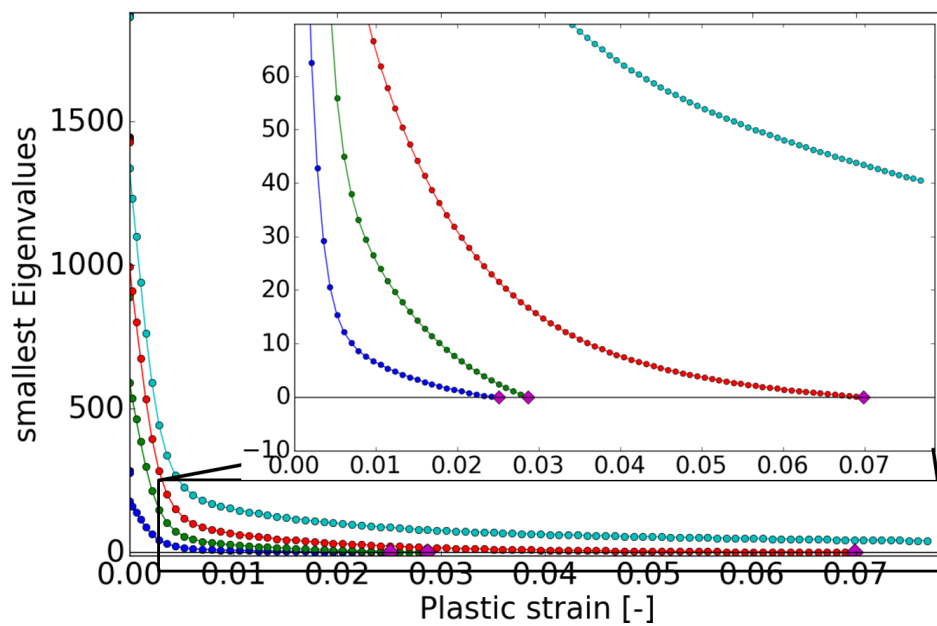


Figure 3.4: Evolution of the smallest eigenvalues during loading process for a bar loaded in tension.

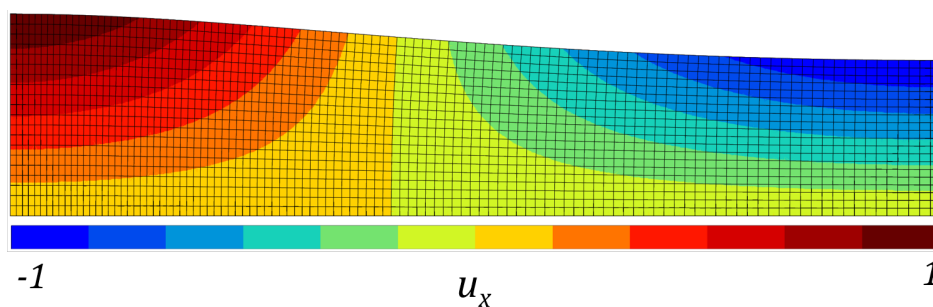


Figure 3.5: Eigenmode associated with the first vanishing eigenvalue for a bar loaded in tension.

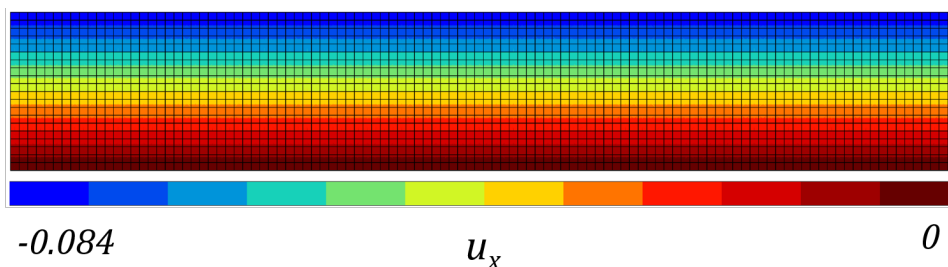


Figure 3.6: Contour of field u_x at the end of computation: necking has been bypassed and the bar stayed homogeneous.

In [Petryk, 2000, Durand and Combescure, 1999], similar results are observed. In [Thermann, 2000], the bifurcated branch is followed using a minimization approach of the velocity potential that exists for material law for which \mathcal{L} possesses major symmetry [Hill, 1958].

3.2 Structural applications

In this section relatively simple structural applications are presented. First, the necking in a tensile sample is analyzed and shows some limits of this criterion with respect to a loss of geometrical symmetry. Then comes the analysis of the buckling of a tube loaded in torsion. This application illustrates the use of this criterion to detect the failure of a tube due to buckling, as presented in section 1.2. Finally, the effects of DBCs on the instability analysis will be discussed in the case of a thin plate loaded in tension.

3.2.1 Necking in a tensile sample

Necking is a well known and deeply studied phenomenon [Considère, 1885, Hutchinson and Miles, 1974, Durand and Combescure, 1999, Mazière, 2007, Okazawa, 2010, Ben-Bettaieb and Abed-Meraim, 2017]. It is common nowadays to simulate experimental samples to characterize the post-necking constitutive law [Cooke and Kanvinde, 2015, Gerbig et al., 2016, Defaisse et al., 2018]. For instance, in [Defaisse et al., 2018] the necking in a tensile specimen is analyzed with direct image correlation in order to compare with the simulated sample and fit a post-necking material behavior. Therefore, capturing necking in the simulation is critical for such characterizations.

As shown in the previous section, necking can be missed when simulating only the gauge part for the sample. In order to avoid this problem, the heads of the sample are commonly introduced in the mesh as a remedy. To illustrate this problem a simulation is run on a axi-symmetric tensile sample ($L/D = 5$, with L the gauge length and D the gauge diameter) with the same material properties as for the previous example. Only half of a section of the sample is simulated. Symmetry conditions are applied on the axi-symmetry axis and on the middle section, and displacement BCs on the head (as shown in Figure 3.7):

- $u_x = 0$ for $x = 0$ (symmetry condition);
- $u_y = 0$ for $y = 0$ (symmetry condition);
- $u_y = u^d$ for $y = L_{tot}$, where L is half the length of the total sample (heads included);
- Free traction forces on the rest of the boundary.

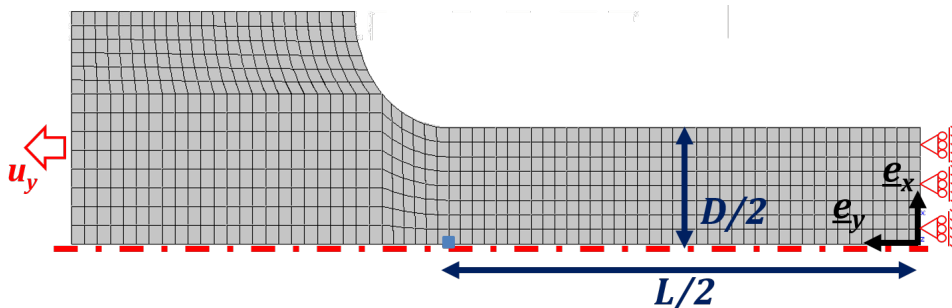


Figure 3.7: Mesh and boundary conditions of the tensile sample. In blue, the position of the virtual extensometer.

In fact, Figure 3.8 shows that such a change in the geometry, induces a non homogeneous strain field that leads to necking in the middle section, as displayed in figure 3.11. Also, the instability analysis on the global stiffness matrix shows that stability is never lost since all eigenvalues remain positive (see Figure 3.9). In the gauge length, the eigenmode associated with the smallest eigenvalue when necking occurs, see Figure 3.10 is similar to the eigenmode observed in Figure 3.5³. These similarities will be discussed in chapter 5.

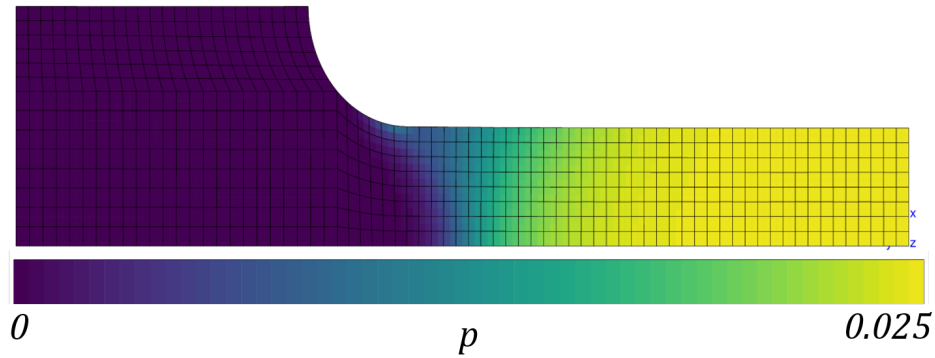


Figure 3.8: Non homogeneous plastic strain field just before necking in the tensile sample (when smallest eigenvalue reaches a minimum).

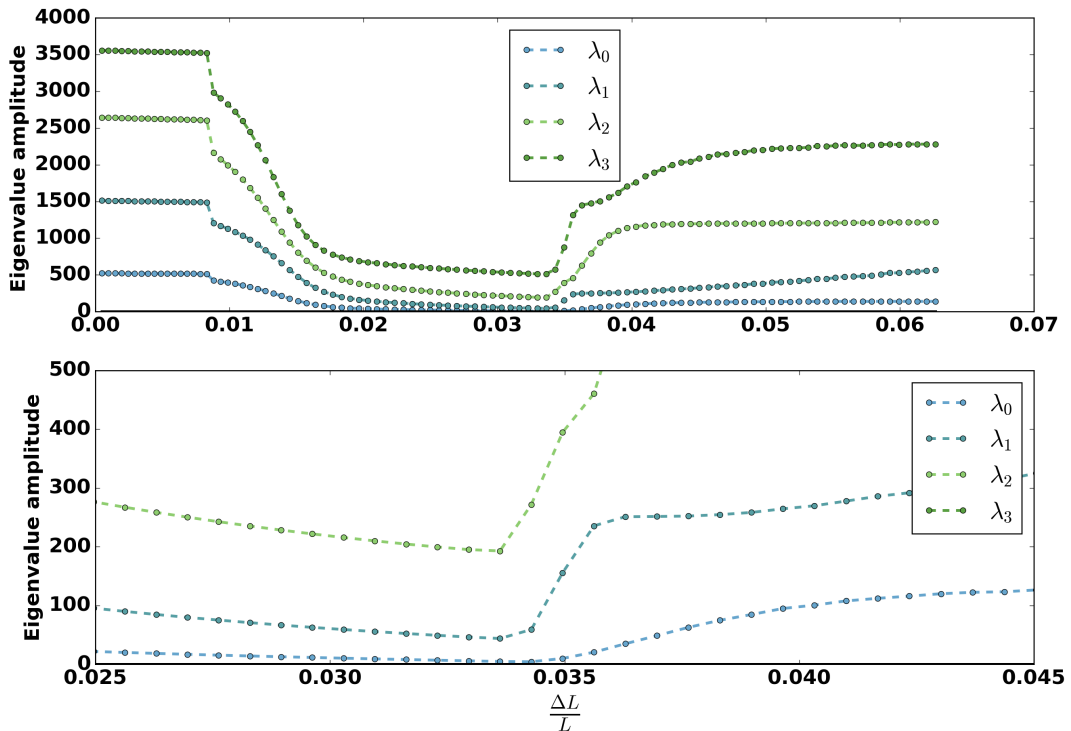


Figure 3.9: Eigenvalue analysis of the tensile sample.

³ Note that in Figure 3.10, before plotting, the mode is multiplied by factor -1 . This has no consequence since eigenmodes have no amplitude and can be normalized or multiplied by any non zero real number.

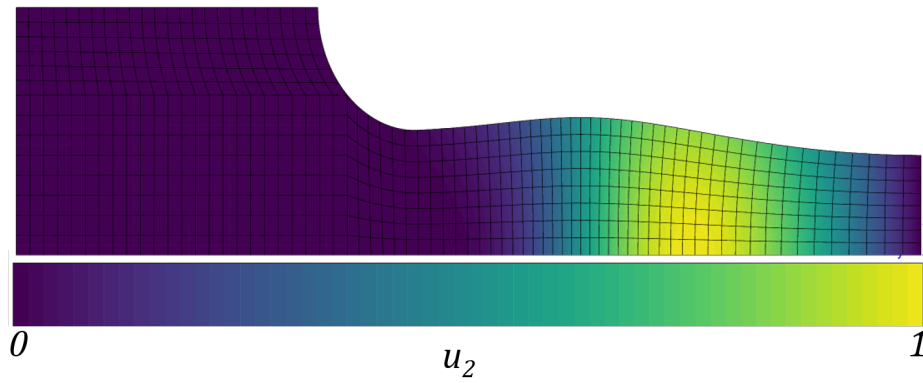


Figure 3.10: Eigenmode associated to the smallest eigenvalue when maximum tensile force is reached.

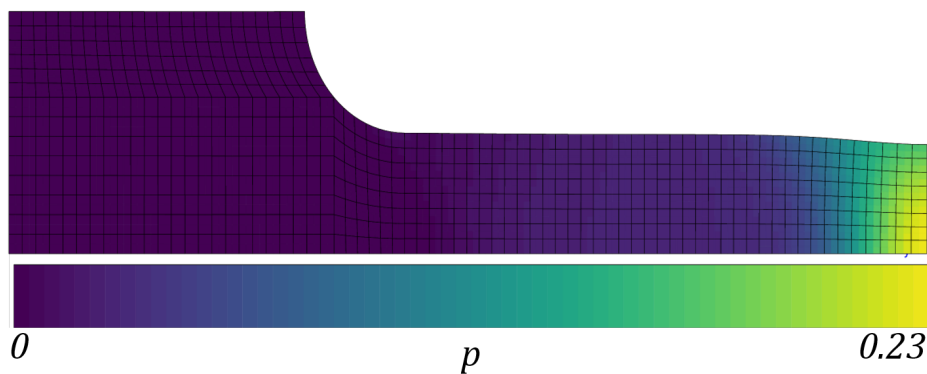


Figure 3.11: Plastic strain at the end of the computation for the tensile sample.

Yet, if the sample is “too long”, for instance $L/D = 12$, it is shown in figure 3.12 that the highest plastic strain just before necking is reached is not in the middle section. As a consequence, the neck develops away from the center leading to a double necking when the symmetry is applied, as shown in Figure 3.13. If the full section had been considered, the eigenvalue analysis would exhibit a negative eigenvalue. In fact, while the symmetry condition leads to a symmetric solution to the problem, it also implies that the instability analysis only admits symmetric modes. Therefore, one should be aware of the consequences on the instability analysis when exploiting symmetries.

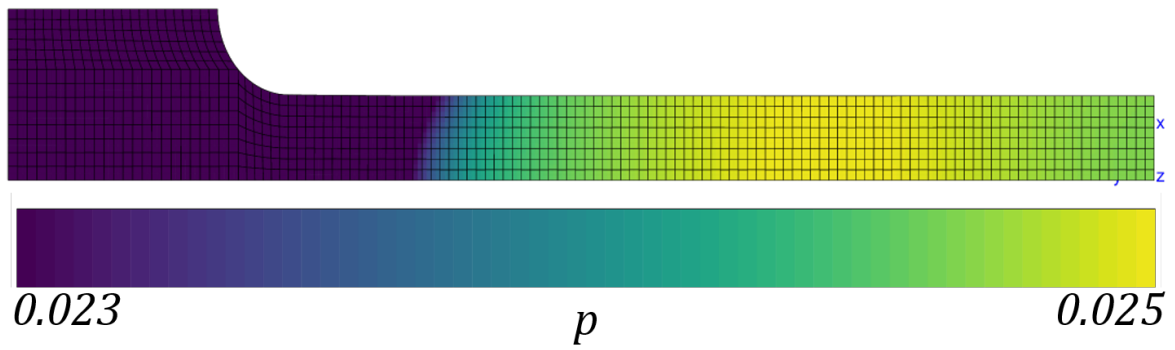


Figure 3.12: Plastic strain field for a long tensile sample ($L/D = 12$).



Figure 3.13: Plastic strain at end of computation for a very long tensile sample ($L/D = 32$). Two necks emerged during the computation.

It is shown in Figure 3.15 and Figure 3.16, the consequences on respectively the post-necking behavior in terms of “Force/Elongation” curves and on the neck profile for an elongation of 0.04. The post necking behavior is of utmost important for [Defaisse et al., 2018] since it is used to identify the material properties in the post-necking regime. These effects become more pronounced for longer samples, as shown in Figure 3.14:



Figure 3.14: Double neck in half a sample for a very long tensile sample ($L/D = 12$).

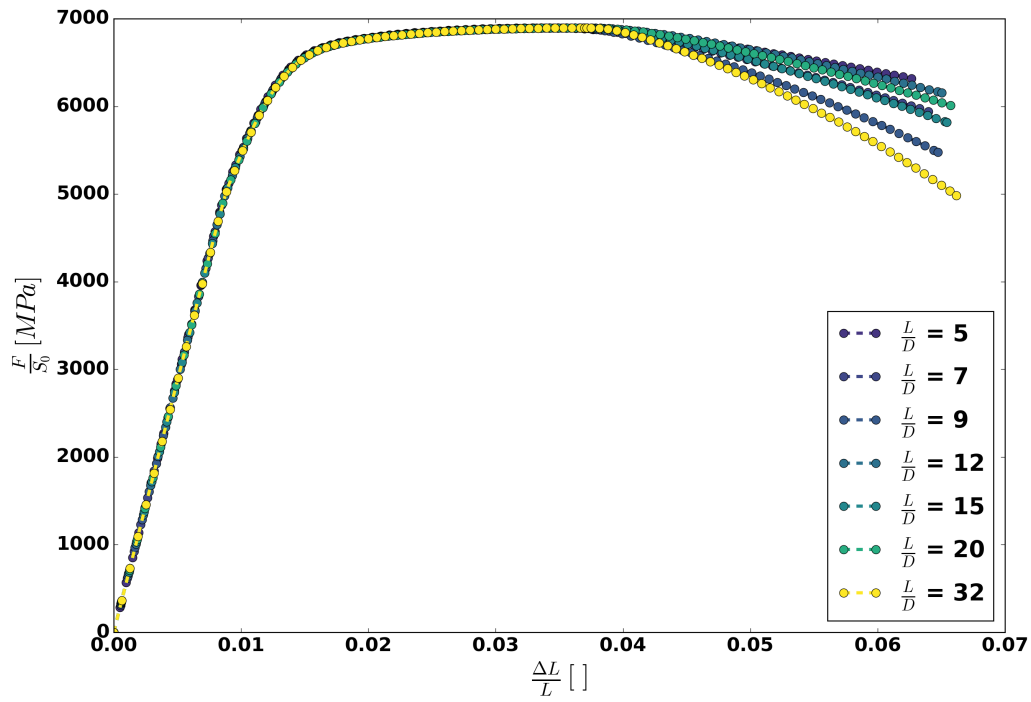


Figure 3.15: Tensile curves for tensile samples of various L/D ratios.

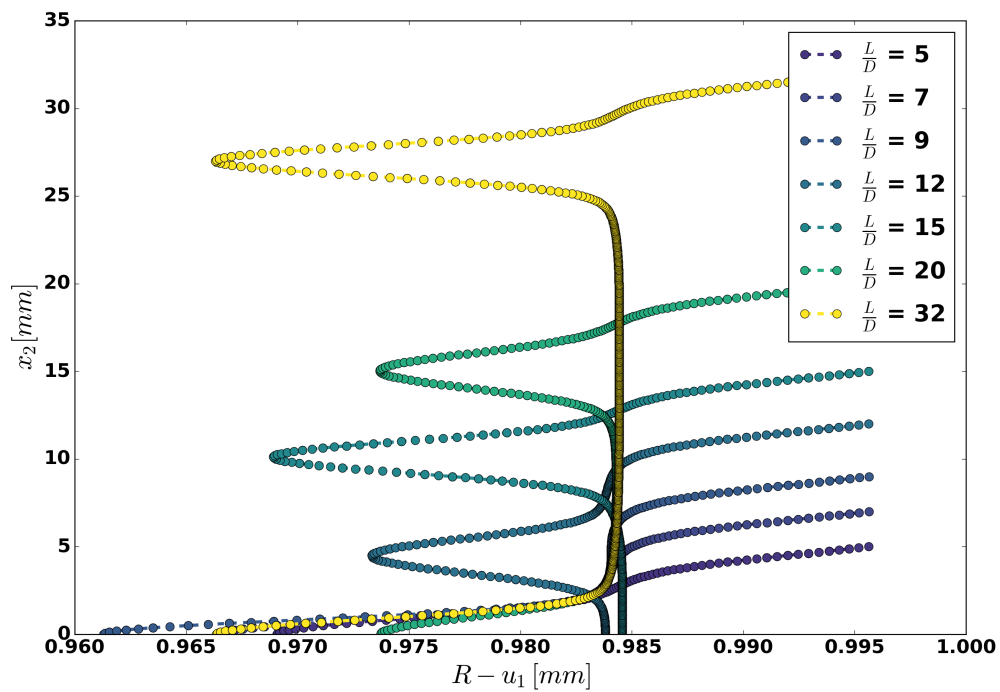


Figure 3.16: Neck profiles taken at $\frac{\Delta L}{L} = 0.04$ in tensile sample of various L/D .

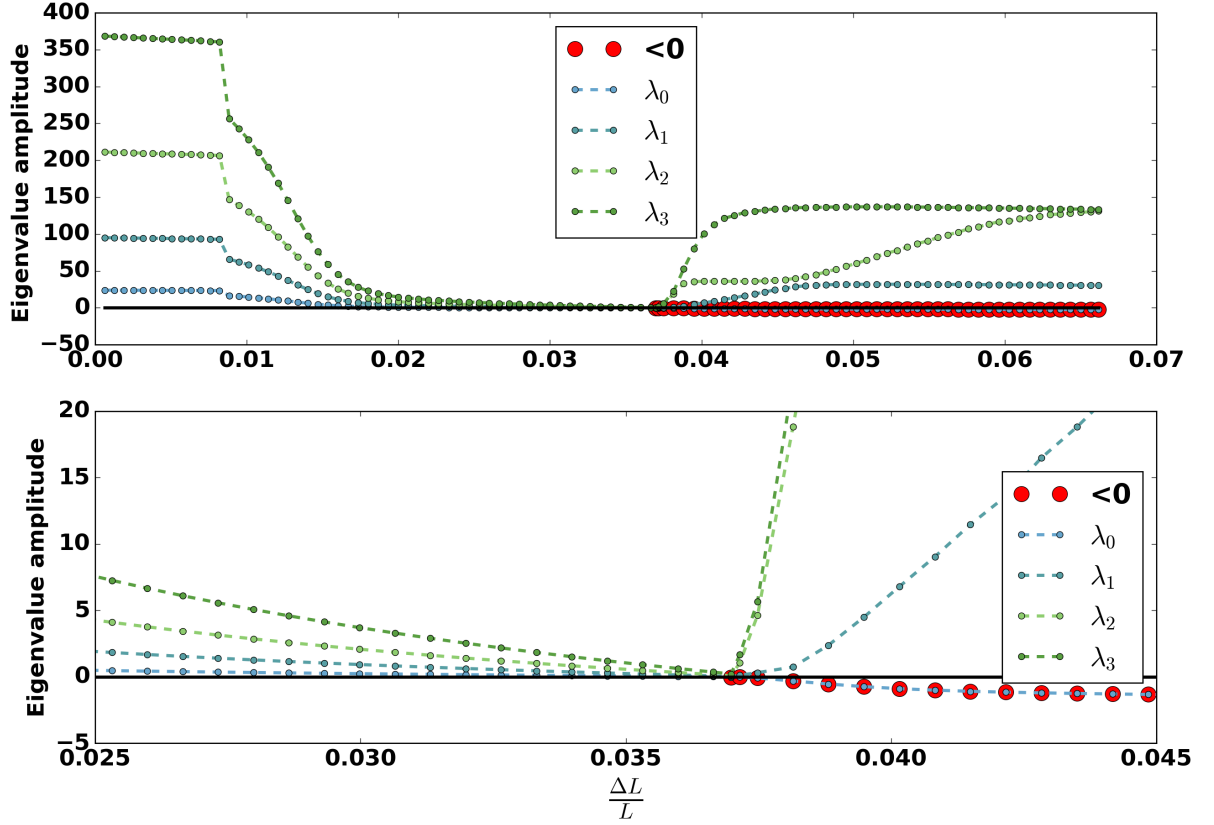


Figure 3.17: Eigenvalue analysis of a very long tensile sample ($L/D = 32$).

This analysis shows that for slight change in the geometry the instability analysis might be significantly modified. Also, the fact that stability is not lost in the some cases is linked to the type of loading (displacement control). The sensitivity to the type of boundary conditions will be discussed in chapter 5.

3.2.2 Buckling of a tube loaded in torsion

Torsional buckling is a geometrical instability, yet it cannot be captured with a simple linear buckling analysis (introduced in section 3.1.4) due to geometrical considerations [Lee and Ades, 1957]. In this paragraph, an elastoplastic tube of external diameter D , length L and thickness t (presented in Figure 3.18) is fixed on the bottom section (S_0) and a rotation is imposed to the top section S_L . Displacement boundary conditions are expressed as:

- $\underline{u} = \underline{0}$ on S_0 ;
- $\underline{u} = (\underline{R}(\theta) - \underline{I})\underline{X}$ on S_L .

where $\underline{R}(\theta)$ is the rotation matrix of an angle θ around the (O, \underline{e}_y) axis.

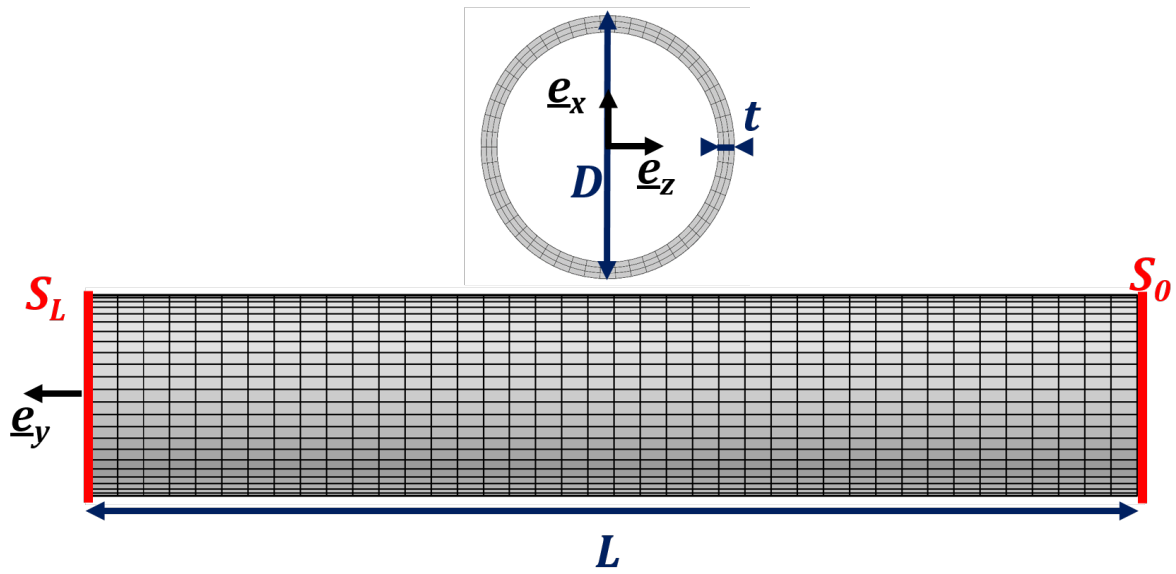


Figure 3.18: Mesh and boundary conditions of the torsion test.

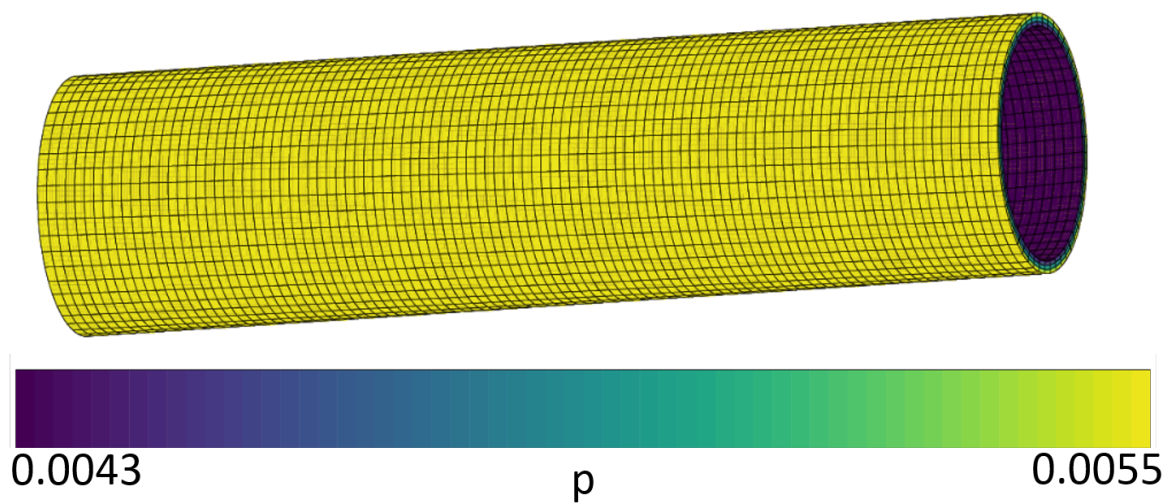


Figure 3.19: Tube at the end of the computation. Strain fields homogeneous in the length, no buckling was captured.

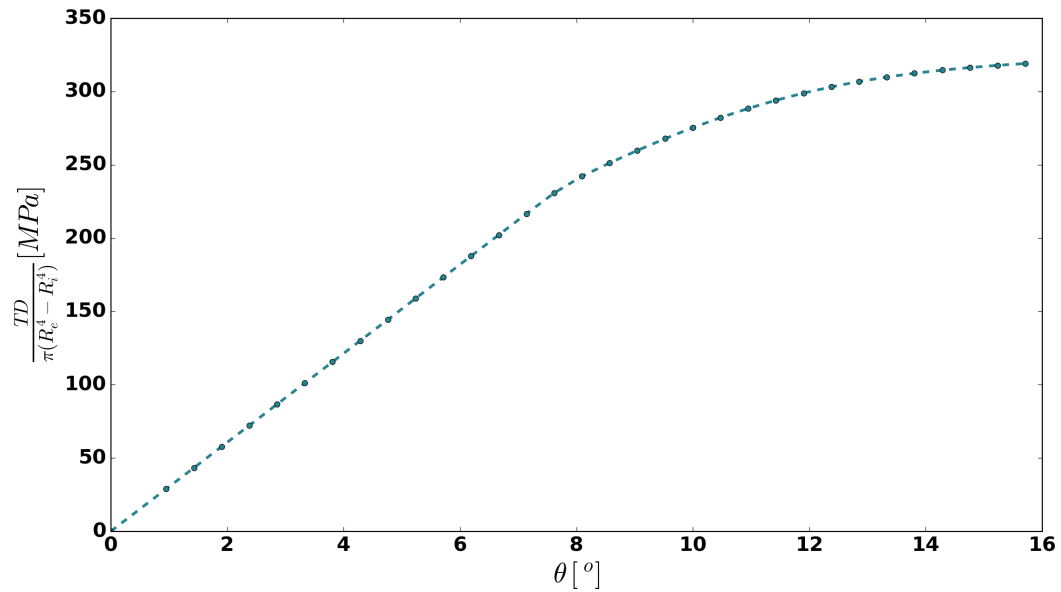


Figure 3.20: Evolution of equivalent shear stress.

As shown in Figure 3.19, no buckling was captured during the simulation. However, the eigenvalue analysis shown in Figure 3.21 exhibits two vanishing eigenvalues. The eigenmodes associated to these vanishing eigenvalues are displayed in Figure 3.22. They correspond to the buckling mode observed experimentally (see section 1.2).

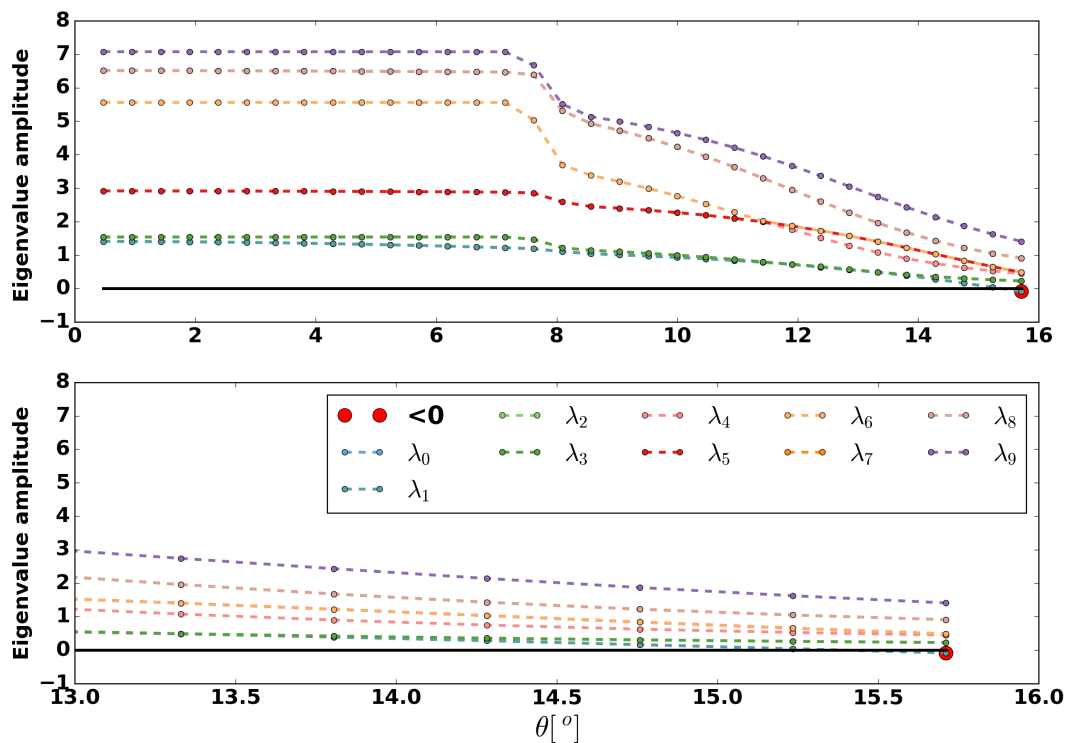


Figure 3.21: Evolution of the eigenvalues during the loading. Two eigenvalues vanish for a rotation angle $\theta = 28^\circ$.

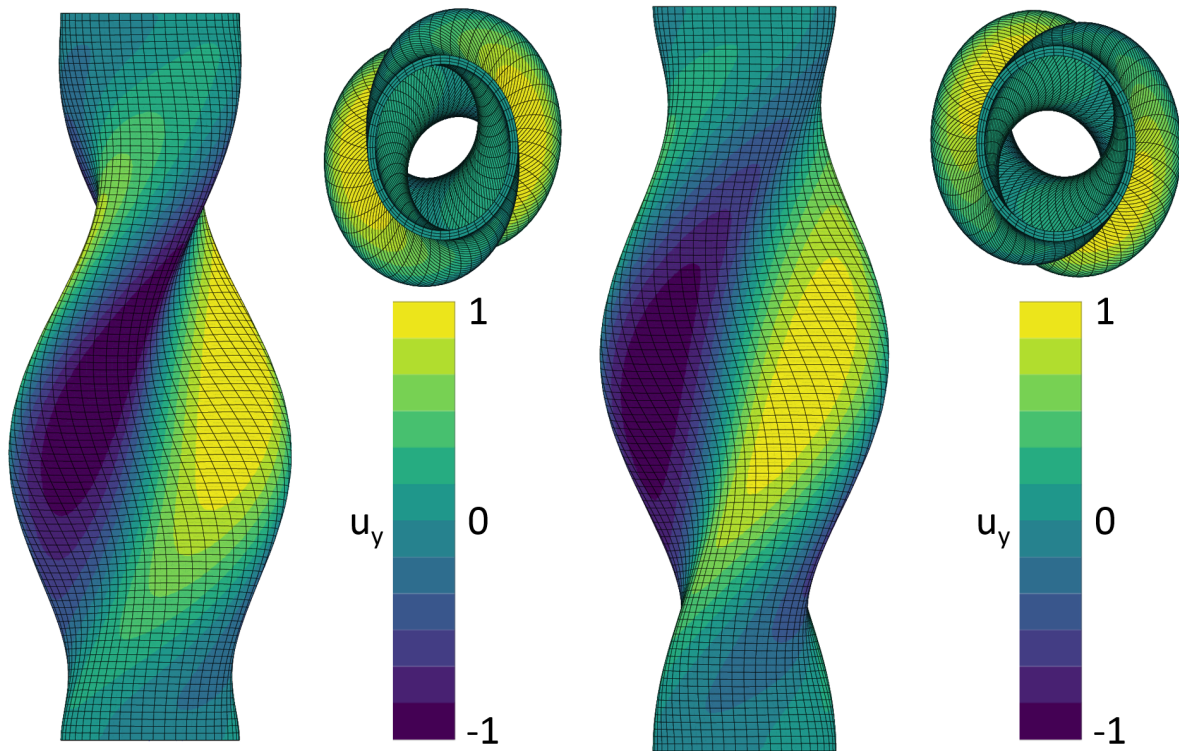


Figure 3.22: Eigenmodes associated to the two vanishing eigenvalues. They only differ by a rotation.

3.2.3 Thin plate loaded in tension: sensitivity to DBCs

The stability analysis of a thin plate loaded in tension is presented in this section. Strain localization⁴ is often studied to analyze metal sheet forming [Hill, 1952, Hill and Hutchinson, 1975, Stören and Rice, 1975, Benallal and Comi, 1996, Abed-Meraim, 2009, Ben-Bettaieb and Abed-Meraim, 2017, Akparna et al., 2017]. These analyzes are generally 2D (plane stress) and based on the loss of ellipticity criterion (discussed in chapter 4). In this example strain localization is interpreted as localized necking in a 3D model, as for instance discussed in [Besson et al., 2010], shown in Figure 3.23.

⁴ Here strain localization comes in a general sense: as soon as the strain gradient in the structure is increases suddenly in a limited narrow area. In chapter 4, localization will be related to the emergence of a strain rate discontinuity.

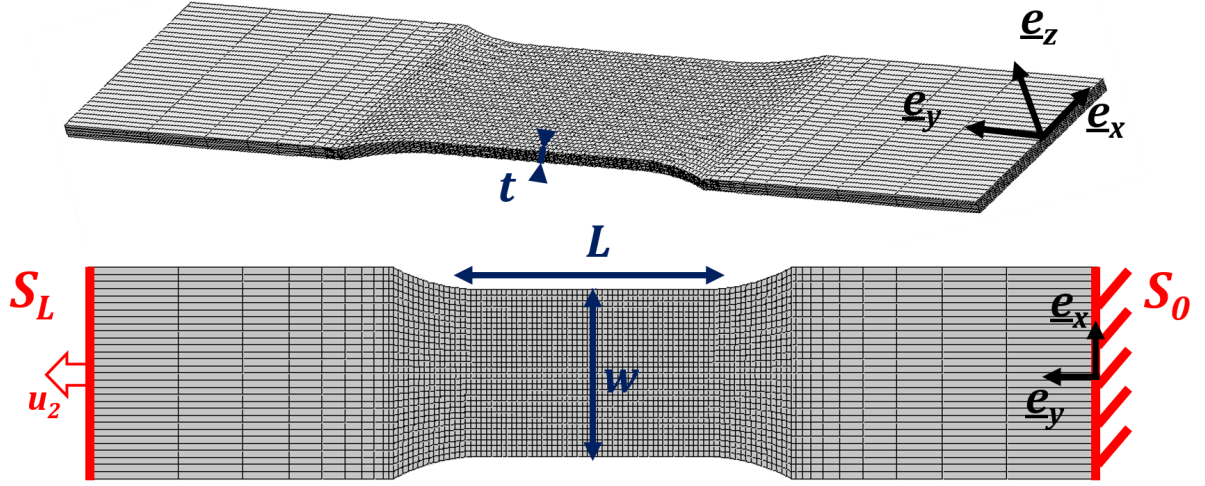


Figure 3.23: Isometric and front view of the thin tensile sample. The mesh of the gauge zone is composed of 10560 quadratic hexahedral elements: 8 through the thickness (1 mm), 44 along the length (22 mm), and 30 in the width (15 mm).

where $L = 22$ mm is the gauge length, $w = 15$ mm the gauge width, and $t = 1$ mm the thickness. Constitutive law formulation is given by [Defaïsse et al., 2018] (see section 2.2.2):

- Corotational: Jaumann derivative of the Kirchhoff stress tensor;
- Elasticity: $E = 184$ GPa and $\nu = 0.29$;
- Criterion: von Mises;
- Isotropic non-linear hardening: $R(p) = R_0 + Q_1(1 - e^{-b_1 p}) + Q_2(1 - e^{-b_2 p}) + Ap$.
 - $R_0 = 1600$ MPa;
 - $A = 236$ MPa;
 - $Q_1 = 510$ MPa ; $b_1 = 773$
 - $Q_2 = 190$ MPa ; $b_2 = 81$

Tensile curves: Two type of BCs are consider: first the “Free case” (or “free to slide”) defined in equation (3.33), that corresponds to a very loose loading; second is the “Fixed case” defined in (3.34), corresponds to a perfectly rigid loading.

$$\text{Free case: } \begin{cases} \underline{\mathbf{u}} = \underline{\mathbf{0}} & \forall \underline{\mathbf{X}} \in S_0 \\ u_2 = u^d & \forall \underline{\mathbf{X}} \in S_L \end{cases} \quad (3.33)$$

$$\text{Fixed case: } \begin{cases} \underline{\mathbf{u}} = \underline{\mathbf{0}} & \forall \underline{\mathbf{X}} \in S_0 \\ \underline{\mathbf{u}} = u^d \underline{\mathbf{e}}_2 & \forall \underline{\mathbf{X}} \in S_L \end{cases} \quad (3.34)$$

While these two sets of boundary conditions might seem similar for this geometry, they differ regarding the loss of stability of the solution⁵. Figure 3.24 shows that both tensile curves are

⁵According to Saint Venant’s principle: the two set of BCs considered here should lead to very similar stress and strain fields in the gauge length, at least before loss of uniqueness.

similar until late in the loading process, while the smallest eigenvalue of each case has a radically different behavior.

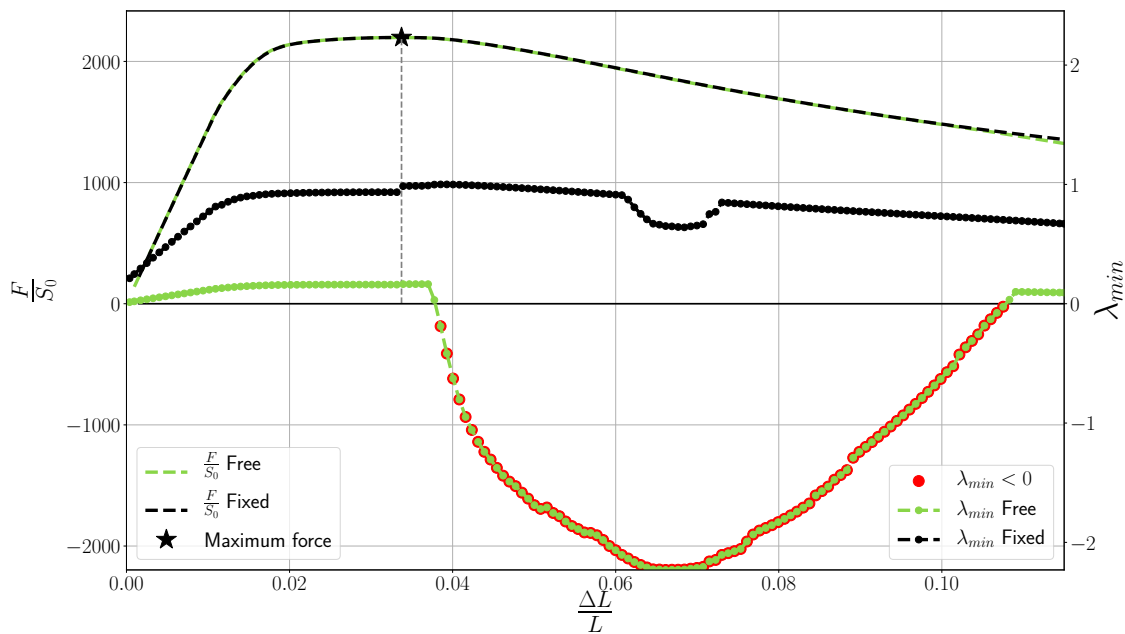


Figure 3.24: Tensile curves for the Free case in green, and in black for the Fixed case. Black stars indicate the maximum load, circles the smallest eigenvalue of the global stiffness matrix.

In the Free case, the eigenvalue analysis of the global stiffness matrix indicates that stability is lost when $\frac{\Delta L}{L} = 0.034$; whereas in the Fixed case, stability is never lost. The accumulated plastic strain contour (when stability is lost) and the eigenmodes associated to the vanishing eigenvalue in the Free case are shown in Figure 3.25.

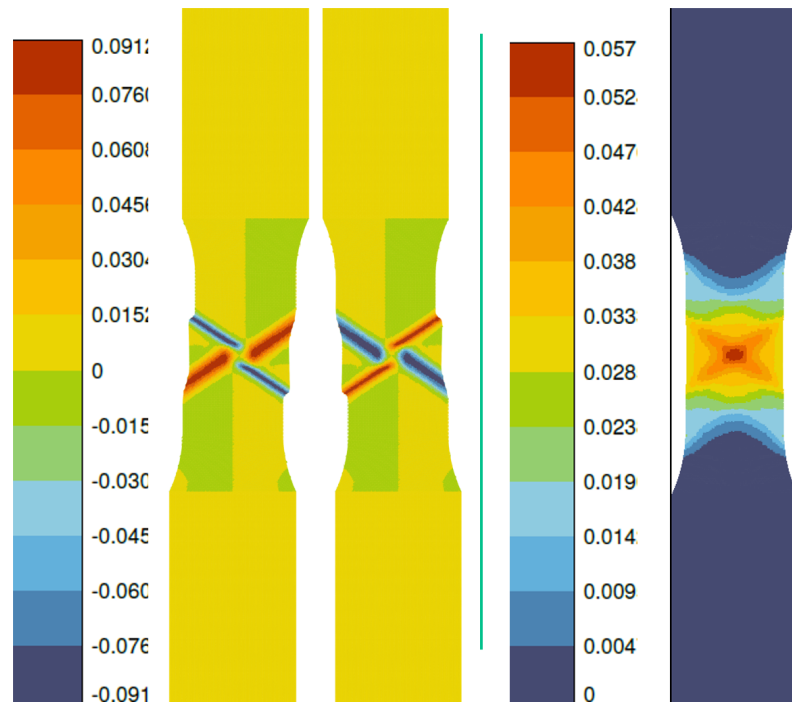


Figure 3.25: On the left, the eigenmode associated to the smallest eigenvalue; on the right, accumulated plastic strain field when stability is lost for the Free case.

This eigenmode, say \underline{v} , either “activates” one band or the other when taking $+\underline{v}$ or $-\underline{v}$, as a bifurcation mode. Also, this mode is captured before the localization properly occurs. Even though uniqueness was lost, this simulation did not bifurcate, and the smallest eigenvalue stays negative for the rest of the computation. Still, as it is shown in Figure 3.26, the plastic strain is highly concentrated in both bands. These bands initially make an angle of 54° with respect the tensile axis when strain localization starts, which is consistent with experimental observations.

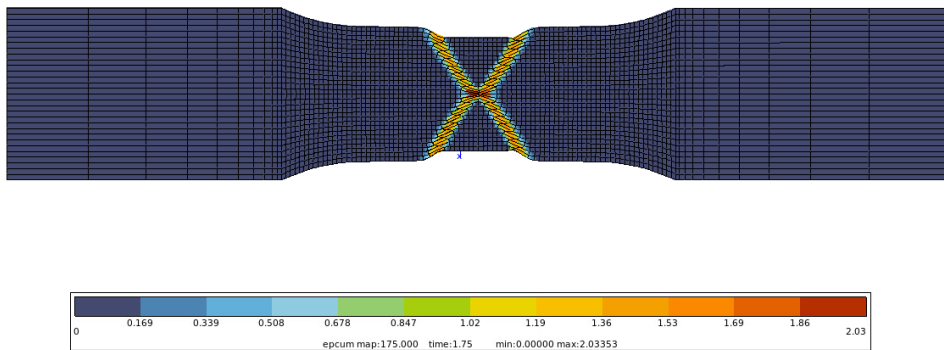


Figure 3.26: Accumulated plastic strain at the end of the computation.

In the Fixed case, though stability is never lost, one of the bands shows higher plastic strain than the other. In fact, numerical error increases in the plastic zone favoring strain localization in one of the bands more than in the other. This was confirmed by running the simulation multiple times on various processors and observing that either band activates randomly. Nevertheless, this still happens long after Free case has lost uniqueness. It is shown in Figure 3.27 that the

eigenmode associated to the smallest eigenvalue (even though it does not vanish) is similar to the one observed in Free case.

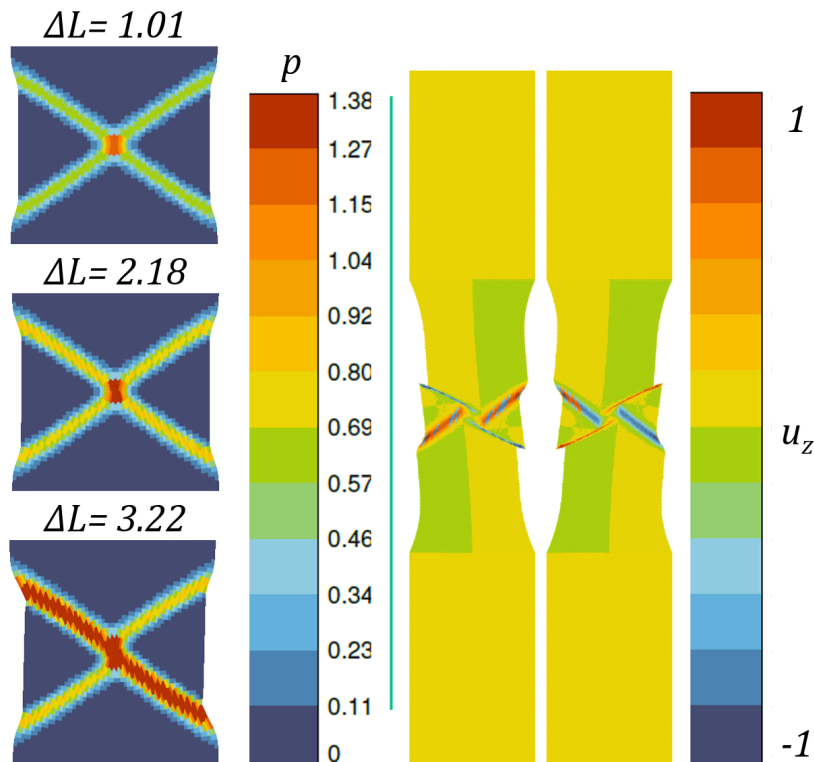


Figure 3.27: Evolution of the localization bands in the Fixed case. Even though the eigenvalues never vanish, the eigenmode shown on the right is the one associated with the smallest eigenvalue around time 0.9 s, which is similar to the vanishing eigenmode of Free case.

It is known that the length of the necking zone is of the same order of magnitude as the diameter of the sample for a tensile bar. In this case, first necking occurs at the maximum tensile load, and its size is of the order of magnitude of the width of the sample⁶. A little later, a necking region of the same order of magnitude in size as the thickness develops in two symmetric bands forming an “X”. At some point (when stability is lost), it is possible to break this symmetry by favoring one band over the other.

Comparison with experiments confirms that the Free case is the most realistic one. These localization bands are observed quickly after the maximum tensile load is reached and only one keeps deforming. This is mainly due to the machine not being infinitely stiff or to the misalignment of the sample with the tensile axis, so one band that is better aligned with the tensile axis and is favored.

3.3 Conclusions

In this chapter, Hill’s loss of stability criterion has been re-derived in order to put notations in consistency with the present work. The formulation of the discrete loss of uniqueness criterion for the rate boundary value problem has been recalled. A link between the common eigenvalue

⁶ Still, stability is not lost since the heads of the sample force the problem to naturally converge on this solution.

analysis of the global stiffness matrix and the eigenvalue analysis of the global tangent matrix has been given, when time-stepping is sufficiently small. This justified the implementation of a numerical method in the FEM software `Zset` and the tool has been validated on the necking of a simple bar.

This tool has then been applied to more “complex” problems and led to the illustration of some the following limitations of this method:

- **Post buckling behavior:** This analysis is not yet sufficient to draw conclusions on the post buckling behavior. A method is proposed in [de Borst et al., 2012] in order to influence the incremental problem to converge on the bifurcated branch. The author proposes to initiate the Newton-Raphson Algorithm with the vanishing eigen mode in order to favor convergence on the bifurcated solution.

- **Bifurcation due to numerical errors:** Bifurcated paths can be chosen by the incremental problem without any imperfections introduced in the modeling of the problem. Necking in a simple bar can also occur due to the accumulated errors at each Gauss point (mainly due to rounding). This numerical error leads to a heterogeneous solution that naturally converges on the bifurcated path (in this case, necking of a homogeneous bar). This can be favored by a fine time-stepping, by fine or random meshes, and multithreading.

- **Existence of a tangent operator:** It was assumed that the elastoplastic formulation chosen had a tangent operator that only depends on the current state. This, for instance, is not the case for viscous materials. Moreover, some elastoplastic (non viscous) formulations do not have such an operator [Rubin and Nadler, 2016]. These formulations are out of the scope of the present work.

- **Contact conditions:** This analysis is by essence formulated for a single body loaded through prescribed displacements and forces. Yet, some boundary conditions are more subtle. In the industry, it is common to study an assembly of mechanical parts. Therefore, a first approach to analyze such problems is proposed in chapter 5.

Bibliography

- Abed-Meraim, F. (2009). *Contributions à la prédiction d'instabilités de type structure et matériau : modélisation de critères et formulation d'éléments finis adaptés à la simulation des structures minces*. Mémoire HDR dissertation, Arts et Métiers ParisTech.
- Akparna, H., Ben-Bettaieb, M., and Abed-Meraim, F. (2017). Prediction of plastic instability in sheet metals during forming processes using the loss of ellipticity approach. *Latin American Journal of Solids and Structures*, 14:1816–1836.
- Ben-Bettaieb, M. and Abed-Meraim, F. (2017). Effect of kinematic hardening on localized necking in substrate supported metal layers. *International Journal of Mechanical Sciences*, 123:177–197.
- Benallal, A. and Comi, C. (1996). Localization analysis via a geometrical method. *International Journal of Solids and Structures*, 33:99–119.
- Besson, J., Cailletaud, G., Chaboche, J.-L., and Forest, S. (2010). *Non-linear mechanics of materials*. Springer.
- Bigoni, D. (2012). *Nonlinear Solid Mechanics: Bifurcation Theory and Material Instability*. Cambridge University Press.
- Considère, A. (1885). Mémoire sur l'emploi du fer et de l'acier dans les constructions. *Annales des Ponts et Chaussées*, 9:574–775.
- Cooke, R. and Kanvinde, A. (2015). Constitutive parameter calibration for structural steel: Non-uniqueness and loss of accuracy. *Journal of Constructional Steel Research*, 114:394–404.
- de Borst, R., Crisfield, M. A., Remmers, J., and Verhoosel, C. (2012). *Non-Linear Finite Element Analysis of Solids and Structures*. Wiley.
- Defaisse, C., Mazière, M., Marcin, L., and Besson, J. (2018). Ductile fracture of an ultra-high strength steel under low to moderate stress triaxiality. *Engineering Fracture Mechanics*, 194:301–318.
- Durand, S. and Combescure, A. (1999). Analytical and numerical study of the bifurcation of a cylindrical bar under uniaxial tension. *Revue européenne des éléments finis*, 8:725–745.
- Gerbig, D., Bower, A., Savic, V., and Hector, L. (2016). Coupling digital image correlation and finite element analysis to determine constitutive parameters in necking tensile specimens. *International Journal of Solids and Structures*, 97-98:496–509.
- Hill, R. (1952). On discontinuous plastic states, with special reference to localized necking in thin sheets. *Journal of the Mechanics and Physics of Solids*, 1:19–30.

- Hill, R. (1958). A general theory of uniqueness and stability in elastic-plastic solids. *Journal of the Mechanics and Physics of Solids*, 6:236–249.
- Hill, R. and Hutchinson, J. (1975). Bifurcation phenomena in the plane tension test. *Journal of the Mechanics and Physics of Solids*, 23:239–264.
- Hutchinson, J. and Miles, J. (1974). Bifurcation analysis of the onset of necking in an elastic/plastic cylinder under uniaxial tension. *Journal of the Mechanics and Physics of Solids*, 22:61–71.
- Lee, L. and Ades, C. (1957). Plastic torsional buckling strength of cylinders including effects of imperfections. *Journal of the Aeronautical Sciences*, 24:241–248.
- Mazière, M. (2007). *Éclatement des disques de Turbomachines*. PhD thesis, École des Mines de Paris.
- Nefussi, G. and Combescure, A. (2002). Coupled buckling and plastic instability for tube hydroforming. *International Journal of Mechanical Sciences*, 44:899–914.
- Nguyen, Q. S. (2000). *Stability and nonlinear solid mechanics*. Wiley.
- Okazawa, S. (2010). Structural bifurcation for ductile necking localization. *International Journal of Non-Linear Mechanics*, 45:35–41.
- Petryk, H. (2000). *Material Instabilities in Elastic and Plastic Solids*. CISM International Centre for Mechanical Sciences 414. Springer, 1 edition.
- Rubin, M. and Nadler, B. (2016). An eulerian formulation for large deformations of elastically isotropic elastic-viscoplastic membranes. *Journal of Mechanics of Materials and Structures*, 11:197–216.
- Stören, S. and Rice, J. (1975). Localized necking in thin sheets. *Journal of the Mechanics and Physics of Solids*, 23(6):421–441.
- Thermann, K. (2000). *Post-critical plastic deformation pattern in incrementally nonlinear materials at finite strain*. CISM International Centre for Mechanical Sciences 414. Springer.

Chapter 4

Material Instabilities

*“Celui qui t’aime, et n’aime pas ton frère ne t’aime pas.”
Mon père*

4.1	Elastoplastic localization bands: Rice 1976	79
4.2	Localization in structures	85
4.3	Numerical methods for detection of loss of ellipticity	89
4.4	Structural applications	102
4.5	Conclusions	122

Résumé : La localisation de la déformation plastique dans une étroite bande de cisaillement est probablement le comportement le plus critique pour une structure. L’apparition de telles bandes est couramment étudiée pour le formage de taule par l’analyse de perte d’ellipticité introduite par Rice dans [Rice, 1976]. Toutefois, ce critère est rarement utilisé dans les massifs autrement que pour expliquer l’initiation de la rupture quand il est vérifié en un unique point. Cependant, l’émergence de bandes de localisation est aussi une possibilité dans les structures massives sous certaines conditions, comme l’apparition d’une bande de localisation dans un tube en torsion dans [Defaisse, 2018].

Dans le présent chapitre, nous rappelons l’analyse de Rice en utilisant les notations introduites au début du manuscrit, tout en attachant une attention particulière aux hypothèses et à la signification du critère. Ensuite, nous proposons un nouvel algorithme pour l’évaluation du critère dans un problème éléments finis, et nous montrons qu’il apporte un gain en coût de calcul et en robustesse pour l’obtention du minimum global qui est associé à la première perte d’ellipticité. Pour mieux comprendre le lien entre perte d’ellipticité locale et perte d’unicité globale, le problème de van Hove est aussi analysé et une extension à son théorème d’unicité est proposée. Enfin, nous présentons les résultats numériques illustrant les conclusions sur le problème de van Hove, ainsi que l’émergence d’une bande de localisation dans un tube en torsion.

Strain localization is one of the most critical phenomena leading to the failure of elastoplastic structures, but its emergence is still not yet fully understood. Indeed, the term “localization” itself is interpreted differently depending on the context. When localization bands emerge in a complex structure and under what conditions they lead to catastrophic failure for the structure are still questions that need to be addressed in many contexts, especially when it comes to certifying industrial pieces. The case of tubes loaded in torsion [Defaisse et al., 2018], shows that even an apparently simple structure can lead to difficulties in defining localization.

When dealing with localization, a first distinction needs to be made between the loss of ellipticity and the loss of strong ellipticity criteria. The loss of ellipticity criterion has commonly been adopted as a strain localization criterion. It has been introduced, for instance, in the analysis of the propagation of acceleration waves in [Hill, 1962], as a stability criterion in small deformation in [Mandel, 1966], the latter being generalized to finite deformation in [Rice, 1976]. Some analyses show that in a homogeneously strained domain, this approach leads to emergence of strain localization bands when two parallel surfaces fulfill the loss of ellipticity criterion [de Borst et al., 2001]. While this is a very restrictive criterion, it is commonly used for the analysis of thin metal sheets forming limits [Ben-Bettaieb and Abed-Meraim, 2017] in a plane stress framework.

The analysis of loss of ellipticity is a local analysis. It was first formulated for an infinite homogeneously strained domain. Nevertheless, the author proposes in [Rice, 1976] to consider this criterion as a good indicator even for a “smoothly varying deformation”. However nothing is said about the structural aspect of this criterion. As discussed in [Abed-Meraim, 2009] around the analysis of localization in poly-crystals, loss of ellipticity in a single material element is not enough for the structure itself to fail. In section 4.2.1, the proof of the uniqueness when the problem is elliptic for the “van Hove rate boundary value problem” is recalled based on [Bigoni, 2012]. Then, a minor extension to [van Hove, 1947] is given in section 4.2.2. This extension will then lead to a discussion about the stability of the discretized problem when ellipticity is lost in part of the structure in section 4.4.1.

Both loss of ellipticity and loss of strong ellipticity can be shown to be equivalent when the tangent operator possesses major symmetry and it is often considered that both conditions are met as soon as the material has an associative flow rule [Rice, 1976]. However, this is not precisely the case. In some particular cases strong ellipticity and ellipticity might differ in a given finite deformation framework even though the material possesses an associative flow rule. In the present chapter the term “localization” is characterized by the possible emergence of a jump in strain rates, as presented in [Rice, 1976].

Regarding numerical methods, section 4.3 shows that the evaluation of the loss of ellipticity criterion leads to a minimization problem on one half of the unit sphere. Different numerical strategies are available in the literature to solve this minimization problem: some evaluate the minimum by iteratively discretizing the half unit sphere [Gruben et al., 2017], some by using a simplex method [Besson et al., 2001], others by defining an eigenvalue problem [Sanborn and Prévost, 2011, Oliver et al., 2010, Ortiz, 1987], and eventually some strategies couple a Newton-Raphson scheme and a line-search method [Mosler, 2005]. It is well known that the iterative discretization of the half unit sphere is time consuming and does not ensure the detection of the global minimum unless one uses a very fine discretization. Hence, when considering a large structural problem, this strategy would require a large amount of computational power on top of being unreliable. The second and third options that are the simplex method and the eigenvalue problem, basically consist of optimization methods. Given that the global minimum is required and that the minimized surface is a sixth order polynomial, it is necessary to take multiple starting points to ensure that the method does not converge on a local minimum. This requires defining a regular discretization of the half unit sphere, which is not obtained using a regular discretization of the angles in a spherical coordinates system [Néda et al., 1999]. As

a consequence, the strategy coupling Newton-Raphson and line-search methods [Mosler, 2005] appears to be the most promising numerical method. Moreover, note that most methods found in the literature are presented in a small deformation framework [Ortiz, 1987, Sanborn and Prévost, 2011], and some only for materials possessing an associative flow rule [Ortiz, 1987]. Their generalization to a finite deformation framework must then be done carefully depending on the finite deformation conventions used.

Finally, it is commonly believed that the loss of ellipticity criterion is limited to perfect plasticity or softening for associative materials. In fact, it can be shown that a non-softening material with an associated flow rule can never lead to localization in the sense of Rice while in a small deformation framework [Bigoni and Hueckel, 1991]. This is however not necessarily the case in a finite deformation framework due to the “geometrical stress” terms. It will be shown in section 4.4, that a material exhibiting non-softening behavior can still exhibit localization bands.

Tangent operators, along with loss of ellipticity and loss of strong ellipticity criteria are derived in a closed form. Then, in section 4.3.3, a new general, efficient, and robust method is presented for an efficient evaluation of the loss of ellipticity criterion based on a Newton-Raphson (NR) scheme. While a similar algorithm was introduced in detail in [Mosler, 2005], a new initialization method is proposed to improve robustness while being computationally more efficient. This method is derived in the most general case as it does not depend explicitly on the formulation of the associativity of the plastic flow, and works for both small and finite deformation frameworks. A comparison with the algorithm given in [Mosler, 2005] in terms of computation cost is performed on the basic example of a unit cube under simple shear loading at the end of this section. A more complex loading on a unit cube underlines that the use of multiple starting points improves the robustness of the method and the interpretation of the results while avoiding artificial effects due to the use of one single starting point. Finally, this new method was implemented and validated in a FEM program (**Zset**: <http://www.zset-software.com/>) and applied in section 4.4 to some structural problems. First, the “van Hove rate boundary value problem” will be illustrated and will lead to a discussion on loss of ellipticity and loss of stability in a FEM framework. Then, this discussion will be illustrated in the case of a simple tube loaded in torsion and a full torsion sample (full geometry) in section 4.4.3 to illustrate the applicability of the method in engineering structural computations.

4.1 Elastoplastic localization bands: Rice 1976

The loss of ellipticity criterion was introduced in [Rice, 1976] in its most general form. It is proposed to rederive some important expressions of this article with in the notations of present work. Note that these results are derived in many articles as [Mandel, 1964, 1966, Ortiz, 1987, Bigoni and Hueckel, 1991, Bigoni and Zaccaria, 1992, 1993, Benallal and Comi, 1996, Neilsen and Schreyer, 1993, Jirásek, 2007, Ben-Bettaieb and Abed-Meraim, 2017, Gourgiotis and Bigoni, 2016, A.R. Aguiar and Prado, 2017].

4.1.1 Loss of ellipticity in a finite deformation framework

For this purpose, let Ω_0 be the reference configuration and Ω the actual (equilibrium) configuration. We will denote $\underline{\mathbf{N}}$ a unit normal in the reference configuration, which becomes $\underline{\mathbf{n}} = J\tilde{\mathbf{F}}^{-T}\underline{\mathbf{N}}$ in the actual configuration.

For the loss of ellipticity analysis, let us also consider a possible strain rate discontinuity surface S_d of normal $\underline{\mathbf{N}}$ in Ω_0 :

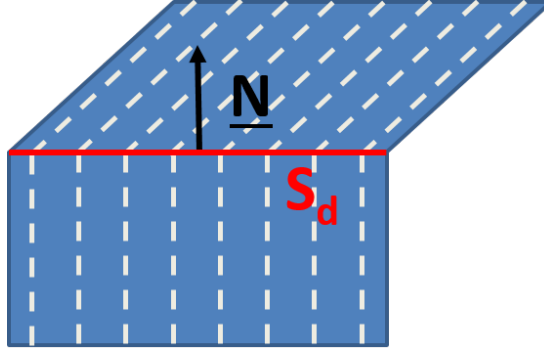


Figure 4.1: Scheme of a jump in strain rates.

Hadamard's compatibility condition for strain and stress rates in the presence of a discontinuity surface is given in finite deformations framework by:

$$\llbracket \dot{\underline{\underline{F}}} \rrbracket = \underline{\underline{g}} \otimes \underline{\underline{N}} \quad (4.1)$$

Stress rates equilibrium compatibility across the surface gives:

$$\llbracket \dot{\underline{\underline{S}}} \rrbracket \cdot \underline{\underline{N}} = \underline{\underline{0}} \quad (4.2)$$

where $\underline{\underline{S}} = J \underline{\underline{\sigma}} \underline{\underline{F}}^{-T}$ is the Boussinesq stress tensor and $J = \det(\underline{\underline{F}})$ the Jacobian of the transformation.

Finally, the present analysis is limited to finite deformation formulations for which the constitutive law in terms of rates can always be expressed in the form:

$$\dot{\underline{\underline{S}}} = \underline{\underline{\mathcal{L}}} : \dot{\underline{\underline{F}}} \quad (4.3)$$

In the most general case, the plastic loading condition is not necessarily identical on both sides of S_d . Therefore combining the previous equations, one gets:

$$(\dot{\underline{\underline{S}}}^+ - \dot{\underline{\underline{S}}}^-) \cdot \underline{\underline{N}} = \underline{\underline{0}} \quad (4.4)$$

$$(4.3) \Rightarrow (\underline{\underline{\mathcal{L}}}^+ : \dot{\underline{\underline{F}}}^+ - \underline{\underline{\mathcal{L}}}^- : \dot{\underline{\underline{F}}}^-) \cdot \underline{\underline{N}} = \underline{\underline{0}} \quad (4.5)$$

$$(\underline{\underline{\mathcal{L}}}^+ : \llbracket \dot{\underline{\underline{F}}} \rrbracket) \cdot \underline{\underline{N}} = -(\llbracket \underline{\underline{\mathcal{L}}} \rrbracket : \dot{\underline{\underline{F}}}^-) \cdot \underline{\underline{N}} \quad (4.6)$$

$$(4.1) \Rightarrow (\underline{\underline{\mathcal{L}}}^+ : (\underline{\underline{g}} \otimes \underline{\underline{N}})) \cdot \underline{\underline{N}} = -(\llbracket \underline{\underline{\mathcal{L}}} \rrbracket : \dot{\underline{\underline{F}}}^-) \cdot \underline{\underline{N}} \quad (4.7)$$

$$(\underline{\underline{N}} \odot \underline{\underline{\mathcal{L}}}^+ \cdot \underline{\underline{N}}) \cdot \underline{\underline{g}} = -(\llbracket \underline{\underline{\mathcal{L}}} \rrbracket : \dot{\underline{\underline{F}}}^-) \cdot \underline{\underline{N}} \quad (4.8)$$

as expressed in [Rice, 1976], and reproduced in Figure 4.2¹:

$$\dot{s}_{ij}^o = L_{ijkl}^o \dot{f}_{kl}^o, \quad \dot{s}_{ij} = L_{ijkl} (\dot{f}_{kl}^o + g_k n_l),$$

and by (2) the kinematical non-uniformity $\underline{\underline{g}}$ must satisfy

$$(n_i L_{ijkl} n_j) g_k = n_i (L^o - L)_{ijkl} \dot{f}_{kl}^o. \quad (5)$$

Figure 4.2: Equation (5) in [Rice, 1976].

¹ One should be aware that these notations are different from Rice's. His "nominal stress tensor" $\underline{\underline{s}}$ is the transposed of the Boussinesq stress tensor : $s_{ji} = S_{ij}$ and $L_{jikl} = \mathcal{L}_{ijkl}$.

Also, if one assumes that the fulfillment of the plastic loading condition is the same on both side of S_d , $\left[\underline{\underline{\mathcal{L}}} \right] = \underline{\underline{\mathbf{0}}}$, equation (4.8) becomes:

$$\exists \underline{\underline{\mathbf{g}}} \quad | \quad (\underline{\underline{\mathbf{N}}} \odot \underline{\underline{\mathcal{L}}} \cdot \underline{\underline{\mathbf{N}}}) \cdot \underline{\underline{\mathbf{g}}} = \underline{\underline{\mathbf{0}}} \Rightarrow \det(\underline{\underline{\mathbf{N}}} \odot \underline{\underline{\mathcal{L}}} \cdot \underline{\underline{\mathbf{N}}}) = 0 \quad (4.9)$$

This fundamental equation, as recognized in [Rice, 1976] (reproduced in Figure 4.3), is also well known as the **loss of ellipticity criterion**:

$$(\underline{\underline{\mathbf{nLn}}})_{jk} \underline{\underline{\mathbf{e}}}_k = 0, \quad \text{or} \quad \det(\underline{\underline{\mathbf{nLn}}}) = 0 \quad (6)$$

for the onset of localization. Here the concise notation $\underline{\underline{\mathbf{nLn}}}$ is introduced for the matrix having the jk component given by the term in parentheses at the left of (5). Later, in applications, it will be preferable to write constitutive rate laws in the form

$$\dot{\underline{\underline{\mathbf{g}}}}_{ij} = \bar{\mathbb{L}}_{ijkl} \frac{\partial \underline{\underline{\mathbf{x}}}_k}{\partial \underline{\underline{\mathbf{x}}}_l} \equiv \mathbb{C}_{ijkl} \mathbb{D}_{kl} - \sigma_{ik} \Omega_{kj} + \Omega_{ik} \sigma_{kj}, \quad (7)$$

where \mathbb{D} and Ω are the respective symmetric and non-symmetric parts of $\partial \underline{\underline{\mathbf{x}}}_k / \partial \underline{\underline{\mathbf{x}}}_l$, and \mathbb{C} relates the co-rotation (or Jaumann) rate of $\underline{\underline{\mathbf{g}}}$, namely $\dot{\underline{\underline{\mathbf{g}}}}$, to \mathbb{D} . Then, following the remark after (2), whenever the current and reference state are instantaneously coincident we have $\underline{\underline{\mathbf{nLn}}} = \underline{\underline{\mathbf{nLn}}}$, whether (6) can be satisfied non-trivially or not, and the localization condition (6) becomes $\det(\underline{\underline{\mathbf{nLn}}}) = 0$.

Figure 4.3: Equation (6) and (7) in [Rice, 1976].

Loss of uniqueness and loss of ellipticity

Finally, in [Rice, 1976] the author makes a link with [Hill, 1958]. Remembering Hill's uniqueness criterion : the solution of a rate boundary value problem is unique as long as:

$$\int_{\Omega_0} (\dot{\underline{\underline{\mathbf{S}}}}(\underline{\underline{\mathbf{v}}}_2) - \dot{\underline{\underline{\mathbf{S}}}}(\underline{\underline{\mathbf{v}}}_1)) : (\dot{\underline{\underline{\mathbf{F}}}}(\underline{\underline{\mathbf{v}}}_2) - \dot{\underline{\underline{\mathbf{F}}}}(\underline{\underline{\mathbf{v}}}_1)) dV > 0 \quad \forall \underline{\underline{\mathbf{v}}}_1, \underline{\underline{\mathbf{v}}}_2 \text{ kinematically admissible} \quad (4.10)$$

Kinematically admissible: All velocity fields that respect velocity boundary conditions.

Let us now consider that the volume is constrained on all $\partial\Omega$ by displacements such that $\dot{\underline{\underline{\mathbf{u}}}} = \dot{\underline{\underline{\mathbf{F}}}}^0 \underline{\underline{\mathbf{X}}}$, where $\dot{\underline{\underline{\mathbf{F}}}}^0$ is the same everywhere. A fundamental solution of such a problem is $\underline{\underline{\mathbf{v}}}^0 = \dot{\underline{\underline{\mathbf{F}}}}^0 \underline{\underline{\mathbf{X}}}$ everywhere. If we assume again that both velocity fields ($\underline{\underline{\mathbf{v}}}_1$ and $\underline{\underline{\mathbf{v}}}_2$) lead to the same loading state everywhere, equation (4.10) leads to a loss of uniqueness when:

$$\int_{\Omega_0} \dot{\underline{\underline{\mathbf{F}}}}(\Delta \underline{\underline{\mathbf{v}}}) : \underline{\underline{\mathcal{L}}} : \dot{\underline{\underline{\mathbf{F}}}}(\Delta \underline{\underline{\mathbf{v}}}) dV = 0 \quad \text{for at least one } \Delta \underline{\underline{\mathbf{v}}} \text{ kinematically admissible to 0} \quad (4.11)$$

Kinematically admissible to 0: all velocity fields that vanish on the velocity boundary $\partial\Omega^u$.

Since the problem is still uniform, one could consider this equation locally and check when $\dot{\underline{\underline{\mathbf{F}}}}(\Delta \underline{\underline{\mathbf{v}}}) = \underline{\underline{\mathbf{g}}} \otimes \underline{\underline{\mathbf{N}}}$ fulfills equation (4.11). This analysis leads to:

$$(\underline{\underline{\mathbf{g}}} \otimes \underline{\underline{\mathbf{N}}}) : \underline{\underline{\mathcal{L}}} : (\underline{\underline{\mathbf{g}}} \otimes \underline{\underline{\mathbf{N}}}) = 0 \quad (4.12)$$

$$\underline{\underline{\mathbf{g}}} \cdot (\underline{\underline{\mathbf{N}}} \odot \underline{\underline{\mathcal{L}}} \cdot \underline{\underline{\mathbf{N}}}) \cdot \underline{\underline{\mathbf{g}}} = 0 \quad (4.13)$$

$$\Rightarrow \det((\underline{\underline{\mathbf{N}}} \odot \underline{\underline{\mathcal{L}}} \cdot \underline{\underline{\mathbf{N}}})^{sym}) = 0 \quad (4.14)$$

This can be read in [Rice, 1976] as:

For any other solution $\underline{\dot{x}}$ meeting the same conditions on S , let $\Delta \underline{\dot{x}} = \underline{\dot{x}} - \underline{\dot{x}}^0$ and observe that this vanishes on S . Accordingly,

$$0 = \int_S n_i \Delta \dot{s}_{ij} \Delta \dot{x}_j dS = \int_V \Delta \dot{s}_{ij} \Delta \dot{F}_{ji} dV,$$

since $\Delta \dot{s}_{ij,i} = 0$, and thus if it is assumed that both the uniform and non-uniform field correspond to the same constitutive cone, a sufficient condition for uniqueness (i.e., the absence of a non-uniform solution) is, as in Hill [3], that the functional

$$I[\Delta \underline{\dot{x}}] \equiv \int_V \Delta \dot{x}_{j,i} L_{ijkl} \Delta \dot{x}_{k,l} dV \quad (13)$$

be positive definite for all fields $\Delta \underline{\dot{x}}$ vanishing on S .

In the restricted case for which the symmetry (4) applies (i.e., for elastic-plastic materials with normality), the equations of continuing equilibrium validate Hill's variational statement $\delta I[\Delta \underline{\dot{x}}] = 0$, and hence the first point in a program of deformation at which $I[\Delta \underline{\dot{x}}]$ becomes semi-definite is also the point at which, at least formally, conditions are met for existence of a non-uniform solution field. In this sense the Hill criterion is necessary as well, but there is no reason for coincidence of the failure of his sufficient condition and the existence of a non-uniform solution when $\underline{\mathcal{L}}$ corresponds to non-normality.

Figure 4.4: Equation (13) in [Rice, 1976]

Which is also well-known as the **loss of strong ellipticity criterion** [Marsden and Hughes, 1983]². Yet, this solution is not necessarily admissible since it does not vanish on $\partial\Omega^u$, as shown in section 4.2.2.

Loss of strong ellipticity criterion

Obviously, when $\underline{\mathcal{L}}$ does possess major symmetry, equations (4.9) and (4.14) are equivalent since the acoustic tensor is symmetric. It is generally not the case when the constitutive law is based on a non-associated flow rule, nor when the material law is formulated with the Jaumann derivative of the Cauchy stress tensor. In other words, the associativity of the plastic flow rule is not a sufficient condition for both criteria to be equivalent: "elasto-plastic materials with normality" [Rice, 1976] is sufficient only in a small deformation framework.

Also, as the problem is formulated above, $\underline{\dot{F}}(\Delta \underline{v}) = \underline{g} \otimes \underline{N}$ cannot be a solution everywhere since the velocity field $\Delta \underline{v}$ is not kinematically admissible to 0 (proof given in section 4.2.2). Therefore, such a velocity field could not be a solution of equation (4.11).

For non-associated materials, the loss of strong ellipticity criterion is not equivalent to the loss of ellipticity criterion. As long as the latter is not fulfilled, jumps in strain rates are not admissible. Therefore, the loss of strong ellipticity criterion can only be seen as the loss of positiveness of the second order work for a velocity gradient of the form $\underline{g} \otimes \underline{N}$ ³. Therefore, it does not satisfy the conditions for the emergence of localization bands in the sense of Rice, since jumps in strain rates are still forbidden.

² Contrary to what is said in [Liu, 2015], the singularity of the acoustic tensor ($\det(\underline{N} \odot \underline{\mathcal{L}} \cdot \underline{N}) = 0$) is not equivalent to the loss of strong ellipticity. The reference he cites is [Marsden and Hughes, 1983] in which the authors talk about elastic materials. These materials' tangent operators necessarily have major symmetry, hence the equivalence between the two criteria.

³ Fulfilling the loss of strong ellipticity criterion ($\det((\underline{N} \odot \underline{\mathcal{L}} \cdot \underline{N})^{sym}) = 0$) would just mean that the work to deform a volume element with a $\underline{\dot{F}}(\Delta \underline{v}) = \underline{g} \otimes \underline{N}$ velocity gradient instantaneously vanishes.

Finally, even if the loss of ellipticity criterion is fulfilled in a volume element in a structure, it does not necessarily mean that localization in the sense of Rice occurs. As discussed in [Mandel, 1966] this criterion corresponds to a volume element with prescribed traction on its boundary, not displacements. In a structure a volume element is obviously not free to deform without considering its neighbors. In fact, as it will be illustrated in section 4.4.2, a tube in simple torsion might exhibit a loss of ellipticity in a part of the structure before localization in the sense of Rice actually occurs in a FEM framework.

Also, as it was expressed in [Rice, 1976], the updated Lagrangian framework⁴ gives:

$$\underline{\mathbf{0}} = \llbracket \hat{\underline{\mathbf{S}}} \rrbracket \cdot \underline{\mathbf{n}} \quad (4.15)$$

$$\underline{\mathbf{0}} = \llbracket \hat{\underline{\boldsymbol{\sigma}}} + \text{Tr}(\underline{\mathbf{L}})\underline{\boldsymbol{\sigma}} - \underline{\boldsymbol{\sigma}}\underline{\mathbf{L}}^T \rrbracket \underline{\mathbf{n}} \quad (4.16)$$

$$\underline{\mathbf{0}} = \llbracket \hat{\underline{\boldsymbol{\sigma}}} \rrbracket \cdot \underline{\mathbf{n}} + (\underline{\mathbf{g}} \cdot \underline{\mathbf{n}})\underline{\boldsymbol{\sigma}} \cdot \underline{\mathbf{n}} - (\underline{\boldsymbol{\sigma}}(\underline{\mathbf{n}} \otimes \underline{\mathbf{g}})) \cdot \underline{\mathbf{n}} \quad (4.17)$$

$$\underline{\mathbf{0}} = \llbracket \hat{\underline{\boldsymbol{\sigma}}} \rrbracket \cdot \underline{\mathbf{n}} + (\underline{\mathbf{g}} \cdot \underline{\mathbf{n}})(\underline{\boldsymbol{\sigma}} \cdot \underline{\mathbf{n}}) - (\underline{\boldsymbol{\sigma}} \cdot \underline{\mathbf{n}})(\underline{\mathbf{g}} \cdot \underline{\mathbf{n}}) \quad (4.18)$$

$$\underline{\mathbf{0}} = \llbracket \hat{\underline{\boldsymbol{\sigma}}} \rrbracket \cdot \underline{\mathbf{n}} \quad (4.19)$$

Passing from equation (4.17) to equation (4.18) is due to the symmetry of $\underline{\boldsymbol{\sigma}}$. As done in equation (2) by [Rice, 1976] (see Figure 4.5)).

$$\underline{\mathbf{n}} \cdot \underline{\dot{\underline{\mathbf{s}}}} = \underline{\mathbf{n}} \cdot \underline{\dot{\underline{\mathbf{s}}}}^0, \quad \text{or} \quad \underline{\mathbf{n}} \cdot \Delta \underline{\dot{\underline{\mathbf{s}}}} = 0. \quad (2)$$

The last condition can be expressed also in terms of $\underline{\mathbf{g}}$. Choosing the reference state to coincide, instantaneously, with the current state, one may show [22] from the relation of $\underline{\mathbf{g}}$ to $\underline{\mathbf{s}}$ that $\underline{\mathbf{n}} \cdot \Delta \underline{\dot{\underline{\mathbf{s}}}} = \underline{\mathbf{n}} \cdot \Delta \underline{\dot{\underline{\mathbf{g}}}}$ whenever (1) is satisfied, and hence the condition (2) is alternatively stated as $\underline{\mathbf{n}} \cdot \Delta \underline{\dot{\underline{\mathbf{g}}}} = 0$. This can, of course, be derived directly.

Figure 4.5: Equation (2) in [Rice, 1976]

This is consistent with the analysis of the propagation of discontinuity waves, given in appendix 8.4, for a vanishing velocity of the discontinuity surface.

Discussion on the symmetries of the acoustic tensor for hypoelastoplastic formulations:

In [Rice, 1976], the author uses a hypoelastoplastic constitutive formulation on the Jaumann derivative of the Cauchy stress tensor : $\underline{\boldsymbol{\sigma}}^J = \underline{\mathcal{L}}^J : \underline{\mathbf{L}}$. In an updated Lagrangian framework, the acoustic tensor can be expressed as [Besson et al., 2001, Rudnicki and Rice, 1975, Mear and Hutchinson, 1985]:

$$\underline{\mathbf{n}} \odot \hat{\underline{\mathcal{L}}} \cdot \underline{\mathbf{n}} = \underline{\mathbf{n}} \odot \underline{\mathcal{L}}^\sigma \cdot \underline{\mathbf{n}} \quad (4.20)$$

$$= \underline{\mathbf{n}} \odot \underline{\mathcal{L}}^J \cdot \underline{\mathbf{n}} + \underline{\mathbf{A}}(\underline{\mathbf{n}}) \quad (4.21)$$

$$\text{with : } \underline{\mathbf{A}}(\underline{\mathbf{n}}) = \frac{1}{2} ((\underline{\mathbf{n}} \cdot \underline{\boldsymbol{\sigma}} \cdot \underline{\mathbf{n}})\underline{\mathbf{I}} + (\underline{\boldsymbol{\sigma}} \cdot \underline{\mathbf{n}}) \otimes \underline{\mathbf{n}} - \underline{\mathbf{n}} \otimes (\underline{\boldsymbol{\sigma}} \cdot \underline{\mathbf{n}}) - \underline{\boldsymbol{\sigma}}) \quad (4.22)$$

In this case $\underline{\mathbf{A}}$ is not symmetric due to the term $(\underline{\boldsymbol{\sigma}} \cdot \underline{\mathbf{n}}) \otimes \underline{\mathbf{n}} - \underline{\mathbf{n}} \otimes (\underline{\boldsymbol{\sigma}} \cdot \underline{\mathbf{n}})$. In fact, even though $\underline{\mathcal{L}}$ does not possess minor symmetries, it may possess major symmetry if the constitutive law is hyper-elastoplastic or hypo-elastoplastic formulated on an objective derivative with Kirchhoff

⁴ $\hat{\underline{\mathbf{F}}} = \underline{\mathbf{I}}$, $\underline{\mathbf{L}} = \hat{\underline{\mathbf{F}}}\hat{\underline{\mathbf{F}}}^{-1} = \hat{\underline{\mathbf{F}}}\hat{\underline{\mathbf{F}}}^{-1} \neq \underline{\mathbf{0}}$, $\hat{J} = 1$ et $\hat{J} = \text{Tr}(\underline{\mathbf{L}})$

stress tensor with an associated flow rule [Petryk, 2000]. In fact, if the law is formulated using the Jaumann derivative of the Cauchy stress tensor (corotational frame) or with a non-associated flow rule (soils for example) $\underline{\underline{\mathcal{L}}}$ has no symmetry at all [Hill, 1958, Szabó, 2000, Sanborn and Prévost, 2011]. $\underline{\underline{\mathcal{A}}}$ is sometimes presented to be a "general finite strain correction". This can be a bit simplistic when one considers the multiplicity of finite strain formulations. For instance, if the constitutive law is formulated using the updated Kirchhoff stress tensor ($\hat{\underline{\tau}} = \hat{\underline{J}}\underline{\underline{\sigma}}$)⁵ instead of the Cauchy stress tensor ($\underline{\underline{\sigma}}$), as proposed in [Bigoni and Zaccaria, 1993, Szabó, 2000, Hill, 1958] and many others, then $\underline{\underline{\mathcal{A}}}$ is symmetric :

$$\underline{\underline{\mathcal{A}}}(\underline{\underline{n}}) = \frac{1}{2} ((\underline{\underline{n}} \cdot \underline{\underline{\sigma}} \cdot \underline{\underline{n}})\underline{\underline{I}} - (\underline{\underline{\sigma}} \cdot \underline{\underline{n}}) \otimes \underline{\underline{n}} - \underline{\underline{n}} \otimes (\underline{\underline{\sigma}} \cdot \underline{\underline{n}}) - \underline{\underline{\sigma}}) \quad (4.23)$$

4.1.2 Loss of ellipticity and loss of strong ellipticity in an infinite homogeneous domain

Let us consider a homogeneous volume homogeneously deformed. In this analysis, one will consider that no "geometrical instabilities" can take place, such as buckling or necking. Also, we consider the domain to be infinite to avoid boundary issues. Let us now assume that the structure is homogeneously loaded in terms of stresses (rigid body motion will be excluded from the analysis)⁶. The fundamental homogeneous solution's quantities are denoted by the superscript " $(\cdot)^0$ ". Hill's loss of uniqueness criterion then gives (assuming no elastic unloading):

$$\int_{\Omega_0} \Delta \underline{\underline{\dot{F}}} : \underline{\underline{\mathcal{L}}} : \Delta \underline{\underline{\dot{F}}} dV = 0 \quad (4.24)$$

where $\Delta \underline{\underline{\dot{F}}} = \underline{\underline{\dot{F}}} - \underline{\underline{\dot{F}}}^0$.

If the loss of strong ellipticity is fulfilled for a given $\underline{\underline{g}}^{se} \otimes \underline{\underline{N}}^{se}$:

$$(\underline{\underline{g}}^{se} \otimes \underline{\underline{N}}^{se}) : \underline{\underline{\mathcal{L}}} : (\underline{\underline{g}}^{se} \otimes \underline{\underline{N}}^{se}) = 0 \quad (4.25)$$

(where the superscript "se" is for "strong ellipticity"), then $\underline{\underline{\dot{F}}} = \underline{\underline{F}}^0 + \underline{\underline{g}}^{se} \otimes \underline{\underline{N}}^{se}$ in all Ω_0 is a solution to equation (4.24). Unless the tangent operator $\underline{\underline{\mathcal{L}}}$ possesses major symmetry, the loss of ellipticity criterion allowing a jump in strain rates is still not necessarily fulfilled. Therefore, $\underline{\underline{\dot{F}}} = \underline{\underline{\dot{F}}}^0 + \underline{\underline{g}}^{se} \otimes \underline{\underline{N}}^{se}$ everywhere⁷.

Now let us assume that the loss of ellipticity criterion is reached for a given $\underline{\underline{N}}^e$:

$$\det(\underline{\underline{N}}^e \odot \underline{\underline{\mathcal{L}}} \cdot \underline{\underline{N}}^e) = 0 \quad (4.26)$$

Then necessarily there exists a vector $\underline{\underline{g}}^e$ (with $\underline{\underline{g}}^e \cdot \underline{\underline{g}}^e = 1$) such that:

$$(\underline{\underline{N}}^e \odot \underline{\underline{\mathcal{L}}} \cdot \underline{\underline{N}}^e) \cdot \underline{\underline{g}}^e = 0 \quad (4.27)$$

Therefore, a strain rate jump through a surface with a normal $\underline{\underline{N}}^e$ is allowed such that:

$$\llbracket \underline{\underline{\dot{F}}} \rrbracket = \alpha \underline{\underline{g}}^e \otimes \underline{\underline{N}}^e \quad (4.28)$$

with α an arbitrary real value.

Let us now consider the possibility of the existence of an infinite band delimited by two plane

⁵ ($\hat{\underline{\tau}} = \hat{\underline{J}}\underline{\underline{\sigma}}$) but $\hat{\underline{\tau}} = \text{Tr}(\underline{\underline{D}})\underline{\underline{\sigma}} + \underline{\underline{\dot{\sigma}}}$

⁶Such an analysis will be illustrated in section 5.3.2.

⁷ $\underline{\underline{\dot{F}}} = \alpha(\underline{\underline{X}} \cdot \underline{\underline{N}}^{se})\underline{\underline{g}}^{se} \otimes \underline{\underline{N}}^{se}$, with α a continuous real valued function, would also be a solution, see section 4.2.2.

surfaces S_d^- and S_d^+ that define three domains (see Figure 4.6): V^+ and V^- where $\dot{\underline{\mathbf{F}}} = \dot{\underline{\mathbf{F}}}^0$ and V^{band} where $\dot{\underline{\mathbf{F}}} = \dot{\underline{\mathbf{F}}}^0 + \alpha \underline{\mathbf{g}}^e \otimes \underline{\mathbf{N}}^e$. This leads to:

$$\Delta \dot{\underline{\mathbf{F}}} = \begin{cases} \alpha \underline{\mathbf{g}}^e \otimes \underline{\mathbf{N}}^e & \text{in the band;} \\ \mathbf{0} & \text{outside the band.} \end{cases} \quad (4.29)$$

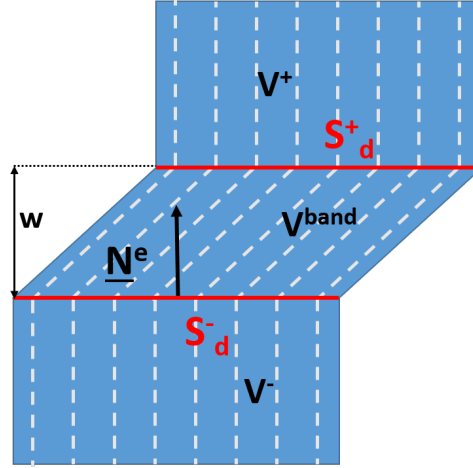


Figure 4.6: Localization band in an infinite homogeneous media.

Since the loss of ellipticity criterion is fulfilled, such a solution is allowed, and trivially fulfills Hill's uniqueness criterion:

$$\int_{\Omega_0} \Delta \dot{\underline{\mathbf{F}}} : \underline{\mathcal{L}} : \Delta \dot{\underline{\mathbf{F}}} dV = \int_{V^{band}} \Delta \dot{\underline{\mathbf{F}}} : \underline{\mathcal{L}} : \Delta \dot{\underline{\mathbf{F}}} dV \quad (4.30)$$

$$= \int_{V^{band}} (\alpha \underline{\mathbf{g}}^e \otimes \underline{\mathbf{N}}^e) : \underline{\mathcal{L}} : (\alpha \underline{\mathbf{g}}^e \otimes \underline{\mathbf{N}}^e) dV \quad (4.31)$$

$$= 0 \quad (4.32)$$

$$(4.33)$$

We just illustrated that when loss of ellipticity is fulfilled in an infinite homogeneous domain, any band of arbitrary width⁸, w , and direction $\underline{\mathbf{N}}^e$ can emerge and it can exhibit jumps in strain rate on its boundaries S_d^- and S_d^+ . Nevertheless, this is only true for the onset of localization. Just after this condition is fulfilled, a new kind of bifurcations becomes possible: localization with plastic loading on one side of S_d and elastic unloading on the other side (see appendix 8.5.2).

4.2 Localization in structures

The work presented above is limited to the analysis of a single material element. Nevertheless, these criteria can virtually be applied to an infinite homogeneous domain. Such a framework is analyzed in section 4.1.2 to compare the loss of ellipticity and the loss of strong ellipticity criterion. However, for our purposes, this analysis is to be used in arbitrary structures. As

⁸ Since it was not specified at any time in the derivations.

pointed out in [Nguyen, 2000, Mandel, 1964, Petryk, 2000], this analysis does not yet include Dirichlet boundary conditions. A proof that $\det(\underline{\mathbf{N}} \odot \underline{\mathcal{L}} \cdot \underline{\mathbf{N}}) > 0$ implies local uniqueness is for instance given in [Bigoni, 2012]. This analysis relies on van Hove's theorem formulated in [van Hove, 1947] and is re-derived in section 4.2.1. Then, a minor extension is proposed in section 4.2.2. Finally, on the basis of this extension, a discussion about the uniqueness of the discretized rate boundary value problem is proposed in section 4.4.1.

4.2.1 Ellipticity and local uniqueness: van Hove's rate boundary value problem

In the present section, the uniqueness of the so-called "van Hove rate boundary value problem" is re-derived based on the proof given in [Bigoni, 2012]. To do so, let us consider a homogeneous finite domain \mathcal{B} homogeneously strained with Dirichlet boundary conditions applied on all $\partial\mathcal{B}$. Then to ensure the uniqueness of the rate boundary value problem, the following condition should be fulfilled:

$$\int_{\mathcal{B}} \dot{\underline{\mathbf{F}}}(\underline{\dot{\mathbf{u}}}) : \underline{\mathcal{L}}^{sym} : \dot{\underline{\mathbf{F}}}(\underline{\dot{\mathbf{u}}}) dV > 0 \quad \forall \underline{\dot{\mathbf{u}}} = \underline{\mathbf{0}} \text{ on } \partial\mathcal{B} \quad (4.34)$$

In order to perform a Fourier transform of $\underline{\dot{\mathbf{u}}}$ and $\dot{\underline{\mathbf{F}}}$, the definition of the velocity field is extended to \mathbb{R}^n ($n = 2, 3$) with $\underline{\dot{\mathbf{u}}} = \underline{\mathbf{0}} \quad \forall \underline{\mathbf{X}} \notin \mathcal{B}$. Then the n dimensional Fourier transform of $\underline{\dot{\mathbf{u}}}$ and $\dot{\underline{\mathbf{F}}}(\underline{\dot{\mathbf{u}}})$ can be expressed as:

$$\underline{\dot{\mathbf{u}}}^*(\underline{\mathbf{w}}_0) = \left(\frac{1}{2\pi}\right)^{\frac{n}{2}} \int_{\mathbb{R}^n} e^{-i\underline{\mathbf{w}}_0 \cdot \underline{\mathbf{X}}} \underline{\dot{\mathbf{u}}}(\underline{\mathbf{X}}) dV \quad (4.35)$$

$$\dot{\underline{\mathbf{F}}}^*(\underline{\mathbf{w}}_0) = \left(\frac{1}{2\pi}\right)^{\frac{n}{2}} \int_{\mathbb{R}^n} e^{-i\underline{\mathbf{w}}_0 \cdot \underline{\mathbf{X}}} \dot{\underline{\mathbf{F}}}(\underline{\mathbf{X}}) dV \quad (4.36)$$

where dV is the volume element in the real space, and $\underline{\mathbf{w}}_0$ is the inverse wave vector in the Fourier space. Using the divergence theorem and that $\underline{\dot{\mathbf{u}}}$ is kinematically admissible to 0 in equation (4.35), one identifies:

$$\dot{\underline{\mathbf{F}}}^* = i\underline{\dot{\mathbf{u}}}^* \otimes \underline{\mathbf{w}}_0 = -\underline{\dot{\mathbf{u}}}_I^* \otimes \underline{\mathbf{w}}_0 + i\underline{\dot{\mathbf{u}}}_R^* \otimes \underline{\mathbf{w}}_0 \quad (4.37)$$

where $i = \sqrt{-1}$, $\underline{\dot{\mathbf{u}}}_R^*$ and $\underline{\dot{\mathbf{u}}}_I^*$ respectively the real and imaginary parts of $\underline{\dot{\mathbf{u}}}^*$. Since \mathcal{B} is homogeneous and homogeneously strained ($\underline{\mathcal{L}}$ is constant in space), using Parseval's theorem, equation 4.34 gives:

$$\int_{\mathcal{B}} \dot{\underline{\mathbf{F}}} : \underline{\mathcal{L}}^{sym} : \dot{\underline{\mathbf{F}}} dV = \underline{\mathcal{L}}^{sym} :: \int_{\mathcal{B}} \dot{\underline{\mathbf{F}}} \otimes \dot{\underline{\mathbf{F}}} dV \quad (4.38)$$

$$= \underline{\mathcal{L}}^{sym} :: \int_{\mathbb{R}^n} \dot{\underline{\mathbf{F}}}^* \otimes \dot{\underline{\mathbf{F}}} dw \quad (4.39)$$

$$= \int_{\mathbb{R}^n} \dot{\underline{\mathbf{F}}}^* : \underline{\mathcal{L}}^{sym} : \dot{\underline{\mathbf{F}}} dw \quad (4.40)$$

where $\bar{(\cdot)}$ is the complex conjugate of the quantity (\cdot) .

Using equation (4.37) in equation (4.40) leads to:

$$\int_{\mathcal{B}} \dot{\underline{\mathbf{F}}} : \underline{\mathcal{L}}^{sym} : \dot{\underline{\mathbf{F}}} dV = \int_{\mathbb{R}^n} (\underline{\dot{\mathbf{u}}}_R^* \otimes \underline{\mathbf{w}}_0) : \underline{\mathcal{L}}^{sym} : (\underline{\dot{\mathbf{u}}}_R^* \otimes \underline{\mathbf{w}}_0) dw + \int_{\mathbb{R}^n} (\underline{\dot{\mathbf{u}}}_I^* \otimes \underline{\mathbf{w}}_0) : \underline{\mathcal{L}}^{sym} : (\underline{\dot{\mathbf{u}}}_I^* \otimes \underline{\mathbf{w}}_0) dw \quad (4.41)$$

$$= \int_{\mathbb{R}^n} \underline{\dot{\mathbf{u}}}_R^* \cdot (\underline{\mathbf{w}}_0 \odot \underline{\mathcal{L}}^{sym} \cdot \underline{\mathbf{w}}_0) \cdot \underline{\dot{\mathbf{u}}}_R^* dw + \int_{\mathbb{R}^n} \underline{\dot{\mathbf{u}}}_I^* \cdot (\underline{\mathbf{w}}_0 \odot \underline{\mathcal{L}}^{sym} \cdot \underline{\mathbf{w}}_0) \cdot \underline{\dot{\mathbf{u}}}_I^* dw \quad (4.42)$$

If $\det(\underline{\mathbf{N}} \odot \underline{\mathcal{L}} \cdot \underline{\mathbf{N}}) > 0$ for any unit vector $\underline{\mathbf{N}}$, then the equations (4.43) and (4.44) are necessarily fulfilled⁹:

$$\dot{\mathbf{u}}_R^* \cdot (\underline{\mathbf{w}}_0 \odot \underline{\mathcal{L}}^{sym} \cdot \underline{\mathbf{w}}_0) \cdot \dot{\mathbf{u}}_R^* > 0 \quad \forall \underline{\mathbf{w}}_0 \neq \mathbf{0} \text{ and } \forall \dot{\mathbf{u}}_R^* \neq \mathbf{0} \quad (4.43)$$

$$\dot{\mathbf{u}}_I^* \cdot (\underline{\mathbf{w}}_0 \odot \underline{\mathcal{L}}^{sym} \cdot \underline{\mathbf{w}}_0) \cdot \dot{\mathbf{u}}_I^* > 0 \quad \forall \underline{\mathbf{w}}_0 \neq \mathbf{0} \text{ and } \forall \dot{\mathbf{u}}_I^* \neq \mathbf{0} \quad (4.44)$$

Since $\underline{\mathbf{w}}_0 = \mathbf{0}$ corresponds to a pure translation, it is excluded from this analysis, uniqueness is proven for the stated rate boundary value problem as long as ellipticity is fulfilled.

4.2.2 A minor extension to van Hove's theorem and loss of uniqueness

Now, it is proposed to take this proof a small step further and prove that the van Hove rate boundary value problem still has a unique solution as long as:

$$\det(\underline{\mathbf{N}} \odot \underline{\mathcal{L}} \cdot \underline{\mathbf{N}}) \geq 0 \quad (4.45)$$

Let $\underline{\mathbf{N}}_0$ and $\underline{\mathbf{g}}_0$ be the only pair of unit vectors¹⁰ that fulfills equation (4.46).

$$(\underline{\mathbf{N}}_0 \odot \underline{\mathcal{L}} \cdot \underline{\mathbf{N}}_0) \underline{\mathbf{g}}_0 = \mathbf{0} \quad (4.46)$$

Let us give a *reductio ad absurdum* to prove that van Hove's rate boundary value problem still possesses a unique velocity solution in such a case. The terms in the integrals in equation (4.42) are strictly positive when $\underline{\mathbf{w}}_0$ is not co-linear with $\underline{\mathbf{N}}_0$ or when $\underline{\mathbf{u}}_R^*$ or $\underline{\mathbf{u}}_I^*$ are not co-linear with $\underline{\mathbf{g}}_0$. Then, for the integral in equation (4.34) to vanish (loss of uniqueness), it is necessary for $\underline{\mathbf{w}}_0$ to be co-linear with $\underline{\mathbf{N}}_0$ and for $\underline{\mathbf{u}}_R^*$ and $\underline{\mathbf{u}}_I^*$ to be co-linear with $\underline{\mathbf{g}}_0$. Then:

$$\dot{\mathbf{u}}_R^* = \begin{cases} \beta(\underline{\mathbf{w}}_0) \underline{\mathbf{g}}_0 & \text{if } \underline{\mathbf{w}}_0 = \alpha \underline{\mathbf{N}}_0 \\ \mathbf{0} & \text{if not} \end{cases} \quad (4.47)$$

$$\dot{\mathbf{u}}_I^* = \begin{cases} \gamma(\underline{\mathbf{w}}_0) \underline{\mathbf{g}}_0 & \text{if } \underline{\mathbf{w}}_0 = \alpha \underline{\mathbf{N}}_0 \\ \mathbf{0} & \text{if not} \end{cases} \quad (4.48)$$

where $\alpha \in \mathbb{R}$, and β and γ denote real valued functions.

Then, $\dot{\mathbf{u}}^*$ is necessarily given by:

$$\dot{\mathbf{u}}^* = (\beta(\underline{\mathbf{w}}_0) + i\gamma(\underline{\mathbf{w}}_0)) \underline{\mathbf{g}}_0 \delta_{\underline{\mathbf{N}}_0}(\underline{\mathbf{w}}_0) \quad (4.49)$$

where $\delta_{\underline{\mathbf{N}}_0}(\underline{\mathbf{w}}_0)$ is a Dirac function of a line in \mathbb{R}^n defined such that:

$$\int_{\mathbb{R}^n} f(\underline{\mathbf{w}}_0) \delta_{\underline{\mathbf{N}}_0}(\underline{\mathbf{w}}_0) dV_{w_0} = \int_{\mathbb{R}} f(\alpha \underline{\mathbf{N}}_0) d\alpha \quad (4.50)$$

⁹ Scaling $\underline{\mathbf{N}}$ with a positive real number covers all $\underline{\mathbf{w}}_0 \neq \mathbf{0}$, and does not change the equation: $\det(\underline{\mathbf{w}}_0 \odot \underline{\mathcal{L}} \cdot \underline{\mathbf{w}}_0) > 0$

¹⁰ The proof would be the same if there are multiple pairs, but a finite number, and would require to use a summation symbol. For simplicity, the proof is derived only with one pair.

Finally, computing the inverse Fourier transform of $\dot{\mathbf{u}}^*$ gives:

$$\dot{\mathbf{u}}(\mathbf{X}) = \left(\frac{1}{2\pi}\right)^{\frac{n}{2}} \int_{\mathbb{R}^n} e^{i\mathbf{w}_0 \cdot \mathbf{X}} \dot{\mathbf{u}}^*(\mathbf{w}_0) dV_{w_0} \quad (4.51)$$

$$= \left(\frac{1}{2\pi}\right)^{\frac{n}{2}} \int_{\mathbb{R}^n} e^{i\mathbf{w}_0 \cdot \mathbf{X}} (\beta + i\gamma) \mathbf{g}_0 \delta_{\mathbf{N}_0}(\mathbf{w}_0) dV_{w_0} \quad (4.52)$$

$$\dot{\mathbf{u}}(\mathbf{X}) = \left(\frac{1}{2\pi}\right)^{\frac{n}{2}} \int_{\mathbb{R}} e^{i\alpha \mathbf{N}_0 \cdot \mathbf{X}} (\beta(\alpha) + i\gamma(\alpha)) \mathbf{g}_0 d\alpha \quad (4.53)$$

where (4.53) is obtained by injecting (4.50) in (4.52). Since \mathbf{N}_0 and \mathbf{g}_0 are given constant vectors (see definition), the result of the whole integral can only be a function of $\mathbf{N}_0 \cdot \mathbf{X}$:

$$\dot{\mathbf{u}}(\mathbf{X}) = \dot{\mathbf{u}}(\mathbf{N}_0 \cdot \mathbf{X}) \quad (4.54)$$

If $\dot{\mathbf{u}}$ has to vanish on all $\partial\mathcal{B}_0^u = \partial\mathcal{B}_0$, then $\dot{\mathbf{u}}$ has to be identically vanishing everywhere. Thus, $\dot{\mathbf{u}}$ is not satisfying as a bifurcation field. Therefore, the van Hove rate boundary problem is always stable as long as the acoustic tensors $\mathbf{N} \odot \mathcal{L} \cdot \mathbf{N}$ is semi-positive definite for any orientation \mathbf{N} .

4.2.3 Discussion

In a structural problem, when $\det(\mathbf{N} \odot \mathcal{L} \cdot \mathbf{N}) = 0$ in a single material element that is surrounded by an elliptic domain, a discussion is necessary. The problem to consider is neither the one constrained in displacements on all the boundary of this material element (also known as “van Hove rate boundary value problem”) [van Hove, 1947] since it is surrounded by something “softer” than strict displacement conditions, nor the one given in section 4.1.2 which is loaded in pure traction conditions¹¹ [Mandel, 1964]. In fact the real structural problem lies in between these two models. Therefore, when $\det(\mathbf{N} \odot \mathcal{L} \cdot \mathbf{N}) = 0$ only in a finite domain inside the bulk of a structure which did not lose ellipticity everywhere, uniqueness is not necessarily lost.

Going a step further would consist of considering the case for which $\det(\mathbf{N} \odot \mathcal{L} \cdot \mathbf{N}) < 0$ for at least a few \mathbf{N} . In Fourier’s space this would mean that the terms in the integral will vanish not only on a line: There will be a whole cone-like shape in which it is negative, outside which it is positive, and on the surface of which it vanishes. In this case, one may probably be able to build a bifurcated solution for the van Hove rate boundary value problem. In fact, the proof for $\det(\mathbf{N} \odot \mathcal{L} \cdot \mathbf{N}) = 0$ implied that $\dot{\mathbf{u}}^*$ has to be defined at least for all directions $\mathbf{w}_0 / \sqrt{\mathbf{w}_0 \cdot \mathbf{w}_0}$ in order to fulfill the Dirichlet boundary conditions¹². Nevertheless, for some materials (like the steel that is considered in the present work) when $\min(\det(\mathbf{N} \odot \mathcal{L} \cdot \mathbf{N})) < 0$, there are some orders of magnitude between the maximum of $\det(\mathbf{N} \odot \mathcal{L} \cdot \mathbf{N})$ (highly positive) and its minimum (slightly negative).

In order to illustrate this problem, let us consider a 2D square domain Ω . $\dot{\mathbf{u}}$ must be defined only inside this domain, then the solution has to fulfill:

$$\dot{\mathbf{u}} = \Pi_{\Omega}(X) \dot{\mathbf{u}} \quad \text{where: } \Pi_{\Omega} = \begin{cases} 1 & \text{if } \mathbf{X} \in \Omega \\ 0 & \text{if not} \end{cases} \quad (4.55)$$

The Fourier transform of Π_{Ω} is similar to a sincard function. Then by the properties of the Fourier transform of a product gives:

$$\dot{\mathbf{u}}^* = \text{sincard}(X) * \dot{\mathbf{u}}^* \quad (4.56)$$

¹¹ Called in the present work “Mandel rate boundary value problem”.

¹² If not, the fields cannot vanish everywhere of $\partial\Omega$.

where $*$ denote the convolution product. This adds a restriction to the possible bifurcation fields. These statements are illustrated in section 4.4.1.

4.3 Numerical methods for detection of loss of ellipticity

In this section, a new method to systematically evaluate the loss of ellipticity criterion is detailed. This method is expressed in the general case of finite deformations. It will be validated by comparison with an analytical case (see section 8.6 for more examples): pure shear, tension in plane strain and simple tension.

4.3.1 Literature review

As discussed, for localization to be possible, one needs to fulfill the loss of ellipticity criterion. Solving $\det(\underline{\mathbf{N}} \odot \underline{\underline{\mathcal{L}}} \cdot \underline{\mathbf{N}}) < 0$ would be computationally too expensive. However, since the acoustic tensor is initially positive definite, one possible method is to evaluate loss of ellipticity by computing the minimum of $C(\underline{\mathbf{N}}) = \det(\underline{\mathbf{N}} \odot \underline{\underline{\mathcal{L}}} \cdot \underline{\mathbf{N}})$ at each Gauss Point (GP) of a finite element mesh, at each time step, and check the sign of this minimum. As long as the minimum is positive, $C(\underline{\mathbf{N}})$ must be positive for all $\underline{\mathbf{N}}$. However, when $\min(\det(\underline{\mathbf{N}} \odot \underline{\underline{\mathcal{L}}} \cdot \underline{\mathbf{N}}))$ is negative, there is at least one $\underline{\mathbf{N}}$ for which ellipticity is lost.

Remark: as $C(\underline{\mathbf{N}})$ is a smooth function of $\underline{\mathbf{N}}$, once ellipticity is lost for one $\underline{\mathbf{N}}$ such that the determinant is negative, there must be a whole cone of normal $\underline{\mathbf{N}}$ for which ellipticity is lost as well. However, it may be the normal that is observed when localization occurs, as shown in the numerical section (8.6.5).

The following two articles propose globally the same method for small strain framework¹³, the only difference being that it is expressed for associative flow rules (symmetric tangent operator) in [Ortiz, 1987], and expressed for non-associative flow rules (non-symmetric tangent operator) in [Sanborn and Prévost, 2011]. For both papers, the method is based on the minimization problem of $C(\underline{\mathbf{n}})$ under the equality condition $\underline{\mathbf{n}} \cdot \underline{\mathbf{n}} - 1 = 0$, given in equation (4.57).

$$\arg \min_{\underline{\mathbf{n}}, \lambda} (M(\underline{\mathbf{n}}, \lambda)) \quad \text{with: } M(\underline{\mathbf{n}}, \lambda) = C(\underline{\mathbf{n}}) - \lambda(\underline{\mathbf{n}} \cdot \underline{\mathbf{n}} - 1) \quad (4.57)$$

where λ denotes the Lagrange multiplier.

Associated and non-associated flow rules only affects the gradient of $C(\underline{\mathbf{n}})$. Therefore, [Ortiz, 1987] and [Sanborn and Prévost, 2011] slightly different expression for the gradient. They respectively use:

$$\left(\frac{\partial C}{\partial n_i} \right) = \det(\underline{\underline{\mathcal{Q}}}) \underline{\underline{\mathcal{Q}}}_{kj}^{-1} L_{ijkl} n_l \quad \text{for associated flow rules} \quad (4.58)$$

$$\left(\frac{\partial C}{\partial n_i} \right) = \det(\underline{\underline{\mathcal{Q}}}) \underline{\underline{\mathcal{Q}}}_{kj}^{-1} (L_{ijkl} + L_{ljki}) n_l \quad \text{for non-associated flow rules} \quad (4.59)$$

where $\underline{\underline{\mathcal{L}}}$ denotes the elastoplastic tangent operator in small strain, and $\underline{\underline{\mathcal{Q}}} = \underline{\mathbf{n}} \odot \underline{\underline{\mathcal{L}}} \cdot \underline{\mathbf{n}}$ the acoustic tensor. These results are derived thanks to the following identity:

$$d(\det(\underline{\underline{\mathcal{A}}})) = \det(\underline{\underline{\mathcal{A}}}) \underline{\underline{\mathcal{A}}}^{-T} : d\underline{\underline{\mathcal{A}}} \quad (4.60)$$

¹³ $\underline{\underline{\mathcal{L}}}$ possesses minor symmetries, $\underline{\mathbf{n}} = \underline{\mathbf{N}}$

which is defined only if $\det(\underline{\mathbf{A}}) \neq 0$.

For the rest of the presentation both gradients will be denoted by:

$$\frac{\partial C}{\partial \underline{\mathbf{n}}} = \underline{\mathcal{J}}(\underline{\mathbf{n}}) \cdot \underline{\mathbf{n}} \quad (4.61)$$

$$\text{with: } J_{il}(\underline{\mathbf{n}}) = \begin{cases} \det(\underline{\mathcal{Q}}) Q_{kj}^{-1} L_{ijkl} & \text{for associated flow rules} \\ \det(\underline{\mathcal{Q}}) Q_{kj}^{-1} (L_{ijkl} + L_{ljki}) & \text{for non-associated flow rules} \end{cases} \quad (4.62)$$

Using this notation, the minimization problem gives:

$$\begin{cases} \frac{\partial M}{\partial \underline{\mathbf{n}}} = \underline{\mathcal{J}} \cdot \underline{\mathbf{n}} - 2\lambda \underline{\mathbf{n}} = \underline{\mathbf{0}} \\ \frac{\partial M}{\partial \lambda} = \underline{\mathbf{n}} \cdot \underline{\mathbf{n}} - 1 = 0 \end{cases} \quad (4.63)$$

To solve this problem the authors propose to rewrite the first equation as a non-linear eigenvalue problem, where the Lagrange multiplier is an eigenvalue of $\frac{1}{2}\underline{\mathcal{J}}(\underline{\mathbf{n}})$:

$$\frac{1}{2}\underline{\mathcal{J}}(\underline{\mathbf{n}}) \cdot \underline{\mathbf{n}} = \lambda \underline{\mathbf{n}} \quad (4.64)$$

Finally, the authors use a “fixed point” algorithm [Besson et al., 2010]. Given a $\underline{\mathbf{n}}^k$, each iteration consists in solving following eigenvalue problem:

$$\frac{1}{2}\underline{\mathcal{J}}(\underline{\mathbf{n}}^k) \cdot \underline{\mathbf{n}}^{k+1} = \lambda^{k+1} \underline{\mathbf{n}}^{k+1} \quad (4.65)$$

At each iteration the eigenvector associated with the smallest eigenvalue is chosen for the next iteration in [Ortiz, 1987], and chosen to be the “closest” to the previous guess in [Sanborn and Prévost, 2011].

In order to choose a “good” starting point, the unit sphere is discretized every 5° , and the point with the smallest $\det(\underline{\mathbf{n}} \odot \underline{\hat{\mathcal{L}}} \cdot \underline{\mathbf{n}})$ is taken to start the analysis.

These methods have four flaws :

1. There is no reason to believe that $C(\underline{\mathbf{n}})$ has a single minimum on the unit sphere. In fact, $(\underline{\mathbf{n}} \odot \underline{\hat{\mathcal{L}}} \cdot \underline{\mathbf{n}})$ components are second order polynomials in terms of $\underline{\mathbf{n}}$'s components. Therefore, $C(\underline{\mathbf{n}})$ is a three dimensional polynomial function of order six. Even if the domain of interest is not entirely \mathbb{R}^3 , there might be multiple local minima on the unit sphere. We are only interested in the smallest one.
2. The discretization to evaluate a starting point is not efficient. First of all, the analysis could be performed on only half of the unit sphere: $C(\underline{\mathbf{n}})$ is a pair function of $\underline{\mathbf{n}}$. Also, “discretizing every 5° ” implies that the spherical angles are taken from 0° to 360° (or 180°) every 5° . This is not an isotropic selection: more points are to be selected on the poles of the unit sphere: either the discretization is too rough on the equator, or too dense at the poles.
3. Finally, as expressed above, these methods are expressed in a small deformation framework.

To avoid these flaws, a new method, that is generalized to the finite deformation framework, is proposed in section 4.3.

4.3.2 Minimization problem

In a finite deformation framework, the loss of ellipticity criterion is fulfilled when:

$$\min(\det(\underline{\mathbf{N}} \odot \underline{\mathcal{L}} \cdot \underline{\mathbf{N}})) \quad \text{becomes negative.} \quad (4.66)$$

where $\underline{\mathcal{L}}$ is the fourth order tensor defined such that:

$$\underline{\dot{\mathbf{S}}} = \underline{\mathcal{L}} : \underline{\dot{\mathbf{F}}} \quad (4.67)$$

As the acoustic tensor $\underline{\mathbf{Q}} = \underline{\mathbf{N}} \odot \underline{\mathcal{L}} \cdot \underline{\mathbf{N}}$ is initially positive definite, the loss of ellipticity will be tracked by using a minimization method on $\det(\underline{\mathbf{N}} \odot \underline{\mathcal{L}} \cdot \underline{\mathbf{N}})$, and then by checking the sign of the minimum. Since $\underline{\mathbf{N}}$ must be a unit vector, it will be expressed in spherical coordinates as:

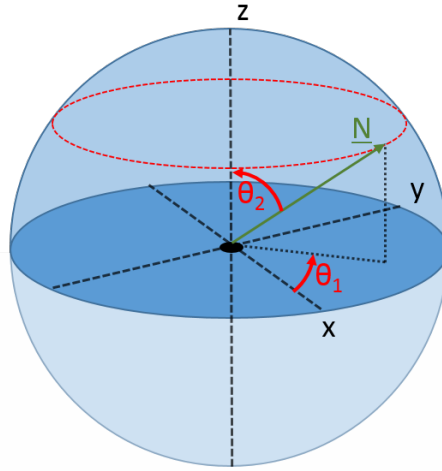


Figure 4.7: Spherical coordinates.

$$\underline{\mathbf{N}}(\{\boldsymbol{\theta}\}) = \begin{pmatrix} \cos(\theta_1) \sin(\theta_2) \\ \sin(\theta_1) \sin(\theta_2) \\ \cos(\theta_2) \end{pmatrix} \quad (4.68)$$

where $\{\boldsymbol{\theta}\} = (\theta_1, \theta_2) \in \mathbb{R}^2$.

In fact, expressed this way, the minimization domain seems to be not bounded. While this is true for the minimization domain, the starting points will only be taken for a given discretization on the half unit sphere such that $N_y \geq 0$.

The minimization problem reduces to:

$$\frac{\partial(\det(\underline{\mathbf{N}} \odot \underline{\mathcal{L}} \cdot \underline{\mathbf{N}}))}{\partial\{\boldsymbol{\theta}\}} = \{\mathbf{0}\} \quad (4.69)$$

$$\left[\frac{\partial(\det(\underline{\mathbf{N}} \odot \underline{\mathcal{L}} \cdot \underline{\mathbf{N}}))}{\partial \underline{\mathbf{N}}} \right] \cdot \left[\frac{\partial \underline{\mathbf{N}}}{\partial \{\boldsymbol{\theta}\}} \right] = \{\mathbf{0}\} \quad (4.70)$$

$$(4.71)$$

where:

$$\left[\frac{\partial \underline{\mathbf{N}}}{\partial \{\boldsymbol{\theta}\}} \right] = \begin{pmatrix} -\sin(\theta_1) \sin(\theta_2) & \cos(\theta_1) \cos(\theta_2) \\ \cos(\theta_1) \sin(\theta_2) & \sin(\theta_1) \cos(\theta_2) \\ 0 & -\sin(\theta_2) \end{pmatrix} \quad (4.72)$$

and:

$$\frac{\partial(\det(\underline{\mathbf{N}} \odot \underline{\mathcal{L}} \cdot \underline{\mathbf{N}}))}{\partial \underline{\mathbf{N}}} = \det(\underline{\mathbf{N}} \odot \underline{\mathcal{L}} \cdot \underline{\mathbf{N}}) (\underline{\mathbf{N}} \odot \underline{\mathcal{L}} \cdot \underline{\mathbf{N}})^{-T} : \frac{\partial(\underline{\mathbf{N}} \odot \underline{\mathcal{L}} \cdot \underline{\mathbf{N}})}{\partial \underline{\mathbf{N}}} \quad (4.73)$$

$$\frac{\partial(\det(\underline{\mathbf{N}} \odot \underline{\mathcal{L}} \cdot \underline{\mathbf{N}}))}{\partial N_p} = \det(\underline{\mathbf{N}} \odot \underline{\mathcal{L}} \cdot \underline{\mathbf{N}}) (\underline{\mathbf{N}} \odot \underline{\mathcal{L}} \cdot \underline{\mathbf{N}})^{-1}_{ji} \frac{\partial(N_k \mathcal{L}_{ikjl} N_l)}{\partial N_p} \quad (4.74)$$

$$= \det(\underline{\mathbf{N}} \odot \underline{\mathcal{L}} \cdot \underline{\mathbf{N}}) (\underline{\mathbf{N}} \odot \underline{\mathcal{L}} \cdot \underline{\mathbf{N}})^{-1}_{ji} (N_k \mathcal{L}_{ikjl} \delta_{pl} + \delta_{pk} \mathcal{L}_{ikjl} N_l) \quad (4.75)$$

$$= \det(\underline{\mathbf{N}} \odot \underline{\mathcal{L}} \cdot \underline{\mathbf{N}}) (\underline{\mathbf{N}} \odot \underline{\mathcal{L}} \cdot \underline{\mathbf{N}})^{-1}_{ji} (\mathcal{L}_{ipjl} + \mathcal{L}_{iljp}) N_l \quad (4.76)$$

where δ is the Kronecker symbol.

Equations (4.62) and (4.76) are in fact equivalent when the tangent operator possesses minor symmetries.

To simplify the coming computations, we will write :

$$(\underline{\mathcal{C}})_{pl} = (\underline{\mathbf{N}} \odot \underline{\mathcal{L}} \cdot \underline{\mathbf{N}})^{-1}_{ji} (\mathcal{L}_{ipjl} + \mathcal{L}_{iljp}) \quad (4.77)$$

$$\underline{\mathbf{D}} = \frac{\partial(\det(\underline{\mathbf{N}} \odot \underline{\mathcal{L}} \cdot \underline{\mathbf{N}}))}{\partial \underline{\mathbf{N}}} = \det(\underline{\mathbf{N}} \odot \underline{\mathcal{L}} \cdot \underline{\mathbf{N}}) \underline{\mathcal{C}} \cdot \underline{\mathbf{N}} \quad (4.78)$$

$$\{\mathbf{d}\} = \{\underline{\mathbf{D}}\}^T \left[\frac{\partial \underline{\mathbf{N}}}{\partial \{\boldsymbol{\theta}\}} \right] = \left\{ \frac{\partial(\det(\underline{\mathbf{N}} \odot \underline{\mathcal{L}} \cdot \underline{\mathbf{N}}))}{\partial \{\boldsymbol{\theta}\}} \right\} \quad (4.79)$$

4.3.3 Algorithm

The minimization algorithm is divided in two steps:

1. Discretization of the half unit sphere to set the starting points;
2. Run a Newton-Raphson algorithm to solve $\{\mathbf{d}\} = \{\mathbf{0}\}$ for each starting point.

Sphere discretization for starting points

Setting multiple starting points means discretizing the half unit sphere. In order to have a regular discretization, and to avoid the clustering at the poles [Néda et al., 1999] which occurs with angular discretization as in [Ortiz, 1987, Néda et al., 1999, Sanborn and Prévost, 2011, Mosler, 2005], only θ_2 is regularly discretized. For a given discretization parameter $n_{\theta_2} \in \mathbb{N}$, n_{θ_2} regularly spaced points are taken in $]0, \pi[$. Then, in order to discretize θ_1 , for a given θ_2 (that defines a circle on the unit sphere, see Figure 4.7) n_{θ_1} is computed in order to keep a constant surface element:

$$\delta\theta_1(\theta_2) = \frac{\delta\theta_2}{|\sin(\theta_2)|} = \frac{\pi}{n_{\theta_2} |\sin(\theta_2)|} \quad (4.80)$$

Finally, to avoid singularities when $\theta_2 = 0[\pi]$, a single point at the pole ($\theta_2 = 0$) is added separately to the discretization.

Implementation remark: we take $n_{\theta_1} = \langle \frac{\pi}{\delta\theta_1} \rangle$ (where “ $\langle \cdot \rangle$ ” denotes the integer part), then $\delta\theta_1$ is recomputed as $\frac{\pi}{n_{\theta_1}}$.

As shown in Figure 4.8, this method has the twin benefits of providing an isotropic distribution as well as reducing the number of discretization points¹⁴:

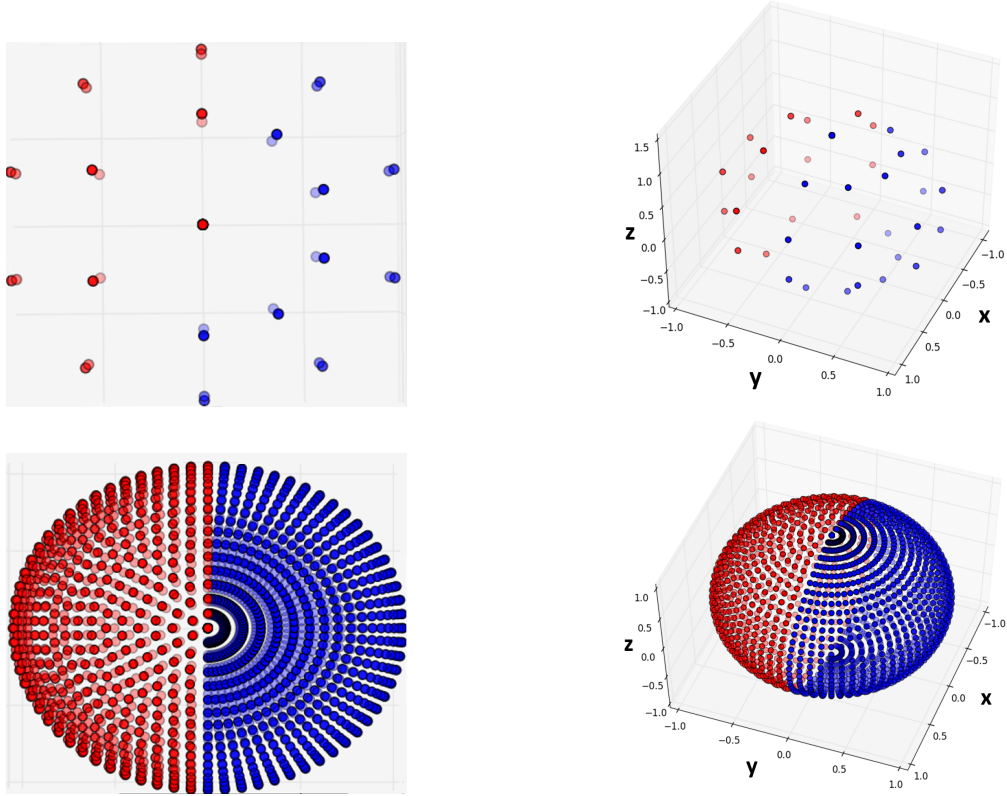


Figure 4.8: In red dots, discretization obtained for constant surface element discretization; in blue dots, discretization obtained for regular angular discretization. Top figures, $n_{\theta_2} = 5$; bottom figures, $n_{\theta_2} = 36$.

Newton-Raphson method

In order to solve our minimization problem, one has to find a solution to:

$$\{d(\{\theta\})\} = \{0\} \quad (4.81)$$

Given a starting point $\{\theta\}^k$, the idea is to compute $\{\Delta\theta^{k+1}\}$ such that:

$$\{d(\{\theta\}^k + \{\Delta\theta\}^{k+1})\} = \{0\} \quad (4.82)$$

Using a Newton Raphson method, we take:

$$\{\Delta\theta\}^{k+1} = -[h(\{\theta\}^k)^{-1}] \cdot \{d(\{\theta\}^k)\} \quad (4.83)$$

¹⁴ In fact the number of points tends to $\frac{2}{\pi}n_{\theta_2}^2$.

where $[\mathbf{h}(\{\boldsymbol{\theta}\}^k)] = \frac{\partial \{d(\{\boldsymbol{\theta}\}^k)\}}{\partial \{\boldsymbol{\theta}\}}$ is the Hessian matrix of $\det(\underline{\mathbf{N}} \odot \underline{\mathcal{L}} \cdot \underline{\mathbf{N}})$.

Iterating this procedure until $\{d(\{\boldsymbol{\theta}\}^k)\}^T \cdot \{d(\{\boldsymbol{\theta}\}^k)\} < \epsilon^2$ gives a second order convergence procedure.

Usually this method is avoided in minimization methodology, because it has two possible major flaws:

1. One cannot ensure that the solution will in fact be a minimum or a maximum; which, in our case, is a major flaw;
2. The second derivative (Hessian matrix) can be very expensive to compute and invert.

While the first flaw cannot be avoided, but by taking multiple starting points, the second one is not a problem in our case. For one thing, we have a two dimensional problem, in other words, the Hessian matrix is a 2×2 matrix, which is almost free to invert. For another, most of the terms of the Hessian matrix are already computed by evaluating the gradient. In fact, the second derivative ($[\mathbf{h}]$) is given by:

$$[\mathbf{h}] = \left[\frac{\partial \underline{\mathbf{N}}}{\partial \{\boldsymbol{\theta}\}} \right]^T \left[\frac{\partial^2 (\det(\underline{\mathbf{N}} \odot \underline{\mathcal{L}} \cdot \underline{\mathbf{N}}))}{\partial \underline{\mathbf{N}}^2} \right] \left[\frac{\partial \underline{\mathbf{N}}}{\partial \{\boldsymbol{\theta}\}} \right] + [\boldsymbol{\eta}] \quad (4.84)$$

where $[\boldsymbol{\eta}]$ is given by:

$$\eta_{\alpha\beta} = D_i \frac{\partial^2 N_i}{\partial \theta_\alpha \partial \theta_\beta} \quad (4.85)$$

$$\left[\frac{\partial}{\partial \theta_1} \left(\frac{\partial N_i}{\partial \theta_\alpha} \right) \right] = \begin{bmatrix} -\cos(\theta_1) \sin(\theta_2) & -\sin(\theta_1) \cos(\theta_2) \\ -\sin(\theta_1) \sin(\theta_2) & \cos(\theta_1) \cos(\theta_2) \\ 0 & 0 \end{bmatrix} \quad (4.86)$$

$$\text{and } \left[\frac{\partial}{\partial \theta_2} \left(\frac{\partial N_i}{\partial \theta_\alpha} \right) \right] = \begin{bmatrix} -\sin(\theta_1) \cos(\theta_2) & -\cos(\theta_1) \sin(\theta_2) \\ \cos(\theta_1) \cos(\theta_2) & -\sin(\theta_1) \sin(\theta_2) \\ 0 & -\cos(\theta_2) \end{bmatrix} \quad (4.87)$$

Finally, $\frac{\partial^2 (\det(\underline{\mathbf{N}} \odot \underline{\mathcal{L}} \cdot \underline{\mathbf{N}}))}{\partial N_p \partial N_q}$ is given by:

$$\begin{aligned} & (C_{pl} N_l) \frac{\partial (\det(\underline{\mathbf{N}} \odot \underline{\mathcal{L}} \cdot \underline{\mathbf{N}}))}{\partial N_q} + \det(\underline{\mathbf{N}} \odot \underline{\mathcal{L}} \cdot \underline{\mathbf{N}}) C_{pq} \\ & + \det(\underline{\mathbf{N}} \odot \underline{\mathcal{L}} \cdot \underline{\mathbf{N}}) (\mathcal{L}_{ipjl} + \mathcal{L}_{iljp}) N_l \frac{\partial (\det(\underline{\mathbf{N}} \odot \underline{\mathcal{L}} \cdot \underline{\mathbf{N}}))_{ji}^{-1}}{\partial N_q} \end{aligned} \quad (4.88)$$

Even though these three expressions seem to be complicated, a few manipulations can help. The first term can be identified as:

$$(C_{pl}N_l) \frac{\partial(\det(\underline{\mathbf{N}} \odot \underline{\mathcal{L}} \cdot \underline{\mathbf{N}}))}{\partial N_q} = (C_{pl}N_l)(\det(\underline{\mathbf{N}} \odot \underline{\mathcal{L}} \cdot \underline{\mathbf{N}}))(\underline{\mathbf{N}} \odot \underline{\mathcal{L}} \cdot \underline{\mathbf{N}})^{-1}(\mathcal{L}_{iljp} + \mathcal{L}_{ipjl})N_l \quad (4.89)$$

$$= \frac{D_p D_q}{\det(\underline{\mathbf{N}} \odot \underline{\mathcal{L}} \cdot \underline{\mathbf{N}})} \quad (4.90)$$

where all the terms are already known. The second expression is already explicitly known. Finally, the third expression requires a little more derivation. In order to take the derivative of the inverse of a tensor, it is possible to use the following identity:

$$d(\underline{\mathbf{A}}^{-1}) = -(\underline{\mathbf{A}}^{-1} \boxtimes \underline{\mathbf{A}}^{-T}) : d\underline{\mathbf{A}} \quad (4.91)$$

$$\frac{\partial((\underline{\mathbf{N}} \odot \underline{\mathcal{L}} \cdot \underline{\mathbf{N}})^{-1})_{ji}}{\partial(\underline{\mathbf{N}} \odot \underline{\mathcal{L}} \cdot \underline{\mathbf{N}})_{rs}} = (\underline{\mathbf{N}} \odot \underline{\mathcal{L}} \cdot \underline{\mathbf{N}})_{jr}^{-1} (\underline{\mathbf{N}} \odot \underline{\mathcal{L}} \cdot \underline{\mathbf{N}})_{si}^{-1} \quad (4.92)$$

thus the third term becomes:

$$\det(\underline{\mathbf{N}} \odot \underline{\mathcal{L}} \cdot \underline{\mathbf{N}})(\mathcal{L}_{ipjl} + \mathcal{L}_{iljp})N_l \frac{\partial(\underline{\mathbf{N}} \odot \underline{\mathcal{L}} \cdot \underline{\mathbf{N}})^{-1}_{ji}}{\partial N_q} \quad (4.93)$$

$$= \det(\underline{\mathbf{N}} \odot \underline{\mathcal{L}} \cdot \underline{\mathbf{N}})(\mathcal{L}_{ipjl} + \mathcal{L}_{iljp})N_l \frac{\partial(\underline{\mathbf{N}} \odot \underline{\mathcal{L}} \cdot \underline{\mathbf{N}})^{-1}_{ji}}{\partial(\underline{\mathbf{N}} \odot \underline{\mathcal{L}} \cdot \underline{\mathbf{N}})_{rs}} \frac{\partial(\underline{\mathbf{N}} \odot \underline{\mathcal{L}} \cdot \underline{\mathbf{N}})_{rs}}{\partial N_q} \quad (4.94)$$

$$= -\det(\underline{\mathbf{N}} \odot \underline{\mathcal{L}} \cdot \underline{\mathbf{N}})(\mathcal{L}_{ipjl} + \mathcal{L}_{iljp})N_l (\underline{\mathbf{N}} \odot \underline{\mathcal{L}} \cdot \underline{\mathbf{N}})_{jr}^{-1} (\underline{\mathbf{N}} \odot \underline{\mathcal{L}} \cdot \underline{\mathbf{N}})_{si}^{-1} (\mathcal{L}_{rqsh} + \mathcal{L}_{rlsq})N_h \quad (4.95)$$

$$= -\det(\underline{\mathbf{N}} \odot \underline{\mathcal{L}} \cdot \underline{\mathbf{N}}) \left[(\underline{\mathbf{N}} \odot \underline{\mathcal{L}} \cdot \underline{\mathbf{N}})_{si}^{-1} (\mathcal{L}_{ipjl} + \mathcal{L}_{iljp})N_l \right] \left[(\underline{\mathbf{N}} \odot \underline{\mathcal{L}} \cdot \underline{\mathbf{N}})_{jr}^{-1} (\mathcal{L}_{rqsh} + \mathcal{L}_{rlsq})N_h \right] \quad (4.96)$$

$$= -\det(\underline{\mathbf{N}} \odot \underline{\mathcal{L}} \cdot \underline{\mathbf{N}}) B_{spj} B_{jqs} = -\det(\underline{\mathbf{N}} \odot \underline{\mathcal{L}} \cdot \underline{\mathbf{N}}) \left(\underline{\mathbf{B}} : \underline{\mathbf{B}}^T \right)_{pq} \quad (4.97)$$

where $B_{jps} = B_{spj} = (\underline{\mathbf{N}} \odot \underline{\mathcal{L}} \cdot \underline{\mathbf{N}})_{si}^{-1} (\mathcal{L}_{ipjl} + \mathcal{L}_{iljp})N_l$.

Finally, the whole Hessian matrix ($[\mathbf{h}]$) can be expressed as follow:

$$[\mathbf{h}] = \left[\frac{\partial \underline{\mathbf{N}}}{\partial \{\boldsymbol{\theta}\}} \right]^T \left[\frac{\underline{\mathbf{D}} \otimes \underline{\mathbf{D}}}{\det(\underline{\mathbf{N}} \odot \underline{\mathcal{L}} \cdot \underline{\mathbf{N}})} + \det(\underline{\mathbf{N}} \odot \underline{\mathcal{L}} \cdot \underline{\mathbf{N}}) \underline{\mathcal{C}} - \det(\underline{\mathbf{N}} \odot \underline{\mathcal{L}} \cdot \underline{\mathbf{N}}) (\underline{\mathbf{B}} : \underline{\mathbf{B}}^T) \right] \left[\frac{\partial \underline{\mathbf{N}}}{\partial \{\boldsymbol{\theta}\}} \right] + [\boldsymbol{\eta}] \quad (4.98)$$

$$[\mathbf{h}] = \frac{\{\mathbf{d}\} \cdot \{\mathbf{d}\}^T}{\det(\underline{\mathbf{N}} \odot \underline{\mathcal{L}} \cdot \underline{\mathbf{N}})} + \det(\underline{\mathbf{N}} \odot \underline{\mathcal{L}} \cdot \underline{\mathbf{N}}) \left[\frac{\partial \underline{\mathbf{N}}}{\partial \{\boldsymbol{\theta}\}} \right]^T \left[\underline{\mathcal{C}} - (\underline{\mathbf{B}} : \underline{\mathbf{B}}^T) \right] \left[\frac{\partial \underline{\mathbf{N}}}{\partial \{\boldsymbol{\theta}\}} \right] + [\boldsymbol{\eta}] \quad (4.99)$$

In equation (4.99), $\underline{\mathbf{B}}$ is the only tensor that has not already been computed when the gradient was evaluated. Therefore computing the Hessian matrix does not require many new calculations and is thus cheaper to evaluate than solving the full eigenvalue problem (as it is done in [Ortiz, 1987] and [Sanborn and Prévost, 2011]); especially since it is a 2×2 matrix and thus trivial to invert.

TTENSOR class

In a FEM software, it is common to use the Voigt notation to manipulate tensors. This approach may be adapted for some mechanical problems, it is not necessarily efficient for large tensor calculations. It goes without saying that there already exist a `TENSOR` class in `Zset` made to handle the tensor-like objects. For our purposes, a specific `C++` class, `TTENSOR`, has been developed to meet the computational efficiency needed for the algorithm to be used in large structural problems. The main improvements were obtained using three basic coding considerations:

- **Compiler optimization:** when writing short and simple methods in `C++` it is important to consider compiler optimization routines, when possible. For instance, when there are simple “for-loops”¹⁵ the compiler might pre-process the code in order to optimize the number of times the memory is accessed and written. This is only possible when the compiler can recognize such loops. For instance, when the size is fixed this process is easier for the compiler. Therefore, it was chosen to fix the size of the matrices to the 3D case (the largest case) so the size is explicitly given to the compiler: 3, 9, 27, and 81 floating numbers for respectively first, second, third, and fourth order tensors.
- **inline:** when a function is “inlined” the compiler directly replaces the call for the method by the expression of the method itself. This reduces the number of method calls, memory copies and temporary objects.
- **Contiguous fixed size memory access:** like humans, computers are much faster at reading and calculating simple operations than storing information (writing memory). Moreover, the reading is obviously more efficient when the words are well ordered. Therefore, the storage and the methods were designed to optimize memory access.

4.3.4 Initialization and general scheme

A multi-point initialization scheme is necessary to ensure the evaluation of the global minimum. Fortunately, the sixth order polynomial surfaces are very smooth, see Figure 4.10, so for any “good starting point” a basic NR scheme converges in very few iterations (4 to 5 for a tolerance of 10^{-8} on the gradient’s norm). Therefore the following scheme is defined (see Figure 4.9) where multiple starting points are chosen, while the number of iterations remains small:

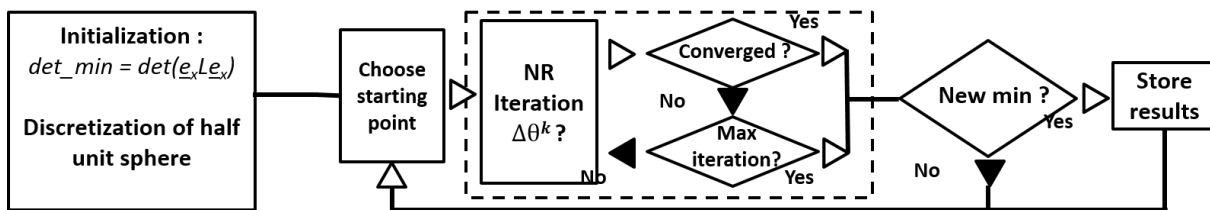


Figure 4.9: Minimization algorithm based on a multi-initialization method and a Newton Raphson algorithm.

Yet, it is important to note that this algorithm captures both minima and maxima. In fact, the determinant of the Hessian matrix is not computed¹⁶. However, by taking enough starting points, the smallest solution found should capture the global minimum. Setting a discretization

¹⁵ Like tensor products.

¹⁶ A positive determinant would confirm that the solution is a local minimum.

parameter n_{θ_2} to 5 (cf. section 4.3.3) for isotropic materials, and up to 6 or 7 for anisotropic materials is expected to be enough.

The algorithm is validated with a simple shear loading test using a finite deformation framework. Performance and robustness are shown and compared to the method proposed in [Mosler, 2005] on a more complex loading. The material laws, especially the values of isotropic hardening parameters, are unrealistic but used to test the robustness of the algorithm.

4.3.5 Validation

For this simulation, a material respecting a von Mises criterion in the corotational framework, formulated on the Kirchhoff stress tensor, with non-linear isotropic hardening is adopted. Its yield surface takes the following form:

$$f(\boldsymbol{\tau}, R) = \sqrt{\frac{3}{2} \boldsymbol{\tau}^{dev} : \boldsymbol{\tau}^{dev}} - R(p) \quad (4.100)$$

where p denotes the cumulative plastic strain, and $R(p)$ the yield stress. Finally, the Young modulus, the Poisson ratio and the isotropic hardening for these simulations are respectively given by:

$$E = 200 \text{ GPa}; \quad \nu = 0.33 \quad (4.101)$$

$$R(p) = 1000 + 100(1 - e^{-300p}) - 700p \quad (4.102)$$

where p is the accumulated plastic strain and $\boldsymbol{\tau}^{dev} = \boldsymbol{\tau} - \frac{\text{Tr}(\boldsymbol{\tau})}{3} \boldsymbol{\mathbb{I}}$ denotes the deviatoric part of the Kirchhoff stress tensor. Within a small deformation framework, it is known that for such a loading and material, the loss of ellipticity criterion is first fulfilled when:

$$H = \frac{dR}{dp} = 0; \quad \underline{\mathbf{n}} = \underline{\mathbf{e}}_x \quad \text{or} \quad \underline{\mathbf{e}}_y \quad (4.103)$$

where H is the hardening modulus [Besson et al., 2010]. In this case it occurs for $p = \log(\frac{300}{7})/300 \simeq 0.0125$ (see Figure 4.11). This result will therefore still be valid for our simulation since deformations are small.

The simulation is run on a Gauss point. Loading is prescribed through the deformation gradient:

$$\boldsymbol{F} = 0.2t(\underline{\mathbf{e}}_x \otimes \underline{\mathbf{e}}_y + \underline{\mathbf{e}}_y \otimes \underline{\mathbf{e}}_x) + \boldsymbol{\mathbb{I}} \quad (4.104)$$

where $t \in [0, 1]$ is the fictitious time (loading parameter). The parameter n_{θ_2} is fixed to 6. Numerical results are shown in Figure 4.10 and Figure 4.12. Three solutions are equivalently obtained: $\pm \underline{\mathbf{e}}_x$ and $\underline{\mathbf{e}}_y$. For each timestep, only one solution is saved at each Gauss point. It would be possible to store all extrema, but that would be too expansive in terms of memory. However, in a FEM problem, the multiplicity of time steps and the large number of Gauss points should be sufficient to ensure that all solutions are observed.

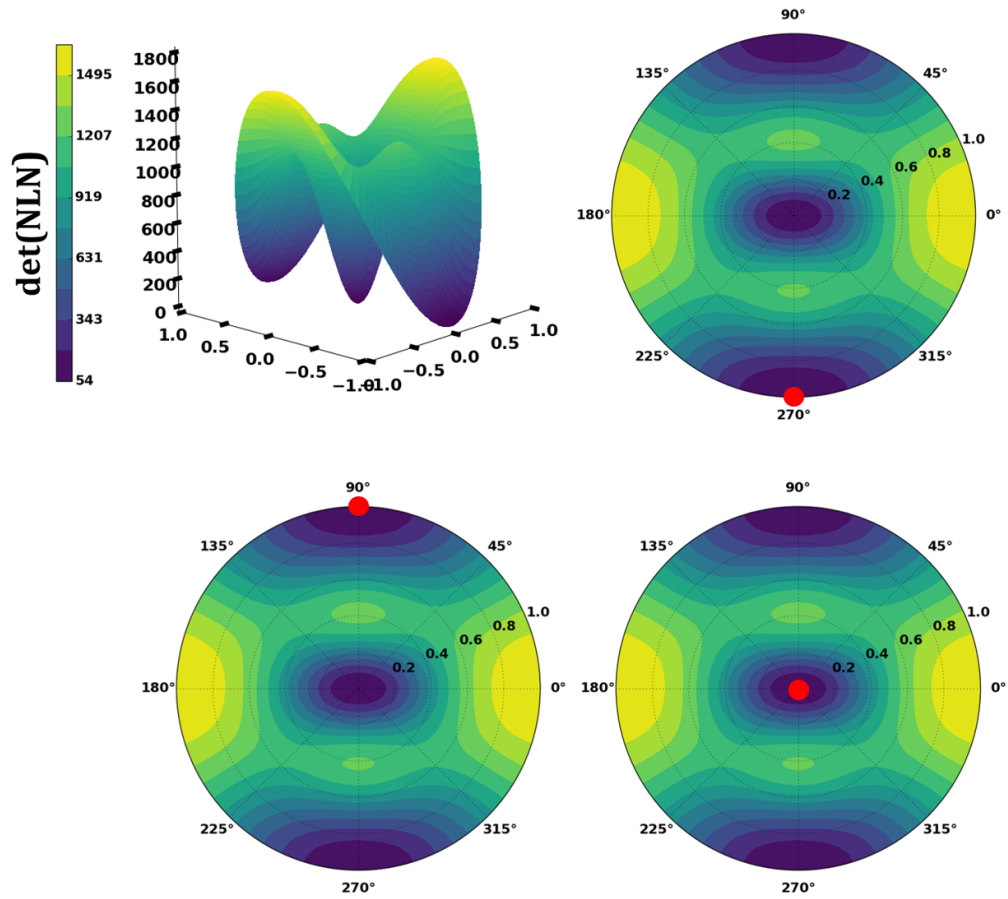


Figure 4.10: Surface $\det(\underline{N} \odot \underline{\mathcal{L}} \cdot \underline{N})$ plotted after stereographic projection in the $(0, \underline{e}_z, \underline{e}_x)$ plane for visualization purposes. The red dots indicate the solutions of the minimization problem at various load increments. Three equivalent solutions are captured.

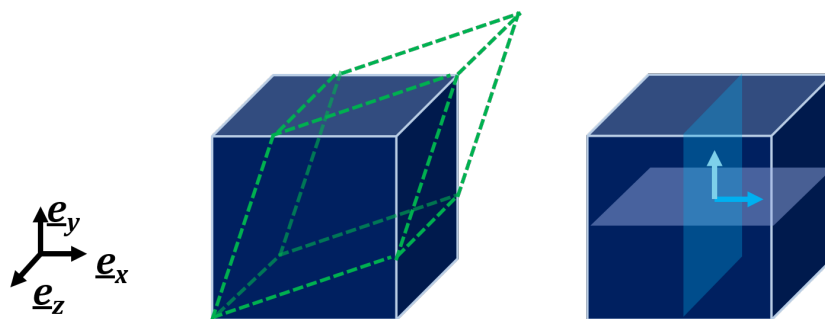


Figure 4.11: Simple shear: localization band with normals \underline{e}_x and \underline{e}_y

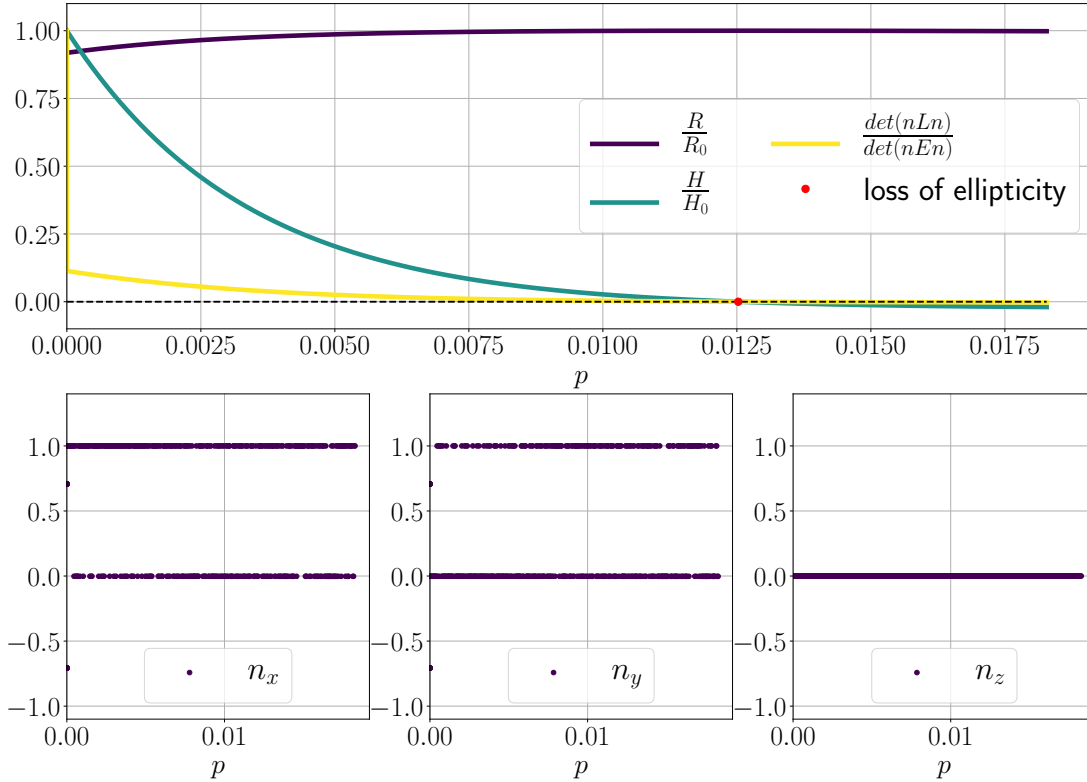


Figure 4.12: Top, the evolution of the yield stress R , the hardening modulus $H = \frac{dR}{dp}$, and the minimum of $\det(\underline{\mathbf{N}} \odot \underline{\mathcal{L}} \cdot \underline{\mathbf{N}})$; both vanish for $p = 0.0125$. Bottom, the component of the normal minimizing $\det(\underline{\mathbf{N}} \odot \underline{\mathcal{L}} \cdot \underline{\mathbf{N}})$; two solutions are found: $\pm \underline{\mathbf{e}}_x$ and $\underline{\mathbf{e}}_y$ ($\underline{\mathbf{e}}_x$ and $-\underline{\mathbf{e}}_x$ are considered to be the same solution). One can remark that both solutions are equivalently obtained while $\min(\det(\underline{\mathbf{N}} \odot \underline{\mathcal{L}} \cdot \underline{\mathbf{N}}))$ evolves smoothly.

4.3.6 Performance and robustness

In the previous section, robustness of the proposed algorithm was demonstrated. In fact, the three equivalent minima have all been captured (see Figure 4.10). In the following example, a comparison between the robustness and computational cost of this method with methods available in the literature is drawn.

As discussed in detail in [Mota et al., 2016], the methods available in the literature propose a two step process: first, a sampling over the unit sphere (unit cube for the method proposed in [Mota et al., 2016]) is performed and the determinant of the acoustic tensor is evaluated for each normal; the normal associated to the smallest determinant is then used to initiate a minimization algorithm. For the sampling, many authors propose to use a spherical discretization and perform a regular discretization of the spherical angles [Sanborn and Prévost, 2011, Oliver et al., 2010, Ortiz, 1987].

In this section, it is shown that this method is not robust enough to always capture the global minimum. The comparison is made with: $n_{\theta_2} = 6$ (cf. section 4.3.3) as the discretization parameter of the proposed method; and for the angular discretization of the spherical angles

$n = 36$ to be consistent with the methods proposed in the literature (every 5°)¹⁷. Using these parameters leads to almost equal computation time for both algorithms (the proposed method being slightly faster by 10% for $n_{\theta_2} = 6$ and 40% for $n_{\theta_2} = 5$).

In the following example the material properties (see section 2.2.2) are given by:

$$E = 20 \text{ GPa}; \quad \nu = 0.33 \quad (4.105)$$

$$f(\boldsymbol{\tau}, R) = \sqrt{\frac{3}{2} \boldsymbol{\tau}^{dev} : \boldsymbol{\tau}^{dev}} - R(p) \quad (4.106)$$

$$R(p) = 1000 + 100(1 - e^{-25p}) - 300p \quad (4.107)$$

The simulation is run on a unit cube element with 8 nodes with 8 integration points. Dirichlet boundary conditions are prescribed on all degrees of freedom such that:

$$u_x = 0.075yt; \quad u_y = 0.225xt; \quad u_z = 0 \quad (4.108)$$

where $t \in [0, 1]$ denote the time-like loading parameter.

Numerical results are shown in Figure 4.14 and Figure 4.13. The solution obtained by the minimization algorithms is the same for both methods when the minimum is unique. However, the results differ when two minima, close to one another, exist (see Figure 4.14). Not only do they lead to different instants for loss of ellipticity, but also to very different normal vectors. The new method is found to be more robust than the methods available in the literature for capturing the global minimum.

¹⁷ Only half of the unit sphere is discretized due to symmetry. This discretization parameter is consistent with what is usually proposed, see [Mosler, 2005, Sanborn and Prévost, 2011, Ortiz, 1987].

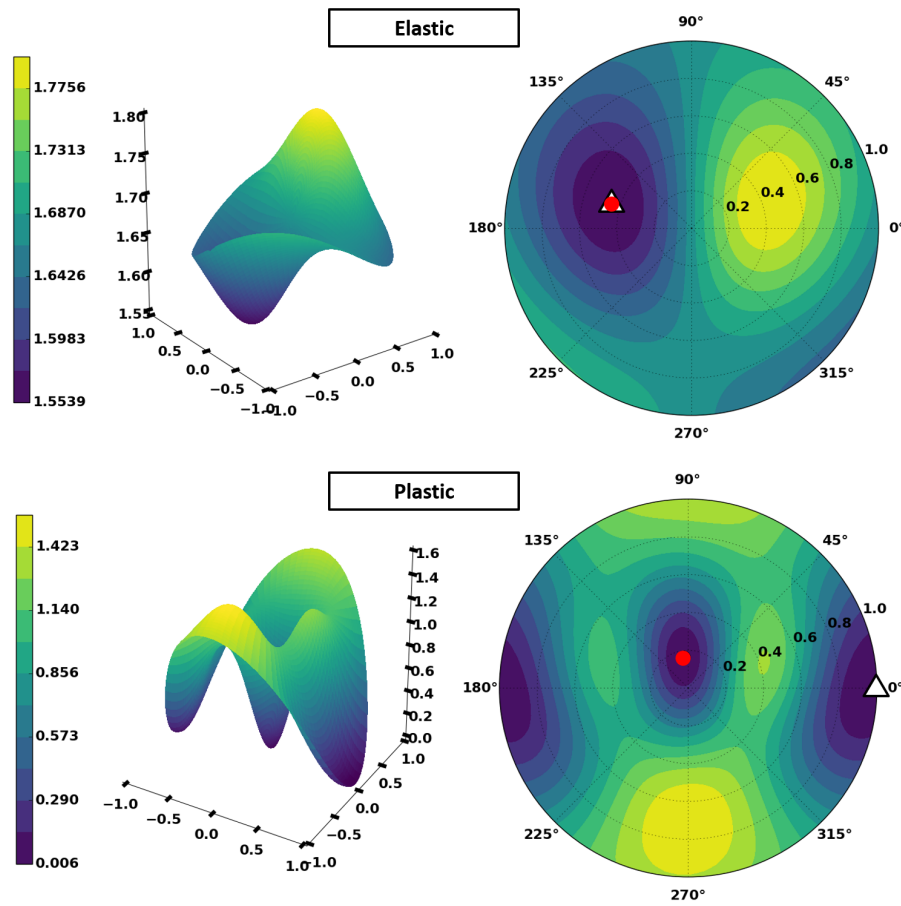


Figure 4.13: On the left, the surface $\det(\underline{N} \odot \underline{\mathcal{L}} \cdot \underline{N})$ plotted after stereographic projection in the $(0, \underline{e}_z, \underline{e}_x)$ plane in the elastic regime; on the right, the surface $\det(\underline{N} \odot \underline{\mathcal{L}} \cdot \underline{N})$ plotted after stereographic projection in the $(0, \underline{e}_z, \underline{e}_x)$ plane in the plastic regime. Red dots indicate the solutions obtained with the proposed algorithm; white triangle give the solutions obtained using the sampling method.

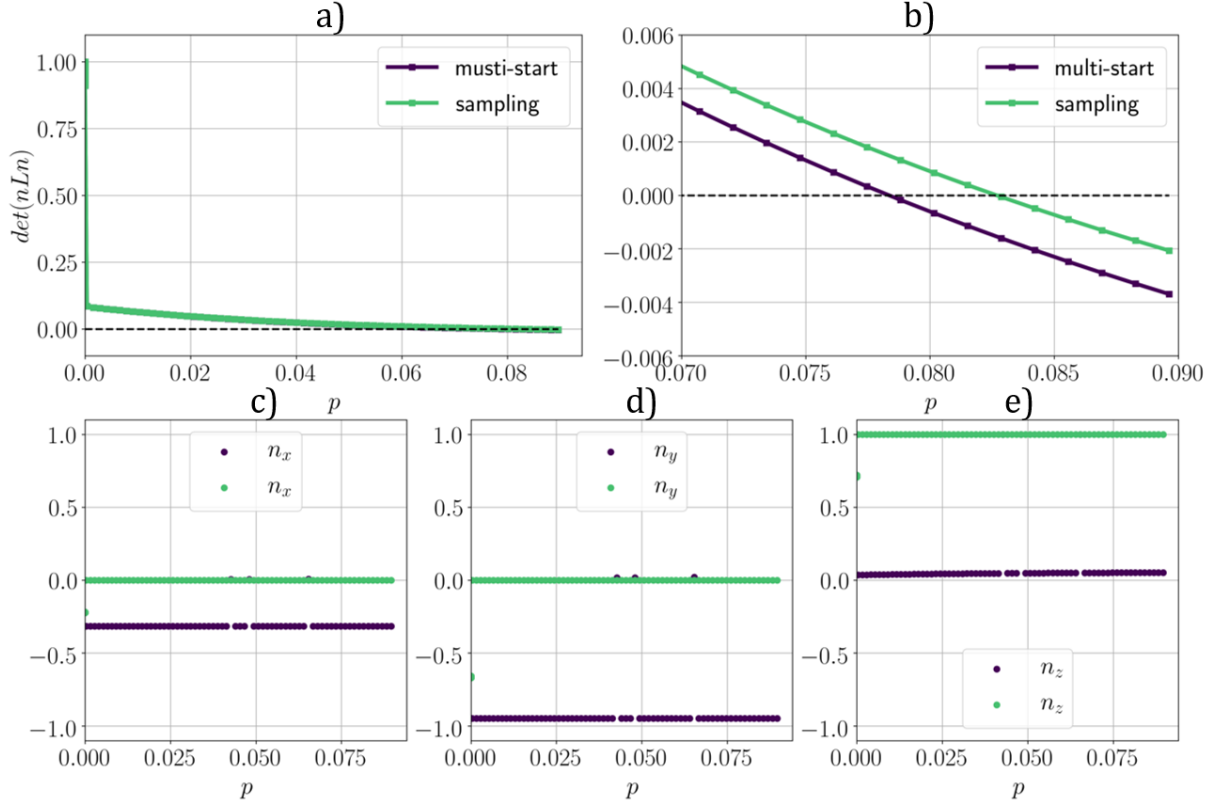


Figure 4.14: Comparison between the proposed method based on multiple initialisation (multi start) and the method available in the literature based on sampling (sampling): a) Evolution of $\min(\det(\underline{\mathbf{N}} \odot \underline{\mathcal{L}} \cdot \underline{\mathbf{N}}))$ for the different algorithms; b) Zoom of a) around the loss of ellipticity instant; c), d) and e) Components of $\arg \min(\det(\underline{\mathbf{N}} \odot \underline{\mathcal{L}} \cdot \underline{\mathbf{N}}))$ for the different algorithms. Results differ in the plastic regime when two close minima exist.

4.4 Structural applications

In this section, three structural examples are studied in order to illustrate the use of such a criterion in structures. First a square homogeneously strained in simple shear is analyzed to illustrate the van Hove rate boundary value problem in the case of simple shear. This analysis will lead to a discussion on the uniqueness of discretized problems and the loss of ellipticity criterion. Then, a simple tube loaded in torsion is presented. In this example the latter discussion will be illustrated for a non-homogeneous problem and the robustness of the proposed minimization algorithm will be highlighted. Finally, a full torsion sample, used in [Defaisse et al., 2018], will be analyzed in section 4.4.3.

4.4.1 Loss of uniqueness and loss of ellipticity in a FEM framework: homogeneous shear in a square

It was shown in section 4.2.1 that when the smallest eigenvalue of the acoustic tensor vanishes there is a straight line in the Fourier space on which the second order work vanishes. While this seems to fulfill Hill's loss of uniqueness criterion, the solution is shown not to be compatible with the DBCs. The next step is to consider the case for which $\det(\underline{\mathbf{N}} \odot \underline{\mathcal{L}} \cdot \underline{\mathbf{N}}) < 0$ for at least

a few \underline{N} . In Fourier's space, this would mean that there is not just a line when $\det(\underline{N} \odot \underline{\mathcal{L}} \cdot \underline{N})$ vanishes, but a whole cone-like shape inside of which it is negative, outside of which it is positive, and on which it vanishes (see Figure 4.15).

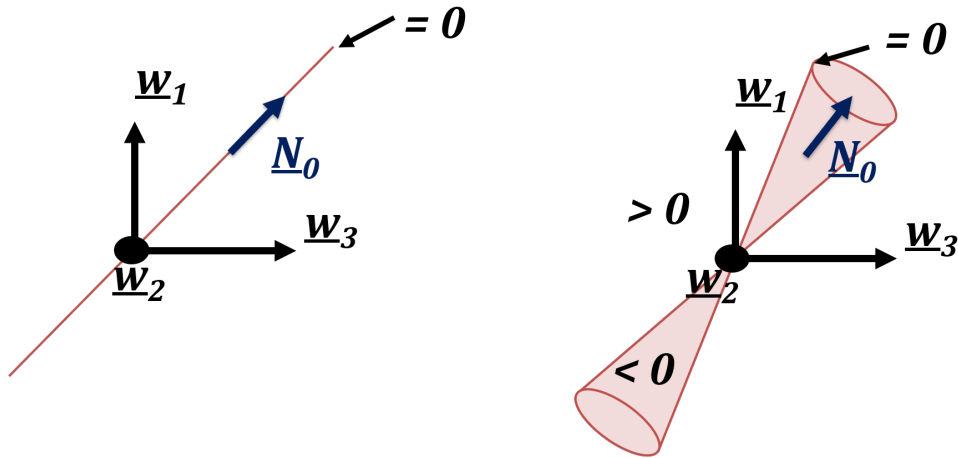


Figure 4.15: On the left, representation of the second order work in the Fourier space when $\det(\underline{N}_0 \underline{\mathcal{L}} \underline{N}_0) = 0$; on the right, representation of the cone of negative second order work in the Fourier space when $\det(\underline{N}_0 \underline{\mathcal{L}} \underline{N}_0) < 0$.

The proof of the uniqueness of the van Hove rate boundary value problem for $\det(\underline{N} \odot \underline{\mathcal{L}} \cdot \underline{N}) = 0$, in section 4.2.1 showed that $\underline{\dot{u}}^*(\underline{w}_0)$ has to be non-vanishing for at least all directions $\underline{w}_0 / \sqrt{\underline{w}_0 \cdot \underline{w}_0}$ in order to fulfill the Dirichlet boundary conditions. Therefore, since the second order work only vanishes on a line in Fourier's space, this condition can not be fulfilled without the global second order work becoming positive. When the smallest eigenvalue of the acoustic tensor becomes negative, it is not necessary for the Fourier transform of the velocity field to be restricted to a line in the Fourier space. Indeed, the global second order work can vanish due to a negative contribution (inside the cone) that compensates the positive contribution (outside the cone).

Other qualitative remarks can be proposed for this problem:

1. Even though there is a negative and a positive part, the positive part may be several orders of magnitude larger than the absolute value of the negative part. Therefore, to compensate a term outside the cone, a large part of the negative cone must be used. The negative part is the interior of the cone, and since the cone is very thin when $\det(\underline{N} \odot \underline{\mathcal{L}} \cdot \underline{N}) < 0$ for the first time, some higher spatial frequencies will be needed¹⁸ in order to exploit the largest part of the negative part.
2. The van Hove rate boundary value problem is defined in a bounded domain. The Fourier transform of any velocity field can be computed if one expands this it is defined on \mathbb{R}^n . In section 4.2.1, this was done by extending the velocity field with $\underline{0}$ outside of the domain \mathcal{B} . As explained in section 4.2.3, this implies that one more condition must be fulfilled by $\underline{\dot{u}}^*$: it must stay unchanged when convoluted with the Fourier transform of a rectangular function. Thus $\underline{\dot{u}}^*$ is most-likely non vanishing on all \mathbb{R}^n .

¹⁸ In the Fourier space, the wavelength is inversely proportional to the distance for the origin.

3. In a FEM framework not all of the Fourier space can be represented. In fact, the finer the mesh, the better Fourier space is described. As it was proposed in the previous item, when $\det(\underline{\mathbf{N}} \odot \underline{\mathcal{L}} \cdot \underline{\mathbf{N}}) < 0$ for some $\underline{\mathbf{N}}$ in van Hove's boundary value problem, $\underline{\mathbf{u}}^*$ is not a trivial function, and higher spatial frequencies are necessary to fulfill Hill's loss of uniqueness criterion. Therefore, it is commonly said that when ellipticity is lost in a finite element framework, uniqueness of the rate boundary value problem is lost too if the mesh is fine enough.

In this section, it is proposed to illustrate these considerations in a FEM framework on a unit square loaded in simple shear. In order to better understand and illustrate the considerations made above, different mesh sizes are considered. The mesh consists of linear fully integrated square elements (4 nodes, 4 Gauss points per element). The number of regular cuts N on one side of the square varies from 3 to 729 (9 to $5e^5$ elements, or 32 to 10^6 degrees of freedom). The meshes for $N = 4, 19, 93,$ and 729 are shown in Figure 4.16.

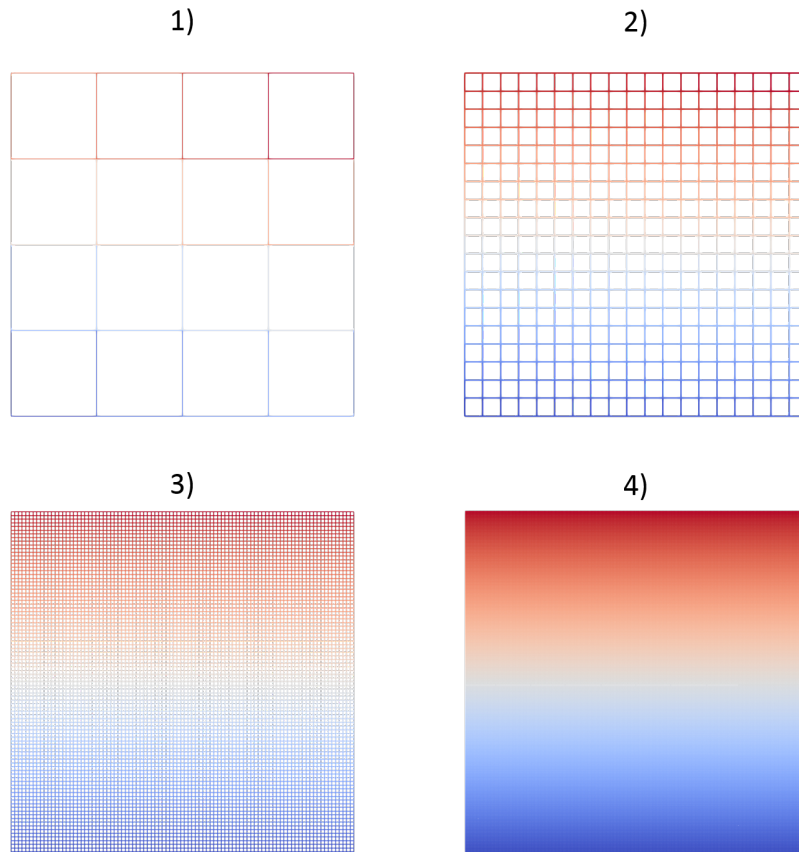


Figure 4.16: From 1) to 4), square meshes for $N = 4, N = 19, N = 93,$ and 729 cuts. Coloring from blue to red is associated to the node number.

Dirichlet boundary conditions of the following form are prescribed at the boundary of the

square under plain strain conditions:

$$\underline{\mathbf{x}} = \underline{\tilde{\mathbf{F}}} \cdot \underline{\mathbf{X}} \quad \forall \underline{\mathbf{X}} \in \partial\Omega \quad (4.109)$$

$$\text{where: } \underline{\tilde{\mathbf{F}}} = \begin{pmatrix} 1 & 0.02t & 0 \\ 0.02t & 1 & 0 \\ 0 & 0 & 1 \end{pmatrix} \quad t \in [0, 1] \quad (4.110)$$

The material is formulated using the Kirchhoff stress tensor in the corotational frame (see section 2.2.2). It follows a von Mises criterion with an isotropic hardening R given by:

$$f(\underline{\boldsymbol{\tau}}, R) = \sqrt{\frac{3}{2} \underline{\boldsymbol{\tau}}^{dev} : \underline{\boldsymbol{\tau}}^{dev}} - R(p) \quad (4.111)$$

$$R(p) = 1000 - 1000p + 100(1 - \exp(-300p)); \quad (4.112)$$

where p is the cumulative plastic strain.

For all meshes, a regular time step of $0.01s$ (100 increments) was applied. The solution is homogeneous during the whole computation for all mesh refinements. The results in terms of stresses and $\det(\underline{\mathbf{N}} \odot \underline{\tilde{\boldsymbol{\mathcal{L}}}} \cdot \underline{\mathbf{N}})$ are shown in Figure 4.17. First loss of ellipticity is captured at $p = 0.01135$.

For each model, the smallest eigenvalue of the global stiffness matrix has been extracted (shown in Figures 4.19 and 4.20) in order to evaluate the loss of uniqueness of the discretized rate boundary value problem. On the one hand, it can be seen that for the given loading some models never lose uniqueness ($N < 36$). On the other hand, when uniqueness is lost (smallest eigenvalue became negative), the critical load gets closer to the loading associated with the first loss of ellipticity when the mesh is finer, see Figure 4.21. This actually illustrates the consideration 3) stated in the paragraph above.

Actually considerations 1) and 3) are illustrated in Figures 5.18 and 4.22. It can be observed that for finer meshes the eigenmodes associated to the vanishing eigenvalues tend to have higher spatial frequencies.

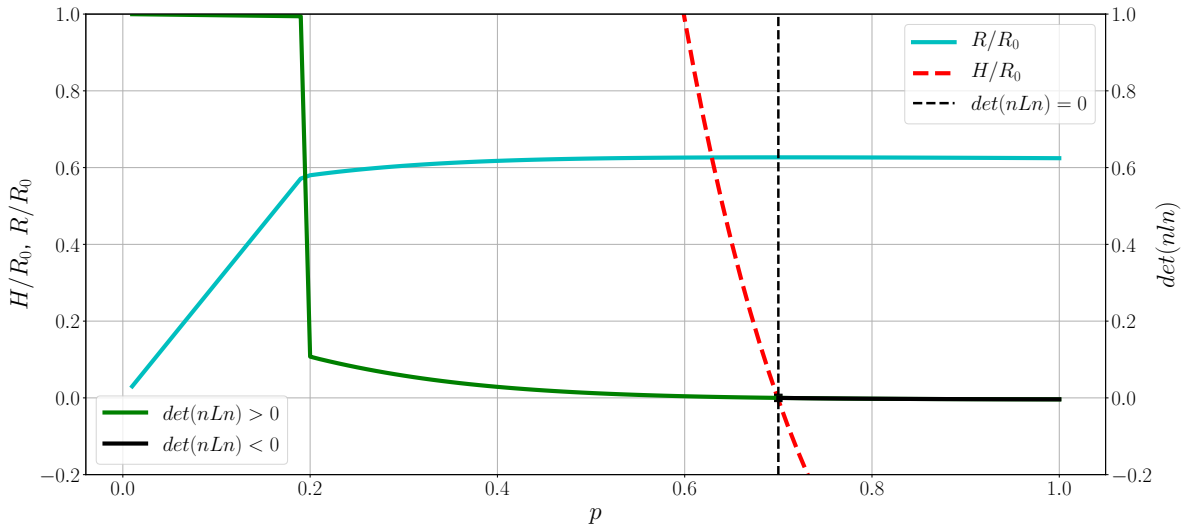


Figure 4.17: The evolution of R , $H = \frac{dR}{dp}$ and $\det(\underline{\mathbf{N}} \odot \underline{\tilde{\boldsymbol{\mathcal{L}}}} \cdot \underline{\mathbf{N}})$ as functions of plastic strain ($R_0 = 1000MPa$) for the square loaded in shear.

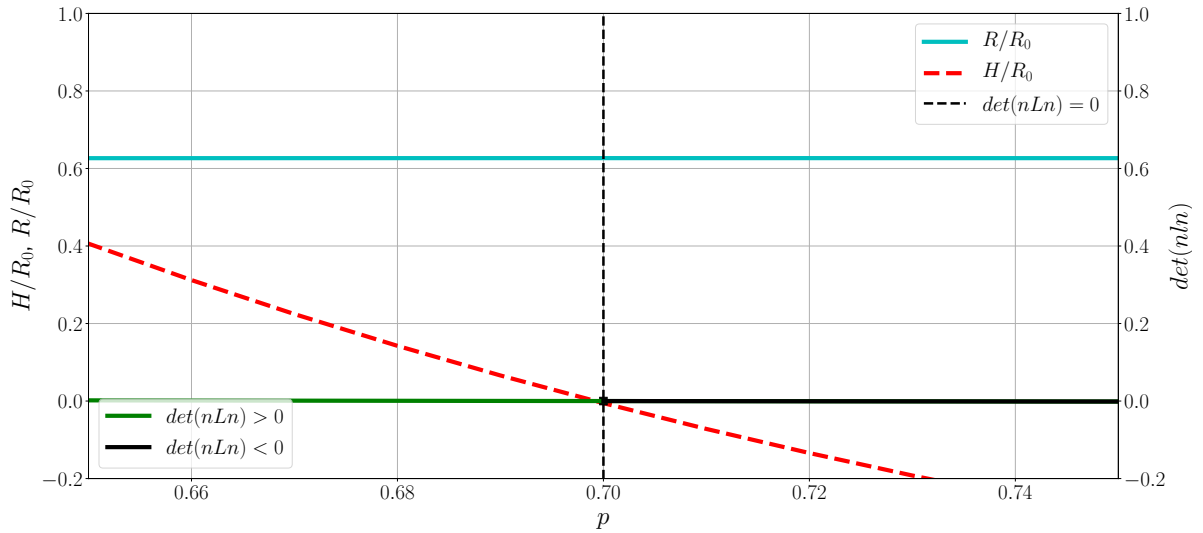


Figure 4.18: The evolution of R , $H = \frac{dR}{dp}$ and $\det(\underline{N} \odot \underline{\mathcal{L}} \cdot \underline{N})$ as functions of plastic strain ($R_0 = 1000MPa$) for the square loaded in shear. Zoom around the instant of loss of ellipticity. Ellipticity lost at $p = 0.01135$ for the square loaded in shear.

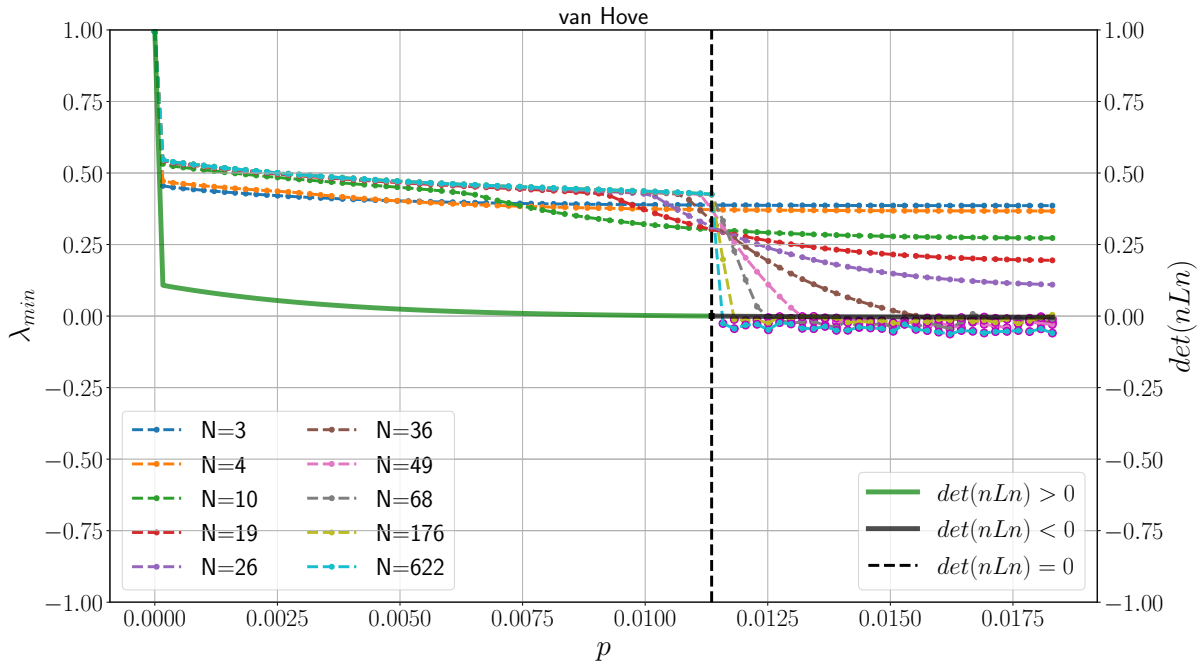


Figure 4.19: Evolution the smallest eigenvalue for different discretizations parameters N . Ellipticity lost for $p = 0.01134$.

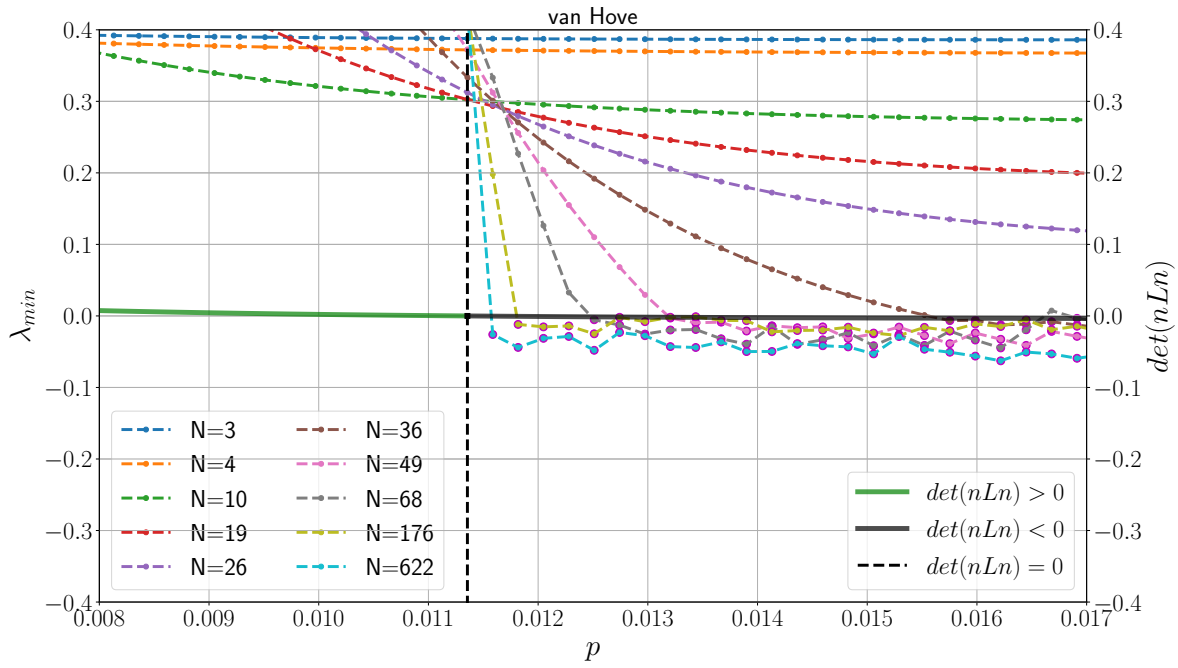


Figure 4.20: Evolution the smallest eigenvalue for different discretizations parameters N . Zoom around the instant of loss of ellipticity ($p = 0.01134$).

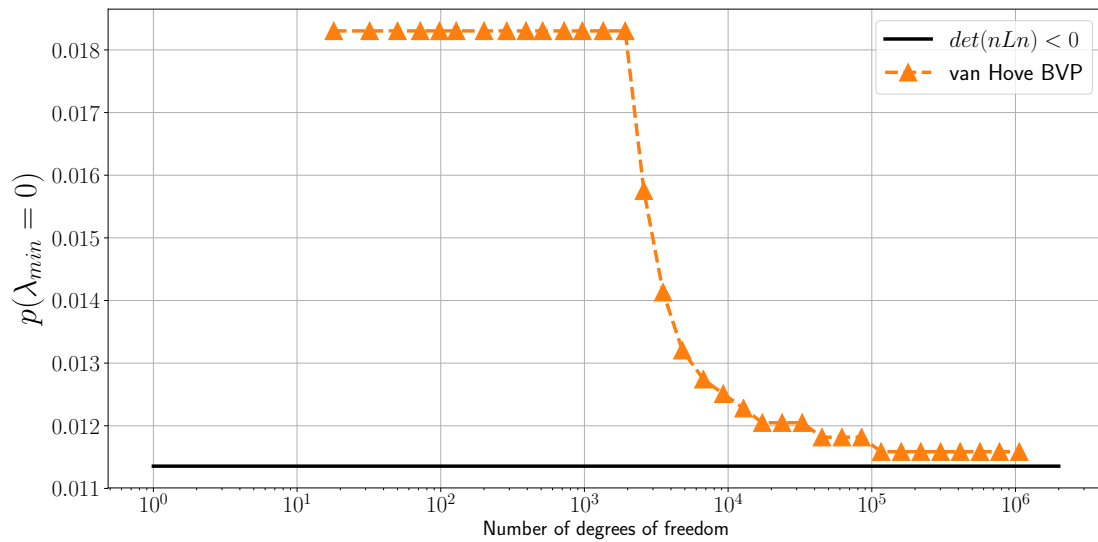


Figure 4.21: Evolution of the plastic strain at loss of uniqueness as a function of the number of degrees of freedom (logarithmic scale).

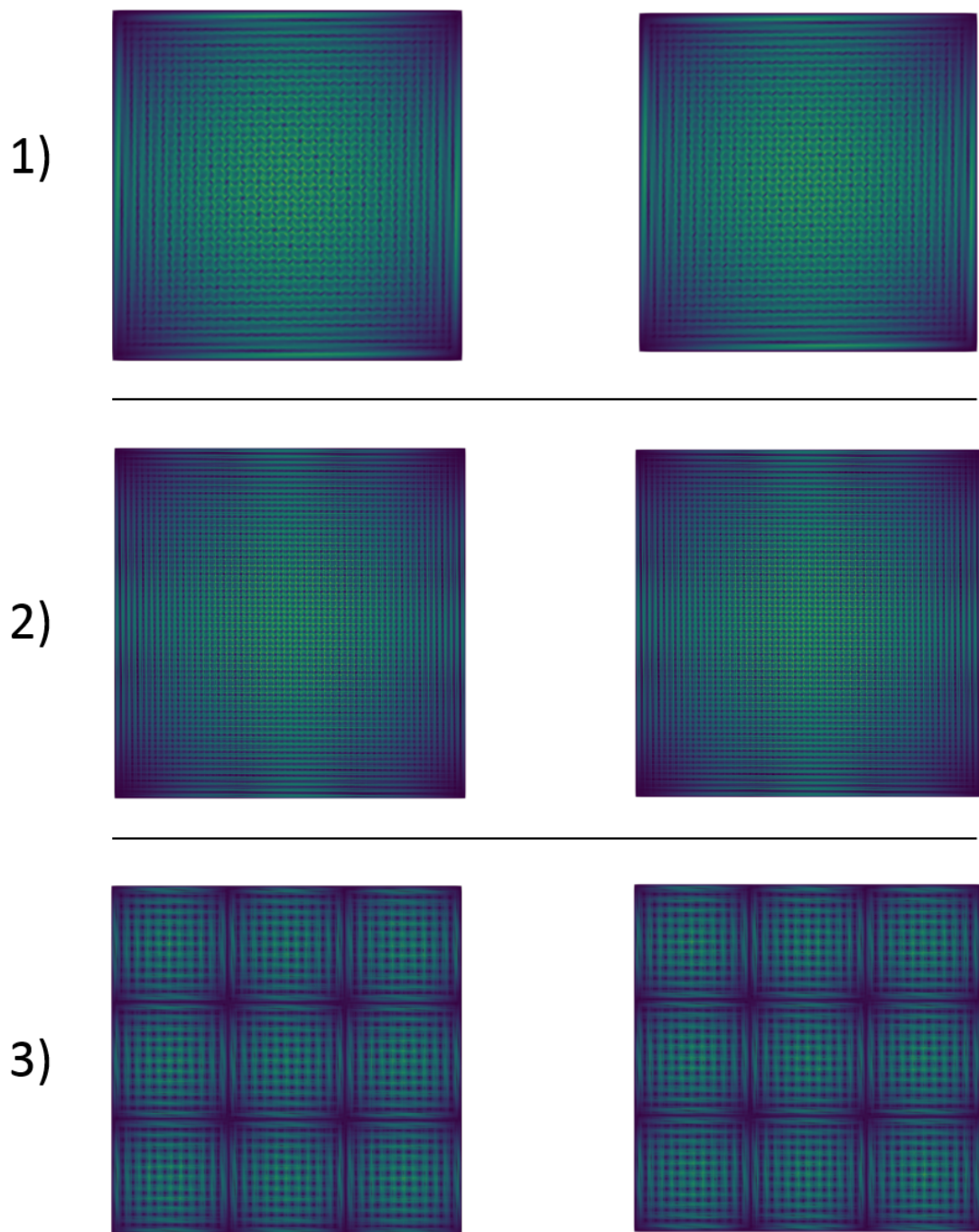


Figure 4.22: First two eigenmodes associated to the first loss of uniqueness of the FEM problem. From 1) to 3): $(N = 110, p = 0.018175)$, $(N = 331, p = 0.011355)$, $(N = 729, p = 0.01355)$.

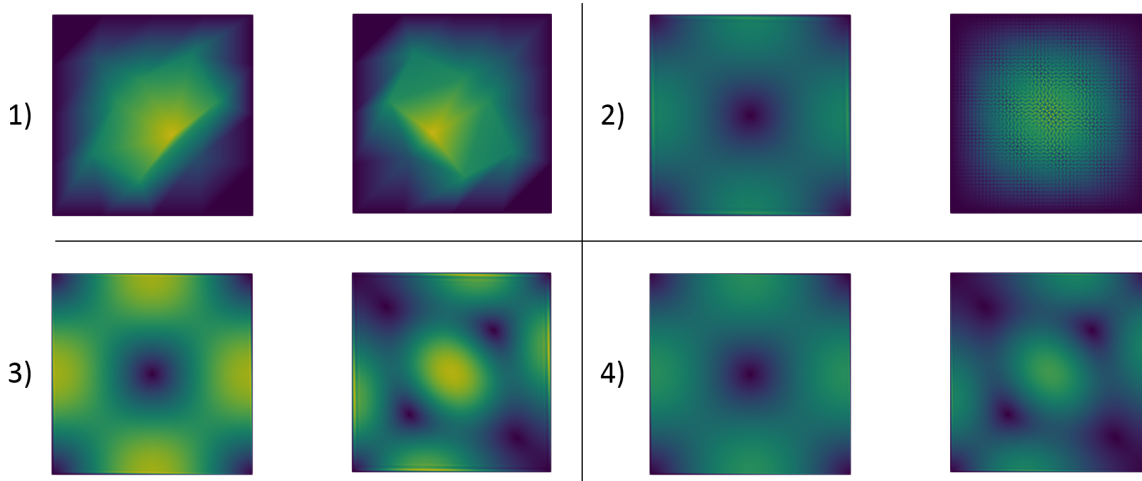


Figure 4.23: Eigenmodes associated to the two smallest eigenvalues at first loss of ellipticity while no loss of uniqueness of the FEM model. From 1) to 4) respectively $N = 4$, $N = 110$, $N = 331$ and $N = 729$.

4.4.2 Application to a simple tube loaded in torsion

In order to demonstrate the efficiency and robustness of the algorithm presented in section 4.3.3, a structural example is given in this section. Some fundamental results given in [Petryk, 1997] about the uniqueness of the FEM problem are illustrated. The implementation of the proposed algorithm and the simulations are performed in the **Zset** software environment [Besson and Foerch, 1997] (<http://www.zset-software.com/>).

Boundary value problem and material properties

A tube of external diameter $D = 1\text{ mm}$, thickness $t = 0.1\text{ mm}$ and length $L = 0.5\text{ mm}$ is loaded in torsion. The tube is oriented along the (O, \underline{e}_y) axis and its lower and upper surfaces are respectively denoted S_0 and S_L , as shown in Figure 4.24. The mesh is made of regular hexahedral elements with 20 nodes, 27 integration points.

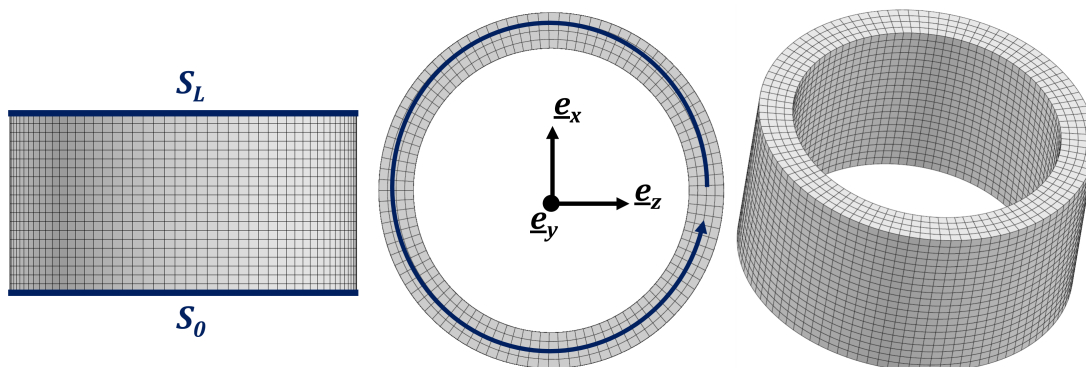


Figure 4.24: Geometry and boundary conditions. S_0 is fixed in all directions, a rotation around (O, \underline{e}_y) is imposed to the nodes on S_L .

On the bottom surface, S_0 , all displacements are fixed; on the top surface, S_L , displacements are imposed to describe a rotation of angle θ as follows:

$$\underline{\mathbf{u}}(y=0) = \underline{\mathbf{0}} \quad \forall \underline{\mathbf{X}} \in S_0 \quad (4.113)$$

$$\underline{\mathbf{u}}(y=L) = (\underline{\mathbf{R}}(\theta) - \underline{\mathbf{I}})\underline{\mathbf{X}} \quad \forall \underline{\mathbf{X}} \in S_L \quad (4.114)$$

Finally, material properties are described by a corotational formulation on the Kirchhoff stress tensor respecting a von Mises criterion such that:

$$E = 200. \text{ GPa}; \quad \nu = 0.33 \quad (4.115)$$

$$f(\underline{\boldsymbol{\tau}}, R) = \sqrt{\frac{3}{2} \underline{\boldsymbol{\tau}}^{dev} : \underline{\boldsymbol{\tau}}^{dev}} - (1000 + 300.(1 - e^{-50p})) \quad (4.116)$$

Evolution of loss of ellipticity:

In the following results, no imperfection is introduced in the mesh, however, since all displacements are prescribed on S_0 and S_L the solution will naturally show some gradient along the longitudinal direction (see Figure 4.25). In fact, this is well known as the ‘‘Swift effect’’ when simulating a simple torsion test of a tube at finite deformation. Therefore, localization occurs in the middle section of the tube as a consequence of this non-homogeneous field.

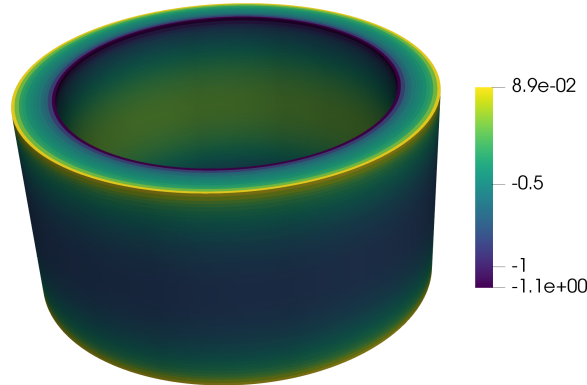


Figure 4.25: Map of the longitudinal stress σ_{yy} (MPa) in the tube.

The evolution of the loss of ellipticity in the thickness of the tube is discussed in this section. Numerical results are given in Figures 4.26 to 4.28 for the second coarsest mesh¹⁹, made of quadratic hexahedral elements with full integration (27 integration points per element): 2 through the thickness, 10 along the length and 50 around the circumference (27000 Gauss points). The proposed minimization algorithm costs 119 μs per Gauss point per increment and per increment (324 s for 100 load increments) with $n_{\theta_2} = 5$, while the sampling method took 190 μs per Gauss point per increment.

¹⁹ It is shown further that such a mesh is sufficiently refined for the convergence before localization. Moreover, this has no consequence on the discussion given in this section.

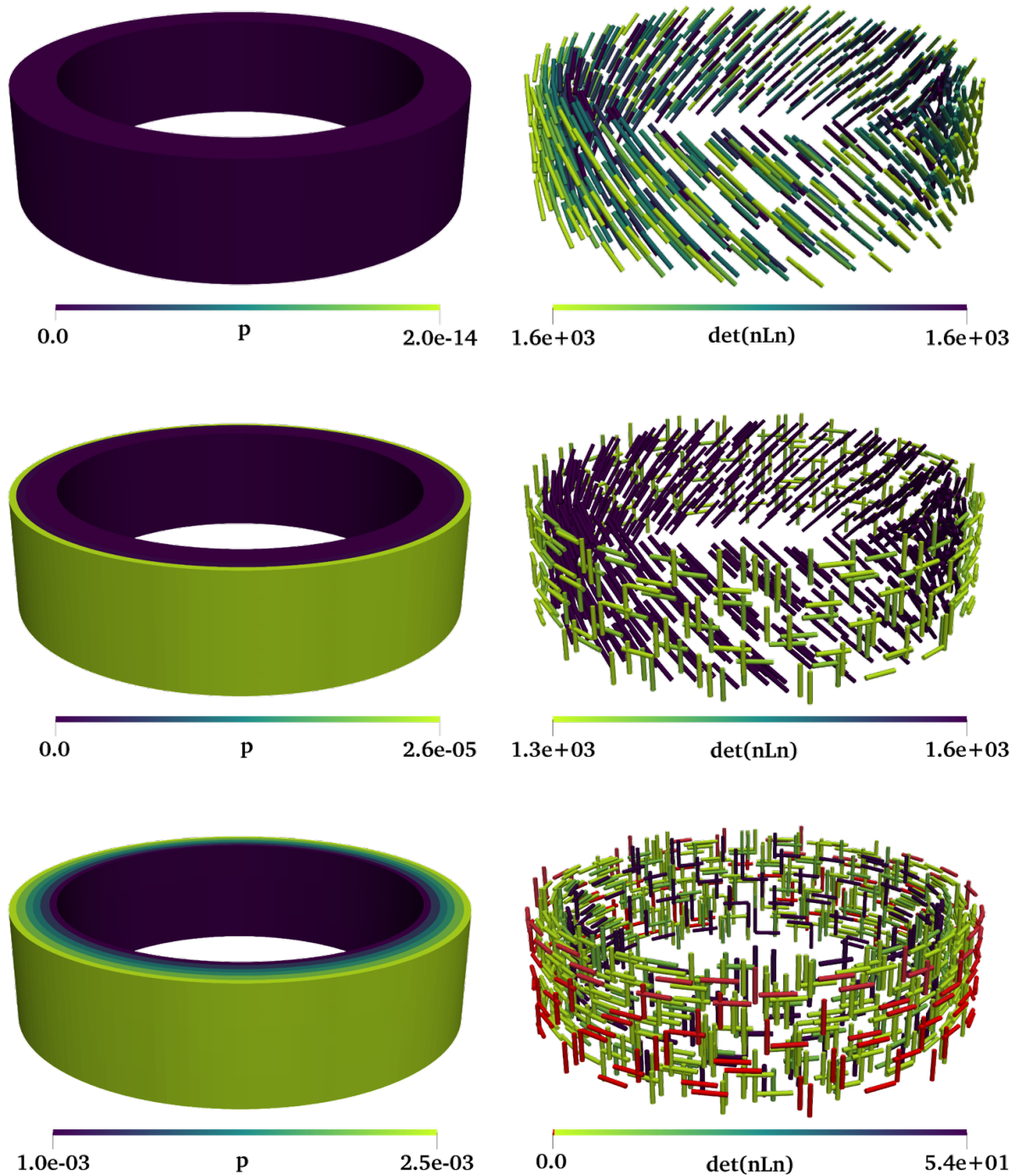


Figure 4.26: Top to bottom: evolution of accumulated plastic strain and $\min(\det(\underline{N} \odot \underline{\mathcal{L}} \cdot \underline{N}))$ in the lower half of the tube for $\theta = \{0.12^\circ, 0.45^\circ, 0.81^\circ\}$. The solution of the minimization problem is plotted with rods aligned with \underline{n} and colored by the amplitude of the minimum obtained in each Gauss point; red indicates loss of ellipticity. For visualization purposes, not all Gauss points are represented on these plots.

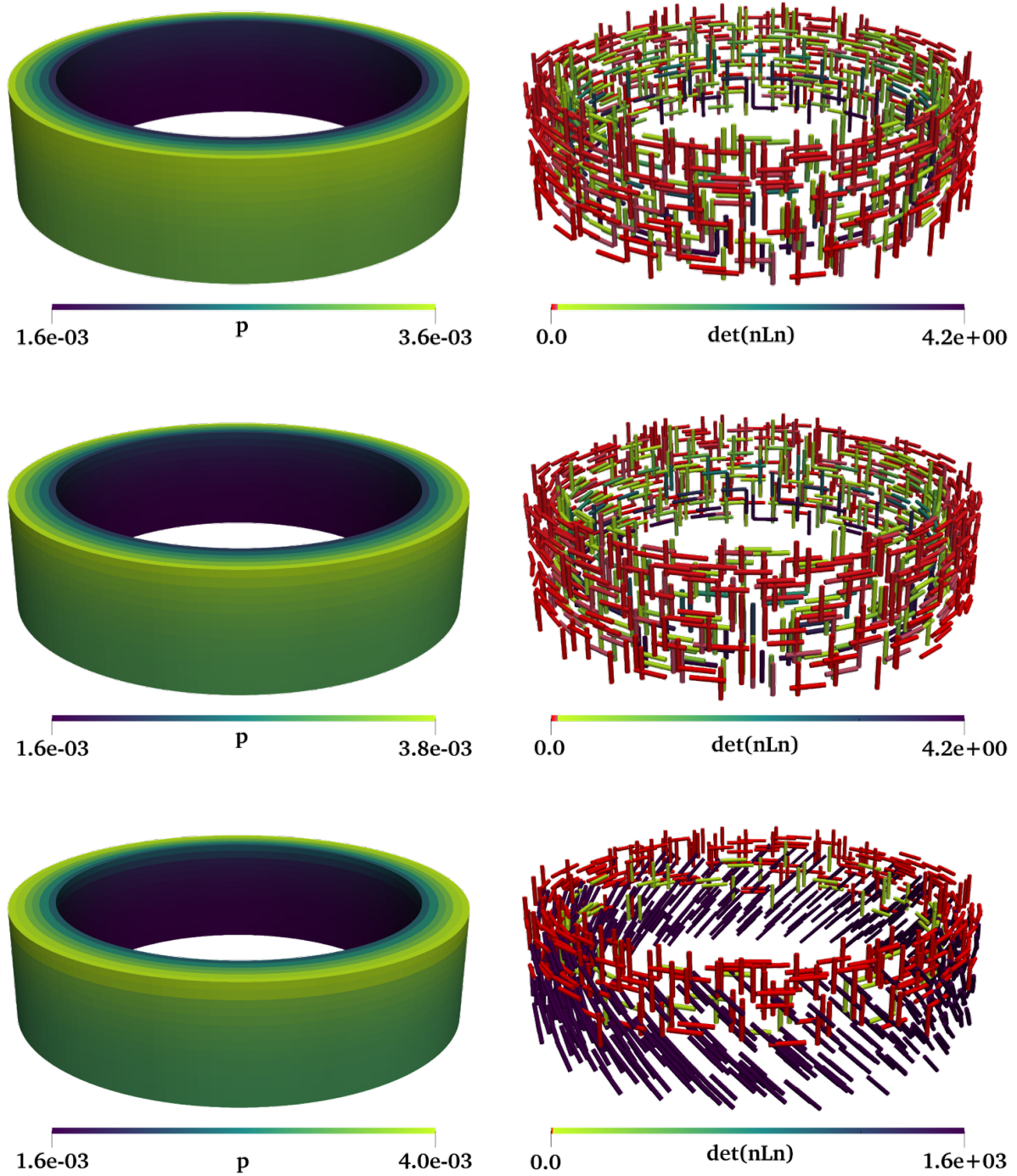


Figure 4.27: Top to bottom: evolution of accumulated plastic strain and $\min(\det(\underline{N} \odot \underline{\mathcal{L}} \cdot \underline{N}))$ in the lower half of the tube for $\theta = \{0.89^\circ, 0.8935^\circ, 0.8975^\circ\}$. The solution of the minimization problem is plotted with rods aligned with \underline{n} and colored by the amplitude of the minimum obtained in each Gauss point; red indicates loss of ellipticity. For visualization purposes, not all Gauss points are represented on these plots.

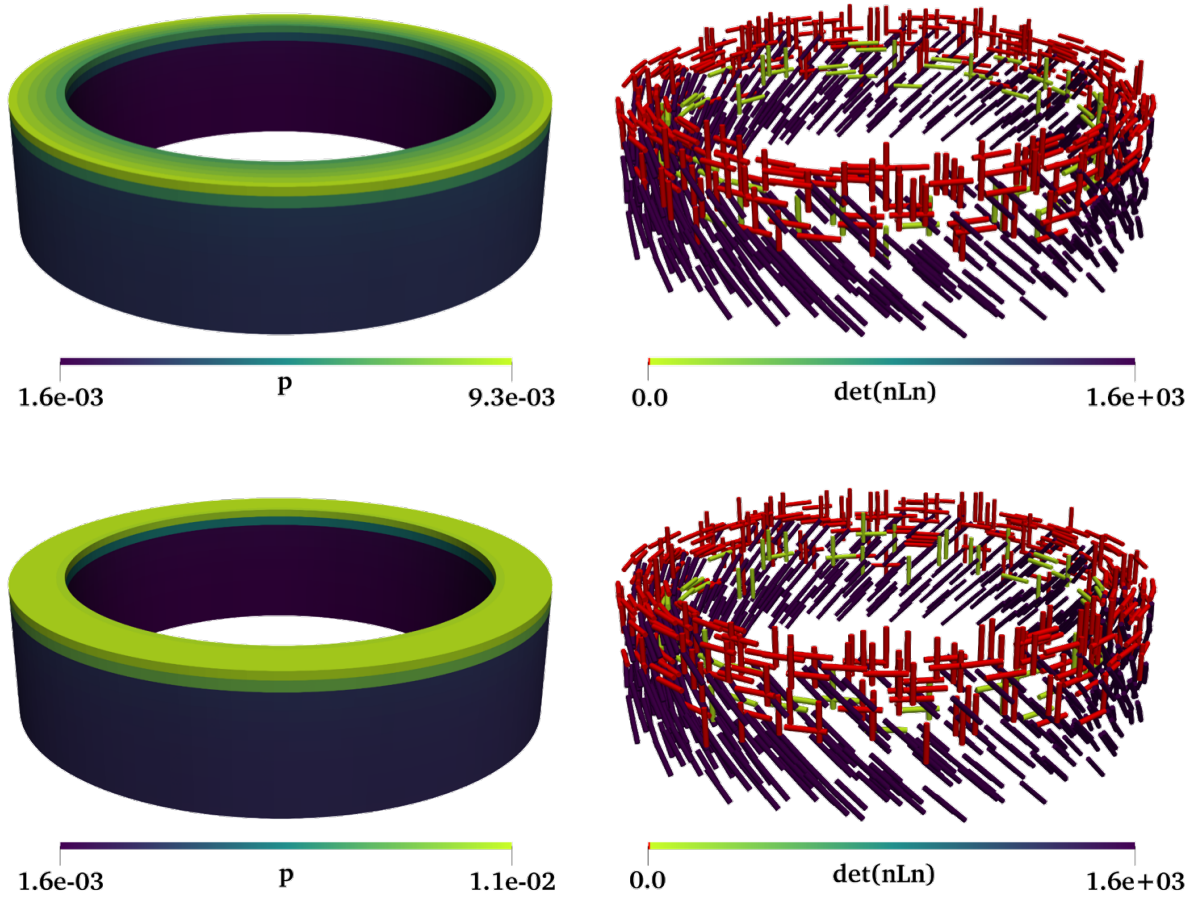


Figure 4.28: Top to bottom: evolution of accumulated plastic strain and $\min(\det(\underline{\mathbf{N}} \odot \underline{\mathcal{L}} \cdot \underline{\mathbf{N}}))$ in the lower half of the tube for $\theta = \{0.94875^\circ, 1.0^\circ\}$. The solution of the minimization problem is plotted with rods aligned with $\underline{\mathbf{n}}$ and colored by the amplitude of the minimum obtained in each Gauss point; red indicates loss of ellipticity. For visualization purposes, not all Gauss points are represented on these plots.

For visualization purposes, only the lower half of the tube is shown in Figures 4.26 to 4.28. The tube is initially elastic and the solution of the minimization problem is constant and positive with $\underline{\mathbf{n}} = \pm(\sqrt{2}/2\mathbf{e}_\theta - \sqrt{2}/2\mathbf{e}_z)$. Once plasticity starts on the outer skin of the tube, $\pm\mathbf{e}_\theta$ and $\pm\mathbf{e}_z$ become equivalent minimizers of $\det(\underline{\mathbf{N}} \odot \underline{\mathcal{L}} \cdot \underline{\mathbf{N}})$ for $\theta = 0.45^\circ$. Ellipticity is first lost on the outer-skin for $\theta = 0.81^\circ$. Then, plastic strain quickly increases in the middle section once the loss of ellipticity reaches the inner-skin ($\theta > 0.8975^\circ$). This occurs in the middle section of the tube due to the longitudinal compression and tension stresses (cf. Figure 4.25). In fact, the strain concentration in the middle section can be observed in some experimental setups [Scales et al., 2016, Defaisse et al., 2018]. Finally, once localization starts in the middle section of the tube, the rest of the structure elastically unloads.

Mesh and time-stepping sensitivity:

In this section one of the main characteristics of loss of ellipticity are investigated: sensitivity of the results with respect to the mesh and time steps sizes. For this purpose, four meshes are modeled (shown in Figure 4.29). From coarsest to finest, models are numbered from 0 to 3.

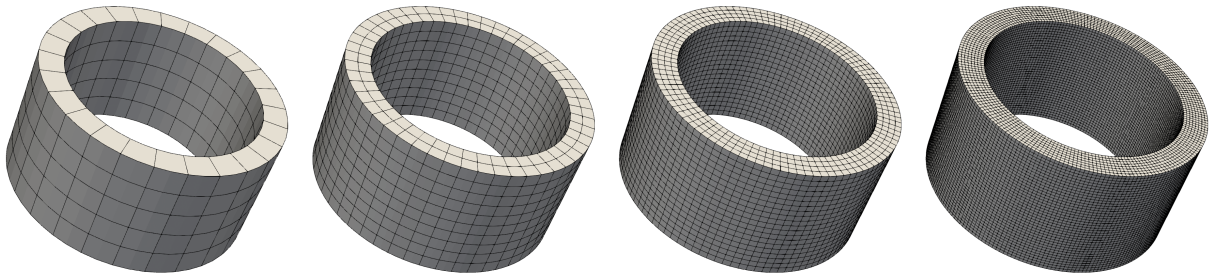


Figure 4.29: Meshes used for the meshes sensitivity analysis. From left to right: 125, 1000, 8080, 64320 elements.

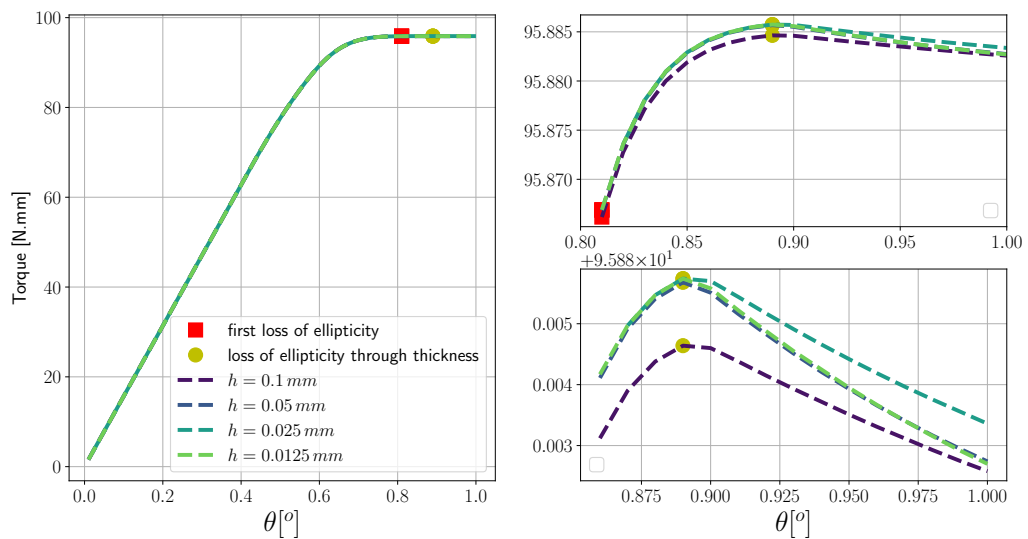


Figure 4.30: Torsion test: On the left, torques obtained for the different mesh sizes (h); on the right, zoom at maximum torque ($\theta \in [0.8, 1.0]$).

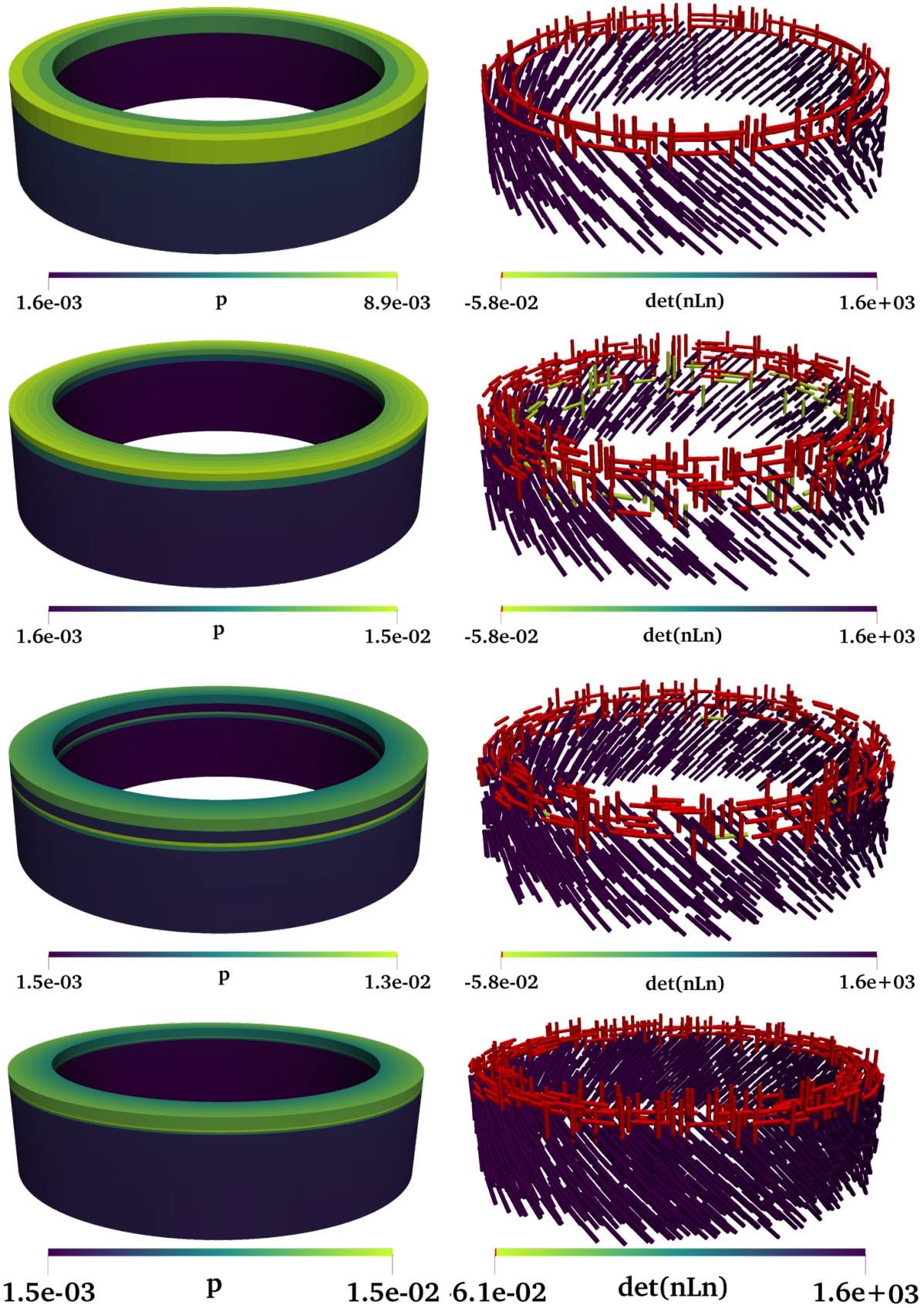


Figure 4.31: From left to right and top to bottom: evolution of accumulated plastic strain and $\min(\det(\underline{\mathbf{N}} \odot \underline{\mathcal{L}} \cdot \underline{\mathbf{N}}))$ in the lower half of the tube for models 0 to 3. The solution of the minimization problem is plotted with rods colored by the amplitude of the minimum obtained in each Gauss point; red indicates loss of ellipticity. For visualization purposes not all Gauss points are represented on these plots.

This example highlights the utmost importance of the algorithm being robust with respect to the existence of multiple equivalent minima. In fact, a single starting point algorithm might have converged to only one solution (sensitivity to the initial discretization of the sphere). If only the solution \underline{e}_θ was found, it would not be possible to put in parallel the loss of ellipticity criterion with the emergence of a localization band in the structure and understand the loss of regularity of the FEM solution.

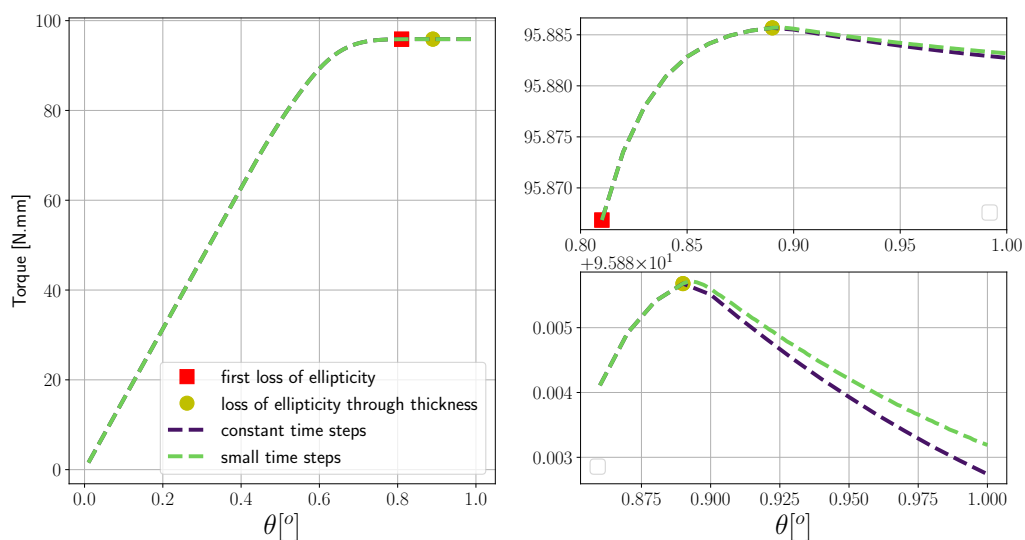


Figure 4.32: Torsion test: On the left, torques obtained for constant and refined time-steps; on the right, zoom at maximum torque ($\theta \in [0.8, 1.0]$)

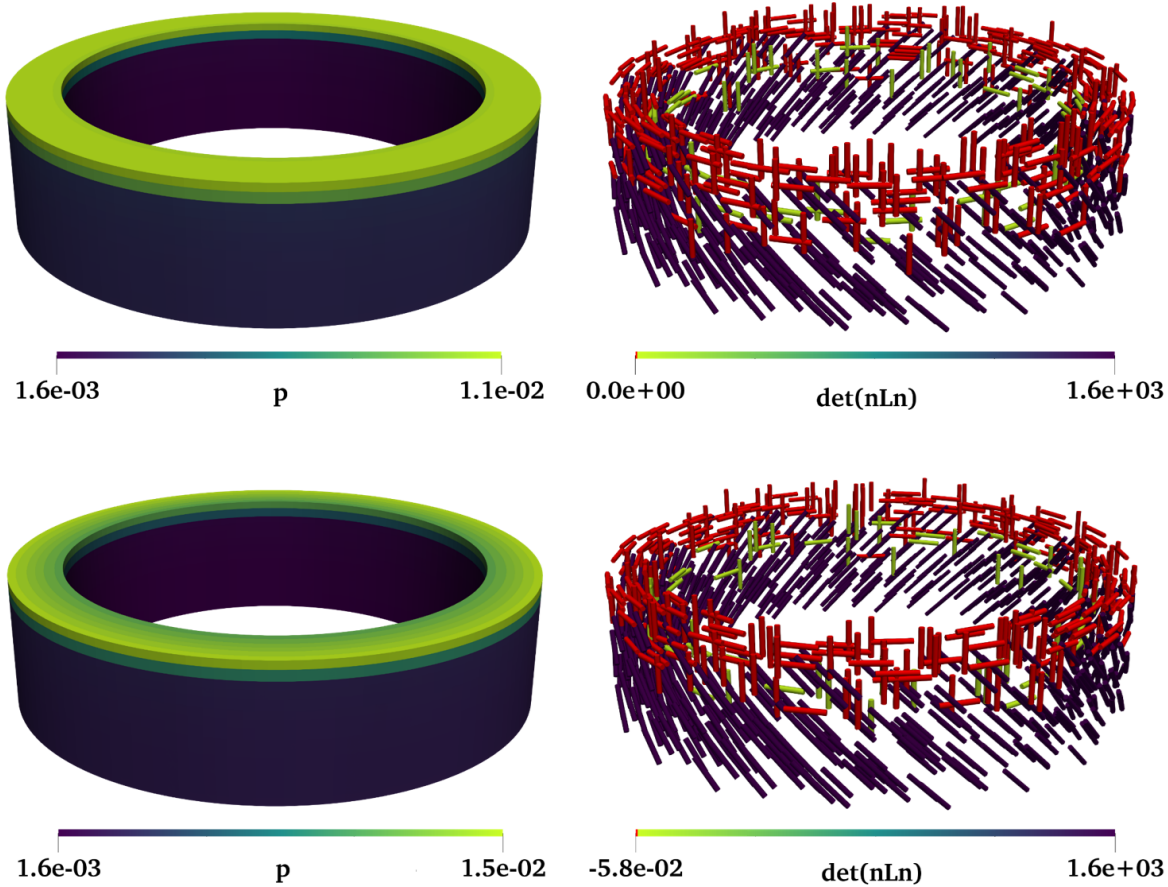


Figure 4.33: Results in terms of accumulated plastic strain and loss of ellipticity for $\theta = 1^\circ$, using mesh of model 1. Top, constant time-steps (0.01°); bottom, refined time-stepping.

The part of the structure in which ellipticity is lost before localization occurs has a finite thickness regardless of the mesh size. This leads to the existence of multiple localization bands of various thickness: infinitely many in a infinite functional space; but as many as there are layers of elements in a FEM model (see section 5.3.2). It is important to note that for a infinite functional space the solution loses uniqueness as soon as ellipticity is lost in an arbitrarily small area [Petryk, 1993]. These localization bands are filtered by the shape functions of the FEM model and only deformations that can be projected on the FEM shape functions can be captured. However, such instabilities are maybe not necessarily critical in order to analyze the structure's integrity since they are confined to an arbitrarily small area [Petryk, 1992].

As proposed in [Petryk, 1997], once a “*disk-like*” zone in which ellipticity is lost has fully emerged, localization in the sense of Rice occurs²⁰. In fact, loss of ellipticity in a single Gauss point is not enough for the FEM model to fail [Petryk, 1997], but it is an indicator of a weak, most likely critical, zone in the structure [Doghri and Billardon, 1995] for softening materials. Another fundamental result is observed: once localization in the sense of Rice occurs (existence of a band with jumps in strain rates), the rest of the structure elastically unloads [Bigoni and

²⁰ In [Petryk, 1997], the author also discusses some geometrical compatibility with the boundary conditions, which is met in this case: the rotation of the upper surface is consistent with the shear band in the middle section.

Zaccaria, 1993, Jirásek, 2007, Besson et al., 2010]. This usually leads to a sudden drop in the structure's stiffness, but shear has almost zero geometric consequences in terms of effective section. Therefore, it does not lead to a sudden drop in the stiffness of the structure but only to a slightly decreasing torque [Jirásek, 2007], as shown in Figure 4.30.

4.4.3 Application to a full torsion sample

In this section the analysis of loss of ellipticity is applied to a real torsion sample, in order to detect a shear localization band. The geometry and mesh are shown in Figure 4.34. This a real sample, tested and modelled in [Defaïsse et al., 2018, Defaïsse, 2018].

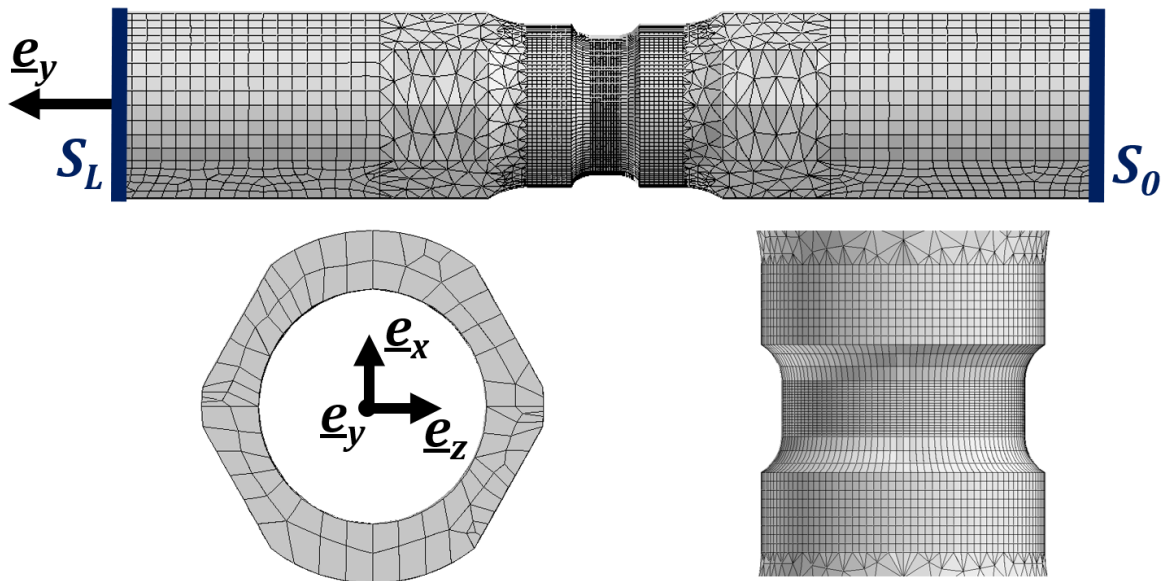


Figure 4.34: Geometry of the torsion sample. A regular mesh (quadratic interpolation) is used in the effective length. Flat surfaces are cut on the sample's heads in order to be able to load it in torsion.

This sample has been loaded in torsion, and exhibits, for the material properties given in [Defaïsse et al., 2018] without the linear hardening term, a localization band in the effective length due to loss of ellipticity. These results are shown in Figure 4.35.

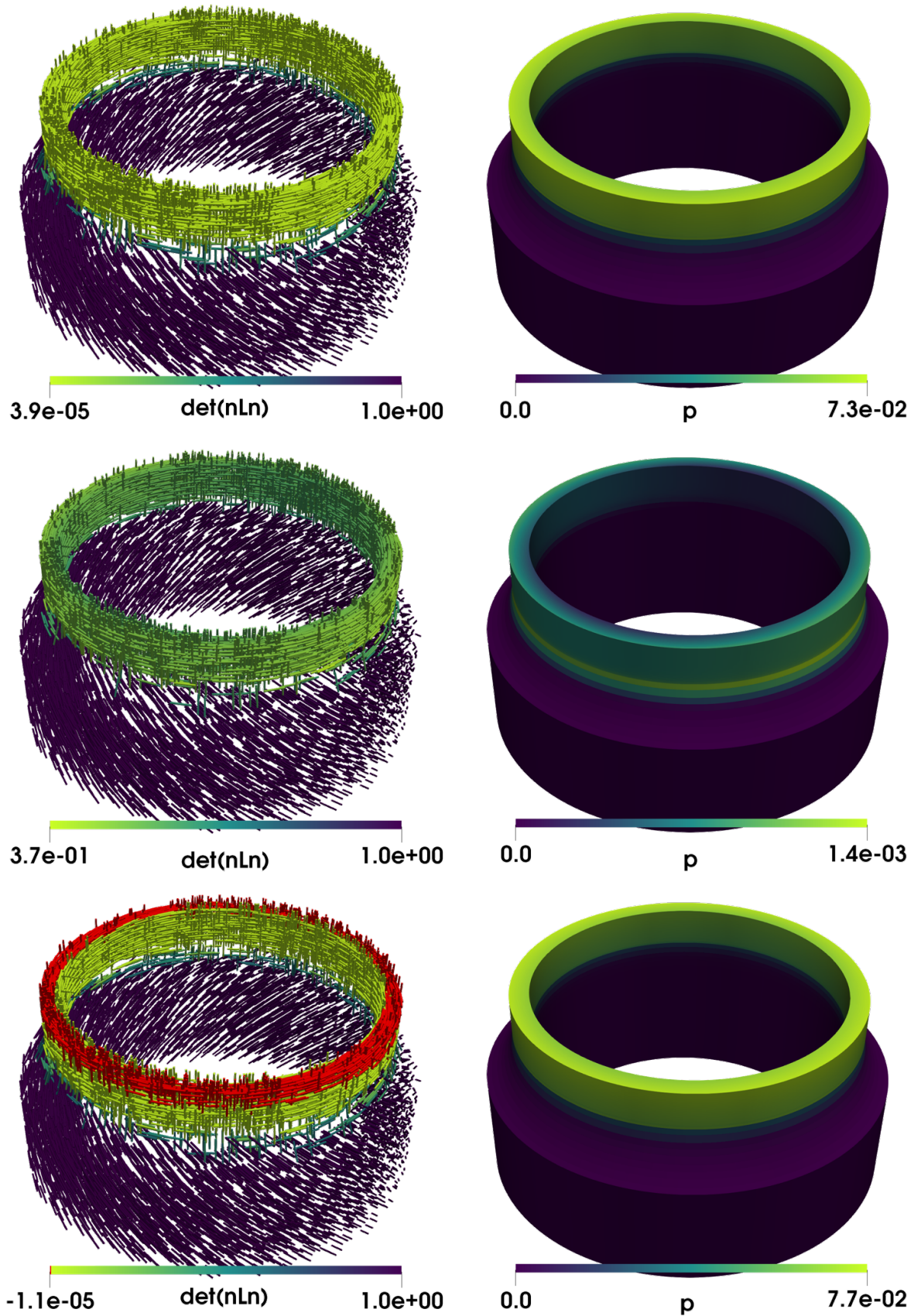


Figure 4.35: From top to bottom: evolution of loss of ellipticity and cumulative plastic strain in the gauge length of the sample. The solution of the minimization problem at each Gauss point is plotted in rods; red rods for loss of ellipticity.

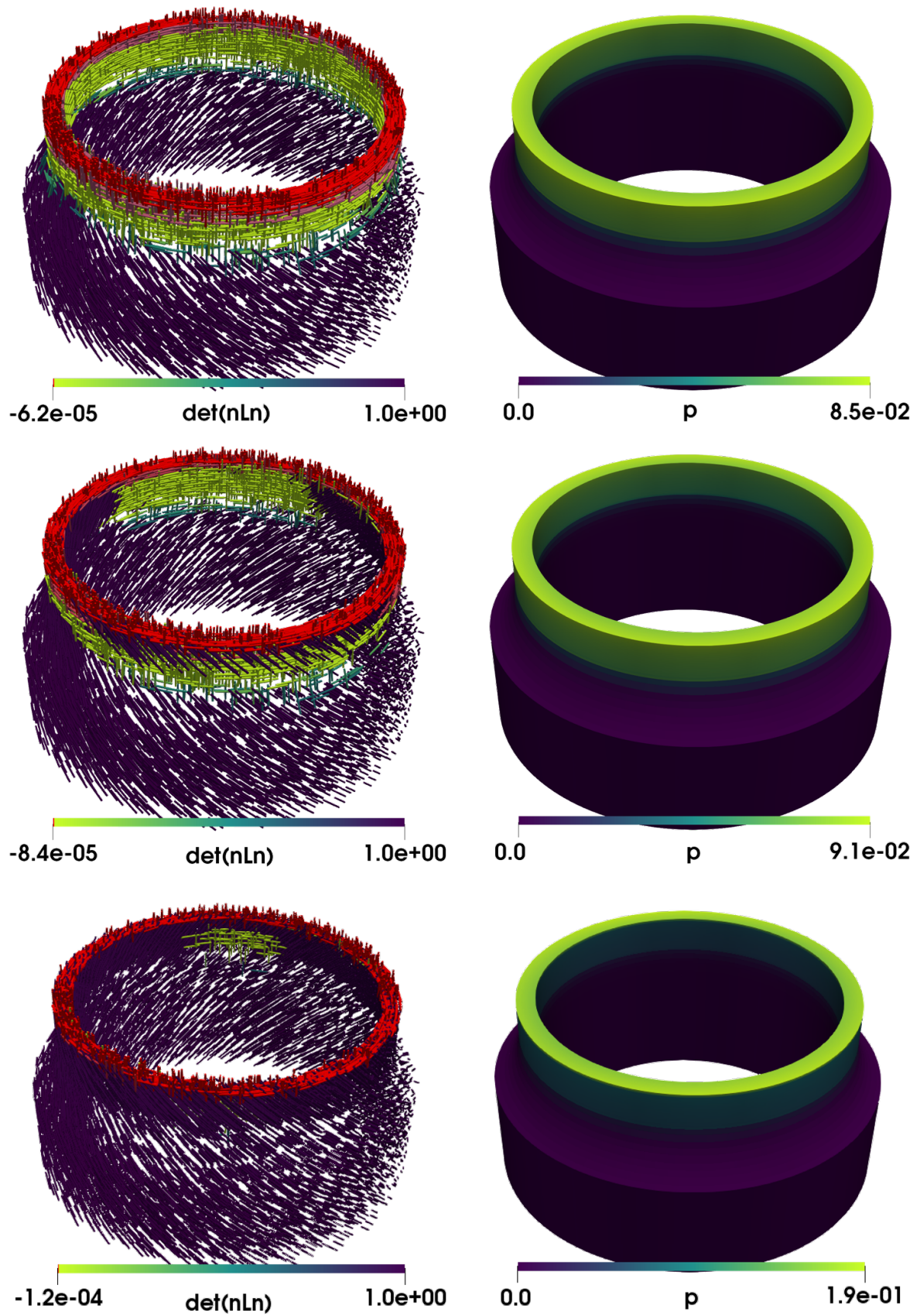


Figure 4.36: From top to bottom, left to right: evolution of loss of ellipticity and cumulative plastic strain in the effective length of the sample. The solution of the minimization problem at each Gauss point is plotted in rods; red rods for loss of ellipticity.

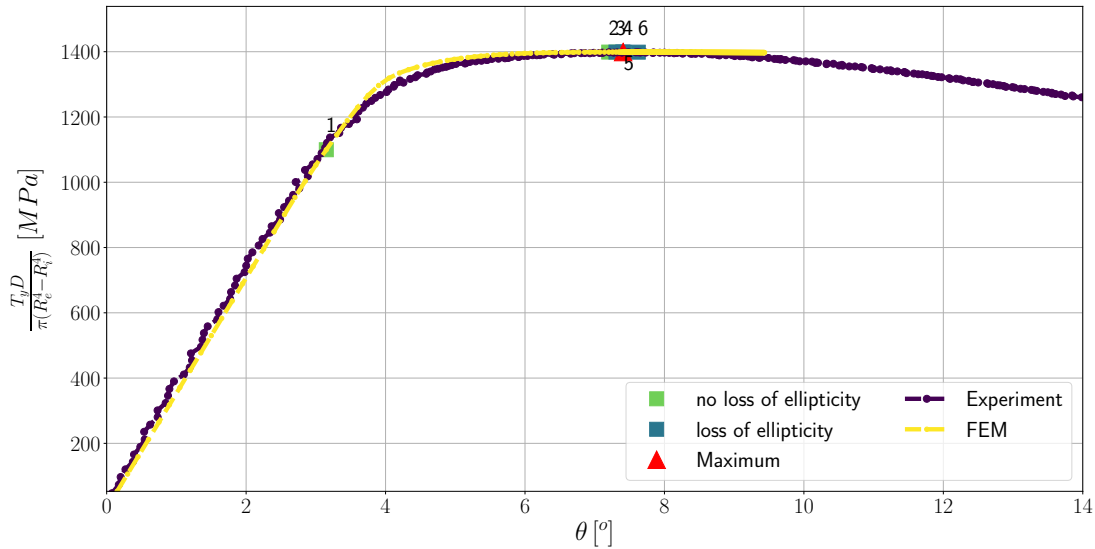


Figure 4.37: Comparison FEM/experiment. Evolution of torques as a function of the loading angle for the whole loading process. In squares, the instants shown in Figures 4.35 and 4.36; the red triangle shows the maximum torque.

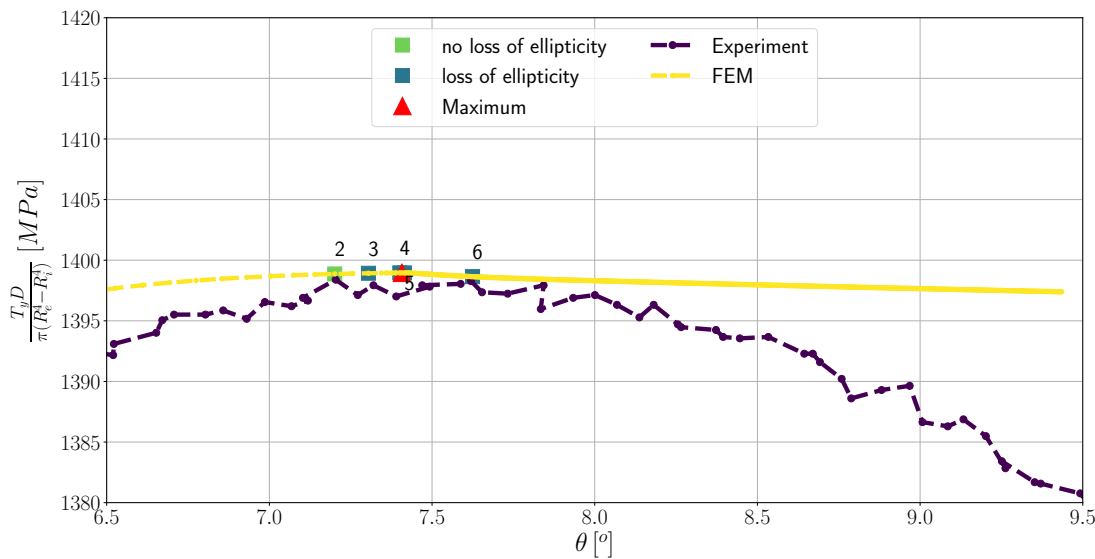


Figure 4.38: Comparison FEM/experiment. Evolution of torques as a function of the loading angle zoom around the localization point. In squares, the instants shown in Figures 4.35 and 4.36; the red triangle shows the maximum torque.

It is shown that the sample has the same kind of behavior for the evolution of loss of ellipticity as for the simple tube presented in section 4.4.2. Yet, a small difference can be observed due to the sample's geometry: the flat surfaces added to the heads for testing purposes induce a non-axisymmetric solution. This leads to the existence of two zones where elastic unloading occurs later. *In fine*, the plastic strain localized in a narrow band (thickness of half an element). As it can be shown in Figures 4.37 and 4.38, the applied torque continues to increase after the

first loss of ellipticity. Once ellipticity is lost through the thickness of the middle section and once there is elastic unloading in the rest of the effective length that the maximum torque is reached. Then, even though the material is non-softening, the applied torque decreases.

Finally, these results seem to be quantitatively consistent with the experimental measures. However, linear hardening had to be neglected in order to have a saturating material. If not, localization would not activate since the hardening modulus would be too large. This is shown in section 6.1, and a more detailed discussion is given about this assumption. Nevertheless, in the identification process of the material law given in [Defaisse et al., 2018], it would have been possible to replace the linear hardening term with a third exponential hardening term. However, this would require some more investigation that has not been done in the present work.

4.5 Conclusions

The loss of ellipticity criterion has been re-derived in order to fit the present work's notations. This criterion has been presented as an indicator for the existence of possible jumps in strain rates²¹. Then, the uniqueness analysis of the van Hove rate boundary value problem has been presented and a minor extension has been given. This led to a discussion on loss of ellipticity and loss of uniqueness of a discretized problem, which has later been illustrated with the case of a square loaded in shear.

A new general and efficient algorithm based on a Newton-Raphson scheme is proposed for evaluating the loss of ellipticity criterion. It is derived in the most general case and does not depend explicitly on the formulation or on the associativity of the flow. This algorithm has been shown to be more robust than what is found in the literature, and more efficient. In order to reach maximal efficiency, a method to discretize the unit sphere has been proposed. This method has the twin benefits of providing an isotropic distribution as well as reducing the number of discretization points. This proposed multi-start method has been compared to the classical sampling method found in the literature [Mosler, 2005]. It is shown to be more robust in terms of finding the global minimum and it has a shorter computation time.

The new method was applied in a structural FEM problem to evaluate the failure of a tube loaded in torsion. It has been shown that, even though the material of the tube is non-softening and possesses an associative flow, the loss of ellipticity criterion is met and localization emerges in the simulation. Also, the use of the multi initialization algorithm proposed in this paper, being robust when there are multiple equivalent global minima, allowed us to properly interpret the results in section 4.4.2.

Finally, it has been observed in a structural problem that loss of ellipticity in a part of the structure in a FEM problem is not enough for the discretized problem itself to lose uniqueness. In fact, it has been shown that localized shear bands appear in the tube only once ellipticity has been lost through the whole thickness of the tube. The section in which loss of ellipticity occurs is parallel to the boundary conditions and the normals minimizing $\det(\underline{\mathbf{N}} \odot \underline{\mathbf{L}} \cdot \underline{\mathbf{N}})$ are also normal to this section. These conditions are discussed in section 5.3.2, where the importance of the compatibility with boundary conditions is illustrated for the localization problem.

²¹ It has been interpreted as such in the rest of the chapter

Bibliography

- Abed-Meraim, F. (2009). *Contributions à la prédiction d'instabilités de type structure et matériau : modélisation de critères et formulation d'éléments finis adaptés à la simulation des structures minces*. Mémoire HDR dissertation, Arts et Métiers ParisTech.
- A.R. Aguiar, L. P.-F. and Prado, E. (2017). Analytical and numerical investigation of failure of ellipticity for a class of hyperelastic laminates. *European Journal of Mechanics A/Solids*, 61:110–121.
- Ben-Bettaieb, M. and Abed-Meraim, F. (2017). Effect of kinematic hardening on localized necking in substrate supported metal layers. *International Journal of Mechanical Sciences*, 123:177–197.
- Benallal, A. and Comi, C. (1996). Localization analysis via a geometrical method. *International Journal of Solids and Structures*, 33:99–119.
- Besson, J., Cailletaud, G., Chaboche, J.-L., and Forest, S. (2010). *Non-linear mechanics of materials*. Springer.
- Besson, J. and Foerch, R. (1997). Large scale object-oriented finite element code design. *Computer Methods in Applied Mechanics and Engineering*, 142(1):165–187.
- Besson, J., Steglich, D., and Brocks, W. (2001). Modeling of crack growth in round bars and plane strain specimens. *International Journal of Solids and Structures*, 38:8259–8284.
- Bigoni, D. (2012). *Nonlinear Solid Mechanics: Bifurcation Theory and Material Instability*. Cambridge University Press.
- Bigoni, D. and Hueckel, T. (1991). Uniqueness and localization - i - associative and non-associative elastoplasticity. *International Journal of Solids and Structures*, 28:197–213.
- Bigoni, D. and Zaccaria, D. (1992). Loss of strong ellipticity in non-associative elastoplasticity. *Journal of the Mechanics and Physics of Solids*, 40:1313–1331.
- Bigoni, D. and Zaccaria, D. (1993). On strain localization analysis of elastoplastic materials at finite strains. *International Journal of Plasticity*, 9:21–33.
- de Borst, R., Wells, G., and Sluys, L. (2001). Some observations on embedded discontinuity models. *Engineering Computations*, 18:241–254.
- Defaïsse, C. (2018). *Étude de la rupture ductile d'un acier à très haute résistance pour des applications aéronautiques*. PhD thesis, École de Mines Paristech.
- Defaïsse, C., Mazière, M., Marcin, L., and Besson, J. (2018). Ductile fracture of an ultra-high strength steel under low to moderate stress triaxiality. *Engineering Fracture Mechanics*, 194:301–318.

- Doghri, I. and Billardon, R. (1995). Investigation of localization due to damage in elasto-plastic materials. *Mechanics of Materials*, 19(2):129–149.
- Gourgiotis, P. and Bigoni, D. (2016). Stress channelling in extreme couple-stress materials part i: Strong ellipticity, wave propagation, ellipticity, and discontinuity relations. *Journal of the Mechanics and Physics of Solids*, 88:150–168.
- Gruben, G., Morin, D., Langseth, M., and Hopperstad, O. (2017). Strain localization and ductile fracture in advanced high-strength steel sheets. *European Journal of Mechanics A/Solids*, 61:315–329.
- Hill, R. (1958). A general theory of uniqueness and stability in elastic-plastic solids. *Journal of the Mechanics and Physics of Solids*, 6:236–249.
- Hill, R. (1962). Acceleration waves in solids. *Journal of the Mechanics and Physics of Solids*, 10:1–16.
- Jirásek, M. (2007). Mathematical analysis of strain localization. *Revue Européenne de Genie Civil*, 11:977–991.
- Liu, P. (2015). Extended finite element method for strong discontinuity analysis of strain localization of non-associative plasticity materials. *International Journal of Solids and Structures*, 72:174–189.
- Mandel, J. (1964). Propagation des surfaces de discontinuité dans un milieu élastoplastique. In *Stress waves in anelastic solids*, pages 331–340. Springer.
- Mandel, J. (1966). Conditions de stabilité et postulat de drucker. In *Rheology and Soil Mechanics*, pages 58–68. Springer.
- Marsden, J. and Hughes, T. (1983). *Mathematical Foundations of Elasticity*. Dover Publications.
- Mear, M. and Hutchinson, J. (1985). Influence of yield surface curvature on flow localization in dilatant plasticity. *Mechanics of Materials*, 4:395–407.
- Mosler, J. (2005). Numerical analyses of discontinuous material bifurcation: strong and weak discontinuities. *Computer Methods in applied Mechanics and Engineering*, 194:979–1000.
- Mota, A., Chen, Q., Foulk, J., Ostien, J., and Lai, Z. (2016). A cartesian parametrization for the numerical analysis of material instability. *International Journal for Numerical Methods in Engineering*, 108(2):156–180.
- Néda, Z., R., and Brechet, Y. (1999). Reconsideration of continuum percolation of isotropically oriented sticks in three dimensions. *Physical Review E*, 59:3717–3719.
- Neilsen, M. and Schreyer, H. (1993). Bifurcations in elastic-plastic materials. *International Journal of Solids and Structures*, 40:521–544.
- Nguyen, Q. S. (2000). *Stability and nonlinear solid mechanics*. Wiley.
- Oliver, J., Huespe, A., Cante, J., and Diaz, G. (2010). On the numerical resolution of the discontinuous material bifurcation problem. *International Journal for Numerical Methods in Engineering*, 6:786–804.
- Ortiz, M. (1987). An analytical study of the localized failure modes of concrete. *Mechanics of Materials*, 6:159–174.

- Petryk, H. (1992). Material instability and strain-rate discontinuities in incrementally nonlinear continua. *Journal of Mechanics and Physics of Solids*, 40:1227–1250.
- Petryk, H. (1993). Theory of bifurcation and instability in time-independent plasticity. In *Bifurcation and Stability of Dissipative Systems*, volume 327, pages 95–152, Vienna. Springer Vienna.
- Petryk, H. (1997). Plastic instability : Criteria and computational approaches. *Archives of Computational Methods in Engineering*, 4:111–151.
- Petryk, H. (2000). *Material Instabilities in Elastic and Plastic Solids*. CISM International Centre for Mechanical Sciences 414. Springer, 1 edition.
- Rice, J. (1976). The localization of plastic deformation. In *W.T. Koiter (Ed.), Theoretical and Applied Mechanics*, pages 207–220. North-Holland.
- Rudnicki, J. and Rice, J. (1975). Conditions for the localization of deformation in pressure sensitive dilatant materials. *Journal of Mechanics and Physics of Solids*, 23:371–394.
- Sanborn, S. and Prévost, J. (2011). Frictional slip plane growth by localization detection and the extended finite element method (xfem). *International Journal for Numerical and Analytical Methods in Geomechanics*, 35:1278–1298.
- Scales, M., Tardif, N., and Kyriakides, S. (2016). Ductile failure of aluminum alloy tubes under combined torsion and tension. *International Journal of Solids and Structures*, 97-98:116–128.
- Szabó, L. (2000). Comments on loss of strong ellipticity in elastoplasticity. *International Journal of Solids and Structures*, 37:3775–3806.
- van Hove, L. (1947). Sur l’extension de la condition de Legendre du calcul des variations aux intégrales multiples à plusieurs fonctions inconnues. *Proceedings of the Koninklijke Nederlandse Akademie van Wetenschappen*, 50:18–23.

Chapter 5

Weakened stability analysis

“Sur l’autoroute, à gauche il y a le terre-plein central, c’est le bord dur, il t’évite le carambolage par la force ; et à droite il y a le bord mou pour les petites déviations. Ta mère c’est le bord mou ... File droit. ”

Mon père

“La partie garde toujours en elle quelque chose de la nature du tout.”

Léonard De Vinci

Résumé : La sensibilité du critère de Hill aux conditions aux limites imposées est un problème bien connu. Généralement, cette dépendance est étudiée en termes de directions de chargement, “quelle serait la conséquence de l’ajout d’un moment de flexion sur le flambement d’un tube en torsion ?”, mais rarement en termes de types de conditions aux limites, comme “la structure est-elle soumise à une force, un déplacement, la raideur d’une autre structure ?”. Cette dernière question est notamment considérée et quantifiée en génie civil. Cependant, pour les structures aéronautiques ce genre d’analyses se révèle être complexe de par la variabilité des matériaux et géométries.

Dans le présent chapitre, nous proposons d’affaiblir le critère d’unicité de Hill en considérant plusieurs ensembles de conditions aux limites. L’introduction de ce “critère affaibli de stabilité” sera d’abord alimenté par l’étude du flambement d’une poutre élastique en compression et par les approches utilisées en génie civil. Par la suite, ce critère sera mis en œuvre pour étudier la relation entre perte d’ellipticité et perte d’unicité du problème de van Hove et retrouver les analyses de Ryzhak et la proposition de Mandel. Aussi, l’analyse de la sensibilité des charges de flambement à différentes conditions aux limites pour un tube en torsion seront présentées.

5.1	Influence of the type of boundary conditions	129
5.2	Weakened stability analysis	133
5.3	Applications of the weakened stability criterion	140
5.4	Conclusions	163

Sensitivity to imperfections is a well-known problem when it comes to the analysis of the uniqueness and stability of a structure's response. While there are many studies which focus on the sensitivity to loading direction, geometrical and material imperfections [Hill and Hutchinson, 1975, Regulation, 2005, Lee and Ades, 1957, Di Pasqua et al., 2016, Remmers and de Borst, 2001, Hutchinson and Tvergaard, 1981, Mear and Hutchinson, 1985, Dæhli et al., 2017, Wang et al., 2017, Asmolovskiy et al., 2015, Kriegsmann et al., 2012, Walport et al., 2018], only a few focus on the sensitivity to the modeling assumptions in the Boundary Conditions (BCs) [Mandel, 1964, Ryzhak, 1994, Nguyen, 2000]. In the present chapter, we propose to investigate on the sensitivity of the critical loads to various assumptions the way loading is prescribed: displacement or dead loads.

In fact, two types of BC imperfections need to be distinguished. The first type focuses on how perfect the loading direction is: for example if the actual tensile axis is not aligned with the sample's axis, or if the tube meant to be loaded in pure torsion is also subject to some bending moment. The second type of BC imperfection analysis questions the nature of boundary conditions to apply in the mathematical or numerical model: "is the tensile machine perfectly stiff so that we can block transverse displacements?", or "is the structure actually loaded in terms of forces or in terms of displacements?" (for example when the load is prescribed through contact).

There are many studies on the effects of imperfections for elastic structures. They are generally based on the existence of a potential energy. Some of them analyze the structure's response to imperfections in either the geometry or loading (partly presented and discussed in chapter 10 in [Nguyen, 2000]). Finally, regarding the analysis of BC imperfections, these studies usually focus on the first type: loading direction. However, a potential energy does not exist for dissipative systems. Thus, the analysis of elastoplastic structures requires the description of every possible evolution of the irreversible quantities, such as plastic strain, and the consequent stress redistribution.

For simple elastoplastic structures, the analysis of small geometrical or loading imperfections might be done analytically as in [Lee and Ades, 1957]. However, they are usually restrictive regarding the material's constitutive law and are limited to simple geometries. When numerical modeling is required for more complex structures, an exhaustive analysis of the sensitivity to geometrical or loading imperfections may be impracticable due to the computation costs and the diversity of possible imperfections. Some recent developments in High Performance Computation (HPC) methods [Gosselet and Rey, 2006], and in Hybrid Reduced Order Modeling (HROM) [Ryckelynck, 2005, Perez et al., 2014, Eftang and Patera, 2014] could possibly provide the required tools for such analyses. However, such modeling is out of the scope of this work.

In a way, imperfections in the geometry or in the loading direction can be seen as a type of lost information. This information could be lost by using the nominal geometry or by idealizing the environment. However, if further details are known, it is possible to add them into the model and evaluate their influence on the critical load. For example, the actual geometry could be measured with scanning tools, as in [Harrison et al., 2016]; for the loading, one could consider a given number of loading imperfections and compute the resulting structural responses. Usually, breaking the symmetry in the loading or in the geometry will lead to a unique solution to the rate problem, see section 3.2.1. In this case, the best evaluation of the structure's critical load is usually obtained by simply computing the incremental responses.

For the second type of BC imperfections, it can be seen as a "modeling imperfection"; information that is not at all taken into account in the modeling. Usually, a structure is loaded through forces or displacements prescribed on the boundaries. Saint Venant's principle states that the behavior of a point far from the boundary where the loading is applied is insensitive to the way it is applied. This is true when the solution is unique. However, it is important to keep in mind that the analysis of the uniqueness of a structure's response with the tools presented in

section 3.1 is by construction highly sensitive to the way the loading is prescribed. In fact, it has been shown in section 3.2.3 that such considerations could have significant consequences on the analysis of the structure's stability.

In the present chapter, a method for evaluating the sensitivity of the critical load to the second type of BC imperfections is proposed. For this purpose, it is assumed that the loading direction and geometry are properly identified, and only the sensitivity to the type of BCs (displacements or traction forces) that are prescribed in the model is discussed. For illustration, the well known analysis of a buckling beam is detailed for various boundary conditions in section 5.1.1. In section 5.1.2, a quick presentation of some approaches used in civil engineering to evaluate critical loads considering various BCs is given. These methods are used to bound the buckling load of some civil engineering steel structures [Regulation, 2005, Gardner, 2018]. Based on these examples, a general numerical method to analyze the sensitivity of the uniqueness analysis of the rate boundary value problem to different BCs is proposed in section 5.2. This method is validated in section 5.2.4 on the reference Euler buckling. Then, the method is illustrated with more complex cases such as the evaluation of the buckling load of a short tube loaded in torsion in section 5.3.1, and the analysis of localization in a square loaded in shear in section 5.3.2. Finally, the latter will lead to the analysis of the emergence of localization bands in the sense of Rice in a thick tube loaded in torsion in section 5.3.3.

5.1 Influence of the type of boundary conditions

The present section aims to illustrate and motivate the “weakened stability” analysis presented in section 5.2. First the analysis of the Euler buckling is presented by linearizing Hill's loss of uniqueness criterion in order to compare the buckling loads obtained with boundary conditions. Then, a short discussion about approaches used in civil engineering is given.

5.1.1 Euler buckling: Sensitivity to BCs

Even though the results of the buckling of a beam loaded in compression are very well-known in elasticity, the aim here is to derive these results starting from Hill's loss of uniqueness criterion: starting from a full finite deformation framework, the analysis will be linearized to small strains but with large displacements. The problem is first analyzed independent of the type of BCs (fixed, simply supported, or free). Then, in order to study the sensitivity to various BCs the critical load is specified for a few specific BCs.

A beam of length L , section S , and Young's modulus E loaded in compression with a force F is analyzed. Before buckling arises, displacements are small enough to consider the initial configuration to be the actual configuration. A point M of the beam is located by the curvilinear coordinate s , as shown in Figure 5.1. The rotation of the section around the (M, \underline{e}_z) axis is given by the angle θ .

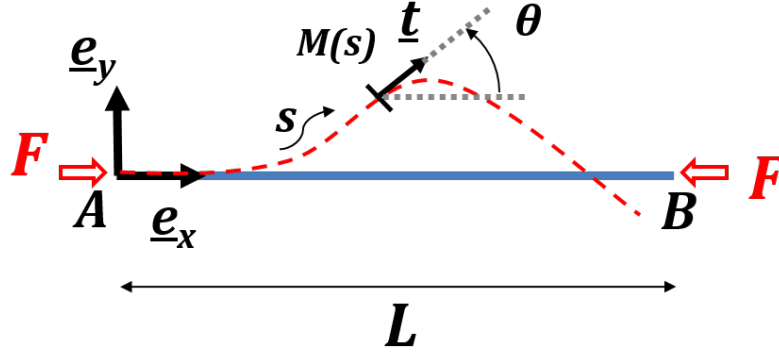


Figure 5.1: Schematic representation of a beam loaded in compression.

Such a coordinate system gives the following set of equations to describe the kinematics:

$$\underline{AM} = x(s)\underline{e}_x + y(s)\underline{e}_y \quad (5.1)$$

$$x(s) = \int_0^s \cos(\theta(s')) ds' \quad (5.2)$$

$$y(s) = \int_0^s \sin(\theta(s')) ds' \quad (5.3)$$

$$\underline{t} = \cos(\theta)\underline{e}_x + \sin(\theta)\underline{e}_y \quad (5.4)$$

It is assumed that the forces on a section of the beam can be reduced to a normal traction N and a torque around the (O, \underline{e}_z) axis M_z , such that the constitutive law can be given by:

$$N = ES \frac{\partial u_x}{\partial s} \quad (5.5)$$

$$M_z = EI \frac{\partial \theta}{\partial s} \quad (5.6)$$

where I denotes the second moment of area of the section. Before buckling occurs, the fundamental solution is trivially given by:

$$\left\{ \begin{array}{l} M_z = 0 \\ N = -F \\ \underline{u} = \frac{-F}{ES} \frac{x}{L} \underline{e}_x \\ \theta = 0 \\ \sigma_{xx} = \frac{-F}{S} \end{array} \right. \quad (5.7)$$

Linearizing Hill's loss of uniqueness criterion to small strains but finite displacements, the buckling analysis gives (see section 3):

$$\int_{\Omega} \underline{\xi}(\Delta \underline{\dot{u}}) : \underline{\tilde{E}} : \underline{\xi}(\delta \underline{\dot{u}}) + \underline{\sigma} : (\underline{\dot{F}}(\Delta \underline{\dot{u}})^T \underline{\dot{F}}(\delta \underline{\dot{u}})) dV = 0 \quad (5.8)$$

where $\underline{\underline{E}}$ is the elasticity fourth order tensor, $\delta\dot{\mathbf{u}}$ a test field, and $\Delta\dot{\mathbf{u}}$ the bifurcation field. Translating this equation into the curvilinear framework of the beam gives:

$$\int_0^L EI \frac{\partial \Delta\dot{\theta}}{\partial s} \frac{\partial \delta\dot{\theta}}{\partial s} ds + \int_0^L N \Delta\dot{\theta} \delta\dot{\theta} ds = 0 \quad (5.9)$$

Applying the divergence theorem leads to:

$$\int_0^L EI \frac{\partial^2 \Delta\dot{\theta}}{\partial s^2} \delta\dot{\theta} + F \Delta\dot{\theta} \delta\dot{\theta} ds = 0 \quad (5.10)$$

$$\int_0^L \left(\frac{\partial^2 \Delta\dot{\theta}}{\partial s^2} + \frac{F}{EI} \Delta\dot{\theta} \right) \delta\dot{\theta} ds = 0 \quad (5.11)$$

For equation (5.11) to be fulfilled for any test field $\delta\dot{\theta}$, the term in brackets must vanish everywhere:

$$\frac{\partial^2 \Delta\dot{\theta}}{\partial s^2} + \frac{F}{EI} \Delta\dot{\theta} = 0 \quad \forall s \in [0, L] \quad (5.12)$$

The solutions of this differential equation are given by:

$$\begin{cases} \Delta\dot{\theta} = A \cos(\lambda s) + B \sin(\lambda s) \\ \lambda^2 = \frac{F}{EI} \end{cases} \quad (5.13)$$

$\Delta\dot{\theta}$ is the difference between two solutions, and one of them is the fundamental straight solution given in the set of equations (5.7). The other solution is then given by:

$$\frac{\partial u_y}{\partial x} = \theta = a \cos(\lambda s) + b \sin(\lambda s) + \gamma \quad (5.14)$$

$$u_y = \alpha \cos(\lambda s) + \beta \sin(\lambda s) + \gamma s + \delta \quad (5.15)$$

This solution is not to be taken as a post bifurcation solution, just as the direction for buckling. Now various boundary conditions can be considered:

- Fixed: $u_y = 0$, $\frac{\partial u_y}{\partial x} = 0$
- Pinned: $u_y = 0$, $\frac{\partial^2 u_y}{\partial x^2} = 0$
- Free: $\frac{\partial^2 u_y}{\partial x^2} = 0$

Using some combinations of these conditions in A and B , one gets drastically different buckling loads:

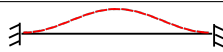
BCs	fixed/free	pinned/pinned	pinned/free	fixed/free
Scheme				
Buckling Force	$F_c = \frac{\pi^2 EI}{4L^2}$	$F_c = \frac{\pi^2 EI}{L^2}$	$F_c = \frac{\eta^2 EI}{L^2}$	$F_c = \frac{4\pi^2 EI}{L^2}$
λ	$\frac{\pi}{2L}$	$\frac{\pi}{L}$	$\frac{\eta}{L}$	$\frac{2\pi}{L}$
Shape ($a \in \mathbb{R}$)	$a(\cos(\lambda s) - 1)$	$a(\sin(\lambda s))$	$a(\sin(\lambda s) - \lambda s)$	$a(\cos(\lambda s) - 1)$

Table 5.1: Summary of the buckling loads for various combinations of BCs of a beam loaded in compression (η is the first positive root of the equation $\tan(\eta) = \eta$), $\eta \simeq 4.493$.

It is then clear that a proper identification of the boundary conditions is necessary when designing a structure that includes beams loaded in compression. In fact, the critical buckling load can vary by a factor of 16. For a given cross section, this could be compensated by doubling its size¹, in other words, quadrupling the mass of the structure. However, not every structural configuration admits such simple boundary conditions. For instance, the assembly of various components may have some play, or the structure can be a substructure of a more complex design.

To illustrate this problem let us consider a simple a hanger holding a coat (see Figure 5.2). Even though this example is not of much interest for aeronautical structures, it will help to illustrate our problem.

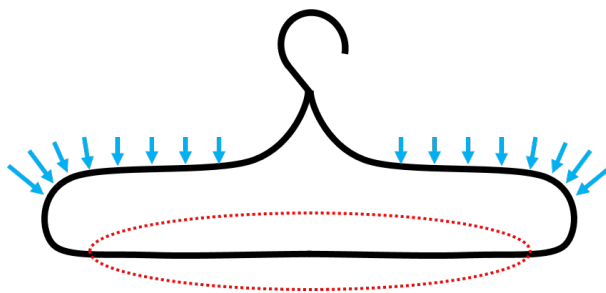


Figure 5.2: Drawing of a hanger. The weak part in a compression state is in the red circle.

It is obvious in this case that the critical part of the hanger is the beam in the red circle. Due to the stiffness of the rest of the structure, this part can neither be considered to be pinned/pinned, nor fixed/fixed, but something in between. Therefore, a design considering a pinned/pinned structure would underestimate the stiffness of the structure and a fixed/fixed structure would overestimate it. For such a problem the engineer might take a conservative approach which leads to a thicker beam. However, in the aeronautical industry, minimizing the mass while optimizing the structure’s stiffness is critical.

5.1.2 External stiffness

The safety of civil structures is naturally of utmost importance. Nevertheless, “over-conservative” methods are not always adapted for civil designs: the weight of the structure itself can become a problem in large buildings or bridges, and the mass may undesirably affect the thermal characteristics. To address this problem, the “Eurocodes” program started in the 1980s in Europe to produce European standards for designing methods. The objective is a set of harmonized technical rules for the design of construction works in order to eliminate technical obstacles to trade [Regulation, 2005].

Some of these methods help evaluate the sensitivity to geometrical imperfections, others are linked to the stability analysis of structures. For the latter, standard geometries are analyzed and “reduction factors” are estimated. For instance, they can depend on the geometrical ratio between the web and the flanges for a “I-beam” as in [Gardner, 2018]. Both kinds of imperfections can be taken into account, and various cases are thoroughly distinguished. In fact, a distinction is made for standard cross sections, slenderness, plasticity and other geometrical or material parameters. For a given set of parameters one can then define an “effective length” that is then applied in the analytical results.

For large structures, two kinds of stability analyses are distinguished: “global stability” and “member stability” in [Regulation, 2005]. In particular, for the analysis of member stability, the

¹ Since I is homogeneous to m^4 .

surrounding environment must be evaluated to assess the buckling load for various boundary conditions. Such a categorization can be made in civil engineering due to the standardization of geometries, materials and assembly methods. In fact, given simple geometries or well-studied joints, it is possible to derive semi-analytical models corrected with experimental results.

5.2 Weakened stability analysis

It has previously been shown that the stability analysis of a structure is sensitive to how the loading is applied. Sometimes, kinematic constraints are applied to structures for modeling purposes; for instance, in order to apply a global quantity (torque, force, torque/force ratio, etc.). These kinematic conditions usually require imposing displacements that are convenient for applying the load, but not relevant for the stability analysis. This also occurs with some kinematic constraints: in order to apply a rotation to a section in finite deformation framework, both radial and ortho-radial displacements have to be specified. As a final consideration, before any loss of stability, applying displacements or the equivalent nodal forces should give the same results especially when the boundary is far from the gauge part. Therefore, when the force tends to saturate (especially for elastoplastic materials like the one we consider in this work that possess a saturating hardening), adequate load-stepping requires an *a priori* knowledge of the solution: if the load steps are not small enough, the displacement increments corresponding to a small force increment will be too large; otherwise convergence will be difficult. The numerical cost is thus another reason to apply kinematic constraints instead of forces.

It is easy to show that the more kinematic constraints that are applied to the structure, the more stable the structure. This is known in the analysis of vibrations of a body: the more a body is kinematically constrained, the higher its fundamental frequency, when rigid body motions are blocked due to some kinematic conditions. As this frequency is directly related to the smallest eigenvalue, it applies to our problem². Therefore, as more unnecessary displacement boundary conditions are applied, the instability analysis becomes less conservative.

Finally, when analyzing a complex structure it is common to analyze sub-parts independently. As discussed in section 5.1.2, the stiffness of the surrounding structure can have a severe consequences on the structure's stability. This "surrounding stiffness" might be possible to evaluate for standard or simple geometries, however for more complex structures this is usually too expensive to evaluate. Still, the usual assumption is to apply kinematic constraints that maintain the *cut surface's* geometry³. In this case, only an upper bound of the critical load can be evaluated due to the added kinematic conditions.

Therefore, a method is proposed here to evaluate a lower bound of the critical load, by replacing kinematic constraints by forces (assuming that the loading direction and geometry are well identified). This method's main purpose is to apply the best boundary conditions for static calculations, while still allowing the evaluation of the uniqueness criterion with the most appropriate BCs. It aims to be the first step toward the evaluation of the uniqueness of the solution of the rate boundary value problem in a complex environment, similar to the civil engineering methods. In this section, the "weakened stability criterion" will first be formulated; then, this criterion will be positioned with respect to the general Hill uniqueness criterion and a physical meaning will be proposed. Finally the numerical method will be detailed and validated on Euler's buckling analysis of a beam.

² This can be justified by considering that the space in which eigen modes are searched when DBCs are applied is a subspace of the one where fewer DBCs are applied. If an eigen mode of the constrained problem corresponds to a vanishing eigenvalue, then it is necessary that this eigen mode is also associated to a vanishing eigenvalue for the unconstrained problem.

³ The *cut surface* here relates to the surface obtained after splitting the sub-part from the larger structure. It is the surface that would appear after "cutting the sub-part out".

5.2.1 Weakened stability criterion

Hill's loss of uniqueness criterion is formulated on the rate boundary value problem. It assumes that the structure is in equilibrium and that the internal variables are known. Then the known solution $\underline{\mathbf{u}}^0$ fulfills the following set of equations:

$$\left\{ \begin{array}{l} \underline{\mathbf{Div}}(\underline{\mathcal{S}}(\underline{\mathbf{u}}^0)) = \underline{\mathbf{0}} \quad \forall \underline{\mathbf{X}} \in \Omega \\ \underline{\mathcal{S}}(\underline{\mathbf{u}}^0)\underline{\mathbf{N}} = \underline{\mathbf{T}}^d \quad \forall \underline{\mathbf{X}} \in \partial\Omega^T \\ \underline{\mathbf{u}}^0 = \underline{\mathbf{u}}^d \quad \forall \underline{\mathbf{X}} \in \partial\Omega^u \end{array} \right. \quad (5.16)$$

Hill's uniqueness criterion for this problem would give:

$$\int_{\Omega^0} \underline{\dot{\mathbf{F}}}(\Delta\underline{\dot{\mathbf{u}}}) : \underline{\mathcal{L}} : \underline{\dot{\mathbf{F}}}(\Delta\underline{\dot{\mathbf{u}}}) \, dV > 0 \quad \forall \Delta\underline{\dot{\mathbf{u}}}, \Delta\underline{\dot{\mathbf{u}}} = \underline{\mathbf{0}} \quad \forall \underline{\mathbf{X}} \in \partial\Omega^u \quad (5.17)$$

As shown in section 3, this gives in a FEM framework (for an equilibrium configuration):

$$\text{eigen} \left(\left[\mathbf{K}^{DBC_s} \right] \right) > 0 \quad (5.18)$$

where $\left[\mathbf{K}^{DBC_s} \right]$ is the global stiffness matrix constrained with the DBCs of the incremental problem.

In order to define a weakened problem, let $\partial\Omega_{fixed}^u$ and $\partial\Omega_{free}^u$ be complementary parts of $\partial\Omega^u$.

$$\partial\Omega_{fixed}^u \cup \partial\Omega_{free}^u = \partial\Omega^u \quad (5.19)$$

$$\partial\Omega_{fixed}^u \cap \partial\Omega_{free}^u = \emptyset \quad (5.20)$$

If the time is fictitiously stopped and the displacement BCs $\partial\Omega_{free}^u$ are replaced by the corresponding forces, the weakened problem becomes:

$$\left\{ \begin{array}{l} \underline{\mathbf{Div}}(\underline{\mathcal{S}}(\underline{\mathbf{u}}^1)) = \underline{\mathbf{0}} \quad \forall \underline{\mathbf{X}} \in \Omega \\ \underline{\mathcal{S}}(\underline{\mathbf{u}}^1)\underline{\mathbf{N}} = \underline{\mathbf{T}}^d \quad \forall \underline{\mathbf{X}} \in \partial\Omega^T \\ \underline{\mathcal{S}}(\underline{\mathbf{u}}^1)\underline{\mathbf{N}} = \underline{\mathcal{S}}(\underline{\mathbf{u}}^0)\underline{\mathbf{N}} \quad \forall \underline{\mathbf{X}} \in \partial\Omega_{free}^u \\ \underline{\mathbf{u}}^1 = \underline{\mathbf{u}}^d \quad \forall \underline{\mathbf{X}} \in \partial\Omega_{fixed}^u \end{array} \right. \quad (5.21)$$

It is clear that $\underline{\mathbf{u}}^1 = \underline{\mathbf{u}}^0$ is a solution of the weakened equilibrium problem defined in equation (5.21). Hill's uniqueness criterion for this case gives:

$$\int_{\Omega^0} \underline{\dot{\mathbf{F}}}(\Delta\underline{\dot{\mathbf{u}}}) : \underline{\mathcal{L}} : \underline{\dot{\mathbf{F}}}(\Delta\underline{\dot{\mathbf{u}}}) \, dV > 0 \quad \forall \Delta\underline{\dot{\mathbf{u}}}, \Delta\underline{\dot{\mathbf{u}}} = \underline{\mathbf{0}} \quad \forall \underline{\mathbf{X}} \in \partial\Omega_{fixed}^u \quad (5.22)$$

in a FEM framework:

$$\text{eigen} \left(\left[\mathbf{K}^{weakened} \right] \right) > 0 \quad (5.23)$$

where $\left[\mathbf{K}^{weakened} \right]$ is the global stiffness matrix constrained with the DBCs of the weakened problem.

With such an approach, it is possible to define a functional \mathcal{F} that depends on the current stress $\boldsymbol{\sigma}$, the local tangent operator \mathcal{L} , the deformation gradient \mathbf{F} and the given set of DBCs $\{DBC\}$ such that:

$$\mathcal{F}(\boldsymbol{\sigma}, \mathcal{L}, \mathbf{F}, \{DBC\}) > 0 \Rightarrow \text{The weakened problem is unique for } \{DBC\} \quad (5.24)$$

$$\mathcal{F}(\boldsymbol{\sigma}, \mathcal{L}, \mathbf{F}, \{DBC\}) \leq 0 \Rightarrow \text{The weakened problem lost uniqueness for } \{DBC\} \quad (5.25)$$

In a FEM framework, this functional can be identified to be the minimum of the Rayleigh quotient under the equality constraints associated to the DBCs defined in $\{DBC\}$:

$$\mathcal{F}(\boldsymbol{\sigma}, \mathcal{L}, \mathbf{F}, \{DBC\}) = \min(\mathcal{R}([\mathbf{K}], \{\mathbf{X}\})) = \frac{\{\mathbf{X}\}^T \cdot [\mathbf{K}] \cdot \{\mathbf{X}\}}{\{\mathbf{X}\}^T \cdot \{\mathbf{X}\}} \quad (5.26)$$

$$\{\mathbf{X}\} \in CA^0\{DBC\} \quad (5.27)$$

where $CA^0\{DBC\}$ is the set of velocity fields that vanish on $\partial\Omega_{fixed}^u$ for the weakened problem.

5.2.2 Hierarchy and interpretation of instabilities

It is possible to show that the weakened problem is at most as stable as the incremental problem when rigid body motions are excluded. In fact, in the FEM problem, each kinematic constraint is associated with a vanishing equality condition on $\{\mathbf{X}\}$. It is known that the minimum of a function under equality or inequality constraints is always larger or equal to the minimum of the unconstrained problem. Therefore, the smallest eigenvalue of the stiffness matrix for the weakened problem is always at most as large as the smallest eigenvalue of the incremental problem.

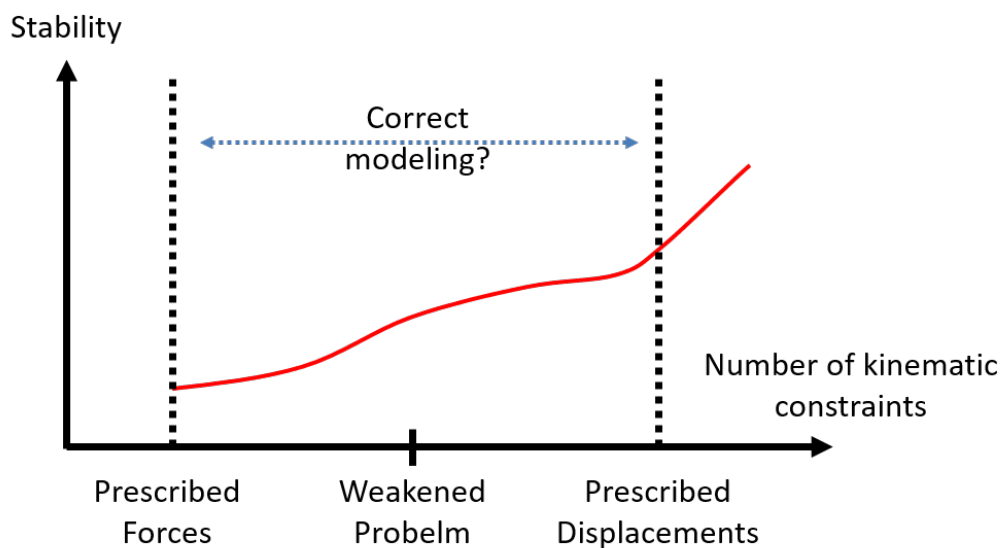


Figure 5.3: Schematic representation of the stability of a sub-structure as a function of the number of kinematic constraints used for modeling.

This result is consistent with the calculation for the buckling of a beam loaded in compression (see Table 5.1.1). A schematic representation is given in Figure 5.4. Only the pinned/pinned

problem and the fixed/free problem cannot be compared *a priori*. In fact, the stability and uniqueness for two BCs sets, say $\{BC_1\}$ and $\{BC_2\}$, can be compared *a priori* if and only if

$$\{BC_1\} \subset \{BC_2\} \quad \text{or} \quad \{BC_1\} \supset \{BC_2\} \quad (5.28)$$

So, in the present case:

$$\{BC(\text{Fixed/Free})\} = \left\{ u_y(0) = 0, \frac{\partial u_y}{\partial x}(0) = 0 \right\} \quad (5.29)$$

$$\{BC(\text{Pinned/Pinned})\} = \{u_y(0) = 0, u_y(L) = 0\} \quad (5.30)$$

In red, the boundary conditions that the two sets do not have in common. Therefore, they can not be compared *a priori*.

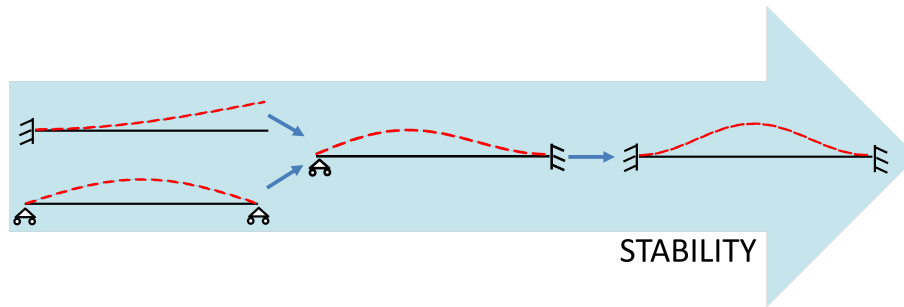


Figure 5.4: Euler buckling: critical load increases with the number of kinematic constraints (from left to right, see Table 5.1.1).

5.2.3 Numerical method

Thanks to the structure of the `Zset` code, it was possible to implement this method with the same approach as the one presented in section 3.1.5. As shown in Figure 3.1, this method is implemented as a `end_increment()` procedure. The only difference lies in the BCs that are applied to the global stiffness matrix. As shown in Figure 5.5, the analysis consists of reassembling the global tangent matrix $[K]$ and applying the weakened BCs one needs to consider. For each $\{DBC\}$ applied, an eigenvalue problem is solved and the eigenvalues and their associated eigenmodes are stored.

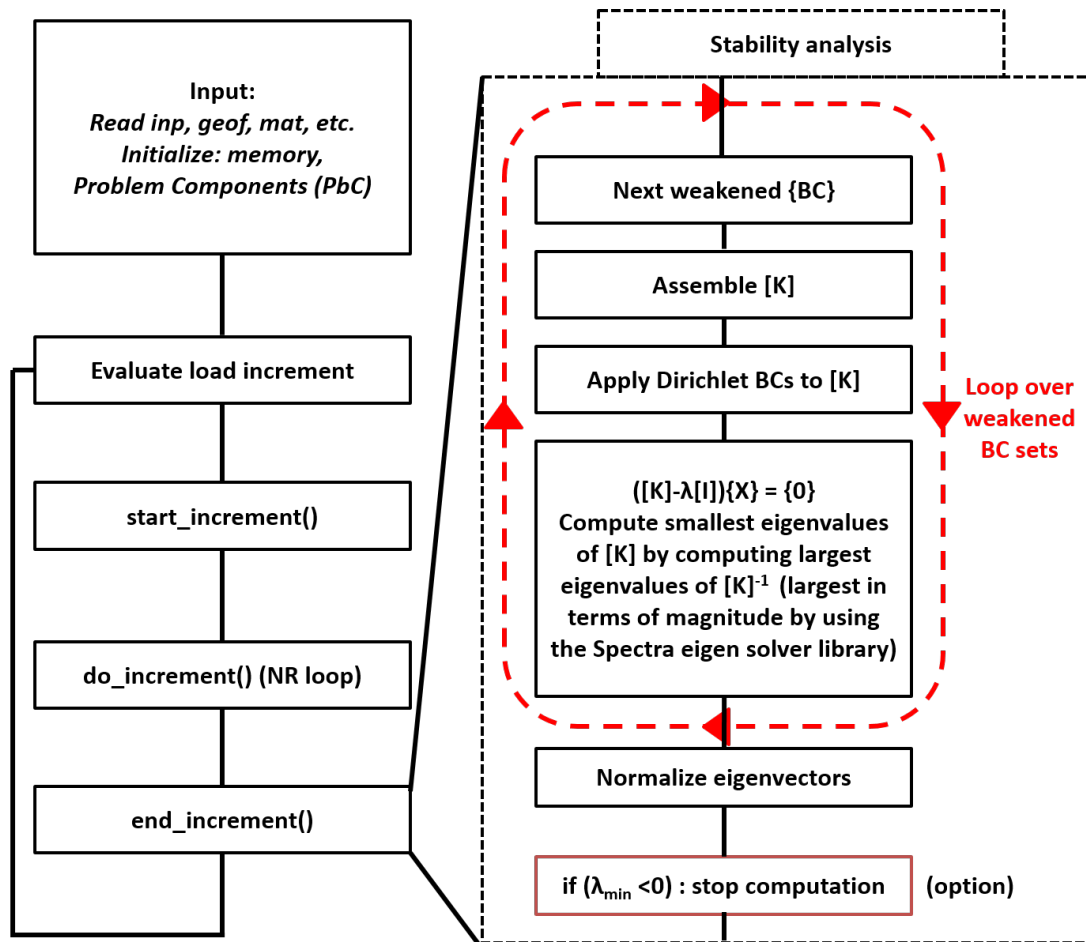


Figure 5.5: Consequences of the modeling assumption on the critical load.

In order to perform this analysis, it is sufficient to insert the following lines in the input file:

```

***global_bifurcation
  [**stop_if_unstable]
  **change_bcs
    *case <number of eigen values> <Size of Krylov subspace>
    <Nset> <DOF>
    <Nset> <DOF>
    ...

    *case <number of eigen values> <Size of Krylov subspace>
    <Nset> <DOF>
    <Nset> <DOF>
    ...
  
```

where for each `*case` a weakened problem can be specified. Finally, to activate the output of the eigen modes and eigenvalues, one must also add the following key words (or the eigenvalues are only output in the “message” file):

```

***output
  **extra global_bifurcation % use global_bifurcation_2D for 2D models
  
```

During the computation, the eigen vectors are output as nodal fields and a file “XXX.eigen” is created to store the eigenvalues.

5.2.4 Validation with Euler buckling

In the following section, the numerical method described in section 5.2.3 is validated by comparison with the analytical results of the Euler buckling derived in section 5.1.1. To do so, a beam shown in Figure 5.6 of length $L = 100\text{ mm}$ with a square cross section of width $w = 1\text{ mm}$ is studied. Material properties are given by:

- Young’s modulus: $E = 60\text{ GPa}$
- Poisson ratio: $\nu = 0$
- Second moment of area: $I = \frac{w^4}{12} = \frac{1}{12}$
- Constitutive law formulation: corotational (see section 2.2.2).

In order to test the method the beam is loaded with displacements imposed on its end sections S_0 ($x = 0$) and S_L ($x = L$):

$$\underline{\mathbf{u}} = \underline{\mathbf{0}} \quad \forall \underline{\mathbf{X}} \in S_0 \quad (5.31)$$

$$\underline{\mathbf{u}} = -u^a \underline{\mathbf{e}}_x \quad \forall \underline{\mathbf{X}} \in S_L \quad (5.32)$$

with $u^a = 0.04\text{ mm}$.

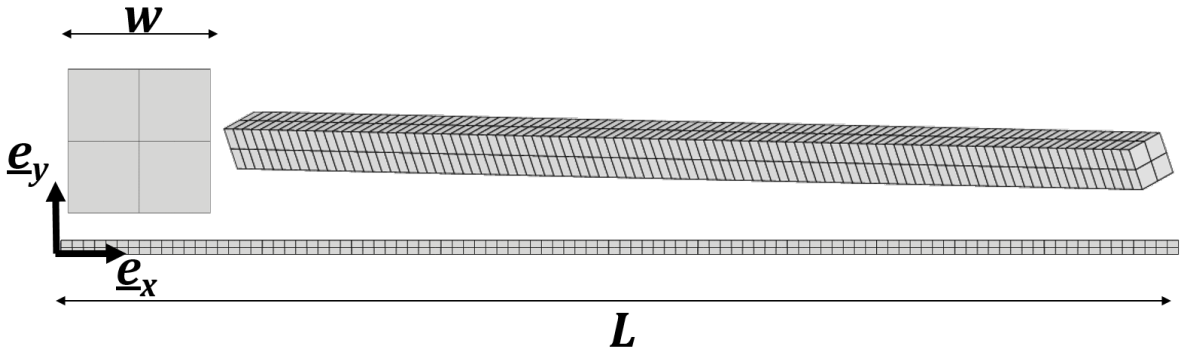


Figure 5.6: Geometry of the square section beam. The mesh is composed of 400 hexahedral quadratic elements: 100 along the length and 2 through each of the thickness and height.

The central nodes of the end sections correspond to the points A and B in section 5.1.1. Only one incremental problem is solved and the four weakened stability problems are solved with the following BCs:

1. Fixed/Free: $\Delta \underline{\mathbf{u}} = \underline{\mathbf{0}}$ for $x = 0$;
2. Pinned/Pinned: $\Delta \underline{\mathbf{u}} = \underline{\mathbf{0}}$ in A and B;
3. Pinned/Fixed: $\Delta \underline{\mathbf{u}} = \underline{\mathbf{0}}$ in A; $\Delta \underline{\mathbf{u}} = \underline{\mathbf{0}}$ $x = L$;
4. Fixed/Fixed: $\Delta \underline{\mathbf{u}} = \underline{\mathbf{0}}$ for $x = 0, L$;

The smallest eigenvalues for each set of boundary conditions are plotted in Figure 5.8. It is shown that for each rate boundary value problem the smallest eigenvalue vanishes for the critical loads derived in table 5.1.1. Moreover, the numerical eigenmodes are displayed in Figure 5.7 and perfectly coincide with the buckling modes obtained analytically.

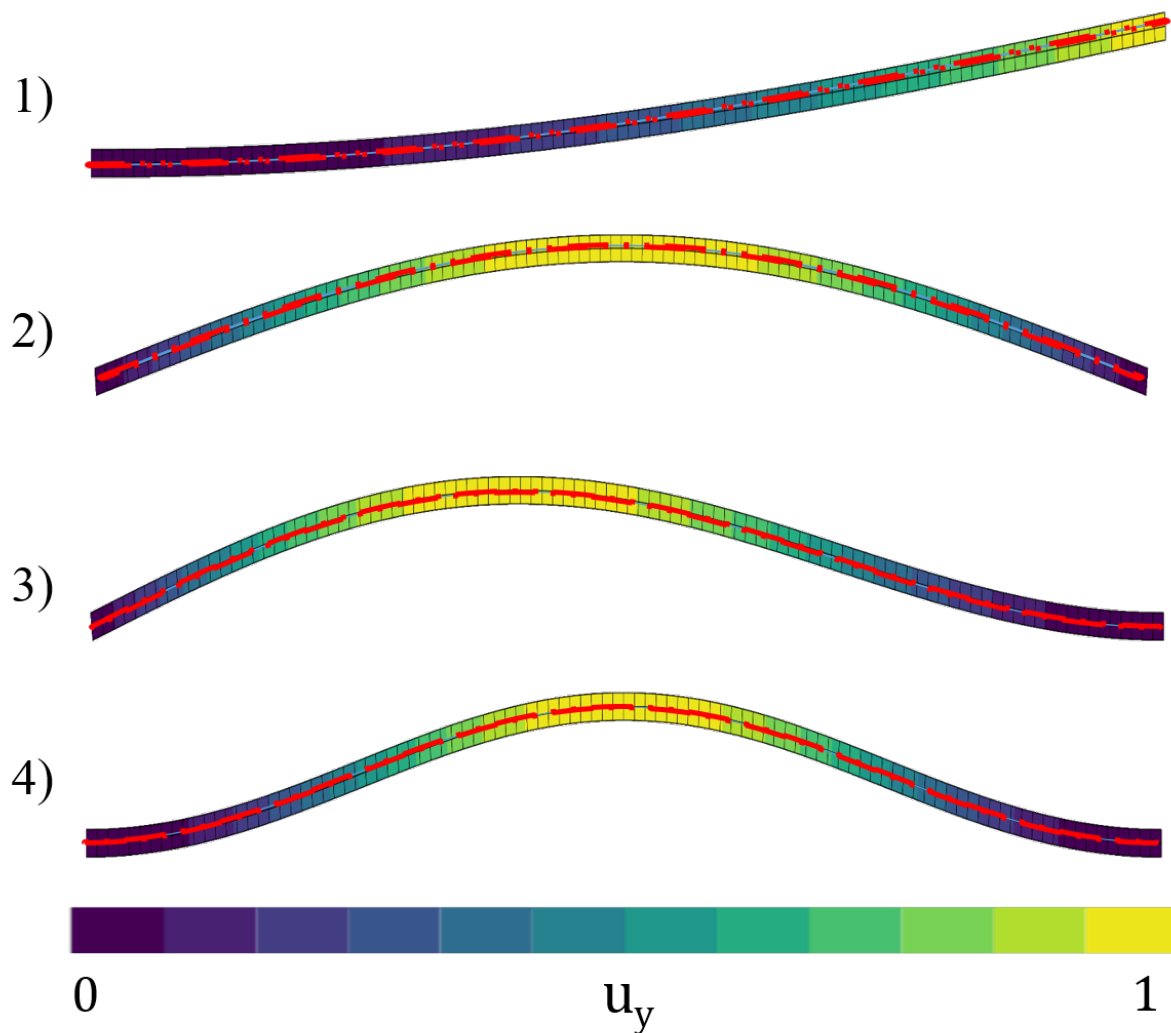


Figure 5.7: Numerical eigenmodes associated to the vanishing eigen values for the weakened problems: 1) Fixed/Free; 2) Pinned/Pinned; 3) Pinned/Fixed; 4) Fixed/Fixed. Analytical solutions are superimposed in red dashed lines.

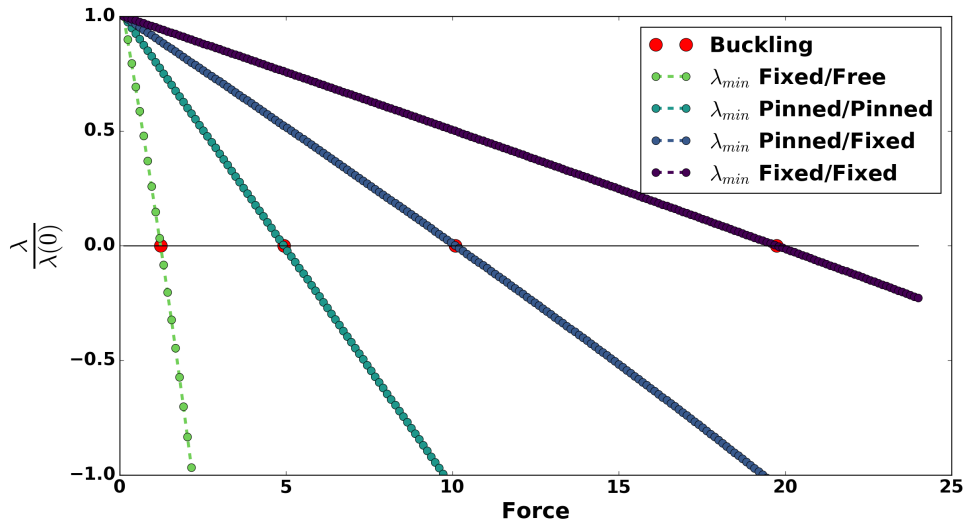


Figure 5.8: Evolution of the smallest eigenvalue for the various weakened boundary conditions. Eigenvalues normalized by the value at first increment.

5.3 Applications of the weakened stability criterion

While the results might seem trivial for the buckling analysis of a beam in compression, this method will allow us to analyze more complex problems in the present section. First a tube loaded in torsion is studied. A discussion of the uniqueness results for various weakened problems are presented and discussed. Then, the analysis of localization in a homogeneously sheared homogeneous square is presented. The application of four BCs sets are discussed: van Hove [van Hove, 1947], Mandel [Mandel, 1964], Ryzhak [Ryzhak, 1994], “Left Fixed” side. The variation of eigen modes obtained for the stated BCs are discussed, as well as the instant of loss of uniqueness of the FEM models. Finally, the case of localization in the tube loaded in torsion presented in section 4.4.2 is compared with the “Left Fixed” case.

5.3.1 Application to a tube loaded in torsion

The analysis of the buckling of tubes under various loadings is very important for the design of aeronautical structures like landing gears and engine shafts⁴. It is common when designing a complex structure to analyze some sub-parts independently. Such analyses are usually done in the first step of a design process and help the designer to have a first evaluation of the structure’s dimensions. A common assumption when modeling subparts is to conserve the interface’s geometry. For instance, in the commonly used reference [Lee and Ades, 1957] the deflection shape totally vanishes on the tube’s ends⁵.

In the present section the analysis of the buckling load for various weakened problems is presented for a single tube loaded in torsion with diameter $D = 70mm$, length $L = 35mm$, and thickness $t = 1mm$ is studied (see Figure 5.9). The material properties are the ones identified

⁴ A thorough study of the buckling and shear band localization in tubes loaded in torsion is given in chapter 6: in section 6.1, the analysis of the competition between buckling and localization is presented for tubes loaded in torsion and made of the material identified in a finite deformation framework in [Defaisse et al., 2018]; in section 6.2, the analysis of two other arbitrary materials are detailed in order to study the consequences of the finite deformation framework on the critical, as well as the comparison for various weakened boundary value problems.

⁵ In [Lee and Ades, 1957], the authors state: “No attempt has been made to obtain the effects of end restraint by an exact solution because of the immense amount of work involved.”

in [Defaïsse et al., 2018] and given bellow. This analysis aims to better understand the influence of the assumed boundary conditions on the buckling loads.

- Elasticity: $E = 189\text{GPa}$ and $\nu = 0.29$;
- von Mises criterion in a corotational framework;
- Isotropic hardening: $R(p) = 1600 + 189(1 - e^{-81p}) + 509(1 - e^{-773p}) + 236p$

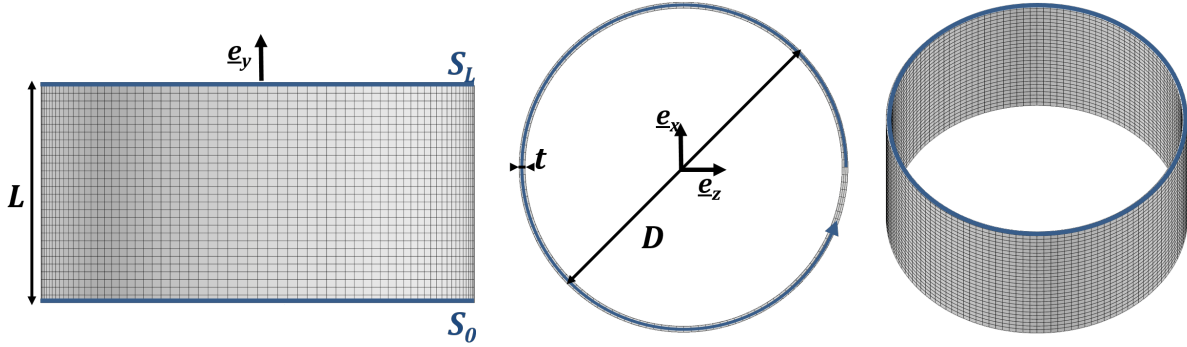


Figure 5.9: Tube with diameter $D = 70\text{ mm}$, length $L = 35\text{ mm}$, and thickness $t = 1\text{ mm}$ loaded in torsion .

The boundary conditions for the incremental problem are given by:

$$\underline{\mathbf{u}} = \underline{\mathbf{0}} \quad \forall \underline{\mathbf{X}} \in S_0 \quad (5.33)$$

$$\underline{\mathbf{u}} = (\underline{\mathbf{R}}(\theta) - \underline{\mathbf{I}}) \cdot \underline{\mathbf{X}} \quad \forall \underline{\mathbf{X}} \in S_L \quad (5.34)$$

where $\underline{\mathbf{R}}$ is the orthogonal matrix that describes a rotation around en $(O, \underline{\mathbf{e}}_y)$ axis.

Finally three different sets of BCs are studied for the uniqueness analysis:

$$\text{Fixed/Fixed: } \begin{cases} \Delta \underline{\mathbf{u}} = \underline{\mathbf{0}} & \forall \underline{\mathbf{X}} \in S_0 \\ \Delta \underline{\mathbf{u}} = \underline{\mathbf{0}} & \forall \underline{\mathbf{X}} \in S_L \end{cases} \quad (5.35)$$

$$\text{Circular/Fixed: } \begin{cases} \Delta \underline{\mathbf{u}} \cdot \underline{\mathbf{e}}_r = 0 & \forall \underline{\mathbf{X}} \in S_0 \\ \Delta \underline{\mathbf{u}} = \underline{\mathbf{0}} & \forall \underline{\mathbf{X}} \in S_L \end{cases} \quad (5.36)$$

$$\text{Flat/Fixed: } \begin{cases} \Delta \underline{\mathbf{u}} \cdot \underline{\mathbf{e}}_y = 0 & \forall \underline{\mathbf{X}} \in S_0 \\ \Delta \underline{\mathbf{u}} = \underline{\mathbf{0}} & \forall \underline{\mathbf{X}} \in S_L \end{cases} \quad (5.37)$$

The results of the incremental problem and the analysis in terms of torque and the evolution of the smallest eigenvalue for various weakened problems are presented in Figure 5.11. The eigenmodes associated to the vanishing eigenvalues are shown in Figure 5.10.

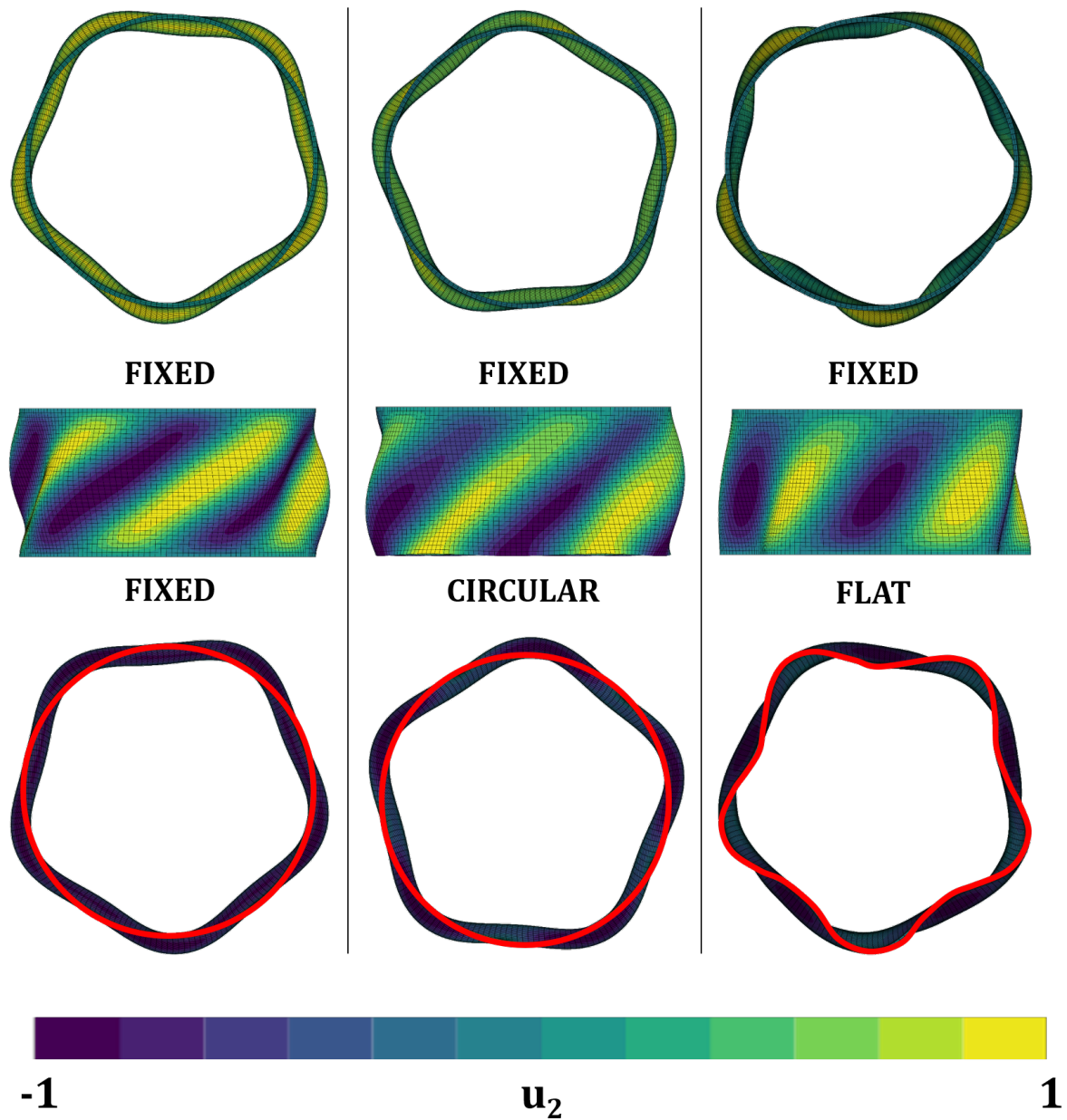


Figure 5.10: Eigen modes associated to the vanishing eigenvalues for the tube loaded in torsion. From left to right (bottom/top): Fixed/Fixed, Circular/Fixed, Flat/Fixed. For visualization purposes, the deformed bottom surface S_0 is outlined in red.

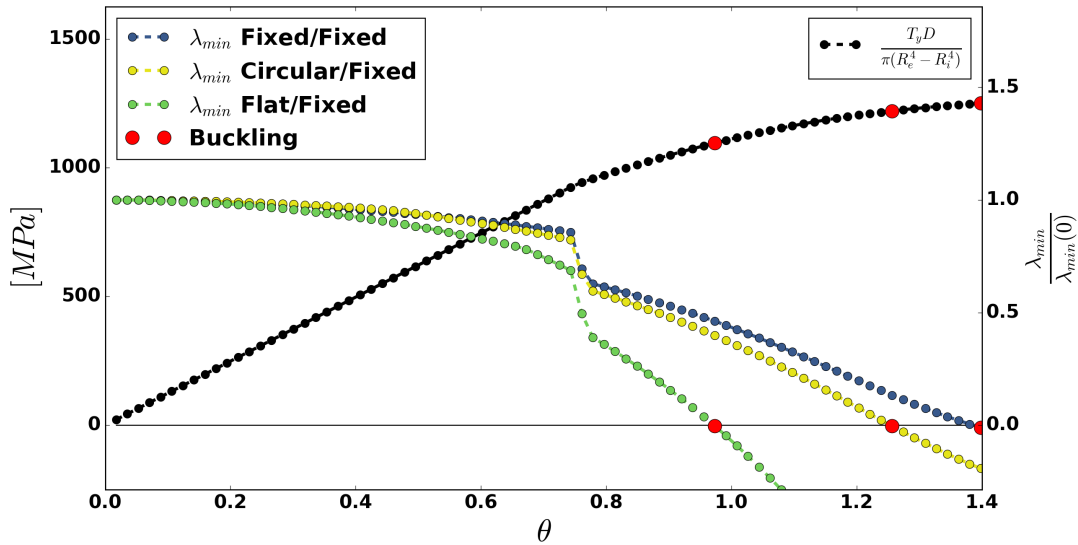


Figure 5.11: Evolution of the torque and the smallest eigen values for each weakened problem for the short thin tube loaded in torsion.

The results in terms of buckling torque and buckling angle are summarized in Table 5.2.

BCs	Flat/Fixed	Circular/Fixed	Fixed/Fixed
Buckling torque	$T_c = 8000 \text{ N.mm}$	$T_c = 8995 \text{ N.mm}$	$T_c = 9216 \text{ N.mm}$
Buckling angle	$\theta_c = 0.97^\circ$	$\theta_c = 1.26^\circ$	$\theta_c = 1.4^\circ$

Table 5.2: Summary of the buckling torques and buckling angles for various weakened boundary value problems for the tube loaded in torsion ($L = 35 \text{ mm}$, $D = 70 \text{ mm}$, $t = 1 \text{ mm}$).

First, let us compare the three instability modes, buckling torques and buckling angles:

- Instability modes: the instability modes associated to the Fixed/Fixed and to the Circular/Fixed weakened problem do not vary substantially. On the other hand, the instability mode for the Flat/Fixed case differs significantly from the first two cases;
- Buckling torque: the critical load is slightly different (only 2.5%) between the Fixed/Fixed and the Circular/Fixed cases. However, for the Flat/Fixed case the instability mode and the critical load differ significantly from the other two cases: The buckling torque is reduced by 15% when compared to the Fixed/Fixed case.
- Buckling angle: the three modeled problems significantly differ in terms of buckling angle: up to a difference of 40% between the Flat/Fixed and the Fixed/Fixed case.

In section 3.1.4, the buckling analysis was presented as a competition between a “geometrical” term and a “material” term. Here, the geometrical term is a function of the shear stress and the material part depends on the hardening modulus. In the present case, the tube is made of a high strength steel (ML340) for which the “true” stress/strain curve is shown in Figure 3.3. For this quickly saturating material, a slight increase in shear stress is associated to a large drop for the hardening modulus. Therefore, the difference in buckling torques is not very large

for the Circular/Fixed and the Fixed/Fixed cases. However, it is shown in section 6.2 that the difference may be much larger for material with slower saturation.

The introduction of section 5.2 stated that the geometry of the *cut-surface* is usually maintained by kinematic constraints when modeling a sub-part. In the present case, this could correspond to the Fixed/Fixed case ⁶, which is not the earliest unstable case. Therefore, this modeling assumption would lead to an overestimation of the buckling load. Still, the Flat/-Fixed case might lead to a large underestimation of the buckling load since the *cut surface* is assumed to be totally free to deform. This is most likely the less realistic modeling assumption of the three investigated weakened boundary value problems since it considers an infinitely soft environment.

5.3.2 Loss of ellipticity and loss of uniqueness in a homogeneous media in FEM

The loss of ellipticity criterion was introduced for the analysis of the propagation of acceleration waves in [Hill, 1962] and as a stability criterion in a small deformation framework in [Mandel, 1966]. The loss of ellipticity criterion in its most general form is introduced in [Rice, 1976] to discuss strain localization in shear bands for a homogeneous domain homogeneously strained. The loss of uniqueness and loss of ellipticity criteria in a finite domain are also discussed by the author in the case of a homogeneous body with displacement imposed on the whole boundary (see section 4.1.2). Using van Hove's theorem [van Hove, 1947], it is shown that the solution in velocity to such a problem (called "van Hove boundary value problem") is necessarily unique when the acoustic tensor is positive definite. In [Ryzhak, 1994], an extension is given to [van Hove, 1947] and [Rice, 1976]: positive definiteness of the acoustic tensor is sufficient to ensure the uniqueness of the rate problem for a homogeneous domain with weaker boundary conditions than van Hove's.

It was proposed in [Mandel, 1966] that such a criterion would lead to the instability of a domain loaded with forces (called in the present work "Mandel boundary value problem"). The author states:

"On doit noter que cette instabilité peut être interdite par la présence de parois fixes qui bloquent les glissements."

En.: *"We should note that this instability (localization bands) can be canceled by fixed boundaries that limit slips."*

He also states:

"Notons à ce propos qu'un élément qui, individuellement, serait instable sous les contraintes qui lui sont imposées si ses déformations étaient libres, peut parfaitement être stable dans un massif."

En.: *"Remark that about this matter (localization bands) that an element that would, individually, be unstable due to the the applied stresses if its deformation were free, can naturally be stable when embedded in a bulk."*

However, it was proven that stability is necessarily lost for the van Hove boundary value problem when the acoustic tensor possesses a negative eigenvalue. Therefore, when the latter is fulfilled in a finite area in an arbitrary structure, the uniqueness of the global problem is necessarily lost in an infinite functional space⁷. When considering softening materials this kind of instability would lead to damage and ultimately fracture. Nonetheless, there exist metallic materials that

⁶ Perhaps to the Circular/Fixed case, but the instability mode does not keep the cut surface flat.

⁷ This results is trivially obtained by considering the instability mode to vanish everywhere but in the area where ellipticity is lost.

do not exhibit softening behavior, like the one used in [Defaisse et al., 2018]. In this case, the emergence of localization instability modes may not necessarily lead to instantaneous failure of the whole structure.

In the present work, it is shown that the velocity solution to van Hove's boundary value problem is still unique as long as the acoustic tensor is semi-positive definite (see section 4.2.2). Based on this result, a discussion was given in section 4.4.1 about the emergence of localization bands in a FEM framework. In particular, it was proposed that the instability modes for the van Hove boundary value problem were most likely composed of very high spatial frequencies (see discussion on the cone in the Fourier space). These modes were, to the author's knowledge, never observed numerically. In the present section, it is proposed to illustrate the latter to discuss and better understand the link between shear band localization, loss of ellipticity and loss of uniqueness for a FEM problem using the weakened stability analysis described in section 5.2.3. For this purpose, the same problem as the one presented in section 4.4.1 is analyzed for various weakened problems:

1. van Hove [van Hove, 1947]: $\Delta \underline{\mathbf{u}} = \underline{\mathbf{0}}$ on all $\partial\Omega$;
2. Ryzhak [Ryzhak, 1994]: $\Delta \underline{\mathbf{u}} \cdot \underline{\mathbf{n}} = 0$ on all $\partial\Omega$;
3. Left Fixed: $\Delta \underline{\mathbf{u}} = \underline{\mathbf{0}}$ for $x = 0$;
4. Mandel [Mandel, 1964]: $\Delta \underline{\mathbf{u}} = \underline{\mathbf{0}}$ for $(x = 0, y = 0)$, and $\Delta \underline{\mathbf{u}} \cdot \underline{\mathbf{e}}_y = 0$ for $(x = 0, y = 1)$ (in order to block rigid body motion).

The same material properties in a corotational frame are used and given in (5.38) and plotted in Figures 5.13 and 5.14 (see section 2.2.2 for the full formulation).

$$f(\underline{\boldsymbol{\tau}}, R) = \sqrt{\underline{\boldsymbol{\tau}}^{dev} : \underline{\boldsymbol{\tau}}^{dev}} - R(p) \quad (5.38)$$

$$E = 200 \text{ GPa}; \quad \nu = 0.33 \quad (5.39)$$

$$R(p) = 1000 + 100(1 - e^{-300p}) - 1000p \quad (5.40)$$

where p denotes the cumulative plastic strain. Finally, boundary conditions for the incremental problem are given by:

$$\underline{\mathbf{u}} = 0.02Yt\underline{\mathbf{e}}_X + 0.02Xst\underline{\mathbf{e}}_Y \quad \forall \underline{\mathbf{X}} \in \partial\Omega \quad (5.41)$$

where $t \in [0, 1]$ is the fictitious time-like loading parameter.

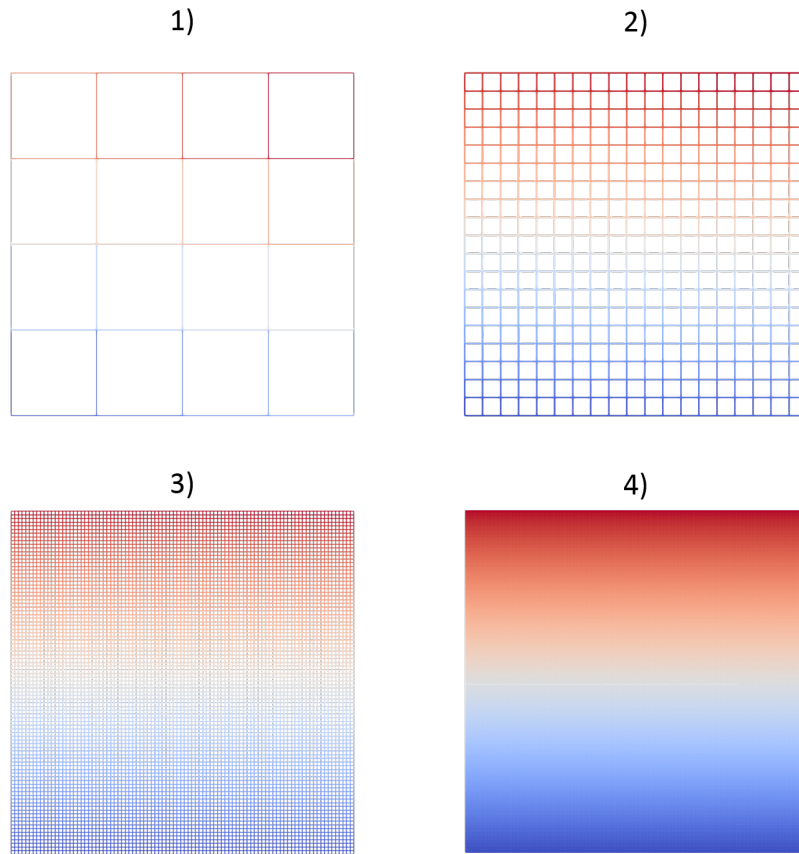


Figure 5.12: From 1) to 4), square meshes for $N = 4$, $N = 19$, $N = 93$, and 729 cuts. Coloring from blue to red is associated to the node number.

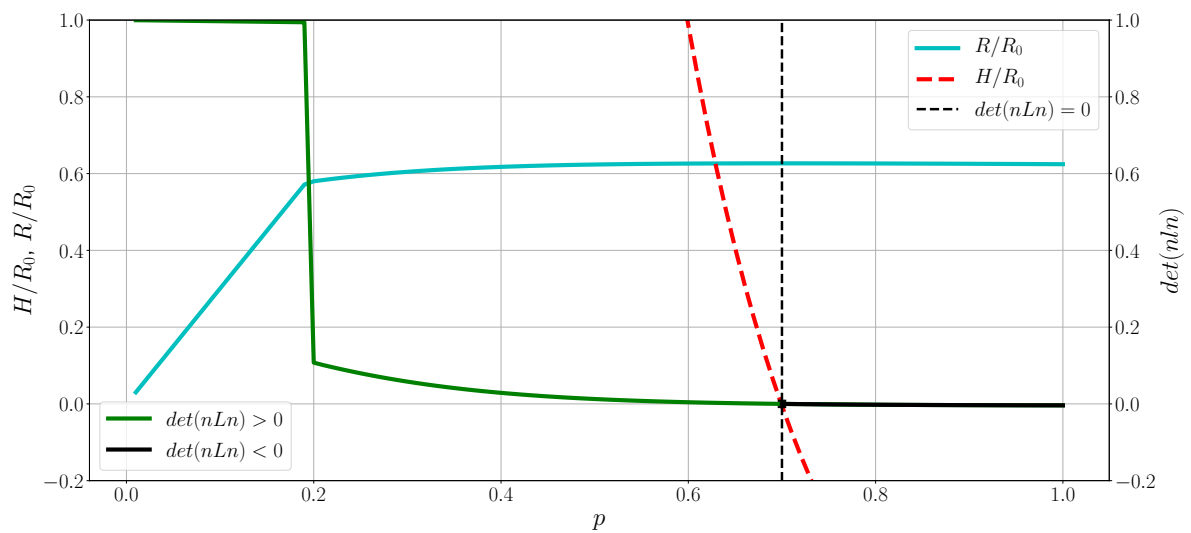


Figure 5.13: The evolution of R , $H = \frac{dR}{dp}$ and $\det(\underline{N} \odot \underline{\mathcal{L}} \cdot \underline{N})$ as functions of plastic strain ($R_0 = 1000MPa$) for the square loaded in shear.

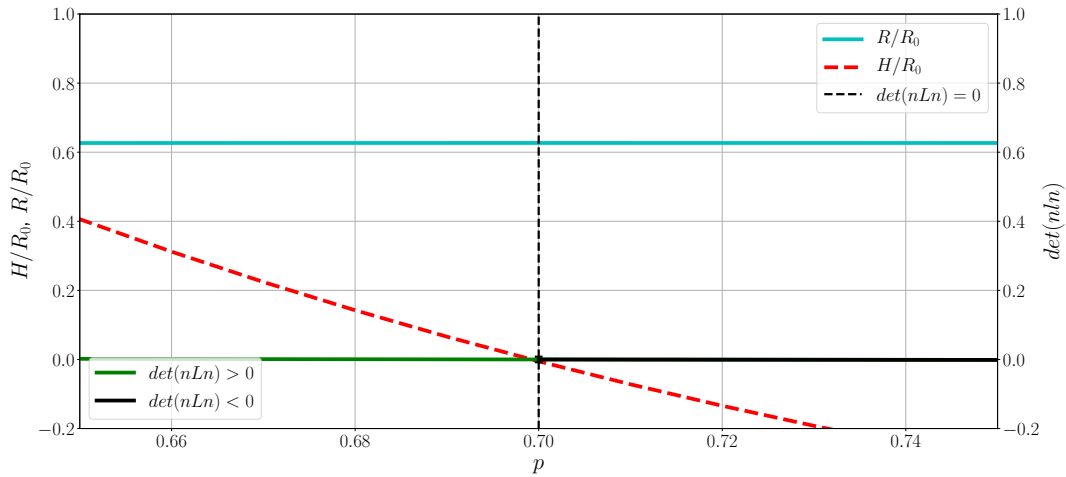


Figure 5.14: The evolution of R , $H = \frac{dR}{dp}$ and $\det(\underline{N} \odot \underline{\mathcal{L}} \cdot \underline{N})$ as functions of plastic strain ($R_0 = 1000MPa$) for the square loaded in shear. Zoom around the instant of loss of ellipticity: ellipticity lost at $p = 0.01134$.

In order to simplify the comparison for the reader, the results in terms of loss of uniqueness and loss of ellipticity for the van Hove BCs are recalled in Figures 5.15 to 5.19, where N is the discretization parameter (number of regular cuts along one edge of the square, see Figure 5.12). It was shown that the instant of emergence of instability modes was sensitive to mesh refinement for a square loaded in simple shear.

The same outputs are shown for the three weakened problems stated above. In Figures 5.20 to 5.22 the results for the Ryzhak rate boundary value problem show the results in terms of smallest eigenvalue and eigen modes at loss of ellipticity. No particular difference can be seen with van Hove's rate boundary problem for the instant of loss of ellipticity, but the eigen modes differ when ellipticity is lost (see Figures 5.18 and 5.22). In fact, the additional degree of freedom (sliding on the boundary is allowed) is enough to drastically change the eigen mode which corresponds to very thin shear bands on the boundary of the square.

Finally, Mandel's rate boundary value problem and the "Left Fixed" rate boundary value problem show a significantly different behavior. In Figures 5.23 to 5.28, it is shown that the loss of uniqueness of the weakened rate boundary value problems is lost as soon as ellipticity is lost for any mesh refinement. This illustrates the statements given by [Mandel, 1964].

The comparison for the various weakened boundary value problems in terms of loss of uniqueness is displayed in Figure 5.29. One can see that both Ryzhak and van Hove's rate boundary value problem lose uniqueness for the same loading but for only one discretization parameter. Actually, the Ryzhak weakened problem should always become unstable before the van Hove rate problem but the load stepping would have to be very fine to capture the difference. Finally, the eigen modes associated to the vanishing eigenvalues are qualitatively the same for both rate problems (see Figure 5.29).

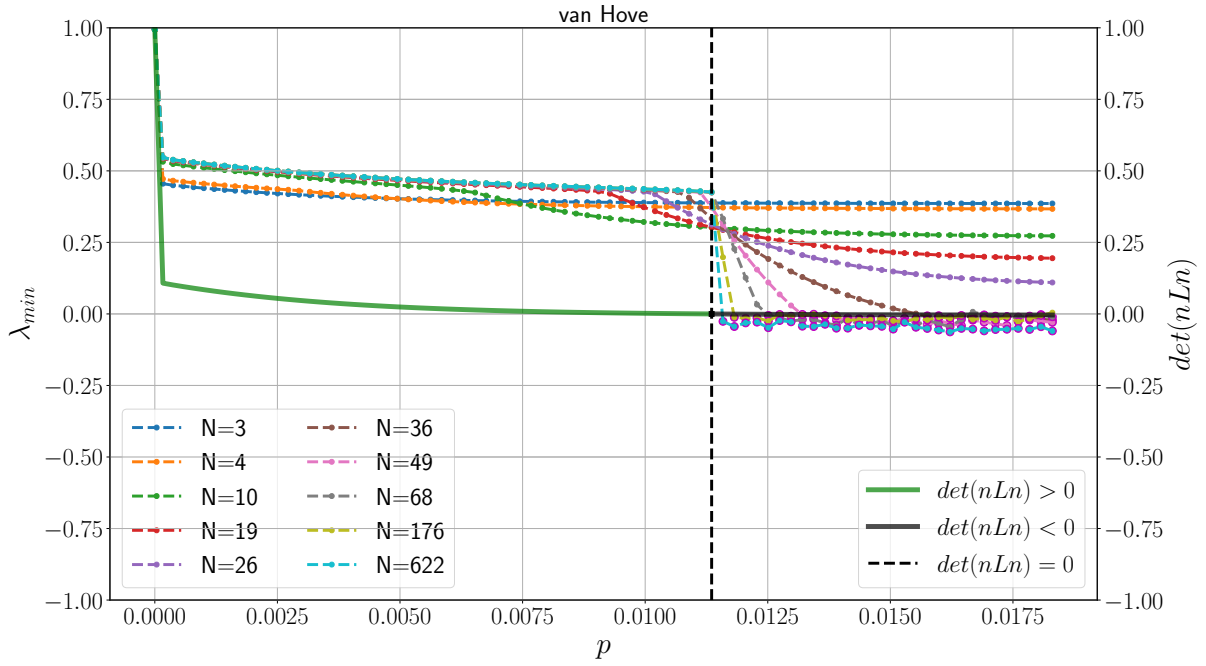


Figure 5.15: Van Hove BCs: Evolution the smallest eigenvalue for different discretization parameters N . Ellipticity lost for $p = 0.01134$.

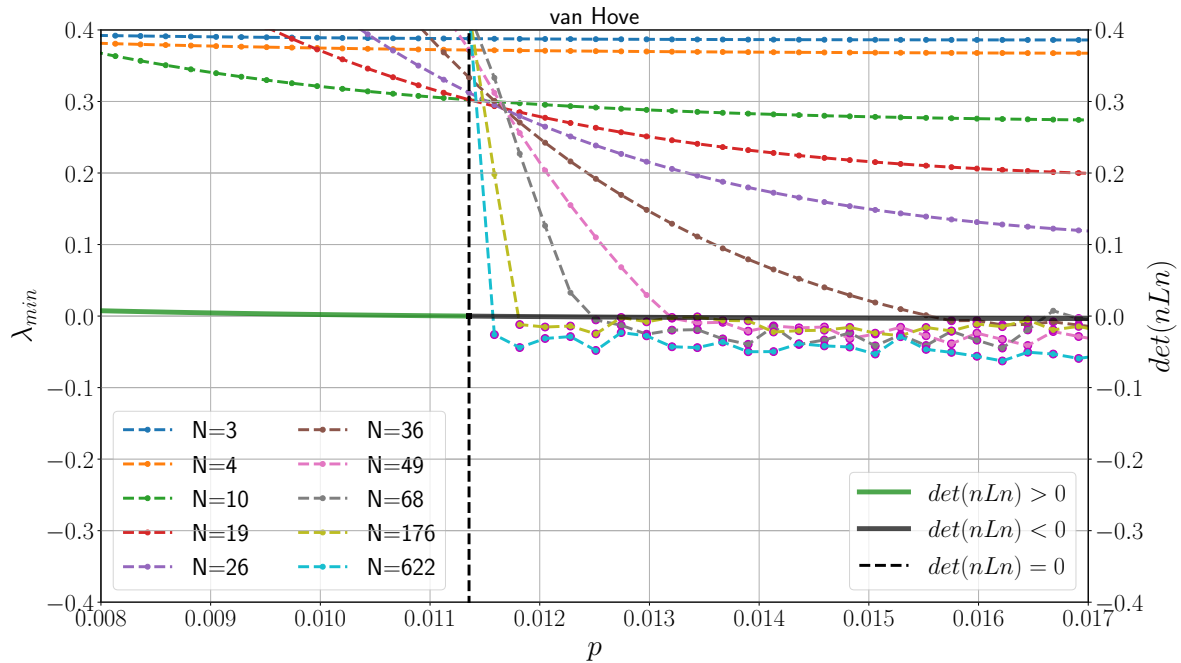


Figure 5.16: Van Hove BCs: Evolution the smallest eigenvalue for different discretization parameters N . Zoom around the instant of loss of ellipticity: ellipticity lost for $p = 0.01134$.

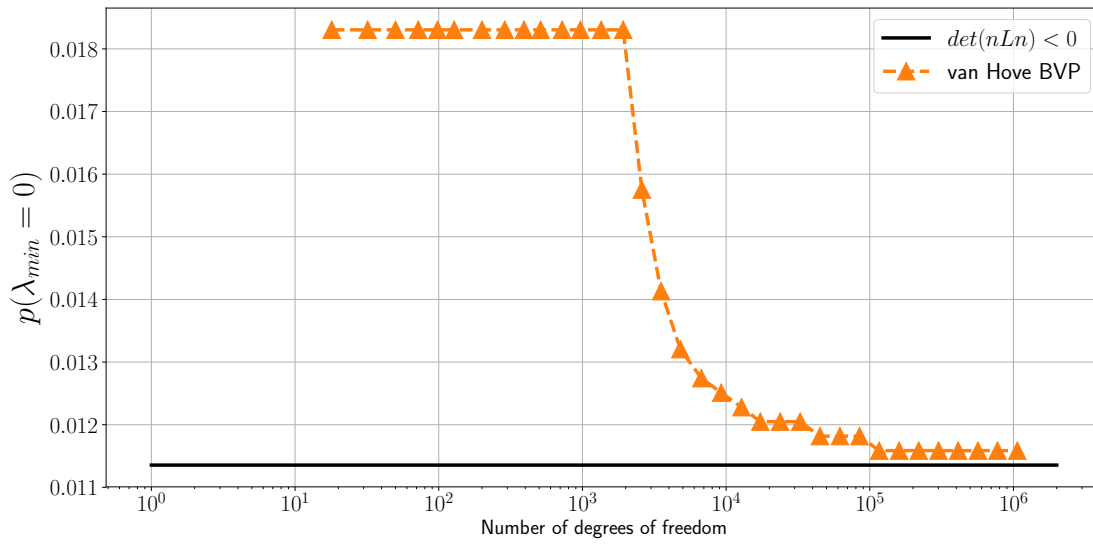


Figure 5.17: Van Hove BCs: Evolution of the plastic strain at loss of uniqueness as a function of the number of degrees of freedom.

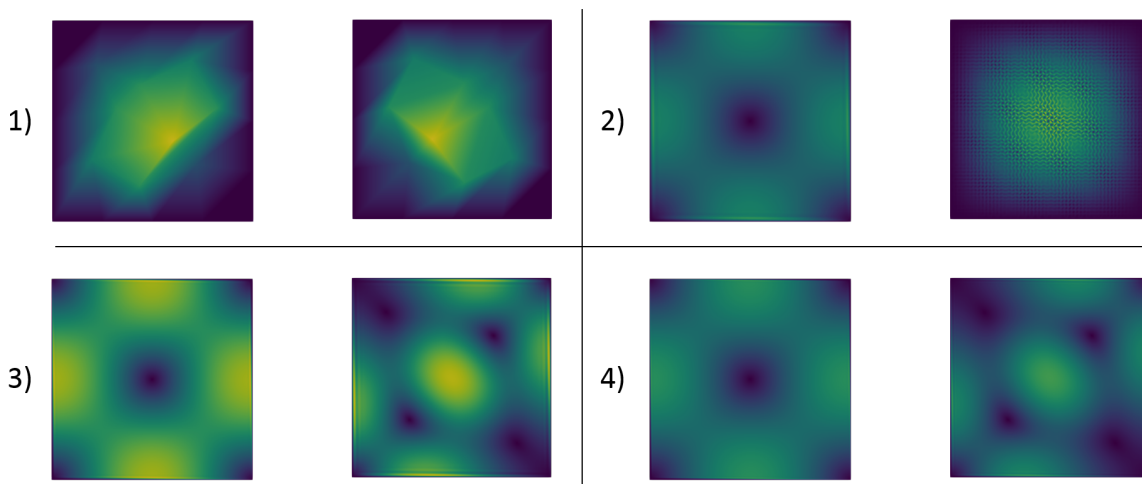


Figure 5.18: Van Hove BCs: Eigenmodes associated to the two smallest eigenvalues at first loss of ellipticity while there is no loss of uniqueness for the FEM model. From 1) to 4) respectively $N = 4$, $N = 110$, $N = 331$, and $N = 729$.

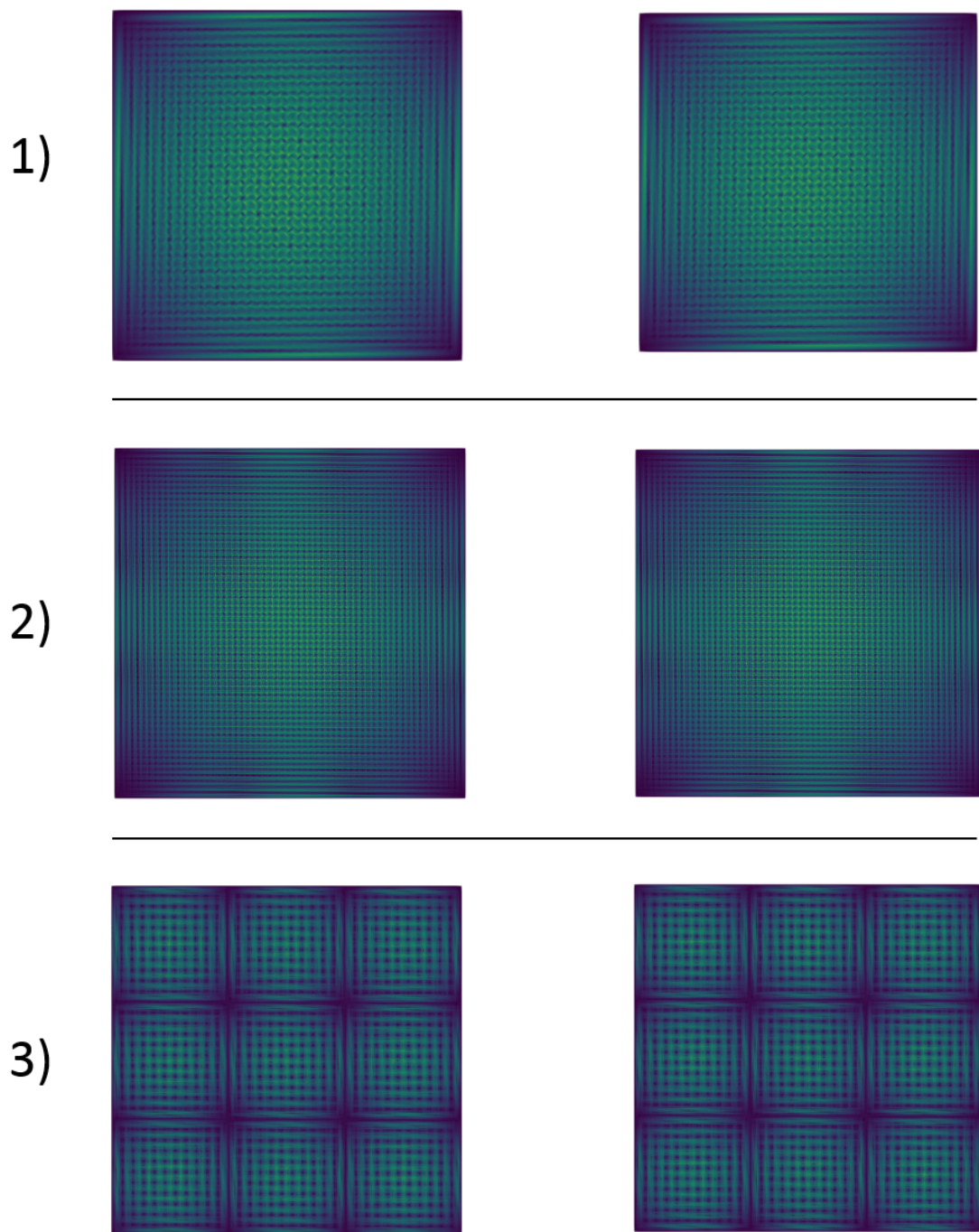


Figure 5.19: Van Hove BCs: Eigenmodes associated to first loss of uniqueness. From 1) to 3) respectively ($N = 110$, $p = 0.01817$), ($N = 331$, $p = 0.01135$), ($N = 729$, $p = 0.01135$).

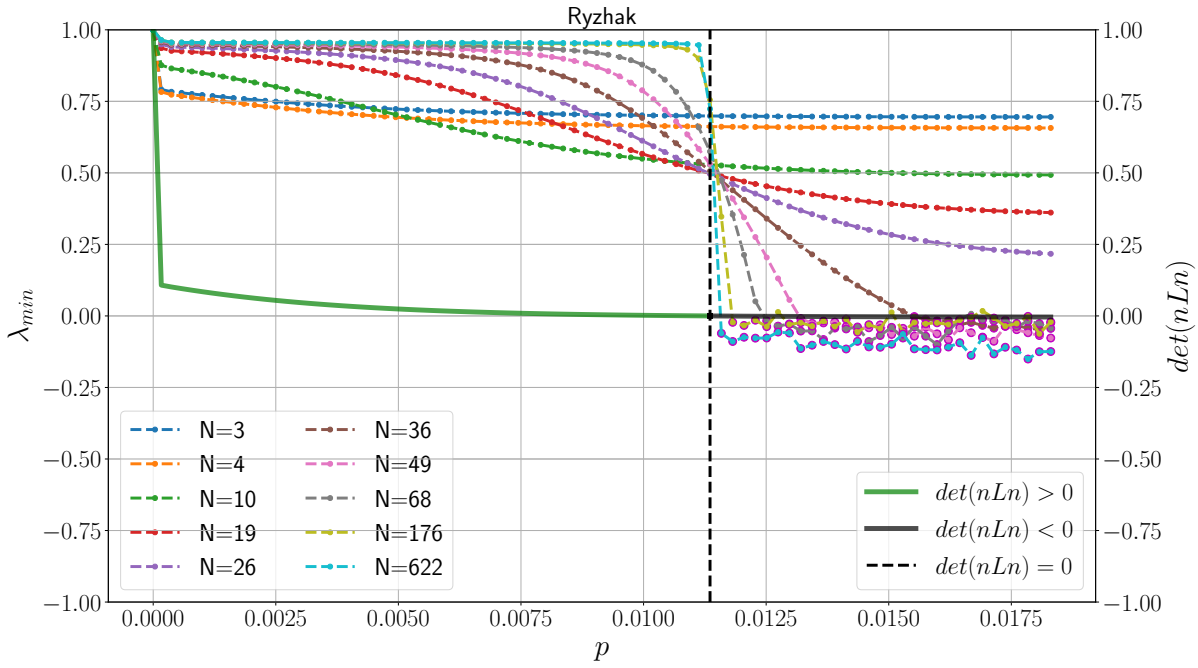


Figure 5.20: Ryzhak BCs: Evolution the smallest eigenvalue for different discretization parameters N . Ellipticity lost for $p = 0.01134$.

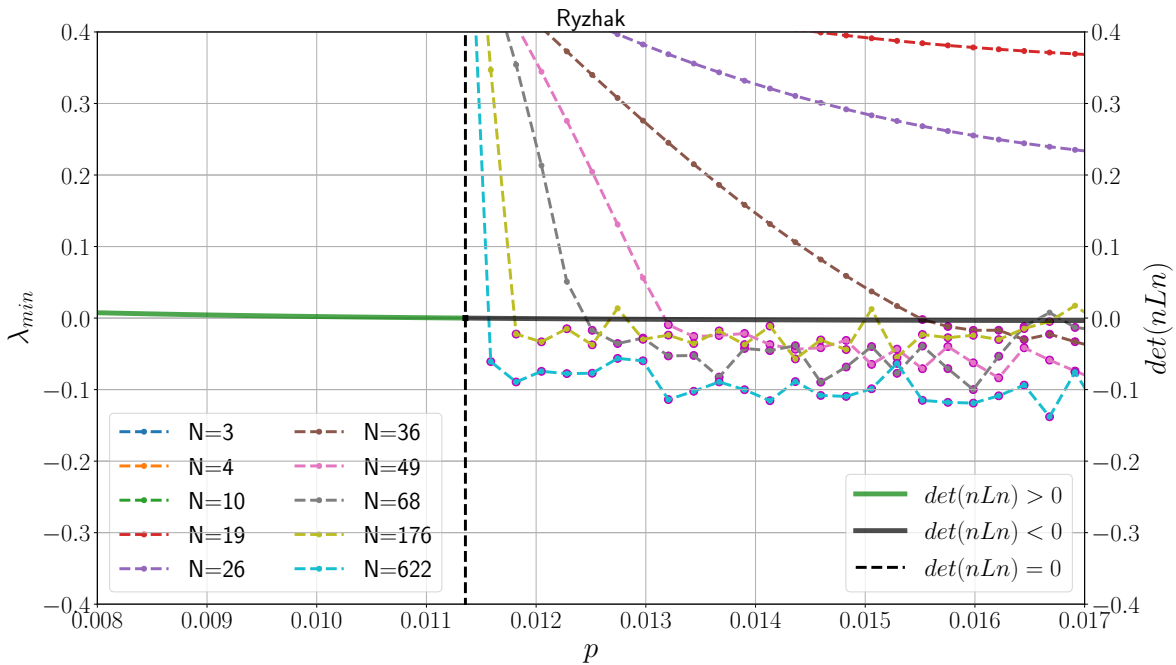


Figure 5.21: Ryzhak BCs: Evolution the smallest eigenvalue for different discretization parameters N . Zoom around the instant of loss of ellipticity: ellipticity lost for $p = 0.01134$.

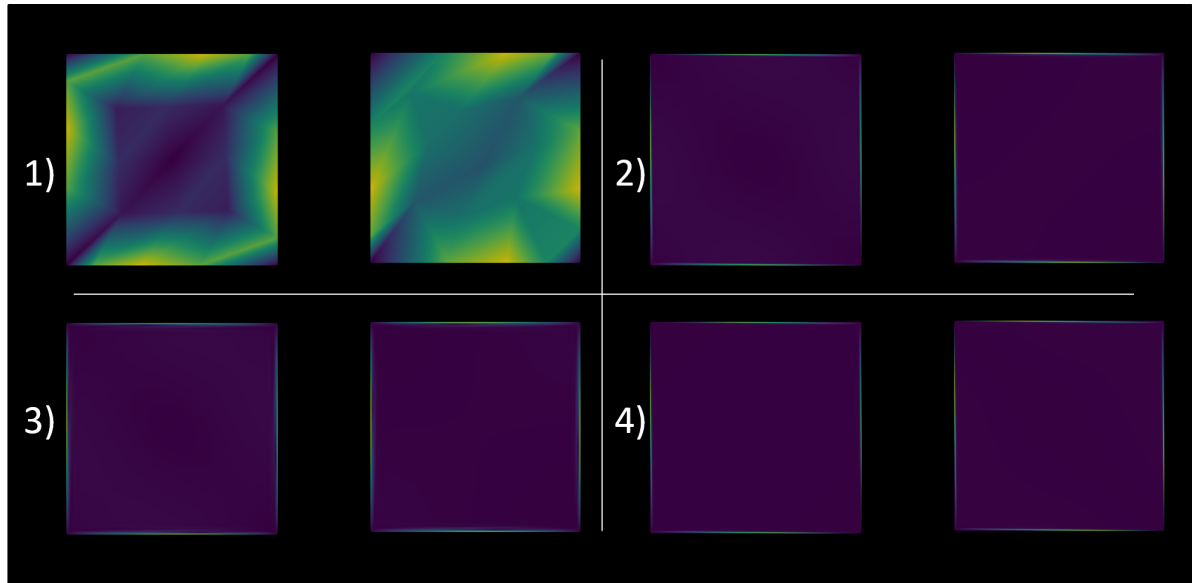


Figure 5.22: Ryzhak BCs: Eigenmodes associated to the two smallest eigenvalues at first loss of ellipticity while there is no loss of uniqueness for the FEM model. From 1) to 4) respectively $N = 4$, $N = 110$, $N = 331$ and $N = 729$.

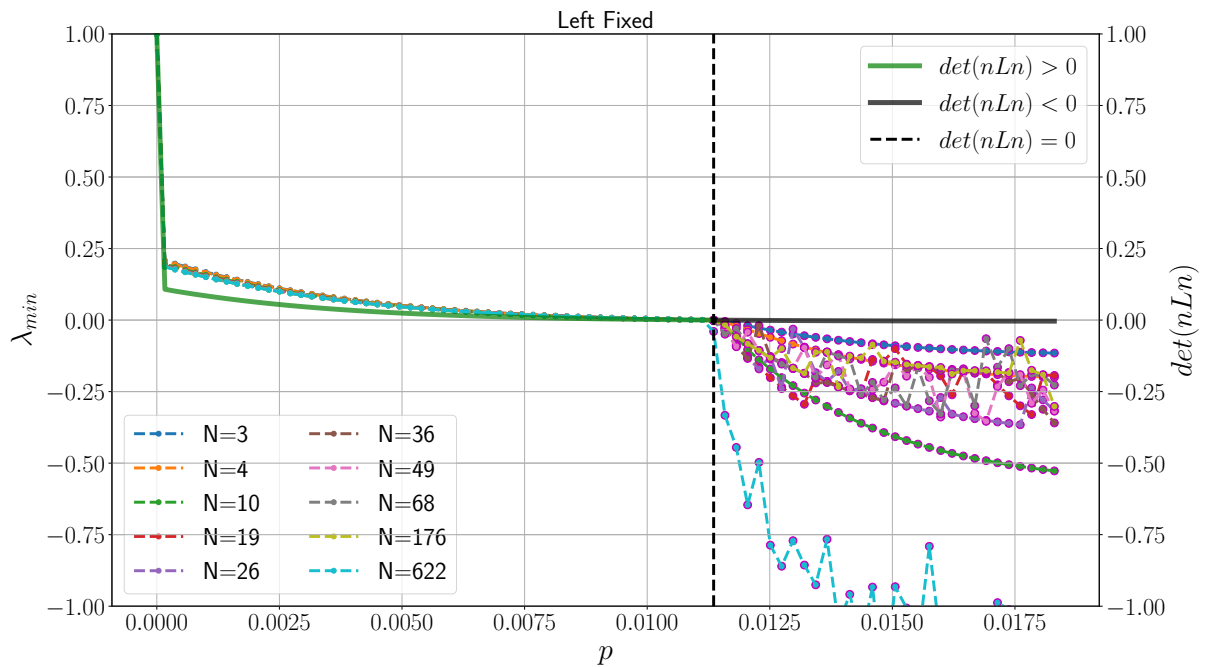


Figure 5.23: Left Fixed BCs: Evolution the smallest eigenvalue for different discretization parameters N . Ellipticity lost for $p = 0.01134$.

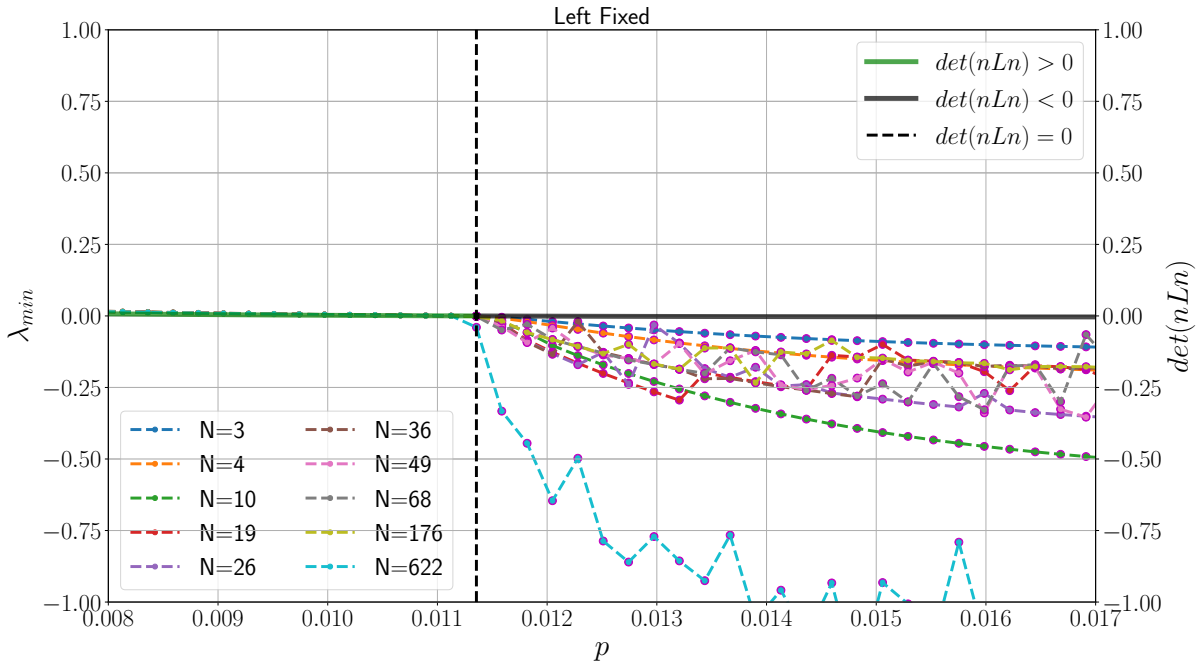


Figure 5.24: Left Fixed BCs: Evolution the smallest eigenvalue for different discretization parameters N . Zoom around the instant of loss of ellipticity: ellipticity lost for $p = 0.01134$.

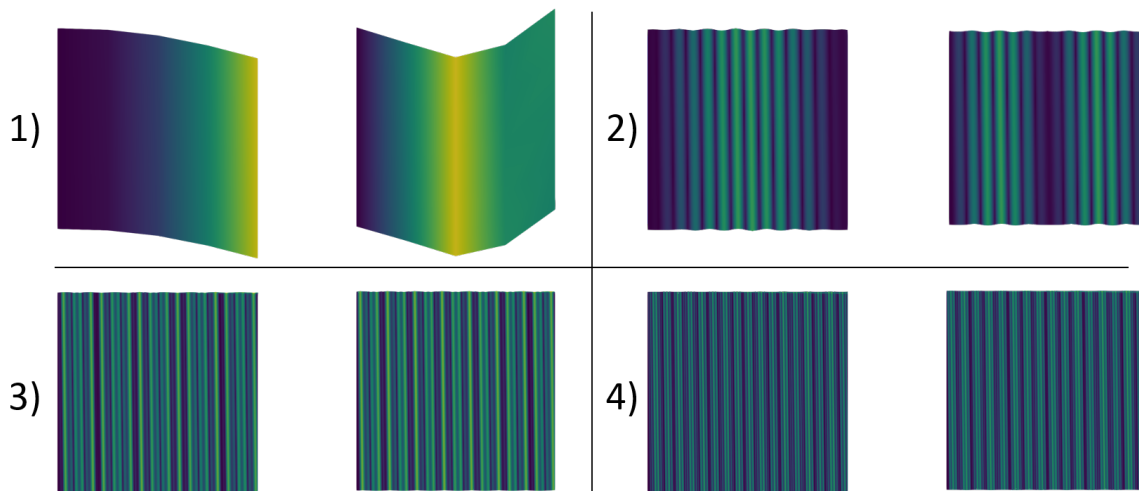


Figure 5.25: Left Fixed BCs: Eigenmodes associated to the two smallest eigenvalues at first loss of ellipticity and loss of uniqueness. From 1) to 4) respectively $N = 4$, $N = 110$, $N = 331$ and $N = 729$.

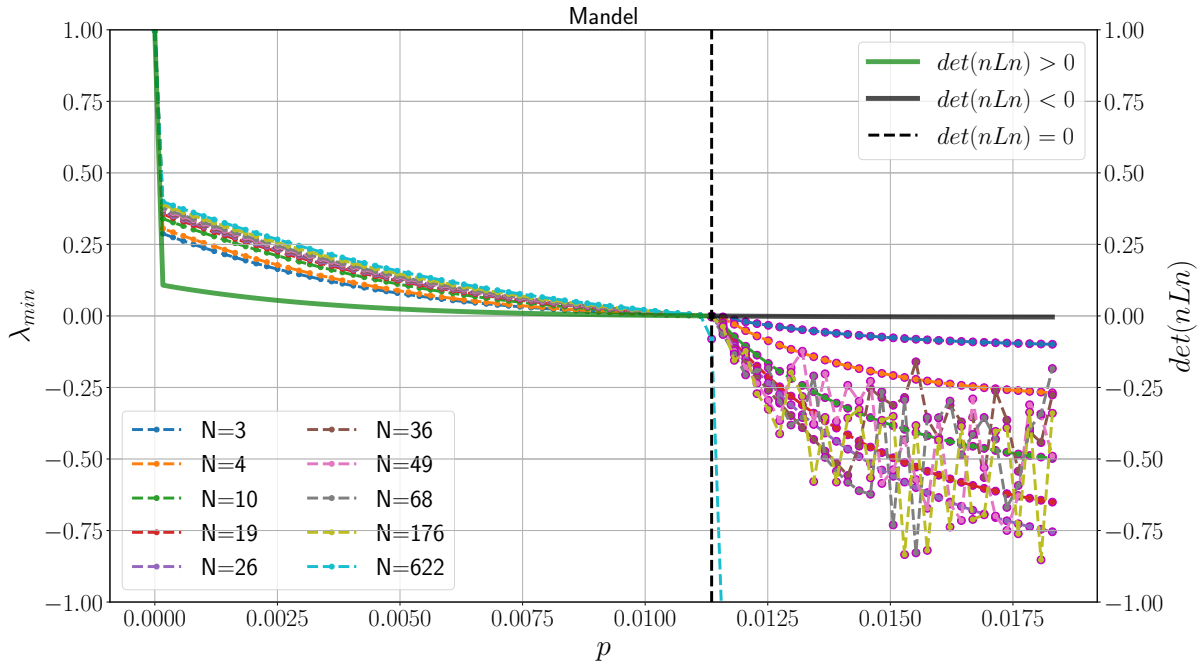


Figure 5.26: Mandel BCs: Evolution the smallest eigenvalue for different discretization parameters N . Ellipticity lost for $p = 0.01134$.

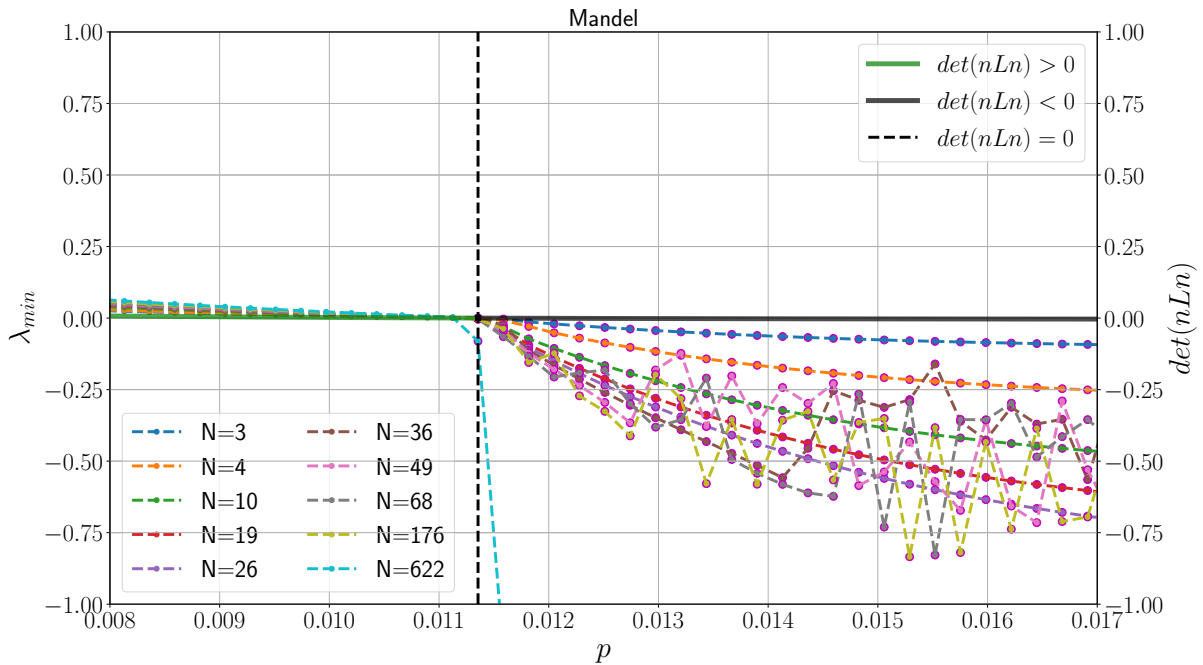


Figure 5.27: Mandel BCs: Evolution the smallest eigenvalue for different discretization parameters N . Zoom around the instant of loss of ellipticity: ellipticity lost for $p = 0.01134$.

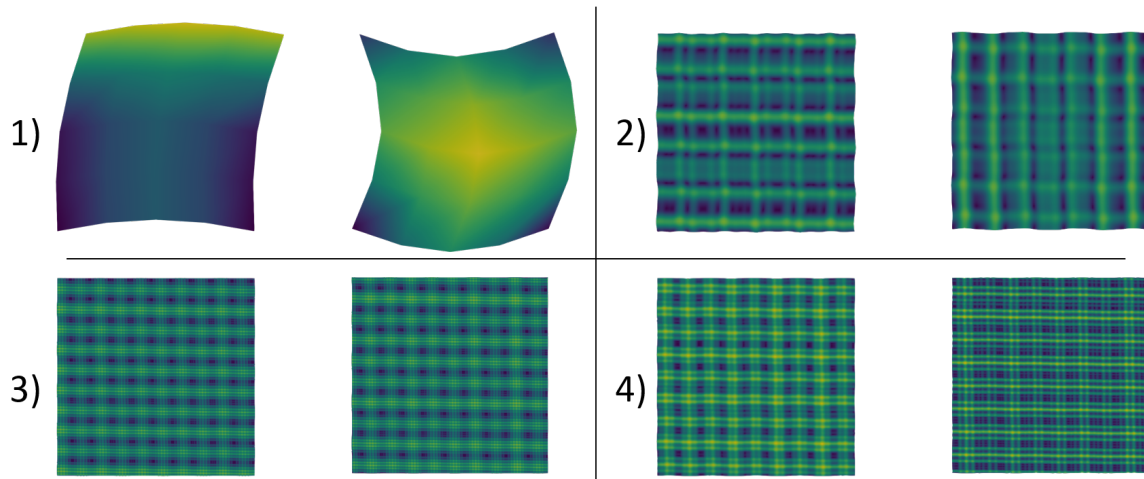


Figure 5.28: Mandel BCs: Eigenmodes associated to the two smallest eigenvalues at first loss of ellipticity and loss of uniqueness. From 1) to 4) respectively $N = 4$, $N = 110$, $N = 331$ and $N = 729$.

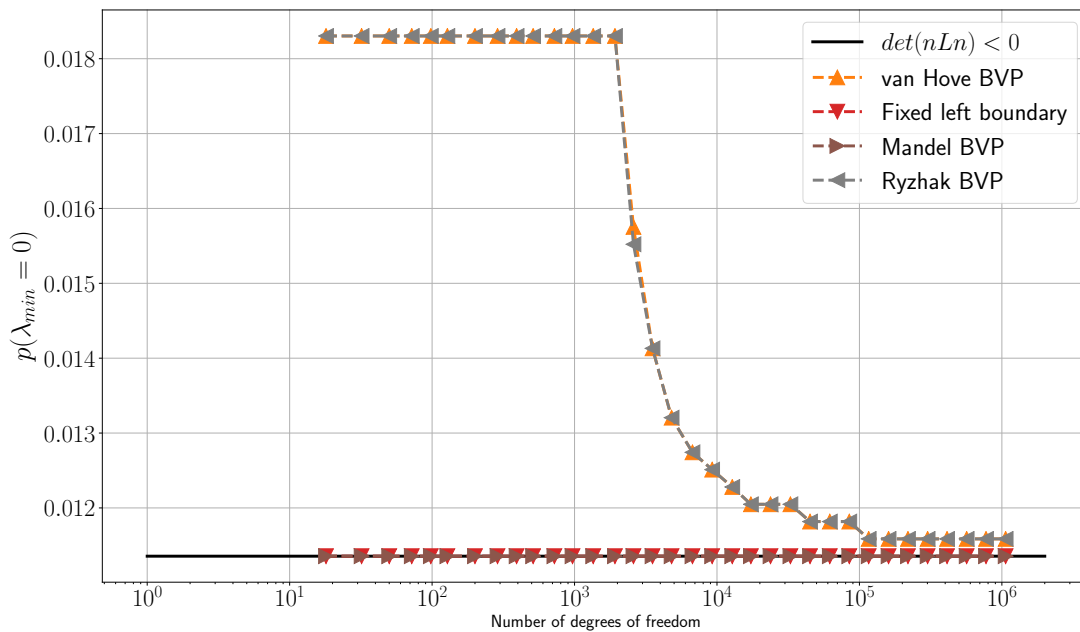


Figure 5.29: Evolution of the plastic strain at first loss of uniqueness as a function of the number of degrees of freedom for the various weakened boundary value problems.

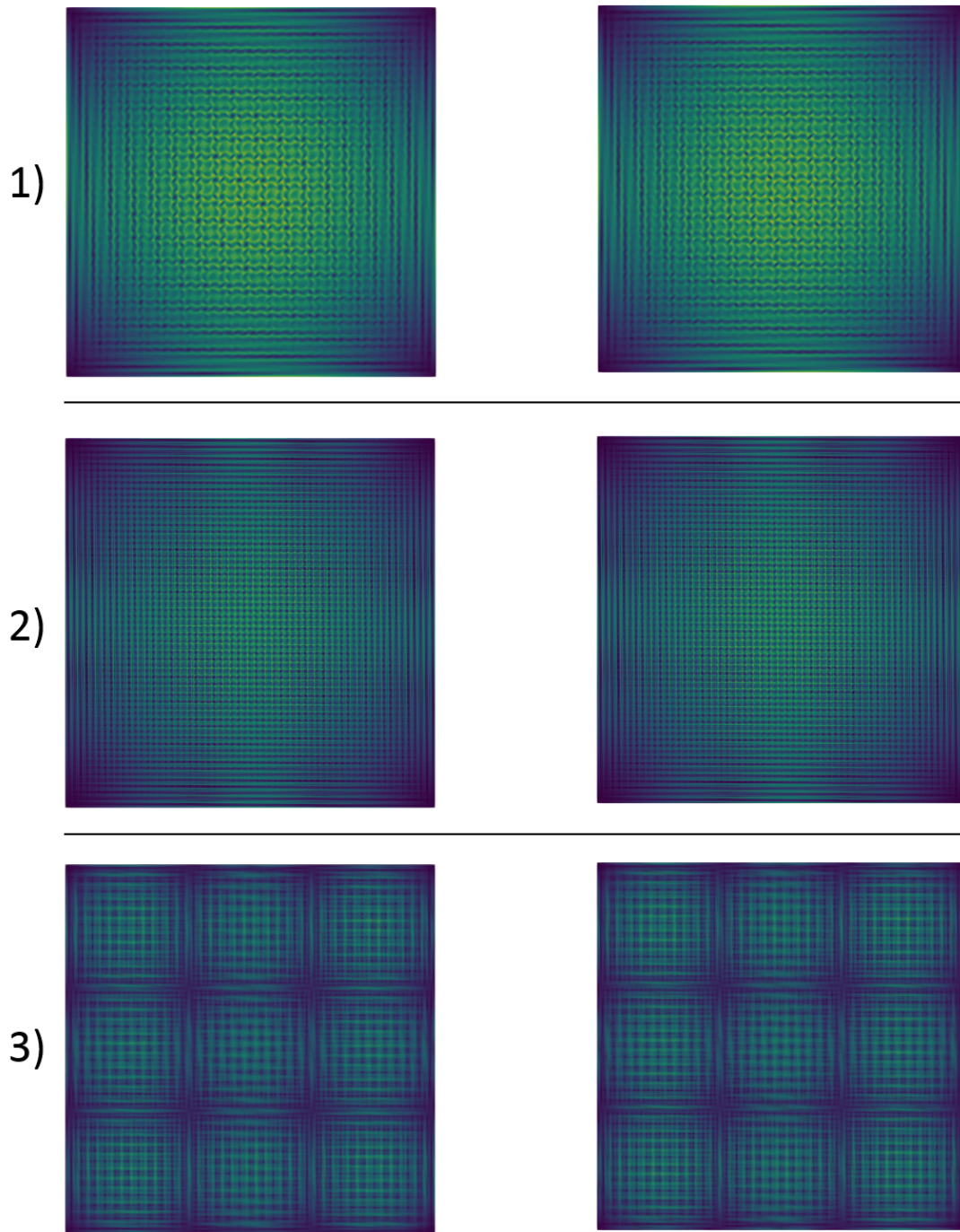


Figure 5.30: Ryzhak BCs: Eigenmodes associated to first loss of uniqueness. From 1) to 3) respectively ($N = 110$, $p = 0.018175$), ($N = 331$, $p = 0.011355$), ($N = 729$, $p = 0.01355$).

It is known that for the simple shear case there are two equivalent normals that minimize the determinant of the acoustic tensor. In our case they correspond to the vertical and horizontal directions. For the Mandel, Ryzhak and van Hove boundary rate value problems both directions

appear in the eigen modes. Yet, for the Left Fixed case, only one directions is favored (see Figure 5.25). Qualitatively, the instability modes observed for this weakened problem are what we would expect from the expression “localization bands”.

Finally, it is shown in Figures 5.31 and 5.32 that for the Left Fixed case with $N = 4$ that there is a correlation between the number of vanishing eigenvalues and the number of modes necessary to describe all possible band formation. Note that it is not a coincidence, and has been observed in other models. But due to computation costs, it is not feasible to compute all the vanishing eigenvalues for the other mesh refinements presented below. This result is consistent with the discussion in section 4.4.1 and the fact that only a finite number of wave lengths can be represented in a discretized problem.

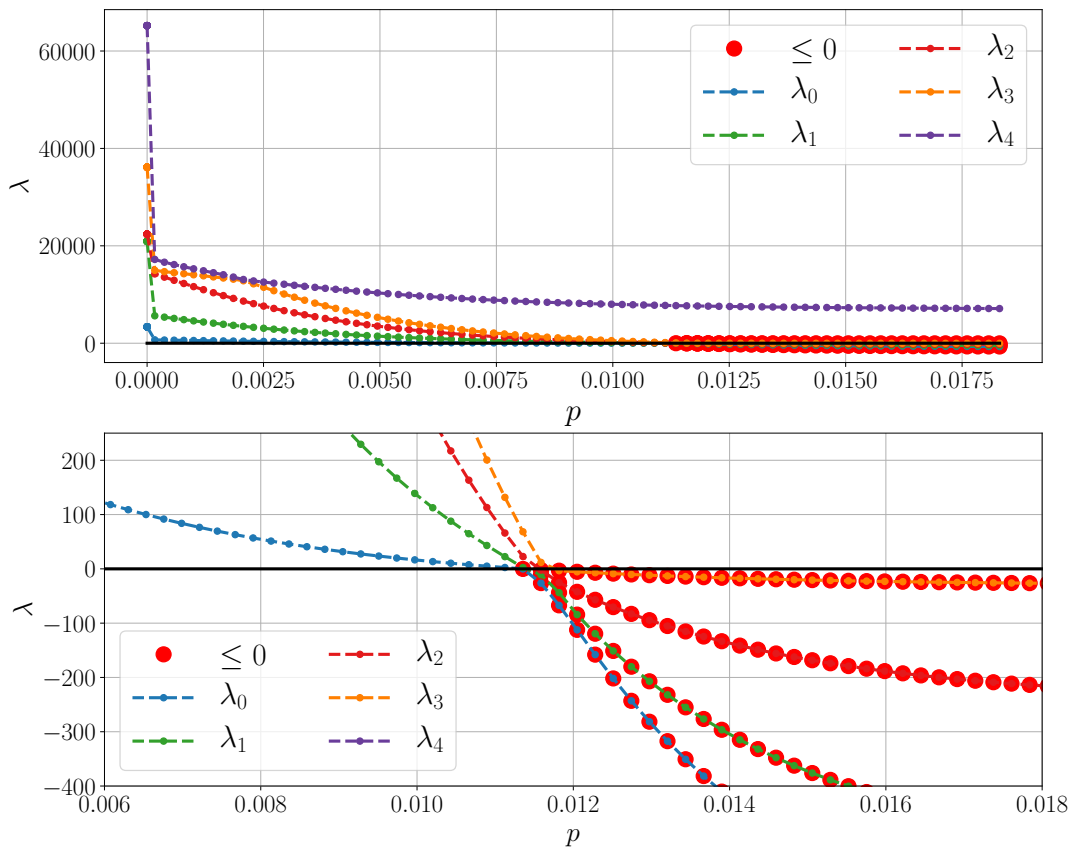


Figure 5.31: Evolution of the smallest eigenvalues for the “Left Fixed” case for $N = 4$. There are N vanishing eigenvalues as number of elements.



Figure 5.32: Eigen modes associated to the four vanishing eigenvalues in Figure 5.31. Any localization mode can be obtained as a linear combination of these four modes.

However, it may not be relevant to discuss whether uniqueness is lost when the smallest eigenvalue of the acoustic tensor vanishes versus when it becomes negative⁸. In fact, the latter happens immediately after the first in an infinite functional space. However, in a finite functional space like the FEM framework and for a given mesh, the uniqueness of the solution of a non-homogeneous problem may be preserved even after loss of ellipticity. This result is due to the essence of the FEM framework in which the solution in velocity/displacements (for our displacement formulation) is investigated in a finite functional space defined by the shape functions at the nodes. These functions do not include velocity fields like the ones obtained for the van Hove or the Ryzhak boundary value problem, unless very fine meshes⁹ are considered.

Another remark concerns the apparent fractal structure obtained for the modes for $N = 729$. In fact, when ellipticity is lost in an arbitrary small domain, these modes could theoretically be able to activate for even arbitrarily smaller wavelengths (see Figure 5.30). A simple proof would consist in considering a smaller square inside the main square that would admit the same instability modes, and iterate this process. This is actually observed in Figure 5.30.

⁸ Yet, this might have some applications for the uniqueness of small deformation and perfect plasticity problems.

⁹ In a 3D structural problem, these meshes would not be reasonable to compute from a time-cost point of view.

The instability modes for van Hove's or Ryzhak's boundary value problems are in fact localized modes since they can theoretically develop in arbitrary small domains, but they are not localization bands in the sense of Rice, in the sense that they do not correspond to the emergence of jumps in strain rates that split the structure. Nevertheless, the instability modes for the Left Fixed boundary value problem (see Figure 5.25) are. Therefore, in the present study, the fact that the FEM framework excludes localization of the first type can be seen as kind of a filter for the shape of the admissible localization modes. This does not regularize the size of the bands and only filters the instability mode's shape; size regularization methods exist and are often based on gradient theories, viscosity, thermal effects or element formulation [Besson et al., 2010, Ibrahimbegovic, 2009, Simo et al., 1993, Petryk, 1997, Bigoni, 2012, Nguyen, 2000].

5.3.3 Competition between loss of ellipticity and global loss of uniqueness in a discretized problem: tube loaded in torsion

It was previously shown that uniqueness may not be lost immediately for the discretized problem as soon as ellipticity is lost in a homogeneous problem depending on the mesh size and boundary conditions. In the present section, it is proposed to study the loss of ellipticity, loss of uniqueness and the emergence of localization bands in the sense of Rice in a non-homogeneous structure with non-softening material properties like the one presented in section 4.4.2. In particular, the aim of the present section is to use the loss of ellipticity criterion to better understand: "when do jumps in strain rates emerge in the structure and lead to the loss of the regularity of the FEM model?" (the aim is not to discuss the uniqueness of the analytical model in an infinite functional space).

For the Mandel and for the Left Fixed boundary value problems, the loss of uniqueness occurred as soon as ellipticity has been lost for the presented homogeneous problem for any mesh size (see section 5.3.2). Nevertheless, if we refer to Mandel's statements in [Mandel, 1964], in a heterogeneous media, the loss of stability of an element under stress conditions which is confined in a stable environment does not necessarily lead to global instability. This is consistent with the discussion in section 5.2.2 and its illustration in section 5.3.1. In the following, Mandel's statement is illustrated in the case of a non-homogeneous domain in which ellipticity, and therefore local stability, is lost in a finite area before global uniqueness of the discretized problem is lost. This is observed by studying a discretized thick tube loaded in pure torsion.

The numerical model is based on the finest mesh presented in section 4.4.2: a tube of external diameter $D = 1 \text{ mm}$, thickness $t = 0.1 \text{ mm}$ and length $L = 0.5 \text{ mm}$ is loaded in torsion. The tube is oriented along the (O, \underline{e}_y) axis and its lower and upper surfaces are respectively denoted S_0 and S_L , as shown in Figure 5.33. The mesh is made of regular hexahedral (0.0125 mm width) elements with 20 nodes, 27 integration points. On the bottom surface, S_0 , all displacements are fixed; on the top surface, S_L , displacements are imposed to describe a rotation of angle θ as follows:

$$\underline{u} = \mathbf{0} \quad \forall \underline{X} \in S_0 \quad (5.42)$$

$$\underline{u} = (\underline{\mathbf{R}}(\theta) - \underline{\mathbf{I}})\underline{X} \quad \forall \underline{X} \in S_0 \quad (5.43)$$

where $\underline{\mathbf{R}}(\theta)$ is the rotation tensor of an angle θ around the (O, \underline{e}_y) axis.

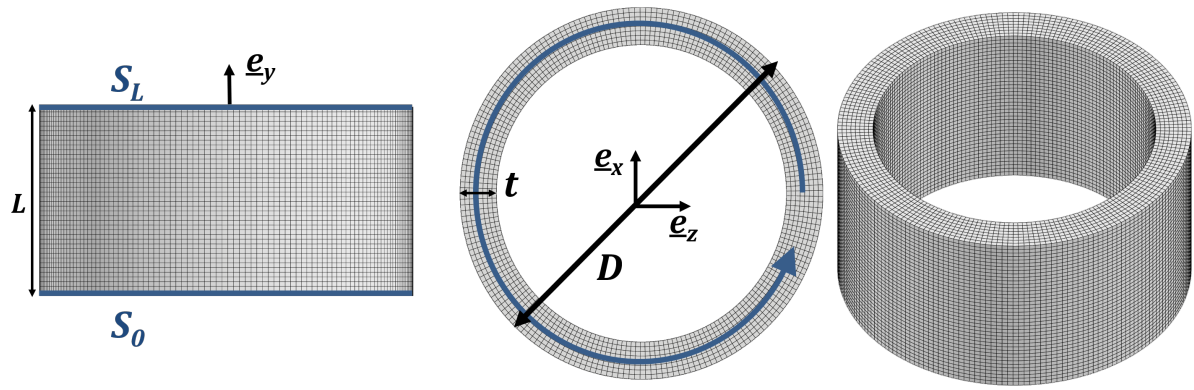


Figure 5.33: Thick tube loaded in torsion. Geometry: diameter $D = 1 \text{ mm}$, thickness $t = 0.1 \text{ mm}$ and length $L = 0.5 \text{ mm}$. The mesh is composed of quadratic hexahedral elements (20 nodes 27 Gauss points), of side length 0.0125 mm .

The evolution of the minimum determinant of the acoustic tensor and the evolution of cumulative plastic strain were already thoroughly presented in section 4.4.2. The contour plot of these two quantities at the critical moments $\theta = 0.89^\circ$ (ellipticity lost in a large part of the tube), and $\theta = 0.90^\circ$ (localization of the cumulative plastic strain and elastic unloading in the rest in the structure are shown in Figures 5.34 and 5.35).

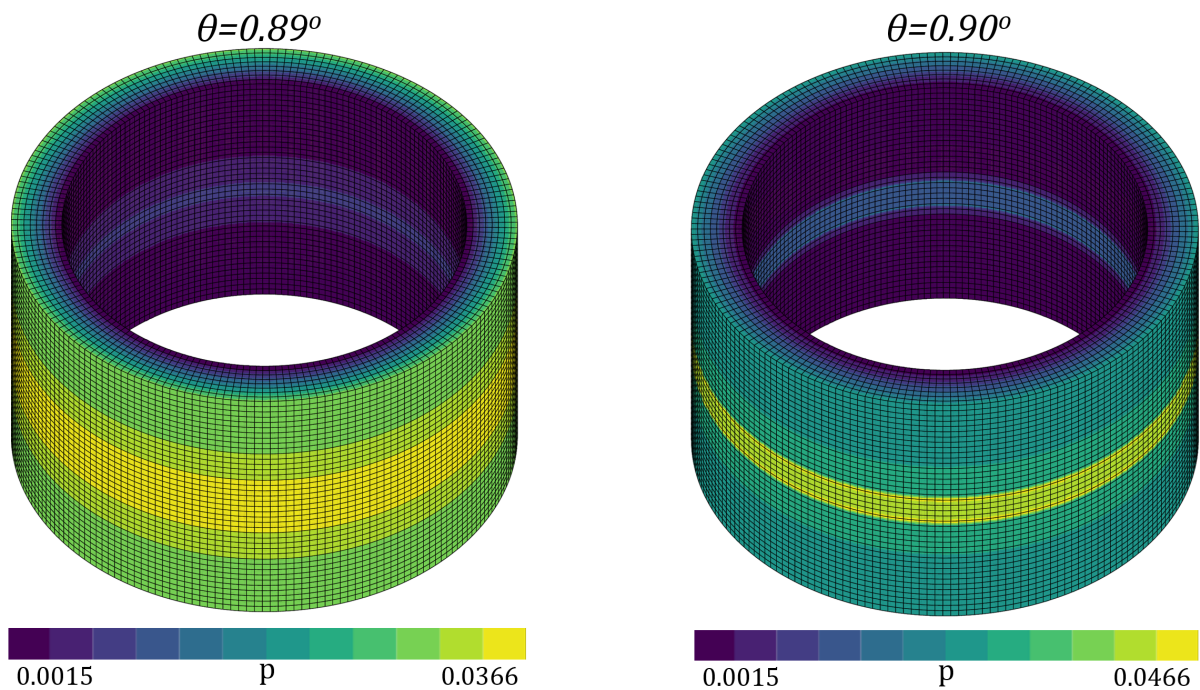


Figure 5.34: Contour of the sign for the minimum of the determinant of the acoustic tensor at $\theta = 0.89^\circ$ and $\theta = 0.90^\circ$.

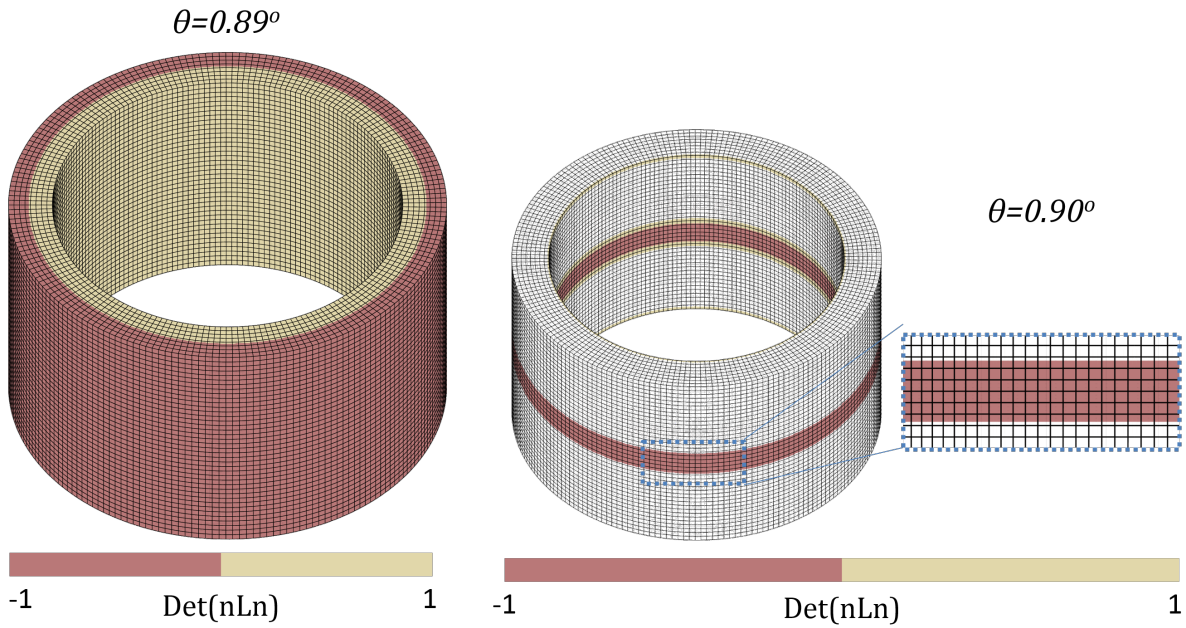


Figure 5.35: Contour of the cumulative plastic strain at $\theta = 0.89^\circ$ and $\theta = 0.90^\circ$.

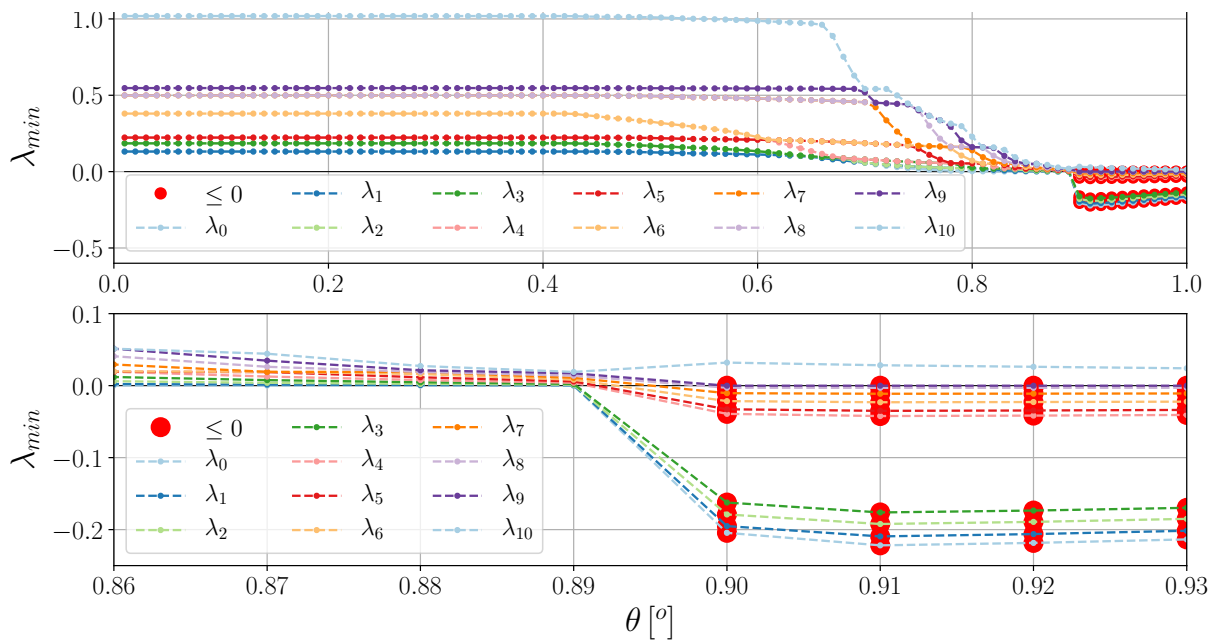


Figure 5.36: Smallest eigenvalues for the global tangent matrix of the tube loaded in torsion for the Fixed/Free weakened problem. First global loss of uniqueness is observed at $\theta = 0.90^\circ$. Ten eigenvalues vanish at once.

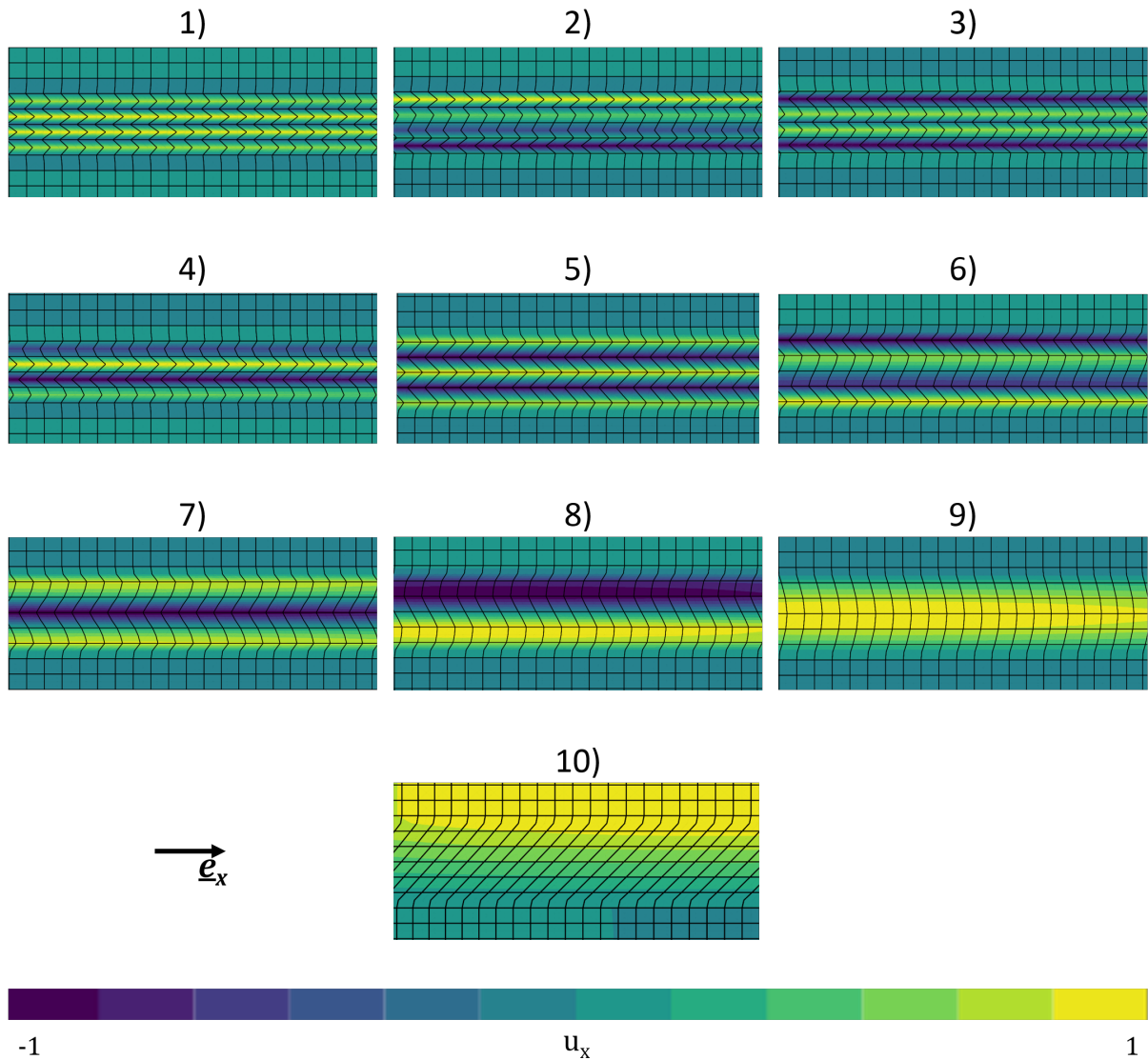


Figure 5.37: Eigen modes associated with the vanishing eigenvalues for the tube loaded in torsion for the Fixed/Free weakened problem. $\theta = 0.90^\circ$.

In order to analyze the global loss of uniqueness of the discretized problem, the weakened stability analysis was performed with fixed boundary conditions on the bottom surface only:

$$\Delta \underline{u} = \underline{0} \quad \forall \underline{X} \in S_0 \quad (5.44)$$

The smallest eigenvalues for this weakened rate boundary value problem were extracted and are presented in Figure 5.36. It is shown that when $\theta = 0.90^\circ$ there are ten eigenvalues that vanish at once. This instant corresponds to the configuration for which ellipticity was lost in the whole middle section. The ten eigenmodes associated to the ten vanishing eigenvalues are shown in Figure 5.37.

The number of instability modes is consistent with the number of two-node layers that are contained in the non-elliptic zone: four full elements and two halves (the mesh is quadratic so it includes middle nodes on the elements edges). This leads to a total of ten layers. In fact, the instability modes observed in Figure 5.37 have a strong resemblance with the “Left Fixed” case presented in the previous section.

The results for the other meshes are not presented, but give similar results. As shown in section 4.4.2, the width of the localized area may change for various mesh sizes, however, the nature of the instability modes are always the same and are consistent with the Left Fixed case presented in section 5.3.2. In the presented case, ellipticity was lost in a large part of the structure before the discretized problem lost global uniqueness.

Note that the weakened uniqueness analysis was not necessary in the present case to capture the global instability. In fact, the weakened problem was defined to have a problem that is similar to the Left Fixed case presented in the previous section. If the instability modes were to vanish on both ends of the tube, only the tenth mode would not be extracted.

Finally, it was observed numerically that when ellipticity is lost through the thickness of the structure, localization bands in the sense of Rice (localization bands that split the structure with a jump in strain rates) are observed to be instability modes. Thus, in a discretized non-homogeneous media, even for a boundary value problems that are much less constrained than van Hove's or Ryzhak's rate problems, uniqueness of the global problem is not necessarily lost, which illustrates Mandel's statement, [Mandel, 1964].

5.4 Conclusions

In this chapter the influence of the kinematic constraints on the structure's stability was investigated thanks to the proposed weakened stability analysis introduced in section 5.2.1. This analysis was built by virtually reducing the number of kinematic constraints on the structure's boundary to formulate a "weakened problem" on which a classical global (in)stability analysis is performed. It was shown that the weakened problem was always at most as stable as the initial problem. This was illustrated with the well known Euler buckling problem which has been studied by linearizing Hill's loss of uniqueness criterion in section 5.1.1. The numerical method for such an analysis was implemented in `Zset` and details are given in section 5.2.3 and validated on the Euler buckling analysis in section 5.2.4. A perfect agreement was obtained between the numerical and analytical results.

In section 5.3.1, it was shown that for various weakened problems the instability modes for a thin tube loaded in torsion were sensitive to the kinematic assumptions at its end surfaces. This analysis allowed us to give lower and upper bounds for the critical load associated with the buckling of the tube loaded in torsion, when assuming that the geometry and loading direction were well identified. This is a first step towards the analysis of instabilities for structures in complex environments. These results actually help us better understand the observations made on the thin plate loaded in tension (see section 3.2.3).

In order to illustrate the discussion given in section 4.2.2, the analysis of a homogeneous 2D square loaded in shear was presented in section 5.3.2. Four weakened rate boundary value problems were analyzed: van Hove [van Hove, 1947], Ryzhak [Ryzhak, 1994], Mandel [Mandel, 1964], and the "Left Fixed" case. On the one hand, the first two weakened problems provided similar conclusions: they did not necessarily lose uniqueness as soon as ellipticity was lost; and the instant for the emergence of instability modes depended on the mesh refinement. Finally, when uniqueness was lost, the instability modes were made of very small wavelength. On the other hand, the last two cases systematically lost uniqueness as soon as ellipticity was lost regardless of the mesh refinement. Also the instability modes were consistent with shear bands that split the structure, like the ones introduced in [Rice, 1976].

Mandel's statement was illustrated by performing both the local and the global instability analysis on a thick tube loaded in torsion in section 5.3.3. The competition between loss of ellipticity and loss of uniqueness was studied to better understand the observations of section 4.4.2. It was observed that when Ryzhak and van Hove's instability modes were excluded due to the FEM framework, global instability modes were consistent with the "Left Fixed" case. These

instability modes were as numerous as the number of possible localization bands (in the sense of Rice) that could kinematically emerge in the non-elliptic area of the FEM problem.

In fact, it was shown that the solution of the FEM model was not necessarily representative of the analytical model in an infinite functional space. If one thinks that there are micro-structural aspects that would forbid the emergence of modes like the ones shown in Figure 5.19, it may probably be considered to be a good thing that the FEM regularizes these modes. Yet, if the material has softening properties, or if highly localized modes like the ones shown in Figure 5.30 are acceptable, then the conclusion about the competition between global and local stability might fail.

Finally, when designing a real structure, it is most likely not safe to wait until loss of ellipticity splits the structure to consider it unreliable. For associative materials the loss of ellipticity criterion is fulfilled only for negative or almost vanishing hardening modulus, which means that the structure already became very weak in some zone; and the analysis of sensitivity to geometrical or material defects was not studied in the present work, yet, it is well known to have a strong impact on the emergence of localization bands or buckling modes. However, these analyses are out of the scope of the present work.

Bibliography

- Asmolovskiy, N., Tkachuk, A., and Bischoff, M. (2015). Numerical approaches to stability analysis of cylindrical composite shells based on load imperfections. *Engineering Computations*, 32(2):498–518.
- Besson, J., Cailletaud, G., Chaboche, J.-L., and Forest, S. (2010). *Non-linear mechanics of materials*. Springer.
- Bigoni, D. (2012). *Nonlinear Solid Mechanics: Bifurcation Theory and Material Instability*. Cambridge University Press.
- Defaisse, C., Mazière, M., Marcin, L., and Besson, J. (2018). Ductile fracture of an ultra-high strength steel under low to moderate stress triaxiality. *Engineering Fracture Mechanics*, 194:301–318.
- Dæhli, L., Morin, D., Børvik, T., and Hopperstad, O. (2017). Influence of yield surface curvature on the macroscopic yielding and ductile failure of isotropic porous plastic materials. *Journal of the Mechanics and Physics of Solids*, 107:253–283.
- Di Pasqua, M., Khakimova, R., Castro, S., Arbelo, M., Riccio, A., Raimondo, A., and Degenhardt, R. (2016). Investigation on the geometric imperfections driven local buckling onset in composite conical shells. *Applied Composite Materials*, 23(4):879–897.
- Eftang, J. and Patera, A. (2014). A port-reduced static condensation reduced basis element method for large component-synthesized structures: approximation and a posteriori error estimation. *Advanced Modeling and Simulation in Engineering Sciences*, 1(1):49 p.
- Gardner, L. (2018). Elastic local buckling stresses for full structural steel cross-sections (oral presentation). In *European Solid Mechanics Conference*. (July-2018) Bologna, Italy.
- Gosselet, P. and Rey, C. (2006). Non-overlapping domain decomposition methods in structural mechanics. *Archives of Computational Methods in Engineering*, 13:515–572.
- Harrison, B., Yuan, L., and Kyriakides, S. (2016). Measurement of lined pipe liner imperfections and the effect on wrinkling and collapse under bending. *International Conference on Offshore Mechanics and Arctic Engineering*, 5.
- Hill, R. (1962). Acceleration waves in solids. *Journal of the Mechanics and Physics of Solids*, 10:1–16.
- Hill, R. and Hutchinson, J. (1975). Bifurcation phenomena in the plane tension test. *Journal of the Mechanics and Physics of Solids*, 23:239–264.
- Hutchinson, J. and Tvergaard, V. (1981). Shear band formation in plane strain. *International Journal of Solids and Structures*, 17(5):451 – 470.

- Ibrahimbegovic, A. (2009). *Geometric and material instabilities*. Springer.
- Kriegsmann, B., Hilburger, M., and Rolfes, R. (2012). The effects of geometric and loading imperfections on the response and lower-bound buckling load of a compression-loaded cylindrical shell. *53rd AIAA/ASME/ASCE/AHS/ASC Structures, Structural Dynamics and Materials Conference*, 1:10 p.
- Lee, L. and Ades, C. (1957). Plastic torsional buckling strength of cylinders including effects of imperfections. *Journal of the Aeronautical Sciences*, 24:241–248.
- Mandel, J. (1964). Propagation des surfaces de discontinuité dans un milieu élastoplastique. In *Stress waves in anelastic solids*, pages 331–340. Springer.
- Mandel, J. (1966). Conditions de stabilité et postulat de drucker. In *Rheology and Soil Mechanics*, pages 58–68. Springer.
- Mear, M. and Hutchinson, J. (1985). Influence of yield surface curvature on flow localization in dilatant plasticity. *Mechanics of Materials*, 4:395–407.
- Nguyen, Q. S. (2000). *Stability and nonlinear solid mechanics*. Wiley.
- Perez, R., Wang, X., and Mignolet, M. (2014). Nonintrusive structural dynamic reduced order modeling for large deformations: Enhancements for complex structures. *Journal of Computational and Nonlinear Dynamics*, 9:12 p.
- Petryk, H. (1997). Plastic instability : Criteria and computational approaches. *Archives of Computational Methods in Engineering*, 4:111–151.
- Regulation, T. E. U. P. (2005). *Eurocode 3: Design of steel structures - Part 1-1: General rules and rules for buildings*. The European Union.
- Remmers, J. and de Borst, R. (2001). Delamination buckling of fibre–metal laminates. *Composites Science and Technology*, 61(15):2207–2213.
- Rice, J. (1976). The localization of plastic deformation. In *W.T. Koiter (Ed.), Theoretical and Applied Mechanics*, pages 207–220. North-Holland.
- Ryckelynck, D. (2005). A priori hyperreduction method: an adaptive approach. *Journal of Computational Physics*, 202(1):346–366.
- Ryzhak, E. (1994). On stability of homogeneous elastic bodies under boundary conditions weaker than displacement conditions. *The Quarterly Journal of Mechanics and Applied Mathematics*, 47(4):663–672.
- Simo, J., Oliver, J., and Armero, F. (1993). An analysis of strong discontinuities induced by strain-softening in rate-independent inelastic solids. *Computational Mechanics*, 12:277–296.
- van Hove, L. (1947). Sur l’extension de la condition de Legendre du calcul des variations aux intégrales multiples à plusieurs fonctions inconnues. *Proceedings of the Koninklijke Nederlandse Akademie van Wetenschappen*, 50:18–23.
- Walport, F., Gardner, L., Real, E., Arrayago, I., and Nethercot, D. (2018). Effects of material nonlinearity on the global analysis and stability of stainless steel frames. *Journal of Constructional Steel Research*, page in press: <https://doi.org/10.1016/j.jcsr.2018.04.019>.
- Wang, H., Yao, X., Li, L., Sang, Z., and Krakauer, B. (2017). Imperfection sensitivity of externally-pressurized, thin-walled, torispherical-head buckling. *Thin-Walled Structures*, 113:104–110.

Chapter 6

Structural Applications

*“La vie est dure, il me l’a dit ;
La vie est amère, il me l’a dit ;
La vie est belle, il me l’a dit plusieurs fois.”
Mon frère au sujet de mon père*

Résumé : Les outils précédemment introduits dans le manuscrit sont utilisés dans ce chapitre pour l’analyse de trois problèmes. D’abord, de nouveaux abaques pour le tube en ML340 chargé en torsion pour différentes combinaisons de L/D (longueur sur diamètre) et D/t (diamètre sur épaisseur) sont présentés et comparés avec [Lee and Ades, 1957], article qui fait toujours office de référence dans l’aéronautique pour le cas des tubes en torsion. Dans un second temps, les résultats pour le tube en torsion pour deux matériaux fictifs possédant la même contrainte conventionnelle maximale que le ML340 mais des limites d’élasticité plus faibles sont présentés pour étudier l’influence de la forme des courbes d’écrouissages sur l’émergence d’instabilités. Pour ces deux premiers cas, le critère affaibli de stabilité a été mis en œuvre pour étudier la sensibilité à différentes conditions aux limites. Enfin, une méthode s’appuyant sur le critère affaibli de stabilité est proposée pour analyser l’émergence d’une instabilité géométrique dans un problème incluant une surface de contact. Cette méthode sera utilisée pour analyser l’apparition de la double striction et d’un mode de perte de symétrie dans le cas d’une chape chargée en traction par un axe rigide.

6.1	Localization and buckling in ML340 tubes loaded in torsion	169
6.2	High yield vs slow saturating hardening	182
6.3	Weakened instability analysis for contact	197

So far we have applied these methods to academic test cases, however the goal is to apply these methods to actual structures. Due to confidentiality aspects, the most complex structures studied during the PhD (actual Safran designs) are not presented. In the present chapter three interesting problems, yet with relatively simple geometries, are detailed.

First, the competition between buckling and localization in ML340 steel tubes loaded in torsion is presented in section 6.1. In this analysis, a wide range of *Length/Diameter* (L/D) and *Diameter/thickness* (D/t) ratios is evaluated. The results are then compared in terms of design curves with the ones given in [Lee and Ades, 1957], which nowadays provides the reference design curves for this problem. This study aims to shed light on the gain in limit load that is a result of C. Defaisse's work on the post-necking material characterization [Defaisse, 2018], and to better understand the competition between buckling and localization in steel tubes loaded in torsion.

Second, the same problem is investigated with two other (fictitious) materials that display large strains: ML340 is a high strength steel that exhibits necking quite early in a tensile experiment (around 2.5% plastic strain), but a long post-necking ductile behavior. It is therefore proposed to compare the corresponding design curves with the ones obtained for materials that undergo large strains before necking, an equivalent maximum tensile force, and a lower yield stress. The purpose of this investigation is to observe the changes in the design curves for various hardening laws. This analysis will allow us to distinguishing two different design criteria for the two different failure modes, and the results for various weakened problems are presented.

Finally, the analysis of a lug loaded in tension is studied. Practically, these structural pieces are loaded through a contact interface. When modeling their behavior, it is necessary to include contact in the numerical model as well. Yet, the global instability analysis is not formulated to take into account such problems. It is proposed to investigate the arising instabilities with the formulation of an adapted weakened rate boundary value problem. This is a method directly comparable to methods that are currently used by mechanical engineers. The numerical results for a lug loaded in tension are detailed and qualitatively compared with experimental results.

6.1 Localization and buckling in ML340 tubes loaded in torsion

In the aeronautical industry, the work presented in [Lee and Ades, 1957] is still a reference for the design of tubes loaded in torsion (see for instance [Department of Defense, 1998]). The authors based their analysis on a small deformation and finite displacement framework. In the present work the numerical methods are not limited to these assumptions. Therefore, it is proposed to compare our numerical results, which are obtained in a full finite deformation framework, with the results presented in [Lee and Ades, 1957] in terms of design curves. The aim is to discuss the possible advantages and limits of the tools presented.

Since the characterization of the post-necking behavior of ML340 was thoroughly investigated by C. Defaisse in [Defaisse, 2018], and since he performed multiple experiments on tubes loaded in torsion, this material will be preferred in this section. In his work, the post-necking behavior was evaluated with a reverse identification method based on the coupling of direct image correlation and FEM modeling within a finite deformation framework. This characterization is essential to capture the true behavior of the material after necking arises. The constitutive law has been identified to be (see section 2.2.2 for more details about the formulation):

- Elasticity: $E = 189 \text{ GPa}$, $\nu = 0.29$;
- Corotational formulation using the Kirchhoff stress tensor;
- von Mises criterion with isotropic hardening:

$$R(p) = 1600 + 189(1 - e^{-81p}) + 509(1 - e^{-773p}) + 236p$$

Moreover, in [Defaisse, 2018], the author defines a ductile failure initiation criterion under multi-axial loading. This criterion relies on the definition of an evolution law of a damage-like parameter based on Rice and Tracey/Johnson Cook formulation with a Lode-dependent term (detailed given in [Defaisse et al., 2018]). This approach is a purely local material approach.

In the present work we propose to investigate the failure of a structure using both global and local instability criteria. The latter was used in section 4.4.2 with a non-softening but saturating material. The material law given above possesses a linear hardening term that prevents localization. Therefore, a strong hypothesis is made in the present section: the damage-like approach is mimicked by removing the linear hardening term. This approach relies on two main arguments:

- The linear hardening term is relatively low and failure in shear in the experiments arises around 10% plastic strain: for the shear stress, this represents 17 MPa out of 1700 MPa; in other words 1%;
- It could technically be replaced with a third exponential hardening term that would saturate.

So for the rest of the present section, the material law used to capture localization is given by:

- Elasticity: $E = 189 \text{ GPa}$, $\nu = 0.29$;
- Corotational formulation using the Kirchhoff stress tensor;
- von Mises criterion with isotropic hardening:

$$R(p) = 1600 + 189(1 - e^{-81p}) + 509(1 - e^{-773p})$$

To verify this assumption, the design curves for both hardening laws are compared in section 6.1.4, and some experimental results are positioned on the design curves. Both "stress/strain" curves are shown in Figures 6.1 and 6.2, respectively in terms of engineering and true "stress/s-trains".

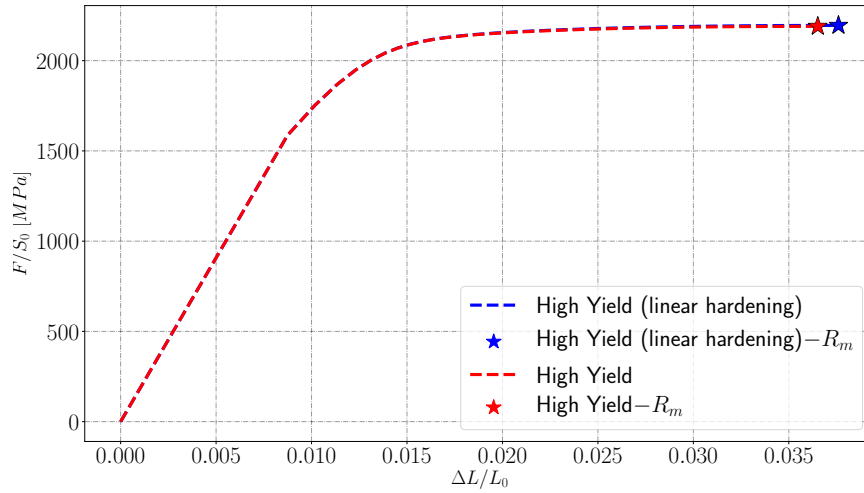


Figure 6.1: Engineering tensile curves for the ML340 steel (identified in [Defaisse, 2018]) with and without linear hardening.

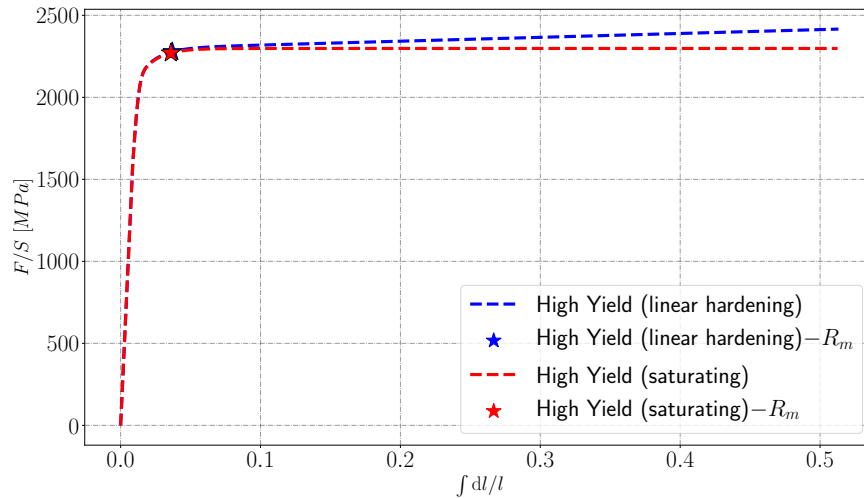


Figure 6.2: True tensile curves for the ML340 steel (identified in [Defaisse, 2018]) with and without linear hardening.

In [Lee and Ades, 1957] the authors split their analysis into two main approaches: a buckling analysis based on the minimization of an energy criterion (deformation theory is used), and shear failure based on the "ultimate shear stress" (in the whole section of the tube), as shown in Figure 6.3. Finally, in order to generalize the results to similar geometries, the "equivalent critical shear stress" $\bar{\tau}$ is evaluated such that:

$$\bar{\tau} = \frac{T_c D}{\pi(R_e^4 - R_i^4)} \quad (6.1)$$

where T_c denotes the critical torque, R_i and R_e respectively the internal and external radii of the tube, and D the external diameter.

The maximum shear stress τ_m is computed from the maximum tensile engineering stress R_m using a von Mises criterion: $\tau_m = \frac{\sigma_{neck}}{\sqrt{3}} = \frac{R_m}{\sqrt{3}}$. When τ_m is reached in the whole section of the tube the equivalent localization shear stress is given by:

$$\bar{\tau}^u = \frac{2\tau_m D(R_e^3 - R_i^3)}{3(R_e^4 - R_i^4)} \tag{6.2}$$

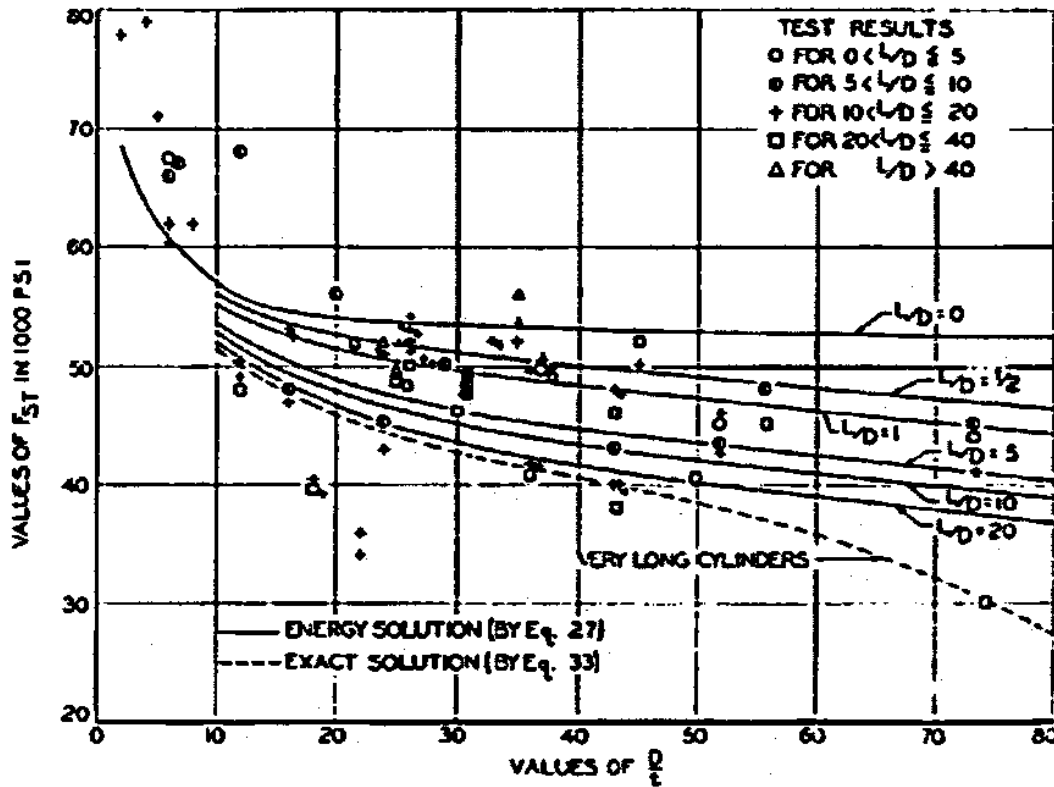


FIG. 11. Comparison of theory with experimental results—steel cylinders.

Figure 6.3: Design curves for tubes loaded in torsion presented in [Lee and Ades, 1957]. The top curve ($L/D = 0$) is evaluated with the "ultimate shear stress" in the whole section of the tube.

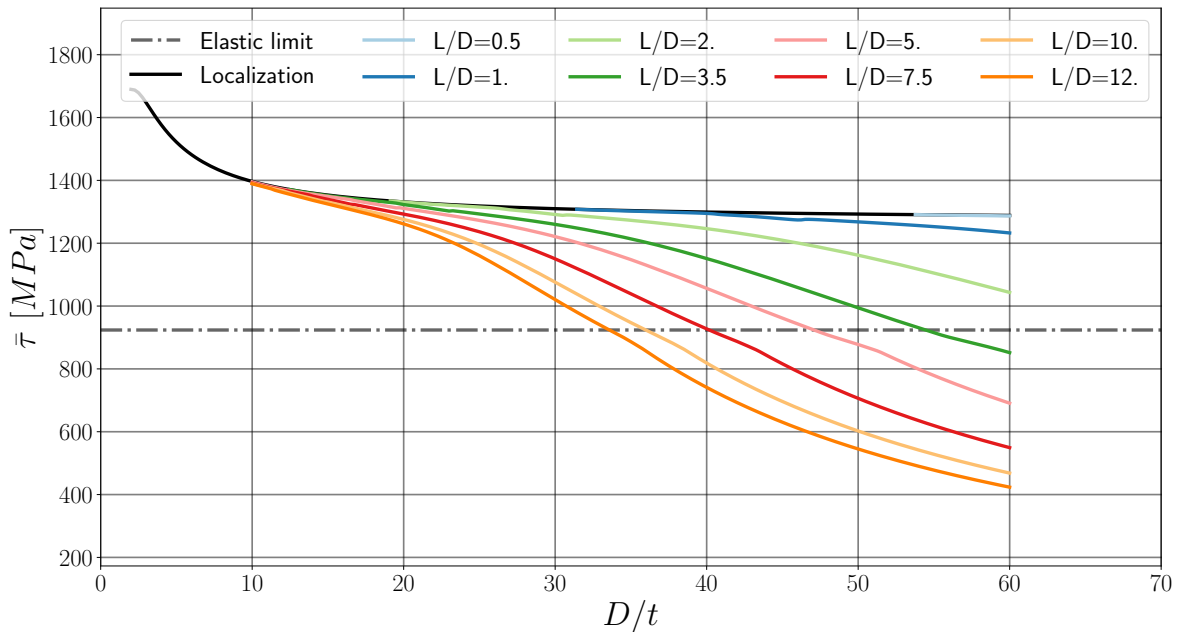


Figure 6.4: Design curves for ML340 tubes loaded in torsion. In black the localization curve: $\bar{\tau} = \bar{\tau}^u$ in the whole section of the tube; in colors, buckling curves for various L/D ratios.

The same approach has been adapted and used with the material law of the ML340 and the resulting design curves are shown in Figure 6.4. They are used in the rest of this section as "reference design curves". The linear hardening term is included whether or no has a negligible effect on the resulting design curves since the engineering stress/strain curves are also almost the same too (see Figure 6.1).

In the present work, both local and global failure modes are studied as instabilities. On the one hand, localization is due to a local material instability, and it was shown in section 4.4 that it can be captured using Rice's localization criterion when the material has a sufficiently small, yet positive, hardening modulus. On the other hand, buckling is a global instability and can be captured using Hill's stability criterion. It was shown in section 5.3.3 that localization in the tube loaded in torsion could also be captured using Hill's uniqueness analysis, and that both criteria are simultaneously fulfilled in the FEM framework once ellipticity is lost through the thickness of the tube. Therefore, in order to distinguish both phenomena, two independent parametric studies are presented: buckling in section 6.1.2 and localization in section 6.1.3.

First the global uniqueness analysis is performed to extract the critical loads for various geometries with the saturating material properties (without linear hardening), and the results presented in section 6.1.2. In section 6.1.3, the localization analysis based on the loss of ellipticity criterion is presented independently and performed to complete the design curves obtained in section 6.1.2. Then in section 6.1.4, the design curves for the non-saturating material properties (with linear hardening), are compared with the one obtained for the saturating material in order to see the influence of the linear hardening term on the critical loads. Finally, in [Lee and Ades, 1957] the authors state: "*No attempt has been made to obtain the effects of end restraint by an exact solution because of the immense amount of work involved.*". Therefore, in section 6.1.5, the design curves obtained with various weakened boundary conditions¹ (Flat/Fixed, Circular/Fixed, and Fixed/Fixed as detailed in section 5.3.1) are presented to evaluate the influence of the BCs on the critical loads.

¹ See chapter 5.

6.1.1 Numerical problem

The parametric studies are performed by computing the torsional response for various tube geometries: with D the external diameter, t the thickness, and L the length as shown in Figure 6.5.

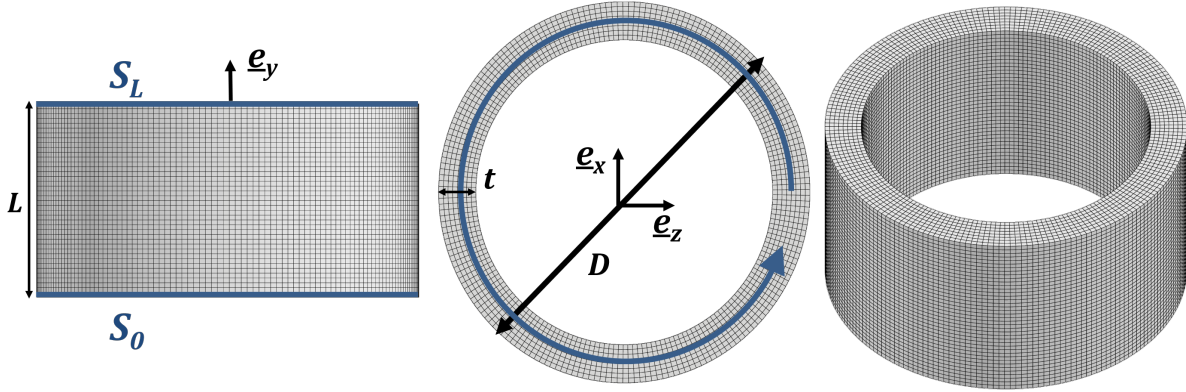


Figure 6.5: Scheme of a tube in torsion.

The end sections of the tube are denoted by S_0 (lower surface: $y = 0$) and S_L (upper surface $y = L$). For each combination of D/t and L/D ratios a regular mesh is designed to have at least three quadratic elements in the thickness for thin tubes, and up to six for thick ones. The loading is prescribed through Dirichlet BCs:

$$\underline{\mathbf{u}} = \underline{\mathbf{0}} \quad \forall \underline{\mathbf{X}} \in S_0 \quad (6.3)$$

$$\underline{\mathbf{u}} = (\underline{\mathbf{R}}(\theta) - \underline{\mathbf{I}}) \underline{\mathbf{X}} \quad \forall \underline{\mathbf{X}} \in S_L \quad (6.4)$$

where θ is the rotation angle (loading parameter).

6.1.2 Buckling analysis

In order to evaluate critical loads, the following parametric analysis is performed for different values of D/t and L/D : D/t varied over fifteen values from 4 to 70 with a logarithmic spacing; L/D is from the set of $\{0.5, 1, 2, 3.5, 5, 7.5, 10, 12\}$. Only L and D vary while $t = 1 \text{ mm}$ is kept constant for all models.

The buckling analysis is based on Hill's loss of uniqueness criterion (see chapter 3), which can be evaluated by computing the smallest eigenvalue of the global stiffness matrix $[\mathbf{K}]$ after convergence for each load increment. Given the boundary conditions defined in equations (6.9) and (6.10), the global uniqueness analysis in the present section can be identified to be the "Fixed/Fixed" case presented in section 5.3.1. Since 120 geometries were computed, the calculations are stopped as soon as an instability mode is captured in order to minimize the calculation time.

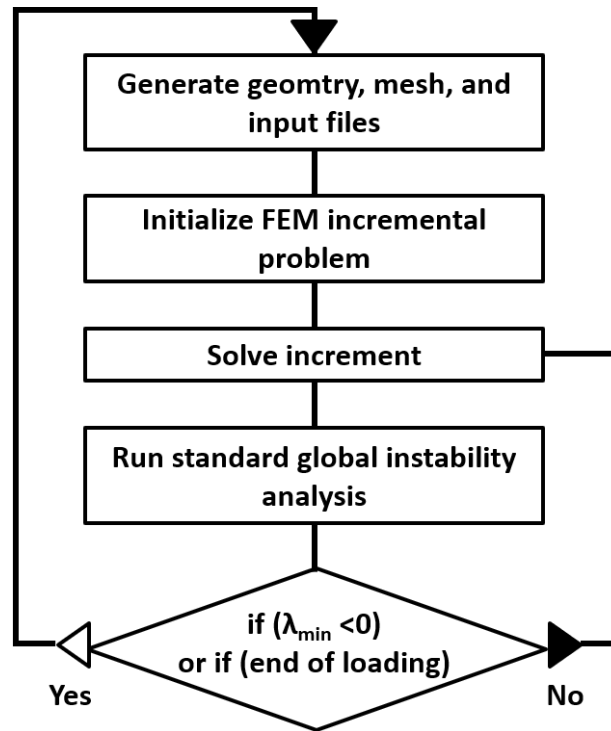


Figure 6.6: Numerical procedure for the evaluation of critical loads for the tube loaded in torsion.

The instability analysis for our range of parameters leads to a classification of the instability modes into five buckling shapes as shown in Figure 6.8. Such results are also observed for the buckling of thin plates loaded in shear for which the number of “bumps” for the first critical load depends on the ratios between width, length and thickness.

In order to compare the critical loads with the reference design curves, both are displayed in Figure 6.7. These critical loads actually contain three types of instabilities: buckling, localization, and maximum equivalent shear stress. The latter is considered separately: when the structure buckles during the simulation² or when localization occurs in one layer of elements, it may or may not be captured as an instability mode depending on the weakened boundary conditions considered (see section 6.1.5). In the present case, the Fixed/Fixed boundary conditions does not necessarily capture this behavior to be an instability. Therefore, there is one simulation for which the equivalent critical shear stress is evaluated as the maximum shear stress obtained during the simulation (it is marked with a black point in Figure 6.7).

Buckling and localization are relatively easy to identify since the structure of the numerical design curves is the same as the reference design curves: for each L/D ratio, there is a buckling curve that decreases when D/t increases, and it coincides with the curves for other L/D ratios when D/t is sufficiently small. These coincident global instability curves for different L/D ratios will be identified as the localization curve in section 6.1.3.

The computed numerical buckling loads are found to be consistent with reference design curves for large L/D and D/t ratios. In the plastic domain, the agreement is still relatively good but larger differences are observed for small L/D and large D/t ratios. These configurations are usually outside of the design domain. This difference is expected since the method presented in [Lee and Ades, 1957] is based on thin shell theory, which is assumed to be valid for thin

² When the solution naturally converges on the bifurcated branch due to numerical errors or slight geometrical imperfections

long structures. Still, the most pronounced differences are actually observed for the localization loads which are systematically higher than the ones obtained in the reference design curves. This is due to the use of a finite deformation framework and a post-necking identification (further explanations are given in section 6.1.3).

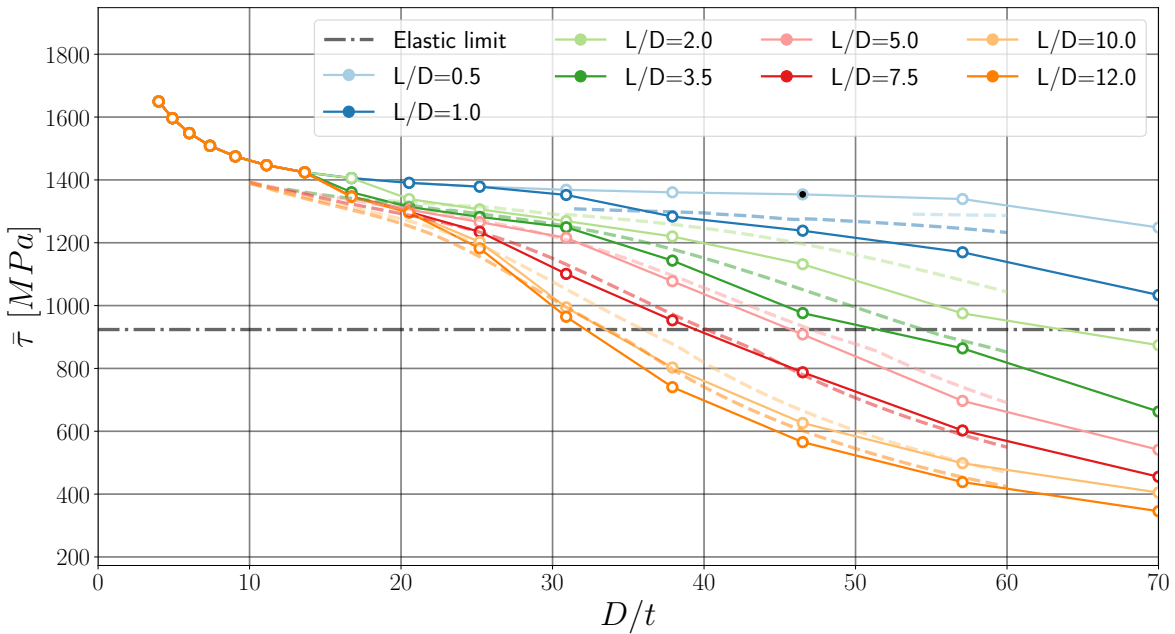


Figure 6.7: Comparison between the global instability results (full lines) and the reference design curves (dashed lines) for ML340 tubes loaded in torsion for various L/D ratios. Black filling: maximum equivalent shear stress obtained during simulation. White filling: global instability modes.

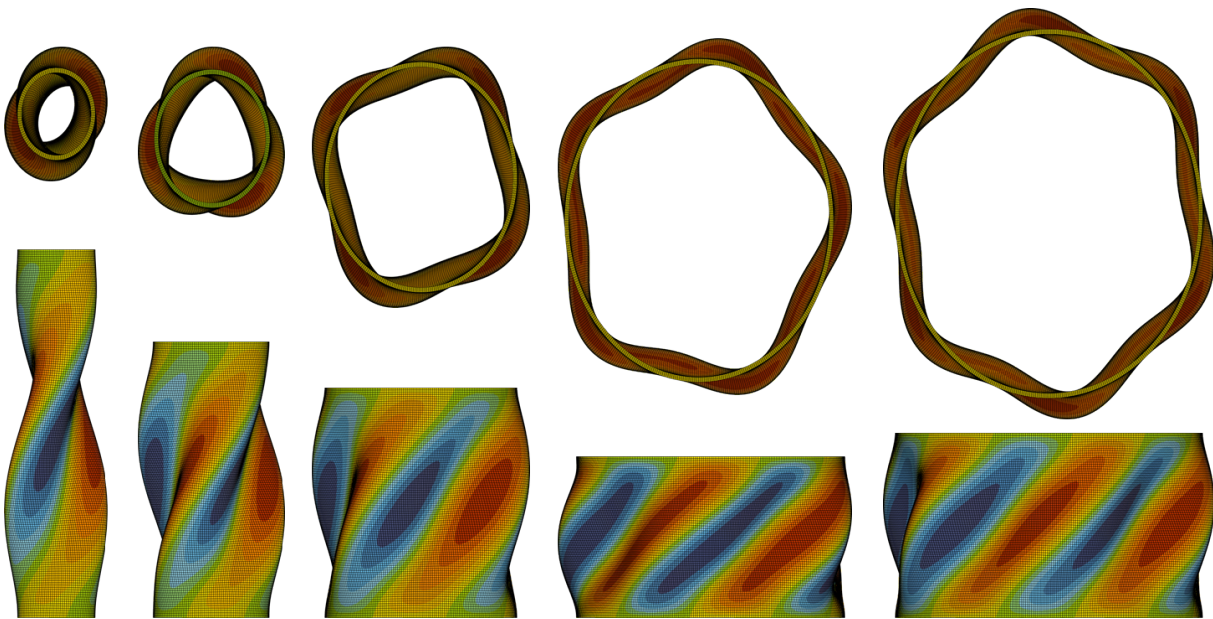


Figure 6.8: Buckling modes for various geometries. From left to right: 2, 3, 4, 5, and 6 lobes.

6.1.3 Localization analysis

In order to study localization (in the sense of Rice), the saturating constitutive law has been preferred (see Figure 6.1). The length L and the thickness t of the tube are fixed:

$$L = 1.5 \text{ mm} \qquad t = 1 \text{ mm} \qquad (6.5)$$

and D/t varied over thirty values from 4 to 70 with a logarithmic spacing. Each model is loaded in torsion as detailed in section 6.1.1.

The loss of ellipticity criterion is evaluated for each geometry at all Gauss Points. The angle θ and equivalent shear stress $\bar{\tau}$ are both extracted at the instant ellipticity is lost on the outer skin (first to occur) and the inner skin (last to occur). Due to the quick saturating properties of this material (see Figure 6.2) no significant difference is observed in the critical torque for those two instants. However, when the D/t ratio decreases, the difference is more pronounced in terms of localization angle (see Figure 6.9).

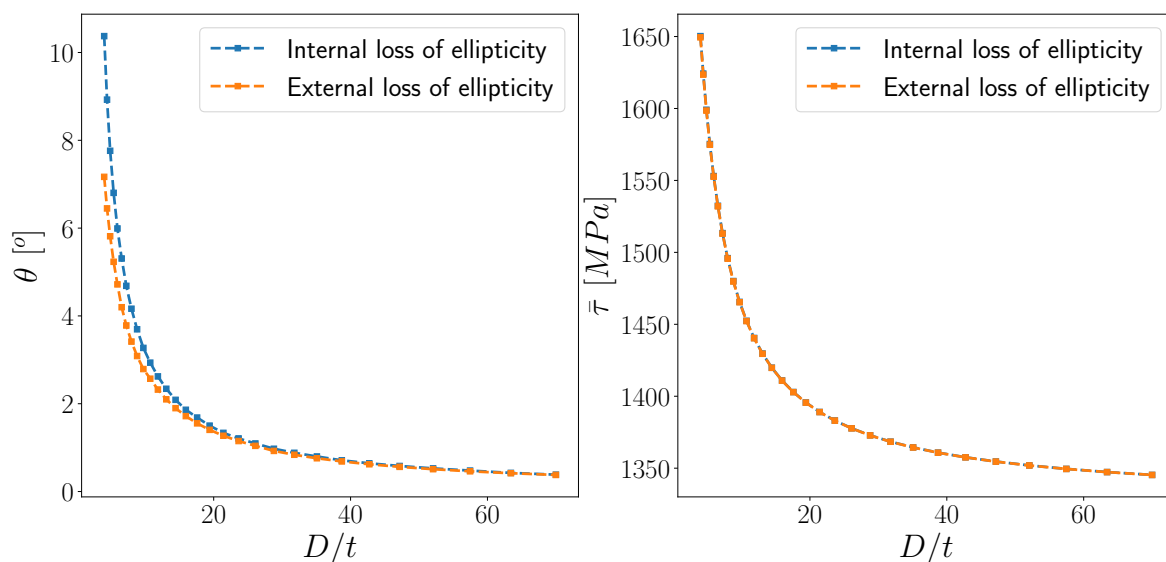


Figure 6.9: ML340 tubes loaded in torsion: angle θ and equivalent shear stress $\bar{\tau}$ at loss of ellipticity on the inner and outer skin for various D/t ratios.

Finally, in order to complete the comparison between the reference design curves and our analysis in a full finite deformation framework³ the localization curves are added to the global instability curves in Figure 6.11. Also, to simplify comparison for the localization alone, both localization curves are plotted in Figure 6.10.

³ This being only possible when a post-necking behavior is well identified.

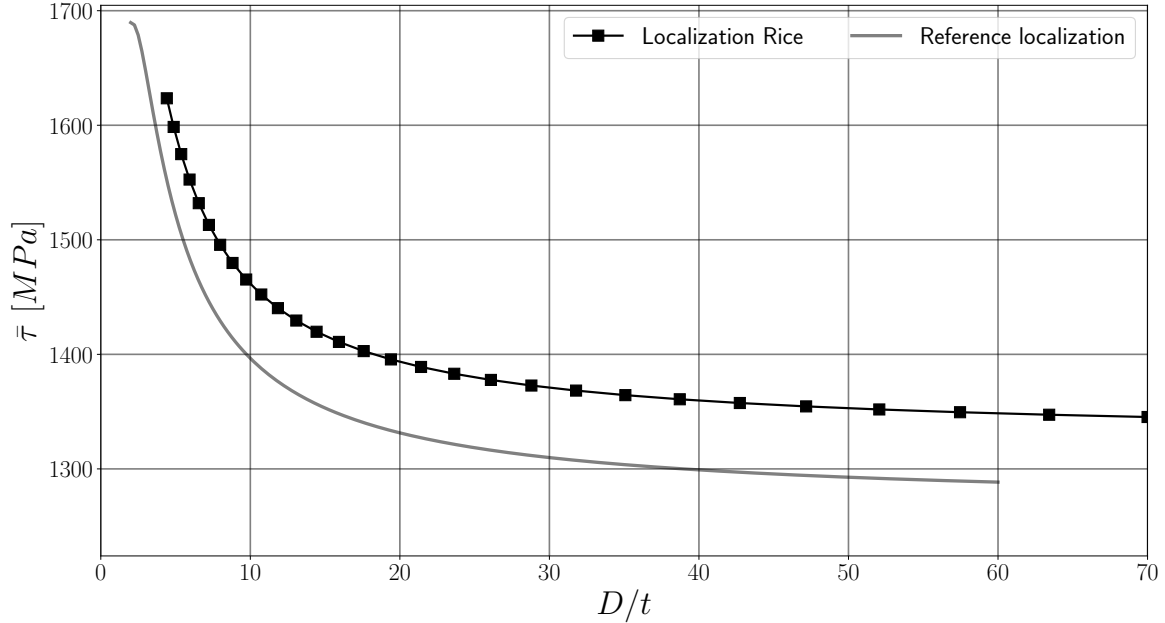


Figure 6.10: Comparison between the local instability results (localization in the sense of Rice) and the reference design curves (maximum engineering shear stress in the whole section) for ML340 tubes loaded in torsion. They differ by 5%.

For large D/t ratios, the difference of 5% is directly related to the finite deformation framework. It can be seen in Figure 6.2, that the maximum tensile stress R_m is reached before the maximum true stress saturates. The difference between the saturating shear stress and the maximum engineering stress is evaluated to be of 5% as well. Since the maximum equivalent shear stress evaluated in [Lee and Ades, 1957] is based on the engineering stress curve, the same difference is observed.

The ML340 steel is a material that possesses a high yield stress and hardening that saturates quickly. In other words, the reduction of section in the tensile experiment does not largely affect the difference between maximum engineering stress and maximum true stress. However, much larger differences can be observed for materials with a slower saturation, as presented in section 6.2.

Finally, by adding the localization curves in figure 6.11, the picture is complete. The global instability modes obtained for small D/t regardless of the L/D ratio merge with the localization curve. This confirms the initial proposal: localization can be evaluated using a material instability criterion and buckling using a global instability analysis. Also, experimental results for samples that failed after strain localized in a thin shear band are positioned on the design curves. They perfectly match the localization analysis.

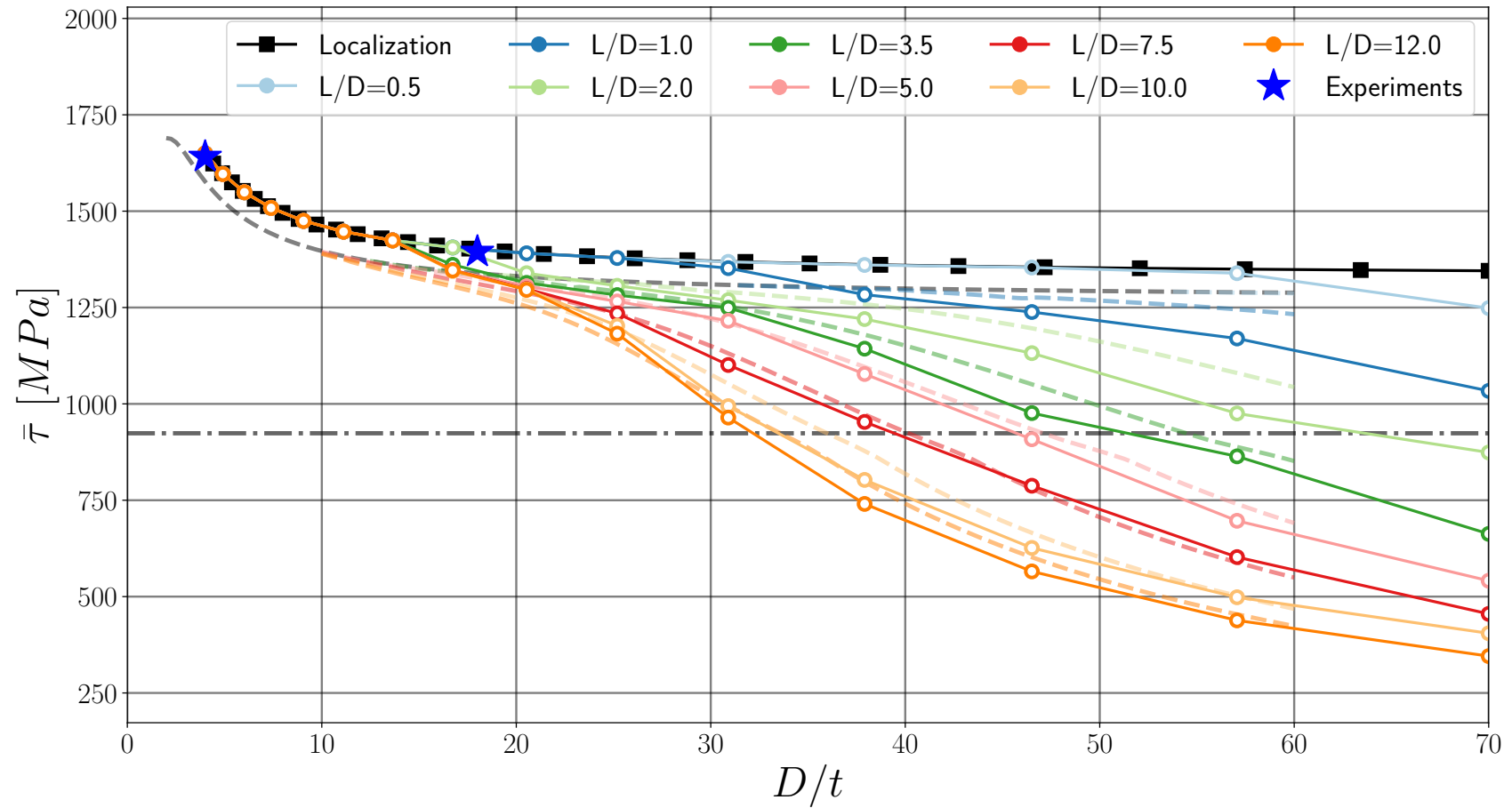


Figure 6.11: Comparison between the global instability results (full lines) and the reference design curves (dashed lines) for ML340 tubes loaded in torsion. Black filling: maximum equivalent shear stress obtained during simulation. White filling: global instability modes. Blue stars: experimental results.

6.1.4 Consequences of linear hardening

At the beginning of this section it was assumed that the linear hardening term could be neglected to study localization and that it would not impact the buckling analysis due to its small magnitude. To verify this assumption, a similar parametric study has been performed with the complete material law identified in [Defaïsse et al., 2018]. However, to reduce the computational costs, fewer D/t and L/D ratios have been investigated. Results are shown in Figure 6.12. On the one hand, both analyses are totally consistent in terms of buckling curves; on the other hand a strong difference is observed for localization. In fact, localization did not emerge when the linear hardening term was considered. It can then be concluded that the material law with the linear hardening term is not a suitable model to capture localization.

6.1.5 Weakened stability analysis

As discussed in section 5.3.1, the kinematic conditions prescribed to load the tube in torsion have an impact on the global instability analysis. In fact, the basic instability analysis corresponds to the Fixed/Fixed case. The weakened stability analysis will now be applied to the Flat/Fixed and Circular/Fixed cases to a wider set of geometries. The weakened boundary conditions are defined by:

$$\text{Fixed/Fixed: } \begin{cases} \Delta \underline{\mathbf{u}} = \underline{\mathbf{0}} & \forall \underline{\mathbf{X}} \in S_0 \\ \Delta \underline{\mathbf{u}} = \underline{\mathbf{0}} & \forall \underline{\mathbf{X}} \in S_L \end{cases} \quad (6.6)$$

$$\text{Circular/Fixed: } \begin{cases} \Delta \underline{\mathbf{u}} \cdot \underline{\mathbf{e}}_r = 0 & \forall \underline{\mathbf{X}} \in S_0 \\ \Delta \underline{\mathbf{u}} = \underline{\mathbf{0}} & \forall \underline{\mathbf{X}} \in S_L \end{cases} \quad (6.7)$$

$$\text{Flat/Fixed: } \begin{cases} \Delta \underline{\mathbf{u}} \cdot \underline{\mathbf{e}}_y = 0 & \forall \underline{\mathbf{X}} \in S_0 \\ \Delta \underline{\mathbf{u}} = \underline{\mathbf{0}} & \forall \underline{\mathbf{X}} \in S_L \end{cases} \quad (6.8)$$

The results are shown in Figure 6.13. Five main trends can be identified:

- The Flat/Fixed case is always less stable than the Circular/Fixed case, which is always less stable than the Fixed/Fixed case;
- The various weakened boundary conditions have no consequence on the localization curve (but they have an impact on the number of instability modes);
- For some geometries, the Flat/Fixed case captures buckling while the other two capture localization;
- The influence of the boundary conditions is less pronounced for large L/D ratios or small D/t ratios;
- The Flat/Fixed and Circular/Fixed always captures instabilities (no markers are filled in black).

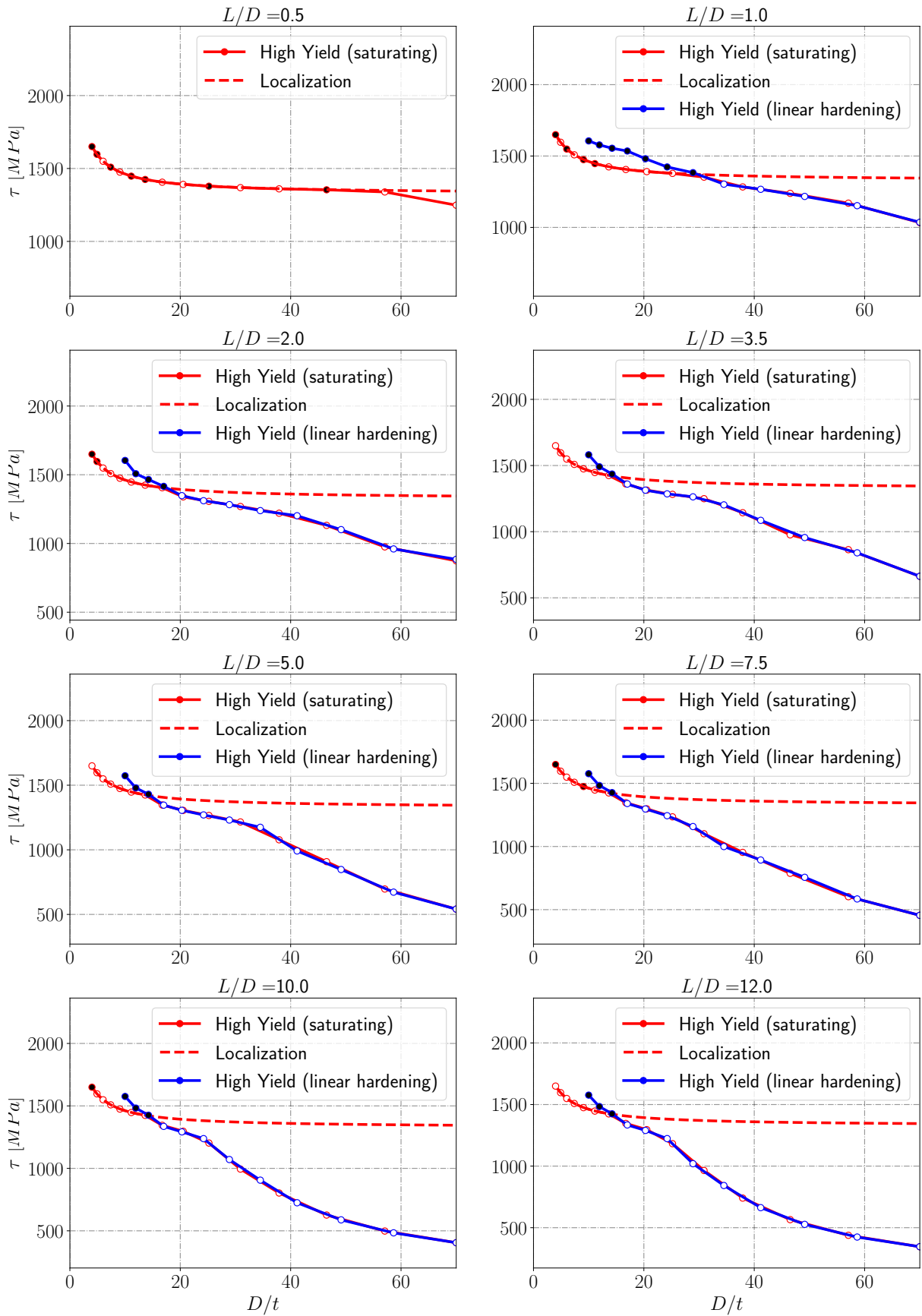


Figure 6.12: Design curves for ML340 tubes loaded in torsion. In blue, material law with the linear hardening term; in red, material law without the linear hardening term (saturating). Black filling: maximum equivalent shear stress obtained during simulation. White filling: global instability modes.

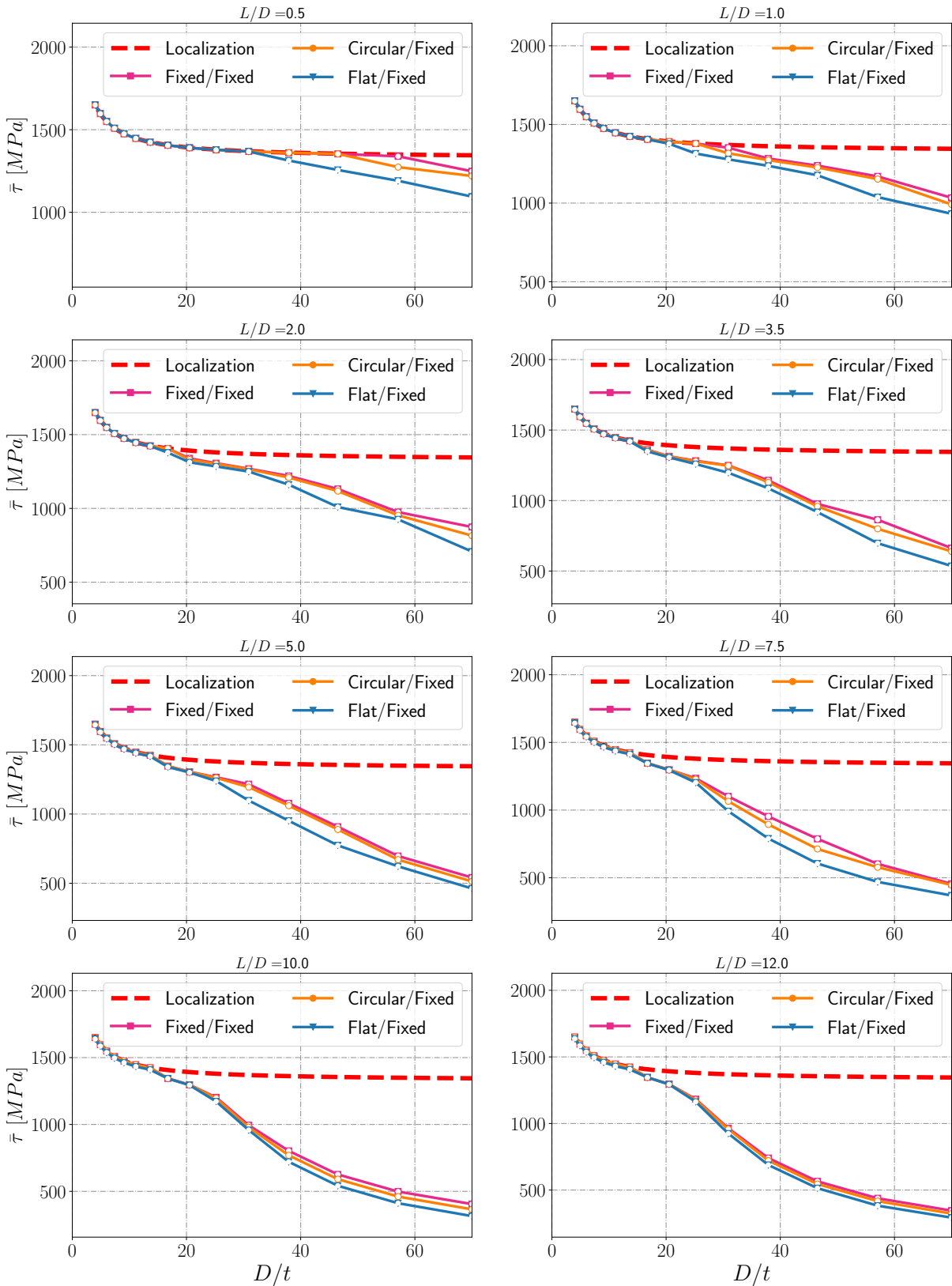


Figure 6.13: Design curves for ML340 tubes loaded in torsion for various weakened boundary value problems. Three cases are considered: Flat/Fixed, Circular/Fixed and Fixed/Fixed (see section 5.3.1).

6.2 High yield vs slow saturating hardening

When designing an aeronautical structure, a number of criteria have to be fulfilled. For some specific structures, these criteria might concern the ultimate load that the structure can sustain for various loading directions. In the present section, it is proposed to focus on the ultimate load that a tube⁴ can sustain in torsion when the yield criterion slowly saturates, and the material reaches large strains.

Generally, two main criteria are used to compare materials: maximum tensile strength, and first yield stress. In this section, two materials with lower yield stresses and the same maximum tensile strength as ML340 are investigated to see how the shape of the tensile curve can impact the design curves for tubes loaded in torsion (see figure 6.14). In fact, ML340 is a material that possesses a quick saturating yield stress while the other two exhibit a slow saturating yield stress, even after necking⁵ (see Figure 6.15). Therefore, another objective in this section is to compare for such materials the critical loads obtained with the method presented in [Lee and Ades, 1957] with the results obtained in the full finite deformation framework.

6.2.1 Materials and weakened problems

Three materials are investigated and shown in Figure 6.14 in terms of engineering stress/s-train curves, and in Figure 6.15 in terms of true stress/strain curves. They are all based on the same formulation as ML340 given in section 6.1 but they differ only in terms of yield criterion:

- High Yield (saturating ML340): $R(p) = 1600 + 189(1 - e^{-81p}) + 509(1 - e^{-773p})$;
- Low Yield (fictitious material): $R(p) = 800 + 800(1 - e^{-30p}) + 800(1 - e^{-50p})$;
- High Ductility (fictitious material): $R(p) = 400 + 1450(1 - e^{-200p}) + 1000(1 - e^{-10p})$.

The loading is prescribed through Dirichlet BCs:

$$\underline{\mathbf{u}} = \underline{\mathbf{0}} \quad \forall \underline{\mathbf{X}} \in S_0 \quad (6.9)$$

$$\underline{\mathbf{u}} = (\underline{\mathbf{R}}(\theta) - \underline{\mathbf{I}}) \underline{\mathbf{X}} \quad \forall \underline{\mathbf{X}} \in S_L \quad (6.10)$$

where θ is the rotation angle (loading parameter). Finally, the three different materials are studied for the following weakened boundary conditions:

$$\text{Fixed/Fixed: } \begin{cases} \Delta \underline{\mathbf{u}} = \underline{\mathbf{0}} & \forall \underline{\mathbf{X}} \in S_0 \\ \Delta \underline{\mathbf{u}} = \underline{\mathbf{0}} & \forall \underline{\mathbf{X}} \in S_L \end{cases} \quad (6.11)$$

$$\text{Circular/Fixed: } \begin{cases} \Delta \underline{\mathbf{u}} \cdot \underline{\mathbf{e}}_r = 0 & \forall \underline{\mathbf{X}} \in S_0 \\ \Delta \underline{\mathbf{u}} = \underline{\mathbf{0}} & \forall \underline{\mathbf{X}} \in S_L \end{cases} \quad (6.12)$$

$$\text{Flat/Fixed: } \begin{cases} \Delta \underline{\mathbf{u}} \cdot \underline{\mathbf{e}}_y = 0 & \forall \underline{\mathbf{X}} \in S_0 \\ \Delta \underline{\mathbf{u}} = \underline{\mathbf{0}} & \forall \underline{\mathbf{X}} \in S_L \end{cases} \quad (6.13)$$

⁴ Tubes are very important for the aeronautical industry since one of the main components of landing gears or an engine is the shafts that links the different rotating parts together.

⁵ Thus, they reach large strains while still possessing a strong hardening modulus.

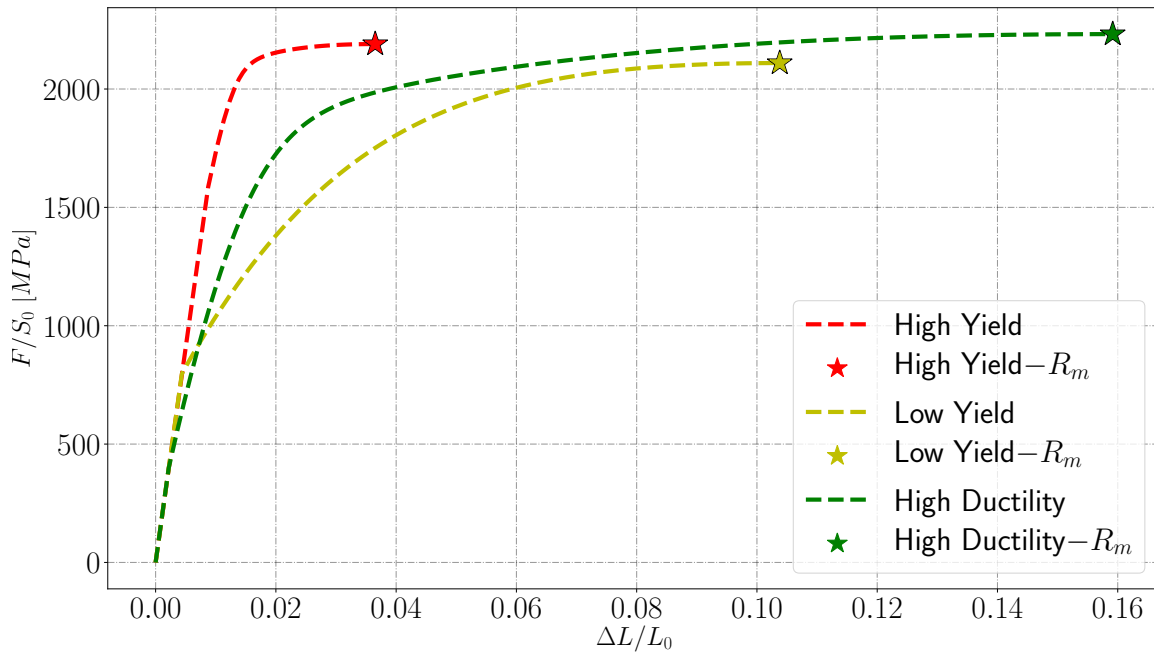


Figure 6.14: Comparison of the three engineering curves with approximately the same maximum tensile force (R_m).

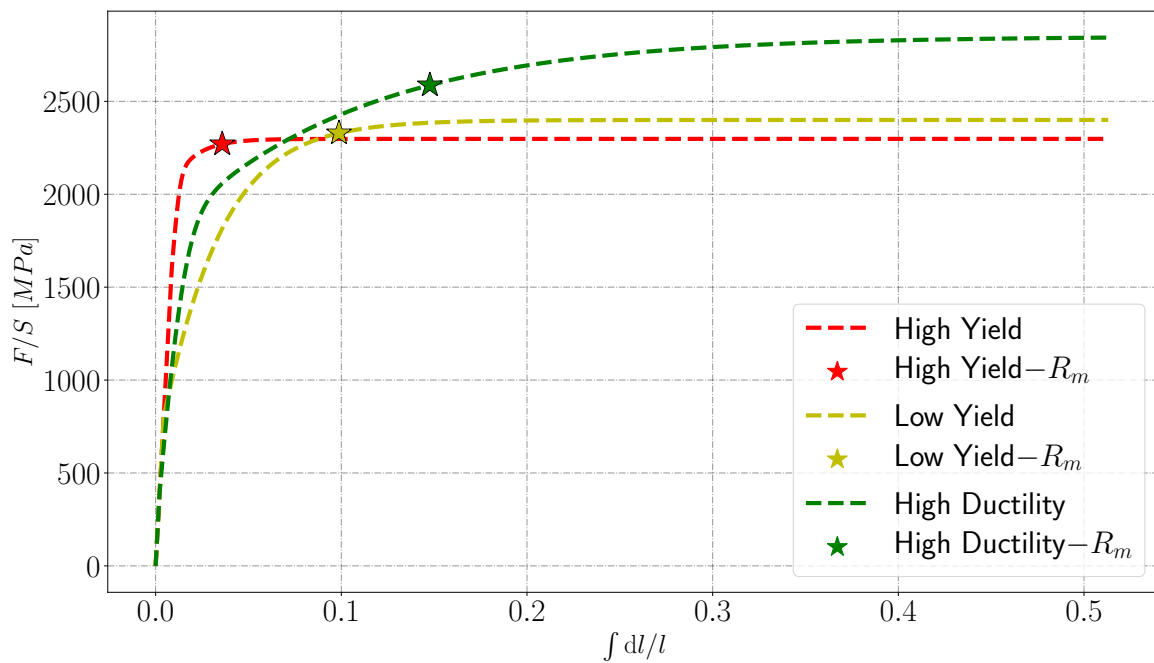


Figure 6.15: Comparison of the three true curves with approximately the same maximum tensile force (R_m).

6.2.2 Influence of the finite deformation framework: comparison with reference curves

Results for ML340 were already thoroughly presented in section 6.1. They correspond to the High Yield material in this section and were shown to be consistent with the reference design curves, excepting the localization domain. The results in terms of design curves obtained in a finite deformation framework are presented for the Low Yield and High Ductility materials and compared with their reference design curves respectively in Figures 6.18 and 6.19.

In particular, it was observed that the localization criterion from the reference design curves was too conservative by 5% (see Figure 6.9). This difference was identified to be due to the post-necking identification of the true behavior. For the Low Yield and High Ductility materials the difference between the maximum engineering tensile stress and the limit true stress is more significant (see Figure 6.15). Therefore, the differences between the reference design curves and the full finite deformation framework are more significant: 14% for the Low Yield material (see Figure 6.16); 28% for the High Ductility material (see Figure 6.17).

It is observed in Figures 6.18 and 6.19 that the differences for the buckling curves are also significant, even for large D/t ratios for the High Ductility material. Also, the transition between localization and buckling for the High Ductility material is relatively abrupt when the equivalent shear stress increases beyond 1200 MPa . This is due to the sudden change in hardening modulus observed around⁶ 2000 MPa for this material (see Figure 6.15).

Finally, for a given L/D ratio, the D/t ratio for which the geometry starts to buckle is larger in the finite deformation framework than in the reference design curves. This is due to the fact that the small deformation framework underestimates the tangent modulus, and thus leads to earlier buckling. This result has very important consequences concerning design methods and is re-discussed in section 6.2.5.

6.2.3 Comparison between materials

In section 6.2.2, it was observed that the finite deformation framework allowed us to identify significantly higher critical loads than the reference method (this result was already moderately observed in section 6.1). In the present section, it is shown that not only the identified critical loads are larger but the conclusions that can be drawn when comparing two materials are also different. For this purpose, the design curves for the three materials considered are compared in Figure 6.20 for the reference results, and in Figure 6.21 for the global instability analysis in the full finite deformation framework.

On the one hand, if materials are compared with the reference method, the following conclusions would be drawn:

- The High Yield material is always preferred to the Low Yield material;
- The High Ductility material is slightly better than the High Yield material in terms of localization but significantly weaker in terms of buckling loads;
- The localization curves are essentially the same.

On the other hand, if the design curves for the various materials are compared within the full finite deformation framework, much richer and opposing conclusions are drawn:

- The High Yield material is always preferred in the buckling;
- The Low Yield material is preferred to the High Yield material in the localization domain;

⁶ $1200\sqrt{3} \simeq 2000$.

- The High Ductility material is significantly better than the High Yield material in terms of localization but relatively weaker in terms of buckling domain;
- The localization curves for the High yield and Low Yield materials are essentially the same (but interchanged) and both are significantly weaker than the High Ductility material.

6.2.4 Weakened stability analysis

Finally, to complete the analysis for the High Ductility and Low Yield materials, the results for various weakened stability problems are presented in Figure 6.22 and in Figure 6.23 respectively. The conclusions are qualitatively the same as the one drawn in section 6.1.5 but are more pronounced.

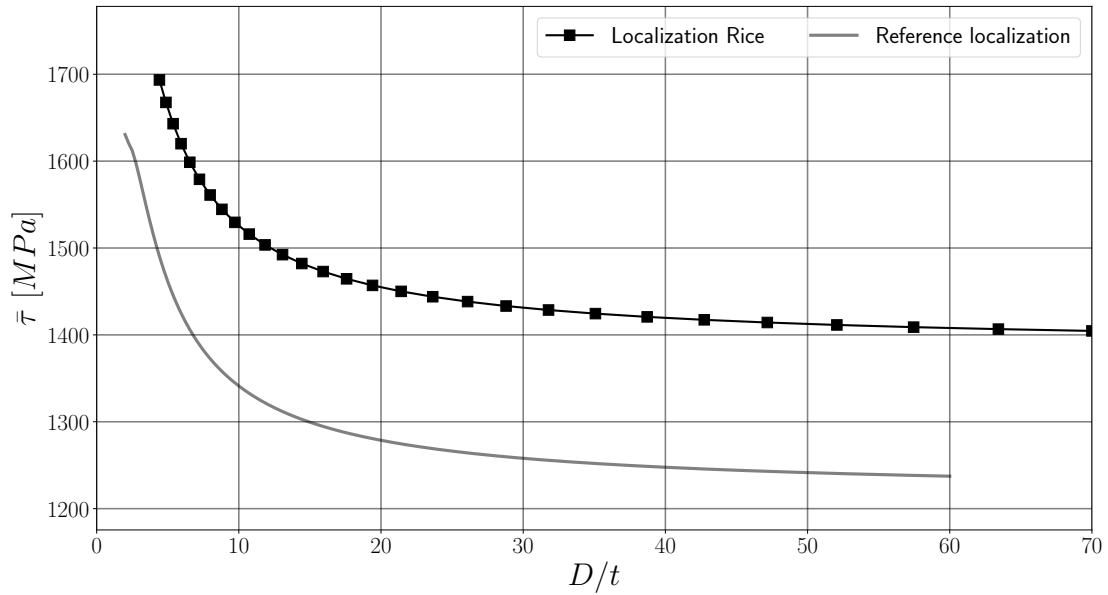


Figure 6.16: Comparison between the local instability results (localization in the sense of Rice) and reference design curves (maximum engineering shear stress in the whole section) for ML340 tubes loaded in torsion. for the Low Yield material. They differ by 14%.

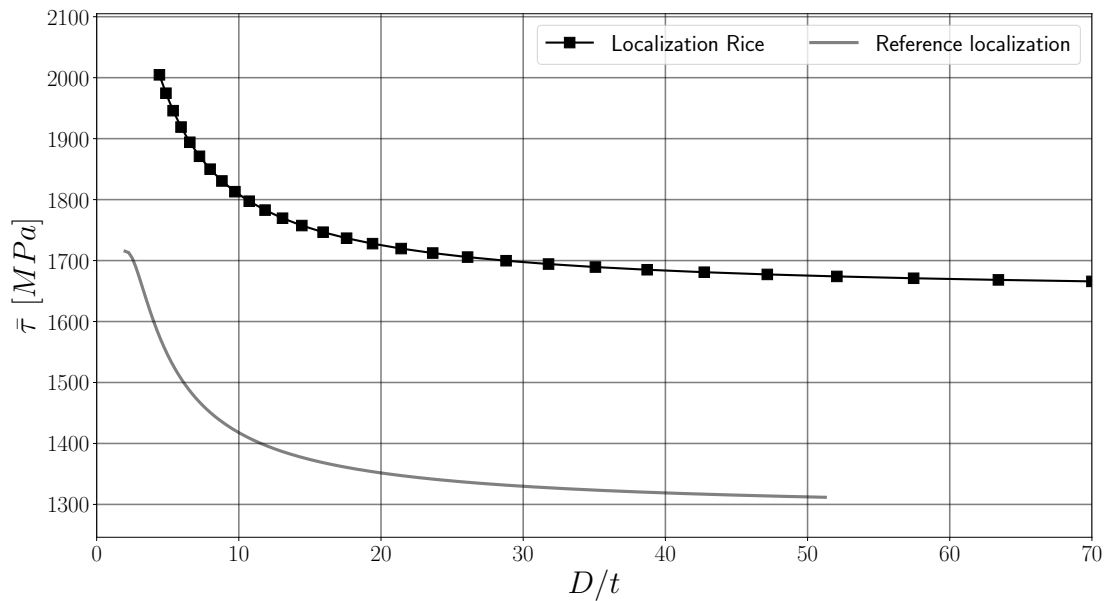


Figure 6.17: Comparison between the local instability results (localization in the sense of Rice) and reference design curves (maximum engineering shear stress in the whole section) for ML340 tubes loaded in torsion. for the High Ductility material. They differ 25%.

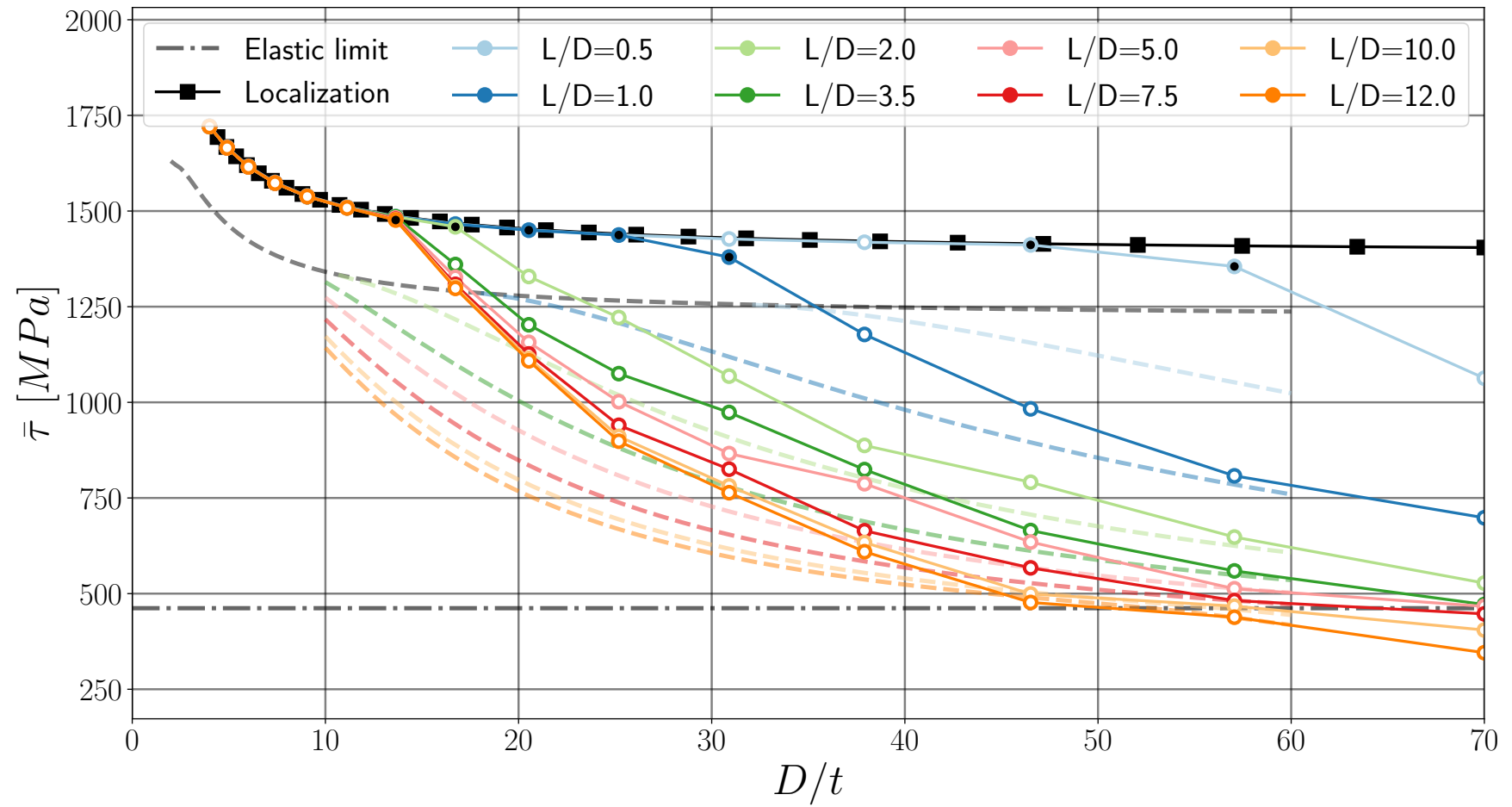


Figure 6.18: Low Yield material: Comparison between the global instability results (full lines) and the reference design curves (dashed lines) for tubes loaded in torsion. Black filling: maximum equivalent shear stress obtained during simulation. White filling: global instability modes.

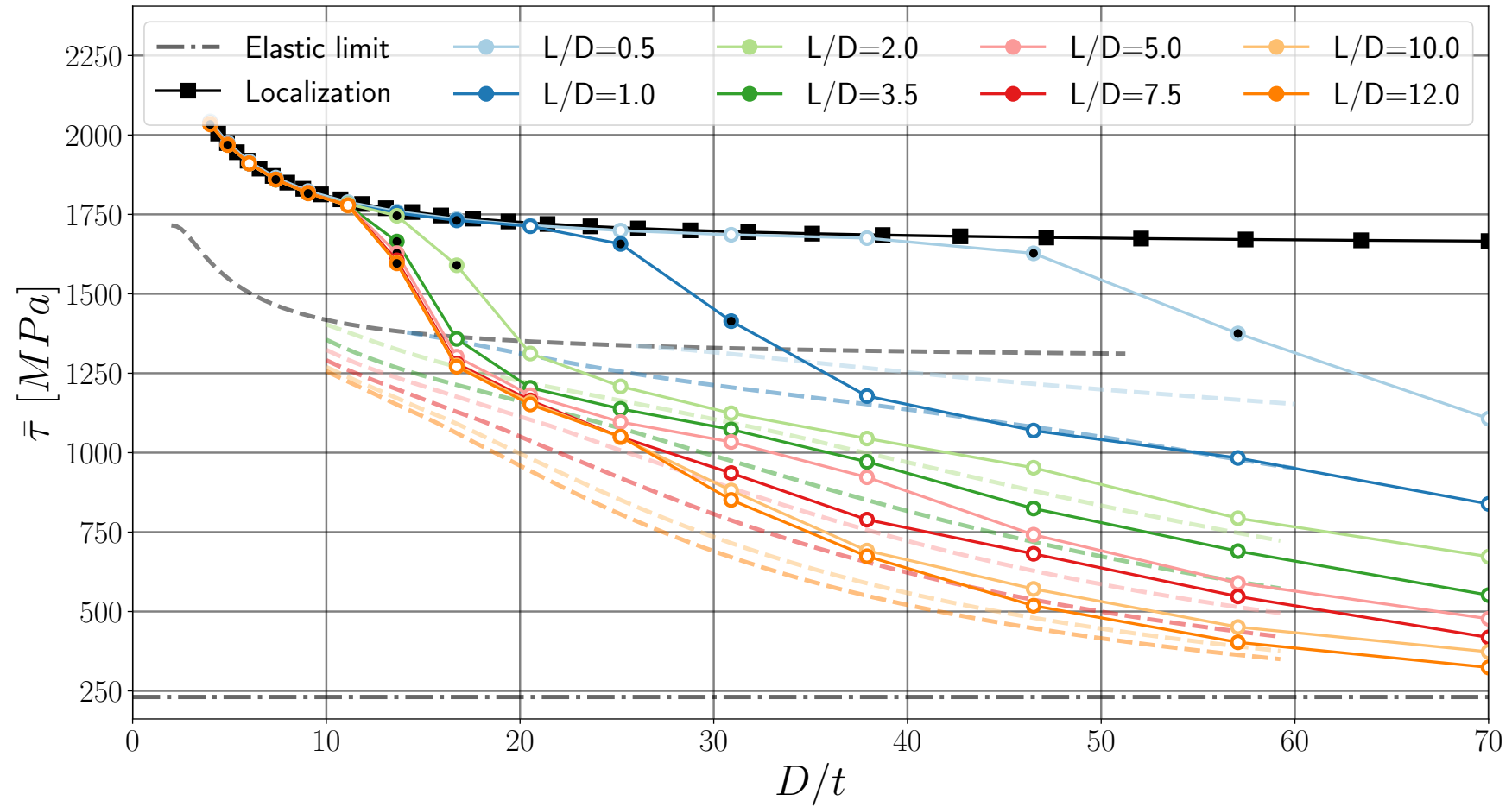


Figure 6.19: High Ductility material: Comparison between the global instability results (full lines) and the reference design curves (dashed lines) for tubes loaded in torsion. Black filling: maximum equivalent shear stress obtained during simulation. White filling: global instability modes.

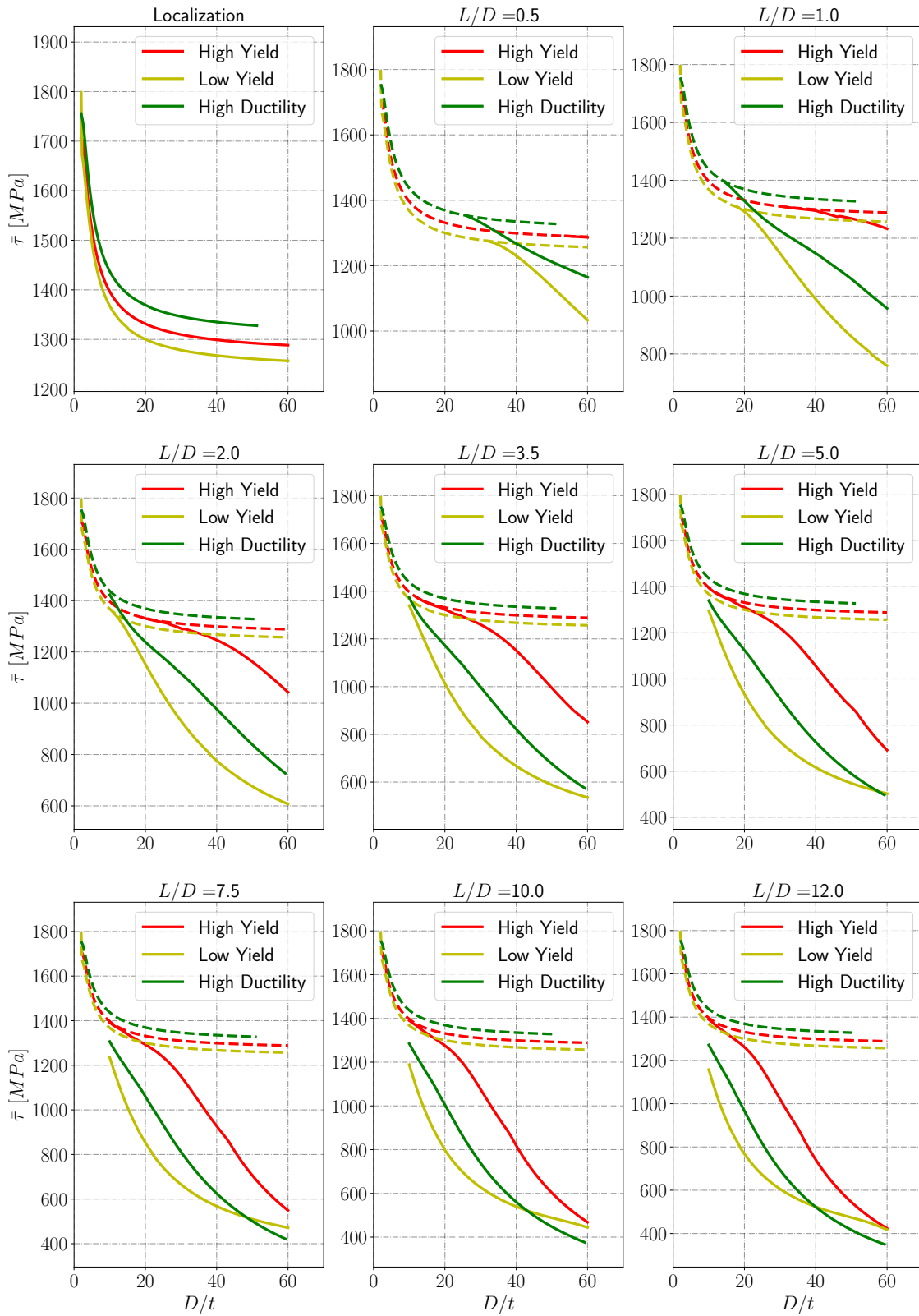


Figure 6.20: Reference design curves for the three materials considered for tubes loaded in torsion. Dashed lines: localization.

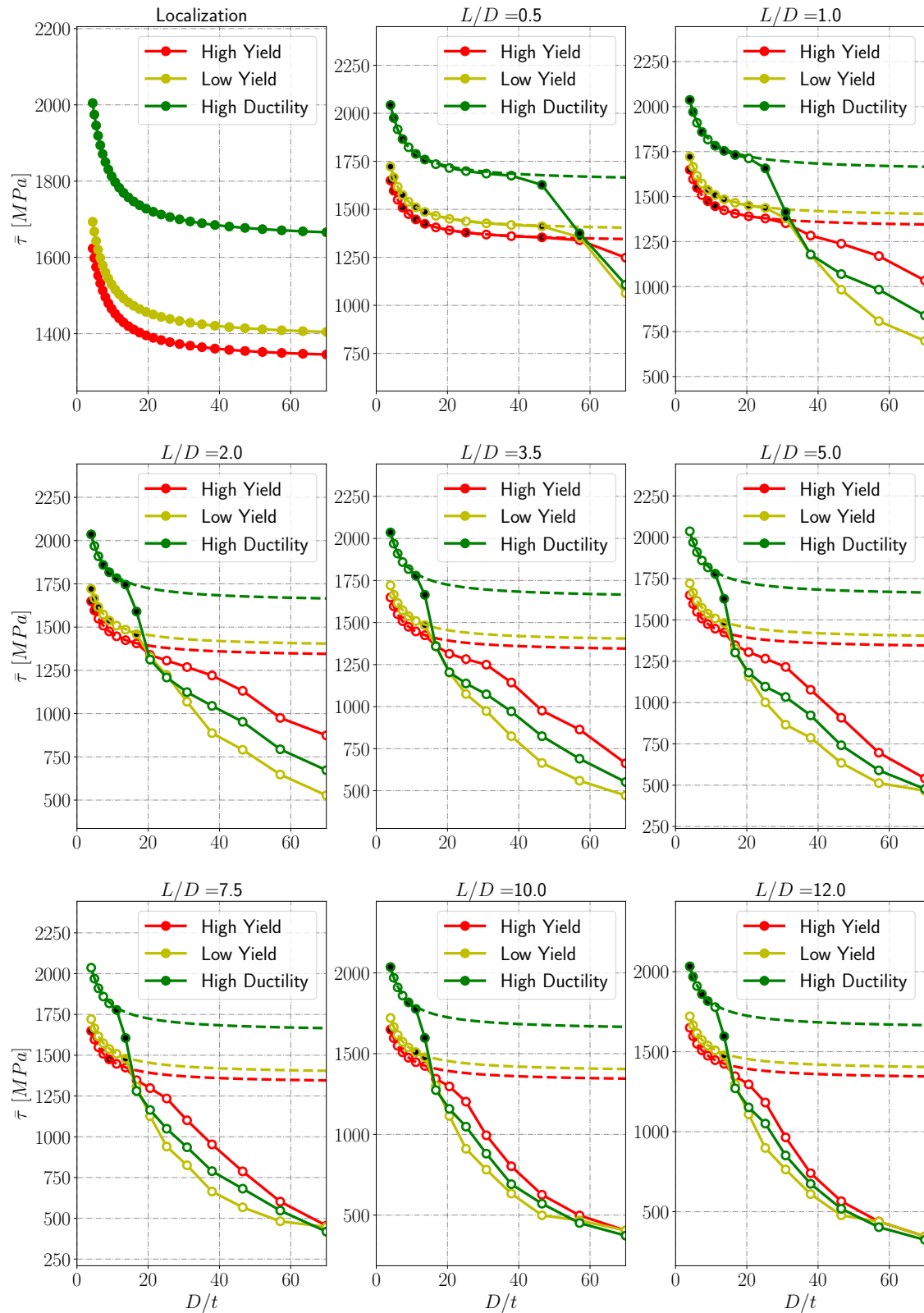


Figure 6.21: Design curves obtained with the global and local instability analyses in a full finite deformation for the three materials considered for tubes loaded in torsion. Dashed lines: localization. Black filling: maximum equivalent shear stress obtained during simulation. White filling: global instability modes.

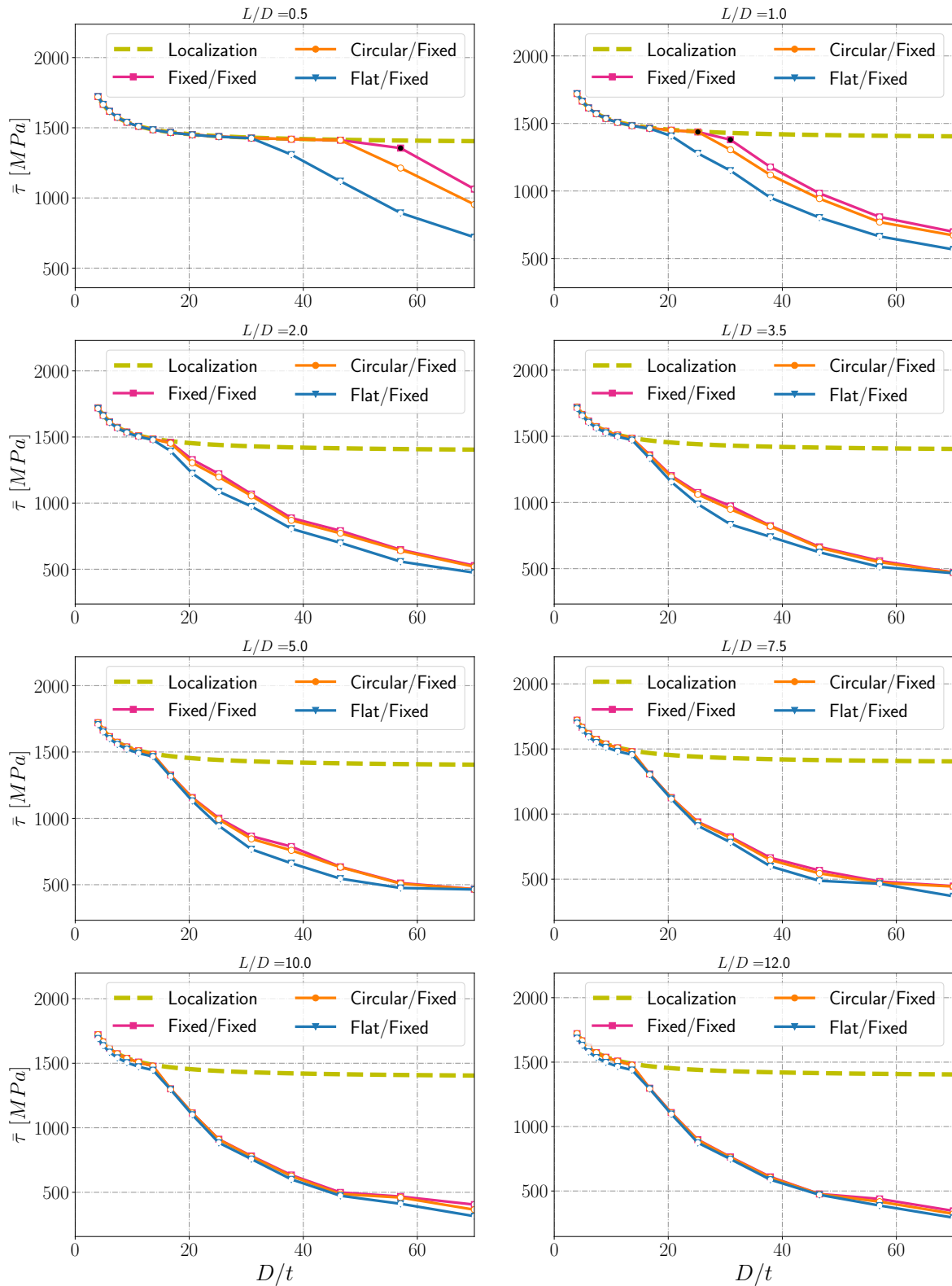


Figure 6.22: Low Yield material: Comparison of the design curves obtained with the weakened stability analysis for various BCs: Flat/Fixed, Circular/Fixed, Fixed/Fixed. Dashed lines: localization. Black filling: maximum equivalent shear stress obtained during simulation. White filling: global instability modes.

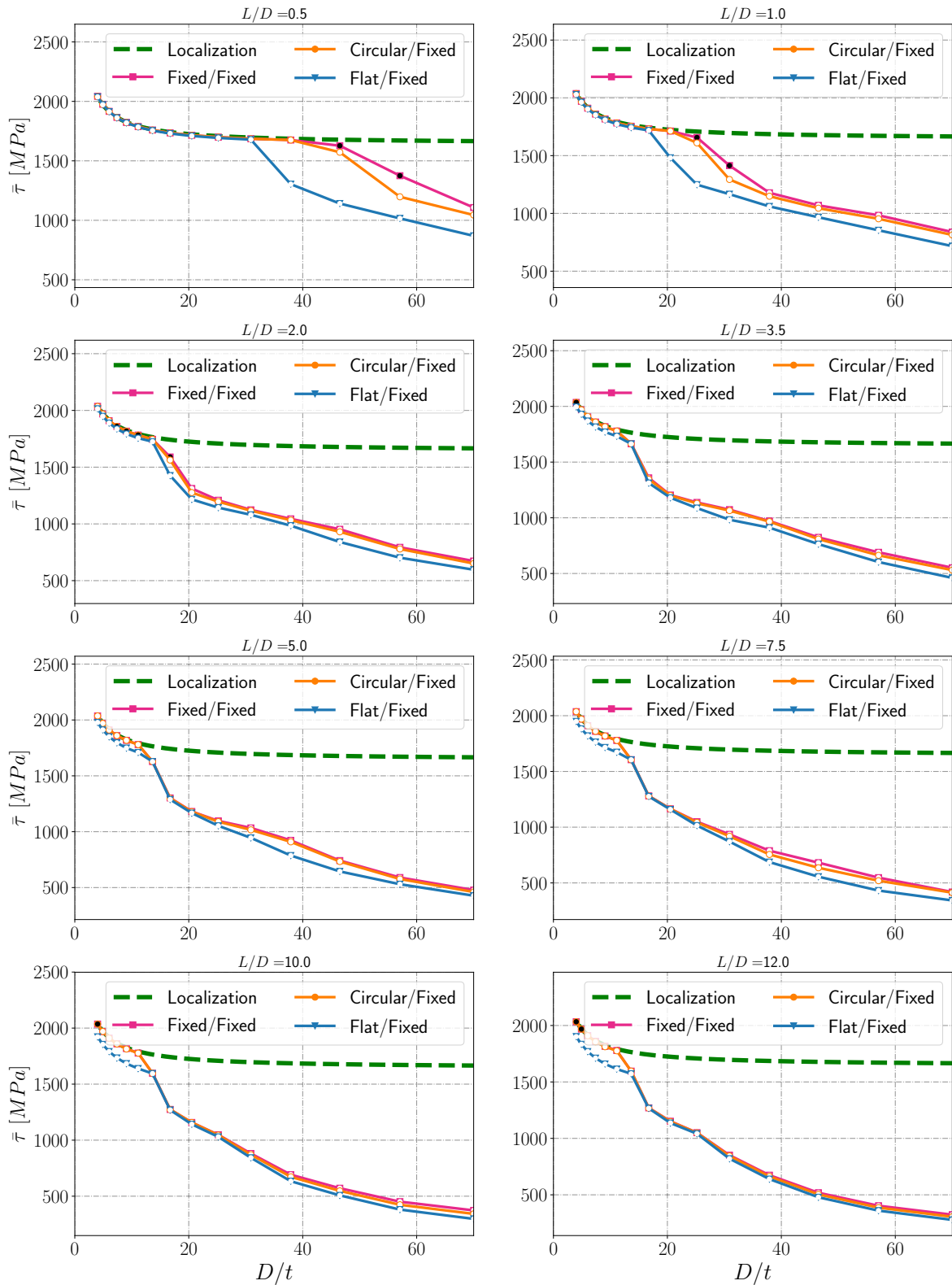


Figure 6.23: High Ductility material: Comparison of the design curves obtained with the weakened stability analysis for various BCs: Flat/Fixed, Circular/Fixed, Fixed/Fixed. Dashed lines: localization. Black filling: maximum equivalent shear stress obtained during simulation. White filling: global instability modes.

6.2.5 Discussion about design methods

Before starting the discussion about the design methods, it is important to remark that the present section is specific to tubes loaded in simple torsion and only focuses on the ultimate loads. Other loading directions might lead to different conclusions due to geometric effects: an obvious example is simply the case of a bar loaded in tension. Still there are structures like engine shafts, that are mainly loaded in simple torsion for which these conclusions seem to be useful.

Another remark concerns the analysis of the sensitivity to geometrical imperfections that was not performed in the present work. Even though the authors in [Lee and Ades, 1957] observe no significant effects of the imperfections on the critical loads, it must be kept in mind that their analysis was performed with a material that seems to have quick saturating properties. With slower saturating materials, like the High Ductility or Low Yield materials, the effects of geometrical imperfections may be more significant⁷. This would need further investigation.

Finally, it must be kept in mind that for aeronautical designs, there are other requirements than the ultimate load. Some requirements may concern the load associated to the first yield in the structure, in which case the two fictitious materials would most likely fail. Therefore, the aim of this section is not to propose new general design methods, but to gather the main tendencies observed in this parametric study in order to better understand the role of the various parameters.

First, it was observed that the buckling loads were mainly sensitive to the tangent modulus: for a given shear stress, the higher the tangent modulus, the more stable the structure is. In fact, it is shown in Figure 6.24 that plotting stress as a function of the hardening modulus already allows a relatively good comparison of the three materials. The trends observed for the buckling curves in Figure 6.21 are well reproduced.

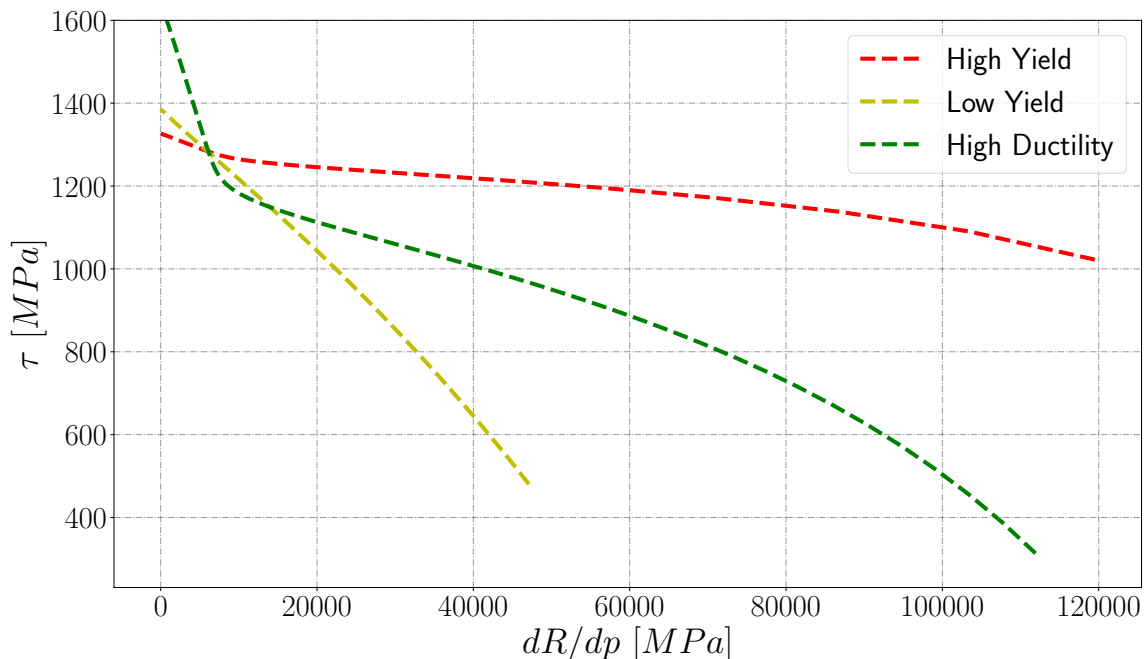


Figure 6.24: Evolution of shear stress τ as a function of the the tangent modulus dR/dp .

⁷ There always are extremely small errors in a numerical framework that could be interpreted as imperfections. It can be remarked in Figures 6.13 and 6.23 that there are more black points for the High Ductility material (that reaches large strains) than for the High Yield material. This could be an indicator of this statement.

For localization, it was observed that the driving parameter for the critical load was directly correlated with the maximum true shear stress. By reproducing the approach given in [Lee and Ades, 1957] for the localization criterion one gets (maximum shear stress in the whole section):

$$\tau^m = \lim_{p \rightarrow \infty} R(p)/\sqrt{3} \quad (6.14)$$

$$\bar{\tau}^u = \frac{2\tau^m D(R_e^3 - R_i^3)}{3(R_e^4 - R_i^4)} \quad (6.15)$$

where $\bar{\tau}^u$ denotes the maximum equivalent shear stress, and τ^m the maximum true shear stress. Comparing this approach with Rice's localization criterion leads to a perfect fit, as shown in Figure 6.25. This was naturally expected since the loss of ellipticity criterion is fulfilled for a vanishing hardening modulus in simple shear.

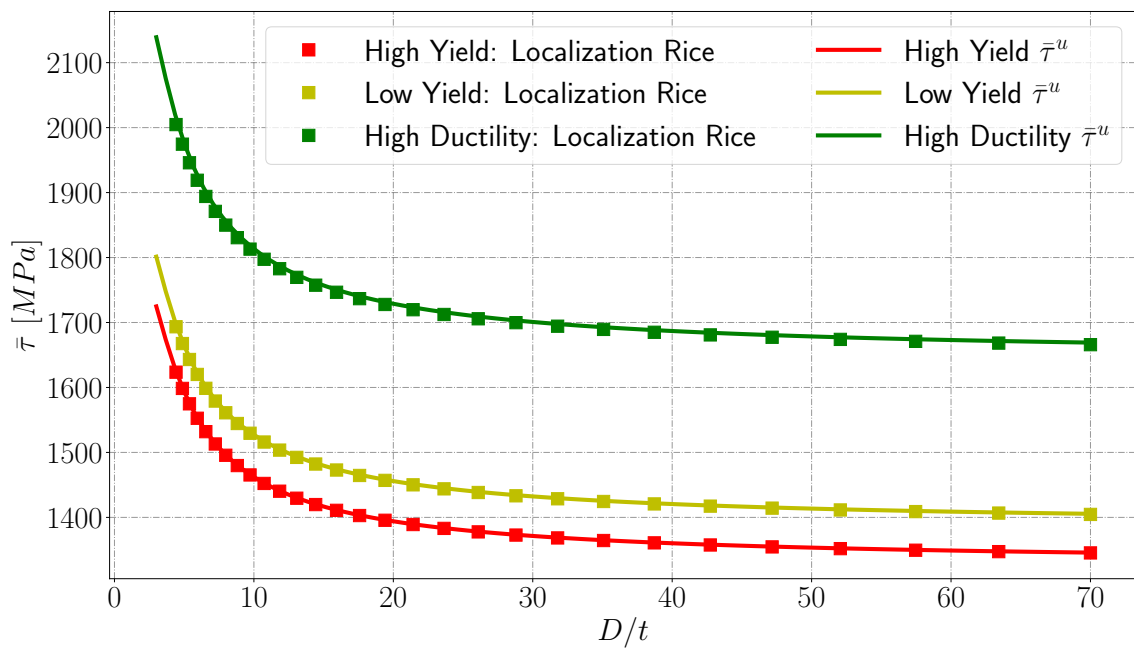


Figure 6.25: Comparison of the maximum equivalent true shear stress ($\bar{\tau}^u = \frac{2\tau^m D(R_e^3 - R_i^3)}{3(R_e^4 - R_i^4)}$) with the local instability analysis (Rice).

It was observed that the reference design curves did not necessarily identify the correct instability modes (see Figures 6.18 and 6.19): some geometries (D/t ratios around 10 for large L/D ratios) were identified to buckle in the reference curves while the global instability analysis identified localization. Then, using the reference design curves would lead to highly conservative results: buckling loads are usually more sensitive to geometrical imperfections than localization and would require higher safety coefficients; the identified buckling loads were significantly lower than the localization loads.

However, such an over-conservative design leaves room for weight optimization. To illustrate this statement, let us take an example:

Let us assume that we aim to build a tube that can sustain a torque $T^o = 20 \text{ kN.m}$, and that for some design restrictions its length must be of $L^o = 6 \text{ m}$ and its diameter of $D^o = 0.8 \text{ m}$. The question is now to know what is the minimal thickness t required to sustain the load T^o . For a

given thickness t , the required equivalent shear stress can be expressed:

$$\bar{\tau}^o(x) = \frac{T^o D^o}{\pi(R_e^o{}^4 - (R_e - \frac{D^o}{x})^4)} \quad (6.16)$$

where $x = D^o/t$. In this example (wisely chosen), $L/D = 7.5$. In Figures 6.26 and 6.27 , the design curves for $L^o/D^o = 7.5$ and $\bar{\tau}^o(x)$ are displayed for both the Low Yield and High Ductility materials. The critical D^o/t ratio can be identified to be the abscissa of the intersection point of $\bar{\tau}^o$ with the design curves. This gives:

- Low Yield material: $D^o/t^{ref} = 26$ with the reference curves and $D^o/t^{insta} = 30$ with the full finite deformation analysis. This means $t^{ref} = 30.8\text{ mm}$ and $t^{insta} = 26.7\text{ mm}$. This implies a reduction of 13% of the total mass of the tube.
- High Ductility material: $D^o/t^{ref} = 29.5$ with the reference curves and $D^o/t^{insta} = 32.5$ with the full finite deformation analysis. This means $t^{ref} = 27.1\text{ mm}$ and $t^{insta} = 24.6\text{ mm}$. This implies a reduction of 9% of the total mass of the tube.

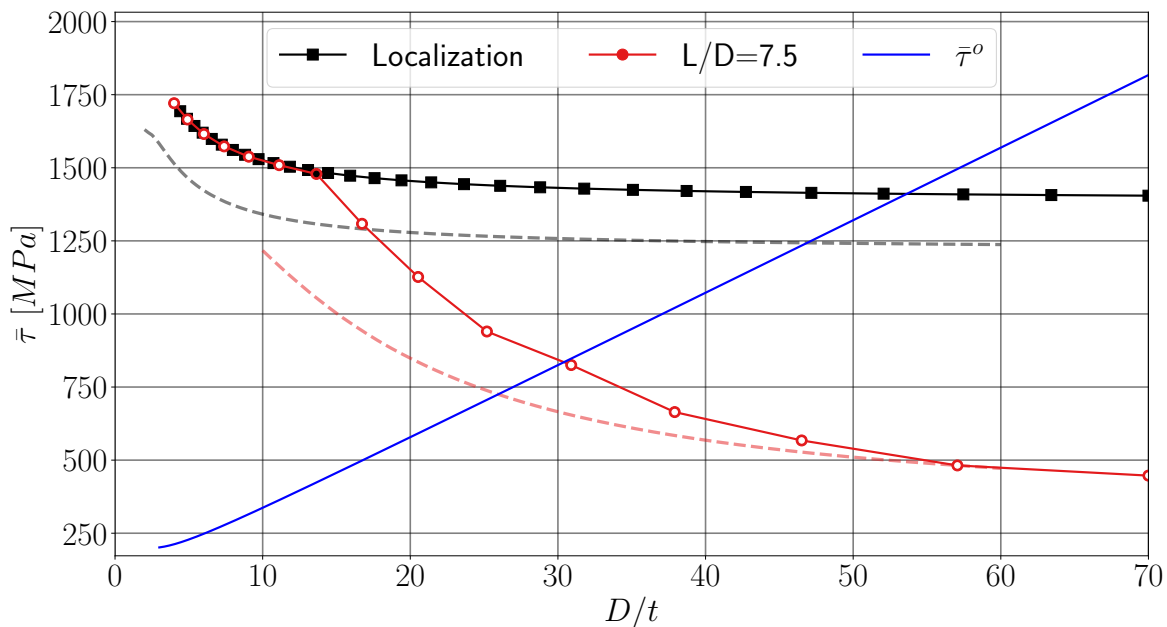


Figure 6.26: Design curves for the Low Yield material: Localization and buckling curve for $L^o/D^o = 7.5$ for both reference and instability analyses. $\bar{\tau}^o$ the equivalent shear stress to sustain a load of 20 kN.m with a diameter of $D^o = 0.8\text{ m}$.

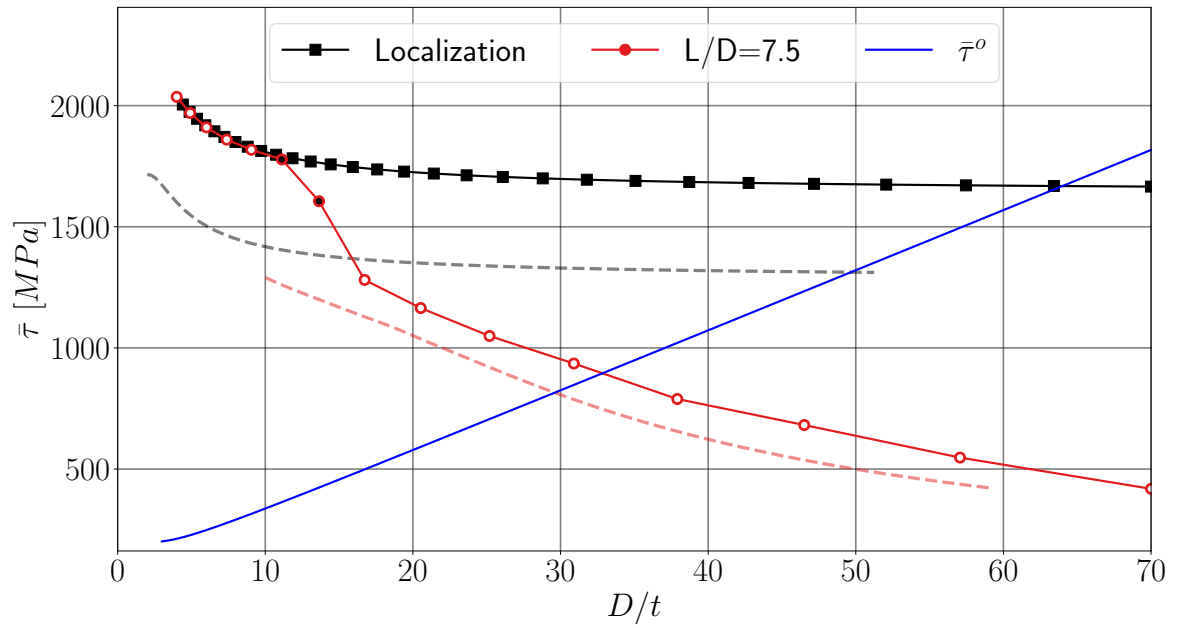


Figure 6.27: Design curves for the High Ductility material: Localization and buckling curve for $L/D = 7.5$ for both reference and instability analyses. $\bar{\tau}^o$ the equivalent shear stress to sustain a load of $20kN.m$ with a diameter of $D = 0.8m$.

All results in terms of design curves (comparison reference/instability, material comparisons, and weakened boundary conditions) are gathered in section 8.7.

6.3 Weakened instability analysis for contact

Seemingly simple, lugs are a complex design problem in a simple geometry and are important members of landing gears. These parts of the structure are used for pivot connections, and are therefore commonly subject to tension or bending loads. In the present section it is proposed to analyze a simplified geometry of a lug loaded in tension in order to better understand their failure modes. For confidentiality reasons, the material properties cannot be specified, nor the exact geometries.

The aim of the present chapter is not to perform a thorough study of the lugs loaded in tension (as it was done in the previous sections for tubes loaded in torsion), but to propose a method to study instabilities in engineering problems where contact is involved. As presented in this problem, the method is restricted to "two body contact" but could be expanded to self contact (detailed in the outlooks).

6.3.1 Mechanical problem

In order to perform tension experiments on steel lugs, an experimental setup was defined as shown in Figure 6.28. The simplified setup consists of a lug (in blue) loaded by pulling a mechanical cylinder (gray) inserted in the bore. In the present analysis the mechanical cylinder is assumed to be perfectly rigid. The broken pieces from experiments using this configuration are shown in Figure 6.29.

The geometry and loading for this problem possess two symmetry planes. It can be conjectured that the solution will be symmetric unless the stability of the straight configuration is lost. As shown in Figure 6.29, the failure mode is not necessarily symmetric. Thus, it is proposed to study the stability of the FEM model in order to detect the emergence of the failure modes. However, the stability analyses defined up until here were not explicitly adapted to the contact problem. For this reason, a method based on the weakened stability analysis is proposed in section 6.3.2. This method is applied to a FEM model of the lug loaded in tension and the results are presented in section 6.3.3. Finally, in section 6.3.4, the results are discussed to propose some prospects to this analysis.

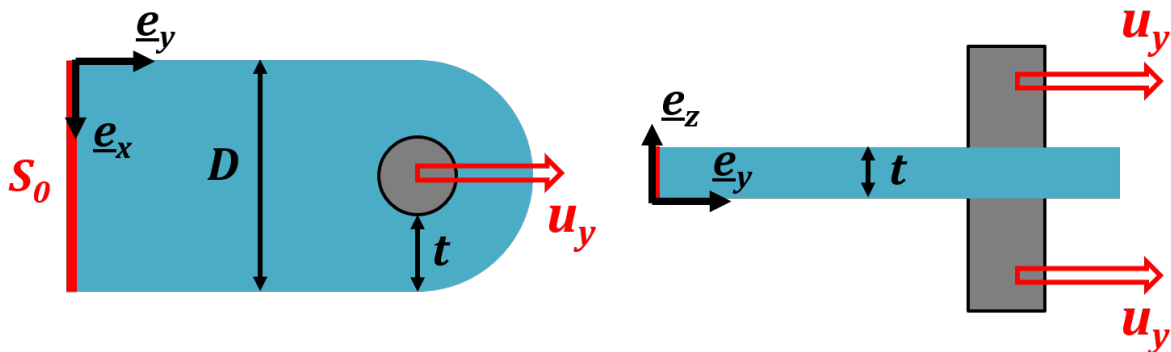


Figure 6.28: Schematic representation of the experimental setup for lugs loaded in tension.



Figure 6.29: Broken lugs after a tension experiment (source: Safran Landing Systems).

6.3.2 Proposed approach for instabilities with contact

As discussed in chapter 5, the analysis of the stability of a structure is sensitive to the type of prescribed boundary conditions. In the presence of a contact condition, neither forces nor displacements are actually prescribed. Nevertheless, it was shown that the problem is always less stable when forces were prescribed instead of displacements. Therefore, as a first approach to study the stability of a structure in a contact problem, it is proposed to analyze the structure's response by fictitiously replacing the contact conditions by the corresponding dead loads, as shown in Figure 6.30. Some other approaches are proposed and discussed in section 6.3.4.

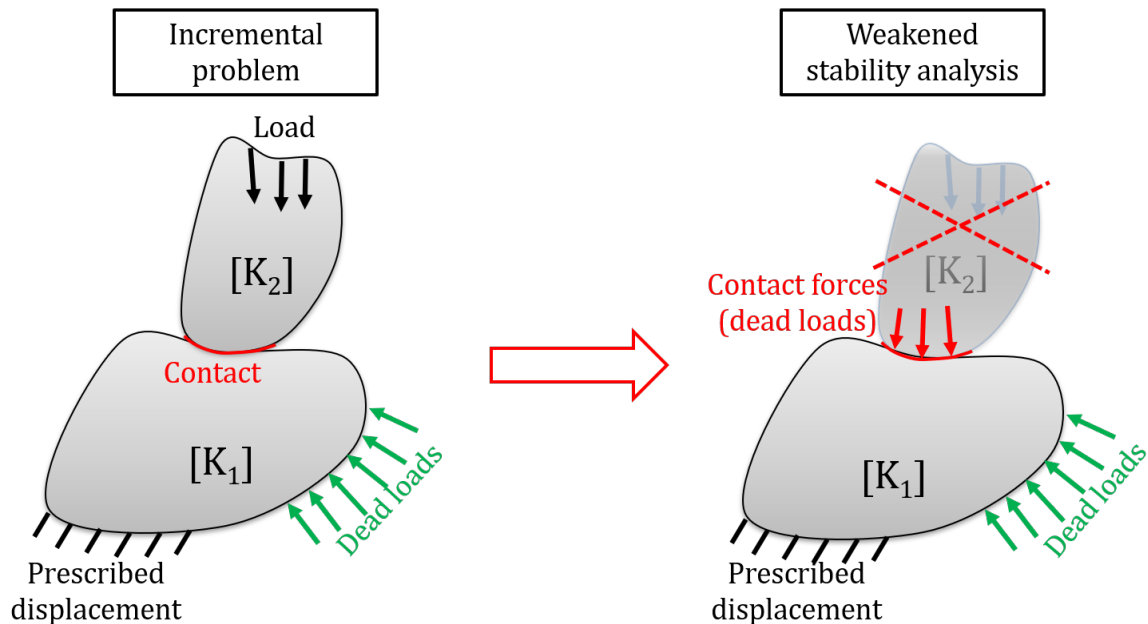


Figure 6.30: Schematic representation of the proposed method to analyze global stability in presence of contact.

Before adding the contact terms to the global stiffness matrix $[K^{tot}]$, it can be decomposed

into two square matrices $[\mathbf{K}_1]$ and $[\mathbf{K}_2]$ and two rectangular zero matrices:

$$[\mathbf{K}^{tot}] = \begin{bmatrix} [\mathbf{K}_1] & [\mathbf{0}] \\ [\mathbf{0}] & [\mathbf{K}_2] \end{bmatrix} \quad (6.17)$$

with $[\mathbf{K}_i]$ is the assembled stiffness matrix associated to the solid i . Let us assume that we want to analyze the stability of solid 1 with a given set of weakened boundary conditions and exclude solid 2 from the analysis by replacing the contact zone by the equivalent dead loads, as shown in Figure 6.30. A good way to do this is to simply build $[\mathbf{K}_1]$ independently and apply the required weakened boundary conditions before performing an eigenvalue analysis.

However, this would require some developments that we could not afford in the present work. Moreover, some FEM software are not designed to be able to change the size of the global matrix during the computation. To bypass this problem, the adopted method consists in prescribing vanishing displacements to all the degrees of freedom associated to solid 2. By doing so, the eigenvalue problem to solve is given by:

$$\begin{bmatrix} [\mathbf{K}_1] & [\mathbf{0}] \\ [\mathbf{0}] & [\mathbf{K}_2] \end{bmatrix} \cdot \begin{Bmatrix} \{\mathbf{D}_1\} \\ \{\mathbf{0}\} \end{Bmatrix} = \lambda \begin{Bmatrix} \{\mathbf{D}_1\} \\ \{\mathbf{0}\} \end{Bmatrix} \quad (6.18)$$

where λ is the eigenvalue, and $\{\mathbf{D}_1\}$ are the degrees of freedom associated to the solid 1. By doing so, the $[\mathbf{K}_2]$ matrix is excluded from the analysis. Finally, any additional displacement boundary condition can be applied to $[\mathbf{K}_1]$.

6.3.3 Numerical results

In the present section the results in terms of plastic strain, tensile force and weakened stability analysis are presented for the lug loaded in tension. The mesh and geometry used for the FEM problem are shown in Figure 6.31. Boundary conditions for the incremental problem are given by:

- Vertical displacement is prescribed to all the node of the cylinder, in order to mimic a rigid body condition: $\underline{\mathbf{u}} = u^d \underline{\mathbf{e}}_y \quad \forall \underline{\mathbf{X}} \in cylinder$;
- All displacements are fixed on the lower surface: $\underline{\mathbf{u}} = \mathbf{0} \quad \forall \underline{\mathbf{X}} \in S_0$.

The weakened boundary value problem for the analysis of the stability of the lug is given by:

$$\Delta \underline{\mathbf{u}} = \mathbf{0} \quad \forall \underline{\mathbf{X}} \in cylinder \quad ; \quad \Delta \underline{\mathbf{u}} = \mathbf{0} \quad \forall \underline{\mathbf{X}} \in S_0 \quad (6.19)$$

The tensile force and for the eigenvalues computed with weakened stability analysis are shown in Figure 6.32 as functions of the prescribed vertical displacement u^d . The results can be decomposed into four stages:

1. Elastic response: the lug is stable, all eigenvalues are positive;
2. Hardening elastoplastic response: first instability mode is captured slightly before maximum tensile force is reached (around $u^d = 3.34 \text{ mm}$) and is associated to a symmetric double necking (see Figure 6.34);
3. Slightly softening response: a second instability mode emerges for $u^d = 8.12 \text{ mm}$ and is associated to an anti-symmetric mode that favors one necking or the other (see Figure 6.35);

4. Highly softening response: this last response emerges when the second instability mode does not exist anymore. This can be observed due to the fact that the second negative eigenvalue jumps back into the positive domain (see Figure 6.32).

The fact that the first instability mode that corresponds to a double necking is captured slightly before the maximum force can be explained by the fact that contact condition has been replaced by dead loads and not displacements. In fact, the contact is an inequality equation prescribed to the displacements: $g - \Delta u > 0$ with g the gap and Δu the relative displacements of two nodes. Therefore, if the instability modes require displacements that are not compatible with the geometry of the cylinder, they might not develop in the contact problem.

The second instability mode is anti-symmetric: it leads to favoring one necking zone over the other. Even though it is associated to a negative eigenvalue, it cannot necessarily emerge in the incremental problem due to the presence of the cylinder that is kinematically constrained in all directions. Yet, due to the possible play in the experimental setup and imperfection in the alignment of the tensile cylinder, this symmetry breaking mode could probably occur earlier in the loading process. It is still unclear if the second mode emerges long after it became unstable due to the boundary conditions (as it was observed for the thin plate in tension), or due to the fact that the FEM problem keeps converging on the symmetric unstable configuration. This would require further investigation and possible approaches are discussed in section 6.3.4. Finally, a qualitative comparison between experimental failure and the second instability mode is shown in Figure 6.36 and a good correlation regarding the failure shape is found.

Finally, the eigenvalue associated to the second mode becomes positive around $u^d = 17.5 \text{ mm}$, after what the tensile force quickly reduces. This is due to the fact that second instability mode emerged and broke symmetry. Once symmetry is broken, this anti-symmetric instability mode does not exist anymore. Therefore its associated eigenvalue "disappears" and the second eigenvalue is associated to another mode that is stable. Since only one necking zone develops after this happened, the load decreases faster (similar results were observed with the double necking problem presented in section 3.2.1).

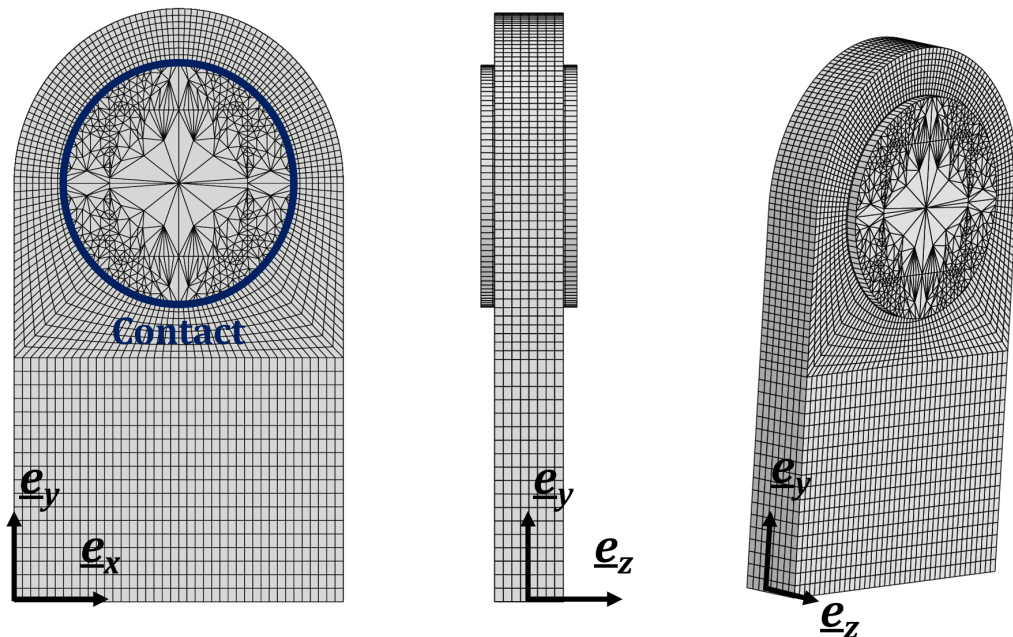


Figure 6.31: Mesh and geometry of a lug loaded in tension.

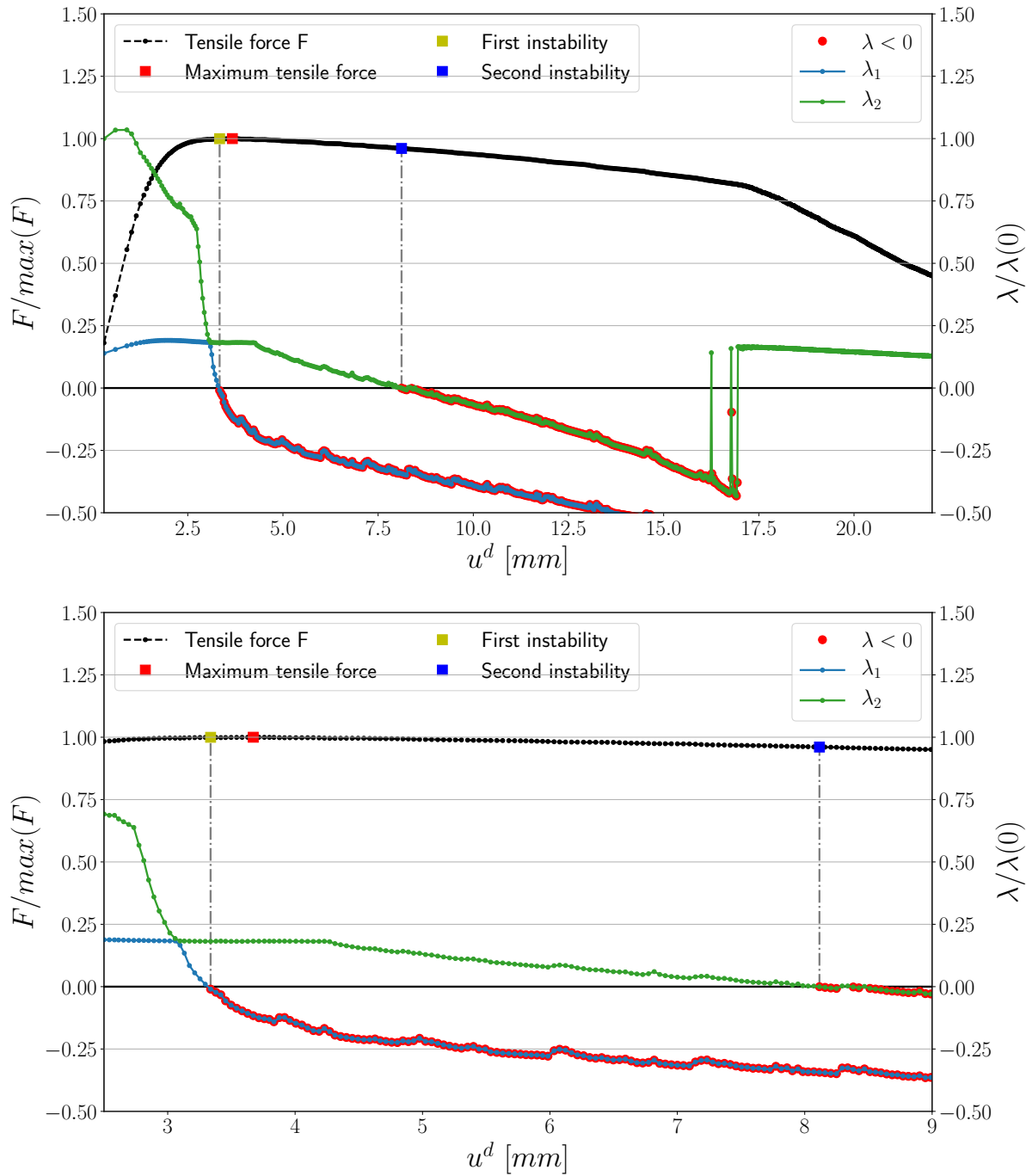


Figure 6.32: Evolution of the tensile force and the two smallest eigenvalues for the lug loaded in tension.

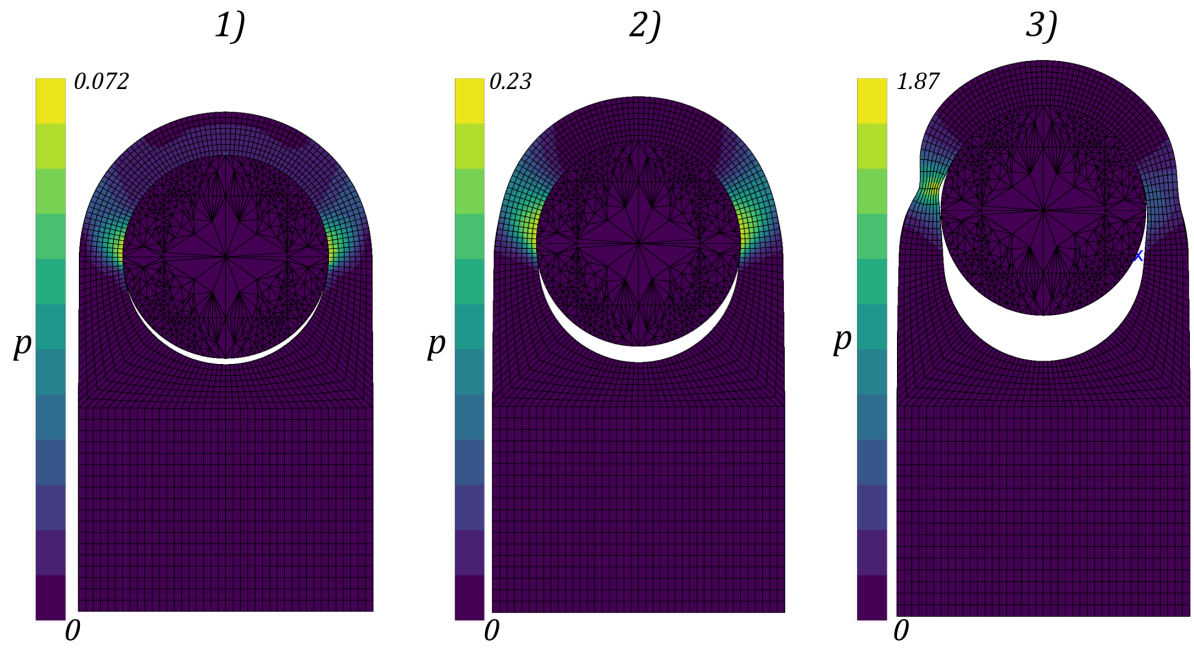


Figure 6.33: Accumulated plastic strain in a lug loaded in tension. From 1) to 3) $u^d = 3.34 \text{ mm}, 8.12 \text{ mm}, 22 \text{ mm}$.

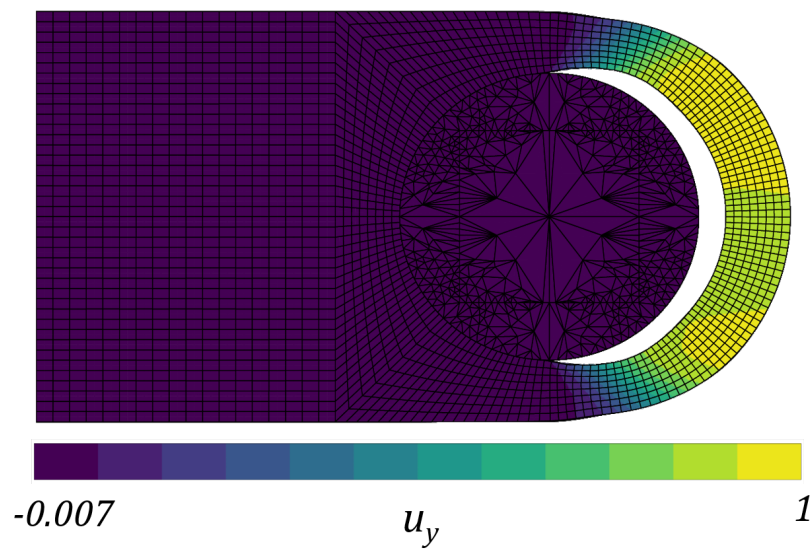


Figure 6.34: Eigen mode associated to the first vanishing eigenvalue for the lug loaded in tension.

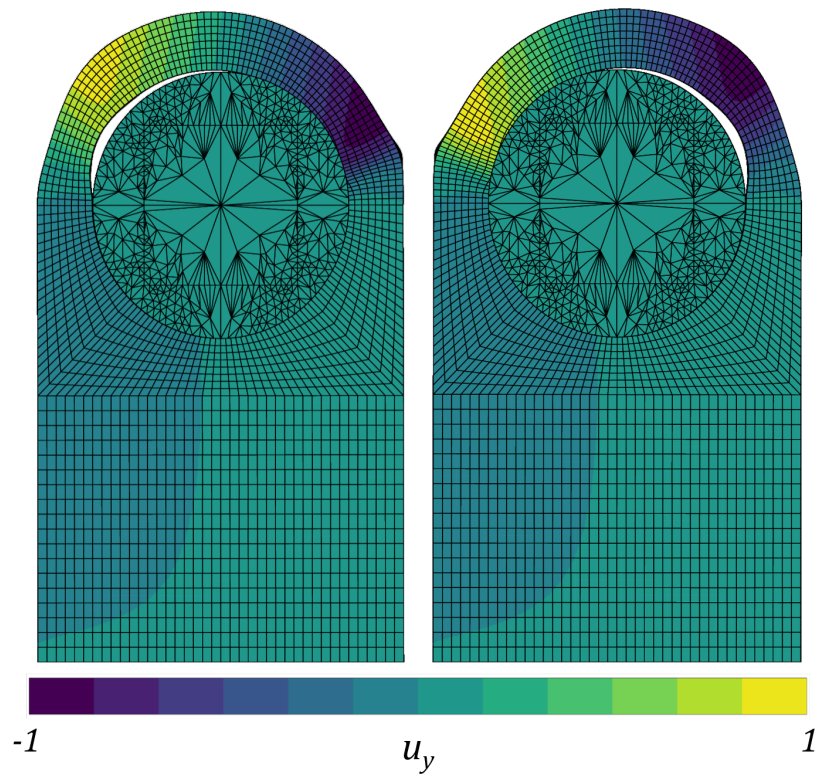


Figure 6.35: Eigen mode associated to the second vanishing eigenvalue for the lug loaded in tension. Deformed shape obtained by plotting $+\underline{\mathbf{X}}_2$ on the left, and $-\underline{\mathbf{X}}_2$ on the right.

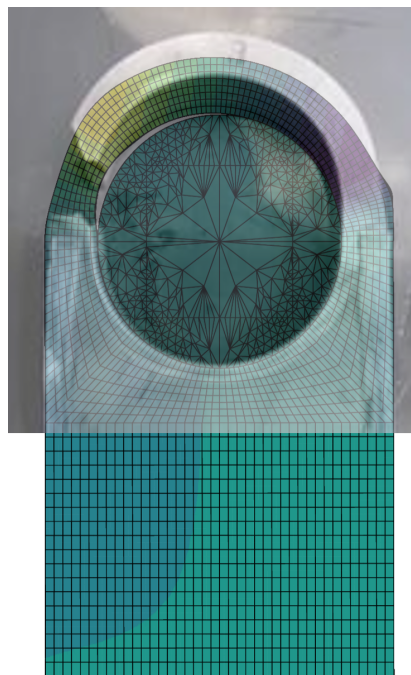


Figure 6.36: Qualitative comparison FEM/experiment of the failure of a lug loaded in tension.

6.3.4 Discussions and prospects

In the example of the lug loaded in tension, the weakened instability analysis helped us have a first evaluation of the stability of the structure. The results were, as expected, conservative since the first instability mode has been captured before the maximum load. This analysis was performed on other geometries of lugs loaded in tension and the same conclusions were observed. Also, a qualitative comparison of a real broken lug with the instability modes observed in the FEM problem was displayed, and a good match was observed.

In the FEM problem, the anti-symmetric mode became unstable long before the symmetry was broken in the incremental problem. There is still an indeterminacy about the cause: Is it because the mode is not compatible with the geometry of the cylinder ? or is it because the FEM problem kept converging on the straight unstable configuration ? Two approaches to dispel the doubts are proposed:

- The weakened stability analysis allows the user to apply any desired kinematic condition for the stability analysis. A type of kinematic constraints commonly used in FEM problems is MPCs (Multi Point Constraints). These conditions could be used in the weakened stability analysis to maintain the geometry of the contact interface. Unfortunately, the developments required to apply this approach could not be implemented in the present work. If available, this would allow us to tie the displacements of the nodes of the lug and the cylinder at the contact interface. However, this approach might lead to an over-constrained analysis, and the anti-symmetric mode may or may not be observed. Finally, this approach may be useful when self contact is involved since it is impossible to exclude the body itself from the analysis, and replacing contact by dead loads might lead to awkward interpenetration;
- The Newton-Raphson algorithm applied to solve the incremental problem depends on an initialization term (see section 2.3.3). Usually the first estimation of the displacement increment is taken to be 0 or the same as the displacement increment computed for the previous load increment. A third option could be proposed: when the anti-symmetric mode becomes unstable, it could be used to initialize the algorithm. Of course, eigen modes have no intrinsic norm, and an amplification/reduction factor should be evaluated. An expression for this factor can be found in [de Borst et al., 2012] page 134.

Bibliography

- de Borst, R., Crisfield, M. A., Remmers, J., and Verhoosel, C. (2012). *Non-Linear Finite Element Analysis of Solids and Structures*. Wiley.
- Defaisse, C. (2018). *Étude de la rupture ductile d'un acier à très haute résistance pour des applications aéronautiques*. PhD thesis, École de Mines Paristech.
- Defaisse, C., Mazière, M., Marcin, L., and Besson, J. (2018). Ductile fracture of an ultra-high strength steel under low to moderate stress triaxiality. *Engineering Fracture Mechanics*, 194:301–318.
- Department of Defense (1998). *Military Handbook: Metallic Materials and Elements for Aerospace Vehicle Structures*. USA.
- Lee, L. and Ades, C. (1957). Plastic torsional buckling strength of cylinders including effects of imperfections. *Journal of the Aeronautical Sciences*, 24:241–248.

Chapter 7

Conclusions – Prospects

“En général, il n’y a pas deux personnes qui s’entendent sans qu’elles ne soient indulgentes l’une envers l’autre.”

Mon père

“C’est que malheureusement, on ne se doute pas que le livre le plus précieux du plus savant serait celui où il dirait tout ce qu’il ne sait pas, c’est qu’on ne se doute pas qu’un auteur ne nuit jamais à ses lecteurs que quand il dissimule une difficulté. Quand la concurrence c’est à dire l’égoïsme ne règnera plus dans les sciences, quand on s’associera pour étudier, au lieu d’envoyer aux académies des paquets cachetés, on s’empressera de publier ses moindres observations pour peu qu’elles soient nouvelles, et on ajoutera : “je ne sais pas le reste” .”

Évariste Galois

Résumé : Les principales conclusions sont rassemblées dans ce chapitre de façon concise et indépendante et respectent la structure du manuscrit. La concaténation de ces résultats mène ensuite à la proposition de quelques ouvertures et propositions pour la continuation ou l’utilisation des travaux présentés.

7.1	Main results and tools	208
7.2	Prospects	212

For obvious safety reasons, engineers of the aeronautical industry are requested to comply with numerous strict regulations. In order to succeed in this task, they commonly rely on analytical approaches that provide exact or approximate solutions to “simple” problems. However, when the geometry, the material behavior, and/or the loading path are too complex, it becomes necessary to use numerical approaches such as the Finite Elements Method. The latter provides a convenient tool for the analysis of elastoplastic problems in a finite deformation framework. Nonetheless, these analyses are subject to loss of uniqueness and loss of stability problems which cannot be neglected.

In order to have a better understanding of these phenomena, two types of instabilities have been studied in the present work: global instabilities such as necking or buckling; and material instabilities such as the emergence of localized shear bands. These two types of instability are generally studied separately and together only for homogeneous problems. In the present work, it was chosen to study them both together in a finite element framework.

In the section 7.1, the various numerical and analytical results and numerical developments proposed in the present work concerning the competition between local and global instabilities (localization and buckling) are summarized. In order to motivate future works on the topic, some prospects are given in section 7.2.

7.1 Main results and tools

The main theoretical and numerical results are presented in five topics that meet the manuscript’s structure. The numerical developments are presented separately in section 7.1.6 and were implemented in **Zset** (<http://www.zset-software.com/>).

7.1.1 Incremental and rate boundary value problems

The finite deformation framework has been introduced in chapter 2. In particular, the equilibrium boundary value problem and rate boundary value problem were detailed and discretized in a finite element framework. These derivations allowed us to make a detailed link between the global stiffness matrix and global tangent matrix. This link is necessary to justify the discretized form of Hill’s loss uniqueness and stability criterion in the following chapter.

7.1.2 Discretized Hill’s loss of uniqueness criterion

In chapter 3, the discretized form of Hill’s loss of uniqueness criterion has been detailed. A numerical procedure based on the analysis of the eigenvalues of the global stiffness matrix has been implemented in **Zset** and validated with the analysis of necking in a homogeneous bar loaded in tension. Three structural cases have then been studied:

- Necking in a tensile sample (whole geometry): it was observed that the stability and uniqueness of this problem was never lost if the slenderness ratio was sufficiently small (length/diameter). This result is necessary for reverse identification methods like [Kamaya and Kawakubo, 2011, Gerbig et al., 2016, Defaisse et al., 2018, Li et al., 2018];
- It was demonstrated that Hill’s uniqueness criterion allows us to capture buckling in an elastoplastic tube loaded in torsion;
- The analysis of a thin plate loaded in tension with slightly varying boundary conditions highlighted the sensitivity of the global uniqueness analysis to a change in the boundary conditions, even though the incremental problem is not apparently impacted by these changes.

7.1.3 Localization and loss of ellipticity

Rice's localization criterion, also known as the loss of ellipticity criterion, based on the possible emergence of jumps in strain rates was recalled in chapter 4. It is defined by the loss of positive definiteness of the acoustic tensor $\underline{\mathbf{N}} \odot \underline{\underline{\mathcal{L}}} \cdot \underline{\mathbf{N}}$ for at least one orientation $\underline{\mathbf{N}}$. The analysis of localization with this criterion led to three principal developments: a minor extension of the uniqueness theorem of the van Hove rate boundary value problem to semi positive definite acoustic tensors, which led to distinguish two types of localization; the numerical analysis of the instability modes in a homogeneous square loaded in shear; the development and implementation of a minimization algorithm; the analysis of the emergence of jumps in strain rates and the loss of regularity of the solution in a non-homogeneous discretized problem.

In [Rice, 1976], the author shows that as long as the acoustic tensor $\det(\underline{\mathbf{N}} \odot \underline{\underline{\mathcal{L}}} \cdot \underline{\mathbf{N}})$ is positive definite for all orientations $\underline{\mathbf{N}}$, van Hove's rate boundary value problem still possesses a unique solution. In section 4.2.2, this analysis has been extended and it was shown that van Hove's rate boundary value problem still possesses a unique solution even when $\det(\underline{\mathbf{N}} \odot \underline{\underline{\mathcal{L}}} \cdot \underline{\mathbf{N}}) = 0$ for a finite number of $\underline{\mathbf{N}}$, and led to a discussion of the shape of the instability modes in section 4.2.3. This discussion leads to a distinction of two types of strain localization phenomena:

- Localization in the sense of Rice: defined by the emergence of jumps in strain rate that split a body;
- Localization in the sense of van Hove: defined by the emergence of confined localization modes possessing a high spatial frequency in an arbitrary small domain.

The discussion about loss of ellipticity and loss of uniqueness of the van Hove rate boundary value problem and the shape of the instability modes has been illustrated in section 4.4.1. It was shown that the load for which the discretized problem becomes unstable is related to the mesh size, and that it tends to coincide with the loss of semi-positive definiteness of the acoustic tensor when the mesh size decreases. This result illustrates the following statement in [Rice, 1976]: “*Conversely, if the localization condition has been met and exceeded by any finite amount, in the sense that nLn is indefinite for some range of orientations, then it is elementary to construct a field such that $I[\Delta \dot{\underline{\underline{\mathbf{x}}}]$ is negative [1,3], implying that a bifurcation point has been passed.*”

When considering softening materials (for instance void nucleation and coalescence), these instability modes might lead to failure. However, the consequences of these instability modes on the overall stiffness of the structure for non-softening materials that does not exhibit damage (no void nucleation as in ML340 steel) is still unclear. The conclusion is then that these instability modes could not justify alone the emergence of thin shear bands that split the structure. Nevertheless, the area in which ellipticity is lost must be considered extremely weak, if not critical, and the design of a structure should be limited to the first loss of ellipticity.

In order to evaluate the loss of ellipticity criterion in a numerical framework, a new minimization algorithm has been presented in section 4.3.3 and implemented in `Zset`. This algorithm, further detailed in section 7.1.6, has been shown to be more robust and more efficient than the methods available in the literature. It has been used to study the emergence of strain localization bands in a tube loaded in torsion in section 4.4.2. In particular, it was observed that the regularity of the solution was lost as soon as ellipticity was lost in the whole section of the tube. These results were also shown in section 4.4.3 in the study of a real ML340 steel torsional sample used in [Defaisse et al., 2018, Defaisse, 2018].

7.1.4 Modeling assumptions and weakened stability analysis

In chapter 5, the weakened stability analysis has been introduced and applied in the investigation of the consequences of the loading definition (displacements or traction forces) on the

stability of the structure. It has been motivated in section 5.1 and aims to be a first step towards the analysis of the stability of a sub-structure extracted from a larger part. This method has been thoroughly presented in section 5.2. The numerical algorithm has been implemented in *Zset* and validated on the analysis of the buckling of a beam loaded in compression in section 5.2.4. Also, it was shown that for a given equilibrium the fewer Dirichlet boundary conditions were applied for the stability analysis, the less stable was the structure (see section 5.2.2).

The weakened stability analysis has then been applied in section 5.3 to three structural problems¹:

- In section 5.3.1, the analysis of the buckling of a short tube loaded in torsion showed that the way the loading is prescribed can have a significant impact on the critical loads;
- In section 5.3.2, the analysis of the emergence of strain localization bands in a homogeneous square loaded in shear has been analyzed for various weakened boundary value problems². In particular, it was demonstrated that when ellipticity was lost, the uniqueness of the “Left Fixed” weakened boundary conditions was lost as well, and that the number of instability modes was equivalent to the numerically possible number of localization bands in the model;
- In section 5.3.3, the analysis of the emergence of shear localization bands in the tube loaded in torsion, first studied in section 4.4.2, were reevaluated in light of the results obtained in section 5.3.2. It has been observed that the uniqueness of the FEM problem was lost only once ellipticity has been lost through the whole thickness of the tube. Also, the instability modes were as numerous as the number of possible localization bands (in the sense of Rice) that could kinematically emerge in the non-elliptic area.

7.1.5 Structural applications

While simple structural examples were presented at the end of each chapter, Chapter 6 focuses on applying all of the previously developed methods to more complex problems. In particular the effects of different material properties are explored, as well as more complex geometries.

First, the competition between localization and buckling in ML340 steel tubes loaded in torsion has been studied in section 6.1 and compared to [Lee and Ades, 1957], the actual reference for this problem in the aeronautical domain. Buckling curves were shown to be in good agreement; but a gain of 5% in equivalent shear stress has been observed and linked to finite deformation effects (see Figure 6.11). These results have been confirmed by the critical loads obtained in two experiments performed in [Defaïsse, 2018]. Also, the effects of the end restrains, not analyzed in the reference method, were investigated by using the weakened stability criterion: significant differences were observed for short tubes and almost none for long tubes (see Figure 6.13). Finally, the effects of a small linear hardening term were shown to be negligible for the buckling curves and non-conservative for the localization curves (see Figure 6.12).

The second study involved taking the latter parametric study and applying it to two other (fictitious) materials in order to study the effects of the shape of the hardening curve on the various instability criteria, and highlight the consequences of the finite deformation framework. This analysis led to the extraction of the following major conclusions:

- The reference design curves were highly conservative in the plastic domain;

¹ More detailed conclusions can be found in section 5.4.

² Named: “van Hove” due to [van Hove, 1947], “Ryzhak” due to [Ryzhak, 1994], “Mandel” due to [Mandel, 1964], and “Left Fixed”.

- The critical load for strain localization in tubes loaded in torsion could simply be extracted using the maximum true shear stress criterion;
- When comparing two materials, the most resistant one to buckling could be identified in a shear stress/hardening modulus plot;
- When comparing two materials, the reference design (based on [Lee and Ades, 1957]) provided trends which were opposed to the ones obtained in our full finite deformation analysis for localization. The differences were related to the use of the material’s true behavior.

In the final study, the weakened instability analysis has been adapted to capture the emergence of structural instability modes in a FEM problem involving contact³. The method was thoroughly detailed in section 6.3.2 and seemed to properly capture the instability modes in the case of a lug loaded in tension.

7.1.6 Numerical developments

The numerical developments represent a significant part of the work shown in the present manuscript. The main difficulty was to implement new specific methods in the large C++ architecture that is the `Zset` software. The most important developments are summarized in this section. Since the developments were done in C++, the standard vocabulary of “classes”, “methods”, and “attributes” is used in this section.

`lagrangian_pk1` and `updated_lagrangian_pk1` elements

One of the earliest and most important numerical developments for the present work was the implementation of Lagrangian finite deformation elements formulated with the Boussinesq stress tensor and the Lagrangian velocity gradient (see section 2.3.3). The formulation of this element is based on the tangent operator $\underline{\underline{\mathcal{L}}}$, as shown in equation (7.1). This not compulsory, yet very convenient, has the twin benefits of simplicity and efficiency: a time gain of approximately 5% to 10% was obtained on the construction of the elementary stiffness matrix.

$$\left[\mathbf{K}^k \right]_{elem} = \int_{\Omega_0^e} [\mathbf{B}_{\dot{\mathbf{F}}}]^T \cdot \left[\underline{\underline{\mathcal{L}}}(\underline{\mathbf{u}} + \underline{\Delta \mathbf{u}}^k) \right] \cdot [\mathbf{B}_{\dot{\mathbf{F}}}] dV_0^e \quad (7.1)$$

Also, the equivalent element in an updated Lagrangian framework was required in order to be consistent with the contact formulations that were available in `Zset` at the time. The expression of the elementary matrix is given in equation (7.2).

$$\left[\mathbf{K}^k \right]_{elem} = \int_{\Omega_0^e} [\mathbf{B}_{\dot{\mathbf{F}}}]^T \cdot \left[\hat{\underline{\underline{\mathcal{L}}}}(\underline{\mathbf{u}} + \underline{\Delta \mathbf{u}}^k) \right] \cdot [\mathbf{B}_{\dot{\mathbf{F}}}] dV^e \quad (7.2)$$

`TTENSOR` class

For the development of the multi-starting point minimization algorithm presented below, a very fast evaluation of the Hessian matrix was compulsory to meet the computational efficiency needed for the algorithm to be used in large structural problems. Therefore, a specific C++ class, `TTENSOR`, has been developed and oriented for an efficient evaluation of the various tensors products. It is important to note that the `TTENSOR` class might be efficient for a specific type of operations, it is not necessarily adapted for other calculations or memory storage. Therefore, this class was only used for the evaluation of the Hessian matrix in the minimization algorithm detailed in the following section.

³ Here we focused on the emergence of a structural instability like necking or buckling. This analysis does not concern the analysis of “contact instabilities” as it might be understood by the contact community.

****min_det_nln: Multi-starting point minimization algorithm for loss of ellipticity**

Detailed in section 4.3.3, a new robust and efficient minimization algorithm for the evaluation of the loss of ellipticity criterion has been proposed. The method is based on the following considerations:

- The function to minimize $\det(\underline{\mathbf{N}} \odot \underline{\mathcal{L}} \cdot \underline{\mathbf{N}})$ is a sixth order polynomial. Thus, a Newton-Raphson algorithm is assumed to provide a quadratic convergence when the initialization point is close enough to an extremum;
- Since there is a finite number of extrema, taking enough starting points will most likely be sufficient to capture the global minimum (which necessarily exist since the function is defined on a bounded domain: the unit sphere);
- In order to avoid unnecessary clustering at the poles provided by a regular angular discretization, the starting points we selected by using a constant surface element discretization.
- If a sufficient number of starting points are selected, the number of Newton-Raphson iterations can be limited: if convergence is not obtained after 5 to 6 iterations (parameter to specified by the user), the initialization point is considered to be a “bad” starting points and the next point is considered;
- Calculating and inverting the Hessian matrix is not computationally expensive when the `TTENSOR` class is used.

Since the loss of ellipticity analysis can be performed independently for each Gauss Points, the method has been multi-threaded in order to take advantage of all available processors.

*****global_bifurcation: Hill’s uniqueness and weakened stability criteria**

Both Hill’s uniqueness analysis (discretized form) and the weakened stability analysis have been gathered in the `***global_bifurcation` problem component. As detailed in sections 3.1.4 and 5.2.3, these analyses are mainly based on the eigenvalue analysis of the global stiffness matrix with various Dirichlet boundary conditions applied.

The most challenging part of this development does not lie in the problem component itself, but on the interfacing of the `SPECTRA C++` (<https://spectralib.org/>) library with the `Zset` code. This library was chosen for its non intrusive character, and its capacity to extract vanishing and negative eigenvalues.

7.2 Prospects

Like any time-limited research project, many problems are still to be solved concerning the analysis of elastoplastic instabilities. In the present section a few prospects are proposed.

7.2.1 Stability of sub-part

The weakened stability analysis was mainly motivated by the need to analyze the effects of over-constraining kinematic conditions. As presented in this manuscript, it is possible to use any boundary conditions for the incremental problem while still applying the most appropriate ones for the stability analysis. However, such an approach might lead to over-conservative methodologies and left to the user to specify.

It would be interesting to develop a systematic method to identify the surrounding stiffness and use it to better identify the buckling loads and modes. This surrounding stiffness could take into account the global stiffness of the surrounding structure, and its non-homogeneity. Such information might probably be found in the “Schur Complement” matrix that is already investigated in Domain Decomposition (DD) methods.

7.2.2 Curvature and corners on the yield surfaces and non-associative flows

Corners and high curvatures on yield surfaces are generally avoided when possible in numerical models due to a difficult convergence. Nonetheless, it is known that such yield surfaces could significantly promote strain localization. However difficult, this problem cannot be fully neglected, especially for metals: some materials that possess a smooth yield surface in their natural form might develop corners due to the micro-structure.

To efficiently solve an incremental problem, it could be possible to resolve the incremental problem with a smooth yield surface, and evaluate the strain localization criterion by using a meta-model that has been evaluated *a priori* [Olivier, 2017]. This meta-model could take into account the possible emergence of corners on the yield surface, the loading path, and other determinant parameters.

7.2.3 Localization in the sense of Rice in heterogeneous media

A distinction has been made between localization in the sense of van Hove, and localization in the sense of Rice. In the analysis of the tube loaded in torsion, there was a perfect coincidence of various geometrical characteristics: the surface in which ellipticity was lost was parallel to the boundary loaded in displacements; the orientations that minimized the determinant of the acoustic tensor were orthogonal to the latter surface; the strain rate vectors (denoted \underline{g} in our analysis) were parallel to the loading direction; the surface in which ellipticity is lost splits the structure and exhibits traction free surfaces on its edges.

These geometrical considerations are believed to be important for the emergence of localization bands in the sense of Rice in a heterogeneous structure (heterogeneous in the sense of material heterogeneity or strain/stress gradients). The tube loaded in torsion was heterogeneous but still relatively simple. If these geometrical considerations are in fact necessary for the emergence of a strain localization surface⁴, then it would be interesting to investigate on a general localization in the sense of Rice criterion.

7.2.4 Reduced order modeling

Reduced Order Modeling (ROM) is a numerical method which has been abundantly investigated during the last decade. This modeling technique relies on the identification of a small number of modes that are sufficient to represent the structure’s behavior⁵. These modes are identified with preliminary calculations with different loading directions, and then used to evaluate the structural response for various combined loading directions: the unknowns of the problem are reduced to the amplitude of each mode⁶.

⁴ The term “band” is not used on purpose: in the present discussion the surface is not necessarily flat.

⁵ Similar approaches were first introduced during the XIXth century by Castigliano and Menabrea.

⁶ Such reduction methods have been used for a long time in dynamics, the main difference relies in the way the reduction modes are identified. In dynamics a natural way to identify the latter is to extract the eigen modes of a generalized eigenvalue problem involving the global stiffness matrix and the mass matrix.

Basis enrichment using the weakened stability analysis

By the nature of ROM analyses, the global instability analysis might not be possible or interesting to perform. In particular: when Hyper Reduction methods are used [Ryckelynck, 2005], the classical global stiffness matrix is not evaluated exactly; the eigenvalue analysis of a global stiffness matrix is time consuming and would ruin the time gain obtained with ROM. Still, as the basis for the incremental solution is computed *a priori*, a basis for the instability modes could be evaluated as well. Including these modes in the analysis would most likely provide very valuable information.

Imperfection sensitivity for stability

The analysis of sensitivity to imperfections is of utmost importance to conclude about the emergence of instability modes. Such analyses are key for the thorough study of emergence of instabilities in elastoplastic structures with finite deformations. While the critical load might decrease, the shape of the instability mode is not necessarily strongly impacted. Analyses of local defects using ROM has recently been strongly investigated, especially in the laser welding problems [Lacourt et al., 2017]. Coupling the latter with the enrichment of the ROM basis with the weakened instability analysis may allow a numerical imperfection analysis for instabilities.

Instabilities for lattice structures

The design of lattice structures is particularly active field of research since the appearance and improvement of additive manufacturing technologies [Combescure et al., 2016, Combescure and Elliott, 2017]. These structures are especially interesting for aeronautical structures. They reduce the number of separate parts to produce and assemble; they can be used as fillers to improve the stiffness of certain parts without considerably increasing their mass; they may provide “unnatural” behaviors that standard metallic materials can not provide (energy absorption for impact, auxetics, noise damping, ...); “controlled instabilities” are being investigated to make actuators.

From a numerical point of view, these mechanical structures are very difficult to model. They are sometimes replaced by an equivalent periodic homogenized material. In large lattice structures, this behavior might be suitable; however, when there is no scale transition the results are not satisfactory. Moreover, instabilities in such structures are often driven by local buckling instabilities.

Lattice structures are generally obtained by juxtaposing identical elementary cells in a cubic or hexahedral repetition. Elementary cells can generally be decomposed into simpler geometrical elements: joints and links. The latter could be thoroughly studied independently in some preliminary computations to extract a ROM basis for various loading directions. In this way, the global problem to solve would have significantly fewer degrees of freedom while still providing precise local results. Finally, if the ROM basis is enriched with instability modes extracted from the weakened stability analysis, both local and global buckling phenomena could be captured. If needed, the sensitivity to local defects could simply be analyzed by enriching the ROM basis as described above.

Bibliography

- Combescure, C. and Elliott, R. S. (2017). Hierarchical honeycomb material design and optimization: Beyond linearized behavior. *International Journal of Solids and Structures*, 115-116:161 – 169.
- Combescure, C., Henry, P., and Elliott, R. S. (2016). Post-bifurcation and stability of a finitely strained hexagonal honeycomb subjected to equi-biaxial in-plane loading. *International Journal of Solids and Structures*, 88-89:296 – 318.
- Defaisse, C. (2018). *Étude de la rupture ductile d'un acier à très haute résistance pour des applications aéronautiques*. PhD thesis, École de Mines Paristech.
- Defaisse, C., Mazière, M., Marcin, L., and Besson, J. (2018). Ductile fracture of an ultra-high strength steel under low to moderate stress triaxiality. *Engineering Fracture Mechanics*, 194:301–318.
- Gerbig, D., Bower, A., Savic, V., and Hector, L. (2016). Coupling digital image correlation and finite element analysis to determine constitutive parameters in necking tensile specimens. *International Journal of Solids and Structures*, 97-98:496–509.
- Kamaya, M. and Kawakubo, M. (2011). A procedure for determining the true stress–strain curve over a large range of strains using digital image correlation and finite element analysis. *Mechanics of Materials*, 43(5):243 – 253.
- Lacourt, L., Figliuzzi, B., Forest, S., Ryckelynck, D., Willot, F., Flouriot, S., Rancourt, V. D., and Thomas, A. (2017). étude de la nocivité des défauts dans les soudures et les pièces obtenues par fabrication additive. In *ColloqueMECAMAT Fatigue des Structures et des Matériaux*. Aussois, France.
- Lee, L. and Ades, C. (1957). Plastic torsional buckling strength of cylinders including effects of imperfections. *Journal of the Aeronautical Sciences*, 24:241–248.
- Li, J., Yang, G., Siebert, T., Shi, M. F., and Yang, L. (2018). A method of the direct measurement of the true stress–strain curve over a large strain range using multi-camera digital image correlation. *Optics and Lasers in Engineering*, 107:194 – 201.
- Mandel, J. (1964). Propagation des surfaces de discontinuité dans un milieu élastoplastique. In *Stress waves in anelastic solids*, pages 331–340. Springer.
- Olivier, C. (2017). *Décompositions tensorielles et factorisations de calculs intensifs appliquées à l'identification de modèles de comportement non linéaire*. PhD thesis, École des Mines de Paris.
- Rice, J. (1976). The localization of plastic deformation. In *W.T. Koiter (Ed.), Theoretical and Applied Mechanics*, pages 207–220. North-Holland.

- Ryckelynck, D. (2005). A priori hyperreduction method: an adaptive approach. *Journal of Computational Physics*, 202(1):346–366.
- Ryzhak, E. (1994). On stability of homogeneous elastic bodies under boundary conditions weaker than displacement conditions. *The Quarterly Journal of Mechanics and Applied Mathematics*, 47(4):663–672.
- van Hove, L. (1947). Sur l'extension de la condition de Legendre du calcul des variations aux intégrales multiples à plusieurs fonctions inconnues. *Proceedings of the Koninklijke Nederlandse Akademie van Wetenschappen*, 50:18–23.

Chapter 8

Appendix

“Good better best, never let it rest, until your good is better and your better is best.”
Mon père

Résumé : Dans ce chapitre d’annexes se trouvent plusieurs sections indépendantes ayant pour but de compléter le manuscrit. On y trouve tout d’abord les formulations lagrangiennes à décomposition additive et multiplicative qui n’ont pas été utilisées dans le manuscrit ; bien qu’adaptées aux critères et outils présentés. Vient ensuite une exégèse de la partie concernant la perte d’unicité globale dans l’article [Hill, 1958]. Les trois sections suivantes concernent la perte d’ellipticité : la première développe le lien entre la propagation d’ondes de discontinuité en vitesse de déformation et le critère de perte d’ellipticité ; dans la deuxième nous détaillons les développements analytiques pour la perte d’ellipticité dans le cas des petites déformations pour un chargement quelconque avec un critère d’écrouissage isotrope de von Mises, ainsi que la condition de charge/décharge de chaque coté de la surface de discontinuité ; enfin, la troisième rassemble quelques cas de chargement permettant de valider et mettre à l’épreuve l’algorithme de minimisation proposé dans le manuscrit. Pour finir, une comparaison plus complète en termes d’abaques pour le cas des tubes en torsion est présentée.

8.1 Additive Lagrangian formulations	218
8.2 Multiplicative decomposition formulations	222
8.3 Loss of uniqueness in elastoplastic solids: Rodney Hill 1958	229
8.4 Dynamic discontinuity and acoustic tensor	236
8.5 Loss of ellipticity specified to small deformation	238
8.6 Loss of ellipticity: analytical simple cases (small deformation)	243
8.7 Design curves summary	257

8.1 Additive Lagrangian formulations

8.1.1 Seth-Hill strain measures

Les lois lagrangiennes additives se définissent par rapport à une configuration de référence. Les tenseurs observés dans cette configuration respecteront alors automatiquement le principe d'indifférence matériel. Comme précédemment, la déformation sera décomposée additivement en une partie plastique et une partie élastique. Nous retrouverons alors un système d'équation de la même nature. La dérivation de l'opérateur tangent élastoplastique se fera alors selon le même procédé. On remarquera que ces lois se formulent à l'aide d'un potentiel thermodynamique.

8.1.2 Mesures des contraintes et déformations

On notera $\mathcal{C} = \mathbf{F}^T \mathbf{F} = \mathbf{U}^2$ le tenseur des dilatations (ou tenseur de Cauchy-Green droit). À l'aide de ce dernier, on définit classiquement le tenseur des déformations de Green-Lagrange :

$$\mathbf{E} = \frac{1}{2}(\mathcal{C} - \mathbf{I}) \quad (8.1)$$

\mathbf{F} est un tenseur mixte, il associe à un vecteur matériel défini dans la configuration de référence le vecteur matériel associé dans la configuration déformée ; \mathbf{F} est donc lagrangien/eulérien. Il s'ensuit que \mathbf{F}^T est un tenseur eulérien/lagrangien. La composition de ces tenseurs (\mathbf{F} puis \mathbf{F}^T : $\mathbf{F}^T \mathbf{F} = \mathcal{C} = \mathbf{U}^2$) donne un tenseur purement lagrangien. De ce fait, \mathbf{E} est un tenseur purement lagrangien. Les tenseurs lagrangiens ont pour propriété d'être invariants par changement de référentiel.

Un tenseur de déformation doit respecter certaines propriétés, comme celle de tendre vers $\boldsymbol{\varepsilon} = \frac{1}{2}(\nabla \mathbf{u} + \nabla^T \mathbf{u})$ (tenseur des déformations infinitésimales) lorsque $\mathbf{F} - \mathbf{I} \ll \mathbf{I}$. On définit plus généralement une famille des mesures lagrangiennes de déformations, dite de Seth-Hill [Hill, 1968], respectant ce critère par :

$$\mathbf{E}_m = \frac{1}{m}(\mathbf{U}^m - \mathbf{I}) \quad \forall m > 0, \quad \text{et} \quad \mathbf{E}_0 = \log(\mathbf{U}) \quad (8.2)$$

Le tenseur des contraintes conjuguées à une mesure donnée des déformations est alors défini en assurant la conservation de densité massique de puissance virtuelle des efforts intérieurs p_m :

$$p_m = \frac{1}{\rho} \boldsymbol{\sigma} : \mathcal{D} \quad (8.3)$$

avec $\boldsymbol{\sigma}$ le tenseur des contraintes ("vraies") de Cauchy défini sur la configuration actuelle, et $\mathcal{D} = \mathbf{L}^{sym} = (\dot{\mathbf{F}} \mathbf{F}^{-1})^{sym}$ la partie symétrique de \mathbf{L} (gradient eulérien des vitesses), aussi appelé "tenseur des taux de déformation" et ρ la masse volumique dans la configuration actuelle.

On définit par exemple le tenseur des contraintes de Piola : $\mathbf{\Pi} = J \mathbf{F}^{-1} \boldsymbol{\sigma} \mathbf{F}^{-T}$ où $J = \frac{\rho_0}{\rho} = \frac{dV}{dV_0} = \det(\mathbf{F})$, la mesure de contrainte conjuguée du tenseur des déformation de Green-Lagrange \mathbf{E} . Ce résultat se démontre immédiatement en remarquant que $\dot{\mathbf{E}} = \mathbf{F}^T \mathcal{D} \mathbf{F}$ et en passant par les notations indicielles :

$$\begin{aligned} \frac{1}{2} \frac{\mathbf{\Pi}}{\rho_0} : \dot{\mathcal{C}} &= \frac{\mathbf{\Pi}}{\rho_0} : \dot{\mathbf{E}} = \frac{1}{\rho_0} J (F_{ik}^{-1} \sigma_{kl} F_{lj}^{-T}) (F_{im}^T D_{mn} F_{nj}) \\ &= \frac{1}{\rho_0} \frac{\rho_0}{\rho} (F_{mi} F_{ik}^{-1}) (F_{nj} F_{jl}^{-1}) (\sigma_{kl} D_{mn}) \\ &= \frac{1}{\rho} \delta_{km} \delta_{ln} \sigma_{kl} D_{mn} \\ &= \frac{1}{\rho} \sigma_{kl} D_{kl} = \frac{\boldsymbol{\sigma}}{\rho} : \mathcal{D} \end{aligned}$$

De ce résultat on peut définir la mesure de contrainte conjuguée de n'importe quelle mesure de déformation définie par (8.2) :

$$\begin{aligned}\dot{\underline{\mathbf{E}}}_m &= \frac{\partial \underline{\mathbf{E}}_m}{\partial \underline{\mathbf{C}}} : \dot{\underline{\mathbf{C}}} = \frac{1}{2} \frac{\partial \underline{\mathbf{E}}_m}{\partial \underline{\mathbf{E}}} : \dot{\underline{\mathbf{C}}} \\ \Rightarrow \dot{\underline{\mathbf{C}}} &= \left(\frac{1}{2} \frac{\partial \underline{\mathbf{E}}_m}{\partial \underline{\mathbf{E}}} \right)^{-1} : \dot{\underline{\mathbf{E}}}_m \\ \Rightarrow \frac{\underline{\mathbf{\Pi}}}{2} : \dot{\underline{\mathbf{C}}} &= \underline{\mathbf{\Pi}} : \dot{\underline{\mathbf{E}}} = \underline{\mathbf{\Pi}}_m : \dot{\underline{\mathbf{E}}}_m \quad \text{avec} \quad \underline{\mathbf{\Pi}}_m = \underline{\mathbf{\Pi}} : \left(\frac{\partial \underline{\mathbf{E}}_m}{\partial \underline{\mathbf{E}}} \right)^{-1}\end{aligned}\quad (8.4)$$

On continue la suite de la démarche avec le tenseur des déformation de Green-Lagrange $\underline{\mathbf{E}}$ ($m=1$) dans un souci d'allègement des notations. Une démarche identique peut se faire pour toutes les mesures de déformation définies par (8.2) et de contraintes conjuguées définies par (8.4).

8.1.3 Formulation thermodynamique

La formulation lagrangienne de l'inégalité de Clausius-Duhem s'écrit [Besson et al., 2010] :

$$-\rho_0 (\dot{\psi} + s\dot{T}) + \underline{\mathbf{\Pi}} : \dot{\underline{\mathbf{E}}} - \frac{\underline{\mathbf{Q}}}{T} \cdot \nabla T \geq 0 \quad (8.5)$$

avec $\underline{\mathbf{Q}} = J\underline{\mathbf{F}}^{-1}\mathbf{q}$ le vecteur flux de chaleur lagrangien, T la température, ψ la densité massique d'énergie libre de Helmholtz et s l'entropie. Cette inégalité décrit la positivité de la dissipation ϕ au cours d'un processus thermodynamique. On sépare classiquement cette quantité en un taux de dissipation thermique $\phi^{th} = -\frac{\underline{\mathbf{Q}}}{T} \cdot \nabla(T)$ et une intrinsèque $\phi^i = -\rho_0 (\dot{\psi} + s\dot{T}) + \underline{\mathbf{\Pi}} : \dot{\underline{\mathbf{E}}}$. Une hypothèse courante consiste à exiger que ces deux quantités restent indépendamment positives ou nulles :

$$\begin{cases} \phi^{th} \geq 0 \\ \phi^i \geq 0 \end{cases} \quad (8.6)$$

La formulation de la loi élasto-plastique se base alors sur une décomposition additive de la mesure de la déformation :

$$\underline{\mathbf{E}} = \underline{\mathbf{E}}^e + \underline{\mathbf{E}}^p \quad (8.7)$$

En faisant le choix des variables d'état : $\underline{\mathbf{E}}^e$, T et $\underline{\boldsymbol{\alpha}}$ (variable interne tensorielle), on a $\psi = \psi(T, \underline{\mathbf{E}}^e, \underline{\boldsymbol{\alpha}})$. La positivité de la dissipation intrinsèque devient :

$$\left(\underline{\mathbf{\Pi}} - \rho_0 \frac{\partial \psi}{\partial \underline{\mathbf{E}}^e} \right) : \dot{\underline{\mathbf{E}}}^e - \rho_0 \left(\frac{\partial \psi}{\partial T} + s \right) \dot{T} + \underline{\mathbf{\Pi}} : \dot{\underline{\mathbf{E}}}^p - \rho_0 \frac{\partial \psi}{\partial \underline{\boldsymbol{\alpha}}} : \dot{\underline{\boldsymbol{\alpha}}} \geq 0 \quad (8.8)$$

Pour les matériaux vicoplastiques que nous traitons ici, la positivité de cette expression doit être vérifiée quels que soient $\dot{\underline{\mathbf{E}}}^e$ et \dot{T} . Les termes qui leurs sont associés sont des formes linéaires. La positivité de la dissipation ne saura alors être respectée que si :

$$\begin{cases} \underline{\mathbf{\Pi}} = \rho_0 \frac{\partial \psi}{\partial \underline{\mathbf{E}}^e} \\ s = -\frac{\partial \psi}{\partial T} \end{cases} \quad (8.9)$$

La dissipation intrinsèque se réduit donc à :

$$\phi^i = \underline{\mathbf{\Pi}} : \dot{\underline{\mathbf{E}}}^p - \underline{\mathbf{X}} : \dot{\underline{\boldsymbol{\alpha}}} \geq 0 \quad (8.10)$$

avec $\underline{\mathbf{X}} = \rho_0 \frac{\partial \psi}{\partial \underline{\boldsymbol{\alpha}}}$. Le matériau est alors dit standard généralisé s'il respecte l'hypothèse de dissipation maximale sous la contrainte d'un critère de plasticité $F(\underline{\boldsymbol{\Pi}}, \underline{\mathbf{X}})$ ($F < 0$ et $\dot{\lambda} = 0$ comportement élastique, $F = 0$ et $\dot{\lambda} > 0$ écoulement plastique). Cela mène alors à écrire le problème de maximisation de la fonction :

$$\mathcal{F}(\underline{\boldsymbol{\Pi}}, \underline{\mathbf{X}}) = \phi^i - \dot{\lambda} F$$

avec $\dot{\lambda}$ le multiplicateur de Lagrange, appelé dans les problèmes élasto-plastiques "multiplicateur plastique" (il s'identifiera pour de nombreux modèles à \dot{p} , le "taux de déformation plastique cumulée"). On aboutit à :

$$\begin{cases} \dot{\underline{\mathbf{E}}}^p = \dot{\lambda} \frac{\partial F}{\partial \underline{\boldsymbol{\Pi}}} \\ \dot{\underline{\boldsymbol{\alpha}}} = -\dot{\lambda} \frac{\partial F}{\partial \underline{\mathbf{X}}} \end{cases} \quad (8.11)$$

que l'on complète par la condition de cohérence $\dot{F} = 0$ si $\dot{\lambda} > 0$. Cette condition permet de déterminer le multiplicateur plastique :

$$\begin{aligned} \dot{F} = 0 &\Rightarrow \frac{\partial F}{\partial \underline{\boldsymbol{\Pi}}} : \dot{\underline{\boldsymbol{\Pi}}} + \frac{\partial F}{\partial \underline{\mathbf{X}}} : \dot{\underline{\mathbf{X}}} = 0 \\ &\Rightarrow \underline{\mathbf{N}} : \dot{\underline{\boldsymbol{\Pi}}} + \frac{\partial F}{\partial \underline{\mathbf{X}}} : \left(\frac{\partial \underline{\mathbf{X}}}{\partial \underline{\boldsymbol{\alpha}}} : \dot{\underline{\boldsymbol{\alpha}}} \right) = 0 \quad \text{avec} \quad \underline{\mathbf{N}} = \frac{\partial F}{\partial \underline{\boldsymbol{\Pi}}} \\ (8.11) &\Rightarrow \underline{\mathbf{N}} : \dot{\underline{\boldsymbol{\Pi}}} - \dot{\lambda} \frac{\partial F}{\partial \underline{\mathbf{X}}} : \frac{\partial \underline{\mathbf{X}}}{\partial \underline{\boldsymbol{\alpha}}} : \frac{\partial F}{\partial \underline{\mathbf{X}}} = 0 \end{aligned}$$

$$\text{en notant } h = \frac{\partial F}{\partial \underline{\mathbf{X}}} : \frac{\partial \underline{\mathbf{X}}}{\partial \underline{\boldsymbol{\alpha}}} : \frac{\partial F}{\partial \underline{\mathbf{X}}} \Rightarrow \dot{\lambda} = \frac{\underline{\mathbf{N}} : \dot{\underline{\boldsymbol{\Pi}}}}{h} \quad (8.12)$$

8.1.4 Tangent operator

Nous avons exprimé l'opérateur tangent élastoplastique local sous la forme suivante :

$$\begin{cases} \dot{\underline{\boldsymbol{\Pi}}} = \underline{\mathcal{L}}^{\Pi} : \dot{\underline{\mathbf{E}}} \\ \underline{\mathcal{L}}^{\Pi} = \underline{\underline{\underline{\Lambda}}} - \frac{(\underline{\underline{\underline{\Lambda}}} : \underline{\underline{\underline{N}}}) \otimes (\underline{\underline{\underline{N}}} : \underline{\underline{\underline{\Lambda}}})}{h + \underline{\underline{\underline{N}}} : \underline{\underline{\underline{\Lambda}}} : \underline{\underline{\underline{N}}}} \\ \dot{\underline{\boldsymbol{\Pi}}} = (\underline{\mathbf{F}}^{-1} \boxtimes \underline{\mathbf{F}}^{-1}) : (\dot{\underline{\boldsymbol{\tau}}} - \underline{\mathbf{L}} \underline{\boldsymbol{\tau}} - \underline{\boldsymbol{\tau}} \underline{\mathbf{L}}^T) \end{cases}$$

On en déduit sans difficulté l'opérateur tangent global :

$$\begin{aligned} \dot{\underline{\boldsymbol{\tau}}} - \underline{\mathbf{L}} \underline{\boldsymbol{\tau}} - \underline{\boldsymbol{\tau}} \underline{\mathbf{L}}^T &= (\underline{\mathbf{F}} \boxtimes \underline{\mathbf{F}}) : \dot{\underline{\boldsymbol{\Pi}}} \\ \dot{\underline{\boldsymbol{\tau}}} - \underline{\boldsymbol{\tau}} \underline{\mathbf{L}}^T &= (\underline{\mathbf{F}} \boxtimes \underline{\mathbf{F}}) : \underline{\mathcal{L}}^{\Pi} : \dot{\underline{\mathbf{E}}} + \underline{\mathbf{L}} \underline{\boldsymbol{\tau}} \\ &\Rightarrow J \dot{\underline{\boldsymbol{\sigma}}} = (\underline{\mathbf{F}} \boxtimes \underline{\mathbf{F}}) : \underline{\mathcal{L}}^{\Pi} : (\underline{\mathbf{F}}^T \boxtimes \underline{\mathbf{F}}^T) : \underline{\mathbf{D}} + \underline{\mathbf{L}} \underline{\boldsymbol{\tau}} \\ (\text{Symétries de } \underline{\mathcal{L}}^{\Pi}) &\Rightarrow J \dot{\underline{\boldsymbol{\sigma}}} = (\underline{\mathbf{F}} \boxtimes \underline{\mathbf{F}}) : \underline{\mathcal{L}}^{\Pi} : (\underline{\mathbf{F}}^T \boxtimes \underline{\mathbf{F}}^T) : \underline{\mathbf{L}} + (\underline{\mathbf{I}} \boxtimes \underline{\boldsymbol{\tau}}) : \underline{\mathbf{L}} \\ &\Rightarrow \dot{\underline{\boldsymbol{\sigma}}} = \left[\frac{1}{J} (\underline{\mathbf{F}} \boxtimes \underline{\mathbf{F}}) : \underline{\mathcal{L}}^{\Pi} : (\underline{\mathbf{F}}^T \boxtimes \underline{\mathbf{F}}^T) + \underline{\mathbf{I}} \boxtimes \underline{\boldsymbol{\tau}} \right] : \underline{\mathbf{L}} \end{aligned} \quad (8.13)$$

8.1.5 Summary

- $\forall \underline{\mathbf{X}} \in \Omega_0$:

$$\left\{ \begin{array}{ll} \underline{\tilde{\mathbf{F}}} = \frac{\partial \underline{\mathbf{x}}}{\partial \underline{\mathbf{X}}} & \text{Gradient de la transformation} \\ \underline{\tilde{\mathbf{C}}} = \underline{\tilde{\mathbf{F}}}^T \underline{\tilde{\mathbf{F}}} & \text{Tenseur des dilatations} \\ \underline{\tilde{\mathbf{E}}}_m = \frac{1}{m} (\underline{\tilde{\mathbf{C}}}^m - \underline{\mathbf{I}}) = \underline{\tilde{\mathbf{E}}}_m^e + \underline{\tilde{\mathbf{E}}}_m^p & \text{Mesure des déformations} \\ \underline{\tilde{\mathbf{\Pi}}}_m = \rho_0 \frac{\partial \psi}{\partial \underline{\tilde{\mathbf{E}}}_m^e} \Rightarrow \dot{\underline{\tilde{\mathbf{\Pi}}}}_m = \rho_0 \left(\frac{\partial^2 \psi}{\partial \underline{\tilde{\mathbf{E}}}_m^e \partial \underline{\tilde{\mathbf{E}}}_m^e} \right) : \dot{\underline{\tilde{\mathbf{E}}}}_m^e & \text{Loi élastique} \\ \underline{\tilde{\mathbf{\Pi}}}_m = \underline{\tilde{\mathbf{\Pi}}} : \left(\frac{\partial \underline{\tilde{\mathbf{E}}}_m}{\partial \underline{\tilde{\mathbf{E}}}} \right)^{-1} & \text{Mesure des contraintes} \\ \underline{\text{Div}}(\underline{\tilde{\mathbf{F}}} \underline{\tilde{\mathbf{\Pi}}}) + J \underline{\mathbf{f}} = \underline{\mathbf{0}} & \text{Équilibre local} \end{array} \right.$$

- Écoulement plastique ($F(\underline{\tilde{\mathbf{\Pi}}}_m, \underline{\tilde{\mathbf{X}}}_m) = 0$) :

$$\left\{ \begin{array}{ll} \dot{\underline{\tilde{\mathbf{E}}}}_m^p = \dot{\lambda} \frac{\partial F}{\partial \underline{\tilde{\mathbf{\Pi}}}_m} & \text{Loi d'écoulement} \\ \underline{\tilde{\mathbf{N}}} = \frac{\partial F}{\partial \underline{\tilde{\mathbf{\Pi}}}_m} & \text{Direction d'écoulement} \\ h = \frac{\partial F}{\partial \underline{\tilde{\mathbf{X}}}} : \frac{\partial \underline{\tilde{\mathbf{X}}}}{\partial \underline{\tilde{\alpha}}} : \frac{\partial F}{\partial \underline{\tilde{\mathbf{X}}}} & \text{Module d'écrouissage} \\ \dot{\lambda} = \underline{\tilde{\mathbf{N}}} : \frac{\dot{\underline{\tilde{\mathbf{\Pi}}}}_m}{h} > 0 & \text{Multiplicateur plastique} \\ \underline{\tilde{\mathbf{\Pi}}}_m : \dot{\underline{\tilde{\mathbf{E}}}}_m^p - \underline{\tilde{\mathbf{X}}}_m : \dot{\underline{\tilde{\alpha}}} \geq 0 & \text{Puissance dissipée} \end{array} \right.$$

- Opérateurs tangents :

$$\left\{ \begin{array}{l} \dot{\underline{\tilde{\mathbf{\Pi}}}} = \underline{\tilde{\mathcal{L}}}^{\Pi} : \dot{\underline{\tilde{\mathbf{E}}}} \\ \dot{\underline{\tilde{\mathbf{S}}}} = \underline{\tilde{\mathcal{L}}} : \dot{\underline{\tilde{\mathbf{F}}}} \\ \underline{\tilde{\mathcal{L}}} = (\underline{\tilde{\mathbf{F}}} \boxtimes \underline{\mathbf{I}}) : \underline{\tilde{\mathcal{L}}}^{\Pi} : (\underline{\tilde{\mathbf{F}}}^T \boxtimes \underline{\mathbf{I}}) + (\underline{\mathbf{I}} \boxtimes \underline{\tilde{\mathbf{\Pi}}}) \end{array} \right.$$

8.2 Multiplicative decomposition formulations

Les lois lagrangiennes présentées au paragraphe 8.1.1 sont basées sur une décomposition additive de la déformation en une partie élastique et une partie plastique. Dans cette section la loi de comportement est construite en se basant sur une décomposition multiplicative du gradient de la transformation : $\underline{\mathbf{F}} = \underline{\mathbf{F}}^e \underline{\mathbf{F}}^p$. Cette formulation est plus longuement détaillée dans [Mandel, 1971].

8.2.1 Gradient de la transformation

Ces lois de comportement ont initialement été développées pour les mono-cristaux. On retrouve dans ces matériaux une micro-structure périodique. La plasticité modélise des glissements selon certains plans bien définis dans le cas des mono-cristaux. La micro-structure est donc localement conservée (cf. Figure 8.1). La démarche sera la suivante : la structure subit une transformation élasto-plastique décrite par son gradient $\underline{\mathbf{F}}$. Localement, l'état de contrainte est la conséquence de la déformation élastique (partie réversible de la transformation). On suppose alors localement l'existence d'une configuration déformée plastiquement seulement (aussi appelée configuration relâchée), par rapport à laquelle la transformation élastique s'opère. La transformation $\underline{\mathbf{F}}$ se décompose localement en une première partie $\underline{\mathbf{F}}^p$ décrivant la transformation plastique, suivie d'une transformation purement élastique $\underline{\mathbf{F}}^e$:

$$\underline{\mathbf{F}} = \underline{\mathbf{F}}^e \underline{\mathbf{F}}^p \quad (8.14)$$

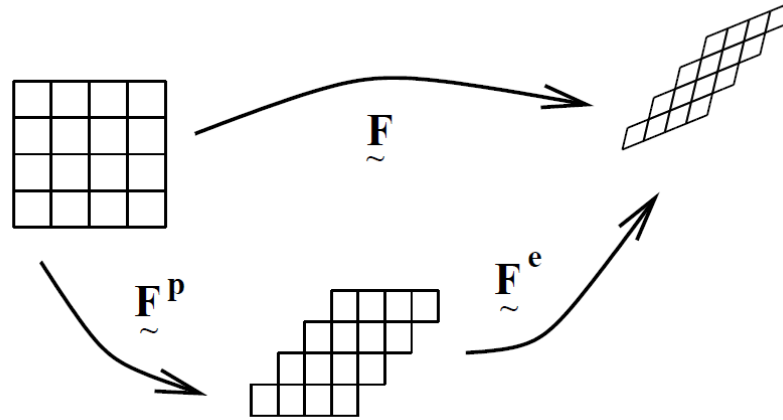


Figure 8.1: Schéma de la décomposition multiplicative locale.

Cette décomposition n'est pas chronologique. Les parties élastique et plastique de la transformation évoluent en même temps. Cependant, à un instant t donné, il sera possible de décomposer localement le gradient de la transformation en ces deux composantes.

8.2.2 Formulation thermodynamique

Pour une telle décomposition du gradient de la transformation, le gradient eulérien des vitesses s'écrit alors :

$$\underline{\mathbf{L}} = \dot{\underline{\mathbf{F}}} \underline{\mathbf{F}}^{-1} = \dot{\underline{\mathbf{F}}}^e \underline{\mathbf{F}}^{e-1} + \underline{\mathbf{F}}^e \dot{\underline{\mathbf{F}}}^p \underline{\mathbf{F}}^{p-1} \underline{\mathbf{F}}^{e-1} = \underline{\mathbf{L}}^e + \underline{\mathbf{F}}^e \dot{\underline{\mathbf{F}}}^p \underline{\mathbf{F}}^{p-1} \underline{\mathbf{F}}^{e-1} \quad (8.15)$$

On identifie $\underline{\mathbf{L}}^e$ qui se comprend comme le gradient eulérien des vitesses de la transformation élastique qui, rappelons le, s'effectue par rapport à une configuration "relâchée localement". On définit alors le tenseur des déformations élastiques de Green-Lagrange par rapport à la configuration relâchée comme :

$$\underline{\mathbf{E}}^e = \frac{1}{2} (\underline{\mathbf{C}}^e - \underline{\mathbf{I}}) = \frac{1}{2} (\underline{\mathbf{F}}^{eT} \underline{\mathbf{F}}^e - \underline{\mathbf{I}}) \quad (8.16)$$

On en déduit :

$$\dot{\underline{\mathbf{E}}}^e = \underline{\mathbf{F}}^{eT} (\underline{\mathbf{L}}^e)^{sym} \underline{\mathbf{F}}^e = \underline{\mathbf{F}}^{eT} \underline{\mathbf{D}}^e \underline{\mathbf{F}}^e \quad (8.17)$$

Ces considérations faites, nous pouvons réécrire la positivité de la dissipation ϕ comme suit :

$$\begin{aligned} \underline{\boldsymbol{\sigma}} : \underline{\mathbf{L}} - \rho (\dot{\boldsymbol{\psi}} + s\dot{T}) &\geq 0 \\ \underline{\boldsymbol{\sigma}} : \underline{\mathbf{L}}^e + \underline{\boldsymbol{\sigma}} : (\underline{\mathbf{F}}^e \dot{\underline{\mathbf{F}}}^p \underline{\mathbf{F}}^{p-1} \underline{\mathbf{F}}^{e-1}) - \rho (\dot{\boldsymbol{\psi}} + s\dot{T}) &\geq 0 \end{aligned} \quad (8.18)$$

Il ne reste alors qu'à faire le choix des variables d'état pour suivre le même développement qu'au paragraphe 8.1.1, on choisit : T la température, $\underline{\mathbf{E}}^e$ le tenseur des déformations élastiques et $\underline{\boldsymbol{\alpha}}$ tenseur des variables internes. L'inéquation (8.18) donne :

$$\underline{\boldsymbol{\sigma}} : \underline{\mathbf{D}}^e + \underline{\boldsymbol{\sigma}} : (\underline{\mathbf{F}}^e \dot{\underline{\mathbf{F}}}^p \underline{\mathbf{F}}^{p-1} \underline{\mathbf{F}}^{e-1}) - \rho \frac{\partial \psi}{\partial \underline{\mathbf{E}}^e} : \dot{\underline{\mathbf{E}}}^e - \rho \frac{\partial \psi}{\partial \underline{\boldsymbol{\alpha}}} : \dot{\underline{\boldsymbol{\alpha}}} - \rho \left(\frac{\partial \psi}{\partial T} + s \right) \dot{T} \geq 0 \quad (8.19)$$

Avec un raisonnement similaire à celui fait au paragraphe 8.1.1, on a :

$$\mathbf{s} = - \frac{\partial \psi}{\partial T} \quad (8.20)$$

En utilisant (8.17), (8.19) devient :

$$\begin{aligned} \underline{\boldsymbol{\sigma}} : (\underline{\mathbf{F}}^{e-T} \dot{\underline{\mathbf{E}}}^e \underline{\mathbf{F}}^{e-1}) - \rho \frac{\partial \psi}{\partial \underline{\mathbf{E}}^e} : \dot{\underline{\mathbf{E}}}^e + (\underline{\mathbf{F}}^{eT} \underline{\boldsymbol{\sigma}} \underline{\mathbf{F}}^{e-T}) : (\dot{\underline{\mathbf{F}}}^p \underline{\mathbf{F}}^{p-1}) - \rho \frac{\partial \psi}{\partial \underline{\boldsymbol{\alpha}}} : \dot{\underline{\boldsymbol{\alpha}}} &\geq 0 \\ \Rightarrow \left(\underline{\mathbf{F}}^{e-1} \underline{\boldsymbol{\sigma}} \underline{\mathbf{F}}^{e-T} - \rho \frac{\partial \psi}{\partial \underline{\mathbf{E}}^e} \right) : \dot{\underline{\mathbf{E}}}^e + (\underline{\mathbf{F}}^{eT} \underline{\boldsymbol{\sigma}} \underline{\mathbf{F}}^{e-T}) : (\dot{\underline{\mathbf{F}}}^p \underline{\mathbf{F}}^{p-1}) - \rho \frac{\partial \psi}{\partial \underline{\boldsymbol{\alpha}}} : \dot{\underline{\boldsymbol{\alpha}}} &\geq 0 \end{aligned} \quad (8.21)$$

Cette inégalité doit être vérifiée quel que soit $\dot{\underline{\mathbf{E}}}^e$, on a donc :

$$\begin{aligned} \underline{\mathbf{F}}^{e-1} \underline{\boldsymbol{\sigma}} \underline{\mathbf{F}}^{e-T} &= \rho \frac{\partial \psi}{\partial \underline{\mathbf{E}}^e} \\ \Rightarrow \underline{\boldsymbol{\Pi}}^e &= J \underline{\mathbf{F}}^{e-1} \underline{\boldsymbol{\sigma}} \underline{\mathbf{F}}^{e-T} = \rho_0 \frac{\partial \psi}{\partial \underline{\mathbf{E}}^e} \end{aligned} \quad (8.22)$$

L'inégalité (8.21) devient :

$$\begin{aligned} (\underline{\mathbf{F}}^{eT} \underline{\boldsymbol{\sigma}} \underline{\mathbf{F}}^{e-T}) : (\dot{\underline{\mathbf{F}}}^p \underline{\mathbf{F}}^{p-1}) - \rho \frac{\partial \psi}{\partial \underline{\boldsymbol{\alpha}}} : \dot{\underline{\boldsymbol{\alpha}}} &\geq 0 \\ \Rightarrow (J \underline{\mathbf{F}}^{eT} \underline{\boldsymbol{\sigma}} \underline{\mathbf{F}}^{e-T}) : (\dot{\underline{\mathbf{F}}}^p \underline{\mathbf{F}}^{p-1}) - \rho_0 \frac{\partial \psi}{\partial \underline{\boldsymbol{\alpha}}} : \dot{\underline{\boldsymbol{\alpha}}} &\geq 0 \end{aligned} \quad (8.23)$$

On voit apparaître le tenseur des contraintes de Mandel [Mandel, 1971] : $\underline{\mathbf{M}} = \underline{\mathbf{C}}^e \underline{\boldsymbol{\Pi}}^e = J \underline{\mathbf{F}}^{eT} \underline{\boldsymbol{\sigma}} \underline{\mathbf{F}}^{e-T}$. En notant $\underline{\mathbf{X}} = \rho_0 \frac{\partial \psi}{\partial \underline{\boldsymbol{\alpha}}}$, l'inéquation (8.23) devient :

$$\underline{\mathbf{M}} : (\dot{\underline{\mathbf{F}}}^p \underline{\mathbf{F}}^{p-1}) - \underline{\mathbf{X}} : \dot{\underline{\boldsymbol{\alpha}}} \geq 0 \quad (8.24)$$

On aboutit à une équation similaire à celle obtenue précédemment en (8.10). Une démarche similaire pourra donc être adoptée pour développer les équations décrivant l'écoulement plastique et l'écroutissage de la matière.

On définit alors une fonction de charge $F = F(\underline{\underline{M}}, \underline{\underline{X}})$, et le multiplicateur plastique $\dot{\lambda}$. On aboutit aux équations suivantes (équivalentes aux équations en équation (8.11)) :

$$\begin{cases} \dot{\underline{\underline{F}}}^p \underline{\underline{F}}^{p-1} = \dot{\lambda} \frac{\partial F}{\partial \underline{\underline{M}}} \\ \dot{\underline{\underline{\alpha}}} = -\dot{\lambda} \frac{\partial F}{\partial \underline{\underline{X}}} \end{cases} \quad (8.25)$$

ainsi que :

$$\dot{\lambda} = \frac{\underline{\underline{N}}^e : \dot{\underline{\underline{M}}}}{h} \quad (8.26)$$

$$\text{avec } h = \frac{\partial F}{\partial \underline{\underline{X}}} : \frac{\partial \underline{\underline{X}}}{\partial \underline{\underline{\alpha}}} : \frac{\partial F}{\partial \underline{\underline{X}}} \text{ et } \underline{\underline{N}}^e = \frac{\partial F}{\partial \underline{\underline{M}}}.$$

8.2.3 Opérateur tangent élastoplastique (configuration locale relachée)

La formulation de l'opérateur tangent pour cette famille de lois sera moins "directe". Nous avons eu l'occasion jusqu'ici de formuler les opérateurs tangents liant entre les mesures de déformations considérées et les mesures de contraintes qui leur sont associée. Dans le cas présent nous considérons deux mesures de contraintes différentes.

Reformulons la loi élastique :

$$\begin{aligned} \dot{\underline{\underline{\Pi}}}^e &= \underline{\underline{\Lambda}}^e : \dot{\underline{\underline{E}}}^e \quad \text{avec : } \underline{\underline{\Lambda}}^e = \rho_0 \frac{\partial^2 \psi}{\partial \underline{\underline{E}}^e \partial \underline{\underline{E}}^e} \\ \underline{\underline{F}}^{e-1} (\dot{\underline{\underline{\tau}}}^e - \underline{\underline{L}}^e \underline{\underline{\tau}} - \underline{\underline{\tau}} \underline{\underline{L}}^{eT}) \underline{\underline{F}}^{e-T} &= \underline{\underline{\Lambda}}^e : (\underline{\underline{F}}^{eT} \underline{\underline{D}}^e \underline{\underline{F}}^e) \\ \underline{\underline{\tau}}^c &= \dot{\underline{\underline{\tau}}}^e - \underline{\underline{L}}^e \underline{\underline{\tau}} - \underline{\underline{\tau}} \underline{\underline{L}}^{eT} = \underline{\underline{F}}^e \cdot [\underline{\underline{\Lambda}}^e : (\underline{\underline{F}}^{eT} \underline{\underline{D}}^e \underline{\underline{F}}^e)] \cdot \underline{\underline{F}}^{eT} \\ \underline{\underline{\tau}}^c &= \underline{\underline{\Lambda}} : \underline{\underline{D}}^e \quad \text{avec : } \Lambda_{ijkl} = F_{ip}^e F_{jq}^e F_{kr}^e F_{ls}^e \Lambda_{pqrs}^e \end{aligned} \quad (8.27)$$

On note que $\underline{\underline{\tau}}^c$ est une dérivée convective de $\underline{\underline{\tau}} = J \underline{\underline{\sigma}}$, c'est donc une dérivée objective, le principe d'indifférence matérielle est bien respecté. Pour exprimer le multiplicateur plastique $\dot{\lambda}$ en fonction du taux de déformation total, il nous faudra aussi développer $\dot{\underline{\underline{M}}}$:

$$\begin{aligned} \dot{\underline{\underline{M}}} &= \underline{\underline{F}}^{eT} (\dot{\underline{\underline{\tau}}} + \underline{\underline{L}}^{eT} \underline{\underline{\tau}} - \underline{\underline{\tau}} \underline{\underline{L}}^{eT}) \underline{\underline{F}}^{e-T} \\ &= \underline{\underline{F}}^{eT} (\underline{\underline{\tau}}^c + \underline{\underline{L}}^{eT} \underline{\underline{\tau}} + \underline{\underline{L}}^e \underline{\underline{\tau}}) \underline{\underline{F}}^{e-T} \\ &= \underline{\underline{F}}^{eT} (\underline{\underline{\tau}}^c + 2\underline{\underline{D}}^e \underline{\underline{\tau}}) \underline{\underline{F}}^{e-T} \end{aligned} \quad (8.28)$$

Pour simplifier la suite des calculs, nous noterons $\underline{\underline{D}} = \frac{1}{2}(\underline{\underline{L}} + \underline{\underline{L}}^T)$ et $\underline{\underline{D}}^p = \underline{\underline{D}} - \underline{\underline{D}}^e$. On a :

$$\begin{aligned} \underline{\underline{D}}^p &= (\underline{\underline{F}}^e \dot{\underline{\underline{F}}}^p \underline{\underline{F}}^{p-1} \underline{\underline{F}}^{e-1})^{sym} \\ \underline{\underline{D}}^p &= (\underline{\underline{F}}^e \dot{\lambda} \underline{\underline{N}}^e \underline{\underline{F}}^{e-1})^{sym} \\ \underline{\underline{D}}^p &= \dot{\lambda} \underline{\underline{N}}_s \quad \text{avec : } \underline{\underline{N}}_s = (\underline{\underline{N}})^{sym} = (\underline{\underline{F}}^e \underline{\underline{N}}^e \underline{\underline{F}}^{e-1})^{sym} \end{aligned} \quad (8.29)$$

Le multiplicateur plastique peut alors s'écrire :

$$\begin{aligned}
h\dot{\lambda} &= \underline{\underline{N}}^e : \dot{\underline{\underline{M}}} \\
h\dot{\lambda} &= \underline{\underline{N}}^e : (\underline{\underline{F}}^{eT}(\underline{\underline{\tau}}^c + 2\underline{\underline{D}}^e \underline{\underline{\tau}}) \underline{\underline{F}}^{e-T}) \\
h\dot{\lambda} &= (\underline{\underline{F}}^e \underline{\underline{N}}^e \underline{\underline{F}}^{e-1}) : (\underline{\underline{\tau}}^c + 2\underline{\underline{D}}^e \underline{\underline{\tau}}) \\
h\dot{\lambda} &= \underline{\underline{N}} : (\underline{\underline{\tau}}^c + 2\underline{\underline{D}}^e \underline{\underline{\tau}}) \\
h\dot{\lambda} &= \underline{\underline{N}} : (\underline{\underline{\Lambda}} : (\underline{\underline{D}} - \underline{\underline{D}}^p) + 2(\underline{\underline{D}} - \underline{\underline{D}}^p) \underline{\underline{\tau}}) \\
(h + \underline{\underline{N}} : \underline{\underline{\Lambda}} : \underline{\underline{N}}_s + 2\underline{\underline{N}} : (\underline{\underline{N}}_s \underline{\underline{\tau}})) \dot{\lambda} &= \underline{\underline{N}} : \underline{\underline{\Lambda}} : \underline{\underline{D}} + 2\underline{\underline{N}} : (\underline{\underline{D}} \underline{\underline{\tau}}) \\
\dot{\lambda} &= \frac{\underline{\underline{N}} : \underline{\underline{\Lambda}} : \underline{\underline{D}} + 2(\underline{\underline{N}} \underline{\underline{\tau}}) : \underline{\underline{D}}}{h + \underline{\underline{N}} : \underline{\underline{\Lambda}} : \underline{\underline{N}}_s + 2(\underline{\underline{N}} \underline{\underline{\tau}}) : \underline{\underline{N}}_s} \quad (8.30)
\end{aligned}$$

L'opérateur tangent élastoplastique liant $\underline{\underline{\tau}}^c$ à $\underline{\underline{D}}$ s'obtient en repartant de l'équation (8.27) :

$$\begin{aligned}
\underline{\underline{\tau}}^c &= \underline{\underline{\Lambda}} : \underline{\underline{D}} - \underline{\underline{\Lambda}} : \underline{\underline{D}}^p \\
\underline{\underline{\tau}}^c &= \underline{\underline{\Lambda}} : \underline{\underline{D}} - \dot{\lambda} \underline{\underline{\Lambda}} : \underline{\underline{N}}_s \\
\underline{\underline{\tau}}^c &= \left(\underline{\underline{\Lambda}} - \frac{(\underline{\underline{\Lambda}} : \underline{\underline{N}}_s) \otimes (\underline{\underline{N}} : \underline{\underline{\Lambda}} + 2\underline{\underline{N}} \underline{\underline{\tau}})}{h + \underline{\underline{N}} : \underline{\underline{\Lambda}} : \underline{\underline{N}}_s + 2(\underline{\underline{N}} \underline{\underline{\tau}}) : \underline{\underline{N}}_s} \right) : \underline{\underline{D}} \\
\underline{\underline{\tau}}^c &= \underline{\underline{\mathcal{L}}}^{\underline{\underline{\tau}}^c} : \underline{\underline{D}} \quad (8.31)
\end{aligned}$$

Les symétries mineures de $\underline{\underline{\mathcal{L}}}^{\underline{\underline{\tau}}^c}$ ne sont à priori pas vérifiées dans l'équation (8.31). Elles s'obtiennent sans difficultés en symétrisant les termes brisant la symétrie. Cela est tout à fait valide étant donné que les termes antisymétriques qui en seront éliminés seront de toute façon évincés suite à la double contraction avec le taux de déformation $\underline{\underline{D}}$. Toutefois, l'opérateur ne possède pas la symétrie majeure, il n'existe donc pas de potentiel en vitesse dont dérive cette équation ¹.

On peut remarquer que cette absence de symétrie vient du numérateur du second terme. Nous ne pourrions pas remédier à ce problème. On peut toutefois simplifier l'expression. Définissons la dérivée objective suivante :

$$\begin{aligned}
\underline{\underline{\tau}}^M &= \underline{\underline{\tau}}^c + 2\underline{\underline{D}}^e \underline{\underline{\tau}} \quad (8.32) \\
\Rightarrow \underline{\underline{\tau}}^M &= \underline{\underline{\Lambda}} : \underline{\underline{D}}^e + 2(\underline{\underline{I}} \boxtimes \underline{\underline{\tau}}) : \underline{\underline{D}}^e \\
\Rightarrow \underline{\underline{\tau}}^M &= \left(\underline{\underline{\Lambda}} + 2\underline{\underline{I}} \boxtimes \underline{\underline{\tau}} \right) : \underline{\underline{D}}^e \\
\Rightarrow \underline{\underline{\tau}}^M &= \underline{\underline{\Lambda}}' : \underline{\underline{D}}^e \quad \text{avec} : \underline{\underline{\Lambda}}' = \underline{\underline{\Lambda}} + 2\underline{\underline{I}} \boxtimes \underline{\underline{\tau}} \quad (8.33)
\end{aligned}$$

Cette opérateur ne possède que la symétrie majeure (interversión de ij et kl). En exploitant

¹ Contrairement à ce qui est énoncé dans [Nguyen, 2000]

l'équation (8.33) dans l'équation (8.31), on obtient :

$$\begin{aligned}
\tau^M &= \underline{\mathcal{L}}^{\tau^c} : \underline{\mathcal{D}} + 2\underline{\mathcal{D}}^e \tau \\
&= \left(\underline{\Lambda} - \frac{(\underline{\Lambda} : \underline{N}_s) \otimes (\underline{N} : \underline{\Lambda} + 2\underline{N}\tau)}{h + \underline{N} : \underline{\Lambda} : \underline{N}_s + 2(\underline{N}\tau) : \underline{N}_s} \right) : \underline{\mathcal{D}} + 2(\underline{\mathcal{D}} - \underline{\mathcal{D}}^p)\tau \\
&= \left(\underline{\Lambda} - \frac{(\underline{\Lambda} : \underline{N}_s) \otimes (\underline{N} : \underline{\Lambda}')}{h + \underline{N} : \underline{\Lambda} : \underline{N}_s + 2(\underline{N}\tau) : \underline{N}_s} \right) : \underline{\mathcal{D}} + (2\underline{I} \boxtimes \tau) : \underline{\mathcal{D}} - 2\lambda \underline{N}_s \tau \\
&= \left(\underline{\Lambda}' - \frac{(\underline{\Lambda} : \underline{N}_s) \otimes (\underline{N} : \underline{\Lambda}') + (2\underline{I} \boxtimes \tau) \otimes (\underline{N} : \underline{\Lambda}')}{h + \underline{N} : \underline{\Lambda}' : \underline{N}_s} \right) : \underline{\mathcal{D}} \\
&= \left(\underline{\Lambda}' - \frac{(\underline{\Lambda}' : \underline{N}_s) \otimes (\underline{N} : \underline{\Lambda}')}{h + \underline{N} : \underline{\Lambda}' : \underline{N}_s} \right) : \underline{\mathcal{D}} \\
\tau^M &= \underline{\mathcal{L}}^{\tau^M} : \underline{\mathcal{D}}
\end{aligned} \tag{8.34}$$

8.2.4 Operateur tangent

La l'opérateur tangent du comportement élastoplastique dans le cadre de lois multiplicatives lagrangienne peut prendre les deux formes suivantes :

$$\left\{ \begin{array}{l} \tau^c = \underline{\mathcal{L}}^{\tau} : \underline{\mathcal{D}} \\ \text{avec } \underline{\mathcal{L}}^{\tau} = \underline{\Lambda} - \frac{(\underline{\Lambda} : \underline{N}_s) \otimes (\underline{N} : \underline{\Lambda} + 2\underline{N}\tau)}{h + \underline{N} : \underline{\Lambda} : \underline{N}_s + 2(\underline{N}\tau) : \underline{N}_s} \\ \text{et } \underline{\Lambda} = \rho_r \frac{\partial^2 \psi}{\partial \underline{E}^e \partial \underline{E}^e} \end{array} \right. \tag{8.35}$$

ou

$$\left\{ \begin{array}{l} \tau^M = \underline{\mathcal{L}}^{\tau^M} : \underline{\mathcal{D}} \\ \text{avec } \underline{\mathcal{L}}^{\tau^M} = \underline{\Lambda}' - \frac{(\underline{\Lambda}' : \underline{N}_s) \otimes (\underline{N} : \underline{\Lambda}')}{h + \underline{N} : \underline{\Lambda}' : \underline{N}_s} \\ \text{et } \underline{\Lambda}' = \rho_r \frac{\partial^2 \psi}{\partial \underline{E}^e \partial \underline{E}^e} + 2\underline{I} \boxtimes \tau \end{array} \right. \tag{8.36}$$

Comme pour les deux autres familles de lois nous allons chercher à développer un opérateur tangent global, nécessaire à l'analyse de bifurcation. Pour simplifier la suite des calculs nous

noterons $\underline{\mathcal{L}}^p = \underline{\mathcal{F}}^e \underline{\dot{\mathcal{F}}}^p \underline{\mathcal{F}}^{p-1} \underline{\mathcal{F}}^{e-1} \neq \underline{\dot{\mathcal{F}}}^p \underline{\mathcal{F}}^{p-1}$. On en déduit alors :

$$J\dot{\underline{\mathcal{S}}} = \dot{\underline{\mathcal{T}}} - \underline{\mathcal{T}} \underline{\mathcal{L}}^T \quad (8.37)$$

$$= (\underline{\mathcal{T}}^c + \underline{\mathcal{L}}^e \underline{\mathcal{T}} + \underline{\mathcal{T}} \underline{\mathcal{L}}^{eT}) - \underline{\mathcal{T}} \underline{\mathcal{L}}^T \quad (8.38)$$

$$= (\underline{\mathcal{L}}^{\tau^c} : \underline{\mathcal{D}} + \underline{\mathcal{L}} \underline{\mathcal{T}} + \underline{\mathcal{T}} \underline{\mathcal{L}}^T - \underline{\mathcal{L}}^p \underline{\mathcal{T}} - \underline{\mathcal{T}} \underline{\mathcal{L}}^{pT}) - \underline{\mathcal{T}} \underline{\mathcal{L}}^T \quad (8.39)$$

$$= \underline{\mathcal{L}}^{\tau^c} : \underline{\mathcal{L}} + \underline{\mathcal{L}} \underline{\mathcal{T}} + \underline{\mathcal{T}} \underline{\mathcal{L}}^T - \dot{\lambda}(\underline{\mathcal{N}} \underline{\mathcal{T}} + \underline{\mathcal{T}} \underline{\mathcal{N}}^T) - \underline{\mathcal{T}} \underline{\mathcal{L}}^T \quad (8.40)$$

$$= \underline{\mathcal{L}}^{\tau^c} : \underline{\mathcal{L}} + \underline{\mathcal{L}} \underline{\mathcal{T}} - \frac{\underline{\mathcal{N}} : \underline{\Lambda} : \underline{\mathcal{D}} + 2(\underline{\mathcal{N}} \underline{\mathcal{T}}) : \underline{\mathcal{D}}}{h + \underline{\mathcal{N}} : \underline{\Lambda} : \underline{\mathcal{N}}_s + 2(\underline{\mathcal{N}} \underline{\mathcal{T}}) : \underline{\mathcal{N}}_s} (\underline{\mathcal{N}} \underline{\mathcal{T}} + \underline{\mathcal{T}} \underline{\mathcal{N}}^T) \quad (8.41)$$

$$= \underline{\mathcal{L}}^{\tau^c} : \underline{\mathcal{L}} + (\underline{\mathcal{I}} \boxtimes \underline{\mathcal{T}}) : \underline{\mathcal{L}} - \left[\frac{(\underline{\mathcal{N}} \underline{\mathcal{T}} + \underline{\mathcal{T}} \underline{\mathcal{N}}^T) \otimes (\underline{\mathcal{N}} : \underline{\Lambda} + 2(\underline{\mathcal{N}} \underline{\mathcal{T}})^{sym})}{h + \underline{\mathcal{N}} : \underline{\Lambda} : \underline{\mathcal{N}}_s + 2(\underline{\mathcal{N}} \underline{\mathcal{T}}) : \underline{\mathcal{N}}_s} \right] : \underline{\mathcal{D}} \quad (8.42)$$

$$= \left[\underline{\mathcal{L}}^{\tau^c} + \underline{\mathcal{I}} \boxtimes \underline{\mathcal{T}} - \frac{(\underline{\mathcal{N}} \underline{\mathcal{T}} + \underline{\mathcal{T}} \underline{\mathcal{N}}^T) \otimes (\underline{\mathcal{N}} : \underline{\Lambda} + 2(\underline{\mathcal{N}} \underline{\mathcal{T}})^{sym})}{h + \underline{\mathcal{N}} : \underline{\Lambda} : \underline{\mathcal{N}}_s + 2(\underline{\mathcal{N}} \underline{\mathcal{T}}) : \underline{\mathcal{N}}_s} \right] : \underline{\mathcal{L}} \quad (8.43)$$

Nous pouvons aussi formuler cette opérateur en partant de $\underline{\mathcal{T}}^M$ au lieu de $\underline{\mathcal{T}}^c$:

$$J\dot{\underline{\mathcal{S}}} = \dot{\underline{\mathcal{T}}} - \underline{\mathcal{T}} \underline{\mathcal{L}}^T$$

$$= \underline{\mathcal{T}}^M - \underline{\mathcal{L}}^{eT} \underline{\mathcal{T}} + \underline{\mathcal{T}} \underline{\mathcal{L}}^{eT} - \underline{\mathcal{T}} \underline{\mathcal{L}}^T$$

$$= \underline{\mathcal{L}}^{\tau^M} : \underline{\mathcal{D}} - \underline{\mathcal{L}}^T \underline{\mathcal{T}} + \underline{\mathcal{T}} \underline{\mathcal{L}}^T + \underline{\mathcal{L}}^{pT} \underline{\mathcal{T}} - \underline{\mathcal{T}} \underline{\mathcal{L}}^{pT} - \underline{\mathcal{T}} \underline{\mathcal{L}}^T$$

$$= \underline{\mathcal{L}}^{\tau^M} : \underline{\mathcal{L}} - \underline{\mathcal{L}}^T \underline{\mathcal{T}} + \underline{\mathcal{T}} \underline{\mathcal{L}}^T - \dot{\lambda}(\underline{\mathcal{T}} \underline{\mathcal{N}}^T - \underline{\mathcal{N}}^T \underline{\mathcal{T}} - \underline{\mathcal{T}} \underline{\mathcal{L}}^T)$$

$$= \underline{\mathcal{L}}^{\tau^M} : \underline{\mathcal{L}} - \underline{\mathcal{L}}^T \underline{\mathcal{T}} - \frac{\underline{\mathcal{N}} : \underline{\Lambda}' : \underline{\mathcal{D}}}{h + \underline{\mathcal{N}} : \underline{\Lambda}' : \underline{\mathcal{N}}_s} (\underline{\mathcal{T}} \underline{\mathcal{N}}^T - \underline{\mathcal{N}}^T \underline{\mathcal{T}})$$

$$= \underline{\mathcal{L}}^{\tau^M} : \underline{\mathcal{L}} - (\underline{\mathcal{I}} \boxplus \underline{\mathcal{T}}) : \underline{\mathcal{L}} - \left[\frac{(\underline{\mathcal{T}} \underline{\mathcal{N}}^T - \underline{\mathcal{N}}^T \underline{\mathcal{T}}) \otimes (\underline{\mathcal{N}} : \underline{\Lambda}')}{h + \underline{\mathcal{N}} : \underline{\Lambda}' : \underline{\mathcal{N}}_s} \right] : \underline{\mathcal{D}} \quad (8.44)$$

$$= \left[\underline{\mathcal{L}}^{\tau^M} - \underline{\mathcal{I}} \boxplus \underline{\mathcal{T}} - \frac{(\underline{\mathcal{T}} \underline{\mathcal{N}}^T - \underline{\mathcal{N}}^T \underline{\mathcal{T}}) \otimes (\underline{\mathcal{N}} : \underline{\Lambda}')}{h + \underline{\mathcal{N}} : \underline{\Lambda}' : \underline{\mathcal{N}}_s} \right] : \underline{\mathcal{L}} \quad (8.45)$$

Le passage de (8.44) à (8.45) se fait à condition de symétriser $\underline{\Lambda}'$ tel que : $\Lambda'_{ijkl} = \Lambda'_{ijlk}$. En combinant les équations (8.36) et (8.45) ou les équations (8.36) et (8.45), on obtient :

$$J\dot{\underline{\mathcal{S}}} = \left[\underline{\Lambda} + \underline{\mathcal{I}} \boxtimes \underline{\mathcal{T}} - \frac{(\underline{\Lambda} : \underline{\mathcal{N}} + \underline{\mathcal{N}} \underline{\mathcal{T}} + \underline{\mathcal{T}} \underline{\mathcal{N}}^T) \otimes (\underline{\mathcal{N}} : \underline{\Lambda} + \underline{\mathcal{T}} : \underline{\mathcal{N}}^T + \underline{\mathcal{N}} \underline{\mathcal{T}})}{H + \underline{\mathcal{N}} : \underline{\Lambda} : \underline{\mathcal{N}} + 2(\underline{\mathcal{N}} \underline{\mathcal{T}}) : \underline{\mathcal{N}}^{sym}} \right] : \underline{\mathcal{L}} \quad (8.46)$$

Ce résultat diffère très légèrement de celui présenté dans [Halphen, 1975] : dans cet article, l'auteur n'a pas l'opération de symétrie sur le tenseur $\underline{\mathcal{N}}$ au dénominateur. Cette différence, qui n'est pas compensée par les autres symétries, peut s'expliquer par le fait que $\underline{\Lambda}^{-1} : \underline{\Lambda} : \underline{\mathcal{N}} = \underline{\mathcal{N}}^{sym} \neq \underline{\mathcal{N}}$. Cette considération est omise par l'autre, mais peut avoir un impacte négligeable sur les résultats : si $\underline{\Lambda}$ est d'un ordre de grandeur plus élevé que $\underline{\mathcal{T}}$, les conséquences sur le dénominateur seront *a priori* minimales.

Enfin, cet opérateur possède la symmétrie majeure. Il existe donc un potentiel en vitesse.

En résumé

- $\forall \underline{\mathbf{X}} \in \Omega_0$:

$$\left\{ \begin{array}{ll} \underline{\tilde{\mathbf{F}}} = \frac{\partial \underline{\mathbf{x}}}{\partial \underline{\mathbf{X}}} = \underline{\tilde{\mathbf{F}}}^e \underline{\tilde{\mathbf{F}}}^p & \text{Gradient de la transformation} \\ \underline{\tilde{\mathbf{C}}}^e = \underline{\tilde{\mathbf{F}}}^{eT} \underline{\tilde{\mathbf{F}}}^e & \text{Tenseur des dilatations élastiques} \\ \underline{\tilde{\mathbf{E}}}^e = \frac{1}{2}(\underline{\tilde{\mathbf{C}}}^e - \underline{\mathbf{I}}) = & \text{Tenseur des déformations élastiques} \\ \underline{\tilde{\mathbf{\Pi}}}^e = \rho_r \frac{\partial \psi}{\partial \underline{\tilde{\mathbf{E}}}^e} \Rightarrow \underline{\dot{\tilde{\mathbf{\Pi}}}}^e = \rho_r \left(\frac{\partial^2 \psi}{\partial \underline{\tilde{\mathbf{E}}}^e \partial \underline{\tilde{\mathbf{E}}}^e} \right) : \underline{\dot{\tilde{\mathbf{E}}}}^e & \text{Loi élastique} \\ \underline{\tilde{\mathbf{M}}} = \underline{\tilde{\mathbf{C}}}^e \underline{\tilde{\mathbf{\Pi}}}^e & \text{Tenseur des contraintes de Mandel} \\ \underline{\text{Div}}(\underline{\tilde{\mathbf{F}}} \underline{\tilde{\mathbf{\Pi}}}) + J \underline{\mathbf{f}} = \underline{\mathbf{0}} & \text{Équilibre local} \end{array} \right.$$

- Écoulement plastique ($F(\underline{\tilde{\mathbf{M}}}, \underline{\tilde{\mathbf{X}}}) = 0$) :

$$\left\{ \begin{array}{ll} \underline{\dot{\tilde{\mathbf{F}}}}^p \underline{\tilde{\mathbf{F}}}^{p-1} = \dot{\lambda} \frac{\partial F}{\partial \underline{\tilde{\mathbf{M}}}} & \text{Loi d'écoulement} \\ \underline{\tilde{\mathbf{N}}}^e = \frac{\partial F}{\partial \underline{\tilde{\mathbf{M}}}} & \text{Direction d'écoulement} \\ h = \frac{\partial F}{\partial \underline{\tilde{\mathbf{X}}}} : \frac{\partial \underline{\tilde{\mathbf{X}}}}{\partial \underline{\dot{\alpha}}} : \frac{\partial F}{\partial \underline{\tilde{\mathbf{X}}}} & \text{Module d'écrouissage} \\ \dot{\lambda} = \underline{\tilde{\mathbf{N}}}^e : \frac{\underline{\dot{\tilde{\mathbf{M}}}}}{h} > 0 & \text{Multiplicateur plastique} \\ \underline{\tilde{\mathbf{M}}} : (\underline{\dot{\tilde{\mathbf{F}}}}^p \underline{\tilde{\mathbf{F}}}^{p-1}) - \underline{\tilde{\mathbf{X}}} : \underline{\dot{\alpha}} \geq 0 & \text{Puissance dissipée} \end{array} \right.$$

- Opérateur élastoplastique :

$$\left\{ \begin{array}{l} \underline{\tau}^c = \underline{\tilde{\mathcal{L}}}^{\tau^c} : \underline{\mathcal{D}} \\ \text{avec } \underline{\tilde{\mathcal{L}}}^{\tau^c} = \underline{\tilde{\Lambda}} - \frac{(\underline{\tilde{\Lambda}} : \underline{\tilde{\mathbf{N}}}_s) \otimes (\underline{\tilde{\mathbf{N}}} : \underline{\tilde{\Lambda}} + 2 \underline{\tilde{\mathbf{N}}} \underline{\tilde{\mathcal{T}}})}{h + \underline{\tilde{\mathbf{N}}} : \underline{\tilde{\Lambda}} : \underline{\tilde{\mathbf{N}}}_s + 2(\underline{\tilde{\mathbf{N}}} \underline{\tilde{\mathcal{T}}}) : \underline{\tilde{\mathbf{N}}}_s} \\ \text{et } \underline{\tilde{\Lambda}} = \rho_r \frac{\partial^2 \psi}{\partial \underline{\tilde{\mathbf{E}}}^e \partial \underline{\tilde{\mathbf{E}}}^e} \end{array} \right. \text{ ou } \left\{ \begin{array}{l} \underline{\tau}^{eM} = \underline{\tilde{\mathcal{L}}}^{\tau^M} : \underline{\mathcal{D}} \\ \text{avec } \underline{\tilde{\mathcal{L}}}^{\tau^M} = \underline{\tilde{\Lambda}}' - \frac{(\underline{\tilde{\Lambda}}' : \underline{\tilde{\mathbf{N}}}_s) \otimes (\underline{\tilde{\mathbf{N}}} : \underline{\tilde{\Lambda}}')}{h + \underline{\tilde{\mathbf{N}}} : \underline{\tilde{\Lambda}}' : \underline{\tilde{\mathbf{N}}}_s} \\ \text{et } \underline{\tilde{\Lambda}}' = \rho_r \frac{\partial^2 \psi}{\partial \underline{\tilde{\mathbf{E}}}^e \partial \underline{\tilde{\mathbf{E}}}^e} + 2 \underline{\mathbf{I}} \boxtimes \underline{\tau} \end{array} \right.$$

- Opérateur tangent :

$$\underline{\hat{\mathcal{L}}} = \frac{1}{J} \left[\underline{\tilde{\Lambda}} + \underline{\mathbf{I}} \boxtimes \underline{\tau} - \frac{(\underline{\tilde{\Lambda}} : \underline{\tilde{\mathbf{N}}} + \underline{\tilde{\mathbf{N}}} \underline{\tilde{\mathcal{T}}} + \underline{\tilde{\mathcal{T}}} \underline{\tilde{\mathbf{N}}}) \otimes (\underline{\tilde{\mathbf{N}}} : \underline{\tilde{\Lambda}} + \underline{\tilde{\mathcal{T}}} : \underline{\tilde{\mathbf{N}}}) + \underline{\tilde{\mathbf{N}}} \underline{\tilde{\mathcal{T}}}}{H + \underline{\tilde{\mathbf{N}}} : \underline{\tilde{\Lambda}} : \underline{\tilde{\mathbf{N}}} + 2(\underline{\tilde{\mathbf{N}}} \underline{\tilde{\mathcal{T}}}) : \underline{\tilde{\mathbf{N}}}^{sym}} \right]$$

8.3 Loss of uniqueness in elastoplastic solids: Rodney Hill 1958

8.3.1 Contraintes, déformations et équilibre

Les problèmes élastoplastiques sont généralement décrits par des lois incrémentales. Nous considérons une configuration d'équilibre à un instant τ (champ de déplacements, contraintes, d'écroissage et de température). On note $\underline{\mathcal{S}}$ le tenseur des contraintes nominales (Boussinesq), non symétrique, qui associe à un élément de surface dans la configuration initial \mathcal{C}_0 , de normale $\underline{\mathbf{N}}$, le vecteur contrainte dans la configuration déformée, $\underline{\mathbf{T}}$. En notant $\underline{\mathbf{F}}$ le gradient de la transformation, $J = \det(\underline{\mathbf{F}})$ le jacobien de la transformation, on le relie à $\underline{\boldsymbol{\sigma}}$, tenseur des contraintes "vraies" de Cauchy exprimé sur les mêmes axes, par le transport suivant :

$$\underline{\mathcal{S}} = J \underline{\boldsymbol{\sigma}} \underline{\mathbf{F}}^{-T} \quad (8.47)$$

Avec la notation d'Einstein et la sommation sur les indices répétés : $(\underline{\mathbf{A}}\underline{\mathbf{B}})_{ij} = A_{ik}B_{kj}$. Ainsi, l'expression des efforts nominaux sur un élément de surface dans la configuration de référence, $\underline{\mathbf{T}}$, s'écrit :

$$\underline{\mathbf{T}} = \underline{\mathcal{S}}\underline{\mathbf{N}}$$

$\underline{\mathbf{N}}$ étant défini sur la configuration de référence, il ne dépend pas du temps. En notant $(\dot{\cdot}) = \frac{d(\cdot)}{dt}$, on a directement :

$$\underline{\dot{\mathbf{T}}} = \underline{\dot{\mathcal{S}}}\underline{\mathbf{N}} \quad (8.48)$$

On remarquera que le tenseur de Boussinesq est transposé dans l'article de Hill [1958] ($\underline{\mathcal{S}} = \underline{\mathcal{S}}^T$). En notant $\underline{\mathbf{L}} = \underline{\dot{\mathbf{F}}}\underline{\mathbf{F}}^{-1}$ le gradient eulérien des vitesses, $\underline{\mathbf{D}}$ sa partie symétrique, $\underline{\boldsymbol{\Omega}}$ sa partie antisymétrique et $\underline{\dot{J}} = J \operatorname{tr}(\underline{\mathbf{L}}) = J \operatorname{div}(\underline{\mathbf{v}})$ on peut écrire :

$$\begin{aligned} \underline{\dot{\mathcal{S}}} &= J \operatorname{div}(\underline{\mathbf{v}}) \underline{\boldsymbol{\sigma}} \underline{\mathbf{F}}^{-T} + J \underline{\dot{\boldsymbol{\sigma}}}\underline{\mathbf{F}}^{-T} - J \underline{\boldsymbol{\sigma}} \underline{\mathbf{F}}^{-T} \underline{\dot{\mathbf{F}}}^T \underline{\mathbf{F}}^{-T} \\ &\Rightarrow \underline{\dot{\mathcal{S}}} = J(\operatorname{div}(\underline{\mathbf{v}}) \underline{\boldsymbol{\sigma}} + \underline{\dot{\boldsymbol{\sigma}}} - \underline{\boldsymbol{\sigma}} \underline{\mathbf{L}}^T) \underline{\mathbf{F}}^{-T} \end{aligned} \quad (8.49)$$

L'étude se fera par la suite en "Lagrangien réactualisé", soit : la configuration actuelle (\mathcal{C}) est prise comme configuration de référence. De façon plus générale, on peut considérer une configuration intermédiaire de référence $\hat{\mathcal{C}}$ à $t = \tau$. Les grandeurs lagrangiennes exprimées par rapport à cette configuration s'écriront $(\hat{\cdot})$. Par exemple $\hat{\underline{\mathbf{F}}}(t)$ s'écrit $\underline{\mathbf{F}}(t)\underline{\mathbf{F}}^{-1}(\tau)$. À $t = \tau$, on a $\hat{\underline{\mathbf{F}}} = \underline{\mathbf{I}}$ mais $\hat{\underline{\dot{\mathbf{F}}}} \neq \underline{\mathbf{0}}$. Un changement de configuration de référence pour une configuration intermédiaire à un instant τ donne alors :

$$\begin{aligned} \hat{\underline{\mathbf{F}}}(t) &= \underline{\mathbf{F}}(t)\underline{\mathbf{F}}^{-1}(\tau) \Rightarrow \hat{\underline{\mathbf{F}}}(\tau) = \underline{\mathbf{I}} \\ \hat{\underline{\dot{\mathbf{F}}}}(t) &= \underline{\dot{\mathbf{F}}}(t)\underline{\mathbf{F}}^{-1}(\tau) \Rightarrow \hat{\underline{\dot{\mathbf{F}}}}(\tau) = \underline{\dot{\mathbf{F}}}(\tau)\underline{\mathbf{F}}^{-1}(\tau) \\ \hat{\underline{\mathbf{L}}}(t) &= \hat{\underline{\dot{\mathbf{F}}}}(t)\hat{\underline{\mathbf{F}}}^{-1}(t) = \underline{\dot{\mathbf{F}}}(t)\underline{\mathbf{F}}^{-1}(\tau)\underline{\mathbf{F}}(\tau)\underline{\mathbf{F}}^{-1}(t) = \underline{\dot{\mathbf{F}}}(t)\underline{\mathbf{F}}^{-1}(t) = \underline{\mathbf{L}}(t) \end{aligned} \quad (8.50)$$

$$\hat{\underline{\dot{\mathcal{S}}}} = \operatorname{div}(\underline{\mathbf{v}}) \underline{\boldsymbol{\sigma}} + \underline{\dot{\boldsymbol{\sigma}}} - \underline{\boldsymbol{\sigma}} \underline{\mathbf{L}}^T \quad \text{à } t = \tau \quad (8.51)$$

On reconnaît en équation (8.51) l'équation dans Hill [1958] (à raison de prendre le transposé de $\hat{\underline{\dot{\mathcal{S}}}}$) :

$$\hat{\dot{\sigma}}_{ij} - \dot{\sigma}_{ij}^{\circ} = \sigma_{ij} \frac{\partial v_k}{\partial x_k} - \sigma_{jk} \frac{\partial v_i}{\partial x_k}$$

Equation sans numéro en page 2 Hill [1958].

Dans son égalité $\underline{\sigma}^o$ correspond au tenseur des contraintes de Cauchy. Ce qu'il note $\underline{\sigma}$ correspond à notre $\underline{\sigma}^*$ (cf. §(8.3.2)), et $\underline{s} = \underline{\hat{S}}^T$. L'égalité (8.50) s'obtient directement en notant que \underline{L} est une grandeur eulérienne, et donc insensible à la configuration de référence choisie. Ainsi l'équation (8.52) s'obtient en combinant les équations (8.49) et (8.51) :

$$\underline{\dot{S}}(\tau) = J \underline{\hat{S}} \underline{F}^{-T} \Leftrightarrow \underline{\hat{S}}(\tau) = \frac{1}{J} \underline{\dot{S}} \underline{F}^T \quad (8.52)$$

En particulier, on notera que le travail du second ordre $\int_{\Omega_0} \underline{\dot{S}} : \underline{\dot{F}} dV_0$ (":" l'opérateur de la double contraction $\underline{A} : \underline{B} = A_{ij} B_{ij}$) se conserve par un tel changement de configuration de référence. À $t = \tau$ on a :

$$\mathcal{W}_{ordre2} = \int_{\Omega} \underline{\dot{S}} : \underline{\dot{F}} dV = \int_{\Omega_0} \left(\frac{1}{J} \underline{\dot{S}} \underline{F}^T \right) : (\underline{\dot{F}} \underline{F}^{-1}) J dV_0 = \int_{\Omega_0} \underline{\dot{S}} : \underline{\dot{F}} dV_0 \quad (8.53)$$

L'équation d'équilibre locale peut s'écrire sur la divergence par rapport à la configuration de référence du tenseur des contraintes de Boussinesq. En lagrangien réactualisé la divergence de $\underline{\hat{S}}$ doit alors s'écrire sur la configuration de référence $\underline{\hat{C}}$. L'équilibre quasi-statique dans de telles conditions s'écrit (en négligeant les efforts volumiques) :

$$\underline{Div}(\underline{\hat{S}}) = \underline{0} \quad (8.54)$$

On définit en équation (8.55) la dérivée objective de Jaumann de la contrainte notée $\underline{\sigma}^J$. Cette définition correspond à la dérivée de la contrainte exprimée dans le référentiel correctionnel : c'est le référentiel local objectif dans lequel le taux de rotation est nul.

$$\underline{\sigma}^J = \underline{\dot{\sigma}} + \underline{\sigma} \underline{\Omega} - \underline{\Omega} \underline{\sigma} \quad (8.55)$$

On reconnaît ici l'équation de l'article :

$$\dot{\sigma}_{ij} - \dot{\sigma}_{ij}^{\circ} = \sigma_{ik} \alpha_{kj} + \sigma_{jk} \alpha_{ki}$$

$$\alpha_{ij} = \frac{1}{2} \left(\frac{\partial v_i}{\partial x_j} - \frac{\partial v_j}{\partial x_i} \right)$$

Equation sans numéro en page 3 Hill [1958].

La dérivée objective de Jaumann de la contrainte est définie sur des grandeurs eulériennes uniquement. Le choix de configuration de référence n'a donc pas de conséquences sur l'expression de $\underline{\sigma}^J$.

Enfin l'équation (8.56) s'obtient en combinant les équations (8.51) et (8.55).

$$\underline{\dot{S}} - (\underline{\sigma}^J + tr(\underline{L}) \underline{\sigma}) = \underline{L} \underline{\sigma} - (\underline{\sigma} \underline{D} + \underline{D} \underline{\sigma}) \quad (8.56)$$

On reconnaît dans l'article :

$$\dot{s}_{ij} - \left(\dot{\sigma}_{ij} + \sigma_{ij} \frac{\partial v_k}{\partial x_k} \right) = \sigma_{ik} \frac{\partial v_j}{\partial x_k} - (\sigma_{ik} \epsilon_{jk} + \sigma_{jk} \epsilon_{ik}).$$

Equation (3) dans Hill [1958].

On notera que $\underline{\varepsilon}$ dans l'article correspond au taux de déformation \underline{D} , et non pas au tenseur des déformation.

8.3.2 Loi de comportement en référentiel local objectif

Il existe une multitude de lois de comportement élastoplastiques en grandes déformations. Elles seront détaillées dans un document qui leur sera consacré. Pour ce qui est de l'article qui fait l'objet de ce document, la loi est formulée en référentiel local objectif.

Ces lois se basent sur une décomposition additive du taux de déformation : $\underline{\underline{D}} = \underline{\underline{D}}^e + \underline{\underline{D}}^p$. On peut alors choisir formuler la loi sur le tenseur des contraintes de Cauchy $\underline{\underline{\sigma}}$ ou le tenseur $\underline{\underline{\tau}} = J\underline{\underline{\sigma}}$, appelé tenseur des contraintes de Kirchhoff en lagrangien réactualisé. Les deux choix sont a priori licites : la prise en compte ou non de la variation de volume n'est pas un point tranché, et influera très peu pour les métaux. On choisit ici de développer la loi sur $\underline{\underline{\tau}}$ (l'autre choix s'obtenant en prenant $J \simeq 1$ et $tr(\underline{\underline{L}}) \simeq 0$).

$\underline{\underline{D}}$ et $\underline{\underline{\tau}}$ seront observés dans le référentiel local objectif "*" par la transformation $\underline{\underline{\tau}}^* = \underline{\underline{Q}}^*(\underline{\underline{\tau}})\underline{\underline{Q}}^{*T}$ et $\underline{\underline{D}}^* = \underline{\underline{Q}}^*\underline{\underline{D}}\underline{\underline{Q}}^{*T} = \underline{\underline{D}}^{e*} + \underline{\underline{D}}^{p*}$ le tenseur des taux de déformation lu dans le référentiel local objectif. La loi de comportement élastique dans ce référentiel s'écrit alors :

$$\dot{\underline{\underline{\tau}}}^* = \underline{\underline{\Lambda}} : \underline{\underline{D}}^{e*}$$

On peut facilement la réécrire (cf. Annexe Lois de comportement) :

$$\begin{aligned} \dot{\underline{\underline{\Sigma}}} &= \dot{\underline{\underline{\sigma}}} + tr(\underline{\underline{L}})\underline{\underline{\sigma}} = \underline{\underline{\Lambda}}^* \underline{\underline{D}} \\ \text{avec } \Lambda_{ijkl}^* &= \frac{1}{J} Q_{ip}^* Q_{jq}^* Q_{kr}^* Q_{ls}^* \Lambda_{pqrs} \end{aligned}$$

En faisant le choix du référentiel corotationnel pour référentiel local objectif, on reconnaît la formulation de la loi de comportement exprimée dans l'article Hill [1958], avec $\theta = tr(\underline{\underline{L}})$ et $\underline{\underline{K}} = \underline{\underline{\Lambda}}^*$:

$$\dot{\underline{\underline{\sigma}}} + \theta \underline{\underline{\sigma}} = \underline{\underline{K}} (\underline{\underline{\epsilon}} - \underline{\underline{\epsilon}}_p)$$

Equation (7) dans Hill [1958].

L'intérêt majeur de cette formulation est de pouvoir calquer la loi de comportement élastoplastique incrémentale sur la formulation en petite déformation. Il nous faut alors définir un critère de plasticité (par exemple un critère de von Mises (8.57)) et une loi d'écoulement plastique (par exemple une loi de normalité (8.58)).

$$f(\underline{\underline{\sigma}}, R(p)) = \sqrt{\frac{3}{2} \underline{\underline{\sigma}}^{dev} : \underline{\underline{\sigma}}^{dev}} - R(p) \quad (8.57)$$

$$\underline{\underline{D}}^p = \dot{p} \frac{\partial f}{\partial \underline{\underline{\sigma}}} = \dot{p} \underline{\underline{n}} \quad (8.58)$$

On notera $h = \frac{\partial R}{\partial p}$ le module d'érouissage. En suivant une démarche similaire à celle décrite dans le BCCF Besson et al. [2010] dans la partie 3.5, on aboutit à la formulation élastoplastique incrémentale donnée en équation (8.59).

$$\dot{\underline{\underline{\Sigma}}} = \underline{\underline{\mathcal{L}}} : \underline{\underline{D}} \quad \text{avec} \quad \underline{\underline{\mathcal{L}}} = \begin{cases} \underline{\underline{\Lambda}}^* & \text{si } \underline{\underline{n}} : \underline{\underline{\Lambda}}^* : \underline{\underline{D}} \leq 0 \\ \underline{\underline{\Lambda}}^* - \frac{(\underline{\underline{\Lambda}}^* : \underline{\underline{n}}) \otimes (\underline{\underline{n}} : \underline{\underline{\Lambda}}^*)}{h + \underline{\underline{n}} : \underline{\underline{\Lambda}}^* : \underline{\underline{n}}} & \text{si } \underline{\underline{n}} : \underline{\underline{\Lambda}}^* : \underline{\underline{D}} \geq 0 \end{cases} \quad (8.59)$$

On reconnaît dans l'article :

$$\dot{\sigma} + \theta\sigma = K\epsilon - \begin{cases} \frac{nK\epsilon}{(nKn + h)} Kn & \text{when } nK\epsilon \geq 0 \\ \mathbf{0} & \dots\dots\dots \leq 0. \end{cases}$$

Equation (10) dans Hill [1958].

Les tenseurs $\underset{\approx}{\Lambda}^*$ et $\underset{\approx}{\mathcal{L}}$ (en tout cas pour un matériau standard généralisé) possèdent en plus de la symétrie mineur (interversion de i et j ou de k et l) la symétrie majeure (interversion de ij et kl) : $\Lambda_{ijkl}^* = \Lambda_{klij}^*$ et $\mathcal{L}_{ijkl} = \mathcal{L}_{klij}$. Ces propriétés nous permettent alors d'écrire une loi incrémentale élastoplastique entre $\hat{\underset{\approx}{S}}$ et $\hat{\underset{\approx}{F}}$. En repartant de l'équation (8.56), on a :

$$\begin{aligned} \hat{S}_{ij} &= \mathcal{L}_{ijkl} D_{kl} + L_{ik} \sigma_{kj} - \sigma_{ik} D_{kj} - D_{ik} \sigma_{kj} \\ &= \frac{1}{2} \mathcal{L}_{ijkl} (\hat{F}_{kl} + \hat{F}_{lk}) + \hat{F}_{lk} \delta_{il} \sigma_{kj} - \sigma_{ik} \delta_{jl} D_{kl} - D_{lk} \delta_{il} \sigma_{kj} \\ &= \mathcal{L}_{ijkl} \hat{F}_{kl} + \hat{F}_{kl} \delta_{ik} \sigma_{lj} - \frac{1}{2} \sigma_{ik} \delta_{jl} (\hat{F}_{lk} + \hat{F}_{kl}) - \frac{1}{2} \delta_{il} \sigma_{kj} (\hat{F}_{lk} + \hat{F}_{kl}) \\ &= \left[\mathcal{L}_{ijkl} + \frac{1}{2} (\delta_{ik} \sigma_{jl} - \delta_{il} \sigma_{jk} - \delta_{jk} \sigma_{il} - \delta_{jl} \sigma_{ik}) \right] \hat{F}_{kl} \\ \hat{S}_{ij} &= \mathcal{L}'_{ijkl} \hat{F}_{kl} \end{aligned} \tag{8.60}$$

On reconnaîtra que l'opérateur $\underset{\approx}{\mathcal{L}}'$ possède seulement la symétrie majeure. Ainsi :

$$\hat{\underset{\approx}{S}} = \hat{\underset{\approx}{F}} : \underset{\approx}{\mathcal{L}}' = \underset{\approx}{\mathcal{L}}' : \hat{\underset{\approx}{F}} \tag{8.61}$$

Le le travail du second ordre peut donc s'écrire :

$$\mathcal{W}_{ordre2} = \int_{\Omega} \hat{\underset{\approx}{F}} : \underset{\approx}{\mathcal{L}}' : \hat{\underset{\approx}{F}} dV \tag{8.62}$$

8.3.3 Identités remarquables

Introduisons la quantité suivante proportionnelle à une densité de travail du second ordre :

$$w(\underline{v}) = \frac{1}{2} \hat{\underset{\approx}{S}} : \hat{\underset{\approx}{F}} = \frac{1}{2} \hat{\underset{\approx}{S}} : (\underline{D}) - \frac{1}{2} \underline{\sigma} : (2\underline{D}\underline{D} - \hat{\underset{\approx}{F}}^T \hat{\underset{\approx}{F}}) \tag{8.63}$$

$$\mathbf{E}(\mathbf{v}) = \frac{1}{2} (\dot{\sigma} + \theta\sigma) \epsilon - \frac{1}{2} \sigma_{ik} \left(2\epsilon_{ij} \epsilon_{jk} - \frac{\partial v_j}{\partial x_i} \frac{\partial v_j}{\partial x_k} \right)$$

Equation (11) dans Hill [1958].

L'opérateur $\underset{\approx}{\mathcal{L}}'$ possédant la symétrie majeure, on obtient :

$$dw = \hat{\underset{\approx}{S}} : d\hat{\underset{\approx}{F}} \quad \hat{\underset{\approx}{S}} = \frac{\partial w}{\partial \hat{\underset{\approx}{F}}} \tag{8.64}$$

On reconnaît :

$$\hat{s}_{ij} d \left(\frac{\partial v_j}{\partial x_i} \right) = d\mathbf{E}, \quad \hat{s}_{ij} = \frac{\partial \mathbf{E}}{\partial (\partial v_j / \partial x_i)}$$

Équation sans numéro en page 5 dans Hill [1958].

Introduisons maintenant deux couples de solutions en taux de contrainte et de déformation $(\underline{\mathcal{D}}^*, \underline{\dot{\Sigma}}^*)$ et $(\underline{\mathcal{D}}, \underline{\dot{\Sigma}})$. On note alors $\Delta(\cdot) = (\cdot)^* - (\cdot)$

Lemme 1 :

$$\Delta \underline{\dot{\Sigma}} : \Delta \underline{\mathcal{D}} = \Delta \underline{\mathcal{D}} : \underline{\Lambda}^* : \Delta \underline{\mathcal{D}} \quad \text{si les deux solutions sont élastiques;} \quad (8.65)$$

$$\Delta \underline{\dot{\Sigma}} : \Delta \underline{\mathcal{D}} \geq \Delta \underline{\mathcal{D}} : \underline{\mathcal{L}}' : \Delta \underline{\mathcal{D}} \quad \text{sinon.} \quad (8.66)$$

La première égalité dans le cas de deux solutions élastiques est triviale étant donné la lois de comportement. La seconde inégalité est une égalité stricte si les deux solutions sont plastiques (cf. symétries de $\underline{\mathcal{L}}'$), alors que l'inégalité est stricte dans le cas où une solution est plastique et la seconde élastique. En effet, si on prend $(\cdot)^*$ comme solution élastique alors :

$$\Delta \underline{\dot{\Sigma}} : \Delta \underline{\mathcal{D}} = \Delta \underline{\mathcal{D}} : \underline{\mathcal{L}}' : \Delta \underline{\mathcal{D}} + \frac{\underline{\mathcal{D}}^* : (\underline{\Lambda}^* : \underline{n}) \otimes (\underline{n} : \underline{\Lambda}^*) : (\underline{\mathcal{D}}^* - \underline{\mathcal{D}})}{h + \underline{n} : \underline{\Lambda}^* : \underline{n}} \quad (8.67)$$

Le premier terme du membre de droite est positif pour un matériau durcissant ($\underline{\mathcal{L}}'$ défini positif) et le second aussi étant donné que $\underline{n} : \underline{\Lambda}^* : \underline{\mathcal{D}} \geq 0$ et $\underline{n} : \underline{\Lambda}^* : \underline{\mathcal{D}}^* \leq 0$.

8.3.4 Critère d'unicité

Considérons un domaine Ω à un instant t donné, instant pour lequel les propriétés matériaux et champs de contraintes ont déjà été évalués en tout point. Soit S_F la partie de $\partial\Omega$ sur laquelle est imposé un taux d'effort $\underline{\dot{T}}^d$ et S_v la partie complémentaire de $\partial\Omega$ sur laquelle sont imposées les vitesses de déplacement \underline{v}^d . En équation (8.68), l'ensemble d'équations régissant le système.

$$\left. \begin{aligned} \underline{d\hat{v}}(\underline{\dot{\Sigma}}) &= \underline{0} \\ \underline{\dot{\Sigma}} &= \underline{\mathcal{L}}' : \underline{\dot{\hat{F}}} \\ \underline{\dot{\Sigma}} &= \underline{\mathcal{L}} : \underline{\mathcal{D}} \end{aligned} \right\} \quad \forall x \in \Omega \quad (8.68)$$

$$\underline{\dot{\Sigma}} \underline{N} = \underline{\dot{T}}^d \quad \forall x \in S_F \quad (8.69)$$

$$\underline{v} = \underline{v}^d \quad \forall x \in S_v \quad (8.70)$$

Si deux solutions existent pour un même incrément de charge, en notant $\Delta(\cdot)$ la différence entre deux champs de même nature, on obtient :

$$\begin{aligned} \int_S \Delta \underline{\dot{\hat{F}}} \Delta \underline{v} \, dS &= \int_{S_F} \Delta \underline{\dot{T}}^d \Delta \underline{v} \, dS + \int_{S_v} \Delta \underline{\dot{\hat{F}}} \Delta \underline{v}^d \, dS = 0 \\ &\Rightarrow \int_{\Omega} \Delta \underline{\dot{\Sigma}} : \Delta \underline{\dot{\hat{F}}} \, dV = 0 \end{aligned} \quad (8.71)$$

$$\Rightarrow \int_{\Omega} \Delta \underline{\dot{\Sigma}} : \Delta \underline{\mathcal{D}} \, dV - \Sigma(\Delta \underline{v}) = 0$$

$$\text{avec } \Sigma(\Delta \underline{v}) = \int_{\Omega} \underline{\sigma} : (2\Delta \underline{\mathcal{D}} \Delta(\underline{\mathcal{D}}) - \Delta \underline{\mathcal{L}}^T \Delta \underline{\mathcal{L}}) \, dV$$

De fait, une condition suffisante pour assurer l'unicité de la solution sera la non nullité de (8.71) soit :

$$\int_{\Omega} \Delta \underline{\dot{\Sigma}} : \Delta \underline{\dot{\hat{F}}} \, dV = \int_{\Omega} \Delta \underline{\dot{\Sigma}} : \Delta \underline{\mathcal{D}} \, dV - \Sigma(\Delta \underline{v}) > 0 \quad (8.72)$$

quelque soit $\Delta \underline{v}$ la différence entre deux champs de vitesses continus respectant $\underline{v} = \underline{v}^d$ sur S_v .

On reconnaît en équation (8.72) le critère de perte d'unicité formulé sur le travail du second ordre (aussi appelée condition de Hill). Étant donné l'égalité (8.53), il se réécrit pour une formulation en lagrangien total :

$$\int_{\Omega_0} \Delta \dot{\underline{\mathbf{S}}} : \Delta \dot{\underline{\mathbf{F}}} \, dV_0 > 0 \quad (8.73)$$

Dans le cas d'un matériaux élastoplastique durcissant, et en intégrant le lemme 1 sur le domaine Ω , on obtient :

$$\int_{\Omega} \Delta \dot{\underline{\mathbf{S}}} : \Delta \underline{\mathbf{D}} \geq H(\Delta \underline{\mathbf{v}}) \quad (8.74)$$

$$\text{avec } H(\Delta \underline{\mathbf{v}}) = \int_{\Omega} \Delta \underline{\mathbf{D}} : \underline{\underline{\mathbf{\Lambda}}}^* : \Delta \underline{\mathbf{D}} dV - \int_{\Omega_P^{\cup}} \frac{(\underline{\mathbf{n}} : \underline{\underline{\mathbf{\Lambda}}}^* : \Delta \underline{\mathbf{D}})^2}{h + \underline{\mathbf{n}} : \underline{\underline{\mathbf{\Lambda}}}^* : \underline{\mathbf{n}}} dV \quad (8.75)$$

avec $\Omega_P^{\cup} = \Omega_P \cup \Omega_P^*$ l'union des volumes de Ω plastifiés dans chaque solution.

H est un minorant du membre de gauche dans l'inéquation (8.74), une condition plus que suffisante pour l'unicité de la solution est alors :

$$H(\underline{\mathbf{w}}) - \Sigma(\underline{\mathbf{w}}) > 0 \quad \forall \underline{\mathbf{w}} \in \mathcal{V}_0^{adm} \quad (8.76)$$

avec \mathcal{V}_0^{adm} l'ensemble des champs continus à valeurs nulles sur S_v

H admet un minorant et un majorant dans le cadre des matériaux élastoplastiques durcissants :

$$H_0(\underline{\mathbf{w}}) = \lim_{h \rightarrow 0} H(\underline{\mathbf{w}}) \leq H(\underline{\mathbf{w}}) \leq \lim_{h \rightarrow \infty} H(\underline{\mathbf{w}}) = H_{\infty} \quad (8.77)$$

On peut à partir de là distinguer quatre cas dans lesquelles on peut conclure sur l'unicité de la solution :

1. $\Sigma < H_{\infty} \quad \forall \underline{\mathbf{w}} \in \mathcal{V}_0^{adm} \Rightarrow$ La solution est unique pour un matériau élastique.
2. $\Sigma < H_0 \quad \forall \underline{\mathbf{w}} \in \mathcal{V}_0^{adm} \Rightarrow$ La solution est unique pour un matériau durcissant ou parfaitement plastique ($h \geq 0$)
3. $\Sigma \leq H_0 \quad \forall \underline{\mathbf{w}} \in \mathcal{V}_0^{adm}$, et $\Sigma = H_0$ pour au moins un champ $\underline{\mathbf{w}} \Rightarrow$ La solution est unique pour un matériau strictement durcissant ($h > 0$).
4. $\Sigma > H_0$ pour au moins un champs $\underline{\mathbf{w}}$ et $\Sigma < H_{\infty} \quad \forall \underline{\mathbf{w}} \in \mathcal{V}_0^{adm} \Rightarrow$ On peut discuter de l'unicité à raison que le matériaux présente un module d'écroissage suffisamment grand.

Pour illustrer le quatrième cas, nous allons prendre l'exemple suivant : On considère un matériaux homogène isotrope. $\underline{\mathbf{n}}$ étant unitaire et purement déviatorique, on a $\underline{\mathbf{n}} : \underline{\underline{\mathbf{\Lambda}}}^* : \underline{\mathbf{n}} = 2\mu$ avec μ le module de cisaillement de ce matériau. On considère de plus la zone plastifiée, présente un module d'écroissage uniforme $h > 0$. Notons $\tilde{H} = \int_{\Omega_P} \frac{(\underline{\mathbf{n}} : \underline{\underline{\mathbf{\Lambda}}}^* : \underline{\mathbf{D}})^2}{2\mu} dV_P > 0$ on obtient alors :

$$\begin{aligned} H_0 &= H_{\infty} - \tilde{H} \\ \Rightarrow \left\{ \begin{array}{l} H = H_{\infty} - \frac{1}{1 + \frac{h}{2\mu}} \tilde{H} \\ H = H_0 + \frac{\frac{h}{2\mu}}{1 + \frac{h}{2\mu}} \tilde{H} \end{array} \right. & \quad (8.78) \end{aligned}$$

Le critère d'unicité (8.76) donne alors :

$$\begin{cases} H_\infty - \Sigma > \frac{1}{1 + \frac{h}{2\mu}} \tilde{H} \\ H_0 - \Sigma > -\frac{\frac{h}{2\mu}}{1 + \frac{h}{2\mu}} \tilde{H} \end{cases} \quad (8.79)$$

Si $\Sigma \leq H_0$ nous nous ramenons au cas 3, et l'unicité est assurée, sinon $\Sigma - H_0 > 0$, on a donc :

$$\begin{cases} 0 < \Sigma - H_0 < \frac{\frac{h}{2\mu}}{1 + \frac{h}{2\mu}} \tilde{H} \\ \frac{1}{H_\infty - \Sigma} > \frac{1 + \frac{h}{2\mu}}{\tilde{H}} > 0 \end{cases} \quad (8.80)$$

$$\Rightarrow \frac{\Sigma - H_0}{H_\infty - \Sigma} < \frac{h}{2\mu} \forall \underline{\mathbf{w}} \in \mathcal{V}_0^{adm} \quad (8.81)$$

$$\Leftrightarrow \frac{h}{2\mu} > \beta \quad , \quad \beta = \sup_{\underline{\mathbf{w}} \in \mathcal{V}_0^{adm}} \left(\frac{\Sigma - H_0}{H_\infty - \Sigma} \right) \quad (8.82)$$

μ étant constant, cela est valable pour h suffisamment grand ($> \beta$).

8.4 Dynamic discontinuity and acoustic tensor

One way of approaching localization is to consider the propagation of an acceleration wave in a solid body. To do this, we start with Cauchy's law, that can be written as:

$$\underline{\text{div}}(\underline{\sigma}) + \rho \underline{f} = \rho \underline{\ddot{u}} \quad (8.83)$$

where ρ is the mass density, \underline{f} volume forces (which is neglected for this work) and $\underline{\ddot{u}}$ the acceleration of the volume element.

Also, let us consider an elastoplastic constitutive law which can always be expressed in its rate form (with $\underline{\mathcal{L}}$ the elastoplastic tangent operator. Note that it always has minor symmetries which is important for the following analysis):

$$\underline{\dot{\sigma}} = \underline{\mathcal{L}} : \underline{\dot{\epsilon}} = \underline{\mathcal{L}} : \underline{\nabla}(\underline{\dot{u}}) \quad (8.84)$$

at small strains Let S_d be a traveling discontinuity surface across which one observes a jump in acceleration and strain rate. We denote its unit normal by \underline{n} , U its normal velocity, V^- and V^+ the two domains in which the volume is split (see Figure 8.2).

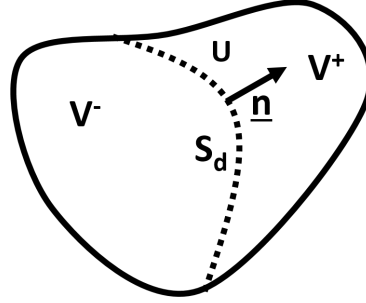


Figure 8.2: Discontinuity surface traveling through the body with a velocity U

Hadamard's compatibility condition states that in the absence of cracks, then any jump in strain rate has to be of the following form [Hadamard, 1903] (with $\llbracket A \rrbracket = A^+ - A^-$):

$$\llbracket \underline{\nabla}(\underline{\dot{u}}) \rrbracket = -\frac{\llbracket \underline{\dot{u}} \rrbracket}{U} \otimes \underline{n} \quad (8.85)$$

Also, the stress jump should respect [Truesdell and Toupin, 1960, Mandel, 1964]:

$$\llbracket \underline{\text{div}}(\underline{\sigma}) \rrbracket = -\llbracket \underline{\dot{\sigma}} \rrbracket \cdot \frac{\underline{n}}{U} \quad (8.86)$$

Let us now consider that the behavior is the same on both side of the discontinuity surface (either both in plastic loading or both in elastic unloading). Combining all previous equations leads to:

$$\llbracket \underline{\text{div}}(\underline{\sigma}) \rrbracket = \rho \llbracket \underline{\dot{u}} \rrbracket \quad (8.87)$$

$$(8.86) \Rightarrow -\llbracket \underline{\dot{\sigma}} \rrbracket \cdot \frac{\underline{n}}{U} = \rho \llbracket \underline{\dot{u}} \rrbracket \quad (8.88)$$

$$(8.84) \Rightarrow -\left(\underline{\mathcal{L}} : \llbracket \underline{\nabla}(\underline{\dot{u}}) \rrbracket \right) \cdot \frac{\underline{n}}{U} = \rho \llbracket \underline{\dot{u}} \rrbracket \quad (8.89)$$

$$(8.85) \Rightarrow -\left(\underline{\mathcal{L}} : \left(-\frac{\llbracket \underline{\dot{u}} \rrbracket}{U} \otimes \underline{n} \right) \right) \cdot \frac{\underline{n}}{U} = \rho \llbracket \underline{\dot{u}} \rrbracket \quad (8.90)$$

$$\left(\underline{n} \odot \underline{\hat{\mathcal{L}}} \cdot \underline{n} \right) \cdot \frac{\llbracket \underline{\dot{u}} \rrbracket}{U^2} = \rho \llbracket \underline{\dot{u}} \rrbracket \quad (8.91)$$

$$\underline{Q} \cdot \llbracket \underline{\dot{u}} \rrbracket = \rho U^2 \llbracket \underline{\dot{u}} \rrbracket \quad (8.92)$$

where \odot denotes the product $(\underline{\mathbf{n}} \odot \underline{\underline{\mathcal{L}}})_{ijkl} = n_k \mathcal{L}_{ikjl}$ and $\underline{\underline{\mathcal{Q}}} = \underline{\mathbf{n}} \odot \hat{\underline{\underline{\mathcal{L}}}} \cdot \underline{\mathbf{n}}$ is the well-known **acoustic tensor** [Bigoni and Zaccaria, 1993].

At small strains $\underline{\underline{\mathcal{L}}}$ possesses minor symmetries (since it relates $\underline{\underline{\dot{\boldsymbol{\epsilon}}}}$ to $\underline{\underline{\dot{\boldsymbol{\epsilon}}}}$, see equation (8.84)), which means the \odot product could be replaced by a \cdot product. However, this is not the case in the finite deformation case (cf. section 4.1.1), so we will keep this notation to avoid misunderstandings.

We recognize in equation (8.92) an eigenvalue problem: ρU^2 is the eigenvalue and $[[\underline{\underline{\dot{\boldsymbol{u}}}}]]$ is the associated eigenvector. While all eigenvalues are positive, the discontinuity surface can propagate. However, when $\underline{\underline{\mathcal{Q}}}$ becomes singular, $\det(\underline{\underline{\mathcal{Q}}}) = 0$, the velocity of the discontinuity surface vanishes and the jump in strain rate leads to localization.

As explained in [Mandel, 1966] this condition is necessary for the existence of a localization band and differs from Drucker's postulate [Drucker, 1951] which requires:

$$\underline{\underline{\dot{\boldsymbol{\sigma}}}} : \underline{\underline{\dot{\boldsymbol{\epsilon}}}} > 0 \quad \forall \underline{\underline{\dot{\boldsymbol{\epsilon}}}} \neq \mathbf{0} \quad \text{to ensure stability of a volume element.} \quad (8.93)$$

In fact, in the particular case where $\underline{\nabla}(\underline{\underline{\dot{\boldsymbol{u}}}}) = \underline{\mathbf{g}} \otimes \underline{\mathbf{n}}$ (see equation 8.85), Drucker's postulate leads to:

$$(\underline{\mathbf{g}} \otimes \underline{\mathbf{n}}) : \underline{\underline{\mathcal{L}}} : (\underline{\mathbf{g}} \otimes \underline{\mathbf{n}}) > 0 \quad (8.94)$$

$$\underline{\mathbf{g}} \cdot \underline{\underline{\mathcal{Q}}} \cdot \underline{\mathbf{g}} > 0 \quad (8.95)$$

$$\underline{\mathbf{g}} \cdot \underline{\underline{\mathcal{Q}}}^{sym} \cdot \underline{\mathbf{g}} > 0 \quad (8.96)$$

$$\text{eigenvalues}(\underline{\underline{\mathcal{Q}}}^{sym}) > 0 \quad (8.97)$$

where $()^{sym}$ denotes the symmetrical part of a tensor.

The latter expression is more restrictive in ensuring stability than $\det(\underline{\mathbf{n}} \odot \hat{\underline{\underline{\mathcal{L}}}} \cdot \underline{\mathbf{n}}) = 0$. While there is no difference for materials that use Hill's maximal dissipation principle because $\underline{\underline{\mathcal{L}}}$ possesses major symmetry leading to $\underline{\underline{\mathcal{Q}}}$ being symmetric, this is not true for all materials. Even though it is the case for most metals, it is generally not true for soils: $\underline{\underline{\mathcal{L}}}$ does not possess major symmetry, so $\underline{\underline{\mathcal{Q}}}$ has no reason to be symmetric. Therefore, the criterion $\det((\underline{\mathbf{n}} \odot \hat{\underline{\underline{\mathcal{L}}}} \cdot \underline{\mathbf{n}})^{sym}) = 0$ is not sufficient to ensure a possible jump in strain rates.

This analysis leads to an interesting discussion in [Mandel, 1966] where the author proposes a link between the celerity of waves and the uniqueness of the system's response. In fact, this phenomenon is observed for elastic beams in compression: the buckling load can be identified as the compression load for which the frequency of the first transverse mode vanishes.

8.5 Loss of ellipticity specified to small deformation

In this section, three main cases are detailed : simple tension in plane strain, simple shear and simple tension. The latter will illustrate a limit of the loss of ellipticity criterion².

To simplify the derivations, the analysis is based on the small deformation theory. This can be justified, since there is not much difference between small and finite strain localization results [Lemaitre et al., 2009] for the following examples. This will be shown in the numerical analysis (section 8.6.5).

8.5.1 General analysis:

In a small deformation analysis the elastoplastic tangent operator $\underline{\underline{\mathcal{L}}}$ can be defined as³:

$$\dot{\underline{\underline{\sigma}}} = \underline{\underline{\mathcal{L}}} : \dot{\underline{\underline{\xi}}} \quad (8.98)$$

$$\text{with : } \underline{\underline{\mathcal{L}}} = \underline{\underline{\Lambda}} - \gamma \frac{(\underline{\underline{\Lambda}} : \underline{\underline{\mathcal{P}}}) \otimes (\underline{\underline{N}} : \underline{\underline{\Lambda}})}{H + \underline{\underline{N}} : \underline{\underline{\Lambda}} : \underline{\underline{\mathcal{P}}}} ; \quad (8.99)$$

$$H \text{ the hardening modulus;} \quad (8.100)$$

$$\underline{\underline{\mathcal{P}}} \text{ the flow direction, such that : } \underline{\underline{\epsilon}}^p = \dot{\lambda} \underline{\underline{\mathcal{P}}} ; \quad (8.101)$$

$$\dot{\lambda} \text{ the plastic multiplier;} \quad (8.102)$$

$$\underline{\underline{N}} = \frac{\partial f}{\partial \underline{\underline{\sigma}}} \text{ the normal to the yield surface with: } f \text{ the yield surface;} \quad (8.103)$$

$$\text{and : } \gamma = \begin{cases} 1 & \text{for plastic loading : } \underline{\underline{N}} : \underline{\underline{\Lambda}} : \dot{\underline{\underline{\xi}}} > 0 ; f = 0 \\ 0 & \text{for elastic unloading : } \underline{\underline{N}} : \underline{\underline{\Lambda}} : \dot{\underline{\underline{\xi}}} \leq 0 ; f = 0 \end{cases} . \quad (8.104)$$

As it has been shown in [Besson et al., 2010, Lemaitre et al., 2009], localization bands with the loading/loading condition are possible before the loading/unloading condition (see section 2.2.3). So we will keep this hypothesis for the following computations, leading to:

$$\gamma = 1 \quad (8.106)$$

Let us explicitly give the acoustic tensor in this case:

$$\underline{\underline{Q}} = \underline{\underline{n}} \odot \underline{\underline{\hat{\mathcal{L}}}} \cdot \underline{\underline{n}} \quad (8.107)$$

$$= \underline{\underline{n}} \odot \underline{\underline{\Lambda}} \cdot \underline{\underline{n}} - \frac{1}{A} (\underline{\underline{n}} \cdot \underline{\underline{\Lambda}} : \underline{\underline{\mathcal{P}}}) \otimes (\underline{\underline{N}} : \underline{\underline{\Lambda}} \cdot \underline{\underline{n}}) \quad (8.108)$$

$$= \underline{\underline{Q}}^e - \frac{\underline{\underline{b}} \otimes \underline{\underline{a}}}{A} \quad (8.109)$$

where $\underline{\underline{Q}}^e = \underline{\underline{n}} \odot \underline{\underline{\Lambda}} \cdot \underline{\underline{n}}$ is the "elastic acoustic tensor", $\underline{\underline{a}} = \underline{\underline{N}} : \underline{\underline{\Lambda}} \cdot \underline{\underline{n}}$, $\underline{\underline{b}} = \underline{\underline{n}} \cdot \underline{\underline{\Lambda}} : \underline{\underline{\mathcal{P}}}$ and $A = H + \underline{\underline{N}} : \underline{\underline{\Lambda}} : \underline{\underline{\mathcal{P}}}$ are here to simplify notation.

² In order to derive the results, we will need to give the explicit expression of the tangent operator. Its expression is given for the general case in the first annual report.

³ Usually denoted $\underline{\underline{n}}$, the normal to the yield surface is denoted $\underline{\underline{N}}$ to avoid any confusion with the normal to the localization surface $\underline{\underline{n}}$

As the loss of ellipticity criterion is formulated on the determinant of the acoustic tensor, we are interested in the analysis of its eigenvalues. Therefore, one might try to solve:

$$\underline{\mathcal{Q}} \cdot \underline{x} = \lambda \underline{x} \quad (8.110)$$

However, expressed like this, solving the problem is not simple.

Nevertheless we show that the elastic acoustic tensor $\underline{\mathcal{Q}}^e$ is positive definite. In fact (of course, neither $\underline{\mathcal{A}}$, \underline{g} or \underline{n} should be identically zero):

$$\underline{\mathcal{A}} : \underline{\underline{\Lambda}} : \underline{\mathcal{A}} > 0 \quad \forall \underline{\mathcal{A}} \neq \underline{\mathbf{0}} \quad (8.111)$$

$$(\underline{g} \otimes \underline{n}) : \underline{\underline{\Lambda}} : (\underline{g} \otimes \underline{n}) > 0 \quad \forall \underline{g} \perp \underline{n} \quad (8.112)$$

$$\underline{g} \cdot (\underline{n} \odot \underline{\underline{\Lambda}} \cdot \underline{n}) \cdot \underline{g} > 0 \quad \forall \underline{g} \perp \underline{n} \quad (8.113)$$

$$\det((\underline{n} \odot \underline{\underline{\Lambda}} \cdot \underline{n})^{sym}) > 0 \quad \forall \underline{n} \quad (8.114)$$

$$\det(\underline{\mathcal{Q}}^e) > 0 \quad \forall \underline{n} \quad (8.115)$$

because $\underline{\underline{\Lambda}}$ possesses all symmetries since it is the elasticity tensor. Then one gets:

$$\det(\underline{\mathcal{Q}}^{e-1} \underline{\mathcal{Q}}) = 0 \Leftrightarrow \det(\underline{\mathcal{Q}}) = 0 \quad (8.116)$$

In other words $\underline{\mathcal{Q}}^{e-1} \underline{\mathcal{Q}}$ and $\underline{\mathcal{Q}}$ both become singular for the same conditions. Therefore, it is chosen to analyze the eigenvalues of $\underline{\mathcal{Q}}^{e-1} \underline{\mathcal{Q}}$ to conclude on the positiveness of the elastoplastic acoustic tensor:

$$\underline{\mathcal{Q}}^{e-1} \underline{\mathcal{Q}} \underline{y} = \lambda \underline{y} \quad (8.117)$$

$$\Rightarrow \left[\underline{\underline{I}} - \frac{1}{A} (\underline{\mathcal{Q}}^{e-1} \cdot \underline{b}) \otimes \underline{a} \right] \cdot \underline{y} = \lambda \underline{y} \quad (8.118)$$

As a matter of fact, equation (8.118) can be solved directly. First two eigenvectors can easily be identified as any two non-colinear vectors orthogonal to \underline{a} . As we are working in three dimensions, we can find a pair a non-co-linear vectors that have this property. Let's call them \underline{y}_1 and \underline{y}_2 . Trivially their eigenvalues are unitary: $\lambda_1 = \lambda_2 = 1$. Finally using the property of the trace of a tensor, we have:

$$\text{Tr}(\underline{\mathcal{Q}}^{e-1} \underline{\mathcal{Q}}) = 3 - \frac{1}{A} (\underline{a} \cdot \underline{\mathcal{Q}}^{e-1} \underline{b}) = 2 + \lambda_3 \quad (8.119)$$

From which one can easily deduce λ_3 . Another way to solve the problem is to remark that $\underline{\mathcal{Q}}^{e-1} \cdot \underline{b}$ is the third eigenvector:

$$\left[\underline{\underline{I}} - \frac{1}{A} (\underline{\mathcal{Q}}^{e-1} \cdot \underline{b}) \otimes \underline{a} \right] \cdot (\underline{\mathcal{Q}}^{e-1} \cdot \underline{b}) \quad (8.120)$$

$$= (\underline{\mathcal{Q}}^{e-1} \cdot \underline{b}) - \frac{1}{A} (\underline{\mathcal{Q}}^{e-1} \cdot \underline{b}) (\underline{a} \cdot \underline{\mathcal{Q}}^{e-1} \cdot \underline{b}) \quad (8.121)$$

$$= \left(1 - \frac{1}{A} \underline{a} \cdot \underline{\mathcal{Q}}^{e-1} \underline{b} \right) (\underline{\mathcal{Q}}^{e-1} \cdot \underline{b}) \quad (8.122)$$

which also directly gives $\lambda_3 = 1 - \frac{1}{A} \underline{a} \cdot \underline{\mathcal{Q}}^{e-1} \underline{b}$.

Finally, as $\lambda_1 = \lambda_2 = 1$, λ_3 is the only eigenvalue that can vanish. Since this quantity depends

on the hardening modulus, it is interesting to extract H as a function of the other variables when λ_3 vanishes:

$$1 - \frac{\underline{\mathbf{a}} \underline{\mathbf{Q}}^{e-1} \underline{\mathbf{b}}}{H + \underline{\mathbf{N}} : \underline{\mathbf{\Lambda}} : \underline{\mathbf{N}}} = 0 \quad (8.123)$$

$$H + \underline{\mathbf{N}} : \underline{\mathbf{\Lambda}} : \underline{\mathbf{N}} = (\underline{\mathbf{N}} : \underline{\mathbf{\Lambda}} \cdot \underline{\mathbf{n}}) \underline{\mathbf{Q}}^{e-1} (\underline{\mathbf{n}} \cdot \underline{\mathbf{\Lambda}} : \underline{\mathbf{P}}) \quad (8.124)$$

$$H(\underline{\mathbf{n}}) = -\underline{\mathbf{N}} : \underline{\mathbf{\Lambda}} : \underline{\mathbf{N}} + (\underline{\mathbf{N}} : \underline{\mathbf{\Lambda}} \cdot \underline{\mathbf{n}}) (\underline{\mathbf{n}} \odot \underline{\mathbf{\Lambda}} \cdot \underline{\mathbf{n}})^{-1} (\underline{\mathbf{n}} \cdot \underline{\mathbf{\Lambda}} : \underline{\mathbf{P}}) \quad (8.125)$$

Equation (8.125) tells us that, for a given plastic flow direction ($\underline{\mathbf{P}}$), a given normal to the yield surface ($\underline{\mathbf{N}}$) and a given normal to a unit surface ($\underline{\mathbf{n}}$), a jump in strain rates proportional to $\left((\underline{\mathbf{n}} \odot \underline{\mathbf{\Lambda}} \cdot \underline{\mathbf{n}})^{-1} (\underline{\mathbf{n}} \cdot \underline{\mathbf{\Lambda}} : \underline{\mathbf{P}}) \right) \otimes \underline{\mathbf{n}}$ becomes possible when the hardening modulus fulfills equation (8.125). These quantities are considered to be “given” because, in the absence of vertices, they are directly derived from the yield surface and the flow rule. They can be constant for a given monotonic loading, while the hardening modulus depends on the current evolution of the stresses⁴. However, if in the current state, multiple ”normals” to the yield surface can be considered (for example in the presence of vertices on the yield surface), this equation has multiple degrees of freedom for a given stress state and monotonic loading, therefore it can be easier to fulfill. In [Rice, 1976] the author talks about an increased softening behavior for materials that develop a vertex on their yield surface. Some analysis of this phenomenon can also be found in [Mear and Hutchinson, 1985].

Let us now make another hypothesis: the hardening modulus only decreases until localization occurs. In fact, this is the case for many materials. One might then try to derive, for a given loading direction, the hardening modulus for which equation (8.125) is fulfilled for the first time. We will denote this quantity H^{cr} :

$$H^{cr} = \text{Sup}_{(\underline{\mathbf{n}} \cdot \underline{\mathbf{n}}=1)} H(\underline{\mathbf{n}}) \quad (8.126)$$

In order to simplify the analysis (the full one is available in [Bigoni and Hueckel, 1991]), the following computations will be expressed for associated flow rules:

$$\text{Tr}(\underline{\mathbf{N}}) = 0 \quad (8.127)$$

$$\underline{\mathbf{N}} = \underline{\mathbf{P}} \quad (8.128)$$

For isotropic elastic materials, equation (8.125) gives:

$$H(\underline{\mathbf{n}}) = 2\mu \left(2(\underline{\mathbf{n}} \underline{\mathbf{P}}) \cdot (\underline{\mathbf{P}} \underline{\mathbf{n}}) - \frac{1}{1-\nu} (\underline{\mathbf{n}} \underline{\mathbf{P}} \underline{\mathbf{n}})^2 - \underline{\mathbf{P}} : \underline{\mathbf{P}} \right) \quad (8.129)$$

where ν is the Poisson ratio and μ the shear modulus.

Given that $\underline{\mathbf{n}}$ is totally undetermined, it will be easier to work in the eigenbasis of $\underline{\mathbf{P}}$. In this basis, $\underline{\mathbf{P}}$ is diagonal and its eigenvalues will be denoted P_i . Equation (8.129) then becomes:

$$H(\underline{\mathbf{n}}) = 2\mu (2n_i^2 P_i^2 - P_i P_i - \frac{1}{1-\nu} (n_i^2 P_i)^2) \quad (8.130)$$

We want to maximize this function under the constrain $\underline{\mathbf{n}} \cdot \underline{\mathbf{n}} = 1$. One can solve the following problem:

$$\begin{cases} \frac{\partial L(\underline{\mathbf{n}}, \lambda)}{\partial \underline{\mathbf{n}}} = \underline{\mathbf{0}} \\ \frac{\partial L(\underline{\mathbf{n}}, \lambda)}{\partial \lambda} = 0 \end{cases} \quad (8.131)$$

$$\text{with } L(\underline{\mathbf{n}}, \lambda) = H(\underline{\mathbf{n}}) - \lambda(\underline{\mathbf{n}} \cdot \underline{\mathbf{n}} - 1) \quad (8.132)$$

⁴ The hardening modulus varies for non linear hardening laws.

where λ is Lagrange multiplier.

The second derivative gives $\underline{\mathbf{n}} \cdot \underline{\mathbf{n}} = 1$.

The first one gives:

$$n_k \left(P_k^2 - \frac{1}{1-\nu} (n_i^2 P_i) P_k - \frac{\lambda}{4\mu} \right) = 0 \quad \text{for } k \in \{1, 2, 3\} \quad (\text{no summation over } k) \quad (8.133)$$

[Besson et al., 2010] states that:

If $n_1, n_2, n_3 \neq 0$ then the system is either undetermined or impossible, depending on $P_1 P_2 P_3$.

If $n_3 = 0$ and $n_1, n_2 \neq 0$, then the system becomes:

$$\begin{cases} 0 = P_1^2 - \frac{P_1}{1-\nu} (n_1^2 P_1 + n_2^2 P_2) \\ 0 = P_2^2 - \frac{P_2}{1-\nu} (n_1^2 P_1 + n_2^2 P_2) \\ n_2^2 = 1 - n_1^2 \end{cases} \quad (8.134)$$

$$\Rightarrow n_1^2 = \frac{P_1 + \nu P_3}{P_1 - P_2} \quad (8.135)$$

$$\Rightarrow H^{cr}(\underline{\mathbf{n}}) = -EP_3^2 \quad (8.136)$$

where E is the Young modulus.

Finally, if $n_2 = n_3 = 0$ and $n_1 = 1$, one gets:

$$H^{cr}(\underline{\mathbf{n}}) = -2E \left(\frac{(P_2 + \nu P_3)^2}{1-\nu^2} + P_3^2 \right) \quad (8.137)$$

$$= -2 \frac{E}{1-\nu^2} (P_2^2 + \nu P_3 P_2 + P_3^2) \quad (8.138)$$

Note that P_i 's are not sorted in any order.

The terms in equations (8.136) and (8.137) are of the same order of magnitude (Young's modulus times variables of the order of unity). For a given flow direction $\underline{\mathbf{P}}$ one can evaluate the different H^{cr} obtained with these equations to deduce the one with the maximum value. Another reason to this, is that we do not know whether each refers to a maximum or a minimum since we only solved to get a null gradient and it is easier to evaluate them all than to compute the second derivative.

8.5.2 Elastic unloading/plastic loading condition

In the previous analysis, a major hypothesis on the loading condition has been made. We need to examine this hypothesis to verify whether it is valid. We need to show that plastic/plastic localization is, in fact, the first to occur.

In a loading process, the material first exhibits an elastic behavior making localization impossible initially⁵ since it was proven already that $\det(\underline{\mathbf{Q}}^e) > 0$ (see section 8.5.1). Moreover, it has been shown that plastic/plastic localization is only possible when the elastoplastic acoustic tensor ($\det(\underline{\mathbf{n}} \odot \underline{\mathbf{L}} \cdot \underline{\mathbf{n}})$) is singular. Thus it remains to consider the elastic/plastic localization.

Let us assume that the behavior in V^+ is in plastic loading while V^- is in elastic unloading while the jump through S_d is such that $[[\underline{\dot{\boldsymbol{\varepsilon}}}}]] = (\underline{\mathbf{g}} \otimes \underline{\mathbf{n}})^{sym}$. One gets:

$$(\underline{\dot{\boldsymbol{\varepsilon}}}^+ - \underline{\dot{\boldsymbol{\varepsilon}}}^-) \cdot \underline{\mathbf{n}} = \underline{\mathbf{0}} \quad (8.139)$$

$$\Rightarrow \left(\underline{\mathbf{L}} : \underline{\dot{\boldsymbol{\varepsilon}}}^+ - \underline{\mathbf{L}} : \underline{\dot{\boldsymbol{\varepsilon}}}^- \right) \cdot \underline{\mathbf{n}} = \underline{\mathbf{0}} \quad (8.140)$$

⁵ We are here working in a small deformation framework. In a finite deformation framework, and with some complex materials one could encounter loss of ellipticity too [d'Avila et al., 2016].

From which one equivalently deduces:

$$\left\{ \begin{array}{l} \left(\underset{\approx}{\mathcal{L}} : \underset{\approx}{\dot{\boldsymbol{\xi}}} \right) \cdot \underline{\mathbf{n}} = \frac{1}{A} \left[\left(\underset{\approx}{\mathcal{P}} : \underset{\approx}{\boldsymbol{\Lambda}} \right) \otimes \left(\underset{\approx}{\boldsymbol{\Lambda}} : \underset{\approx}{\mathcal{N}} \right) : \underset{\approx}{\dot{\boldsymbol{\xi}}}^- \right] \cdot \underline{\mathbf{n}} \\ \text{or: } \left(\underset{\approx}{\boldsymbol{\Lambda}} : \underset{\approx}{\dot{\boldsymbol{\xi}}} \right) \cdot \underline{\mathbf{n}} = \frac{1}{A} \left[\left(\underset{\approx}{\mathcal{P}} : \underset{\approx}{\boldsymbol{\Lambda}} \right) \otimes \left(\underset{\approx}{\boldsymbol{\Lambda}} : \underset{\approx}{\mathcal{N}} \right) : \underset{\approx}{\dot{\boldsymbol{\xi}}}^+ \right] \cdot \underline{\mathbf{n}} \end{array} \right. \quad (8.141)$$

$$\Rightarrow \left\{ \begin{array}{l} \left(\underset{\approx}{\mathcal{L}} : \underset{\approx}{\dot{\boldsymbol{\xi}}} \right) \cdot \underline{\mathbf{n}} = \frac{\alpha}{A} \underset{\approx}{\mathcal{P}} : \underset{\approx}{\boldsymbol{\Lambda}} \cdot \underline{\mathbf{n}} \text{ with: } \alpha = \underset{\approx}{\mathcal{N}} : \underset{\approx}{\boldsymbol{\Lambda}} : \underset{\approx}{\dot{\boldsymbol{\xi}}}^- < 0 \text{ elastic unloading condition} \\ \text{or: } \left(\underset{\approx}{\boldsymbol{\Lambda}} : \underset{\approx}{\dot{\boldsymbol{\xi}}} \right) \cdot \underline{\mathbf{n}} = \frac{\beta}{A} \underset{\approx}{\mathcal{P}} : \underset{\approx}{\boldsymbol{\Lambda}} \cdot \underline{\mathbf{n}} \text{ with: } \beta = \underset{\approx}{\mathcal{N}} : \underset{\approx}{\boldsymbol{\Lambda}} : \underset{\approx}{\dot{\boldsymbol{\xi}}}^+ > 0 \text{ plastic loading condition} \end{array} \right. \quad (8.142)$$

$$(8.143)$$

Combining these two equations, and using Hadamard's compatibility condition, it leads to:

$$\left(\underset{\approx}{\mathcal{L}} : (\underline{\mathbf{g}} \otimes \underline{\mathbf{n}}) \right) \cdot \underline{\mathbf{n}} = \frac{\alpha}{\beta} \left(\underset{\approx}{\boldsymbol{\Lambda}} : (\underline{\mathbf{g}} \otimes \underline{\mathbf{n}}) \right) \cdot \underline{\mathbf{n}} \quad (8.144)$$

$$\Rightarrow \underset{\approx}{\mathcal{Q}} \cdot \underline{\mathbf{g}} = \frac{\alpha}{\beta} \underset{\approx}{\mathcal{Q}}^e \cdot \underline{\mathbf{g}} \quad (8.145)$$

$$\Rightarrow \left(\underset{\approx}{\mathcal{Q}}^{e-1} \underset{\approx}{\mathcal{Q}} \right) \underline{\mathbf{g}} = \frac{\alpha}{\beta} \underline{\mathbf{g}} \quad (8.146)$$

This equation can be identified as the one set in equation (8.118).

Therefore, $\frac{\alpha}{\beta}$ can be identified as the third eigenvalue; the one that is not unity. As a consequence of the plastic loading/elastic unloading condition this ratio is negative. Since the acoustic tensor is initially positive definite, and one assumes that the hardening modulus is a smooth function of the state variables, the elastic/plastic jump occurs necessarily after the plastic/plastic jump.

Still, it happens literally just after [Lemaitre et al., 2009]. This means that plastic/plastic jumps are most likely not to be captured within a problem with finite time steps. This is in fact the same problem as the one encountered with Hill's loss of uniqueness criterion. In a finite element simulation, one can evaluate Hill's loss of uniqueness criterion at each computed time step, however, one can not conclude on uniqueness through the whole time-step.

8.6 Loss of ellipticity: analytical simple cases (small deformation)

For the following cases one should keep in mind that we are working on a single element (in numerical problems we would talk about a "Gauss Point problem"). Geometry is not taken into account. However one can always imagine an equivalent structural problem just by imposing homogeneous conditions on the boundary that satisfy the following cases. This is done in section 8.6.5 to validate the development of a new numerical method to evaluate loss of ellipticity. All results in the following paragraphs are given for a von Mises criterion with an isotropic hardening law:

$$\left\{ \begin{array}{l} \underline{\underline{\sigma}}^{dev} = \underline{\underline{\sigma}} - \frac{\text{Tr}(\underline{\underline{\sigma}})}{3} \underline{\underline{I}} \\ \sigma^{eq} = \sqrt{\frac{3}{2} \underline{\underline{\sigma}}^{dev} : \underline{\underline{\sigma}}^{dev}} \\ f(\underline{\underline{\sigma}}, R) = \sigma^{eq} - R(p) \\ \underline{\underline{N}} = \frac{3}{2} \frac{\underline{\underline{\sigma}}^{dev}}{\sigma^{eq}} \\ H(p) = \frac{\partial R}{\partial p} \end{array} \right. \quad (8.147)$$

8.6.1 Simple shear

Simple shear is characterized by a stress state of the form:

$$\underline{\underline{\sigma}} = \begin{pmatrix} 0 & \tau & 0 \\ \tau & 0 & 0 \\ 0 & 0 & 0 \end{pmatrix} \Rightarrow \sigma^{eq} = \sqrt{3}\tau \quad (8.148)$$

From which we can deduce (using equations in (8.147)):

$$\underline{\underline{N}} = \frac{\sqrt{3}}{2} \begin{pmatrix} 0 & 1 & 0 \\ 1 & 0 & 0 \\ 0 & 0 & 0 \end{pmatrix} \quad (8.149)$$

$$= \frac{\sqrt{3}}{4} \begin{pmatrix} 1 & 1 & 0 \\ 1 & -1 & 0 \\ 0 & 0 & 0 \end{pmatrix} \begin{pmatrix} 1 & 0 & 0 \\ 0 & -1 & 0 \\ 0 & 0 & 0 \end{pmatrix} \begin{pmatrix} 1 & 1 & 0 \\ 1 & -1 & 0 \\ 0 & 0 & 0 \end{pmatrix} \quad (8.150)$$

From equation (8.136) one gets:

$$H^{cr} = 0 \quad \text{or} \quad H^{cr} = -E < 0 \quad (8.151)$$

From equation (8.137) one gets:

$$H^{cr} = -\alpha E \quad (8.152)$$

where $\alpha > 0$ for all combinations.

This gives $H^{cr} = 0$ for which (in the eigenbasis):

$$\underline{\mathbf{n}} = \frac{\sqrt{2}}{2} \begin{pmatrix} 1 \\ 1 \\ 0 \end{pmatrix} \quad \text{or :} \quad \underline{\mathbf{n}} = \frac{\sqrt{2}}{2} \begin{pmatrix} 1 \\ -1 \\ 0 \end{pmatrix} \quad (8.153)$$

which in the global frame gives:

$$\underline{\mathbf{n}} = \begin{pmatrix} 1 \\ 0 \\ 0 \end{pmatrix} \quad \text{or :} \quad \underline{\mathbf{n}} = \begin{pmatrix} 0 \\ 1 \\ 0 \end{pmatrix} \quad (8.154)$$

Which leads to angles of 0° and 90° with the shearing axes ($\underline{\mathbf{x}}$ and $\underline{\mathbf{y}}$ in this case).

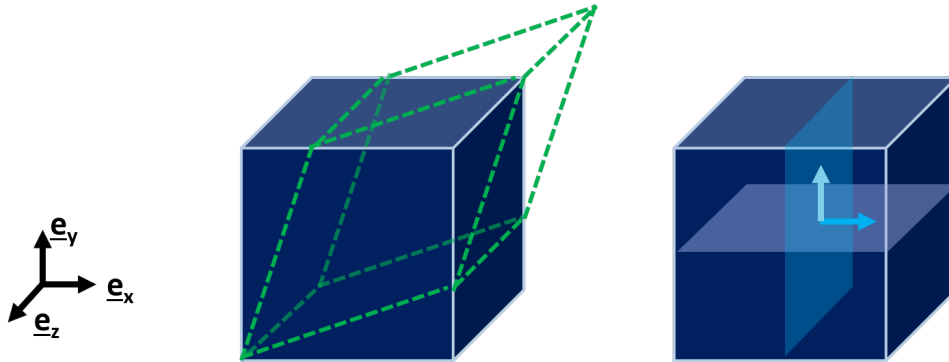


Figure 8.3: Volume element loaded in pure shear: localization bands at 0° and 90° .

8.6.2 Simple tension (or 3D case)

Simple tension is characterized by a stress state of the form:

$$\underline{\underline{\boldsymbol{\sigma}}} = \begin{pmatrix} \sigma & 0 & 0 \\ 0 & 0 & 0 \\ 0 & 0 & 0 \end{pmatrix} \Rightarrow \sigma^{eq} = \sigma \quad (8.155)$$

From which we can deduce:

$$\underline{\underline{\mathbf{N}}} = \begin{pmatrix} 1 & 0 & 0 \\ 0 & -\frac{1}{2} & 0 \\ 0 & 0 & -\frac{1}{2} \end{pmatrix} \quad (8.156)$$

$$(8.157)$$

From equation (8.136) one gets:

$$H^{cr} = -\frac{E}{4} \quad \text{or} \quad H^{cr} = -E < -\frac{E}{4} \quad (8.158)$$

From equation (8.137) one gets:

$$H^{cr} = -\frac{E}{1-\nu} < -\frac{E}{4} \quad \text{or} \quad H^{cr} = -\frac{5-2\nu}{2-2\nu^2}E < -\frac{E}{4} \quad (8.159)$$

This gives $H^{cr} = -\frac{E}{4}$ for which one gets:

$$\underline{\mathbf{n}} = \begin{pmatrix} \sqrt{\frac{2-\nu}{3}} \\ \sqrt{\frac{1+\nu}{3}} \\ 0 \end{pmatrix} \quad \text{or} \quad \underline{\mathbf{n}} = \frac{\sqrt{2}}{2} \begin{pmatrix} \sqrt{\frac{2-\nu}{3}} \\ -\sqrt{\frac{1+\nu}{3}} \\ 0 \end{pmatrix} \quad (8.160)$$

which in the global frame corresponds to an angle of $\arcsin\left(\sqrt{\frac{1+\nu}{3}}\right) \simeq 41.75^\circ$ with the tensile axis (so the band should roughly show an angle of $90^\circ - 41.75^\circ = 48.25^\circ$ angle with the tension axis).

Note that $\underline{\mathbf{e}}_2$ and $\underline{\mathbf{e}}_3$ are strictly equivalent in this analysis, $\underline{\mathbf{n}}$ is inclined at 41.75° angle with respect to the tension axis. so there is a cone of normal that satisfy the loss of ellipticity at the same time.

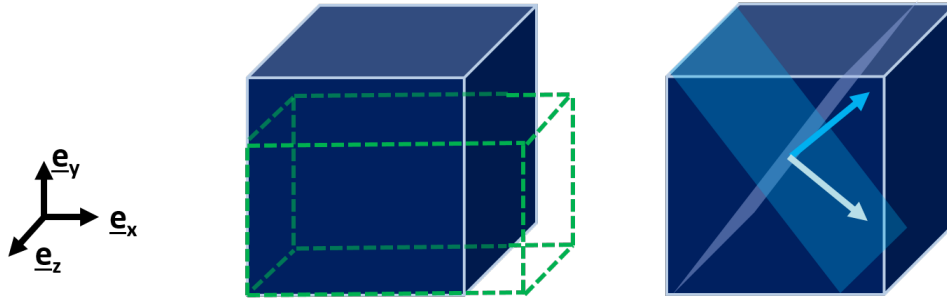


Figure 8.4: Scheme of a volume element loaded in plane stress tension: localization bands at $\sim -48^\circ$ and $\sim 48^\circ$ with the tension axis.

8.6.3 Tension in plane strain

Plane strain is characterized by:

$$\varepsilon_{33} = \varepsilon_{33}^e + \varepsilon_{33}^p = 0 \quad (8.161)$$

However ε_{33}^e and ε_{33}^p are not independently 0, but stay very small. They can usually be neglected when compared with the strains in the other directions. Therefore we will consider $P_3 \simeq 0$.

Also in tension, the strain principal directions are those aligned with the tensile direction and the direction orthogonal to the tension axis, and the third direction:

$$\underline{\underline{\mathbf{N}}} = \begin{pmatrix} P_1 & 0 & 0 \\ 0 & P_2 & 0 \\ 0 & 0 & 0 \end{pmatrix} \quad (8.162)$$

$$(8.163)$$

which gives: $P_1 = -P_2$.

Similarly to the simple shear case, one gets:

$$H^{cr} = 0 \quad \text{and} \quad \underline{\mathbf{n}} = \frac{\sqrt{2}}{2} \begin{pmatrix} 1 \\ 1 \\ 0 \end{pmatrix} \quad \text{or} \quad \underline{\mathbf{n}} = \frac{\sqrt{2}}{2} \begin{pmatrix} 1 \\ -1 \\ 0 \end{pmatrix} \quad (8.164)$$

which corresponds to an angle of 45° with the tension axis.

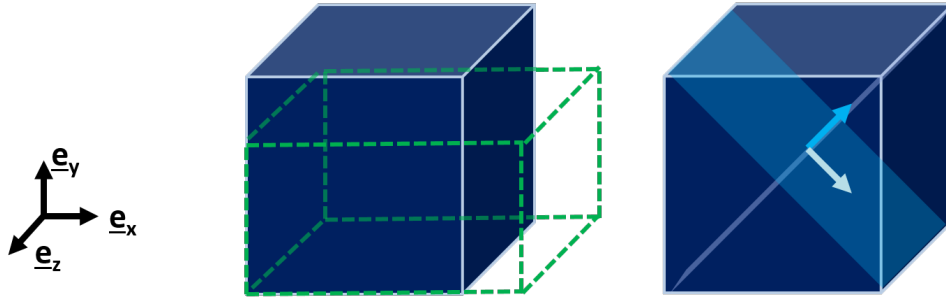


Figure 8.5: Scheme of a volume element loaded in plane strain tension: localization bands at -45° and 45° with the tension axis.

8.6.4 Plane stress bidimensional case

One might wonder why the second case is called "Simple tension (or 3D case)". In fact, the stress state we exposed was trivially plane stress since $\sigma_{33} = 0$. However the result obtained in paragraph 8.6 is obviously not satisfying ... $\frac{\partial R}{\partial p} = -\frac{E}{4}$ is something one might never see in a tensile test! In fact, when we consider the structural problem necking occurs long before⁶. Once it starts, the stress state is not simple tension anymore in the neck area, and this criterion is never reached.

As it has been stated, the loss of ellipticity is the moment when a jump in strain rates is allowed. In fact, Drucker's criterion on the loss of positiveness of second order work occurs first in this case. The eigen analysis of the elastoplastic tangent operator gives only one eigenvalue that depends on the hardening modulus, while the others are only function of the elastic constants. This is given in [Besson et al., 2010]:

$$\lambda = \frac{2\mu H}{H + 3\mu} \quad \text{and} \quad \underline{\underline{\mathbf{d}}} = \frac{2}{\sqrt{6}} \begin{pmatrix} 1 & 0 & 0 \\ 0 & -\frac{1}{2} & 0 \\ 0 & 0 & -\frac{1}{2} \end{pmatrix} \quad (8.165)$$

where λ is the eigenvalue of interest and $\underline{\underline{\mathbf{d}}}$ the associated and normalized eigentensor ($\underline{\underline{\mathbf{d}}} : \underline{\underline{\mathbf{d}}} = 1$). One might recognize that this tensor corresponds to a necking mode. Since this eigenvalue vanishes when $H = 0$, it is consistent with what we know about necking. This can actually be captured by Hill's uniqueness criterion. In fact, this is the case for tensile specimens such as bars, though not for thin plates. In fact, the loss of ellipticity criterion seems to fail to predict

⁶ Considère's criterion would give $H = R$.

localization in this case. Experimentally, it is well known that thin plates in tension break after a thin shear band appears in the specimen with an angle of 54.74° with respect to the tensile axis [Besson et al., 2010].

However to discuss this case properly, we need to numerically evaluate the loss of ellipticity. Some methods are presented in section 4.3.1 and a more efficient method is proposed in section 4.3. The full analysis of tension in thin plates will be derived in 3.2.3.

8.6.5 Application of numerical algo

This section is only about validating the minimization method based on analytical solutions that can be found in appendix (section 8.5). The material laws that are used are not realistic, especially when verifying the plane stress result ($H^{cr} = -\frac{E}{4}$). Therefore, the following results will be presented for a non linear isotropic hardening law formulated such as:

$$R(p) = 10000 - 52000p + 1000(1 - e^{-500p}) \quad (8.166)$$

$$E = 200 \text{ GPa} \quad , \quad \nu = 0.33 \quad (8.167)$$

where $p = \int_{-\infty}^t \sqrt{\frac{2}{3} \dot{\tilde{\epsilon}}^p : \dot{\tilde{\epsilon}}^p} dt$ is the accumulated plastic strain.

A von Mises criterion is used for the comparison with the results derived earlier. Finally, in finite deformation, the formulation is hypo-elastoplastic formulated on the Kirchhoff stress tensor.

Note that all simulations gave homogeneous results in terms of strain and stress until the end of the computation: they were run on a single element (unit cube, eight nodes, see Figure 8.6) where degrees of freedom were all prescribed. Therefore, no localization or diffused necking could take place. This is why all results are presented at a single GP. For each section the boundary conditions will be given, and the results of the simulations in small and finite deformation will be plotted. The instant for which ellipticity is lost will be indicated with a vertical dashed red line in each plot.

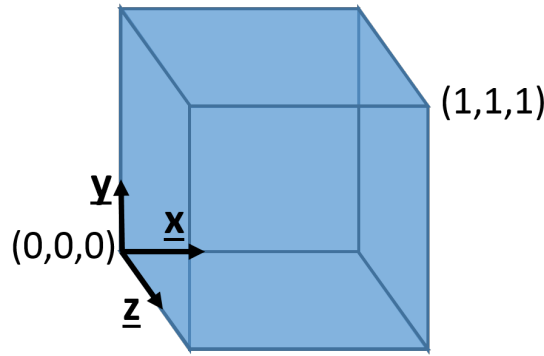


Figure 8.6: Unit cube element used for the following validation cases.

Tension in plane strain

Loading:

$$F_{11} = 1 + u^d t \quad (8.168)$$

$$F_{33} = 1 \quad (8.169)$$

$$\sigma_{22} = \sigma_{12} = \sigma_{23} = \sigma_{31} = 0 \quad (8.170)$$

$$(8.171)$$

Small deform

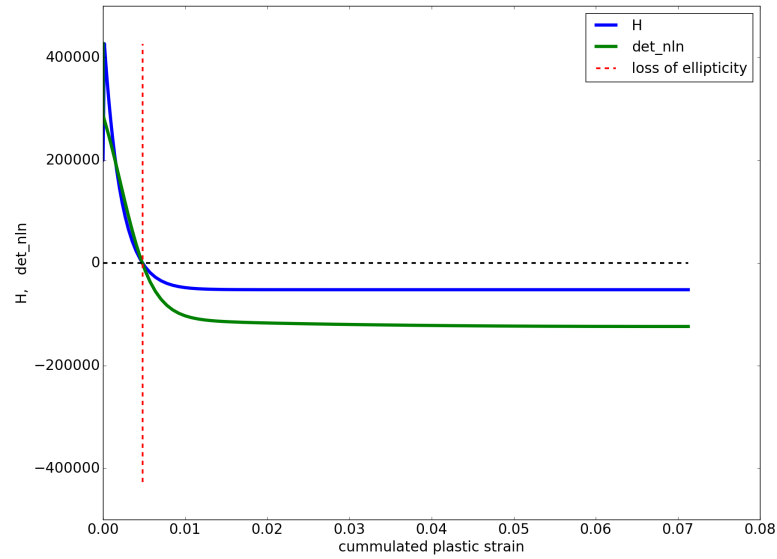


Figure 8.7: $\min(\det(\underline{n} \odot \hat{\underline{\mathcal{L}}} \cdot \underline{n}))$ and hardening modulus as functions of cumulated plastic strain under plane strain conditions.

The loss of ellipticity criterion is met when the hardening modulus vanishes. It is also found, in Figure 8.8, that \underline{n} is inclined at 45° degrees with respect to the tensile axis.

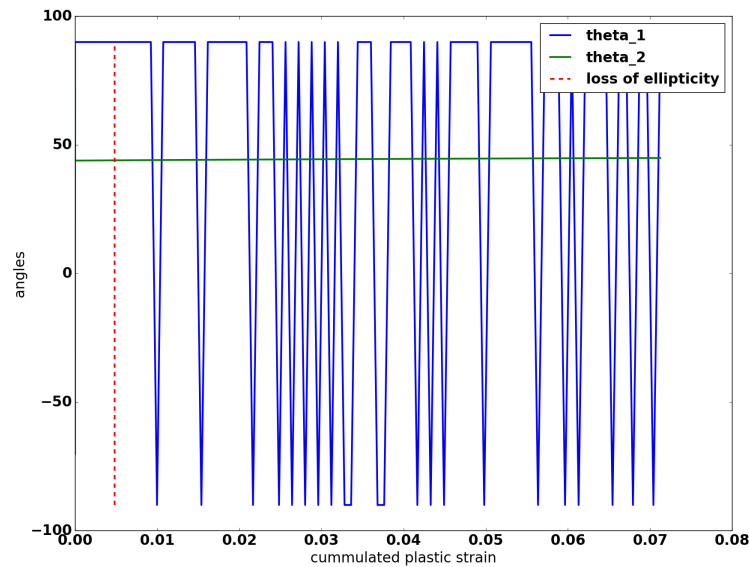


Figure 8.8: Plot of the spherical angles defining \underline{n} as a function of plastic strain in plane strain.

As shown earlier in section 8.6, there are two equivalent directions, so that θ_1 is either -90° or 90° .

Finite deformation:

In a finite deformation framework there are not much difference:

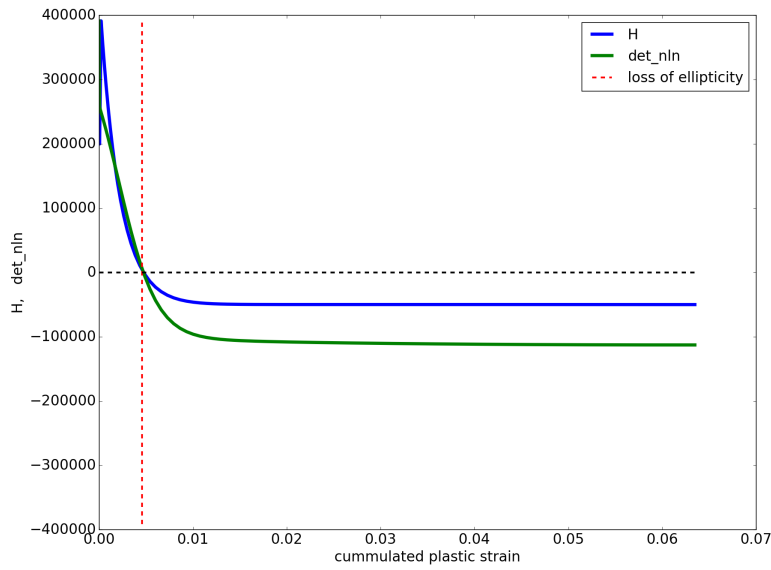


Figure 8.9: $\min(\det(\underline{n} \odot \hat{\mathcal{L}} \cdot \underline{n}))$ and hardening modulus as functions of cumulated plastic strain under plane strain conditions.

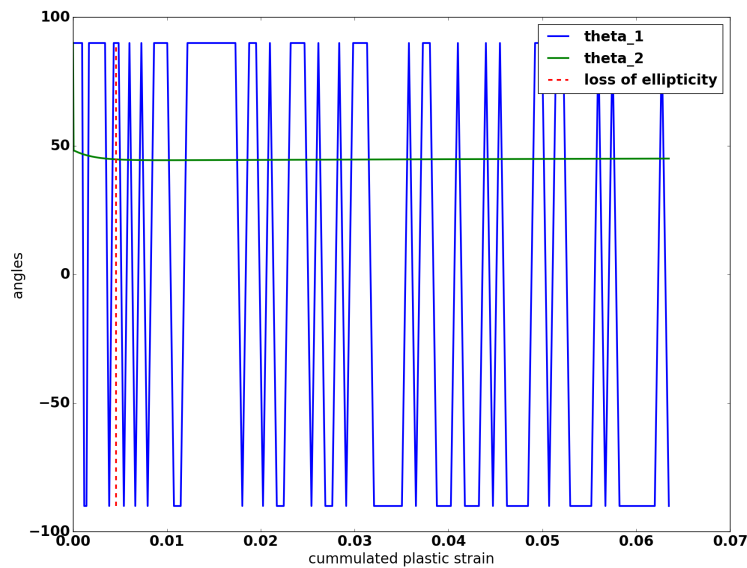


Figure 8.10: Plot of the spherical angles defining \underline{n} (finite deformation) as a function of plastic strain under plane strain conditions.

Simple tension

Boundary Conditions:

$$F_{33} = 1 + U^d t \quad (8.172)$$

$$\sigma_{11} = \sigma_{22} = \sigma_{12} = \sigma_{23} = \sigma_{31} = 0 \quad (8.173)$$

e_3 is chosen to be the tensile axis, so θ_2 represents the angle with respect to the tensile axis (see 8.6.2).

Small deform

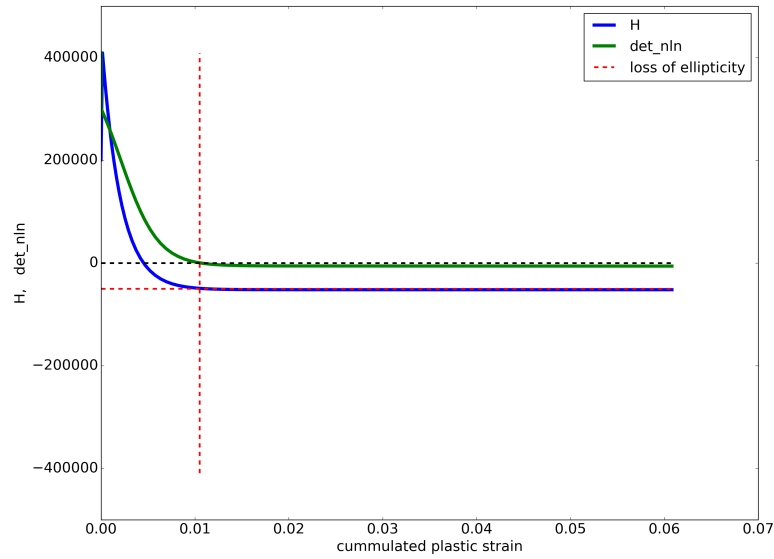


Figure 8.11: $\min(\det(\underline{n} \odot \hat{\mathcal{L}} \cdot \underline{n}))$ and hardening modulus as functions of cumulated plastic strain under plane stress conditions.

The loss of ellipticity criterion is met when the hardening modulus vanishes. It is also found that \underline{n} makes

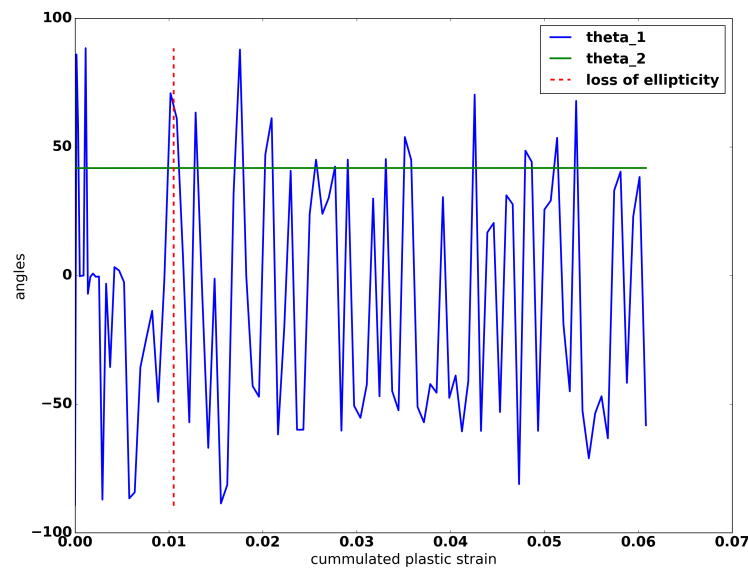


Figure 8.12: Plot of the spherical angles defining \underline{n} as a function of plastic strain under plane stress conditions.

As it was said earlier (cf. Figure 8.4), the solution does not depend on θ_1 , since \underline{x} and \underline{y} are equivalent directions. This is why it seems random.

Finite deformation:

In finite deformation there are not much difference:

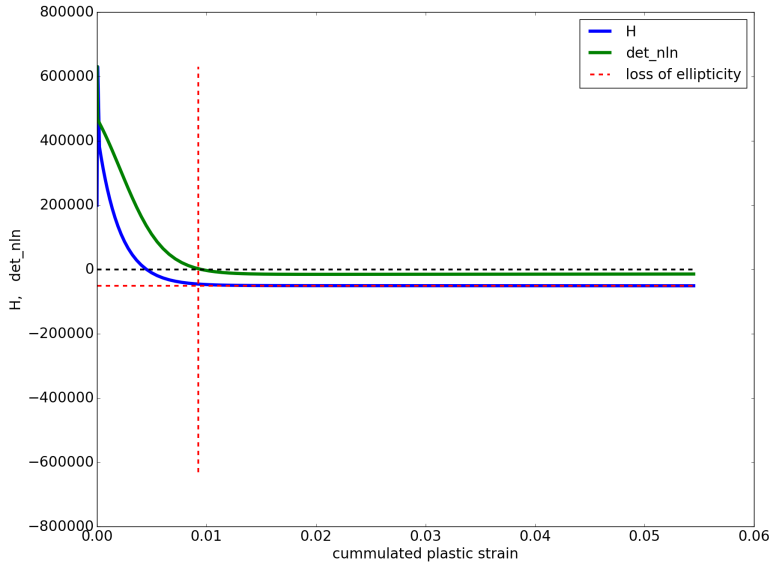


Figure 8.13: $\min(\det(\underline{n} \odot \hat{\mathcal{L}} \cdot \underline{n}))$ and hardening modulus as functions of cumulated plastic strain under plane stress conditions.

The loss of ellipticity criterion is met a little before the hardening modulus vanishes because of the finite deformation stress terms. It is found that \underline{n} makes a 42.38 degrees with the tension axis:

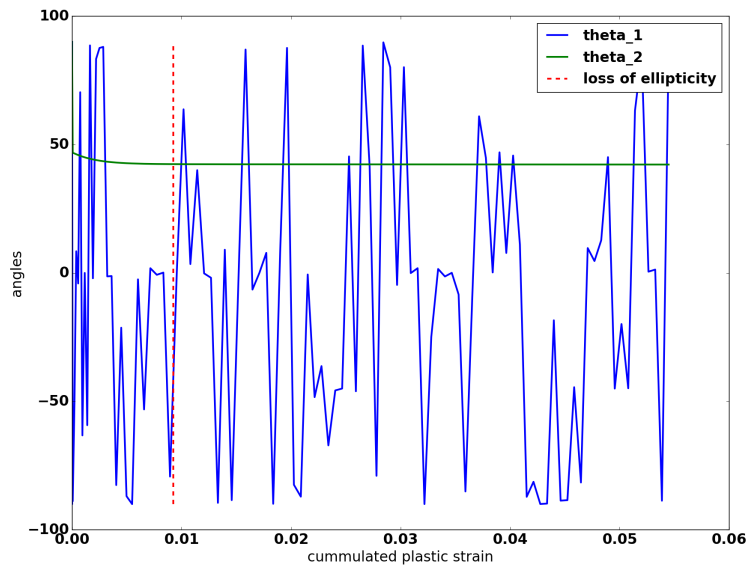


Figure 8.14: Plot of the spherical angles defining \underline{n} (finite deformation) as a function of plastic strain under plane stress conditions.

Pure shear

Deformation gradient:

$$\tilde{\mathbf{F}} = \begin{pmatrix} 1 & \alpha t & 0 \\ \alpha t & 1 & 0 \\ 0 & 0 & 1 \end{pmatrix} \quad (8.174)$$

Small deformation:

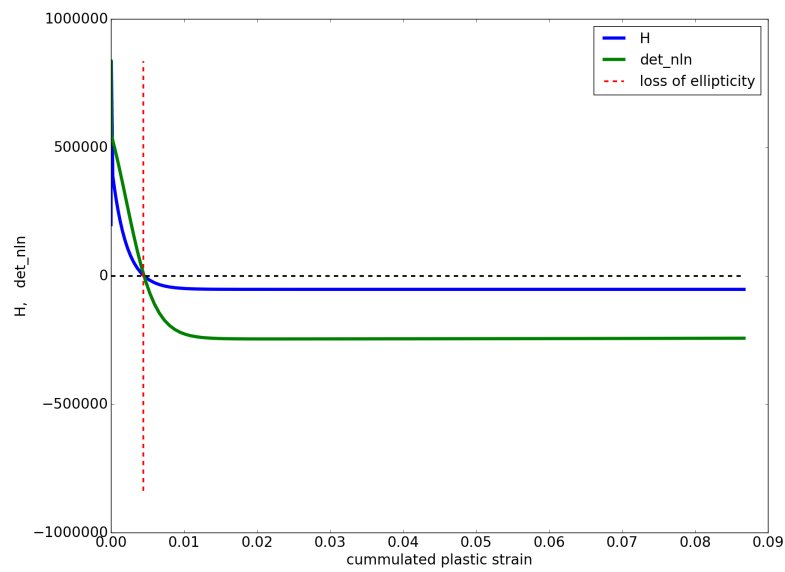


Figure 8.15: $\min(\det(\underline{\mathbf{n}} \odot \hat{\mathcal{L}} \cdot \underline{\mathbf{n}}))$ and hardening modulus as functions of cumulated plastic strain under shear conditions.

The loss of ellipticity criterion is met when the hardening modulus vanishes. Both directions $\underline{\mathbf{n}} = (1; 0; 0)$ and $\underline{\mathbf{n}} = (0; 1; 0)$ are found:

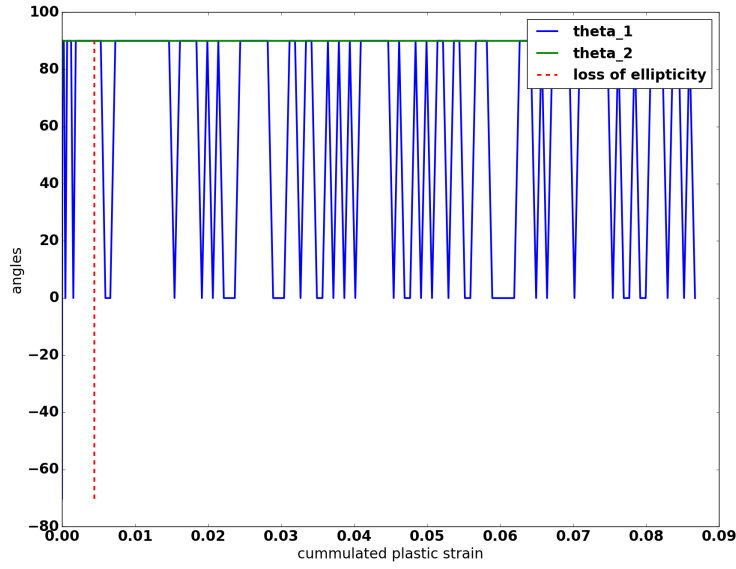


Figure 8.16: Plot of the spherical angles defining \underline{n} as a function of plastic strain under shear conditions.

Note that the stress tensor is consistent with pure shear:

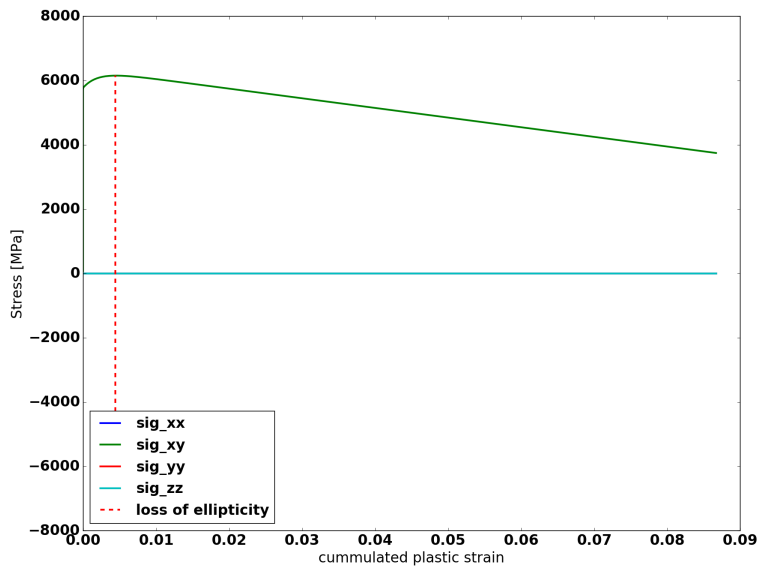


Figure 8.17: Only σ_{xy} is non zero.

Finite deformation:

In finite deformation there are not much difference:

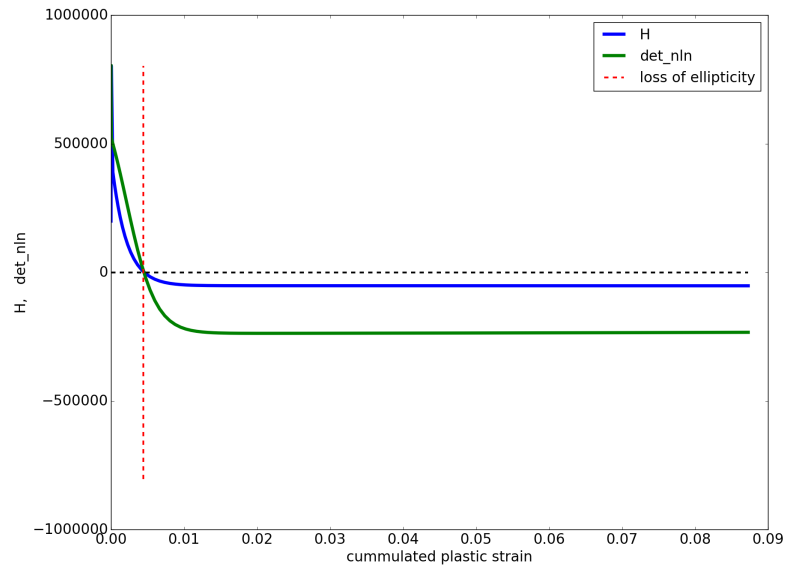


Figure 8.18: $\min(\det(\underline{n} \odot \hat{\mathcal{L}} \cdot \underline{n}))$ and hardening modulus as functions of cumulated plastic strain under shear conditions.

The loss of ellipticity criterion is met when the hardening modulus vanishes. Both directions $\underline{n} = (1; 0; 0)$ and $\underline{n} = (0; 1; 0)$ are found in a finite deformation framework too:

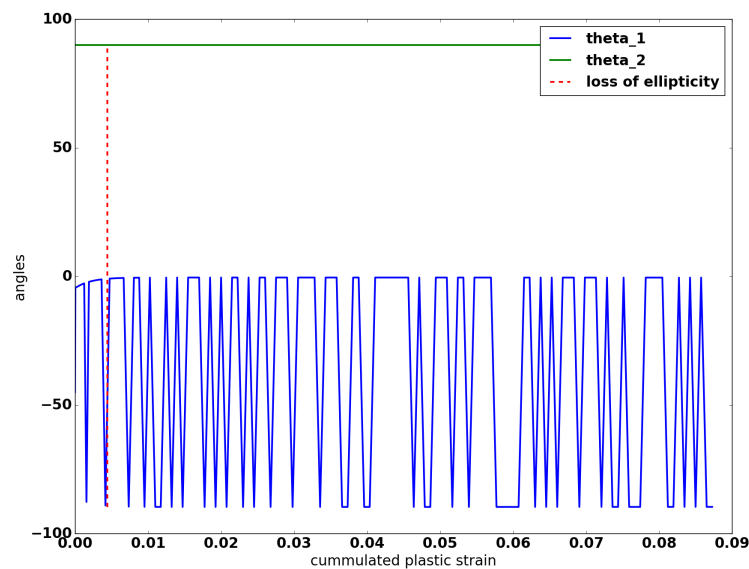


Figure 8.19: Plot of the spherical angles defining \underline{n} (finite deformation) as a function of plastic strain under shear conditions.

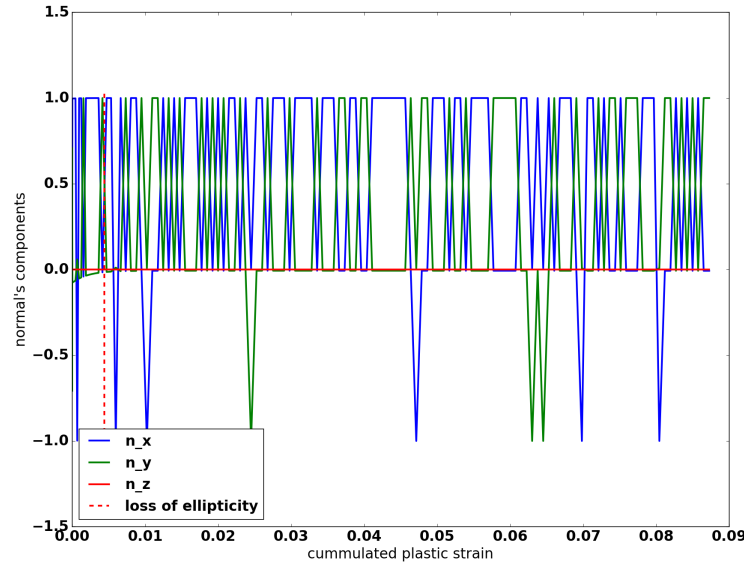


Figure 8.20: Plot of the Cartesian coordinates of \underline{n} (finite deformation) as a function of plastic strain under shear conditions.

In fact, even though σ_{xy} is not the only non zero stress in finite deformation, the angles of the localization:

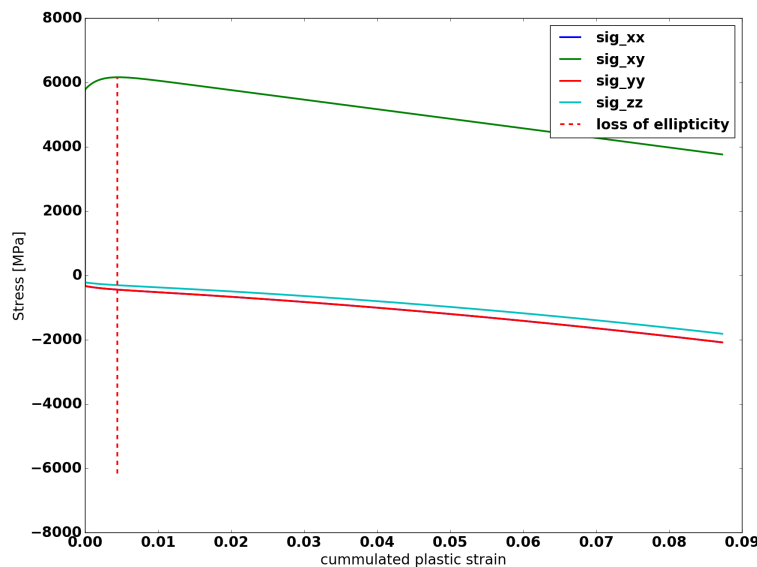


Figure 8.21: Stresses as a function of plastic strain.

However, the difference with small strain is close to be a hydrostatic stress since σ_{xx} , σ_{yy} , and σ_{zz} are very close to one another and very small compared to σ_{xy} . Therefore, the elastoplastic tangent operator is not so different since it only depends on the deviatoric part of the stress tensor for such a formulation.

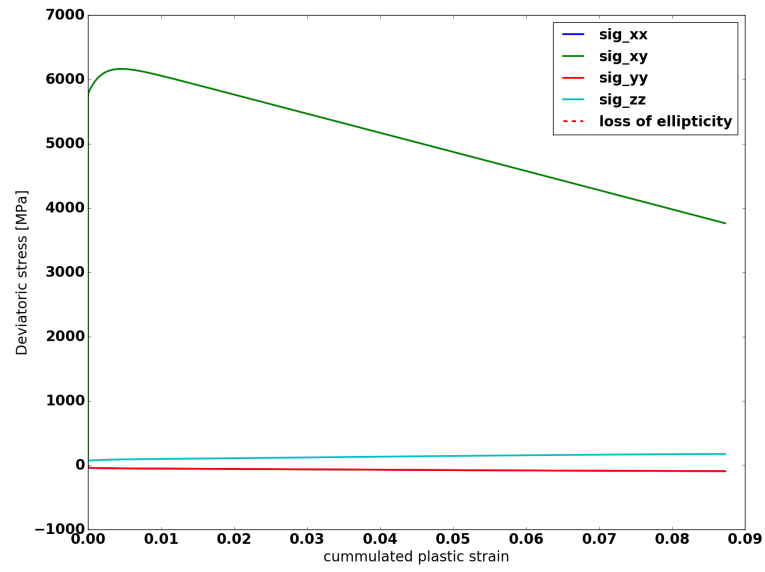


Figure 8.22: Deviatoric stresses as a function of plastic strain. Almost a pure shear stress tensor.

8.7 Design curves summary

In this last appendix section, the results in terms of design curves presented in sections 6.1 and 6.2 are gathered in this section. Some more comparisons are also presented.

8.7.1 Material properties:

The constitutive law formulation is given by:

- Elasticity: $E = 189 \text{ GPa}$, $\nu = 0.29$
- Corotational formulation using the Kirchhoff stress tensor: $\boldsymbol{\tau}^c = \underline{\underline{\Lambda}} : \underline{\underline{D}}$
- von Mises criterion with isotropic hardening: $R(p)$.

Three hardening laws are considered:

- High Yield (saturating ML340): $R(p) = 1600 + 189(1 - e^{-81p}) + 509(1 - e^{-773p})$;
- Low Yield (fictitious material): $R(p) = 800 + 800(1 - e^{-30p}) + 800(1 - e^{-50p})$;
- High Ductility (fictitious material): $R(p) = 400 + 1450(1 - e^{-200p}) + 1000(1 - e^{-10p})$.

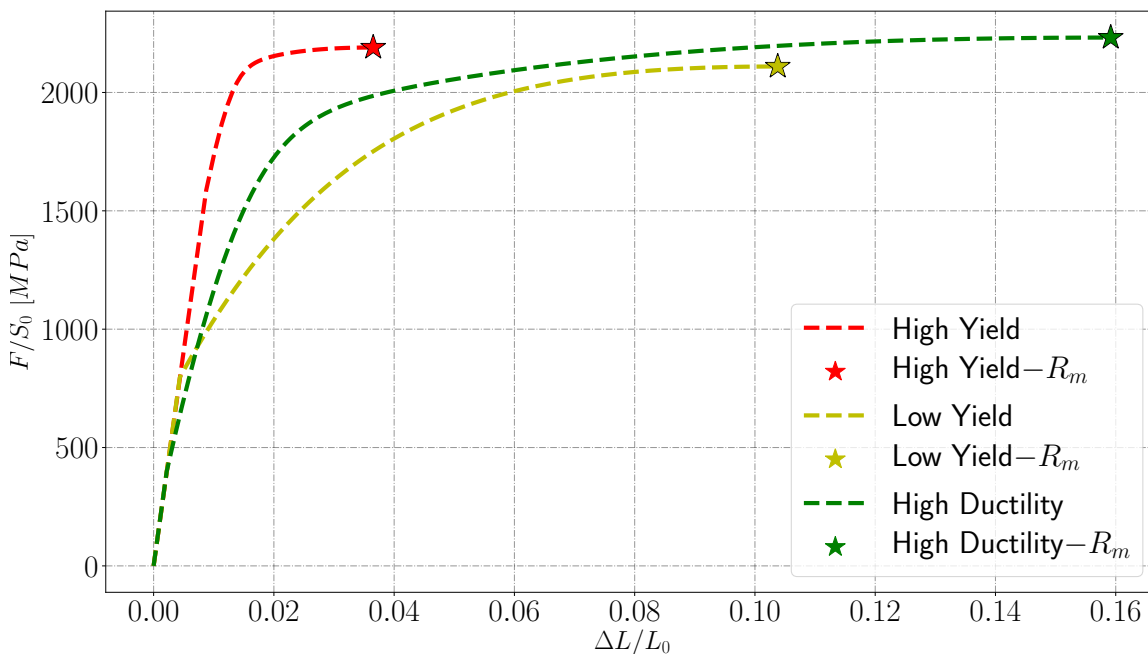


Figure 8.23: Comparison of the three engineering curves with approximately the same maximum tensile force (R_m).

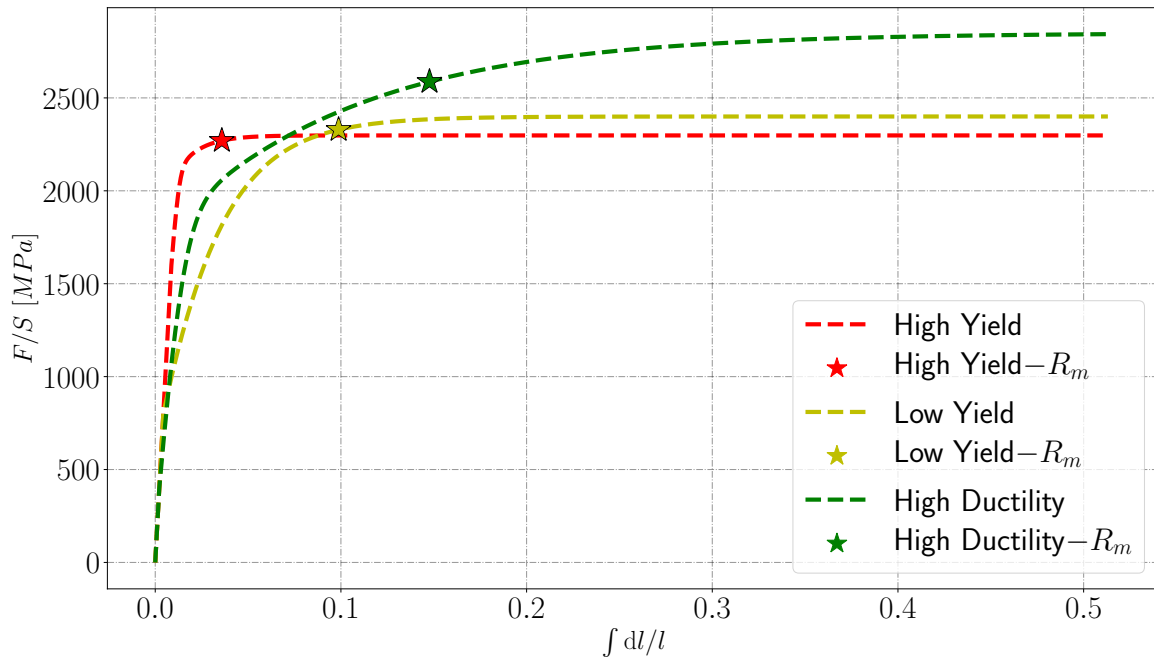


Figure 8.24: Comparison of the three true curves with approximately the same maximum tensile force (R_m).

8.7.2 Comparison of localization curves

Comparison Reference and Rice criterion

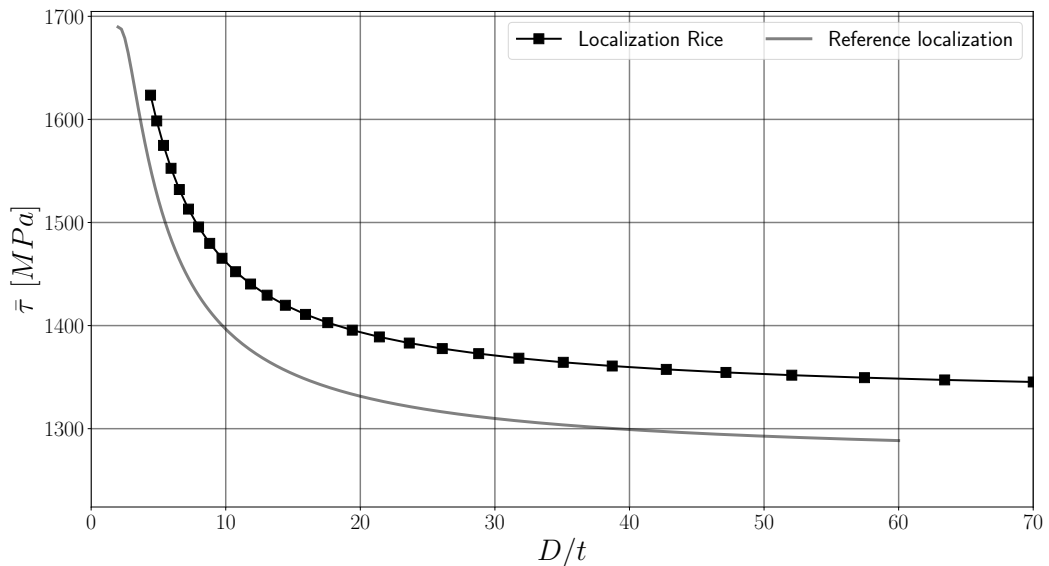


Figure 8.25: Comparison between local instability results (localization in the sense of Rice) and reference design curves (maximum engineering shear stress in the whole section) for ML340 tubes loaded in torsion. They differ by 5%.

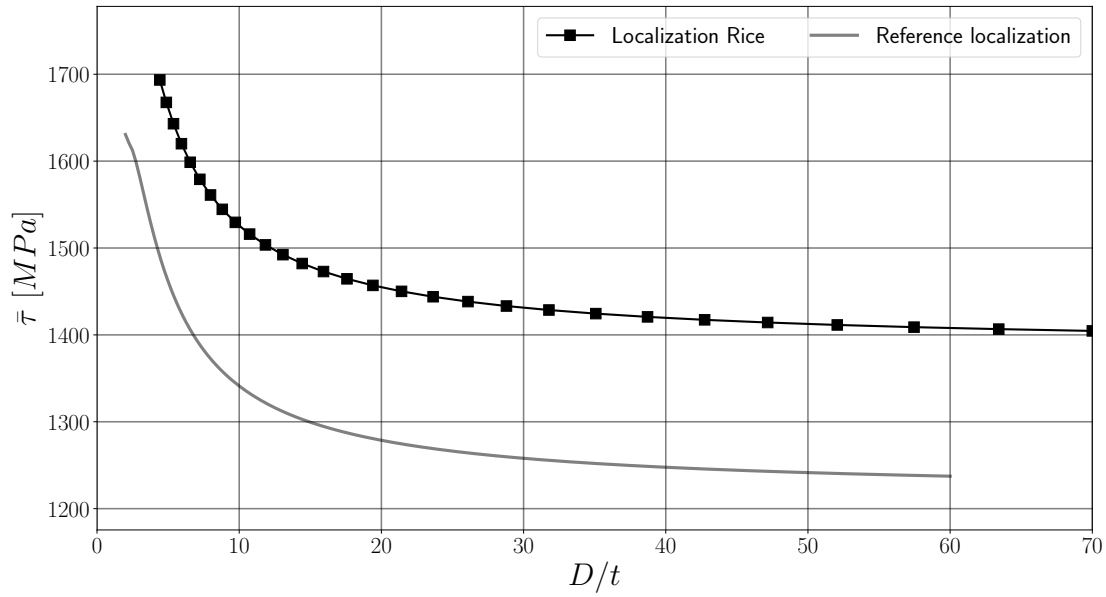


Figure 8.26: Comparison between local instability results (localization in the sense of Rice) and reference design curves (maximum engineering shear stress in the whole section) for the Low Yield material. They differ by 14%.

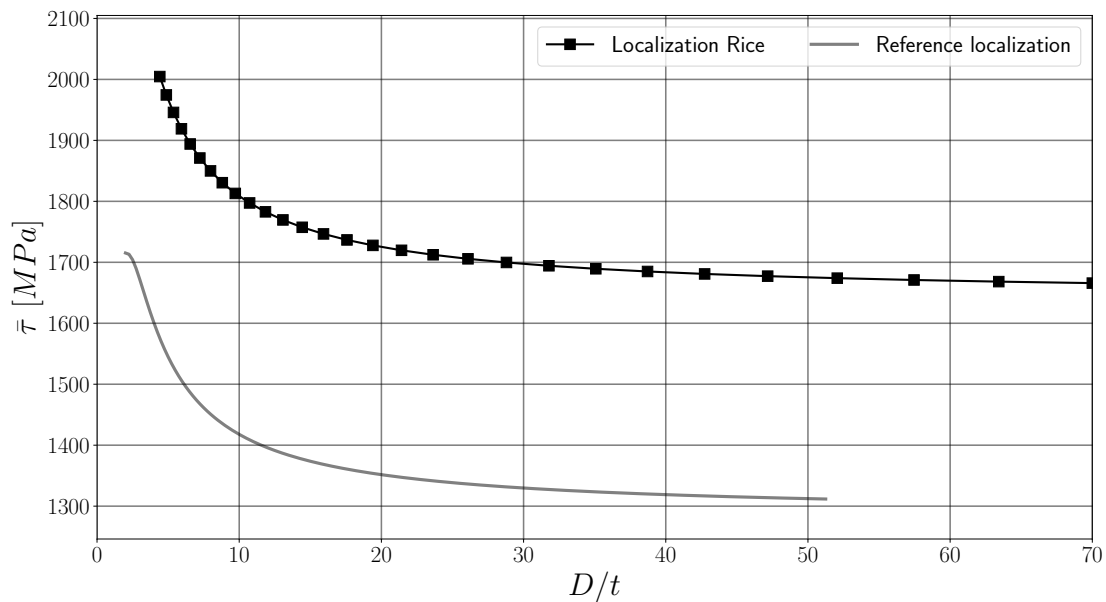


Figure 8.27: Comparison between local instability results (localization in the sense of Rice) and reference design curves (maximum engineering shear stress in the whole section) for the High Ductility material. They differ 25%.

Materials comparison

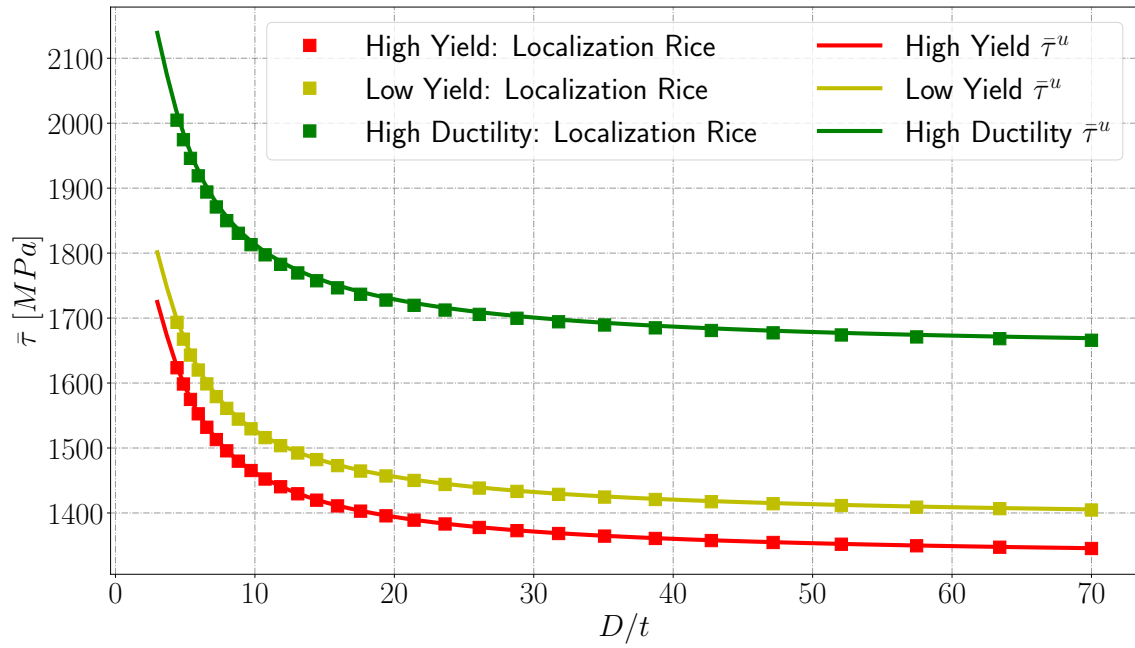


Figure 8.28: Comparison maximum equivalent shear stress ($\bar{\tau}^u = \frac{2\tau^m D(R_e^3 - R_i^3)}{3(R_e^4 - R_i^4)}$) with local instability analysis (Rice).

8.7.3 Comparison of reference curves with instability analysis

High Yield design curves

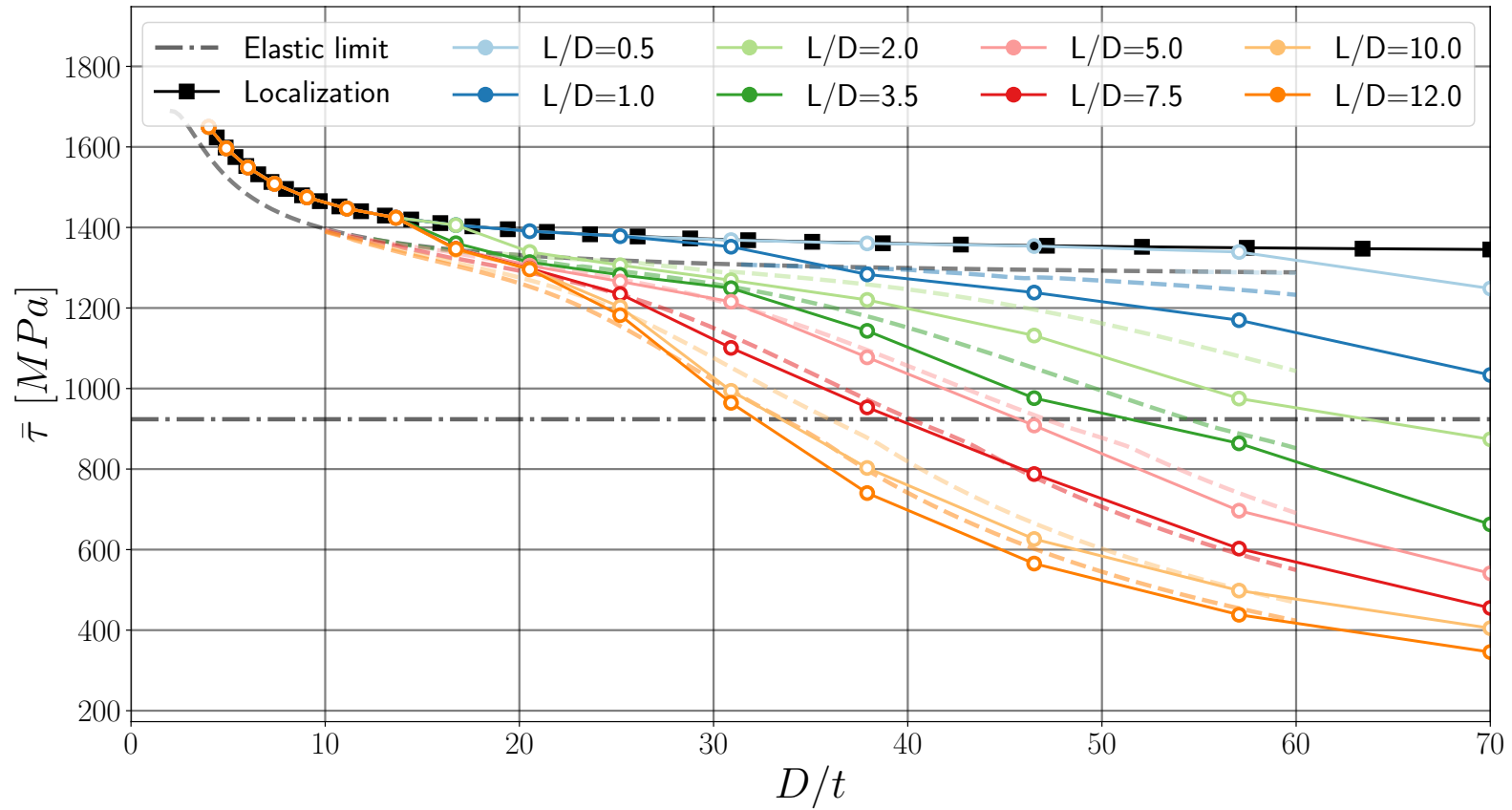


Figure 8.29: High Yield material: Comparison between global instability (Fixed/Fixed case) results (full lines) and reference design curves (dashed lines) for tubes loaded in torsion. Black filling: maximum equivalent shear stress obtained during simulation. White filling: global instability modes.

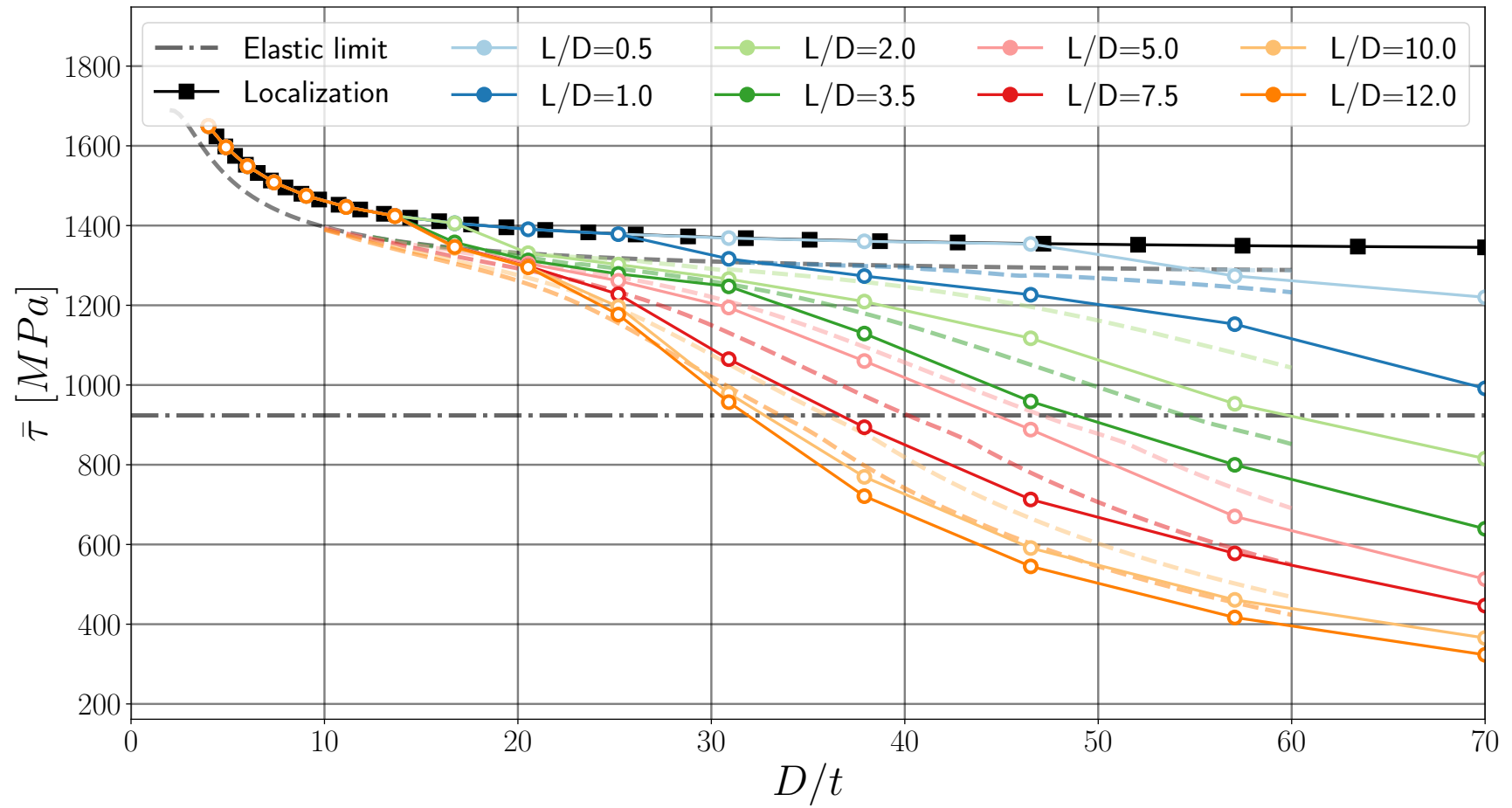


Figure 8.30: High Yield material: Comparison global instability (Circular/Fixed case) results (full lines) with reference design curves (dashed lines) for tubes loaded in torsion. Black filling: maximum equivalent shear stress obtained during simulation. White filling: global instability modes.

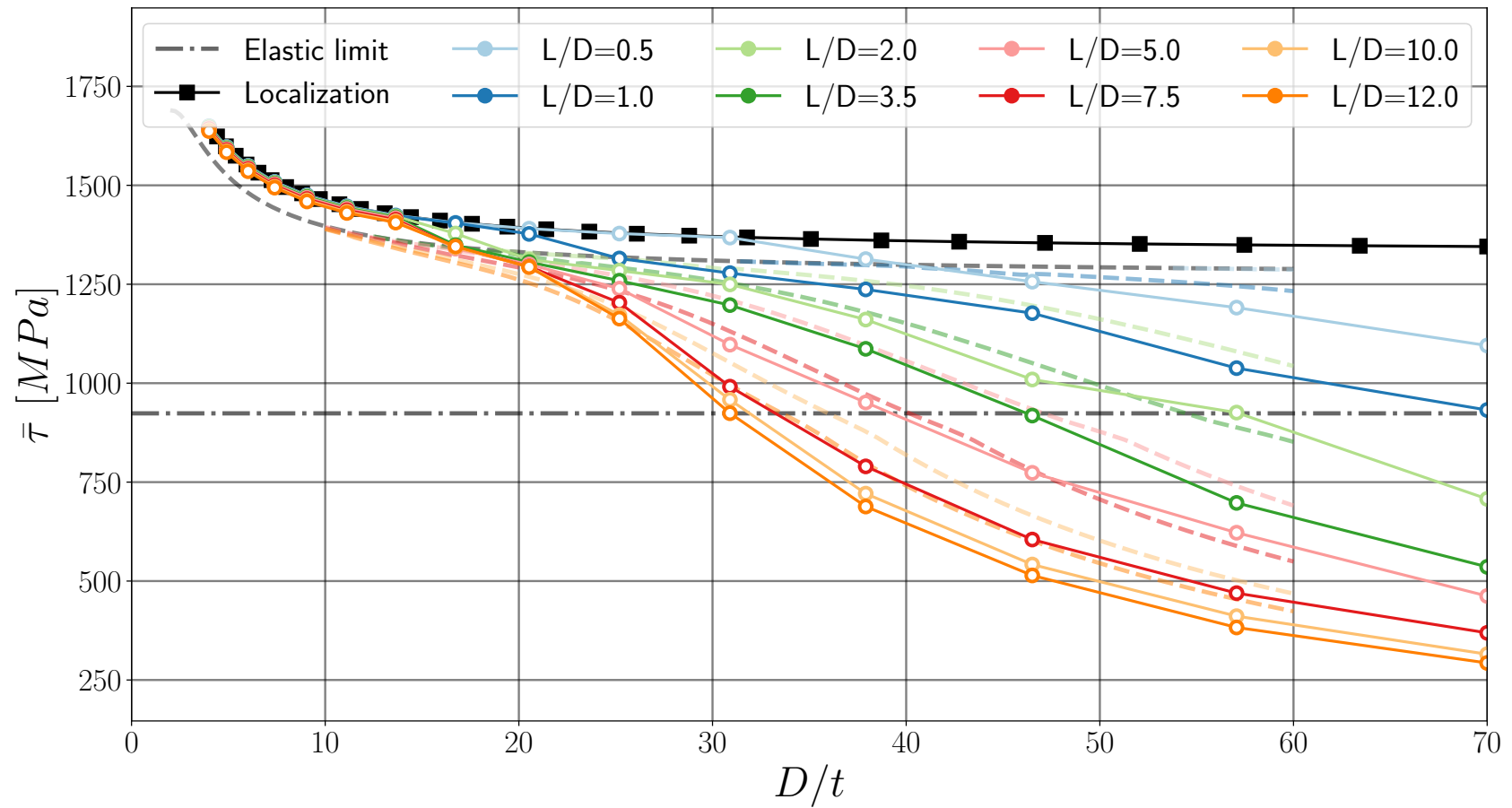


Figure 8.31: High Yield material: Comparison global instability (Flat/Fixed case) results (full lines) with reference design curves (dashed lines) for tubes loaded in torsion. Black filling: maximum equivalent shear stress obtained during simulation. White filling: global instability modes.

Low Yield design curves

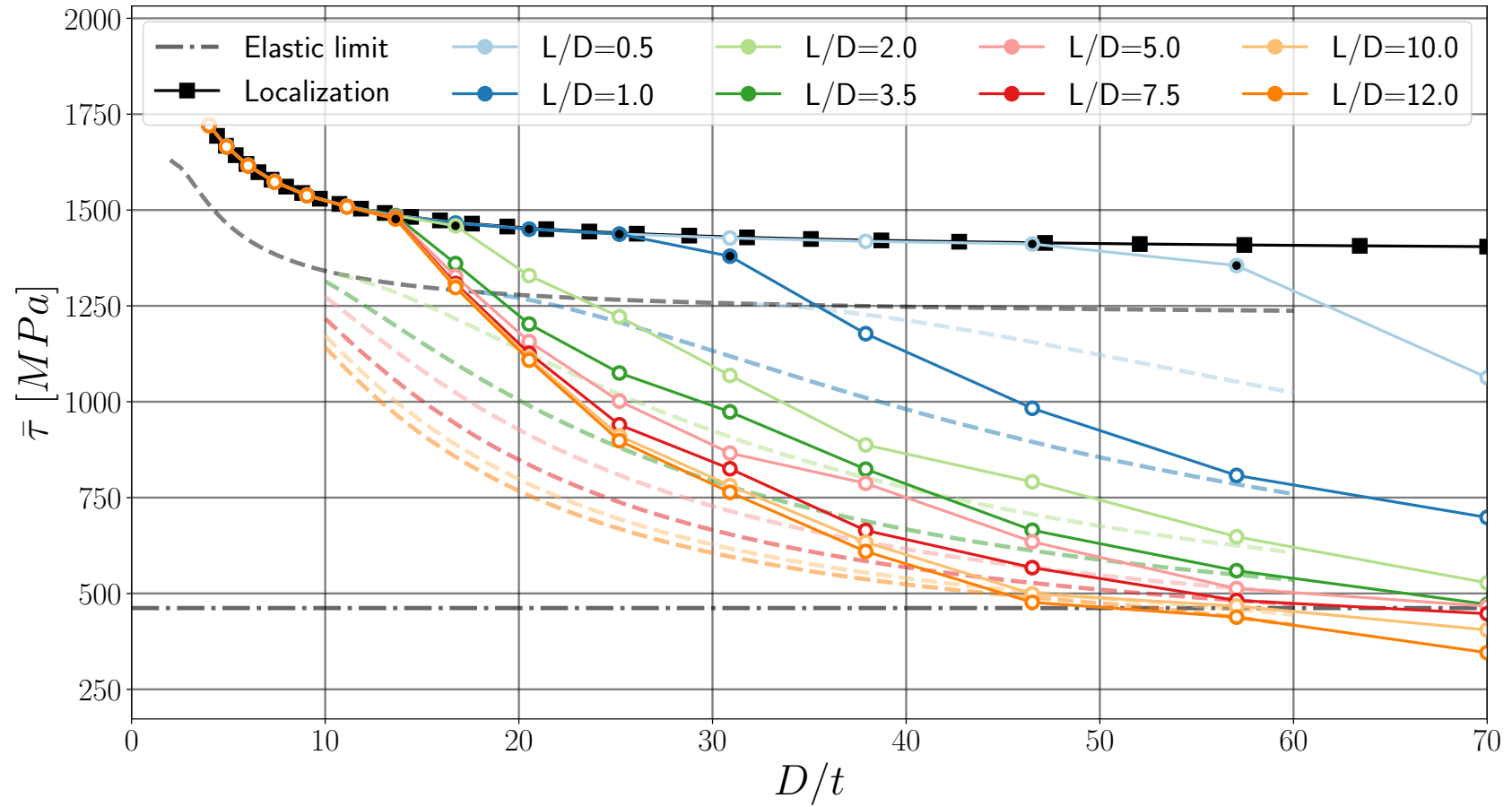


Figure 8.32: Low Yield material: Comparison global instability (Fixed/Fixed case) results (full lines) with reference design curves (dashed lines) for tubes loaded in torsion. Black filling: maximum equivalent shear stress obtained during simulation. White filling: global instability modes.

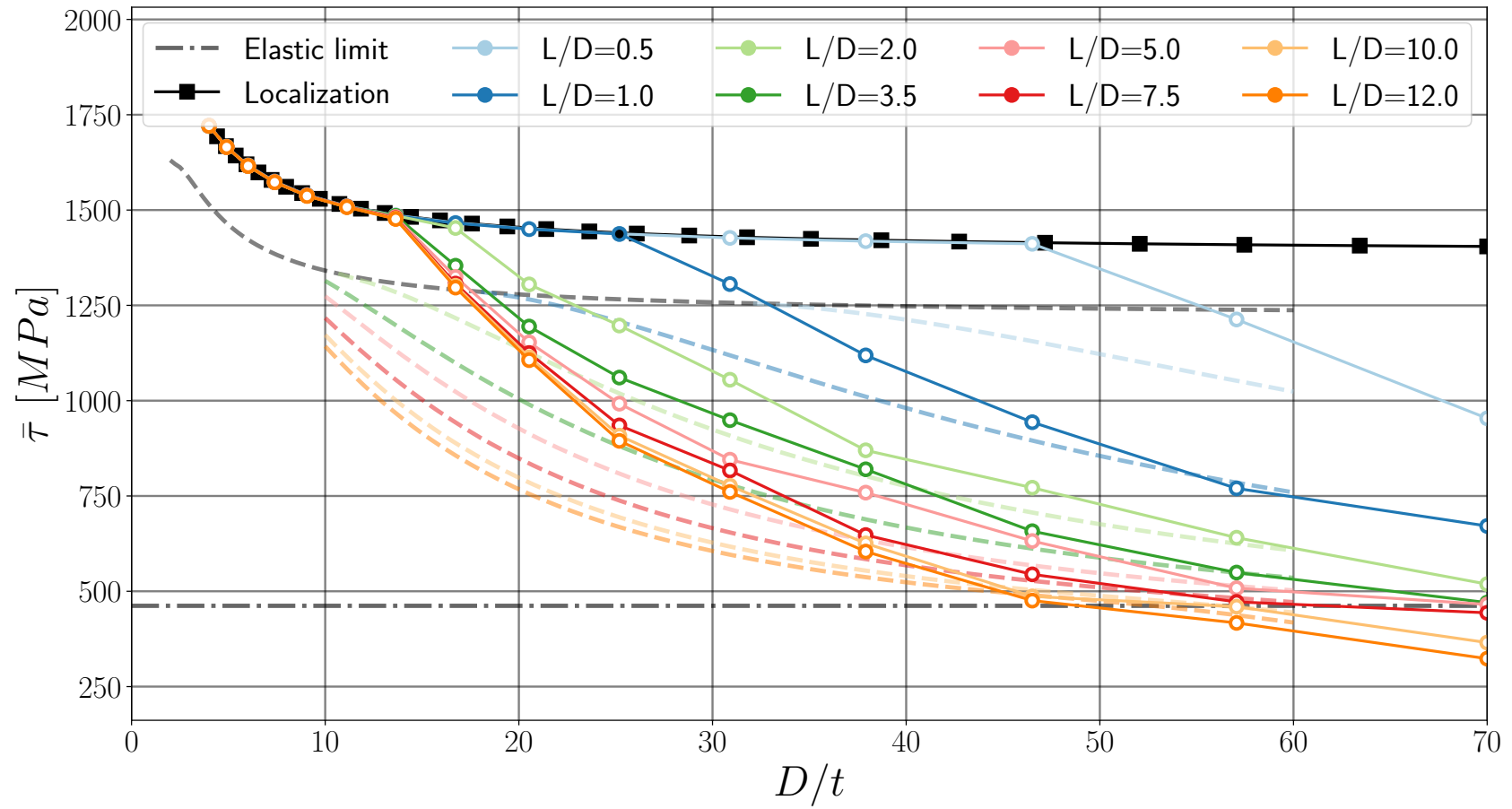


Figure 8.33: Low Yield material: Comparison between the global instability analysis (Circular/Fixed case) results (full lines) and the reference design curves (dashed lines) for tubes loaded in torsion. Black filling: maximum equivalent shear stress obtained during simulation. White filling: global instability modes.

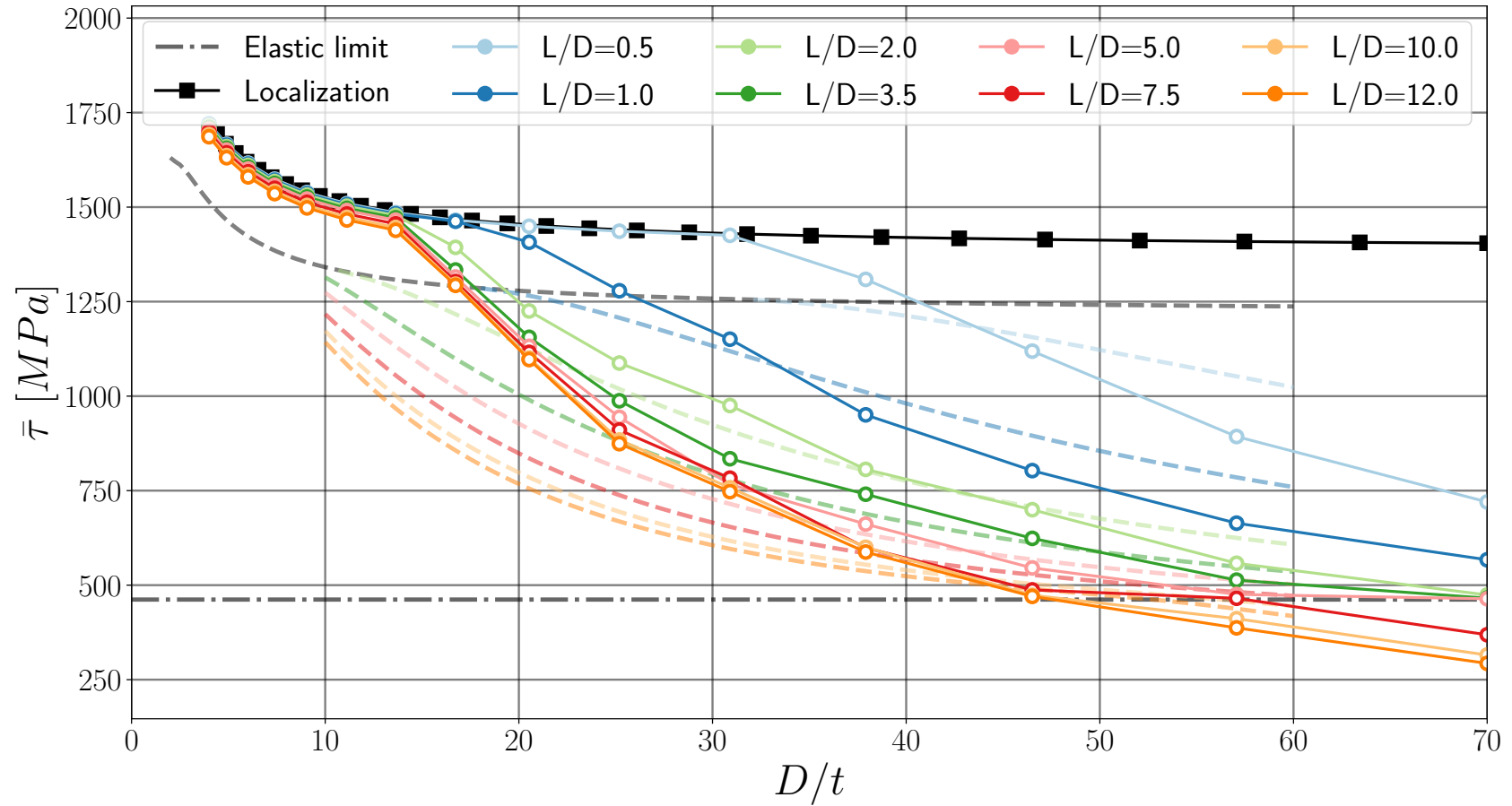


Figure 8.34: Low Yield material: Comparison between global instability (Flat/Fixed case) results (full lines) and reference design curves (dashed lines) for tubes loaded in torsion. Black filling: maximum equivalent shear stress obtained during simulation. White filling: global instability modes.

High Ductility design curves

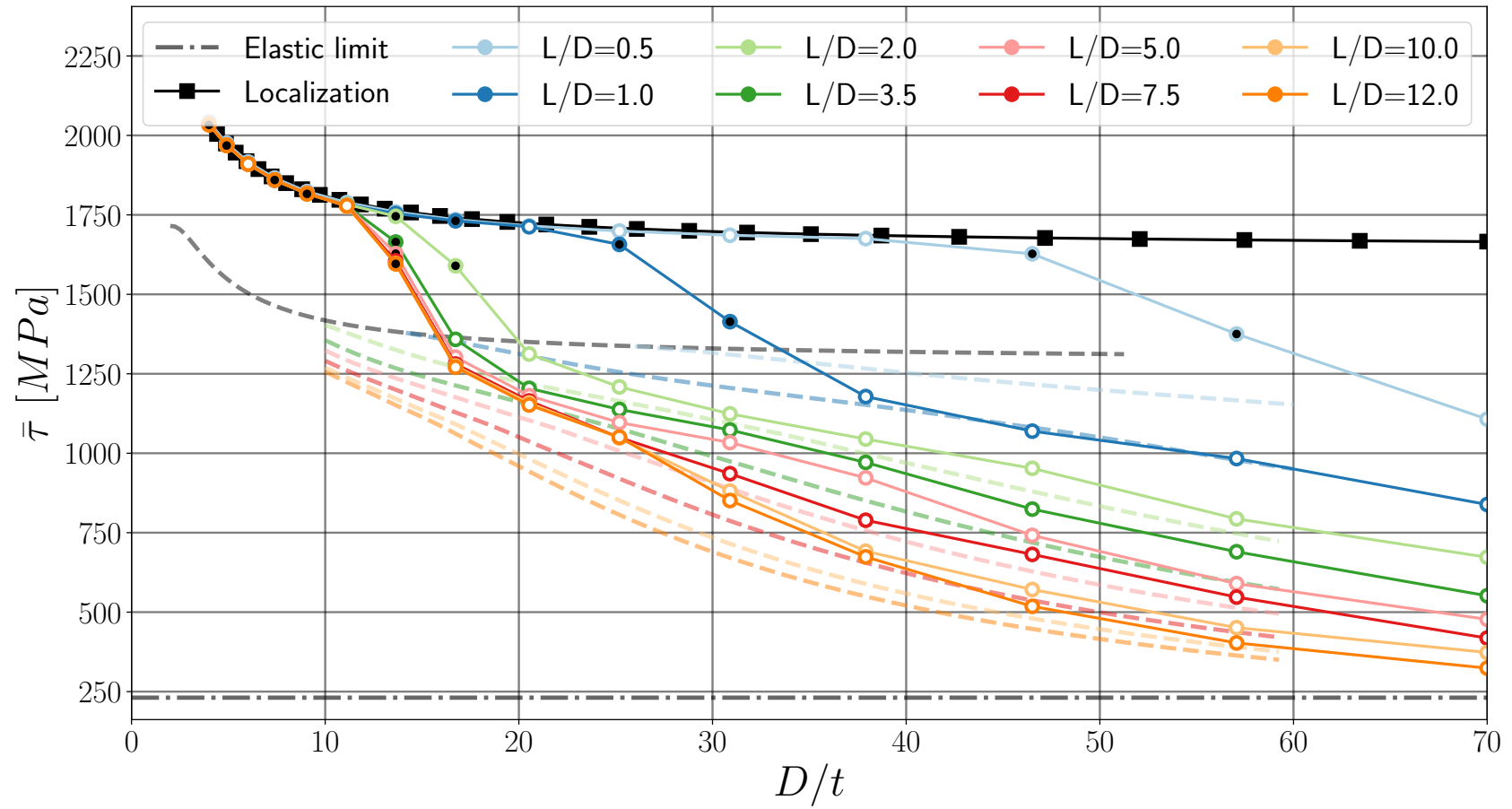


Figure 8.35: High Ductility material: Comparison between global instability (Fixed/Fixed case) results (full lines) and reference design curves (dashed lines) for tubes loaded in torsion. Black filling: maximum equivalent shear stress obtained during simulation. White filling: global instability modes.

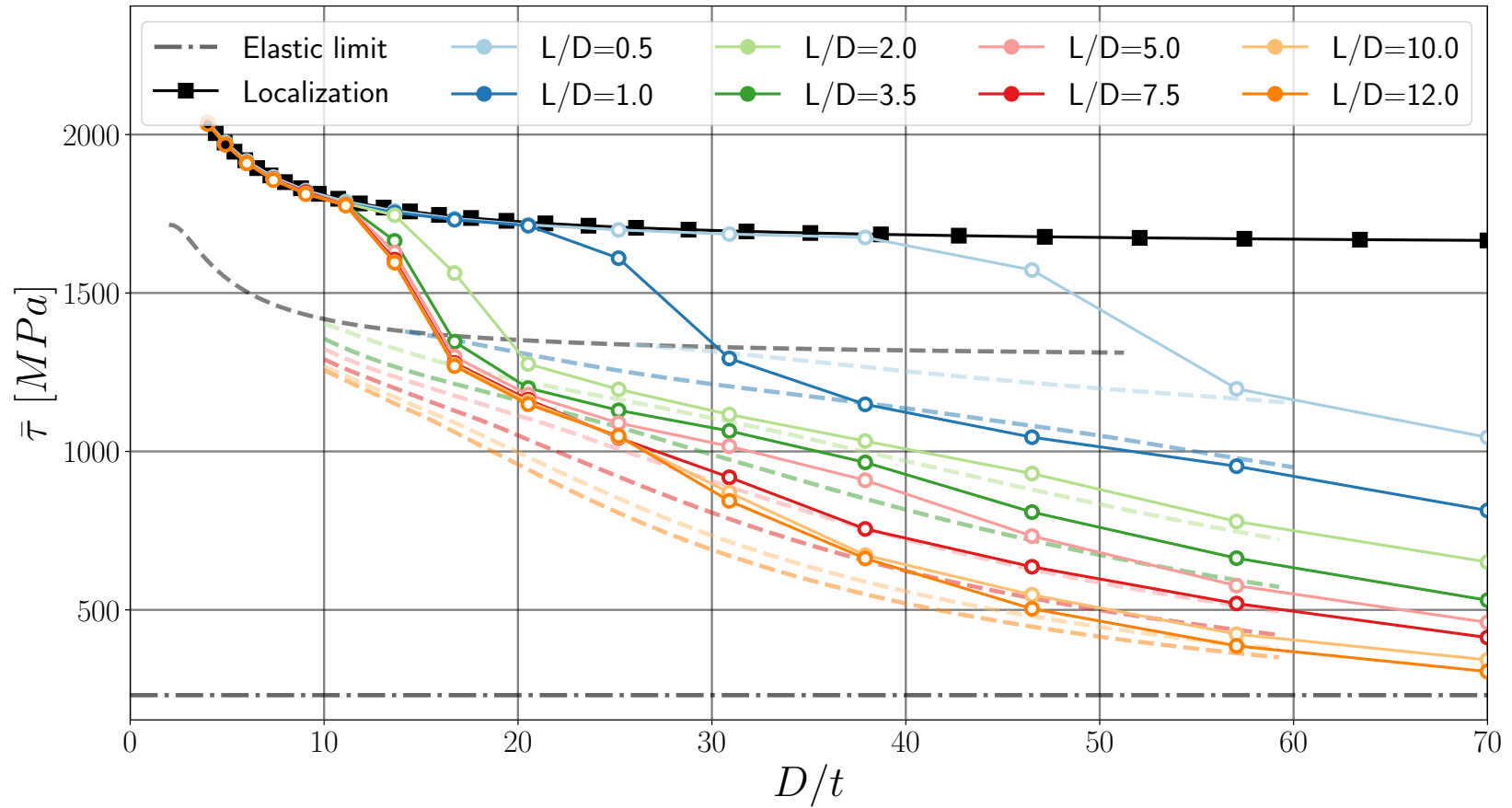


Figure 8.36: High Ductility material: Comparison between global instability (Circular/Fixed case) results (full lines) with reference design curves (dashed lines) for tubes loaded in torsion. Black filling: maximum equivalent shear stress obtained during simulation. White filling: global instability modes.

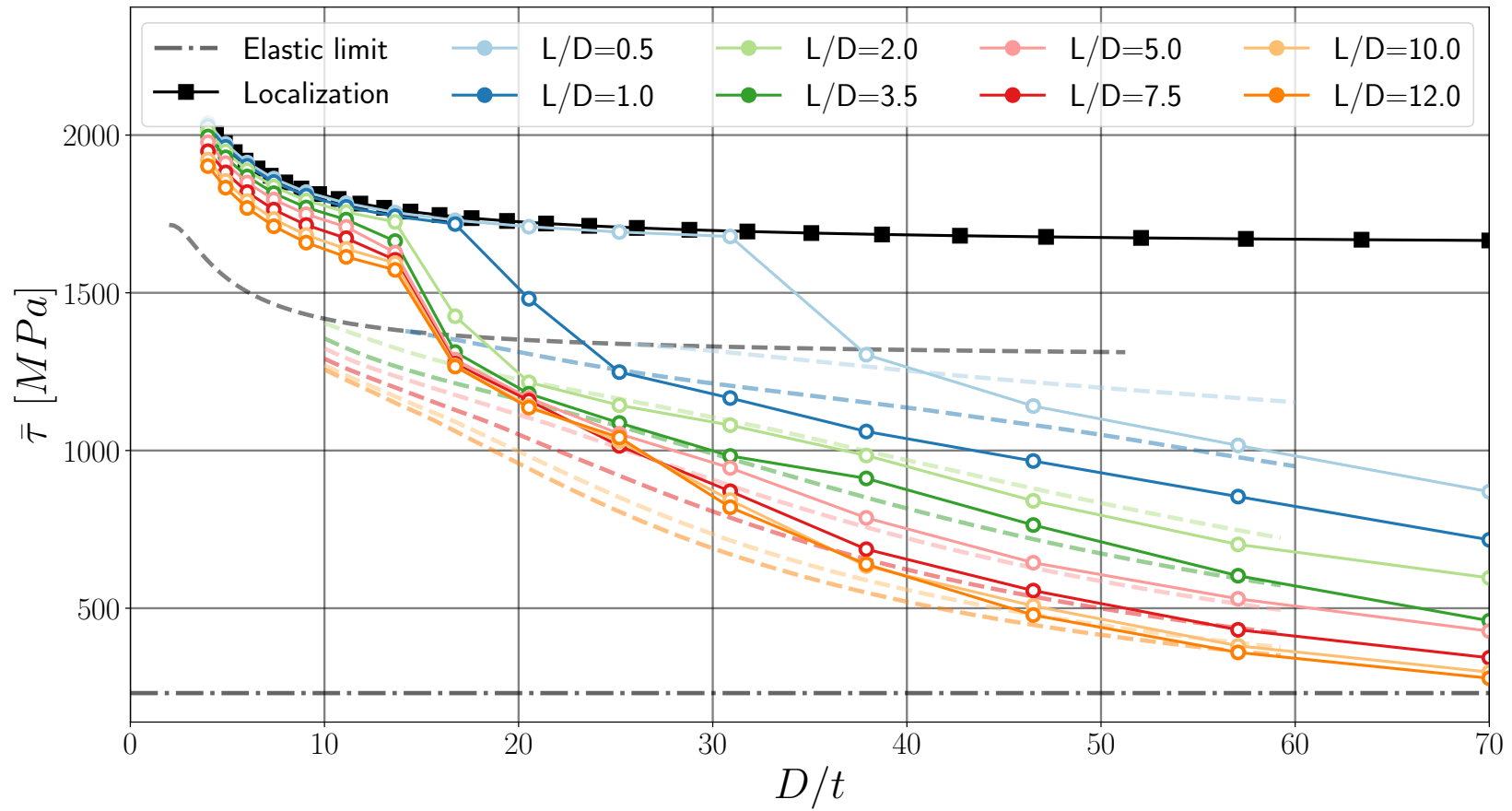


Figure 8.37: High Ductility material: Comparison global instability (Flat/Fixed case) results (full lines) with reference design curves (dashed lines) for tubes loaded in torsion. Black filling: maximum equivalent shear stress obtained during simulation. White filling: global instability modes.

8.7.4 Material comparison : Design curves

Flat/Fixed weakened problem

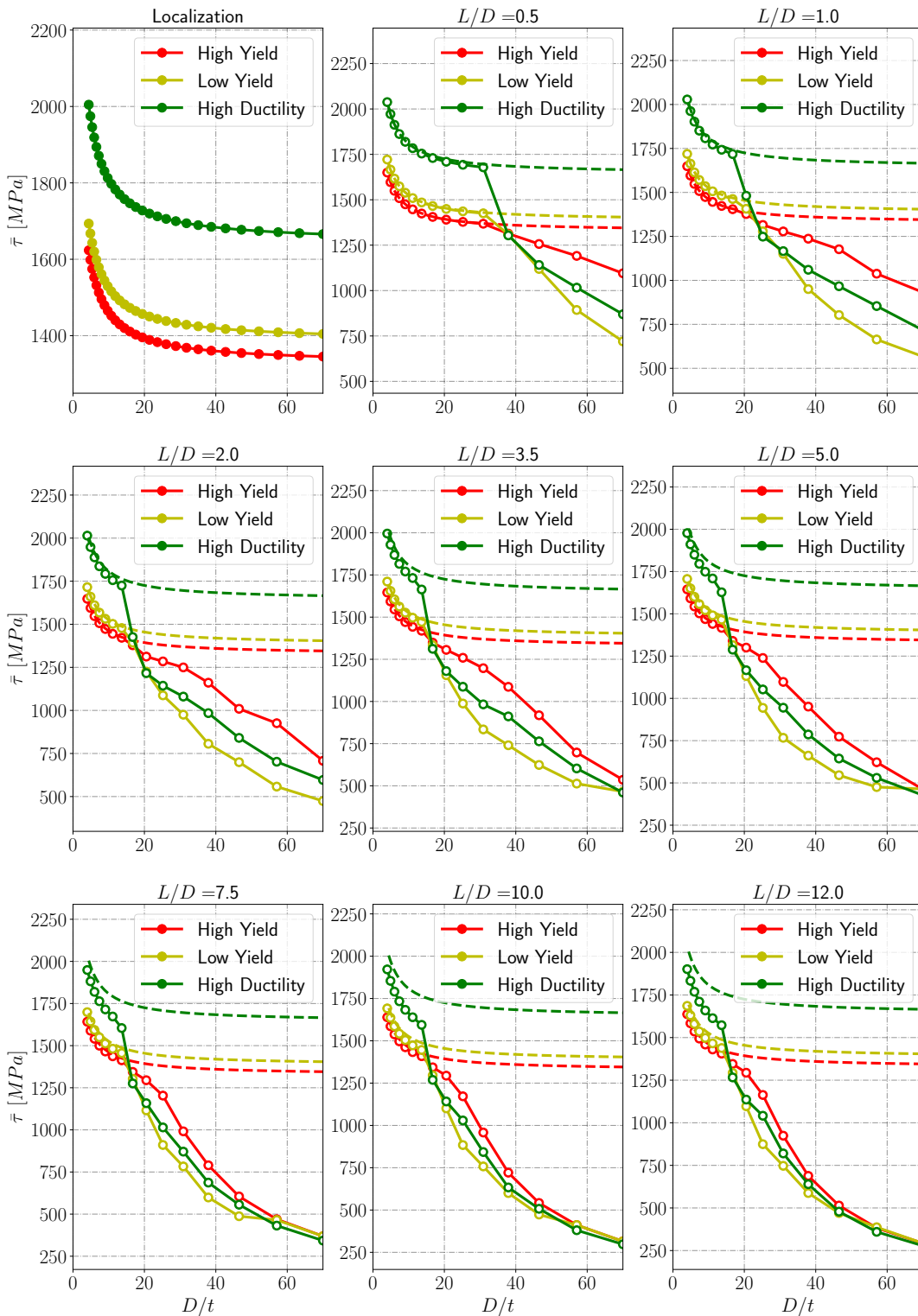


Figure 8.38: Weakened boundary conditions: Flat/Fixed. Design curves obtained with the global and local instability analysis in a full finite deformation for the three materials considered for tubes loaded in torsion.

Circular/Fixed weakened problem

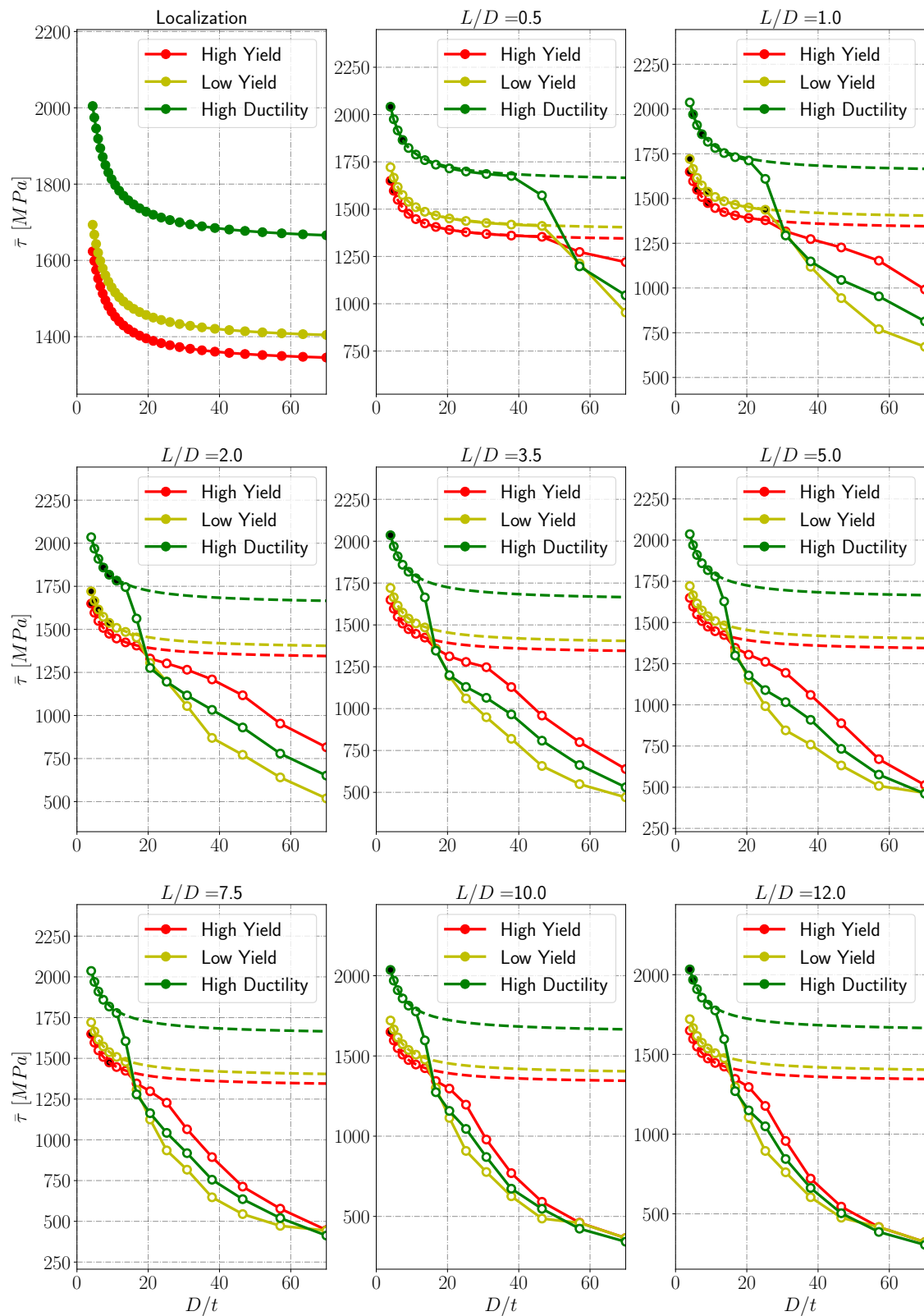


Figure 8.39: Weakened boundary conditions: Circular/Fixed. Design curves obtained with the global and local instability analysis in a full finite deformation for the three materials considered for tubes loaded in torsion.

Fixed/Fixed weakened problem

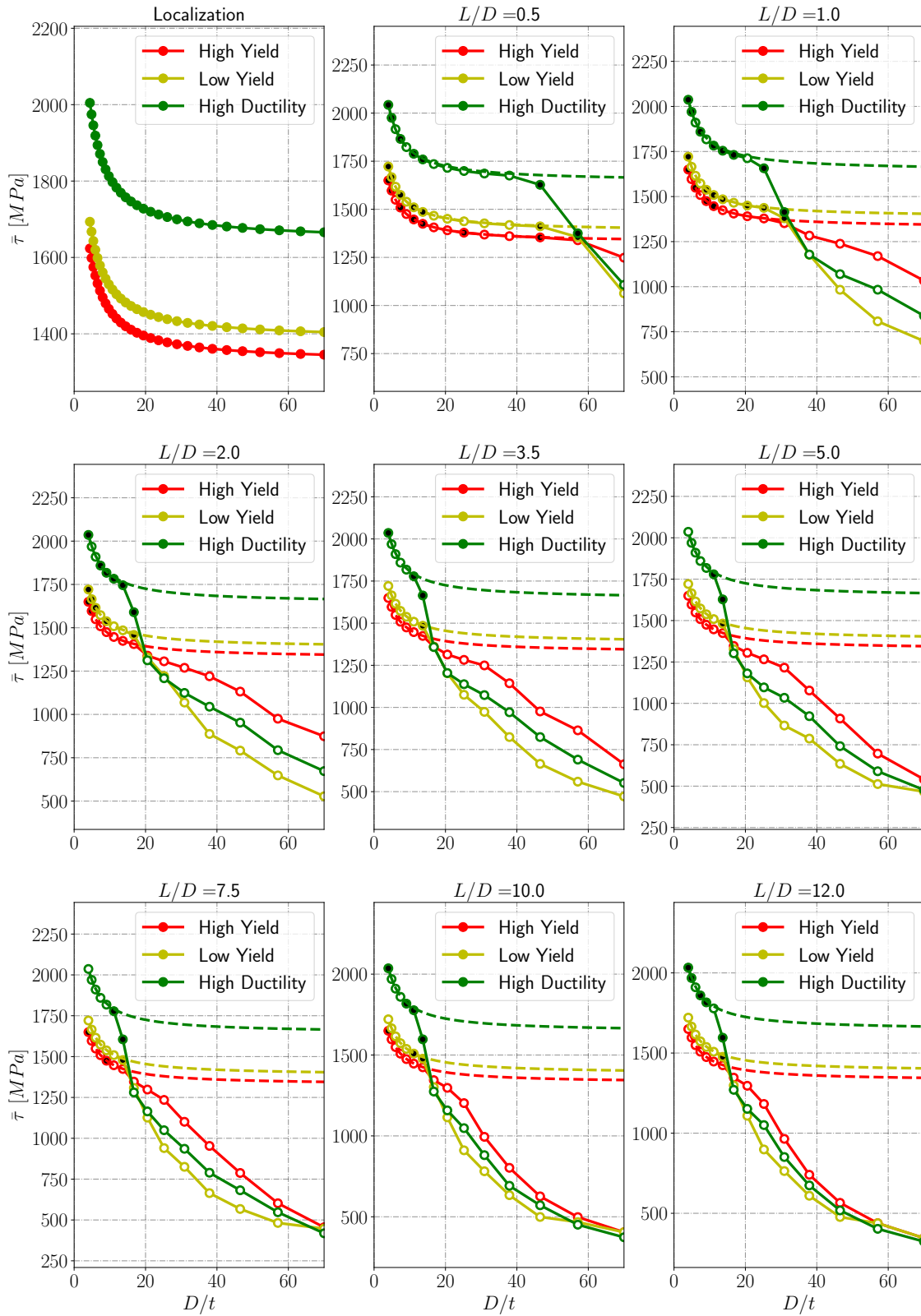


Figure 8.40: Weakened boundary conditions: Fixed/Fixed. Design curves obtained with the global and local instability analysis in a full finite deformation for the three materials considered for tubes loaded in torsion.

8.7.5 Weakened stability analysis comparison

High Yield material

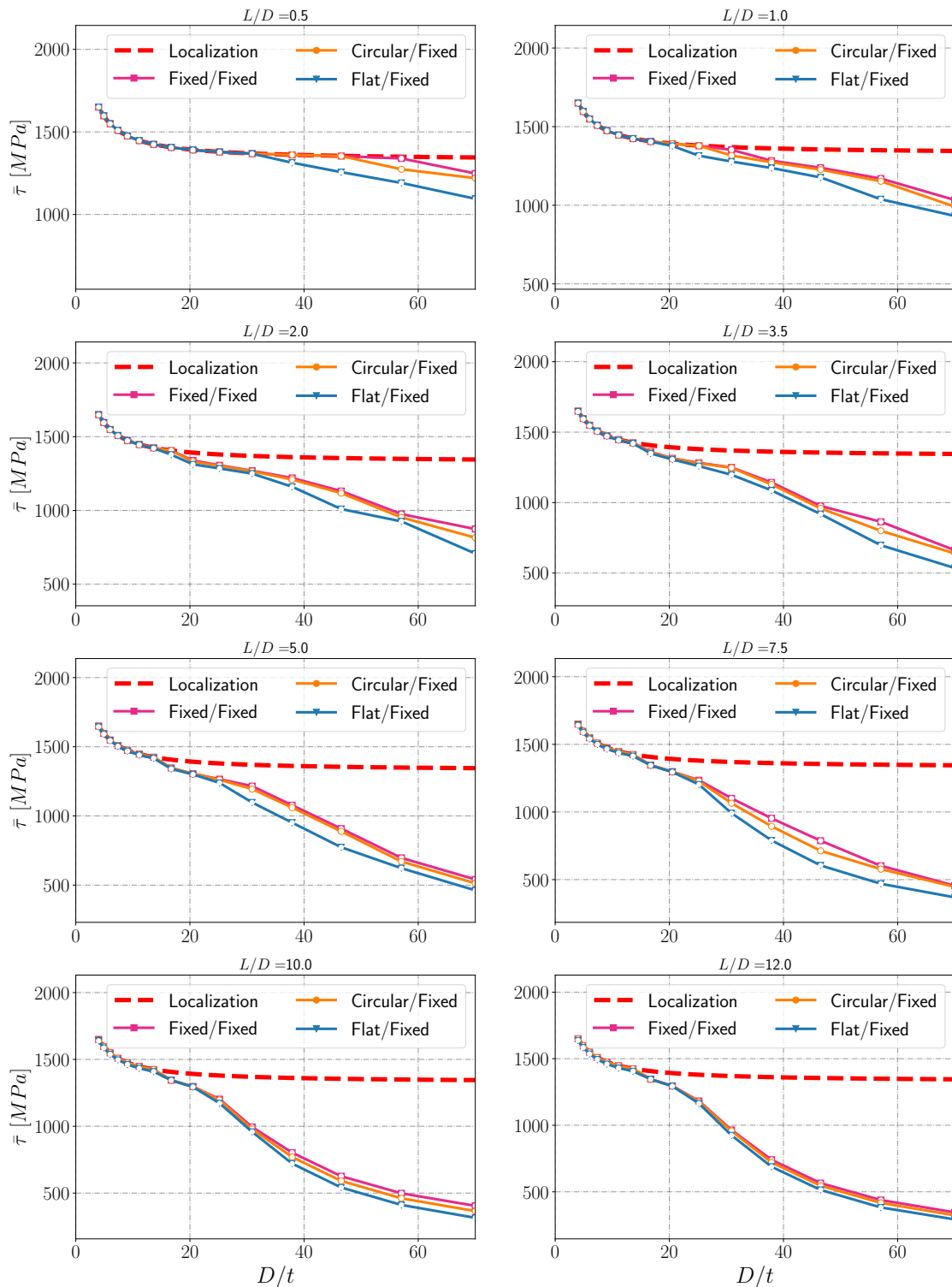


Figure 8.41: High Yield material: Comparison of the design curves obtained with the weakened stability analysis for various BCs: Flat/Fixed, Circular/Fixed, Fixed/Fixed.

Low Yield material

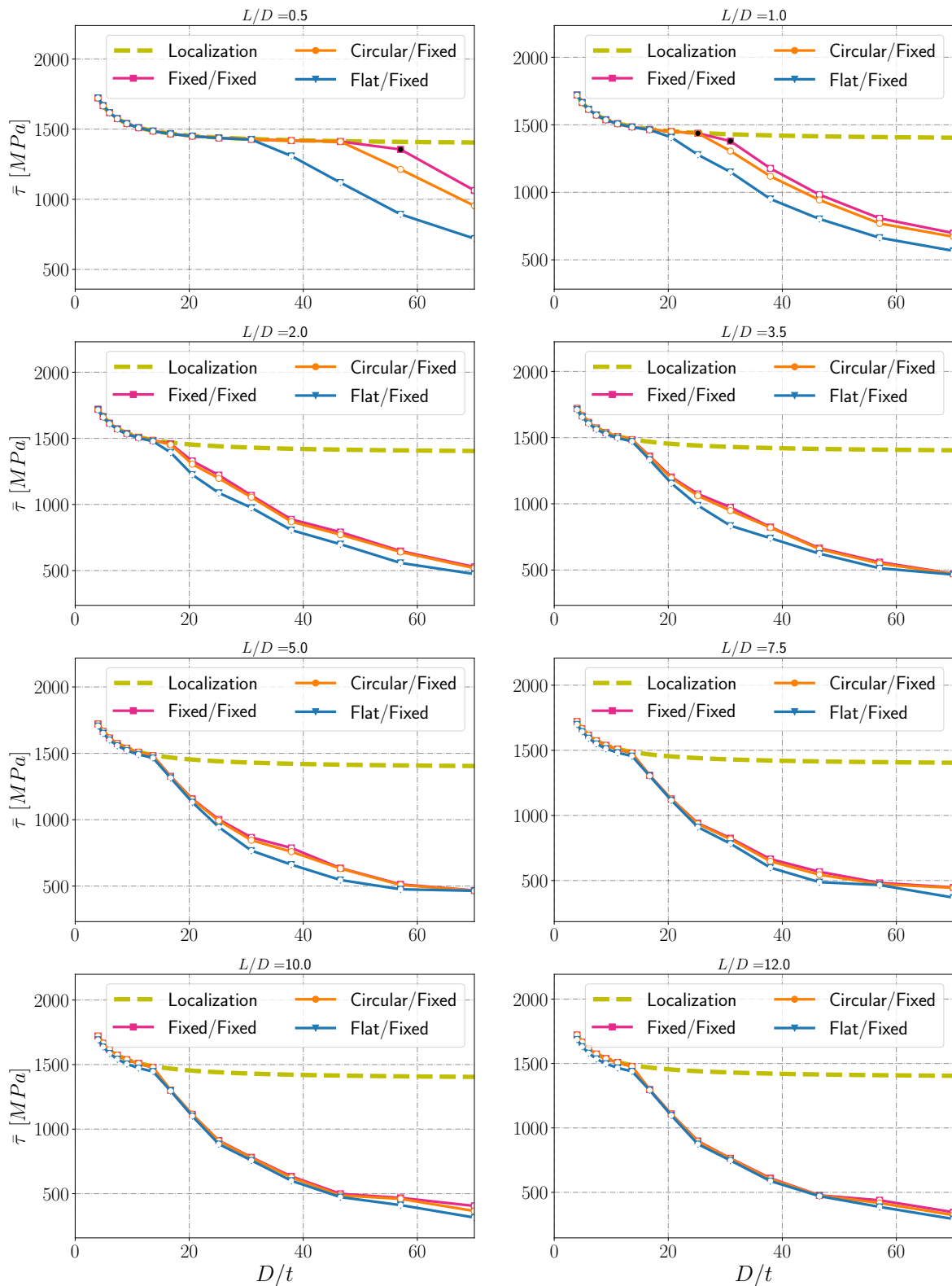


Figure 8.42: Low Yield material: Comparison of the design curves obtained with the weakened stability analysis for various BCs: Flat/Fixed, Circular/Fixed, Fixed/Fixed.

High Ductility material

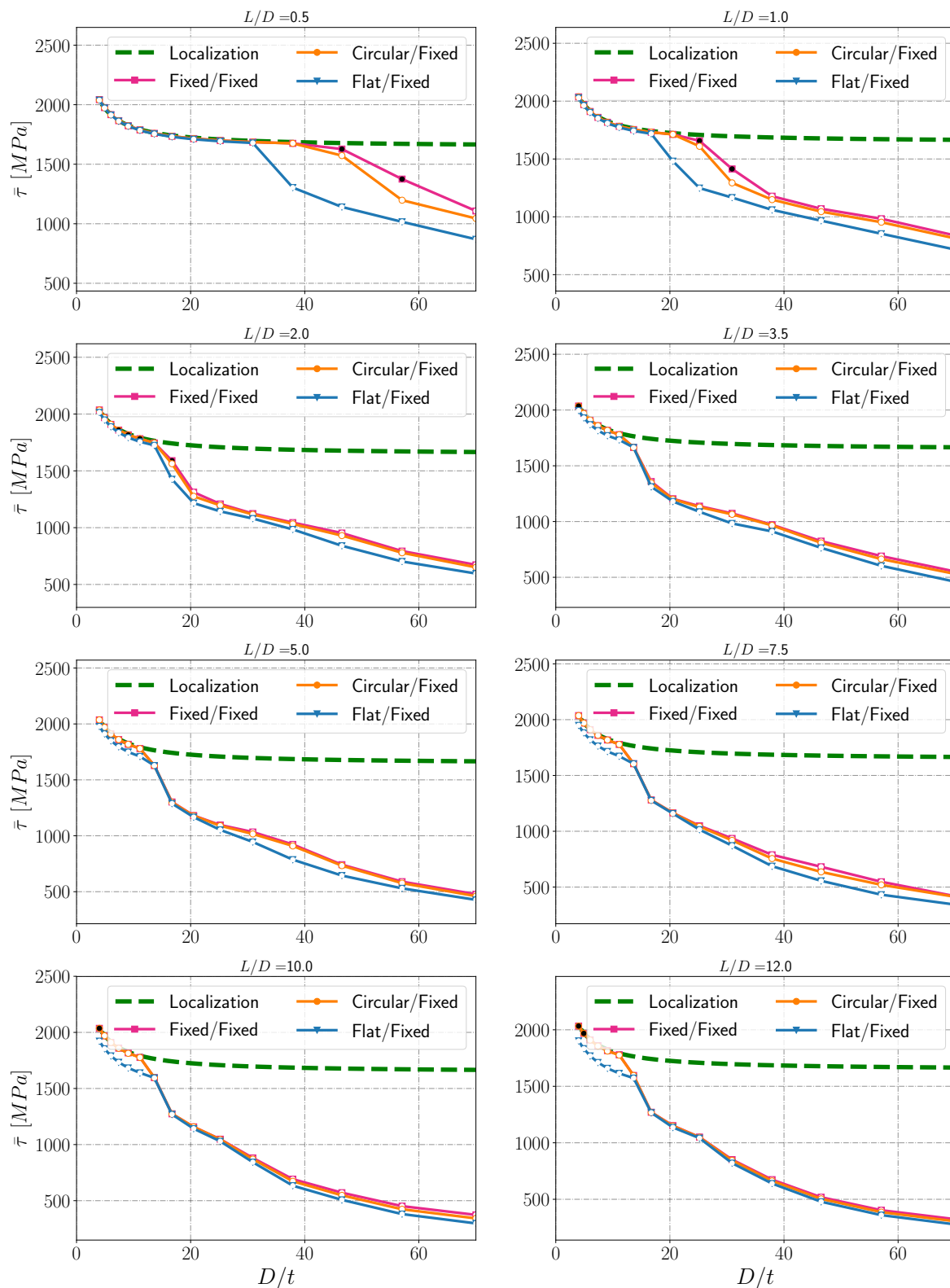


Figure 8.43: High Ductility material: Comparison of the design curves obtained with the weakened stability analysis for various BCs: Flat/Fixed, Circular/Fixed, Fixed/Fixed.

Bibliography

- Besson, J., Cailletaud, G., Chaboche, J.-L., and Forest, S. (2010). *Non-linear mechanics of materials*. Springer.
- Bigoni, D. and Hueckel, T. (1991). Uniqueness and localization - i - associative and non-associative elastoplasticity. *International Journal of Solids and Structures*, 28:197–213.
- Bigoni, D. and Zaccaria, D. (1993). On strain localization analysis of elastoplastic materials at finite strains. *International Journal of Plasticity*, 9:21–33.
- d’Avila, M. S., Triantafyllidis, N., and Wen, G. (2016). Localization of deformation and loss of macroscopic ellipticity in microstructured solids. *Journal of the Mechanics and Physics of Solids*, 97:275–298.
- Drucker, D. (1951). A more fundamental approach to stress-strain relations. *First US National Congress of Applied Mechanics*, pages 487–491.
- Hadamard, J. (1903). *Leçons sur la propagation des ondes et les équations de l’hydrodynamique*. Hermann.
- Halphen, B. (1975). Sur le champ des vitesses en thermoplasticité finie. *International Journal of Solid Structures*, pages 947–960.
- Hill, R. (1958). A general theory of uniqueness and stability in elastic-plastic solids. *Journal of the Mechanics and Physics of Solids*, 6:236–249.
- Hill, R. (1968). On constitutive inequalities for simple materials–ii. *Journal of the Mechanics Physics Solids*, pages 315–322.
- Lemaitre, J., Chaboche, J. L., Benallal, A., and Desmorat, R. (2009). *Mécanique des matériaux solides - 3ème édition*. Dunod.
- Mandel, J. (1964). Propagation des surfaces de discontinuité dans un milieu élastoplastique. In *Stress waves in anelastic solids*, pages 331–340. Springer.
- Mandel, J. (1966). Conditions de stabilité et postulat de drucker. In *Rheology and Soil Mechanics*, pages 58–68. Springer.
- Mandel, J. (1971). Plasticité classique et viscoplasticité. In *CISM Courses and lectures*, volume 97, pages 1–187.
- Mear, M. and Hutchinson, J. (1985). Influence of yield surface curvature on flow localization in dilatant plasticity. *Mechanics of Materials*, 4:395–407.
- Nguyen, Q. S. (2000). *Stability and nonlinear solid mechanics*. Wiley.

- Rice, J. (1976). The localization of plastic deformation. In *W.T. Koiter (Ed.), Theoretical and Applied Mechanics*, pages 207–220. North-Holland.
- Truesdell, C. and Toupin, R. (1960). *The classical field theory of mechanics*. Springer.

RÉSUMÉ

Les ingénieurs sont constamment mis au défi de concevoir des avions plus légers et moins polluants. En même temps, ils se doivent de respecter un certain nombre de critères de dimensionnement établis pour assurer l'intégrité des structures aéronautiques. Pour répondre à ce double défi, les chercheurs du milieu industriel et académique travaillent à l'unisson pour constamment repousser les limites du savoir scientifique. Ces collaborations aboutissent notamment au développement de nouveaux outils mathématiques, numériques, expérimentaux et de production.

On trouve de nombreuses pièces métalliques parmi les composants aéronautiques les plus critiques, comme les trains d'atterrissage, les arbres moteurs ou les chapes. Ces structures subissent des chargements extrêmes de par leur environnement thermique ou leur intense sollicitation mécanique ponctuelle ou cyclique. Pour ces structures élastoplastiques, la ruine peut généralement être causée par l'apparition et la propagation de fissures, ou l'émergence d'instabilités locales, comme la localisation de la déformation plastique, ou d'instabilités globales, comme le flambement.

Dans les travaux présentés dans ce manuscrit, nous nous sommes intéressés à la détection d'instabilités locales et globales dans des structures élastoplastiques en grandes déformations. Alors qu'elles sont classiquement considérées indépendamment, nous avons fait le choix d'étudier les deux types d'instabilités simultanément pour mieux comprendre la compétition entre ces deux phénomènes. Pour ce faire, plusieurs développements analytiques sont présentés et fondés sur le critère de stabilité de Hill (1958) et le critère de localisation de la déformation de Rice (1976), ainsi que la proposition d'une nouvelle méthode d'"analyses de stabilité affaiblie" permettant d'investiguer la sensibilité aux types de conditions limites imposées. Tous ces critères ont été implémentés dans le code de calcul par éléments finis *Zset*, ce qui nous a permis, entre autres, d'analyser l'apparition d'instabilités élastoplastiques dans différentes éprouvettes de traction/torsion, des tubes en torsion et une chape en traction.

MOTS CLÉS

Localisation, Flambement, Elastoplastique, Instabilités, Méthodes Numériques, Structures Aéronautiques

ABSTRACT

Aeronautical engineers are constantly challenged to provide lighter structures in order to reduce fuel consumption, and thus the environmental impact and flight costs. At the same time, the design of aeronautical structures is subjected to strict regulation aimed at ensuring the integrity of the aircraft and the safety of the passengers. To tackle this challenge, the limits of structural and material mechanics are consistently explored which in turn leads to the development of new, mathematical, numerical, experimental and manufacturing tools.

There are numerous metallic parts in the most critical aeronautical structures, like landing gears, engine shafts, or mechanical lugs. These parts are subjected to extreme loading conditions due to the thermal environment or to the intense mechanical ultimate or cyclic loading. The failure of these elastoplastic structures is generally caused by the initiation and propagation of cracks or by the emergence of local instabilities, such as plastic strain localization, or global instabilities, such as buckling.

In the present work, we focus on the detection of local and global elastoplastic instabilities in a finite deformation framework. While they are generally studied separately, it was chosen to study both phenomena together in order to analyze and better understand the competition between localization and buckling in elastoplastic structures. For this purpose, multiple analytical developments are presented founded on Hill's global stability criterion (1958) and Rice's strain localization criterion (1976). The new "weakened stability analysis" has been introduced in order to analyze the sensitivity to the type of prescribed boundary conditions. All these criteria have been implemented in the finite element software *Zset*, which allowed us to analyze the emergence of elastoplastic instabilities in various experimental samples, tubes loaded in torsion, and a lug loaded in tension.

KEYWORDS

Localization, Buckling, Elastoplastic, Instabilities, Numerical Methods, Aeronautical Structures.